Computer Modelling of the Mode of Action of Gas Hydrate Kinetic Inhibitors

by

Mark Timothy Storr

A thesis submitted in partial fulfilment of the requirements for the degree of

Doctor of Philosophy in Chemistry

University of Warwick, Department of Chemistry

May 2001

Table of Contents

CHAPTER 1 GAS HYDRATES–AN INTRODUCTION

CHAPTER 2 SIMULATION TECHNIQUES

CHAPTER 3 ANALYSIS TECHNIQUES

CHAPTER 4 INHIBITOR BEHAVIOUR IN LIQUID WATER

CHAPTER 5 STRUCTURE II HYDRATES–PHASE BEHAVIOUR

CHAPTER 6 INHIBITOR BEHAVIOUR AT GAS HYDRATE SURFACES

CHAPTER 7 EXPERIMENTAL STUDY OF THE INHIBITION PROPERTIES OF tba3S

CHAPTER 8 CONCLUSIONS

Acknowledgements

As with all works of this length the list of people one would like to acknowledge is considerable and unfortunately the space afforded such a section is limited. I would therefore like to apologise to all those people who are not included here and assure them that although their names are not in this thesis they are most certainly in my thoughts.

Firstly I would like to acknowledge Dr. Mark Rodger for his help and support throughout my PhD studies, and for his unending enthusiasm when faced with my constant barrage of requests and questions.

Secondly thanks must go to Dr. Paul Taylor for synthesising tba3S without which the following experimental studies would not have proved so informative. I thank Dr. Jean-Pierre Monfort and Dr Lisebelle Jussaume at ENSIGCT for their assistance with the experiments on ethane hydrate and for allowing a computational chemist loose in a laboratory. In addition I also must acknowledge Marie-Line Zanota at the Universite de Pau et des Pays de l'Adour for her help with the experiments on THF hydrate.

I would like to express appreciation for my parents and grandparents without whose financial and emotional support this work would never have been possible. I would also like to thank them for having the belief in me when even I wasn't sure how things would work out.

Finally I would like to thank my beautiful and loving fiancée for coming to England to be with me during my studies and for always being there when things weren't going well. I love you Nuria and always will.

Declaration

The observations and recommendations in this thesis are those of the author except where acknowledgement has been made to results and ideas previously published. The work was undertaken at the Department of Chemistry, University of Warwick and the Department of Chemistry, University of Reading between October 1997 and September 2000 and has not been previously submitted for a degree at any institution.

Abstract

This thesis reports an investigation of two families of potential gas hydrate inhibitor: quaternary amine carboxylates and sulphonates. Molecular dynamics simulations of the inhibitors have been performed both in liquid water and at the surface of a thin hydrate film under natural gas. Trajectories were analysed to determine inhibitor effects upon the structure of the water and the stability of the gas hydrate lattice. *T/P* conditions for the thin film study were determined from the calculated stability of a structure II gas hydrate under pressure. All three studies were analysed using radial distribution functions, time correlation functions, and order parameters to probe the underlying structure.

To complement the computer modelling study, an experimental investigation of one of the amine sulphonates, *N,N,N*-tributylammonium-1-(3-propylsulphonate), and one established inhibitor, polyvinylpyrrolidone was performed. These measured the effect of the inhibitor on nucleation time, crystal growth and morphology for both tetrahydrofuran and ethane hydrate.

Results from the liquid water simulations indicate that bulk water is largely unaffected by the inhibitors, while solvated water shows increased short- and long-range structure.

Hydrate pressures were determined from the thin film simulations. A transition to a high-pressure phase was also found at around 20 kbar. These results are consistent with experimental data. Pressures in the middle of the hydrate stability zone were adopted for the subsequent inhibitor simulations. Inhibitor behaviour at the interface showed signs of relaxation of the gas hydrate water network, while for solvated water there was a contraction in the water network for the carboxylates headgroup.

The experimental investigation revealed the amine sulphonate to be a more effective kinetic inhibitor of hydrate formation than polyvinylpyrrolidone. This was achieved by delaying nucleation, along with some growth modifying properties.

Abbreviations

BF – Bernal + Fowler model.

BNS – Ben-Naim + Stillinger model.

CI – chemical ionisation.

CPU – central processor unit.

EI – electron ionisation.

erf – error function.

erfc – complementary error function.

ESPD – electrostatic potential derived charges.

EXAFS – Extended X-ray absorption fine structure spectroscopy.

GCR – gas consumption rate.

HF – Hartree-Fock.

HPLC – high-pressure liquid chromatography.

IR/ir – infra red.

MC – Monte Carlo.

MD – molecular dynamics.

MSD – mean square displacement.

NCC – Niesar, Corongiu + Clementi model.

NMR/nmr – nuclear magnetic resonance.

PVcap – polyvinylcaprolactam.

PVP – polyvinylpyrrolidone.

RDF – radial distribution function.

RHF – restricted Hartree-Fock.

RMS/rms – root mean square.

rpm – revolutions per minute.

SCF – self-consistent field.

SD – standard deviation.

SPC – simple point charge model.

SPCE – simple point charge extended model.

ST2 – Stillinger model.

tba1C – *N,N,N*-tributylammonium-1-(2-ethylcarboxylate).

tba1S – *N,N,N*-tributylammonium-1-(1-methylsulphonate).

tba2C – *N,N,N*-tributylammonium-1-(3-propylcarboxylate).

tba2S – *N,N,N*-tributylammonium-1-(2-ethylsulphonate).

tba3C – *N,N,N*-tributylammonium-1-(4-butylcarboxylate).

tba3S – *N,N,N*-tributylammonium-1-(3-propylsulphonate).

THF – tetrahydrofuran.

TIP3P – transferable intermolecular potential three point model.

TIP4P – transferable intermolecular potential four point model.

TIPS – transferable intermolecular potential functions model.

TIPS2 – transferable intermolecular potential functions two model.

UA – united atom model.

VC – vinylcaprolactam.

VC713 – terpolymer of vinylpyrrolidone + vinylcaprolactam + dimethylaminoethyl methacrylate.

VP – vinylpyrrolidone.

CHAPTER 1

GAS HYDRATES–AN INTRODUCTION

1 Introduction

In this chapter a literature review of gas hydrates is outlined. The chapter is divided into nine parts as outlined below.

1.1 A brief introduction to gas hydrates.

1.2 Historical background of gas hydrates.

1.3 The three main gas hydrate structures: I, II and H.

1.4 Occurrence of gas hydrates.

1.5 Stability of gas hydrates.

1.6 Consequences of gas hydrates.

1.7 Primary nucleation.

1.8 Crystal growth.

1.9 Inhibition of gas hydrate formation.

1.1 Gas hydrates–an introduction.

Gas hydrates (or clathrate hydrates as they are alternatively known) are a special type of inclusion compound. Inclusion compounds are compounds that comprise of two, (or more), molecular species that order themselves such that one molecular species, the 'host', entraps the other molecular species, the 'guest'. In clathrates the host molecules are arranged to form hollow polyhedra, or 'cages'. For gas hydrates the host species is water which forms a crystalline lattice based on at least two types of polyhedra. These hollow polyhedra accommodate a variety of guest species, which are conventionally split into the four categories given below.

i) Small hydrophobic compounds such as CH_4, C_2H_6, Ar, Kr, Xe, O_2, N_2 and CCl_4.

ii) Water-soluble acids such as H_2S and CO_2.

iii) Water-soluble polar compounds such as cyclic ethers.

iv) Water soluble ternary/quaternary alkyl ammonium salts.

Gas hydrate formation is a concomitant process requiring the presence of both the host and guest molecular species. The water lattice is thermodynamically unstable by itself and so the stability of the gas hydrate is a direct result of the presence of the guest molecules in the hydrate cavities.[1]

1.2 Historical Background

Gas hydrates have a long and varied history of interest ranging from their discovery in 1810 up to the present day. This interest has been fuelled all the more by the fact that there are massive naturally occurring deposits of methane hydrate, such that they

may well provide the solution to the world's energy requirements in the decades to come.

Sir Humphrey Davy first discovered gas hydrates in 1810.[2] Davy found that a solid formed when an aqueous solution of chlorine was cooled below 9 °C. Faraday[3] confirmed the existence of the solid and suggested that it was composed of 1 part of chlorine and 10 parts of water.

Following the discovery of gas hydrates their history can be roughly separated into three areas of study.[4]

i) 1810 onwards: for the first 100 years after their discovery the interest in gas hydrates stemmed purely from an academic standpoint. It was concerned with the identifying molecular species that would form gas hydrates and in elucidating the pressure/temperature conditions at which their formation was observed. Within the last decade interest in this area has been renewed by the discovery of a new type of gas hydrate.

ii) 1934 onwards: following the discovery by Hammerschmidt[5] that the plugging of natural gas pipelines was not due to ice formation but due to the formation of natural gas hydrate there has been an immense research effort into natural gas hydrates and their implications for the oil and gas industry.

iii) 1960's onwards: more recently there has been much interest in the presence of gas hydrates as natural deposits[6] which exist within and below the permafrost regions of the world, in subsea sediment in the Arctic, Antarctic, tropical and subtropical oceans as well as extra-terrestrially.

1.3 Structure

One of the most important factors following the discovery of a new compound is the elucidation of its constitution and structure. This is not only because it is helpful in gaining insight into how the compound may interact with its environment, but also to help visualise its structure.

The majority of gas hydrates can be identified as being of one of three structures namely I, II or H. To explain these structures it is helpful to begin by describing the basic polyhedral building blocks and then considering how the building blocks fit together. The cavities present in each of these hydrate structures satisfy Euler's theorem,[7] which states

number of faces + number of vertices = number of edges + 2.

Water in the hydrate forms a near-perfect tetrahedral hydrogen bond network and so the vertices of each polyhedra are associated with the oxygen atoms, and the edges formed by the O-H·····O covalent/hydrogen bond pair.

With these definitions in mind the five cavity types found in the structures I, II and H hydrates are as follows.

i) The pentagonal dodecahedron is the basic building block of all three gas hydrate structures; it is composed of twelve pentagons joined together to form a polyhedron, hence the usual notation 5^{12}. The notation is such that the main number describes the faces of the polyhedron while the superscript number indicates how many such faces are present. This cavity is large enough to accommodate molecules such as Kr, Ar, N_2, O_2 and CH_4.

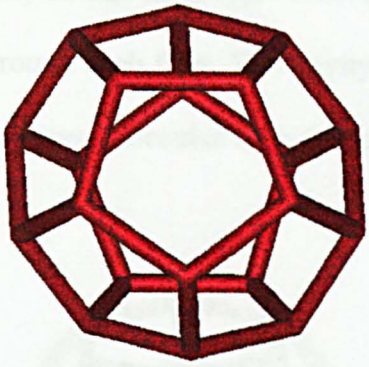

Figure 1.1 The pentagonal dodecahedron.

ii) The tetrakaidecahedron, denoted $5^{12}6^2$, is composed of two facing hexagons; each hexagon is surrounded by five pentagons to form a basket, and two such baskets then fit together to form the whole cavity. This cavity accommodates molecules such as CO_2, C_2H_6 and also CH_4.

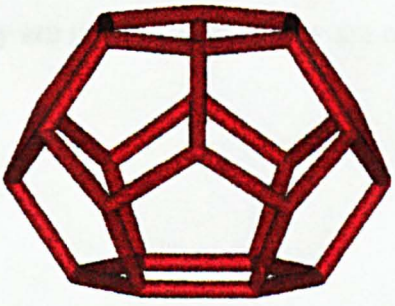

Figure 1.2 The tetrakaidecahedron.

iii) The hexakaidecahedron, denoted $5^{12}6^4$, is composed of four hexagonal faces arranged symmetrically so that their faces form the vertices of a tetrahedron; pentagonal faces surround each face. This cavity is the most spherical of the cavities and accommodates molecules such as C_3H_8 and C_4H_{10}.

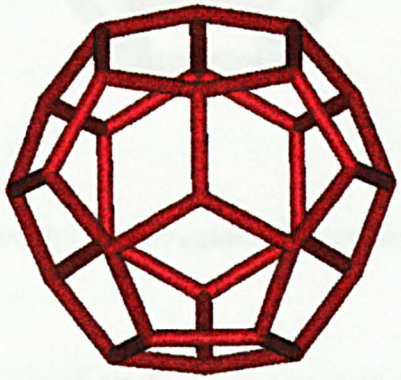

Figure 1.3 The hexakaidecahedron.

iv) The irregular dodecahedron, denoted $4^3 5^6 6^3$, is composed of three square faces, six pentagonal faces and three hexagonal faces. The square faces present in this cavity are unusual in that they are not found in any of the other gas hydrate cavities.

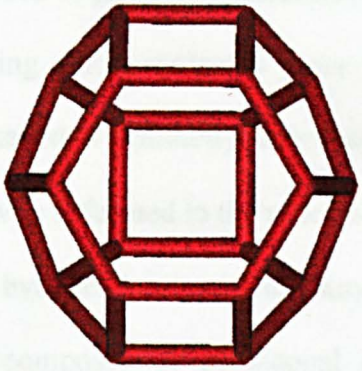

Figure 1.4 The irregular dodecahedron.

v) The icosahedron, denoted $5^{12}6^8$, is composed of twelve pentagonal and eight hexagonal faces, with six hexagons around the equator of the cavity, and a hexagon at both the top and bottom of the cavity.

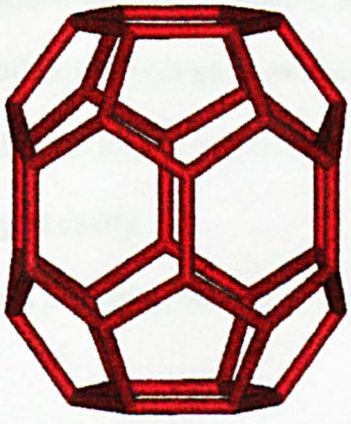

Figure 1.5 The icosahedron.

The two main types of gas hydrate structures are those of structure I and II and were originally described by Von Stackelberg.[8]

i) Structure I (type I) hydrates have a body centred cubic crystal structure. Type I hydrates are composed of pentagonal dodecahdra arranged in space in such a way that a bridging water molecule joins the vertices. Because these polyhedra are of icosahedral symmetry and so cannot pack together to fill 3-D space, a second cavity is formed in the process—the tetrakaidecahedron.

ii) Structure II (type II) hydrates have a cubic diamond lattice structure. Type II hydrates are again composed of pentagonal dodecahedra, but this time arranged in space in such a way that they share faces. Again, a second type of cavity must be formed in order to fill 3-D space, and in this case it is the hexakaidecahedron that is formed.

The third structure, structure H was discovered by Ripmeester *et al.*[6] in 1987 and was so named due to its hexagonal space group symmetry. Structure H was found to be isostructural with clathrasil dodecasil-1H, a clathrate formed with SiO_2 replacing H_2O as the host molecule.[9]

Structure H has been determined as being a double hydrate, since it requires two different guest species to stabilise it. Small guest molecules such as CH_4 reside in the two smaller cavities, and then a larger hydrocarbon compound such as methyl cyclohexane occupies the largest cavity.

The structure types and cavities present in the type I, type II and structure H hydrates are summarised in table 1.1.

	TYPE I	TYPE II	STRUCTURE H
Number of waters per unit cell	46	136	34
Small cavity in hydrate	5^{12}	5^{12}	5^{12}
Diameter of the cavity/Å	7.88	7.82	7.82[b]
Number of cavities	2	16	3
Variation in radius[a]/%	3.40	5.50	Not Available
Medium cavity in hydrate	N.A.	N.A.	$4^3 5^6 6^3$
Diameter of the cavity/Å	N.A.	N.A.	8.12[b]
Number of cavities	N.A.	N.A.	2
Variation in radius[a]/%	N.A.	N.A.	Not Available
Large cavity in hydrate	$5^{12}6^2$	$5^{12}6^4$	$5^{12}6^8$
Diameter of the cavity/Å	8.60	9.46	11.42[b]
Number of cavities	6	8	1
Variation in radius/%	14.4	1.73	Not Available

[a] Variation in distance of oxygen atoms from the centre of the cavity, taken from experimental crystal structures[4]
[b] Estimates of structure H cavities from geometric models.

Table 1.1 Structural properties of the gas hydrates.

1.4 Occurrence

Gas hydrates are widely distributed about the planet in various environments, and new deposits are constantly being found. Naturally occurring hydrate bearing strata have been identified in both on-shore and off-shore sites; such strata generally lie below the seafloor in regions that slope from the continents to the deep ocean basins thousands of meters underwater. Methane hydrate deposits have been identified off

the coasts of Costa Rica, New Jersey, Oregon, Japan, India and hundreds of other sites around the world. Hydrates have also been encountered during drilling operations through Arctic permafrost in Siberia, Alaska and Canada.

AREA	EQUIVALENT VOLUME AT STP/10^{15} m^3	MASS METHANE CARBON/10^{15} kg	YEAR	REFS.
Marine	5-25	2.7-13.7	1977	[10]
	3.1	1.7	1981	[11]
	7600	4100	1981	[12]
	17.6	11	1988	[19]
	19.5	11	1990	[13]
	26.4-139.1	N.A.	1994	[14]
Continental	0.057	0.02	1977	[10]
	0.014	0.005	1981	[15]
	0.031	0.011	1981	[11]
	34	12	1981	[12]

Table 1.2 Estimates of methane gas and methane carbon resources contained in the marine and continental gas hydrate accumulations. Taken from references[16] and[17].

Current estimates of the amount of carbon in natural deposits of methane hydrate suggest that as much as 54% of the worlds organic carbon may be present in these deposits,[18] and twice the amount of carbon in all known fossil fuel deposits (*i.e.* coal, natural gas and oil).[19] Table 1.2 shows the various estimates that have been made of

the amount of methane gas and methane carbon in continental and marine gas hydrate accumulations.

In addition to naturally occurring hydrates on earth Miller[20] has also predicted the existence of methane hydrate on Uranus, Saturn and Jupiter as well as on the satellites of Saturn and Jupiter. Hydrates are also believed to be a major constituent of cometary ice.

1.5 Stability

Knowledge of the thermodynamic formation conditions for gas hydrates is important. It enables oil and gas producers and processors to be aware of areas of danger for the operation of their plants and pipelines. This knowledge is helpful in designing plants to minimise the effects of gas hydrate formation on their operation, for example by lagging the pipes to prevent the temperature from falling below the hydrate formation temperatures. Alternatively, it allows efficient use of additives to inhibit hydrate formation, (see section 1.9).

A schematic phase diagram can be seen in figure 1.6 for the methane/water system.

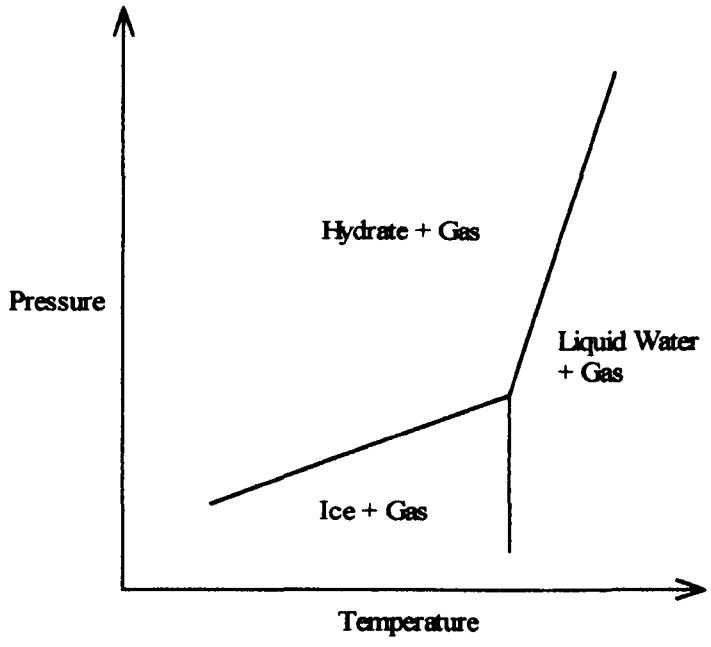

Figure 1.6 A schematic phase diagram for methane hydrate. The quadruple point occurs at 272.9K and 2.563Mpa.

In order to help to understand the various areas of the phase diagram we must first consider the Gibbs phase rule, equation 1.1,

$$F = C - P + 2 \qquad \textit{Equation 1.1}$$

where F is the variance, C is the number of chemical components and P is the number of phases at equilibrium. The definition of 'phase' is a state of matter that is 'uniform throughout not only in chemical composition, but also in physical state', as first defined by Gibbs. For example a gas is a single phase while an alloy of two metals is a two-phase system if the metals are immiscible, but a single-phase system if they are miscible. The number of components is defined as the minimum number of independent species necessary to define the composition of all phases present in the system. In essence, when you have a system where the species do not react then you simply count the number of species *e.g.* pure water is a single-component system whereas water and ethanol is a two-component system. The variance is defined as the

dimension of the co-existence region in the phase diagram, that is to say a plane (d=2), a line (d=1) or a point (d=0) on the diagram. For methane and water there are two components present and so $F + P = 4$; information on the diagram can now be simplified.

NUMBER OF CO-EXISTING PHASES	F	DESCRIPTION OF REGION ON DIAGRAM
4	0	point
3	1	line
2	2	plane

Table 1.3 A table to show the relationship between the number of phases and F for a two component system.

We can now see from figure 1.6 that at the intersection of the three lines all four phases are present in equilibrium, namely water, ice, gas and hydrate. Each of the lines denotes the existence of three phases and each of the planes indicates a region in which two phases coexist at equilibrium. The point of intersection of the three lines is known as the quadruple point and for methane hydrate occurs at 272.9 K and 2.563 MPa. The line defining the barrier between the hydrate + gas plane and the rest of the phase diagram in figure 1.6 can be seen in more detail in graph 1.1. Pressures along this line are often referred to as hydrate pressures as they specify the minimum pressures for which hydrates are stable at the given temperature.

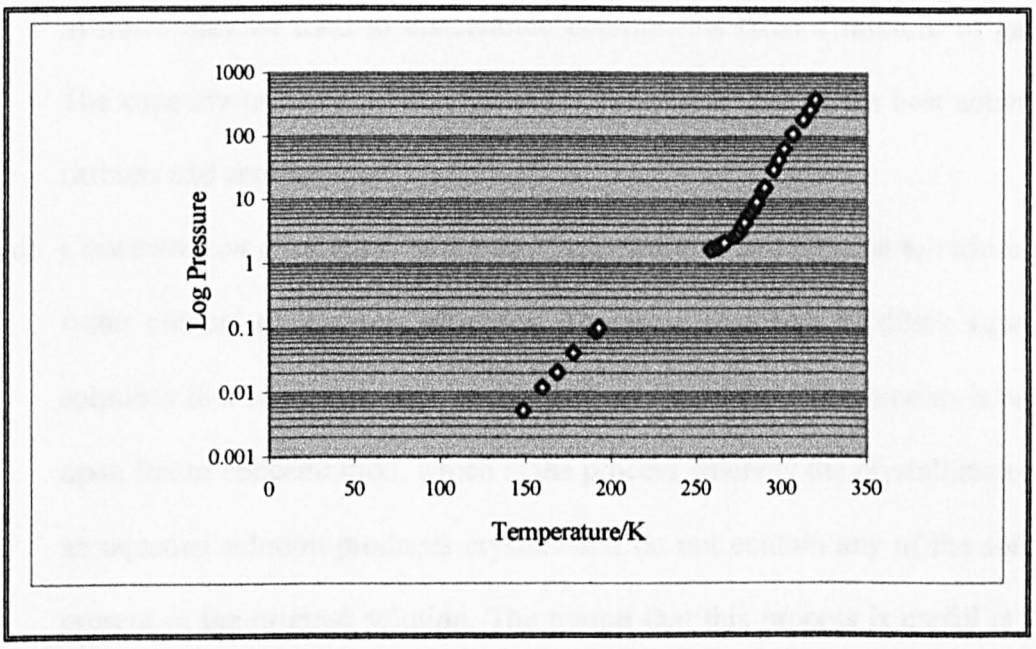

Graph 1.1 Three-phase data for methane hydrate.[4]

1.6 Consequences

The consequences of gas hydrate formation can be split into two classes: applications resulting from the properties of gas hydrates and problems[21] which are associated with gas hydrates.

i) Applications

a) *Desalination of water*:[22] several processes have been patented for the conversion of saline water into drinkable water using hydrate formation. However, although a number of these processes were scaled up and demonstrated on a pilot plant scale none of them ever made it to full industrial scale. The reason for this was that problems were encountered in separating the crystals from the concentrated brine solution and the subsequent removal of the hydrate forming gas from the recovered water.

b) *Fractionation of gases and liquids by selective enclathration*:[23] some gas

hydrates may be used to concentrate components from a mixture of gases. The capacity to take up host molecules is equal to that of the best activated carbons and zeolites.

c) *Concentration of aqueous solutions*:[24] gas hydrates can be used to reduce the water content of aqueous solutions. There are a variety of dilute aqueous solutions that can be concentrated by hydrate formation. The process is based upon freeze concentration, which is the process whereby the crystallisation of an aqueous solution produces crystals that do not contain any of the solutes present in the original solution. The reason that this process is useful is that gas hydrates can be formed at temperatures above the normal freezing point of water, and consequently there is an energy advantage in replacing the crystallisation step of a freeze concentration system with gas hydrate formation. This process has been applied to the concentration of fruit juices such as apple, orange and tomato[25] and was able to remove approximately 80 % of the water present in the original solution. The resulting crystals produced were removed by using a centrifuge. This area of gas hydrate chemistry is most applicable to temperature-sensitive solutions.

d) *Storage of gases*:[26] gas hydrates with low critical temperatures may be used to store gases at considerably lower pressures or in smaller volumes than required for the gases themselves. Gases such as ClO_2 and O_3, which are explosive, can be more safely transported as hydrates than as dense fluids.

e) *Waste minimisation*:[27] over the past few years environmental regulations have become increasingly tougher and have forced process industries to develop innovative water strategies. These strategies include development of cost-effective technologies to recover clean water from effluent by inducing the

formation of gas hydrates. The gas hydrates can then be removed and melted to recover the water in the lattice.

f) *Future source of natural gas*: in future as fossil fuel reserves are depleted production of methane from natural hydrates may become economically viable. There are still some technical problems associated with mining such hydrates, however.

i) Problems

a) *Greenhouse effect*:[28] it is now well known to most people that methane is an important greenhouse gas which is estimated to be 21 times[29] more effective than carbon dioxide at promoting the Greenhouse effect. As a result the sheer size of gas hydrate deposits may mean that they provide an important positive feedback mechanism for global warming: an increase in the global temperature could possibly cause the gas hydrate deposits to begin to decompose releasing more methane into the atmosphere; this would then enhance the Greenhouse effect, causing a further rise in temperature and so further destabilising the gas hydrate deposits The overall process can be seen in figure 1.7.

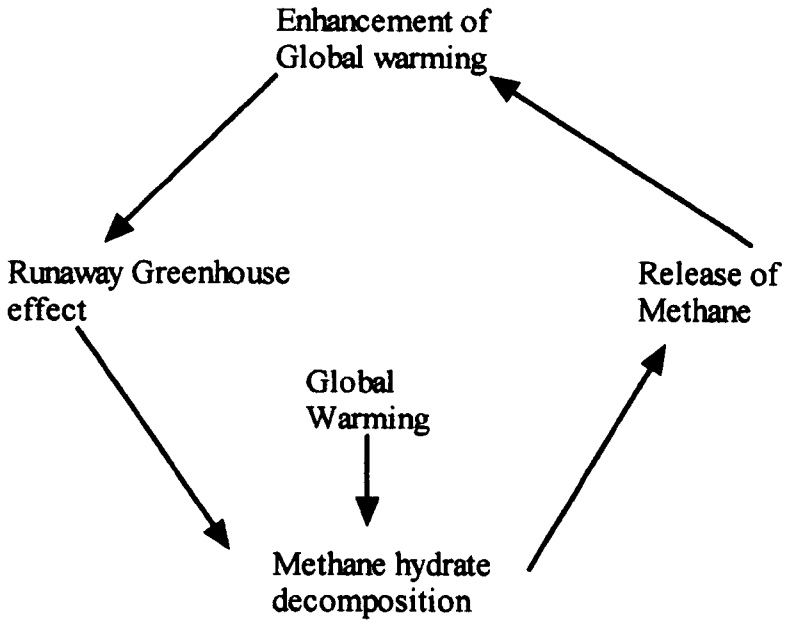

Figure 1.7 The positive feedback mechanism for global warming.

Kvenvolden[30] has proposed that a similar mechanism may have released large amounts of hydrates at the end of the last ice age. At the time of the last ice age as the continental ice melted, the global sea levels increased by more than 90 meters. This rise in the sea level caused Arctic regions (where hydrates exist) to be submerged. Since the water was relatively warm ocean water this would have caused the hydrate deposits to melt, releasing huge amounts of methane into the atmosphere. It has been shown that the carbon isotopic ratios in the sea shifted several times in the last 70, 000 years consistent with large amounts of methane pouring into the oceans. These increases in the carbon isotopic ratios coincide with the well-known Dansgaard-Oeschger episodes when the Earth's ice age climate suddenly increased in temperature. If this theory is correct then the same ideas could apply to the modern world. Sea levels are currently rising at a few centimetres per decade and these rates

are expected to increase as the amount of greenhouse gas pollution increases. If this is then coupled with the expected increase in ocean temperatures, hydrate deposits may well play a large role in the future climate changes of the planet.

b) *Formation during oil and gas production or transport*: in the deep waters where the sea floor is cold and the hydrostatic pressures are high, gas hydrates may be formed during the drilling process. This can lead to the blockage of riser lines and blow-out preventers. Indeed a situation similar to this cost one company twelve million dollars and the loss of two wells.

1.7 Nucleation of Gas Hydrates

In order to consider the kinetics of gas hydrate formation we must study two distinct areas as outlined below:

a) primary nucleation; and

b) crystal growth.

1.7.1 Primary Nucleation

As shown in figure 1.8 there are two types of primary nucleation, namely homogeneous and heterogeneous. During primary nucleation subcritically sized crystals may either shrink or grow before eventually reaching a larger critical size, upon which for homogeneous nucleation monotonic growth occurs and for heterogeneous nucleation catastrophic growth occurs.

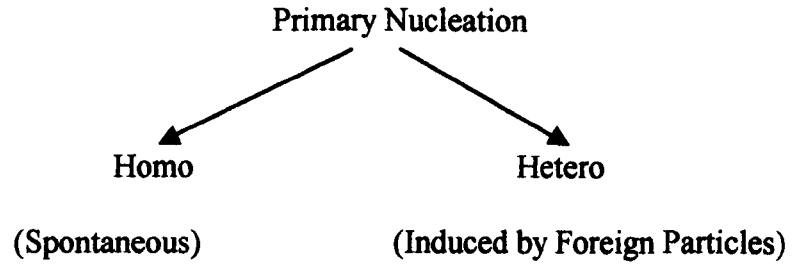

Figure 1.8 Types of primary nucleation.

Homogeneous Nucleation

Homogeneous nucleation refers to the process whereby crystallisation from solution in the absence of impurities takes place. This process involves many more molecules than could collide simultaneously and therefore it is thought that a sequence of autocatalytic bimolecular collisions are taking place as shown in figure 1.9, where A refers to a molecule in the system and A_i refers to a cluster of *i molecules of type* A and A_n is a cluster of critical size for monotonic growth to occur.

$$A + A \leftrightarrows A_2$$

$$A_2 + A \leftrightarrows A_3$$

$$A_3 + A \leftrightarrows A_4$$

.....

$$A_{n-1} + A \leftrightarrows A_n \text{ (critical cluster size)}$$

Figure 1.9 Homogeneous Nucleation.

Before attaining the critical cluster size groups of molecules will tend to shrink, although entropy-driven fluctuations to larger cluster sizes will still occur. Once the cluster of molecules reaches the critical cluster size then the tendency will be for monotonic growth to occur (although entropy-driven fluctuations to smaller cluster sizes can still occur). Attainment of the critical cluster size is a balance of two factors: the first is the surface excess free energy which follows an r^2 relationship, is proportional to the surface area of the cluster and opposes growth; the second is the volume excess free energy which follows an r^3 relationship, is proportional to the volume of the cluster and favours growth. These two factors are of opposite sign and addition of the two leads to the excess Gibbs free energy between a small solid particle of solute and the solute in solution, with a maximum corresponding to the critical nucleus size. An example of homogeneous nucleation is the formation of methane hydrate from methane dissolved in water; it can be thought of as an equilibrium fluctuation of the methane solution such that methane hydrate nucleates.

Heterogeneous Nucleation

Heterogeneous nucleation is by far the more common process by which primary nucleation takes place. This is simply due to the fact that it is virtually impossible to remove all the impurities from a solution and these impurities then act as the sites for subsequent nucleation. In addition the presence of a surface in the system can also act as a nucleation site, be it the walls of the container, or the surface at an interface. An example of heterogeneous nucleation would be the formation of methane hydrate at a water/methane interface.

Primary Nucleation of Gas Hydrates

The research on the nucleation of gas hydrates can be split into two areas:

a) nucleation from ice; and

b) nucleation from water.

The data available concerning the nucleation from ice is considerably less than that for nucleation from water. This is probably due to the fact that industry is a large driving force in deciding the direction of current research. Consequently, because the formation of ice in pipelines and gas processing is avoided at most operating conditions, the research concerning nucleation of gas hydrates from ice is limited.

Primary Nucleation of Gas Hydrates from Ice

Barrer and Ruzicka[31] carried out some of the earliest experiments on the nucleation of hydrates from ice in 1962. Their work suggested that a very limited amount of hydrate would form from ice in a nonagitated chamber at temperatures below the ice point. In addition they indicated that more rapid hydrate formation from ice occurred when the ice surface was renewed by grinding with a ball-mill-like apparatus. They therefore suggested that without agitation the exposed ice surface area is growth limiting and was therefore acting as a kinetic parameter.

The first experiments to measure the induction times from ice using noble gases as hydrate formers were carried out by Barrer and Edge.[32] They studied the formation of simple hydrates of argon, xenon and krypton by using a ball-mill-type apparatus to renew the ice surface that was converted to hydrates. They found that there was no induction period for the hydrates of xenon and argon, but an induction time of 1 hour was observed for krypton that was followed by a rapid growth of hydrate then a slow decline due to the depletion of the ice. The work of Barrer and Ruzicka[31] has since

been validated by experiments carried out at Holder's laboratory by Wright[33] and Hwang *et al.*[34] The latter work has suggested that the melting ice acted as a template for the hydrogen bonds of hydrate formation.

Eight years after the work of Barrer and Edge,[32] Falabella[35] carried out an investigation into the equilibrium and kinetic properties of the hydrates of methane, ethane, ethylene, acetylene, carbon dioxide and krypton. Hydrates of these molecules were formed from ice at temperatures ranging from 148–240 K and at constant sub-atmospheric pressures. Using a similar experimental setup to that of Barrer and Edge[32] Falabella was able to duplicate their induction time results for krypton. Falabella's results were of two distinct types: those for methane and krypton, where there was a clearly defined induction time, and those for the other molecules studied, where there was no observable induction time.

In 1991, Sloan and Fleyfel[36] carried out experiments on the kinetics of cyclopropane hydrate formation from ice. Cyclopropane is able to occupy either the large cavity of structure I ($5^{12}6^2$) or the large cavity of structure II ($5^{12}6^4$), depending on the temperature. This choice of hydrate former stemmed from the suggestion of Glew[37] in 1959 that when the size of a guest molecule approached the limiting size of a cavity a high degree of thermodynamic nonstoichiometry was observed. A similar behaviour on a kinetic level was thought to be responsible for the induction periods observed for methane and krypton hydrates. In essence it was suggested that the induction periods for the simple hydrates of methane and krypton represent a period of oscillation between the 5^{12} cavities of structure I and structure II before structure I achieves the critical nuclei radius stability, (the size of several unit crystals), for simple methane hydrates, or before structure II reaches the critical size for stability of krypton hydrate. Indeed, their experimental findings validated the reasoning that

hydrate formation from molecules of a van der Waals size intermediate to the hydrate cavity size did lead to a measurable induction time. They then went on to propose a mechanism for hydrate primary nucleation, which is summarised in figure 1.10.

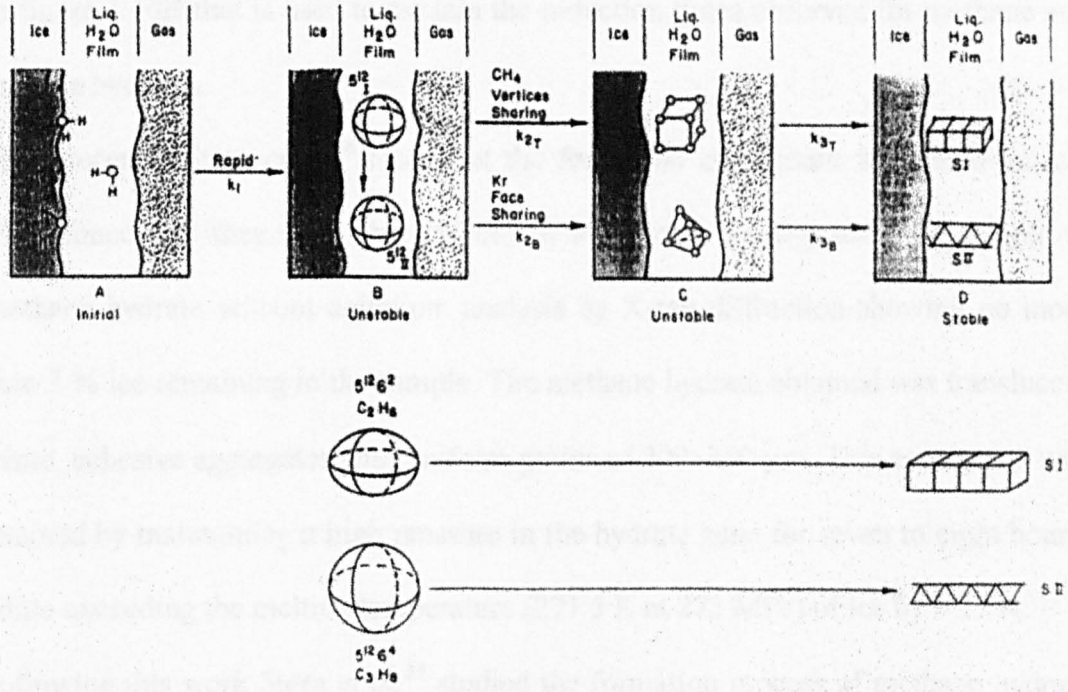

Figure 1.10 Kinetic mechanism for hydrate formation from ice, reproduced from Sloan and Fleyfel.[36]

In figure 1.10A ice is shown together with gas and liquid water. In figure 1.10B the basic hydrate cavity, the 5^{12} cavity, is shown as a labile species in the liquid film at the ice interface, with melting ice acting as the template for hydrogen bond formation which is required for hydrate formation. Following figure 1.10B two parallel paths are shown. The top path represents the path followed for the construction of type I hydrates such as methane, while the bottom path is the path followed for the construction of type II hydrates such as krypton. In figure 1.10C the unit cells of either of the two hydrate types are formed; however these unit cells are not beyond

the critical size for growth and so some of them may shrink back to figure 1.10B or combine to give the structures seen in figure 1.10D. In figure 1.10D the species are of sufficient size that they have progressed beyond critically-sized crystals and therefore grow monotonically. It is the transition between the upper and lower path in figure 1.10B that is used to explain the induction times observed for methane and krypton hydrates.

More recently Stern *et al.*[38] looked at the formation of methane hydrate from ice. They found that they were able to convert 97 % of a small-grained ice sample to methane hydrate without agitation: analysis by X-ray diffraction showing no more than 3 % ice remaining in the sample. The methane hydrate obtained was translucent white, cohesive aggregates with uniform grains of 200–350 μm. This conversion was attained by maintaining a high pressure in the hydrate zone for seven to eight hours, while exceeding the melting temperature (271.5 K at 273 MPa) of ice by ~ 17 K.

Following this work Stern *et al.*[39] studied the formation process of methane hydrate from ice in greater detail. Methane hydrate was formed under static conditions by combining cold, pressurised CH_4 gas with granulated H_2O ice, with subsequent heating of the reactants to promote the reaction

$$CH_{4(g)} + 6H_2O_{(s\rightarrow l)} \rightarrow CH_4.6H_2O_{(s)}$$

They observed that hydrate formation occurs at the ice/liquid water interface on ice grain surfaces with complete reaction being achieved by warming the system above the ice melting point and up to 290 K, at 25–30 MPa for approximately 8 hours; the methane hydrate dissociation point is 292 K at 30 MPa. The material obtained was pure, cohesive, polycrystalline methane hydrate with controlled grain size. From their experiments they concluded that methane hydrate formation initially occurs in the ice subsolidus region, producing a thin plating of hydrate on the ice grain

surfaces and that further hydrate formation occurs by diffusion of the hydrate-forming species through the hydrate crust to the ice core. In addition they concluded that under hydrate-forming conditions H_2O ice can persist metastably to temperatures well above its ordinary melting point while reacting to form hydrate, that is to say the H_2O ice is superheated. This was explained by the fact that the reaction of a hydrate-forming species with 'premelting' at the hydrate-ice core interface may inhibit the formation of an equilibrium solid-liquid water interface required for bulk melting and therefore allows for superheating of the remainder of the unreacted ice. Stern *et al.*[40] confirmed this hypothesis of superheating of ice during the formation of either methane or carbon dioxide hydrate by means of optical cell observations.

Hemming *et al.*[41] used neutron diffraction at temperatures ranging from 230–290 K to study the formation of carbon dioxide hydrate. The hydrate was formed from deuterated ice crystals at 230, 243, 253 and 263 K by pressurising the system with carbon dioxide to produce hydrate in approximately 70 % yield, with nearly complete conversion being observed as the temperature was slowly increased through the melting point of deuterated ice. They suggested that the formation of carbon dioxide hydrate was initially fast with fast conversion on the surface of the ice particles, but after the initial period the process is controlled by the diffusion rate of carbon dioxide molecules through the accumulating hydrate layer—a suggestion also proposed by Hwang *et al.*[34] and Stern *et al.*[42]

Primary Nucleation of Gas Hydrates from Liquid

Some of the earliest work in this area was carried out by Vysniauskus and Bishnoi.[43,44,45] They investigated the kinetics of methane and ethane hydrate formation by contacting gas with water at temperatures above the freezing point of

water. The results showed that hydrate formation consists of the appearance of nuclei and their subsequent growth. The history of the water affects the induction period but it does not have any observable effect on the growth of the nuclei. A lower mean induction period was observed when water obtained from thawed ice was used when compared to that obtained with hot tap water. The mean induction period was also lower when water obtained from dissociated hydrates was used compared to that observed for hot tap water. This effect is known as the 'memory effect' and has been observed in various studies.[46,47,48,49,50]

In addition to their experimental results they developed a semi-empirical model for the gas-consumption rate. The work of Vysniauskas and Bishnoi[43,44,45] was followed by that of Englezos *et al.*[51] who studied the formation of methane and ethane hydrates. They used a semi-batch stirred tank reaction to study the formation kinetics at four different temperatures (274, 276, 279 and 292 K) for methane in the pressure range 3.294–8.903 MPa and ethane hydrate in the pressure range of 0.636–2.188 MPa and at stirring rates of 300–450 rpm. They observed that hydrate formation was not restricted to a thin layer close to the gas/liquid interface but could occur anywhere in the liquid as long as supersaturation exists. In addition they observed that the induction period was shorter at higher stirring speeds. From their experimental results they developed a mechanistic model with only one adjustable parameter, which represents the rate constant for hydrate growth, for the formation of methane and ethane hydrates.

This work was immediately followed up by Englezos *et al.*[52] who studied the formation of gas hydrates from mixtures of methane and ethane. They used the same experimental equipment as in their previous paper[51] at temperatures from 274–283 K for three methane/ethane mixtures at a stirring rate of 400 rpm. From their results

they extended their previous model for pure gases[51] to describe the formation of gas hydrates from mixtures of methane and ethane.

In 1988 Englezos and Bishnoi[53] studied the formation of methane hydrates. They measured the turbidity point of the system, *i.e.* the first visual appearance of hydrate nuclei, at typical methane solubilities, to be a factor of twenty less than the calculated thermodynamic limit.

Lingelem and Majeed[54] measured the time for natural gas hydrate crystals to appear in a sapphire cell at high pressure and found that the induction time was exponential with respect to subcooling; however Muller-Bongartz *et al.*[55] were unable to reproduce these findings.

Further work was carried out on the nucleation of methane hydrate by Levkam and Ruoff.[56] From their study they developed a five-step reaction kinetic model for the formation of methane hydrate from liquid water and methane gas, which contained three dynamic elements as outlined below:

a) the dissolution of methane gas into the water phase;

b) the build up of an oligomeric precursor of methane hydrate;

c) growth of methane hydrate by an autocatalytic process.

They found that their relatively simple model gave close agreement with experimentally observed behaviour.

This was followed by an investigation by the same authors into the kinetics and mechanism of methane hydrate decomposition in liquid water with particular attention to hysteresis.[57] They used their previous model,[56] supplemented with one additional step to account for bubble formation during hydrate melting to model the melting of hydrate.

Malegaonkar *et al.*,[58] 1997, modified and used the model of Englezos[52] to study the formation of carbon dioxide and methane hydrate along with an experimental investigation of carbon dioxide formation. They found that the solubility of carbon dioxide in water increased with pressure at constant temperature and that the kinetic rate constant for carbon dioxide hydrate formation was greater than that for methane hydrate formation.

Bowron *et al.*[59] used extended X-ray absorption fine structure (EXAFS) spectroscopy to study the formation of krypton hydrate. EXAFS was used to follow the local structure around krypton atoms on either side of the liquid-to-solid phase transition. EXAFS is an ideal choice for comparison of the local structure around atoms in the two phases because it is insensitive to the onset of long-range order in the crystalline phase. The krypton–oxygen partial radial distribution function for the krypton solution and the krypton hydrate was obtained and it was found that the first peak in the radial distribution function occurred at the same distance of 3.8 Å for both, indicating that the size of the liquid state hydration shell is directly comparable to the small cage of the structure II hydrate. In addition they showed that the full width at half maximum of the first peak was 0.9 Å for the hydrate and 1.1 Å for the liquid state indicating a hydration 'cage' exists in the liquid state but that it is less well-defined than in the hydrate. A final observation was that the position of the large cage hydration shell coincides with the minimum in the liquid state radial distribution function. This indicated that molecules that contribute to the formation of the hydrate from the liquid state must be drawn into the local vicinity of the gas atoms as the cage structure is established. This led to the proposal that clathrate hydrate formation could possibly be inhibited if some way could be found of blocking this process.

Recently, Uchida *et al.*[60] studied the formation process of carbon dioxide hydrate. They found that during the induction period carbon dioxide and water molecules dissolved each other to nucleate hydrate. Primary nucleation occurred at the interface and sometimes secondary nucleation was observed. In addition they found that the hydrate propagation rate was mainly temperature dependent, indicating that the main process determining the propagation rate is heat diffusion from the reaction sites.

A number of studies have used light scattering to study the nucleation of hydrates. These include Nerheim,[61] who determined the critical radius of hydrate formation in a system stirred at 50 rpm, 1 mm below the liquid surface for a 94 % methane and 6 % propane mixture. The critical radius for hydrate formation was estimated to be in the region of 30–800 Å, 30 Å being the lower limit for observation by light scattering.

In the same year, 1993, Monfort and Nzihou[47] used light scattering to study the formation and growth of cyclopropane hydrate. In their study they showed that at high degrees of subcooling (> 1.5 K) in the reactor, the onset of nucleation was followed by a very rapid crystal growth. Once the particles were observed primary nucleation ceased because the energy barrier to form a new nucleus was greater than that of enclathrating gas into existing nucleation centres. Also in the same year Parent[62] showed that light scattering could be used to observe particles with sizes between 10^3–10^6 Å. However, the onset of hydrate formation was too quick for their equipment to observe particles of this size.

Several researchers have also investigated the phenomenon of induction time. The two major bodies of work are those of Skovborg *et al.*[63] and Natarajan.[64] Skovborg *et al.*[63] in 1993 studied the induction time of methane and ethane gas hydrates along

with a 90 % (mole) methane and 10 % (mole) ethane mixture. They found that the duration of the induction time was affected by:

a) the stirring rate; and

b) temperature.

In addition, they suggested that the relative stability of the type I and II structures might also affect the induction period. Natarajan[64] looked at the induction time of methane, ethane and carbon dioxide hydrate as well as methane/ethane, methane/sodium chloride and carbon dioxide/sodium chloride mixtures.

In the same year Parent[62] investigated the nucleation of methane hydrate. The experiments were carried out at 90 bar and 275 K with a stirring rate of 1000 rpm. In a series of eleven experiments the induction times varied from 0–5 hours; indeed, in four of the experiments no nucleation was observed.

Nerheim *et al.*[65] studied the induction time for a 94 % methane and 6 % ethane mixture at 35 bar and temperatures between 1.7 and 3.2 °C. Results for seven of the experiments were presented with induction times ranging from 25–110 minutes: no systematic trends were observed.

Parent[66] carried out further work in 1995 at the laboratory of Bishnoi. Fifteen experiments were carried out to study the induction time of methane hydrate. In each of the experiments the pressure was 90 bar, the temperature 275 K and the stirring rate was 1000 rpm, and each used the same source of water. In four of the experiments no nucleation was observed and in the rest induction times ranged from 0–6 hours.

1.8 Crystal Growth

In the crystal growth region monotonic growth takes place from the nuclei that in the primary nucleation region attained critical size, *i.e.* this process follows the primary nucleation stage. This stage of crystallisation marks the beginning of very rapid crystal growth.

1.8.1 Crystal Growth of Gas Hydrates

The research on the crystal growth of gas hydrates can be split into three main areas:

a) crystal morphology studies,

b) growth from ice;

c) growth from water.

As mentioned in the section on primary nucleation of gas hydrates the relevant data available concerning growth from ice is limited in comparison with the data available for growth from water.

Gas Hydrate Crystal Morphology Studies

Morphology studies have been carried out on all three of the gas hydrate structures I, II and H. In all of these crystal studies it must be remembered that the slowest growing faces are observed, while the rapidly growing planes disappear.

Experiments on structure I hydrates were carried out by Larsen *et al.*[67] who studied the melt growth of ethylene oxide hydrate. Their studies showed that the ethylene oxide crystals were dodecahedral with rhombic faces like those of garnet and exhibited the {1 1 0} crystallographic planes.

Makogon *et al.*[68] studied structure II hydrates with THF hydrate. The crystals obtained were octahedral and exhibited the {1 1 1} crystallographic planes.

Smelik and King[69] studied both structure I and II as well as structure H. Structure I hydrates were formed from pure methane and were found to be dodecahedral with rhombic faces and exhibited the {1 1 0} crystallographic planes as found by Larsen *et al.*[33] for ethylene oxide hydrate. However they did observe another, rare, crystal form that was trapezohedral with 24 trapezium-shaped faces, however these crystals were hard to identify due to their close similarity to cubes.

Structure II hydrates were formed from a 95 % methane and 5 % propane mixture. The crystals obtained were of two main morphologies, octahedral or thin platelets, with the platelets being hexagonal, trigonal or triangular in shape. Structure II hexagonal plates have been observed by McMullan and Kvick[70] for $8CCl_4.3½Xe.136D_2O$ hydrate. For both the octahedral and platelet forms the {1 1 1} crystallographic planes were exhibited.

Structure H hydrates were formed from methane and methylcyclopentane. The crystals obtained were hexagonal prisms. Hexagonal prisms can crystallise as one of two possible forms, which are identical in appearance. The two forms are a first order prism {1 0 0} or a second order prism {1 1 0}. Results presented by the authors suggest that the prisms are first order. Growth twins were also observed in this system.

From the above studies some important conclusions may be drawn:

a) structure I hydrates form as dodecahedral crystals bounded by {1 1 0} faces, with relative growth rates for the primary crystallographic planes being {1 1 1} > {1 0 0} > {1 1 0};

b) structure II hydrates form as octahedral crystals or hexagonal platelets, both exhibiting the {1 1 1} plane with relative growth rates for the primary crystallographic planes being {1 0 0} > {1 1 0} > {1 1 1 };

c) structure H hydrates form as a first order hexagonal prism with similar growth rates for the {1 0 0} and {0 0 1} families of planes.

Crystal Growth of Gas Hydrates from Ice

The work of Barrer and Edge[32] was some of the earliest work carried out in this area. They studied the formation of argon, krypton and xenon hydrates by reaction of ice crystals with the inert gases at temperatures ranging from 269–290 K; agitation was provided by small steel ball bearings. From their results they derived a second order kinetic model for the rate of ice transformation into hydrate.

Bertie *et al.*[71,72,73,74,75] carried out a number of spectroscopic studies on the hydrates of cyclopropane, ethylene oxide, trimethylene oxide, oxetane, 1,3-dioxolane, tetrahydrofuran, cyclobutanone, xenon and oxirane over a period of almost ten years. Devlin and his co-workers[76,77,78,79] at various departments continued this work over the next five years. This work culminated in the conclusions that hydrates grew from an amorphous phase only when Bjerrum L-type defects induced by ethylene oxide propagated through the bulk of the crystal to the surface in an annealing process. In essence the defects were required to minimise the disorder in the crystal. In addition it was found that the mobility of the defects for structure II hydrates tended to be lower than for structure I hydrates, and that in either case the defect mobility was positively correlated with the magnitude of the guest dipole moment. This may reflect the relative tendency of the guest molecules to generate L-type defects through the formation of a hydrogen bond to the host lattice molecules.

Hwang *et al.*[80] studied the crystal growth of methane hydrate from water/ice. They found that hydrates would only form at a measurable rate from ice and when the temperature was above the ice point, suggesting that melting plays an important role in hydrate crystallisation. This is consistent with the findings of Stern *et al.* reported above.[40] They also found that the rate of hydrate growth increased with increased temperatures and pressures. In addition they proposed a kinetic model for hydrate growth.

Crystal Growth of Gas Hydrates from Water

A significant amount of data exists surrounding kinetic studies of gas hydrates from water, beginning with the work of Knox *et al.*[81] on propane hydrate. They examined the growth of hydrates in a stirred slurry pilot plant reactor as part of a study on desalination. They proposed that the sizes of crystals grown depended on the degree of subcooling. A higher degree of subcooling produced, in general, smaller crystals.

Barrer and Ruzicka[1] studied the growth of argon and tetrahydrofuran hydrates and suggested that the hydrate growth rates were controlled by transport of the guest to the hydrate surface.

Grauuw and Rutten[82] in 1970 showed that interfacial mass transport was rate limiting for chlorine and propane hydrate. As a result of this observation a number of researchers decided to study the hydrates of miscible guests such as ethylene oxide and tetrahydrofuran in an attempt to overcome this phenomenon in their experiments.

Glew and Haggett[83,84] studied the kinetics of ethylene oxide hydrate. They concluded that the formation of ethylene oxide hydrate could be described by three consecutive reactions as shown overleaf:

$$EO + xH_2O \xrightarrow{k_{2a}} EO(H_2O)_x + Q_{Surface}$$

$$Q_{Surface} \xrightarrow{k_{2b}} Q_{Bulk}$$

$$Q_{Bulk} \xrightarrow{k_1} Q_{Thermostat}$$

where Q represents the heat produced by the hydrate crystallisation. In all of their experiments they found that:

$$k_1 << \frac{1}{1/k_{2a} + 1/k_{2b}}$$

and therefore heat of transfer by conduction through the glass wall of their experimental apparatus was the controlling step in hydrate formation.

Pinder[85] studied the formation of THF hydrate and showed that the rate of hydrate formation could be diffusion dependent.

However the majority of the work in this area has come from the laboratory of Bishnoi. The earliest work was that of Vysniauskas and Bishnoi[43,44,45] who investigated the kinetics of methane and ethane hydrate formation. They observed that the growth of hydrates is dependent on the interfacial area, pressure, temperature and the degree of subcooling. In addition they developed a semi-empirical model for the gas consumption rate.

This work was followed by that of Englezos *et al.*[51,52] who developed a mechanistic model for hydrate formation fitted to data for methane and ethane hydrates which was then extended to growth data for mixtures of methane and ethane to match hydrate growth at times less than 200 minutes. Englezos assumed that hydrate formation was composed of three steps:

a) transport of gas from the vapour phase to the liquid phase;

b) diffusion of gas from the liquid phase through a boundary layer around the hydrate particles;

c) reaction of particles at the hydrate interface.

As water is in excess the reaction at the interface is assumed to be of first order in gas concentration. The model contains only one adjustable parameter which represents the rate constant for hydrate growth. Dholabhai[86] then extended this model to the kinetics of methane hydrate formation in electrolyte solutions without the need for further parameters.

Other work in this area includes that of Shindo *et al.*[87,88] who proposed a model for carbon dioxide hydrate formation at the interface between liquid carbon dioxide and water. Hydrate formation was assumed to occur mainly in the liquid carbon dioxide and not in the water and was considered as a first order homogeneous reaction between carbon dioxide and water.

Skovborg and Rasmussen[89] in 1994 proposed a simplification of the Englezos model to account only for mass transfer effects *i.e.* transport of gas through the liquid film at the gas-liquid interface. The model was extrapolated to much longer times than the Englezos model, *e.g.* 25 hours, and showed an acceptable fit for both methane and ethane hydrates as well as methane/ethane mixtures.

Ohmura *et al.*[90] studied the growth of CH_3CCl_2F (*i.e.* R141b) hydrate—a structure II hydrate. Each experiment consisted of immersing a drop of R141b at a temperature higher than the water/hydrate/liquid R141b equilibrium temperature, T_{trip}, into a pool of water, the water being either pure (having had no prior contact with R141b) or water presaturated with R141b. Hydrate formation was induced by sprinkling a trace amount of hydrate particles into the system which had been prepared in advance.

For presaturated water held at subcoolings of ~ 6.5 K below T_{trip}, two stages of hydrate crystal growth were observed, which were significantly different in both the crystal growth morphology and time span. The first stage was characterised by lateral

growth of a thin, fine-grained polycrystalline layer along the surface of each R141b drop for a period of several tens of seconds. The second stage began after a delay of about 10 minutes and continued for a few tens of hours; it was characterised by radial growth of plate-like crystals that stood upright on the outer surface of the drop-enclosing hydrate shell formed in the first stage, and protruded into the liquid water phase. The second stage was never observed with pure water and/or at small subcoolings $\leq$ 2 K.

Uchida *et al.*[60] studied the formation of clathrate hydrate films at an interface between water and carbon dioxide. They found that the growth rate was mainly temperature dependent, suggesting that the limiting process for growth is heat diffusion from reaction sites In addition the thickening of the hydrate film was observed to occur mainly in the water phase.

1.9 Inhibition of Gas Hydrate Formation

The inhibition of gas hydrate formation is necessitated by the fact that during the exploration process of natural gas and oil the conditions can be conducive to the formation of gas hydrates. It is therefore essential to have the ability to suppress the formation/growth of gas hydrates in order to prevent them from reducing the efficiency of the pipeline, or possibly blocking it completely.

At present the formation of gas hydrates may be inhibited in one of several ways:

a) by removing free water from the system;
b) by maintaining the temperature of the system above the hydrate equilibrium formation temperature for the given operating pressure;
c) by maintaining the pressure of the system below the hydrate equilibrium formation pressure for the given operating temperature;

d) using chemical inhibition, whereby the formation or growth of gas hydrates is modified by adding particular chemicals to the pipeline.

Options a) and b) are very expensive with option a) requiring expensive equipment at the gas source and option b) estimated to cost ~ $1million per mile to insulate subsea pipelines.[91] Option c) is not practical in subsea transmission pipelines or on drilling platforms. Therefore option d) is the favoured choice of industry.

1.9.1 Chemical Inhibition of Gas Hydrate Formation

Chemical inhibition may be one of two main types:

a) thermodynamic; or

b) kinetic.

Thermodynamic inhibitors act by disrupting the hydrogen-bonding network characteristics of the gas hydrate lattice. The result of this is that the gas hydrate formation temperature is shifted to a lower value. In thermodynamic terms they increase the activity of water in the liquid state or decrease its chemical potential. Examples of such chemicals used by the gas/oil industry are glycol and methanol. The problem with these types of inhibitor is that they are required in large quantities, anything from 10–50 % by weight of water, which makes them a major financial consideration. It is estimated that the worldwide operational expenditure on methanol as a gas hydrate inhibitor is in excess of $500 million per annum.[92] In addition there is a large capital expenditure in engineering plants to process the inhibitors: Sloan[93] estimated that 5–8 % of the total cost of building a plant is the capital cost required to prevent gas hydrate formation.

Kinetic inhibitors are inhibitors that affect the crystallisation process of the gas hydrates. This can occur in one of two ways:

a) by delaying the onset of nucleation; or

b) by modifying the crystal growth patterns, thereby leading to crystals of a different shape and size, and thus giving a suspension with acceptable rheological properties.

Examples of such chemicals are polyvinylpyrrolidone (PVP) and vinylcaprolactam based polymers such as polyvinylcaprolactam (PVcap) and VC-713 (a terpolymer of vinylcaprolactam, vinylpyrrolidone and dimethylaminoethyl methacrylate). The great advantage of these types of inhibitors is that they are required in much lower concentrations. Kinetic inhibitors are effective at concentrations of less than 1 wt. % in the aqueous phase.[94] This is because kinetic inhibitors are only needed to modify the crystallisation process, and for natural gas hydrates this occurs only at the water/hydrocarbon interface.

1.9.2 Mode of Action of Kinetic Inhibitors

The theoretical picture of the mode of action of kinetic inhibitors draws ideas from two areas:

a) the anti-freeze glycopeptides found in Antarctic fish, especially Winter Flounder;

b) growth inhibition of crystalline salts.

Antarctic fish use a class of glycopeptide molecules capable of acting as cryoprotectants which allow them to live in temperatures below 0 °C. These glycopeptides are thought to act by adsorption to a planar ice front through hydrogen-bonding to oxygen atoms in the ice lattice.[95,96] This binding is assumed to occur between polar groups on the peptide and water molecules in the surface of the

ice lattice. Initial modelling studies supported this, but found van der Waals forces to be more important than hydrogen-bonding.

Lal *et al.*[97] carried out a molecular modelling study of the inhibition of ice crystal growth by the anti-freeze peptide found in the Winter Flounder. They studied the relative binding of the anti-freeze peptide to the faces and internal planes of the ice (Ih) crystal, in particular the *c*-face and $20\bar{2}1$ plane. They found that the *in-vacuo* binding energies of the anti-freeze peptide for the *c*-face and the $20\bar{2}1$ plane differed by more than three, which they suggested could account for the preferential adsorption of the anti-freeze peptide to the $20\bar{2}1$ plane than for the *c*-face. In addition they concluded that the mode of adsorption was due to a near-perfect steric fit of the $20\bar{2}1$ plane to the anti-freeze peptide in a 'lock and key' fashion, as the propensities of the anti-freeze peptide to hydrogen bond with the *c*-face and $20\bar{2}1$ plane are almost identical.

Mullin[98] presented a model of salt crystal growth inhibition in 1993. In this theoretical model inhibitor molecules adsorb to terraces, steps and kink sites. The adsorbed molecules then prevent crystal growth at the molecular adsorption site.

Kinetic inhibition of gas hydrates is envisaged to be an amalgam of these two theoretical pictures.

The research into kinetic inhibitors and their mode of action can be split into three main areas as follows:

a) computational studies;

b) experimental studies;

c) crystal growth studies, which constitute neither computational nor experimental studies.

Computational Studies of Gas Hydrate Kinetic Inhibitors

Carver *et al.*[99] studied the mechanism of kinetic inhibition by PVP on a structure I gas hydrate. Monte Carlo calculations were carried out on PVP monomers, dimers, tetramers and octamers adsorbed to the {0 0 1} gas hydrate surfaces. Adsorption was found to occur predominantly through the formation of two hydrogen bonds between the pyrrolidone oxygen and the gas hydrate lattice, with adsorption being dependent on the availability of pendant hydrogens on the gas hydrate surface. The hydrogen-bonding distances observed were similar to those in the gas hydrate lattice itself and it was suggested that the pyrrolidone oxygen was being built into the gas hydrate lattice. The method of inhibition was proposed as PVP adsorption to the gas hydrate lattice surface preventing further crystal growth.

A second study[100] looked at the mechanism of kinetic inhibition by PVP on a structure II gas hydrate. Monte Carlo studies were used to study the adsorption of N-ethylpyrrolidone onto the {1 1 1} gas hydrate surface. Once again hydrogen bonds were observed between the pyrrolidone oxygen and the gas hydrate lattice, however this was complemented by a van der Waals contribution derived by adsorption of the pyrrolidone ring into a partially formed hexakaidecahedral cage. Makogon[101] with PVcap also observed adsorption into the hexakaidecahedral cages of structure II gas hydrates.

The technique of molecular dynamics was used by Kvamme *et al.*[102] to study a PVP monomer in water and water/gas hydrate systems. Adsorption was found to occur through hydrogen-bonding between the gas hydrate lattice and PVP, with PVP preferring to be orientated perpendicular to the gas hydrate surface.

Jussaume *et al.*[103] developed an efficiency scale to allow for the identification of potential gas hydrate inhibitors. The method was found to be suitable for small

molecules and could be used to identify monomer units for inclusion in new polymeric inhibitors.

Experimental Studies of Gas Hydrate Kinetic Inhibitors

Kelland *et al.*[104] studied the control of gas hydrate formation by surfactants and polymers. Their study identified three types of kinetic inhibitor:

a) gas hydrate growth delay inhibitors which delay the growth of gas hydrate crystals for substantial periods but after a certain gas uptake eventually allow blockage of pipelines;

b) chemicals that allow the gas hydrate to form but prevent agglomeration of the crystals so that a transportable slurry is maintained (anti-agglomerants);

c) dual purpose inhibitors which display characteristics of a) and b).

However, the dual purpose inhibitors they reported generally showed poor gas hydrate growth delay properties.

Notz *et al.*[94] reported the successful use of PVP in three gas wells in southwestern Wyoming and in five gas pipelines in east Texas. In the Wyoming case PVP was used at 0.3 wt.% or less in the aqueous phase and gas hydrate plugging was eliminated. In the east Texas case PVP was at < 0.1 wt.% in the aqueous phase and the problem of plugging was reduced but not totally eliminated; however it must be noted that the residence times for gas in the pipeline were much greater in this case than in the southwestern Wyoming application. They concluded that use of PVP instead of methanol as a gas hydrate inhibitor should be considered when the subcooling is less than 5–10 °F and/or if the residence time is less than a few minutes. The advantages in favour of this recommendation were that: (i) only minor modifications were required to existing methanol injection facilities; (ii) PVP is non-

toxic in contrast to methanol; and (iii) treatment costs were reduced by 50 % or more in the Wyoming test.

Bloys *et al.*[105] presented results of a field trial of VC713 in a 9.4 km transmission line in the southern North Sea Gas Basin. VC713 effectively inhibited gas hydrate formation at both 0.5 and 0.25 wt.% concentrations with the maximum effective subcooling being 9 °C; at higher subcoolings gas hydrates began to form at steady rates. It was concluded that for a new platform the economics of kinetic inhibition were 'more attractive'.

Pakulski[106] presented results for experimental tests on PVP, VC713 and an experimental compound. The inhibitors were tested at 0.5 wt.% and found to be more effective than existing ethylene glycol thermodynamic inhibitors.

Urdahl *et al.*[107] tested a number of surfactants, polymers and patented chemicals in a high-pressure test wheel. For the surfactants tested, anionic surfactants showed no improvements, non-ionic surfactants showed some positive effects but the concentration required was several percent of the aqueous phase and they did not prevent gas hydrate deposition on the pipe wall. No effect was observed with the polymers tested. Tyrosine was tested as a patented chemical but did not exhibit gas hydrate kinetic inhibition; in fact they concluded that experimental verification of the efficiency of patented chemicals had not been adequate.

Lederhos *et al.*[91] tested the efficiency of PVcap, VC713 and a copolymer of vinylpyrrolidone and vinylcaprolactam, VP/VC, with different ratios of each constituent homopolymer. VC713 was found to be unable to inhibit massive amounts of gas hydrates at high pressures (10.3 MPa) however at moderate pressures VC713 was able to delay gas hydrate formation for at least 20 hours at 0.5 wt.%. PVcap was found to allow a large amount of gas hydrate to form at high pressures (10.3 MPa)

while at pressures less than 6.9 MPa little gas was consumed at 0.5 wt.%. VP/VC with ratios of VP/VC equal to or less than 25/75 were as effective inhibitors as either PVcap or VC713 alone.

Lederhos *et al.*[91] also proposed a hypothesis for inhibition due to the fact that the sizes of the five- and seven-member lactam rings are similar to the five- and six-member faces respectively in the gas hydrate cages. This suggested that the lactam rings of PVcap and VC713 adsorb onto the gas hydrate crystals through hydrogen-bonding by the amide group and sterically block gas hydrate growth. The polymer network was envisaged to extend between small, stabilised gas hydrate particles simultaneously providing an inhibiting structure to the surrounding water while blocking the most active growth sites of the gas hydrate crystals.

Cohen *et al.*[108] observed that glycol ethers provided powerful synergism with kinetic inhibitors. They tested VC713, PVcap and VC/VP polymers at 0.5 wt.% with various glycol ethers at 0.75 wt.% and found that glycol ethers with three or four carbons in the alkoxy group enhanced gas hydrate inhibition. For example with 0.5 wt.% VC713 the gas hydrate induction time was increased from 40 minutes to 1200 minutes on the addition of 0.75 wt.% 2-butoxyethanol. They suggested that due to the fact that glycol ethers, especially the higher homologs, have surfactant-like properties the hydrophobicity of the alkoxy group might cause the molecules to associate with the dissolved polymer. This may affect the conformation of the polymer with an extended polymer having more of its length available for interaction with the gas hydrate crystal.

Sloan *et al.*[109] studied the effectiveness of PVcap on gas hydrate formation. They found that increasing concentration of PVcap gave an asymptotic increase in subcooling with increasing concentration, and that low molecular weights of PVcap

were more effective. In addition it was found that PVcap was less effective in the presence of methanol and that salt concentrations above 5.0 wt.% showed improved subcooling with PVcap.

Recently King *et al.*,[110,111] used neutron scattering to study the conformation of polymeric gas hydrate kinetic inhibitors. They studied three kinetic inhibitors, namely PVP, PVcap and N-vinylacetamide/N-vinyl-2-caprolactam as well as polyethylene as a control. They found that the kinetic inhibitors change their conformation in the temperature range where gas hydrate crystals coexist with a liquid, and ascribed this to an adsorbed polymer layer on the gas hydrate crystals. In addition, low-q scattering was used as a measure of the inhibitor adsorption and a correlation was found between inhibitor activity and the amplitude of scattering. From this they suggested that the principle mechanism of gas hydrate kinetic inhibition involves surface adsorption onto growing gas hydrate crystals with resultant slowing of growth.

Crystal Growth Studies of Gas Hydrate Kinetic Inhibitors

Larsen *et al.*[112] studied the growth of THF hydrate with and without kinetic inhibitors. They studied the effect of PVP, PVcap and VC713 on the crystal growth habit and found that with inhibitor present crystal morphology changed from 3-D octahedrons to 2-D hexagonal plates at inhibitor concentrations lower than 0.1 wt.%. Higher concentrations of inhibitors were enough to stop growth completely at low subcoolings. They believed that the inhibitors affect the THF hydrate crystals by surface adsorption on already established crystal faces, and that the inhibition effect was strongly dependent on the pendant groups of the polymers. Once adsorbed to the THF hydrate crystal surface the polymers were thought to be hard to remove and that

the backbone acts as a barrier to further availability of hydrate former molecules on the growing surface.

Makogon *et al.*[68] also studied the growth of THF hydrate and its inhibition. The effect of PVP, PVcap and VC713 was investigated. Once again it was observed that upon addition of an inhibitor the THF hydrate crystals changed their morphology from 3-D octahedrons to 2-D hexagonal plates. In addition it was found that the hexagonal plate thickness decreased with increasing inhibitor concentration until growth was completely inhibited. The concentration of polymer required to inhibit growth completely was dependent on the subcooling.

Larsen *et al.*[67] have recently carried out a study into the inhibition of ethylene oxide hydrate by PVP, PVcap and VC713. It was found that upon the addition of PVP no crystal habit changes were observed. However the growth rate was reduced by more than 50 % at 0.1 wt.% polymer concentrations. Upon the addition of PVcap or VC713 at concentrations of between 0.05–0.25 wt.% small scale branching of the crystals resulting in spherical globules composed of flimsy branches was observed. At higher concentrations, dependent on the subcooling, PVcap and VC713, completely inhibited the crystal growth.

1.10 References

[1] Rodger P.M., *J. Phys. Chem.*, **93**, 1989, 6850.

[2] Davy H., *Philos. Trans. R. Soc.*, **101**, 1811, 1.

[3] Faraday M., *Philos. Trans. R. Soc.*, **113**, 1823, 160.

[4] Sloan E.D., *Clathrate Hydrates of Natural Gases*, Marcel Dekker, Inc., 1990.

[5] Hammerschmidt E.G., *Ind. Eng. Chem.*, **26**, 1934, 851.

[6] Ripmeester J.A., Tse J.S., Ratcliffe C.I., Powell B.M., *Nature*, **325**, 1987, 135.

[7] Lyusternik L.A., *Convex Figures and Polyhedra*, Dover, 1963.

[8] Von Stackelberg M., *Rev. Trav. Chim.*, **75**, 1956, 902.

[9] Gerke H., Gies H., *Zeit. Fur Kristall.*, **11**, 1984, 166

[10] Trofimuk A.A., Cherski N.V., Tsaryov V.P., *The Future Supply of Nature-made Petroleum and Gas*, R. F. Meyer ed., Pergamon Press, 1977.

[11] McIver R.D., *Long-term Energy Resources*, R.F. Meyer and J.C. Olson eds., Pitman, 1981.

[12] Dobrynin V.N.M., Korotajev Y.P., Plyuschev D.V., *Long-term Energy Resources*, R.F. Meyer and J.C. Olson eds., Pitman, 1981.

[13] MacDonald G.J., *Annual Review of Energy*, **15**, 1993, 53.

[14] Gornitz V., Fung I., *Global Biogeochemical Cycles*, **8**, 1994, 335.

[15] Meyer R.F., *Long-term Energy Resources*, R.F. Meyer and J.C. Olson eds., Pitman, 1981.

[16] Prensky S.E., Meeting of the Society of Professional Well Log Analysts, Paris, France, 26–29 June, 1995.

[17] Kvenvolden K.A., *The Future of Energy Gases: U.S. Geological Survey Professional Paper*, **1570**, 1993, 555.

[18] Chersky N.J., Makogon Y.F., *Oil Gas Int.*, **10**, 1970, 82.

[19] Kvenvolden K.A., *Chemical Geology*, **71**, 1988, 51.

[20] Miller S.L. Delsemme A.H., *Planet. Space Sci.*, **18**, 1970, 709.

[21] Englezos P., *Ind. Eng. Che. Res.*, **32**, 1993, 1251.

[22] McDermott J., *Desalination by Freeze Concentration*, Noyes Data Corp., Park Ridge, New Jersey, USA, 1971.

[23] Berecz E., Balla-Achs M., *Studies in Inorganic Chemistry 4: Gas Hydrates*, Elsevier, Amsterdam, Holland, 1983.

[24] Werezac G.N., *AIChE Symp. Ser.*, **65**, 1969, 6.

[25] Huang C.P., Fennema O., Powrie W.D., *Cryobiology*, **2**, 1965, 109.

[26] Berner D., Proceedings of the 2nd International Offshore and Polar Engineering Conference, San Francisco, USA, 14–19 June, 1992.

[27] Stevenson S., *Pulp. Paper Can.*, **93**, 1992, 13.

[28] Bell P.R., *Carbon Dioxide Review*, W.C. Clark ed., Oxford University Press, New York, USA, 1982.

[29] Taylor F.W., *Rep. Prog. Phys.*, **54**, 1991, 881.

[30] Kvenvolden K.A., *Global Biogeochem. Cycles*, **2**, 1988, 221.

[31] Barrer R.M., Ruzicka D.J., *Trans. Far. Soc.*, **58**, 1962, 2262.

[32] Barrer R.M., Edge A.V.J., *Proc. Roy. Soc.*, **A300**, 1967, 1.

[33] Wright D.A., A Kinetic Study of Methane Hydrate Formation from Ice, MS Thesis, U. of Pittsburgh, 1985.

[34] Hwang M.J., Wright D.A., Kapur A., Holder G.D., *J. Inclusion Phenomena*, D.W. Davidson Memorial Issue, **8**, 1990, 103.

[35] Falabella B.J., A Study of Natural Gas Hydrates, PhD Diss., U. of Mass., 1975.

[36] Sloan E.D., Fleyfel F., *AIChE Journal*, **37**, 1991, 1281.

[37] Glew D.N., *Nature*, **184**, 1959, 545.

[38] Stern L.A., Kirby S.H., Durham W.B., *Science*, **273**, 1996, 1843.

[39] Stern L.A., Kirby S.H., *Energy and Fuels*, **12**, 1998, 201.

[40] Stern L.A., Hogenboom D.L., Durham W.B., Kirby S.H., Chou I.M., *J. Phys. Chem. B*, **102**, 1998, 2627.

[41] Henning R.W., Schultz A.J., Mori Y.H., Halpern Y., *J. Phys. Chem*, **104**, 2000, 5066.

[42] Stern L.A., Kirby S.H., *Energy and Fuels*, **12**, 1998, 201.

[43] Vysniauskas A., Bishnoi P.R., Natural Gas Hydrates: Properties, Occurrence and Recovery, J.L. Cox ed., Butterworths, 1983.

[44] Vysniauskas A., Bishnoi P.R., *Chem. Eng. Sci.*, **38**, 1983, 1061.

[45] Vysniauskas A., Bishnoi P.R., *Chem. Eng. Sci.*, **40**, 1985, 299.

[46] Nerheim R.A., Svartaas T.M., Samuelson E.K., Proceedings of the 2nd International Offshore and Polar Engineering Conference, San Francisco, USA, 14–19 June, 1992, 620.

[47] Monfort J.P., Nzihou A., *J. Crystal Growth*, **128**, 1993, 1182.

[48] Monfort J.P., Nzihou A., Annals of New York Academy of Sciences, **715**, 1994, 555.

[49] Fleyfel F., Song K.Y., Kook A., Martin R., Kobayashi R., Annals of New York Academy of Sciences, **715**, 1994, 212.

[50] Baez A.L., Clancy P., Annals of New York Academy of Sciences, **715**, 1994, 177.

[51] Englezos P., Kalogerakis N., Dholabhai P.D., Bishnoi P.R., *Chem. Eng. Sci.*, **42**, 1987, 2647.

[52] Englezos P., Kalogerakis N., Dholabhai P.D., Bishnoi P.R., *Chem. Eng. Sci.*, **42**, 1987, 2659.

[53] Englezos P., Bishnoi P.R., *Fluid Phase Equil.*, **42**, 1988, 129.

[54] Lingelem M., Majeed A., Challenges in Areas of Multiphase Transport and Hydrate Control for a Subsea Gas Condensate Production System, Proceedings of the 68th Annual Gas Processors Association Convention, San Antonio, USA, 13–14 March, 1989.

[55] Muller-Bongartz B., Wildeman T.R., Sloan E.D., A Hypothesis for hydrate Nucleation Phenomena, Proceedings of the 2nd International Offshore and Polar Engineering Conference, San Francisco, USA, 14–19 June, 1992, 628.

[56] Levkam K., Ruoff P., *J. Am. Chem. Soc.*, **115**, 1993, 8565.

[57] Levkam K., Ruoff P., *J. Crystal Growth*, **179**, 1997, 618.

[58] Malegainkar M.B., Dholabhai P.D., Bishnoi P.R., *Can. J. Chem. Eng.*, **75**, 1997, 1090.

[59] Bowron D.T., Filipponi A., Roberst M.A., Finney J.L., *Physical Review Letters*, **81**, 1998, 4164.

[60] Uchida T., Ebinuma T., Kawabata J., Norita H., *J. Crystal Growth*, **204**, 1999, 348.

[61] Nerheim A.R., Investigation of Gas Hydrate Formation Kinetics by Laser Light Scattering, D.Ing. Thesis, Norwegian Institute of Technology, Trondheim, 1993.

[62] Parent J.S., Investigations into the Nucleation Behaviour of Natural Gas Components, MSc Thesis, U. of Calgary, 1993.

[63] Skovborg P., Ng H.J., Rasmussen P., Mohn U., *Chem. Eng. Sci.*, **48**, 1993, 445.

[64] Natarajan V., Thermodynamics and Nucleation Kinetics of Gas Hydrates, PhD Diss., U. of Calgary, 1993.

[65] Nerheim A.R., Svartaas T.M., Samuelson E.K., Proceedings of the 4th International Offshore and Polar Engineering Conference, Osaka, April, 1994, 323.

[66] Parent J.S., Bishnoi P.R., *Chem. Eng. Comm.*, **144**, 1996, 51.

[67] Larsen R., Knight C.A., Rider K.T., Sloan E.D., *J. Crystal Growth*, **204**, 1999, 376.

[68] Makogon T.Y., Larsen R., Knight C.A., Sloan E.D., *J. Crystal Growth*, **179**, 1997, 258.

[69] Smelik E.A., King H.E., *American Mineralogist*, **82**, 1997, 88.

[70] McMullan R.K., Kvick A., *Acta Crystallograhica B*, **46**, 1990, 390.

[71] Bertie J.E., Bates F.E., Hendricksen D.K., *Can. J. Chem.*, **53**, 1975, 71.

[72] Bertie J.E., Jacobs S.M., *Can. J. Chem.*, **55**, 1977, 1777.

[73] Bertie J.E., Jacobs S.M., *J. Chem. Phys.*, **69**, 1978, 4105.

[74] Bertie J.E., Jacobs S.M., *J. Chem. Phys.*, **77**, 1982, 3230.

[75] Bertie J.E., Devlin J.P., *J. Chem. Phys.*, **78**, 1983, 6340.

[76] Richardson H.H., Wooldridge P.J., Devlin J.P., *J. Chem. Phys.*, **83**, 1985, 4387.

[77] Richardson H.H., Wooldridge P.J., Devlin J.P., *J. Phys. Chem.*, **89**, 1985, 3552.

[78] Wooldridge P.J., Richardson H.H., Devlin J.P., *J. Chem. Phys.*, **87**, 1987, 4126.

[79] Fleyfel F., Devlin J.P., *J. Phys. Chem.*, **92**, 1988, 631.

[80] Hwang M.J., Wright D.A., Kapur A., Holder G.D., *J. Inclusion Phenomena*, **8**, 1990, 103.

[81] Knox W.G., Hess M., Jones G.E., Smith H.B., *Chem. Eng. Prog.*, **57**, 1961, 66.

[82] Grauuw J.D., Rutten J.J., *Proc. Int. Fresh Water Sea*, **3**, 1970, 103.

[83] Glew D.N., Haggett M.L., *Can. J. Chem.*, **46**, 1968, 3857.

[84] Glew D.N., Haggett M.L., *Can. J. Chem.*, **46**, 1968, 3867.

[85] Pinder K.L., *Can. J. Chem. Eng.*, **10**, 1965, 271.

[86] Dholabhai P.D., Kalogerakis N., Bishnoi P.R., *SPE Prod. & Facil.*, August, 1993, 185.

[87] Shindo Y., Lund P.C., Fujioka Y., Komiyama H., *Int. J. of Chem. Kin.*, **25**, 1993, 777.

[88] Shindo Y., Lund P.C., Fujioka Y., Komiyama H., *Energy Conversion and Management*, **34**, 1993, 1073.

[89] Skovborg P., Rasmussen P., *Chem. Eng. Sci.*, **49**, 1994, 1131.

[90] Ohmura R., Shigetomi T., Mori Y.H., *J. Crystal Growth*, **196**, 1999, 164.

[91] Lederhos J.P., Long J.P., Sum A., Christiansen R.L., *Chem. Eng. Sci.*, **51**, 1996, 1221.

[92] Anderson F.E., Prausnitz J.M., *AIChE Journal*, **32**, 1986, 1321.

[93] Sloan E.D., *J. Pet. Technol.*, **43**, 1991, 1414.

[94] Notz P.K., Bumgartner S.B., Schaneman B.D., Todd J.L., The Application of Kinetic Inhibitors to Gas Hydrate Problems, Offshore Technology Conference, Houston, USA, 1–4 May, 1995.

[95] Knight C.A., Cheng C.C., DeVries A.L., *Biophys. J.*, **59**, 1991, 409.

[96] Chakrabartty A., Yang D.S.C., Hew C.L., *J. Biol. Chem.*, **264**, 1989, 11313.

[97] Lal M., Clark A.H., Lips A., Ruddock J.N., White D.N.J., *Faraday Discuss.*, **95**, 1993, 299.

[98] Mullin J.W., Crystallization, 3rd Edition, Butterworth-Heinemann, 1993

[99] Carver T.J., Drew M.G.B., Rodger P.M., *J. Chem. Soc. Faraday Trans.*, **91**, 1995, 3449.

[100] Carver T.J., Drew M.G.B., Rodger P.M., *J. Chem. Soc. Faraday Trans.*, **92**, 1996, 5029.

[101] Makogon T.Y., Kinetic Inhibition of Natural Gas Hydrates, PhD Thesis, Colorado School of Mines, 1997.

[102] Kvamme B., Huseby G., Forrisdahl O.K., *Molecular Physics*, **90**, 1997, 979.

[103] Jussaume L., Canselier J.P., Monfort J.P., Rodger P.M., Molecular Modelling of the Interaction of Additives on Type II Gas Hydrate Surfaces: Development of an Efficiency Parameter, Proceedings AIChE Meeting, Miami-Beach, USA, 15–20 November, 1998.

[104] Kelland M.A., Svartaas T.M., Dybvik L.A., Control of Hydrate Formation by Surfactants and Polymers, SPE 69th Annual Technical Conference and Exhibition, New Orleans, USA, 25–28 September, 1994.

[105] Bloys B., Lacey C., Lynch P., Laboratory Testing and Field Trial of a New Kinetic Hydrate Inhibitor, Offshore Technology Conference, Houston, USA, 1–4 May, 1995.

[106] Pakulski M., High Efficiency Non-Polymeric Gas Hydrate Inhibitors, International Symposium on Oilfield Chemistry, Houston, USA, 18–21 February, 1997.

[107] Urdahl O., Lund A., Mork P., Nilsen T.N., *Chem. Eng. Sci.*, **50**, 1995, 863.

[108] Cohen J.M., Wolf P.F., Young W.D., *Energy and Fuels*, **12**, 1998, 216.

[109] Sloan E.D., Subramanian S., Matthews P.N., Lederhos J.P., Khokhar A.A., *Ind. Eng. Chem. Res.*, **37**, 1998, 3124.

[110] King H.E., Hutter J.L., Lin M.Y., Sun T., *J. Chem. Phys.*, **112**, 2000, 2523.

[111] Hutter J.L., King H.E., Lin M.Y., *Macromolecules*, **33**, 2000, 2670.

[112] Larsen R., Makogon T.Y., Knight C.A., Sloan E.D., Hydrates in Multiphase Flow and Kinetic Inhibition in a Model System, Proceedings of the 2nd International Conference on Natural Gas Hydrates, Toulouse, France, 2–6 June, 1996.

CHAPTER 2

SIMULATION TECHNIQUES

2 Introduction

In this chapter the techniques used to carry out the simulations in this thesis are outlined. The chapter is divided into eight parts as outlined below.

2.1 Statistical mechanics.

2.2 Molecular Dynamics.

2.3 Simulation cell.

2.4 Periodic boundary conditions.

2.5 Force fields.

2.6 Charges.

2.7 Conformational search methods.

2.8 Minimising algorithms.

2.1 Statistical Mechanics

The fundamental postulate of statistical mechanics states that the observed properties of a system are the average of the microscopic properties of all possible micro-states consistent with the thermodynamic state of the system. Statistical mechanics therefore provides us with a mechanism by which we can determine macroscopic thermodynamic properties such as entropy or enthalpy. In principle, any observable that can be expressed as a function of atomic positions and velocities can be evaluated.

For a system containing N atoms, $6N$ values are required to define the state of the system (3 co-ordinates per atom and 3 components of momentum). Each combination of $3N$ positions and $3N$ momenta defines a point in the $6N$ dimensional space, known as phase space. If Γ denotes a point in phase space, then it can be assumed that an experimental observable associated with a property A, denoted A_{obs} may be expressed as an average of the microscopic value $A(\Gamma)$:

$$A_{obs} = \langle A \rangle = \int A(\Gamma) f(\Gamma) d\Gamma \qquad \textit{Equation 2.1}$$

where $f(\Gamma)$ is the normalised probability density. Over time, the instantaneous value of the property A fluctuates as a result of interactions between particles. The value of A derived is therefore an average over the time of interest and is therefore known as a time average. As time increases to infinity so the value of the following integral approaches the 'true' average value of the property.

$$\int_0^\infty A(\Gamma(t))dt = \int A(\Gamma_i) f(\Gamma_i) d\Gamma \qquad \textit{Equation 2.2}$$

To calculate the average values of the properties of the system, it would therefore appear necessary to simulate the dynamical behaviour of the system. The difficulty is that for

'macroscopic' numbers of atoms or molecules (of the order of 10^{23}) it is not even feasible to determine an initial configuration of the system. Gibbs recognised this difficulty and suggested replacing the time average with an ensemble average, this suggestion was the basis of the Ergodic Hypothesis which states that the time average is equal to the ensemble average (*i.e.* equation 2.2 is valid). An ensemble is therefore a collection of points Γ in phase space, distributed according to a probability density $\rho(\Gamma)$. Each microstate that is generated then becomes part of the ensemble of microstates, such that the microstates are consistent with the fixed macroscopic variables. The four main ensembles in statistical mechanics and their fixed macroscopic variables are:

i) microcanonical–fixed N, V, E;

ii) canonical–fixed N, V, T;

iii) isothermal-isobaric–fixed N, P, T;

iv) grand canonical–fixed μ, V, T.

The ensemble average of a system $\langle A \rangle_{ens}$ is given by:

$$\langle A \rangle_{ens} = \frac{1}{Q_{ens}} \sum_{\Gamma_i} A(\Gamma_i)\rho(\Gamma_i) \qquad \textit{Equation 2.3}$$

where

$$Q_{ens} = \sum_{\Gamma_i} \rho(\Gamma_i) \qquad \textit{Equation 2.4}$$

and

$$f(\Gamma) = \frac{1}{Q_{ens}} \rho(\Gamma) \qquad \textit{Equation 2.5}$$

where Q_{ens} is the partition function or 'sum over states' and $\langle A \rangle_{ens}$ indicates an ensemble average.

In order to calculate a particular property a method must be found of searching phase space. There are two methods that are commonly used to carry this out: molecular dynamics, (MD) and Monte Carlo, (MC). MD uses Newton's equations of motion to follow the time evolution of the system. Monte Carlo generates the configurations of the system by generating random moves and accepting or rejecting the new configuration on the basis of a Boltzmann probability. Both of these methods require the energy to be calculated and this normally involves the use of empirical force fields. In the following sections an outline of the theory of the molecular dynamics technique and the force fields used in this work is given.

2.2 Molecular Dynamics

The Molecular Dynamics method is used to produce a trajectory that specifies how the positions and velocities of the particles in a system vary with time. Central to the molecular dynamics method are two mathematical concepts and these are:

i) finite difference methods based upon a Taylor series expansion;

ii) Newton's second law of motion.

In the simplest of cases, where the acceleration of the particles is constant, then Newton's second law of motion can be used to integrate the equations of motion to determine the velocities and positions of the particles in the system. However in the majority of systems studied this is not the case and the acceleration is not constant. Therefore one is faced with a many-body problem that cannot be solved analytically in this way. In order to overcome this difficulty finite difference methods are employed. Finite difference methods are based upon the assumption that the positions and

dynamical properties (velocities, accelerations *etc.*) of a system can be approximated by a Taylor series expansion:

$$\boldsymbol{r}(t+\delta t)=\boldsymbol{r}(t)+\delta t\boldsymbol{v}(t)+\frac{1}{2}\delta t^{2}\boldsymbol{a}(t)+\frac{1}{6}\delta t^{3}\boldsymbol{b}(t)+\frac{1}{24}\delta t^{4}\boldsymbol{c}(t)+\ldots. \quad \textit{Equation 2.6}$$

$$\boldsymbol{v}(t+\delta t)=\boldsymbol{v}(t)+\delta t\boldsymbol{a}(t)+\frac{1}{2}\delta t^{2}\boldsymbol{b}(t)+\frac{1}{6}\delta t^{3}\boldsymbol{c}(t)+\ldots. \quad \textit{Equation 2.7}$$

$$\boldsymbol{a}(t+\delta t)=\boldsymbol{a}(t)+\delta t\boldsymbol{b}(t)+\frac{1}{2}\delta t^{2}\boldsymbol{c}(t)+\ldots. \quad \textit{Equation 2.8}$$

$$\boldsymbol{b}(t+\delta t)=\boldsymbol{b}(t)+\delta t\boldsymbol{c}(t)+\ldots. \quad \textit{Equation 2.9}$$

$\boldsymbol{v}$ is the velocity (the first derivative of the position with respect to time); $\boldsymbol{a}$ is the acceleration (the second derivative of the position with respect to time); $\boldsymbol{b}$ is the third derivative; and so on. It must be noted that this approach is an approximation and therefore there are associated errors, which are:

i) truncation errors–related to the accuracy of the finite difference method with respect to the true solution, which are due to the fact that the Taylor series expansion is truncated at some term;

ii) round-off errors–related to implementation of the finite difference method, which are due to the finite number of digits used in computer arithmetic.

One of the most common implementations based upon this approach is the Verlet algorithm.[1] This algorithm uses the positions and accelerations at time t, and the positions from the previous step, $\boldsymbol{r}(t-\delta t)$ to calculate the new positions at $t+\delta t$, $\boldsymbol{r}(t+\delta t)$. To derive the Verlet algorithm one can write the Taylor series expansions for $\boldsymbol{r}(t+\delta t)$ and $\boldsymbol{r}(t-\delta t)$ shown overleaf:

$$\boldsymbol{r}(t+\delta t)=\boldsymbol{r}(t)+\delta t\boldsymbol{v}(t)+\frac{1}{2}\delta t^2\boldsymbol{a}(t)+\frac{1}{6}\delta t^3\boldsymbol{b}(t)+\frac{1}{24}\delta t^4\boldsymbol{c}(t)+\ldots. \quad \textit{Equation 2.10}$$

$$\boldsymbol{r}(t-\delta t)=\boldsymbol{r}(t)-\delta t\boldsymbol{v}(t)+\frac{1}{2}\delta t^2\boldsymbol{a}(t)-\frac{1}{6}\delta t^3\boldsymbol{b}(t)+\frac{1}{24}\delta t^4\boldsymbol{c}(t)-\ldots. \quad \textit{Equation 2.11}$$

Adding of these two equations gives:

$$\boldsymbol{r}(t+\delta t)=2\boldsymbol{r}(t)-\boldsymbol{r}(t-\delta t)+\delta t^2\boldsymbol{a}(t)+O\delta t^4\boldsymbol{c}(t)+\ldots. \quad \textit{Equation 2.12}$$

Therefore to calculate the new positions of the particles in the system we need the current positions ($\boldsymbol{r}(t)$), the previous positions ($\boldsymbol{r}(t - \delta t)$), and the accelerations, of the particles. In order to calculate the accelerations of the particles in the system we use Newton's second law, which states:

$$F = ma \quad \textit{Equation 2.13}$$

where F is the force exerted on a particle, m is its mass and a its acceleration. By simply rearranging equation 2.13 we see that:

$$a = F/m \quad \textit{Equation 2.14}$$

the acceleration of the particles can then be calculated by using the intermolecular forces employed in the system and the mass of the particles.

The Verlet algorithm has a number of advantages and disadvantages, which are:

i) the storage requirements are modest, comprising two sets of positions ($\boldsymbol{r}(t)$ and $\boldsymbol{r}(t - \delta t)$) and the accelerations $\boldsymbol{a}(t)$;

ii) it is straightforward to implement;

iii) there is no explicit velocity term in the equations which means it is difficult to obtain the velocities, and the velocities are not available until the positions have been computed at the next step;

iv) the positions $\boldsymbol{r}(t + \delta t)$ are obtained by adding a small term $\delta t^2\boldsymbol{a}(t)$ to the difference of two much larger terms, $2\boldsymbol{r}(t)$ and $\boldsymbol{r}(t - \delta t)$ and this may lead to a loss of precision;

v) the algorithm is not self-starting. The new positions are obtained from the current positions $\boldsymbol{r}(t)$ and the positions from the previous step, $\boldsymbol{r}(t - \delta t)$. At time t=0 there is only one set of positions and it is therefore necessary to employ some other means to obtain the positions at $t - \delta t$ in order to start the algorithm.

Other algorithms have been developed to overcome the difficulties associated with the Verlet algorithm, however these algorithms have their own inherent advantages and disadvantages, such that the Verlet algorithm remains the most commonly implemented algorithm due to its simplicity.

2.2.1 Molecular Dynamics Simulation Outline

In systems of interest the setting up of an MD run involves several steps. The first is the creation of an equilibrated box of 'solvent', into which the 'solute' of interest is added, the solute is added in such a way that any solvent molecules that create a bad contact with the solute are removed. Bad contacts are defined using the van der Waals radius of the atoms, hence any solvent atom that overlaps with the solute is removed along with the rest of the solvent molecule. The whole system is then subjected to an energy refinement using an energy minimisation algorithm. This energy refinement relieves local stresses due to non-bonded overlaps, as well as bond-length and bond-angle stresses in the solute and solvent. The atoms are then assigned velocities from a Maxwellian distribution at a temperature below the desired temperature; usually, a

temperature near zero is used as the starting temperature. The system is then equilibrated by integrating the equations of motion while adjusting the temperature and density to appropriate values. The temperature is brought into the range of interest by incrementally increasing the velocities of all the atoms, either by reassignment from a Maxwellian distribution at an increased temperature or by scaling all velocities. The instantaneous temperature, $T(t)$, at any given time t is defined in terms of the mean kinetic energy by,

$$T(t) = \frac{1}{(3N - n)k_B} \sum_{i=1}^{N} m_i \mid v_i \mid^2 \qquad \textit{Equation 2.15}$$

where $(3N - n)$ is the total number of unconstrained degrees of freedom in the system, v_i is the velocity of atom i at time t, and k_B is the Boltzmann constant. From this expression, if the velocities are scaled by a factor of,

$$\sqrt{T'/T(t)} \qquad \textit{Equation 2.16}$$

then this will result in a mean kinetic energy corresponding to a temperature of T'. The aim of the heating and equilibration process is that it decreases the probability that localised fluctuations in the energy (*e.g.* 'hot-spots') will still be present at the beginning of the production stage. It also ensures that highly strained regions, that might otherwise lead to catastrophic numerical integration errors, have been removed from the system. Once the equilibration process has been completed then the actual simulation production run can commence.

2.3 Periodic Boundary Conditions

Periodic boundary conditions enable a simulation to be carried out while only using a relatively small number of particles, in such a manner as the particles experience forces

as if they were part of a bulk system. If we consider the central box in figure 2.1, illustrating periodic boundary conditions in two dimensions, then when the particles move the periodic images of these particles move in exactly the same fashion in the surrounding boxes. Therefore as a particle leaves the central box then one of its images will enter the central box through the opposite face, ensuring that the number of particles in the central box remains constant. In addition particles close to the edge of the central box are able to interact with image particles in surrounding boxes. There are no boundaries at the edge of the central simulation box, and so no surface particles in the simulation.

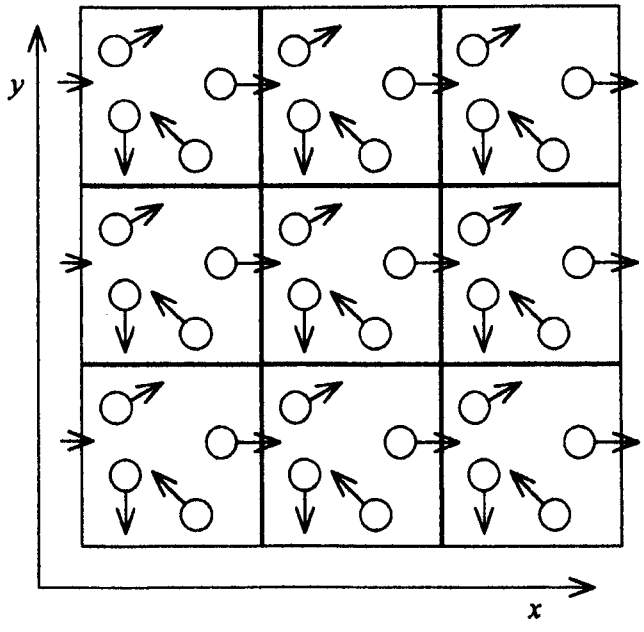

Figure 2.1 Application of periodic boundary conditions.

In principle any cell shape may be used as long as it fills all of space by translation operations of the central box in three dimensions. There are five geometric shapes that satisfy this condition and they are:

i) the cube/parallepiped;

ii) the hexagonal prism;

iii) the truncated octahedron;

iv) the rhombic dodecahedron;

v) the elongated dodecahdron.

In any simulation it is therefore sensible to choose a simulation cell that reflects the underlying symmetry of the system to be studied.

It must be noted however that in some instances that standard periodic boundary conditions in all directions may be inappropriate, for example when studying the adsorption of particles onto a surface. In this instance the surface can be modelled as a true boundary and the opposite side of the box treated in such a way that when a particle strays out of the top it is reflected back into the simulation cell, with usual periodic boundary conditions being employed parallel to the surface.

2.4 Simulation Cell

In order to employ periodic boundary conditions as introduced in section 2.3 a simulation box must be designed. The most obvious way is simply to design a box that is sufficient to include all of one's system. However the problem with this approach is that the size of the calculation becomes prohibitive for large systems. The general approach employed is to use the smallest box possible, although this is not always desirable. If one uses an interaction cut-off for the van der Waals forces of 8–10 Å then the box lengths must be at least twice the cut-off distance. This is to prevent a molecule from interacting

with both another molecule and its image produced by the periodic boundary conditions. An idealised simulation cell can be seen in figure 2.2, in front and side view.

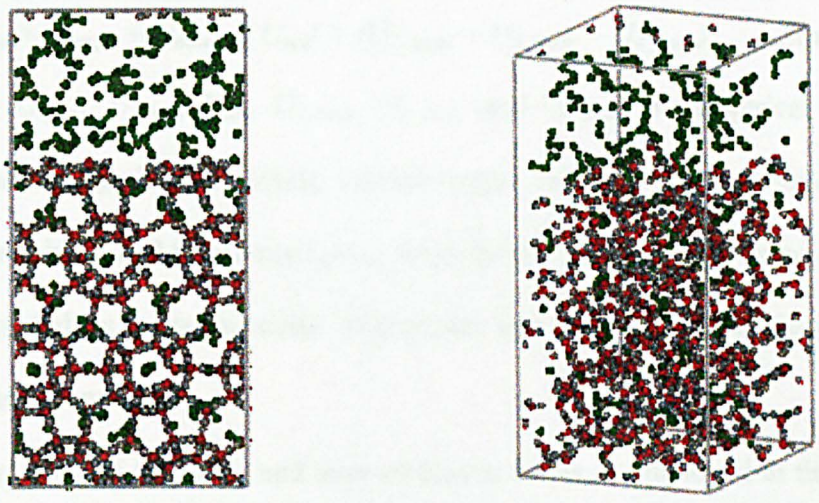

Figure 2.2 An idealised simulation cell, stabilising gas molecules are coloured in green and gas hydrate water molecules in red (oxygen) and grey (hydrogen).

2.5 Force Fields

A force field is ultimately used to calculate the energy of a molecular configuration. In this thesis the force field used was as implemented by DL_POLY[2] with parameters for molecular configurations used in this force field being derived from the CHARMm[3] force field, simple point charge (SPC)[4] model for water molecules and united atom (UA)[5] for hydrocarbon molecules.

2.5.1 DL_POLY Force Field

The energy of the molecular configuration was calculated by DL_POLY[2] using the following equations

$U_{total} = (U_{bond} + U_{angle} + U_{dihed} + U_{inv}) + (U_{2\_body} + U_{3\_body} + U_{4\_body})$ *Equation 2.17*

where U_{bond}, U_{angle}, U_{dihed}, U_{inv}, U_{2_body}, U_{3_body} *and* U_{4_body} are empirical interaction functions representing chemical bonds, valence angles, dihedral angles, inversion angles, two-body, three-body and four-body forces respectively. The first four terms in equation 2.17 are regarded as intra-molecular interactions and the next three terms as inter-molecular interactions.

The functional form of the intra- and inter-molecular terms as employed in this thesis in DL_POLY[2] are outlined in the following sections. The inversion angle potential, three-body and four-body terms were not implemented in this thesis and will therefore not be defined.

Chemical Bond Potential

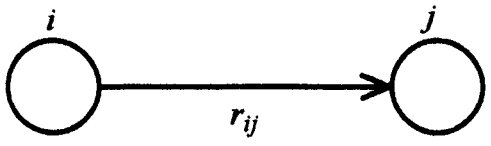

Figure 2.3 Schematic representation of the bond potential.

Given two atoms i and j joined by a bond of length r_{ij}, then the chemical bond energy $U(r_{ij})$ is given by

$$U(r_{ij}) = \frac{1}{2}k(r_{ij} - r_0)^2 \qquad \textit{Equation 2.18}$$

where k is the force constant associated with the bond r_{ij} and r_0 the natural bond length for a bond between atoms of type i and j.

Valence Angle Potential

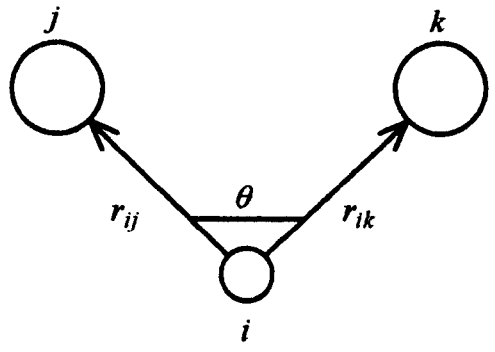

Figure 2.4 Schematic representation of the valence angle potential.

Given any two bonds r_{ij} and r_{ik} bonded to a common atom i, then the bond angle interaction is a function of the angle θ_{jik} between them such that the valence angle energy $U(\theta_{jik})$ is given by

$$U(\theta_{jik}) = \frac{k}{2}(\theta_{jik} - \theta_0)^2 \qquad \textit{Equation 2.19}$$

where k is the force constant associated with the angle θ_{jik} and θ_0 the natural bond angle for bonds between atoms of type i, j and k. The choice of θ_0 and k is specific to each triplet of atom types.

Dihedral Angle Potential

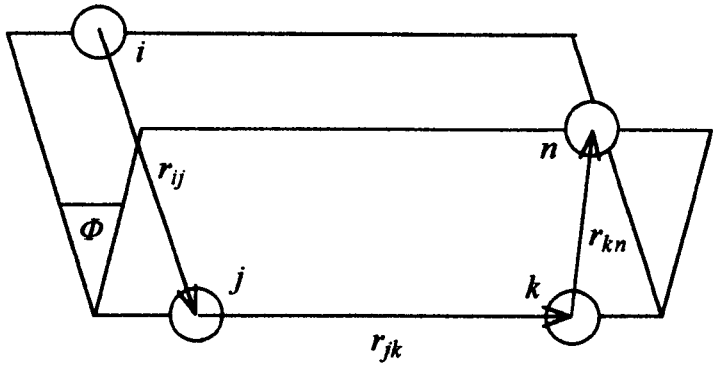

Figure 2.5 Schematic representation of the dihedral angle potential.

Given any two bonds r_{ij} and r_{kn} attached to a common bond r_{jk}, the dihedral angle Φ is defined as the angle between the *ijk* plane and the *jkn* plane such that the dihedral angle energy $U(\Phi_{ijkn})$ is given by

$$U(\Phi_{ijkn}) = A[1 + \cos(m\Phi_{ijkn} - \delta)] \qquad \textit{Equation 2.20}$$

where m is the periodicity of the potential, δ is the phase factor, and A is the rotational barrier.

Pair Potential–van der Waals and/or Electrostatic Terms

The pair potential may be comprised of two components:

i) the first is due to short- intermediate-ranged interactions, namely van der Waals forces;

ii) the second is due to long-ranged interactions, namely electrostatic (Coulombic) forces.

A Lennard-Jones expression was used to describe the van der Waals forces such that

$$U(r_{ij}) = 4\varepsilon\left(\left(\frac{\sigma}{r}\right)^{12} - \left(\frac{\sigma}{r}\right)^{6}\right) \qquad \textit{Equation 2.21}$$

where ε is the well depth and σ is the bond length; and ε and σ depend upon the atom types in the pair.

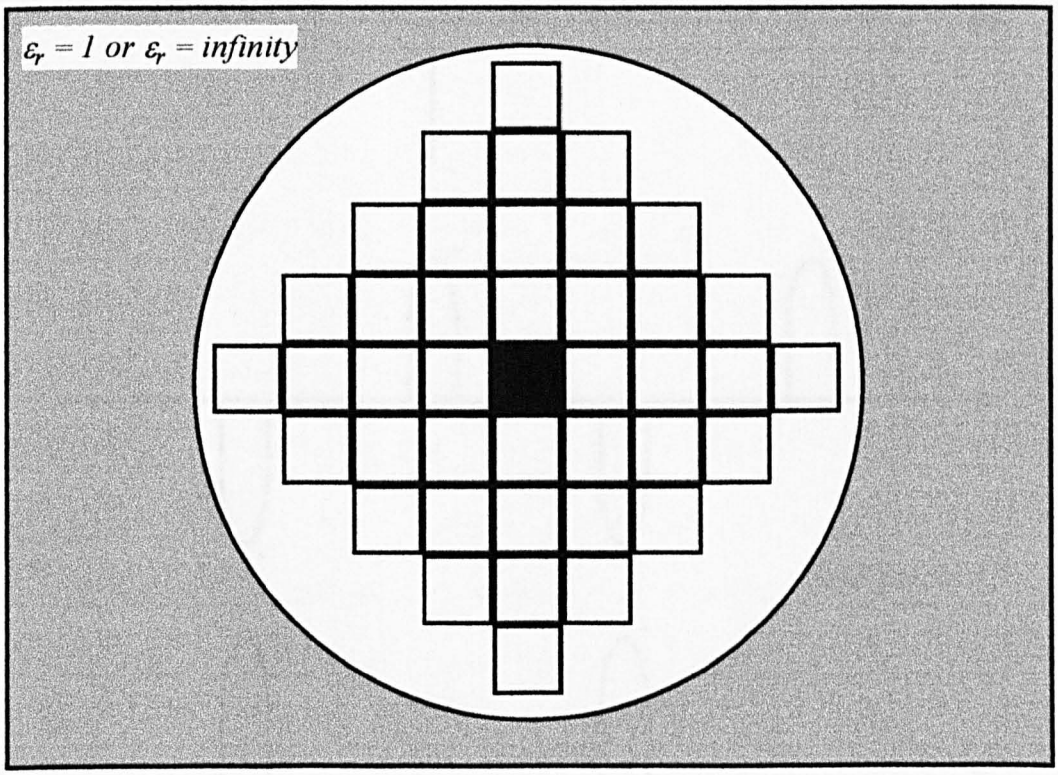

Figure 2.6 Construction of the infinite array of simulation boxes. The central simulation box is coloured in black with the external dielectric medium coloured in grey with relative permittivity ε_r.

The long-ranged electrostatic forces were calculated using the Ewald sum method which was first devised by Ewald in 1921 to study the energetics of ionic crystals.[6] In this

method a particle interacts with all other particles in the simulation box and with all of their images in an infinite array of periodic simulation boxes. A schematic representation of how the simulation boxes are constructed is shown in figure 2.6.

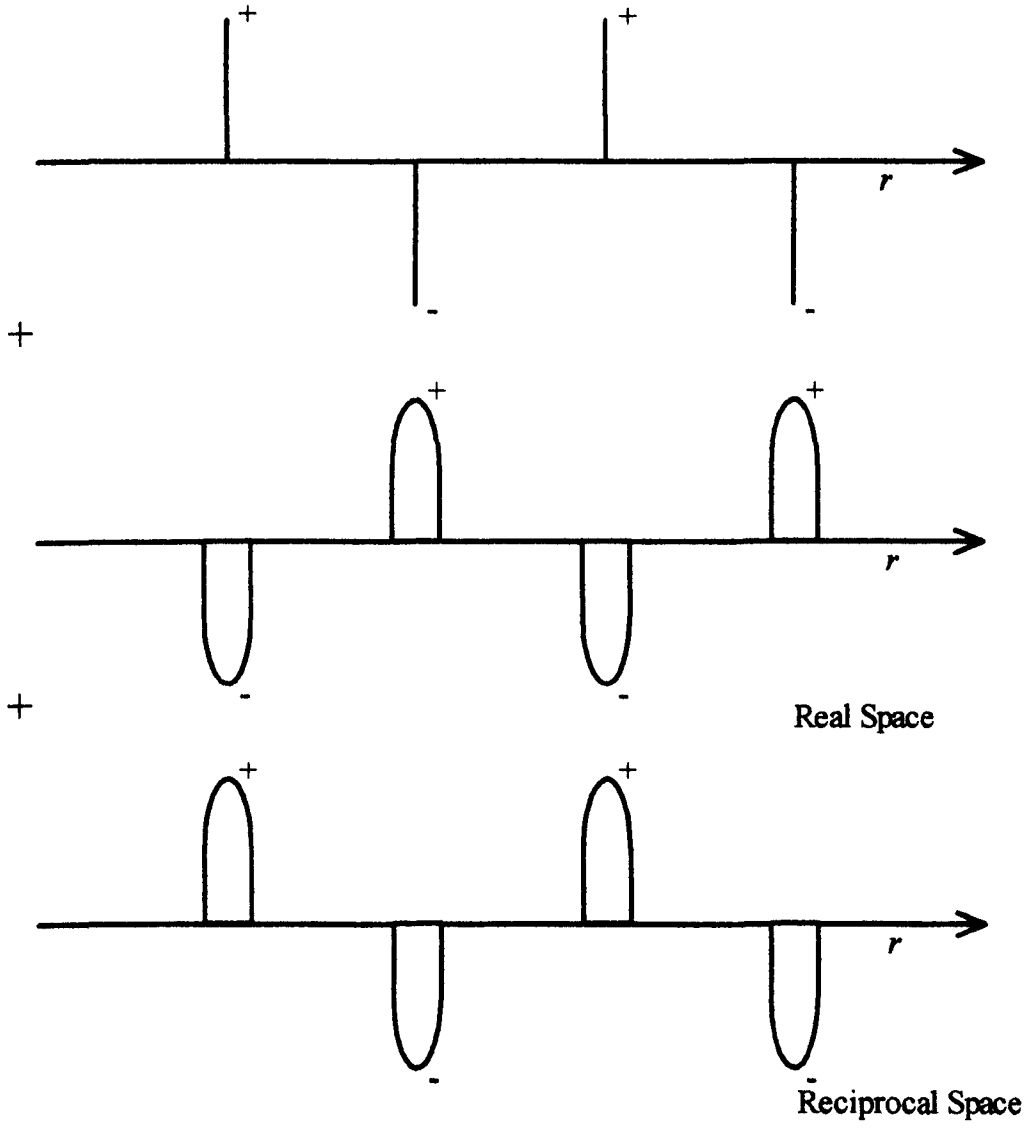

Figure 2.7 Schematic diagram of the charge distribution in the Ewald sum method. The initial set of charges are surrounded by a Gaussian distribution in real and reciprocal space.

The total energy of the system is then comprised of a contribution from the interactions in the central simulation box along with the interactions between the central simulation box and all image simulation boxes. There is also a contribution due to the interaction of the spherical array of unit cells with the surrounding medium. The problem with calculating the total energy is that the summation converges extremely slowly. In the Ewald sum method the summation is converted into two series, each of which converge much more rapidly than the original summation. This is achieved by considering that each charge is surrounded by a diffuse neutralising charge distribution of equal size but of opposite sign and a cancelling charge distribution as illustrated in figure 2.7.

The rate of convergence of the summation depends upon the width of the Gaussian distributions employed: the wider the Gaussian the faster the series will converge. The potential due to the real space part of the Ewald sum is short-ranged and can easily be evaluated directly, while the potential due to the reciprocal space part of the Ewald sum is evaluated as a Fourier series.

In the case of molecular systems, as opposed to systems comprised simply of point ions, additional adjustments are required in order to correct for the excluded (intra-molecular) Coulombic interactions. In the real space part of the Ewald sum these are simply ignored. In reciprocal space the effects of the individual Gaussian charges cannot be easily extracted and as a result the correction is made in real space. In essence the terms corresponding to the potential energy of an ion l due to the Gaussian charge on a neighbouring charge m (or *vice-versa*) are removed.

This correction leads to the final term in the formula for the Ewald sum for the calculation of the total electrostatic energy for a system with relative permittivity $\varepsilon_r = 1$ *i.e.* a vacuum as given overleaf:

$$U_c = \frac{1}{2V_o\varepsilon_0}\sum_{k\neq 0}^{\infty}\frac{\exp(-k^2/4\alpha^2)}{k^2}\left|\sum_j^N q_j \exp(-i\boldsymbol{k}\cdot\boldsymbol{r}_j)\right|^2 + \frac{1}{4\pi\varepsilon_0}\sum_{n<j}^{N^*}\frac{q_j q_n}{r_{nj}}erfc(\alpha r_{nj})$$
$$-\frac{1}{4\pi\varepsilon_0}\sum_{molecules}\sum_{l\leq m}^{M^*} q_l q_m\left\{\delta_{lm}\frac{\alpha}{\sqrt{\pi}} + \frac{erf(\alpha r_{lm})}{r_{lm}^{1-\delta_{lm}}}\right\} \qquad \textit{Equation 2.22}$$

where erf is the error function and erfc is the complementary error function; N is the number of ions in the system and N^* the same number discounting any excluded (intra-molecular) interactions; M^* represents the number of excluded atoms in a given molecule and includes the atomic self correction; V_0 is the simulation cell volume and $\boldsymbol{k}$ is a reciprocal lattice vector which is defined as

$$\boldsymbol{k} = l\boldsymbol{u} + m\boldsymbol{v} + n\boldsymbol{w} \qquad \textit{Equation 2.23}$$

where l, m, n are integers and $\boldsymbol{u}$, $\boldsymbol{v}$, $\boldsymbol{w}$ are the reciprocal space basis vectors. Both V_0 and $\boldsymbol{u}$, $\boldsymbol{v}$, $\boldsymbol{w}$ are derived from the vectors ($\boldsymbol{a}$, $\boldsymbol{b}$, $\boldsymbol{c}$) that define the simulation cell, such that

$$V_0 = |\boldsymbol{a}\cdot\boldsymbol{b}\times\boldsymbol{c}| \qquad \textit{Equation 2.24}$$

and

$$\boldsymbol{u} = 2\pi\frac{\boldsymbol{b}\times\boldsymbol{c}}{\boldsymbol{a}\cdot\boldsymbol{b}\times\boldsymbol{c}}$$

$$\boldsymbol{v} = 2\pi\frac{\boldsymbol{c}\times\boldsymbol{a}}{\boldsymbol{a}\cdot\boldsymbol{b}\times\boldsymbol{c}}$$

$$\boldsymbol{w} = 2\pi\frac{\boldsymbol{a}\times\boldsymbol{b}}{\boldsymbol{a}\cdot\boldsymbol{b}\times\boldsymbol{c}} \qquad \textit{Equations 2.25}$$

2.5.2 Simple Point Charge (SPC) Model

The Simple Point Charge (SPC) model[4] was used to simulate the water of the gas hydrate lattice. SPC water is a rigid, three-site model with a positive charge of +0.41 *e* placed at each of the hydrogen positions and a negative charge of –0.82 *e* placed at each of the oxygen positions. There is also a Lennard-Jones site centred on the oxygen atom, with σ having a value of 3.16 Å and ε having a value of 0.1553 kcal mol^{-1}. Within this model hydrogen-bonding arises as a result of the electrostatic charges on the water atoms, coupled with the lack of an excluded volume for hydrogen atoms (i.e. $\varepsilon_H = 0$), and so no explicit hydrogen-bonding potential is required.

2.5.3 United Atom (UA) Model

The united atom model as developed by Jorgensen *et al.*[5] was used to describe the hydrocarbons in this thesis. In this model CH_n groups ($n = 0, 1, 2, 3$ and 4) are described as a single interaction site centred on the carbon position. The advantage of this type of model is that the interactions due to hydrogen atoms are removed and therefore the amount of time to perform a calculation is reduced; *e.g.* if butane is modelled as a four-site united atom model rather than one with fourteen atoms then the van der Waals interactions between two butane molecules involves the calculation of 16 terms rather than 196 terms.

2.5.4 Cross-Terms

The Lennard-Jones cross-terms, *i.e.* terms arising from non-identical atom-type pairs, were obtained from the Lorenz-Berthelot mixing rules as given overleaf:

$$\varepsilon_{ij} = \sqrt{\varepsilon_i \cdot \varepsilon_j}$$

$$\sigma_{ij} = \frac{(\sigma_i + \sigma_j)}{2} \qquad \textit{Equation 2.26}$$

2.6 Charges

2.6.1 Hartree-Fock Self Consistent Field (HF-SCF)

The GAUSSIAN94 program[7] was used to derive the atomic charges. GAUSSIAN94 implements *ab-initio* quantum mechanical methods to derive charges, and as such provides a more rigorous basis for determining the charges when compared with semi-empirical methods. GAUSSIAN94 is based directly on the Schrodinger equation, equation 2.27, and so gives rise to a wavefunction, which, in turn, summarises the electron distribution for the system:

$$\hat{H}\Psi = E\Psi \qquad \textit{Equation 2.27}$$

where $\hat{H}$ is the Hamiltonian operator and incorporates the nuclear kinetic and potential energy terms as well as the electronic kinetic and potential energy terms, Ψ is the wavefunction and E is the energy of that state of the system. GAUSSIAN94 was used to solve equation 2.27 within the Hartree-Fock self consistent field (HF-SCF) approximation. The Hartree-Fock equations are a set of coupled integro-differential equations that can only be solved by an iterative method such as the SCF method. To solve the Hartree-Fock equations an initial trial set of orbitals is chosen and the Fock operator is constructed. The Fock equation is then solved to obtain a new set of orbitals. The new set of orbitals is then used to construct a new Fock operator, which is then

solved to get yet another set of orbitals; this procedure is repeated until convergence is obtained. The SCF method is based upon guessing the wavefunctions for all the electrons in the system. Then one electron is selected and the potential in which it moves is calculated by freezing the distribution of all the other electrons and treating them as the source of the potential, and as a result a new wavefunction for the electron is obtained. This procedure is repeated for all the other electrons in the system using the electrons in the frozen orbitals as the source of the potential. When the cycle is completed (see figure 2.8) a set of orbitals for all the electrons in the system will have been obtained and in general these will differ from the original guessed set. The cycle is then repeated but the improved wavefunctions generated by the first cycle are used as the initial guess. This sequence is continued until passing a set of orbitals through the cycle leads to no change: the orbitals are then self-consistent.

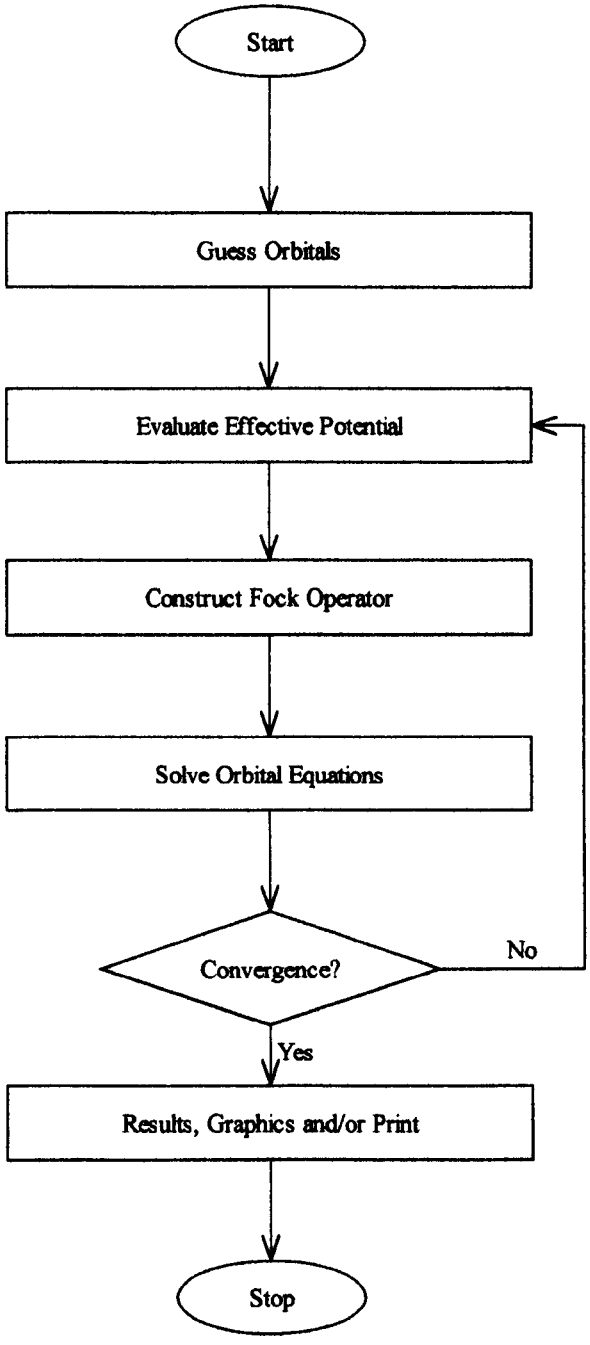

Figure 2.8 The HF-SCF method.

2.6.2 Basis Sets

There are two types of basis sets commonly used to describe atomic orbitals. The first type is comprised of Slater-type orbitals while the second type consists of Gaussian-type orbitals. Slater-type basis sets are based on the solutions to the Schrodinger equation for the hydrogen atom and so they provide a good description of atomic orbitals; however they are not well-suited to numerical work as they involve complicated integrals and so are time consuming to implement. Individual Gaussian-type basis sets are not as good a representation of atomic orbitals as Slater-type orbitals, but their strength is that the resulting integrals are fast to calculate, and so more complex basis sets can be used. Gaussian-type basis sets have a particular nomenclature as outlined below. The general form is, for example, 6-31G**. This indicates that 6 Gaussian-type orbitals were used to describe the core electrons of each of the atoms in the molecule. While the 31 indicates that a split valence set was used with 4 Gaussian-type orbitals being used to describe the valence electrons, 3 for the contracted part and 1 for the diffuse part. The first * indicates that polarisation functions were used on the second row elements and the second * indicates that polarisation functions were also used on hydrogen atoms. Polarisation is included in an attempt to account for the distortion observed of the electron cloud about an atom caused by other atoms in the vicinity *i.e.* the attraction of electrons around one nucleus to the nucleus of another atom.

2.6.3 Charge Calculation

Wavefunctions generated by GAUSSIAN94 were analysed to generate electrostatic potential derived (ESPD)[8] charges. In this method a set of points are defined by

constructing a cubic grid around the molecule which extends not further than 2.8 Å from any nucleus, with points spaced 0.3–0.8 Å apart. If any of the points lie within the van der Waals radius of any atom then they are excluded. This leads to the creation of a homogeneous grid in the region around the molecule. The electrostatic potential at a point is defined to be the energy of a unit positive charge placed at that point, and may be calculated exactly from the wavefunction for the molecule. The HF wavefunction is therefore used to create a reference grid of electrostatic potential energies. The ESPD charge model then derives the set of atomic charges that best reproduces this reference electrostatic potential grid.

2.7 Conformational Search Methods

Conformational searches are used to investigate the possible conformations of a molecule in order to identify the energetically feasible conformations that the molecule may adopt. This is important because the effectiveness of a kinetic inhibitor will depend on how well it fits to the surface of the crystal it inhibits, and this fit will depend strongly on the shape (and hence conformation) of the adsorbate.

Three common methods for carrying out a conformational search are random search, grid scan and molecular dynamics.

2.7.1 Random Search

The random search method, as its name suggests, is a random process for investigating the conformers of a molecule.

In the random search method either the atomic cartesian co-ordinates or the torsion angles of the rotatable bonds are altered by random amounts. The general outline of the process can be seen in figure 2.9.

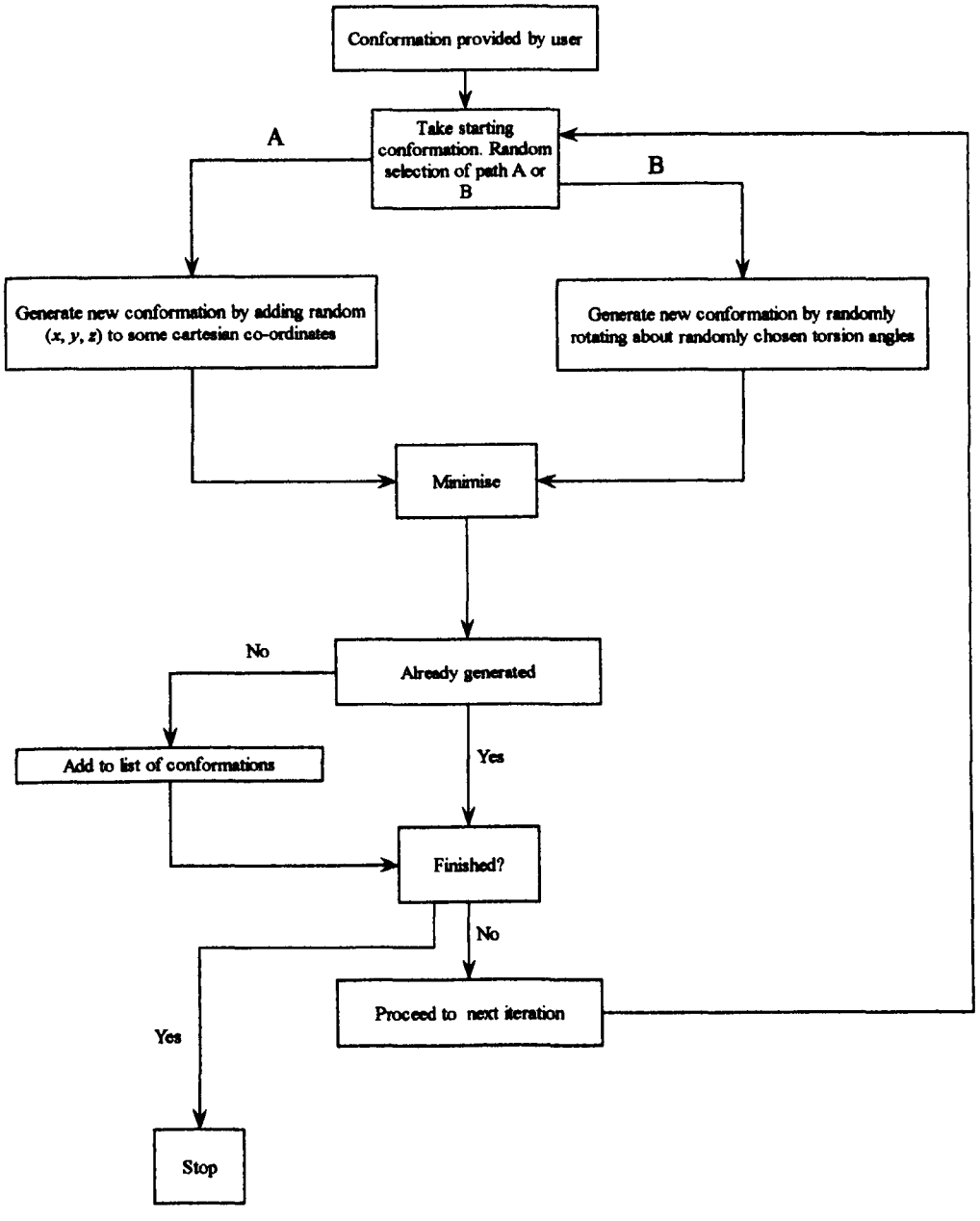

Figure 2.9 Outline of the random search method.

At each iteration a random change is made to the current conformation. The new conformation is then minimised with respect to its energy; if this conformation has not been found before then it is stored. This conformation is then used as the starting point for the next iteration and the cycle starts again. This process continues until the required number of steps have been carried out or it is decided that there are no new conformations to be found. The only difference between the cartesian and dihedral versions of the random search is the way in which new conformations are produced. The cartesian method adds a random value to the x, y and z co-ordinates of the atoms in the molecule; whereas the dihedral method makes random twists to the rotatable bonds, while keeping the bond lengths and bond angles constant. The latter is less likely to generate highly strained conformations as the starting configuration for the subsequent minimisation.

2.7.2 Grid Scan

In the grid scan method all significant rotatable bonds in the molecule are identified. The bond lengths and angles remain fixed throughout the search procedure. Each of the chosen bonds are then systematically rotated through 360° using a set increment. The new conformation produced at each stage is then minimised with respect to its energy and saved. This procedure then continues until all the conformations have been found. The advantage of this method is that it can identify all possible conformations. The problem with this method is that the number of possible conformations, C_N, increases greatly with the number of rotatable bonds such that:

$$C_N = \prod_{i=1}^{N} \frac{360}{\theta_i}$$ *Equation 2.28*

where θ_i is the dihedral increment chosen for the bond i. For example if there are 5 bonds and an increment of 30° is used for each bond then 248 832 (= 12^5) structures will be generated. One way to overcome this problem is to apply an energy filter so that conformations with an energy above a threshold value are not kept, so reducing the number of conformations to be analysed at the end of the procedure. However the discarded conformations still have to be generated and their energies calculated (even if not minimised) and so consume CPU time. The point is rapidly reached where the number of conformations that have to be generated is too great for the amount of time available to derive them.

2.7.3 Molecular Dynamics

In this method the molecule is heated up to an extremely high, physically unrealistic temperature in order to impart kinetic energy to the atoms in the molecule; the kinetic energy is sufficient to get free rotation about all bonds, but not to break bonds. This allows the molecule to move along the energy profile and adopt new conformations rather than getting stuck in local energy minima (see figure 2.10). The co-ordinates of the molecule are saved at regular steps to a file and these are then subsequently minimised.

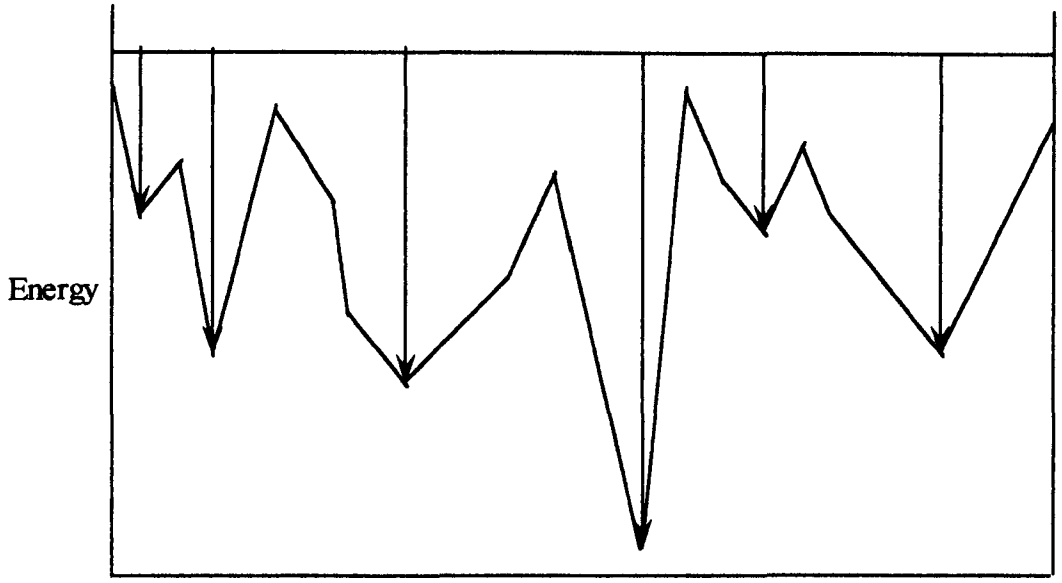

Figure 2.10 The energy profile of a molecule as explored by molecular dynamics.

2.8 Minimising Algorithms

During an energy minimisation the atomic co-ordinates are adjusted in order to reduce the molecular energy. There are three common algorithms designed to carry out this process, conjugate gradient,[9] steepest descent[10] and Fletcher-Powell.[11] The minimisation algorithm used in this project was the conjugate gradient algorithm which is explained below along with a brief description of the other two algorithms.

2.8.1 Conjugate Gradient

The conjugate gradient uses information from previous steps to modify the move in the next step. In the first step where the gradient vector is $\boldsymbol{g}_1$ the move is performed in the direction $\boldsymbol{s}_1$ given by,

$$\boldsymbol{s}_1 = -\boldsymbol{g}_1 \qquad \textit{Equation 2.29}$$

The new search direction for subsequent steps, s_k, takes into account the previous search direction and the current gradient,

$$s_k = -g_k + b_k s_{k-1} \qquad \textit{Equation 2.30}$$

where s_{k-1} is the search direction from the previous step and b_k is a scaling factor given by:

$$b_k = \frac{g_k \cdot g_k}{g_{k-1} \cdot g_{k-1}} \qquad \textit{Equation 2.31}$$

The effect of the second term in equation 2.30 is to release the constraint that the $i + 1^{th}$ gradient should be orthogonal to the i th gradient. As a result better search directions are usually obtained by the method and it has much better convergence properties.

2.8.2 Steepest Descent

In the steepest descent algorithm co-ordinates are displaced in a direction opposite to the gradient of the potential energy at each step. The step size is increased if a lower energy is obtained; alternatively it is decreased if a higher energy is obtained. This process is continued until convergence is reached. The main advantage of the steepest descent method is that it is very efficient when large forces are present. Far away from the minimum it is therefore useful at tidying up structure geometries but final refinement is best achieved with another method.

2.8.3 Fletcher-Powell

Fletcher-Powell is a pseudo second order method, which generates a second order derivative matrix by finite differences. It must be noted that the computation time

increases as the cube of the number of atoms. That makes this algorithm generally not useful for systems larger than three hundred atoms.

2.9 References

[1] Verlet L., *Phys. Rev.*, **159**, 1967, 98.

[2] Smith W., Forester T.R., *J. Mol. Graphics*, **14**, 1996, 136.

[3] Brooks, B.R., Bruccoleri R.E., Olafson B.D., States D.J., Swaminathan S., CHARMm: A Program for Macromolecular Energy, Minimisation and Dynamics Calculations, *J. Comp. Chem.*, **4**, 1983, 187.

[4] Berensden H.J.C., Postma J.P.M., van Gunsteren W.F., Hermans J., *Intermolecular Forces*, B. Pullman ed., D. Reidel Publishing Co., 1981, 331.

[5] Jorgensen W.L., Madura J.D., Swenson C.J., *J. Am. Chem. Soc.*, **106**, 1984, 6638.

[6] Ewald P., *Ann. Phys.*, **64**, 1921, 253.

[7] Gaussian 92/DFT, Revision F.2, Frisch M.J., Trucks G. W., Schlegel H. B., Gill P. M. W., Johnson B. G., Wong M. W., Foresman J. B., Robb M. A., Head-Gordon M., Replogle E. S., Gomperts R., Andres J. L., Raghavachari K., Blinkley J. S., Gonzalez C., Martin R. L., Fox D. J., Defrees D. J., Baker J., Stewart J. J. P., Pople J. A., Gaussian, Inc., Pittsburgh PA, 1993.

[8] Singh U.C., Kollman P.A., *J. Comp. Chem.*, **5**, 1984, 129.

[9] Fletcher R., Reeves C.M., *Comput. J.*, **7**, 1964, 149.

[10] Levitt M., Lifson S., *J. Mol. Biol.*, **46**, 1969, 269.

[11] Press W.H., Flannery B.P., Teukolsky S.A., Vetterling W.T., In *Numerical Recipes, The Art of Scientific Computing*, Chapter 10, Cambridge University Press, Cambridge, 1986.

CHAPTER 3

ANALYSIS TECHNIQUES

3 Introduction

In this chapter the analysis techniques used to investigate the simulations carried out in this thesis are outlined. The chapter is divided into five parts as outlined below.

3.1 Time correlation functions.

3.2 Diffusion Coefficients.

3.3 Radial distribution functions.

3.4 Order parameters.

3.5 Co-ordination Number.

3.1 Time Correlation Functions

A molecular dynamics simulation provides data values at specific times and one of the most interesting properties that may be calculated from such a simulation is time dependent properties. This allows for the value of some property at some instant to be correlated with the value of the same, or another property, at a later time t. The resulting values are known as time correlation functions and have the general form:

$$Cxy(t) = \langle x(t).y(0) \rangle \qquad \textit{Equation 3.1}$$

If the properties x and y are different then the time correlation function is referred to as a cross correlation function, whereas if x and y are the same property then the time correlation function is referred to as an auto correlation function. In this thesis we are concerned with auto correlation functions which therefore have the general form:

$$Cxx(t) = \langle x(t).x(0) \rangle \qquad \textit{Equation 3.2}$$

In order to normalise the auto correlation functions we divide by $\langle x(0).x(0) \rangle$ such that the auto correlation function becomes:

$$Cxx = \frac{\langle x(t).x(0) \rangle}{\langle x(0).x(0) \rangle} \qquad \textit{Equation 3.3}$$

By definition an auto correlation function has an initial value of 1, and will usually decay to a value of 0 at infinite times.

These auto correlation functions are of interest in computer simulation because:

i) they give a clear picture of the dynamics in a system;

ii) their time integrals can often be related, via Green-Kubo relationships, to macroscopic transport coefficients;

iii) their Fourier transforms can often be related to experimental spectra.

Three types of auto correlation functions are used in this thesis:

i) the residence time correlation function, $R(t)$;

ii) the second Legendre polynomial time correlation function, $P_2(t)$;

iii) the mean square displacement function, $MSD(t)$.

In the following chapters it has proved useful to identify the dynamical behaviour in specified spatial regions. For example, as a function of distance away from a hydrate/gas interface, or in the vicinity of key functional groups within an inhibitor. To perform this identification we have defined a function $X_i(t)$ so that $X_i(t)= 1$ if a molecule that started in a region has remained in that region until time t and $X_i(t) = 0$ in all other cases; that is to say that once a molecule has left a region then $X_i(t)$ will be 0 for the rest of the simulation, even if the molecule re-enters the region. This has the effect of causing the auto correlation function to decay to 0 at long times simply because no molecules are indefinitely trapped within a given spatial region. The three auto correlation functions are outlined below.

3.1.1 Residence Time Correlation Function

The residence time correlation function has been calculated for water molecules, such that:

$$R(t) = \frac{1}{N}\sum_{i=1}^{N} X_i(0).X_i(t) \qquad \textit{Equation 3.4}$$

where N is the number of atoms in the system, $X_i(t)$ relates to occupancy of a given solvation shell or slice through the gas hydrate lattice. From $R(t)$ it is possible to calculate an estimate for the residence times of water molecules in the given region.

3.1.2 Second Legendre Polynomial Time Correlation Function

The Legendre polynomials, also called Legendre functions of the second kind, Legendre coefficients, or zonal harmonics, are solutions to the Legendre differential equation and have the following form for the first few Legendre polynomials:

$$P_0(x) = 1$$

$$P_1(x) = x$$

$$P_2(x) = \tfrac{1}{2}(3x^2 - 1)$$

$$P_3(x) = \tfrac{1}{2}(5x^3 - 3x)$$

$$P_4(x) = \tfrac{1}{8}(35x^4 - 30x^2 + 3) \qquad \textit{Equation 3.5}$$

The second Legendre polynomial time correlation functions for the unit vector $\boldsymbol{e}$ is given by:

$$< P_2(t) > = \frac{\sum_{i=1}^{N} (X_i(0).X_i(t).P_2(\boldsymbol{e}_i(0).\boldsymbol{e}_i(t)))}{\sum_{i=1}^{N} (X_i(0).X_i(t))} \qquad \textit{Equation 3.6}$$

where N is the number of atoms in the system and $X_i(t)$ relates to (continual) occupancy of a specified region. $\boldsymbol{e}$ may be chosen to be any characteristic vector for the molecules of interest. In this work we have used two directions. The first is the direction of the water dipole (denoted 'parallel' or '||'), while the second is the vector joining the water hydrogen atoms (denoted 'perpendicular' or '⊥'). From these $<P_2(t)>$ it is possible to estimate the rotational lifetimes of motion parallel and perpendicular to the dipole moment of water molecules.

3.1.3 Mean Square Displacement Time Correlation Function

The mean square displacement time correlation function has been calculated for water molecules such that:

$$MSD(t) = \frac{\sum_{i=1}^{N} X_i(t)((r_i(t) - r_i(0))^2}{\sum_{i=1}^{N} X_i(t)} \qquad \textit{Equation 3.7}$$

where N is the number of atoms in the system, $X_i(t)$ relates to a solvation shell or slice through a hydrate film, and $r_i(t)$ the position of the i th particle at time t.

The $MSD(t)$ is related to the self-diffusion coefficient by the equation:

$$D = \lim_{t \to \infty} \frac{1}{6t} \langle | r(t) - r(0) |^2 \rangle \qquad \textit{Equation 3.8}$$

where D is the self-diffusion coefficient. It must however be noted that, due to the added requirement that molecules *remain* within a specified region throughout the time interval (0, t), the value of D obtained from our MSDs may be an under-estimate of the real value: fast moving molecules are more likely to leave the region after shorter time intervals, and only the slower moving molecules will remain at long times.

3.2 Diffusion Coefficients

The usual method for determining a self-diffusion coefficient from computer simulations is to determine the gradient of the linear region of the mean square displacement function as outlined in section 3.1.3 and is in general the method used in this thesis.

Where a spatial decomposition has been used, the issue of only slow particles remaining in a region has been dealt with by estimating the half life, $t_{½}$, for molecules to remain within the specified region, and then using this as the upper time limit for any linear fit to the MSD.

In some instances the self-diffusion coefficients output from DL_POLY[1] simulations have been quoted and these are calculated in a slightly different way. The equation used to determine the self-diffusion coefficient is derived from:

$$D = \frac{\sum_{i=1}^{N}((r_i(t) - r_i(0))^2}{t} \qquad \textit{Equation 3.9}$$

where N is the number of atoms in the system, $r_i(t)$ the position of the i th particle at time t, and t is the total time of the simulation. DL_POLY therefore assumes that the whole of the mean square displacement function is linear and calculates the average gradient for the whole of the simulation. This approach of course leads to inaccuracies in the value of D as the initial region of the mean square displacement function is not linear, however it is sufficient to gain an indication as to the magnitude of D.

3.3 Radial Distribution Function

The radial distribution function (RDF) is a useful way to describe the structure of a system, especially for liquid systems. Consider a spherical shell of thickness δr at a distance r from a chosen atom, as shown in figure 3.1.

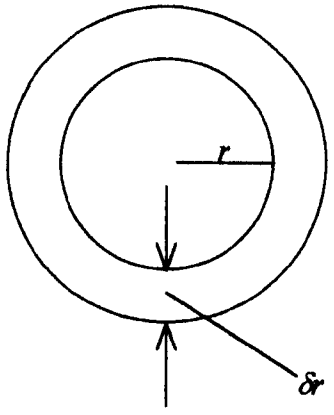

Figure 3.1 Schematic representation of the spherical shell used in the calculation of the radial distribution function.

The volume of the spherical shell is given by:

$$V = \frac{4}{3}\pi(r+\delta r)^3 - \frac{4}{3}\pi r^3$$

$$= 4\pi r^2 \delta r + 4\pi r \delta r^2 + \frac{4}{3}\pi \delta r^3 \qquad \textit{Equation 3.10}$$

For very thin shells ($\delta r \rightarrow 0$) the terms in δr^2 and δr^3 are negligible, and so the volume becomes:

$$V \approx 4\pi r^2 \delta r \qquad \textit{Equation 3.11}$$

If there were ρ particles per unit volume in the system, then the total number of particles expected to lie in the shell would be given by

$$N = 4\pi\rho r^2 \delta r \qquad \textit{Equation 3.12}$$

Thus the number of atoms in the volume element varies as r^2. This describes the probability of finding atoms separated by distance r in a completely homogeneous distribution. However in most instances we do not have an homogeneous distribution and therefore the actual number of particles in this shell ($N(r)dr$) is given by the number

of atoms within the shell of inner radius r and outer radius $r + \delta r$ centred on the central atom i. In computer simulations this is calculated by sorting the neighbours around each atom or molecule into distance 'bins', or histograms, with the number of neighbours in each bin then averaged over the whole simulation. From this $g(r)$ may be determined as:

$$g(r) = \frac{N(r)}{N} \qquad \textit{Equation 3.13}$$

An idealised plot of $g(r)$ for liquid water is shown in figure 3.2.

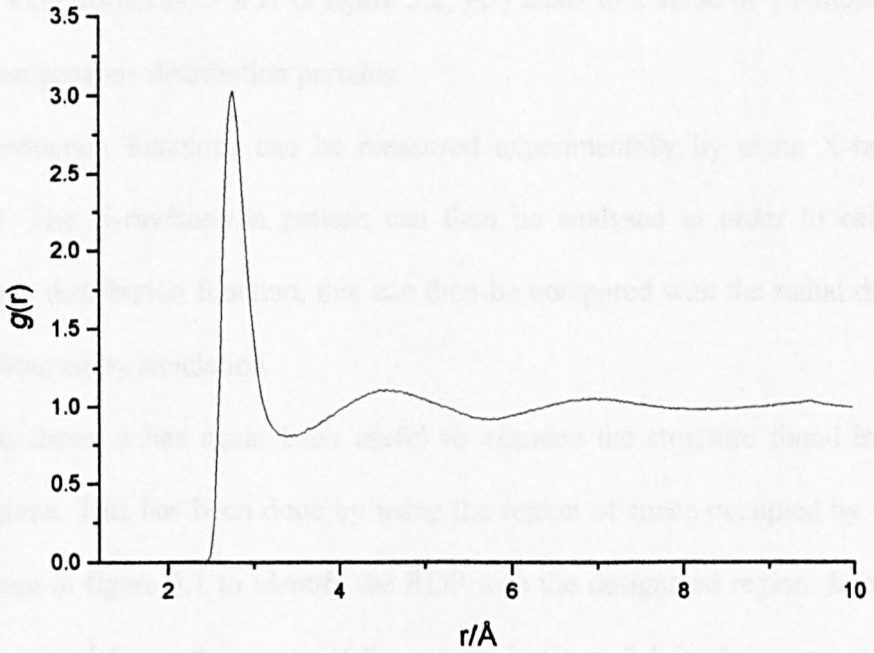

Figure 3.2 An idealised radial distribution function.

A number of salient features are apparent from figure 3.2.

i) At short distances (less than the atomic diameter) $g(r)$ is zero; this is due to the strong repulsive forces between atoms which prevents them from occupying the same region of space.

ii) At intermediate distances, 2–8 Å in figure 3.2, there are a number of well-defined peaks. The value of $g(r)$ for each peak indicates how much more likely you are to find two molecules with this separation than in the corresponding ideal gas.

iii) At long distances, > 8 Å in figure 3.2, $g(r)$ tends to a value of 1 indicating that a homogeneous distribution pertains.

Radial distribution functions can be measured experimentally by using X-ray/neutron diffraction. The X-ray/neutron pattern can then be analysed in order to calculate an experimental distribution function, this can then be compared with the radial distribution function obtained by simulation.

Within this thesis it has again been useful to examine the structure found in different spatial regions. This has been done by using the region of space occupied by the centre of the sphere in figure 3.1 to identify the RDF with the designated region. In calculating RDFs from simulations, the centre of the sphere in figure 3.1 is always associated with an atomic site, and so it is actually the site of this 'central' atom that is used to identify the region with which the RDF should be associated.

3.4 Order Parameters

This discussion is largely based upon the paper by Fidler and Rodger.[2]

An order parameter is a measure of the degree of order (or, equivalently, disorder) in the system. Its usefulness stems from the fact that its value depends on the ordered state of the system, so that it adopts one value in a given ordered state (*e.g.* for water in a hydrate lattice), but a measurably different value in a different ordered state (*e.g.* water in the liquid, or in ice I_h). In this thesis three order parameters have been employed to probe the different types of local water structures: F_3, $F_{4\varphi}$ and F_{4t}.

In order to calculate these order parameters the water hydrogen-bonding network must be defined. This has been done as shown in figure 3.3.

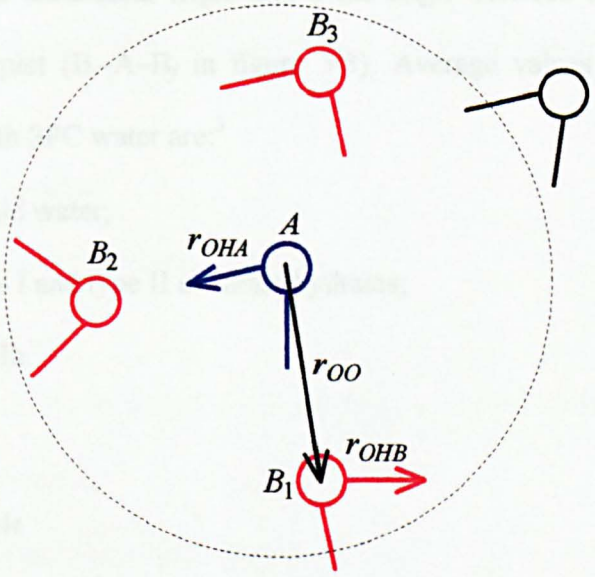

Figure 3.3. Schematic diagram showing how the water hydrogen-bonding network is defined. Water molecule A is in blue, and its solvation shell is illustrated by a dotted line. Three B_i water molecules are depicted in red and a fourth water molecule in black which is not considered as it is outside the solvation shell of water molecule A. The vectors r_{OHA} and r_{OHB} are shown, which lie along the water molecule OH bonds, along with r_{OO}, the vector which joins the two oxygen atoms of the dimer.

3.4.1 F_3

F_3 is a three-body order parameter and measures the average angle between the water oxygens from within a hydrogen-bonded triplet. F_3 actually measures how the average angle deviates from the ideal tetrahedral angle and can be used to distinguish between solid and liquid phases, with low values indicating a well-defined tetrahedral hydrogen-bonding network as found in gas hydrates and ice. F_3 is calculated according to the equation:

$$F_3 = < (Cos\vartheta \,|\, Cos\vartheta \,| + Cos^2 109.47)^2 > \qquad \textit{Equation 3.14}$$

where 109.47° is the tetrahedral angle and θ the angle between the oxygens within a hydrogen-bonded triplet (B_i–A–B_j in figure 3.3). Average values obtained from bulk phase simulations with SPC water are:[3]

0.101 for liquid water;

0.014 for type I and type II clathrate hydrates;

0.011 for ice Ih.

3.4.2 $F_{4\varphi}$ & F_{4t}

These two order parameters probe the torsion angles found within a hydrogen-bonding network and were designed to probe for clathrate-like structure. A suitable order parameter can be defined from a water dimer by assuming that those O–H bonds that are not involved in the dimer hydrogen bond will point towards the next oxygen in the network. Therefore the A–B_i dimers were used to define three normalized vectors.

i) the vector between the two oxygen atoms, r_{OO};

ii) for each of A and B_i, the vector from the oxygen atom to the hydrogen atom not involved in the hydrogen bond, r_{OHA} and r_{OHB}.

In order to provide a unique definition, the hydrogen atom furthest from the oxygen atom on the other molecule was always used to define the r_{OH} vectors. These vectors where then used to calculate order parameters based on the torsion angle φ and the vector triple product, such that:

$$F_{4\varphi} = < Cos3\varphi > \qquad \textit{Equation 3.15}$$

$$F_{4t} = < (r_{OHA} \times r_{OO} . r_{OHB})^2 > \qquad \textit{Equation 3.16}$$

The use of $Cos3\varphi$ for $F_{4\varphi}$ is due to the 3-fold rotational symmetry for torsion angles expected in a tetrahedral network. Average values for $F_{4\varphi}$ in typical water-based phases are:[3]

-0.01 for liquid water;

0.73 for type I and II clathrate hydrates;

-0.39 for ice Ih.

Average values obtained from bulk phase simulations with SPC water for F_{4t} are:[3]

0.26 for liquid water;

0.47 for type I and II clathrate hydrates;

0.29 for ice Ih.

3.5 Co-ordination Number

The calculation of the co-ordination number for atoms associated with certain regions of space (*e.g.* solvation shells) simply involves determining the number of atoms present in the region of space of interest. In the strictest sense the value calculated is in fact the

solvation number and not the co-ordination number as it might be defined in transition metal complexes (where 'co-ordinating' is taken to imply 'forming a complex bond with'). However when we say that the co-ordination number of sodium or chloride in sodium chloride is 6 then we are simply determining the number of atoms surrounding each of the species in one unit cell. To that end we are calculating an analogous quantity with the only difference being that in our definition the unit cell is replaced by a different region of space (*e.g.* solvation shells).

In this thesis, in some instances co-ordination numbers have been calculated from the appropriate RDF, by integrating up to the position of the first trough minimum in the RDF:

$$C_n = \sum_{r=0}^{r=T_{min}} 4\pi r^2 \rho \delta r g(r) \qquad \textit{Equation 3.17}$$

where r is the radius of the shell, ρ the density of the system, δr the thickness of the shell and T_{min} the position of the trough minimum.

Since the RDFs have been calculated for specified spatial regions, the co-ordination numbers calculated from these RDFs will automatically have the same spatial identification.

3.6 References

[1] Smith W., Forester T.R., *J. Mol. Graphics*, **14**, 1996, 136.

[2] Fidler J., Rodger P.M., *J. Phys. Chem. B*, **103**, 1999, 7695.

[3] Rodger P.M., *Annals of the New York Academy of Sciences*, **912**, 2000, 474.

CHAPTER 4

INHIBITOR BEHAVIOUR IN LIQUID WATER

4 Introduction

In this chapter the investigation into the liquid water behaviour of the amine sulphonates and amine carboxylates is outlined. This work was undertaken because kinetic inhibitors act at the liquid water/hydrate interface; however it is not clear whether the kinetic inhibitors affect the hydrate surface or liquid water structure or a mixture of the two. Therefore by investigating the liquid water behaviour alone before considering a more complex system we can identify any activity in this region. The chapter is divided into four parts as outlined below.

4.1 A literature review of water models, both conceptual and also potential-based.

4.2 Simulation details—outlining the 'preparation' of the systems studied along with the simulations carried out.

4.3 Results and discussion.

4.4 Conclusions.

4.1 Literature Review

4.1.1 Models of Water

The models available for water can be split into two general categories:

a) conceptual models; or

b) potential-based models.

Conceptual models are models that are derived as a direct result of a set of experimental observations in an attempt to rationalise/explain the experimental observations. Potential-based models are derived from computer simulation in order to reproduce quantitatively a wide range of experimental observations, with the parameters of the model being adjusted after each simulation in order to achieve the best reproduction of the experimental observations.

It must be noted that this subdivision of water models is not unique, and is not always clear-cut, but for ease of classification we have decided to divide them in this way.

Conceptual Water Models

The conceptual models of water that are currently available can be split into three broad categories as outlined below. These definitions are by no means rigid and may be found in different forms in other texts.

a) Mixture/flickering cluster models propose that equilibrium exists between two or more molecular species with different numbers of hydrogen bonds per molecule, with the equilibrium being temperature and pressure-dependent.

These models date back to the work of Roentgen[1] in 1892 who proposed that water was composed of two basic components, a 'bulky' ice-like component and a comparatively less bulky 'normal liquid'.

b) Interstitial models propose that there is a basic framework of water molecules which create cavities into which water molecules may enter. These models are derived from the idea that the increase in density of ice upon melting arises from invasion by interstitial molecules of some of the empty spaces in the ice lattice—a notion that can be traced back to the work of Pauling[2] in 1959 who proposed that water was a hydrogen-bonded clathrate-like framework with interstitial H_2O molecules that occupy some of the cavities in the clathrate network.

c) Distorted hydrogen bond/continuum models regard hydrogen bonds as distorted to varying degrees, as opposed to either intact or broken. Water molecules in the liquid, like those in ices, are considered to be four-co-ordinate, but the networks of linked molecules in the liquid are envisaged as irregular and varied. These models can be traced back to the work of Bernal and Fowler[3] in 1933 who proposed that water forms a network that is more or less completely hydrogen-bonded, with the effect of temperature being to distort the bonds by bending them rather than formally breaking them.

Potential-based Water Models

The current potential-based water models available of water can also be split into three general areas.

a) *non-polarisable:* these models generally treat water molecules using a fixed number of interaction sites, which can range from three to five; although not

essential, they normally treat the molecule as being a rigid body. The main advantages of such models are that they are easy to implement and are able to predict certain properties, such as the density and enthalpy of vaporisation, well. These models are parameterised by calculating various thermodynamic and structural properties with molecular dynamics or Monte Carlo techniques and then adjusting the parameters until the desired level of agreement is reached between simulation and experiment. The main disadvantages with these models are that they overestimate the dipole moment of water, which is 1.85 D for water molecules in the gas phase, such that the value they predict is nearer to the effective dipole moment of water being 2.6 D and that due to the fact that the majority of them are rigid then it is not possible to calculate the vibrational spectrum.

b) *polarisable:* these models allow for changes in the charge distribution of the water molecule due to an external field acting on it. The main advantages of such models is that they are better suited for simulations in systems that are inhomogeneous, such as where there are strong electric field gradients due to the presence of ions or at a solute–solvent interface, and they should be better at reproducing the behaviour of water in other phases such as solid or vapour. The main disadvantage with these models is that by incorporating polarisation effects the computational effort required can increase significantly;

c) *ab-initio:* these models are based upon *ab-initio* calculations on small clusters of water molecules such as the NCC model.[4]

As we can see from the three model types above each has advantages and disadvantages and therefore when one is considering simulating a system it is

worthwhile considering what properties of the system one is interested in and choosing a model that best predicts such properties. By far the most common models in use today are the non-polarisable models and for that reason we will concentrate our discussion on those models.

Non-polarisable Models

Non-polarisable models can usefully be split into three categories according to the number of interaction sites that they employ: three, four, or five interaction sites. The sites give rise to van der Waals interactions, Coulombic interactions, or both.

The computational effort involved in using these models increases as the number of interaction sites increases. This is because 9 site-site distances must be calculated for a three site model, 16 for a four site model and 25 for a five site model.

In these types of models the van der Waals interaction between two water molecules is usually calculated using a Lennard-Jones interaction. The combination of the electrostatic and van der Waals interactions leads to a pair interaction energy for molecules α and β, $E_{\alpha\beta}$, as given by equation 4.1:

$$E_{\alpha\beta} = \sum_{i}^{\ln\alpha} \sum_{j}^{\ln\beta} \frac{1}{4\pi\varepsilon_0} \frac{q_i q_j}{r_{ij}} + \frac{A_i A_j}{r_{ij}^{12}} - \frac{C_i C_j}{r_{ij}^{6}} \qquad \text{Equation 4.1}$$

where ε_0 is the permittivity of vacuum and is equal to $8.85418782 \times 10^{-12}$ F m^{-1}.

Three Interaction Site Models

A diagram to illustrate the most common implementation of a three interaction site model is shown in figure 4.1.

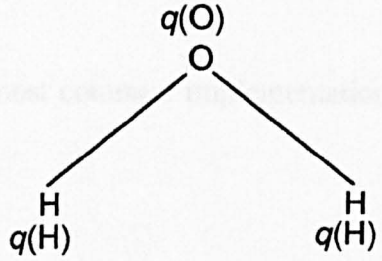

Figure 4.1 A three interaction site model.

Examples of three site models are:

a) transferable intermolecular potential functions, TIPS,[5] TIP3P;[6]

b) simple point charge, SPC;[7]

c) extended simple point charge, SPCE.[8]

The parameters used by these models are given in table 4.1.

	TIPS	TIP3P	SPC	SPCE
r(OH)/Å	0.9572	0.9572	1.0	1.0
HOH/°	104.52	104.52	109.47	109.47
A x 10^{-3} kcal $Å^{12}$ mol^{-1}	580.0	582.0	629.4	629.4
C kcal $Å^{6}$ mol^{-1}	525.0	595.0	625.5	625.5
q(O)/e	-0.80	-0.834	-0.82	-0.8476
q(H)/e	+0.40	+0.417	+0.41	+0.4238

Table 4.1 Three interaction site models constants.

Four Interaction Site Models

A diagram to illustrate the most common implementation of a four interaction site model is shown in figure 4.2.

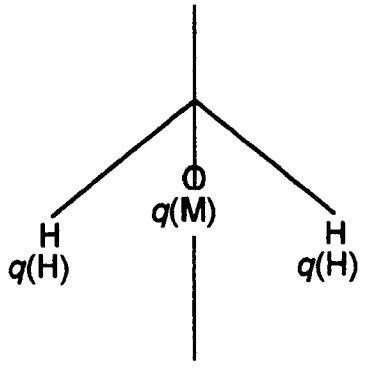

Figure 4.2 A four interaction site model.

Examples of four interaction site models are:

a) Bernal and Fowler, BF;[3]

b) Transferable intermolecular potential functions 2, TIPS2;[9]

c) Transferable intermolecular potential 4 point, TIP4P.[6]

The parameters used by these models are given in table 4.2.

	BF	TIPS2	TIP4P
r(OH)/Å	0.96	0.9572	0.9572
HOH/°	105.7	104.52	104.52
A x 10^{-3} kcal Å^{12} mol^{-1}	560.4	695	600
C kcal Å^{6} mol^{-1}	837.0	600	610
q(O)/e	0	0	0
q(H)/e	+0.49	+0.535	+0.52
q(M)/e	-0.98	-1.07	-1.04
r(OM)/Å	0.15	0.15	0.15

Table 4.2 Four interaction site models constants

Five Interaction Site Models

The most commonly used five interaction site model is the ST2[10] model based upon the four interaction site model of Ben-Naim and Stillinger, BNS.[11] In this model charges are placed on the hydrogen atoms and on two lone pair sites on the oxygens, with a single Lennard-Jones site acting on the oxygen atom. A diagram to illustrate this is shown in figure 4.3.

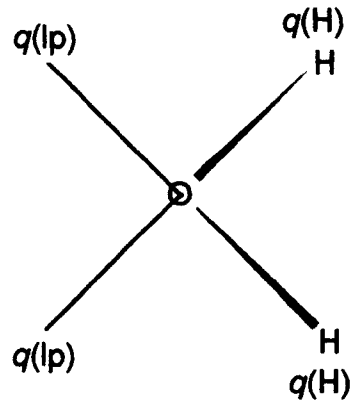

Figure 4.3 A five interaction site model.

Once again the van der Waals interaction between two water molecules is calculated using a Lennard-Jones function. However the electrostatic interaction is scaled by a modulation function so that for oxygen–oxygen distances below 2.016 Å the modulation function is 0 and for distances greater than 3.1287 Å it is 1, and it varies smoothly between these two limits.

The parameters used by this model are given in table 4.3.

	ST2
r(OH)/Å	1.0
HOH/°	109.47
$A \times 10^{-3}$ kcal Å^{12} mol^{-1}	238.7
C kcal Å^{6} mol^{-1}	268.9
q(O), e	0
q(H), e	+0.2375
q(lp), e	-0.2375
r(lp), Å	0.8

Table 4.3 Five interaction site models constants

4.2 Simulation Details

4.2.1 System Overview

In this section the preparation of the systems for the study of the amine carboxylates and amine sulphonates in aqueous solution is outlined.

4.2.2 System Preparation

Molecules Studied

In this project six potential hydrate inhibitors have been studied: three carboxylates and three sulphonates. The carboxylates are a group of zwitterionic compounds. In comparison the sulphonates are synthetic analogues of the carboxylates: they are also zwitterions, with similar structural moieties as present in the carboxylates, that is to say a quaternary nitrogen atom with three alkyl chains and a fourth chain (of varying length) connecting the nitrogen atom to a negatively charged hydrogen-bonding centre. The purpose of the fourth chain varying in length is to investigate the effect of charge separation upon the behaviour of the inhibitors. It was these similarities between the two groups of compounds that we believed would help us to compare and contrast the differences in their water structuring properties in order to determine the mode of action of the carboxylates and ultimately kinetic inhibitors.

The names and formulas of the three amine carboxylates and the three amine sulphonates are shown in table 4.4 along with the abbreviations used throughout this thesis.

MOLECULE	FORMULA	ABBREVIEATION
N,N,N-tributylammonium-1-(2-ethylcarboxylate)	$(C_4H_9)_3N^+CH_2COO^-$	tba1C
N,N,N-tributylammonium-1-(3-propylcarboxylate)	$(C_4H_9)_3N^+(CH_2)_2COO^-$	tba2C
N,N,N-tributylammonium-1-(4-butylcarboxylate)	$(C_4H_9)_3N^+(CH_2)_3COO^-$	tba3C
N,N,N-tributylammonium-1-(1-methylsulphonate)	$(C_4H_9)_3N^+CH_2SO_3^-$	tba1S
N,N,N-tributylammonium-1-(2-ethylsulphonate)	$(C_4H_9)_3N^+(CH_2)_2SO_3^-$	tba2S
N,N,N-tributylammonium-1-(3-propylsulphonate)	$(C_4H_9)_3N^+(CH_2)_3SO_3^-$	tba3S

Table 4.4 Molecular formulas and abbreviations. Note 1, 2, 3 in the abbreviations refers to the number of CH_2 spacer groups, while C and S refers to whether the inhibitor is an amine Carboxylate or amine Sulphonate.

Molecular Conformations/Charges

A set of charges/conformations for each of the six molecules studied has been derived by means of an iterative process involving the calculation of the electrostatic potential derived charges, ESPD,[12] followed by subsequent energy-minimisation of the molecule as outlined below.

The initial structure for each of the six molecules studied was drawn using the 3-D sketcher in Cerius[2],[13] and subsequently minimised using the minimiser option. The default options were used for the minimiser, namely universal force field,[14] conjugate gradient algorithm[15] with termination occurring after 500 steps or the RMS force being 0.1 kcal mol^{-1} $Å^{-1}$. These initial conformations for the six molecules were then used as the starting point for a charge calculation. ESPD charges were calculated for each of the six molecules from a Restricted Hartree Fock, RHF, single point energy calculation with a 6-31G** basis set in GAUSSIAN94.[16] The charges derived from these calculations were then applied to the respective molecules and their geometries re-optimised in Cerius[2].

This cycle of GAUSSIAN94/minimser calculations was iterated for two cycles whence convergence was obtained. It was found at this point that the energy/charges and conformations did not change significantly and hence the conformations were used as the starting point for a series of molecular dynamics simulations.

The initial conformations of the six molecules studied can be seen in figure 4.4.

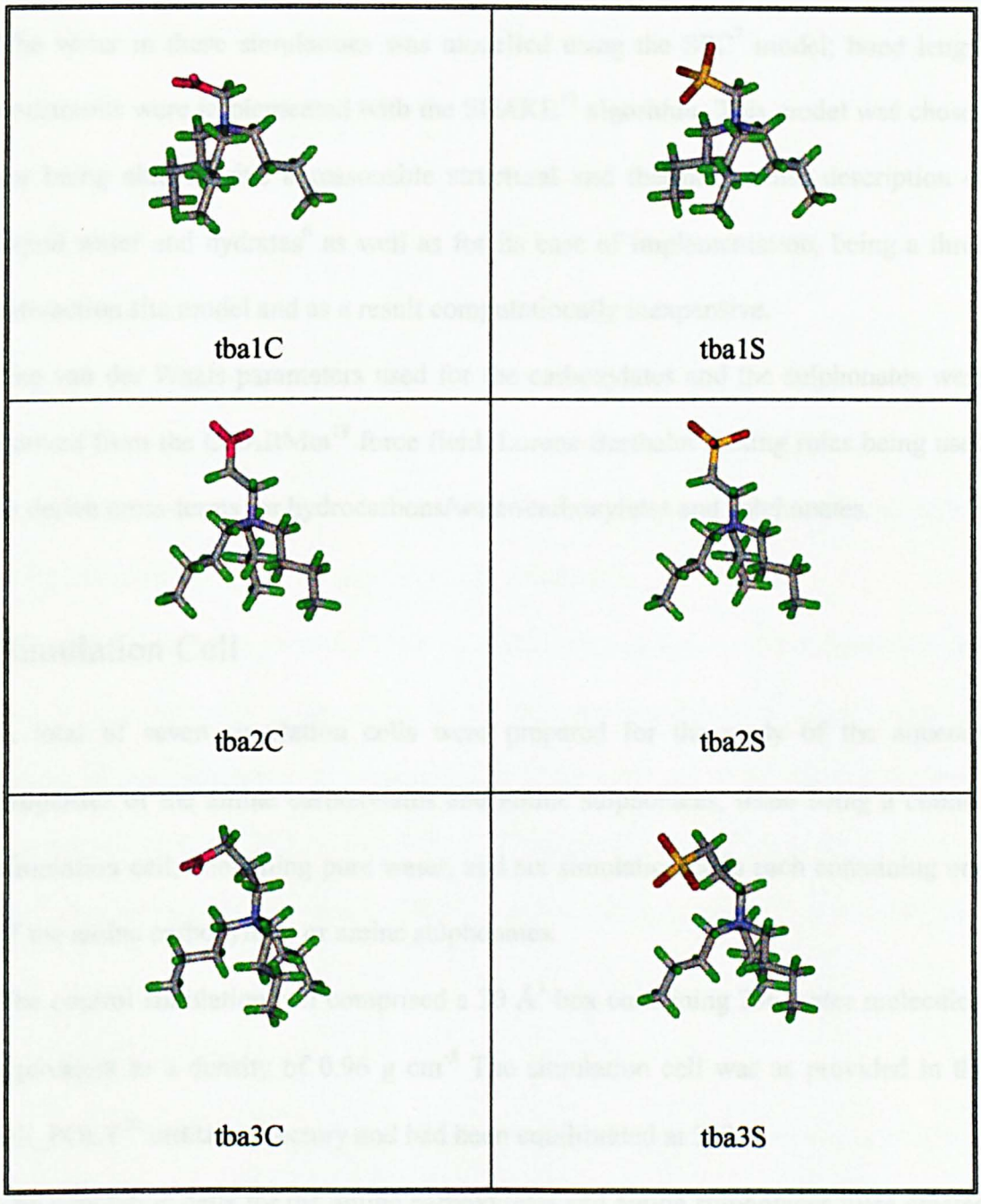

Figure 4.4 The initial conformations of the six potential inhibitors listed in table 4.4. Carbon–grey, hydrogen–green, nitrogen–blue, sulphur–yellow, carboxylate oxygen–pink, sulphonate oxygen–red.

Potentials

The water in these simulations was modelled using the SPC[7] model; bond length constraints were implemented with the SHAKE[17] algorithm. This model was chosen for being able to give a reasonable structural and thermodynamic description of liquid water and hydrates[6] as well as for its ease of implementation, being a three interaction site model and as a result computationally inexpensive.

The van der Waals parameters used for the carboxylates and the sulphonates were derived from the CHARMm[18] force field. Lorenz-Berthelot mixing rules being used to derive cross-terms for hydrocarbons/water/carboxylates and sulphonates.

Simulation Cell

A total of seven simulation cells were prepared for the study of the aqueous properties of the amine carboxylates and amine sulphonates, those being a control simulation cell, containing pure water, and six simulation cells each containing one of the amine carboxylates or amine sulphonates.

The control simulation cell comprised a 20 $Å^3$ box containing 256 water molecules, equivalent to a density of 0.96 g cm^{-3} The simulation cell was as provided in the DL_POLY[19] utilities directory and had been equilibrated at 300 K.

The simulation cells for the amine carboxylates and amine sulphonates were created by taking a copy of the control simulation cell and inserting one of the solute molecules. The molecule was inserted in such a way so that any solvent molecules that created a bad contact were removed, bad contacts being defined using the van der Waals radius of the atoms involved. Therefore any solvent atoms that overlap with the molecule were removed along with the rest of the solvent molecule.

Simulations Performed

The six simulation cells obtained above were then used as the initial configurations for a 5000 step [*N*, *V*, *T*]-molecular dynamics simulation run using DL_POLY[19] with a thermostat value of 0.1 ps, to ensure that the density of the system was equal to 0.96 g cm^{-3}. All simulations were carried out at a temperature of 300 K and with a time step of 1 fs.

Long-range electrostatic interactions were evaluated with an Ewald summation,[20] while all other interactions were truncated for distances in excess of 9.5 Å.

Bond lengths, bond angles and torsions for the amine carboxylates and amine sulphonates were treated dynamically as per chapter 2.

The seven simulation cells obtained were then used as the initial configurations for longer simulations in order to study the aqueous properties of the six potential inhibitors and pure water as a comparison. Once again all of the simulations were carried out using DL_POLY, in the [*N*, *V*, *T*] ensemble with a thermostat value of 0.1 ps. Simulations were carried out at 300 K for 200 000 steps with a time step of 1 fs.

Simulation Analysis

The seven 200 000 step simulations were then analysed using the techniques outlined in chapter 3 to determine time correlation functions, radial distribution functions and order parameters, with the results of these analyses being presented in section 4.3.

In order to calculate the various above-mentioned functions it was decided to split the amine carboxylates and amine sulphonates into chemically/symmetrically similar regions as shown in figure 4.5, which are summarised below:

a) C1, which is the carbons immediately next to the nitrogen atom;

b) C2, which is the central carbons of the butyl chains;

c) C3, which is the terminal carbons of the butyl chains;

d) C4, which is the carbons immediately next to the headgroup moiety.

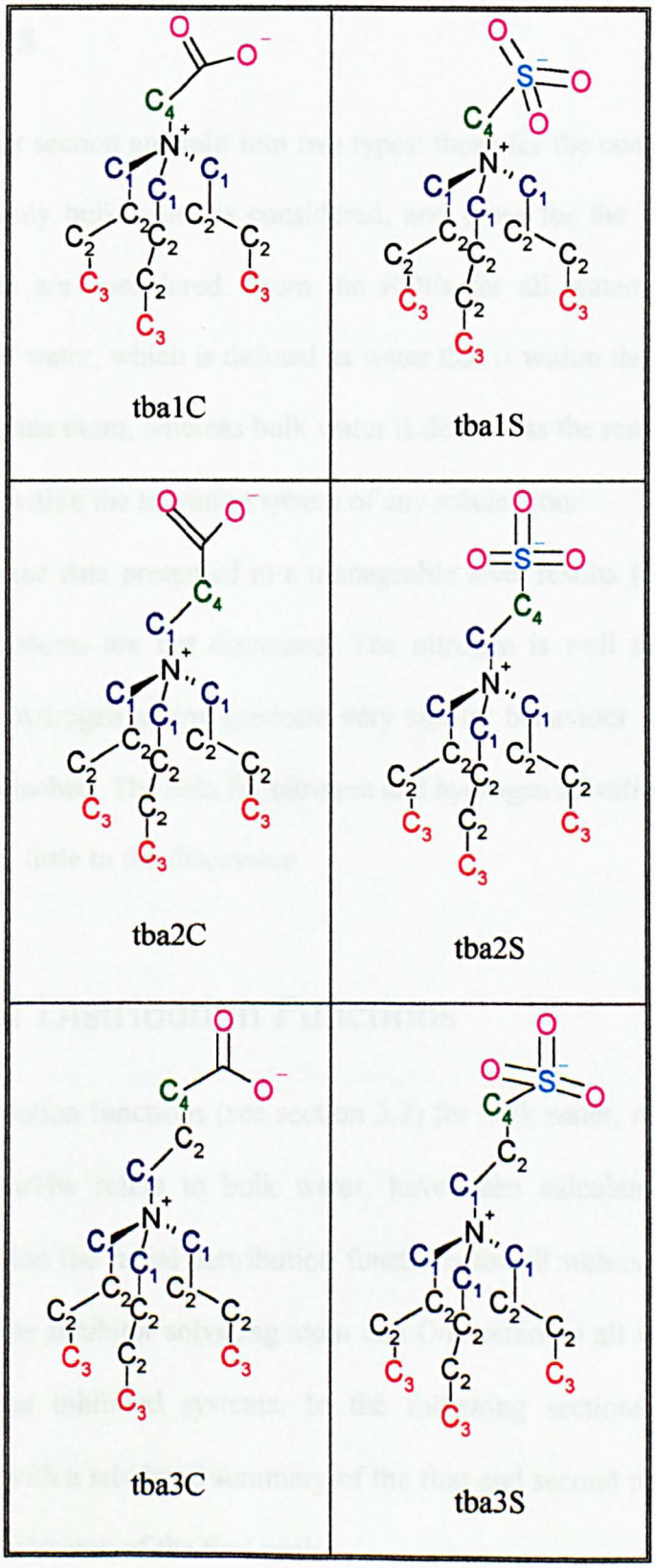

Figure 4.5 Numbering schemes used for the six potential inhibitors. Note the C atom of the amine carboxylates headgroup has not been shown but is colour coded as the S atom of the amine sulphonates.

4.3 Results

The results in this section are split into two types: those for the control and inhibited systems where only bulk water is considered, and those for the inhibited systems where all waters are considered. From the RDFs for all waters we are able to consider solvated water, which is defined as water that is within the solvation sphere of at least one solute atom, whereas bulk water is defined as the remaining water, *i.e.* water that is not within the solvation sphere of any solute atom.

In order to keep the data presented to a manageable level results for the nitrogen or hydrogen solute atoms are not discussed. The nitrogen is well shielded from the solvent and the hydrogen atoms generate very similar behaviour to the carbons to which they are attached. The data for nitrogen and hydrogen solvation were therefore found to add very little to the discussion.

4.3.1 Radial Distribution Functions

The radial distribution functions (see section 3.3) for bulk water, namely g_{OwOw} and g_{OwHw} where Ow/Hw refers to bulk water, have been calculated for the seven systems. In addition the radial distribution functions for all waters, namely g_{XO} and g_{XH} where X is the inhibitor solvating atom and O/H refers to all waters, have been calculated for the inhibited systems. In the following sections these plots are presented along with a tabulated summary of the first and second peak positions and where applicable the area of the first peak.

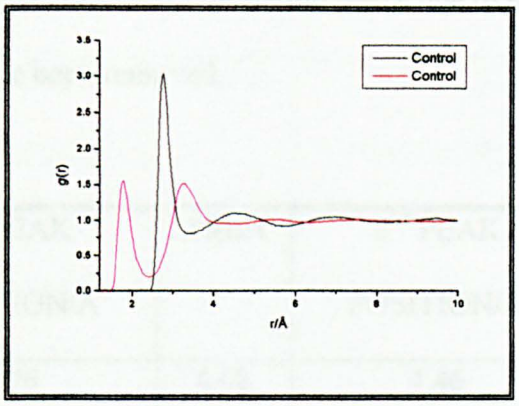

Figure 4.6 The radial distribution functions, of bulk water oxygens about bulk water oxygens (black) and of bulk water hydrogens about bulk water oxygens (red), for the control system.

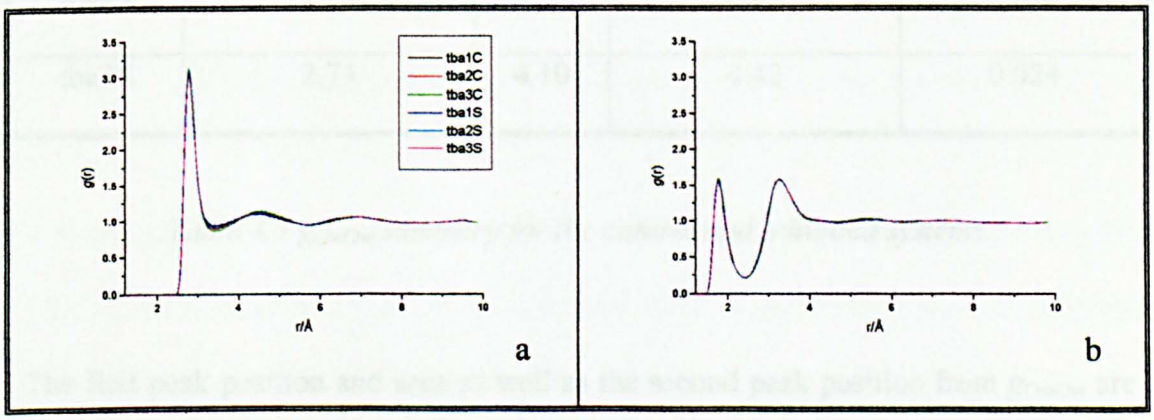

Figure 4.7 The radial distribution functions, of bulk water oxygens about bulk water oxygens (a) and of bulk water hydrogens about bulk water oxygens (b), for inhibited systems. The legend is the same for each plot.

The radial distribution functions g_{OwOw} and g_{OwHw} for the control and inhibited systems can be seen in figures 4.6 and 4.7, g_{OwOw} corresponds to the oxygen

distribution around the oxygen atom, both atoms belonging to bulk water, whereas g_{OwHw} corresponds to the hydrogen distribution around the oxygen atom, both of bulk water. In figures 4.6 and 4.7 the self-correlation peaks due to the internal geometry of the water molecule have been removed.

SYSTEM	1st PEAK POSITION/Å	AREA	2nd PEAK POSITION/Å	RESOLUTION OF PEAKS/Å
Control	2.76	4.08	4.46	0.025
tba1C	2.76	4.05	4.50	0.024
tba2C	2.76	4.07	4.50	0.025
tba3C	2.75	4.02	4.55	0.025
tba1S	2.76	4.03	4.43	0.024
tba2S	2.77	4.09	4.43	0.024
tba3S	2.74	4.10	4.42	0.024

Table 4.5 g_{OwOw} summary for the control and inhibited systems.

The first peak position and area as well as the second peak position from g_{OwOw} are shown for the seven systems in table 4.5. The first peak area is as calculated by the Origin 5.0 peak area tool using the trapezium rule out to a distance of ~ 3.5 Å. In g_{OwOw} this corresponds to the number of nearest neighbour atoms, which in perfectly hydrogen-bonded tetrahedral water would be 4.

The analogous values as in table 4.5 are presented for g_{OwHw} in table 4.6. The first peak area in g_{OwHw} corresponds to the number of hydrogen bond acceptors per water

molecule which, when doubled, gives the number of hydrogen bonds per water molecule.

SYSTEM	1st PEAK POSITION/Å	AREA	2nd PEAK POSITION/Å	RESOLUTION OF PEAKS/Å
Control	1.76	1.79	3.24	0.025
tba1C	1.76	1.78	3.25	0.024
tba2C	1.75	1.80	3.25	0.025
tba3C	1.76	1.78	3.27	0.025
tba1S	1.76	1.76	3.24	0.024
tba2S	1.77	1.79	3.26	0.024
tba3S	1.77	1.79	3.23	0.024

Table 4.6 g_{OwHw} summary for the control and inhibited systems.

The g_{OwOw} summary (table 4.5) and the g_{OwHw} summary (table 4.6) for the control and inhibited systems allow us to determine various parameters from the control system for comparison with the inhibited systems.

The first value of interest is the first peak position in g_{OwOw} at 2.76 Å, which gives us the first neighbour oxygen–oxygen distance and the area under this peak of 4.08. The area under this peak would be expected to be 4.00 if each water molecule accepted two hydrogen bonds from neighbours and donated two as in the simple random tetrahedral network model.

The second value is the first peak position in g_{OwHw} at 1.76 Å whose area of 1.79 gives us the number of hydrogen bond acceptors per water molecule, which doubled

gives the number of hydrogen bonds per water molecule, namely 3.58. This value of 3.58 is a bit smaller than the value of 4.00 assumed in the random tetrahedral network model.

If we now compare the values obtained for the control system with those for the inhibited systems then we see that the first peak position and area for both g_{OwOw} and g_{OwHw} are unaffected by the presence of solutes. This agreement between the control and the inhibited systems values suggest that the short-range water structure is not altered by either the amine carboxylates or the amine sulphonates. However if we consider the second peak position for g_{OwOw} in table 4.5 we do see that there is a slight movement of this peak for the amine carboxylates to longer distances suggesting a weakening in the long-range water structure, with an opposite effect observed for the amine sulphonates. But at best, this effect is very small.

Inhibited Systems: Solvated Waters

The radial distribution functions g_{XO} and g_{XH} for the inhibited systems can be seen in figures 4.8 and 4.9, g_{XO} corresponds to the distribution of water oxygens around the X atom where X is C1, C2, C3, C4 or the headgroup C/S, O, whereas g_{XH} corresponds to the distribution of water hydrogens around the X atom.

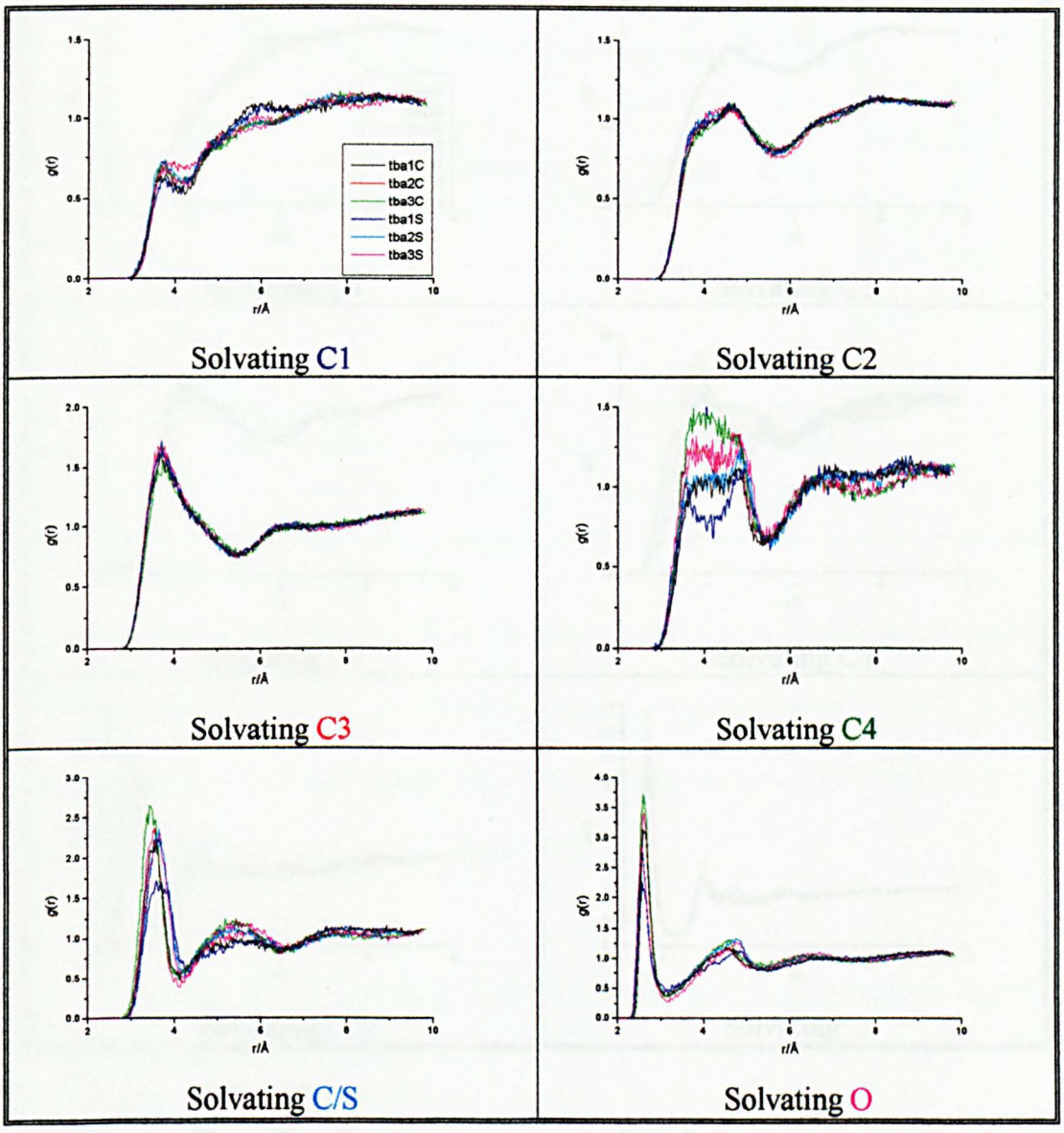

Figure 4.8 The radial distribution functions of the oxygen atom of all waters around various solute atoms for the inhibited systems. The legend is the same for each plot and atom numbers are coloured as per figure 4.5.

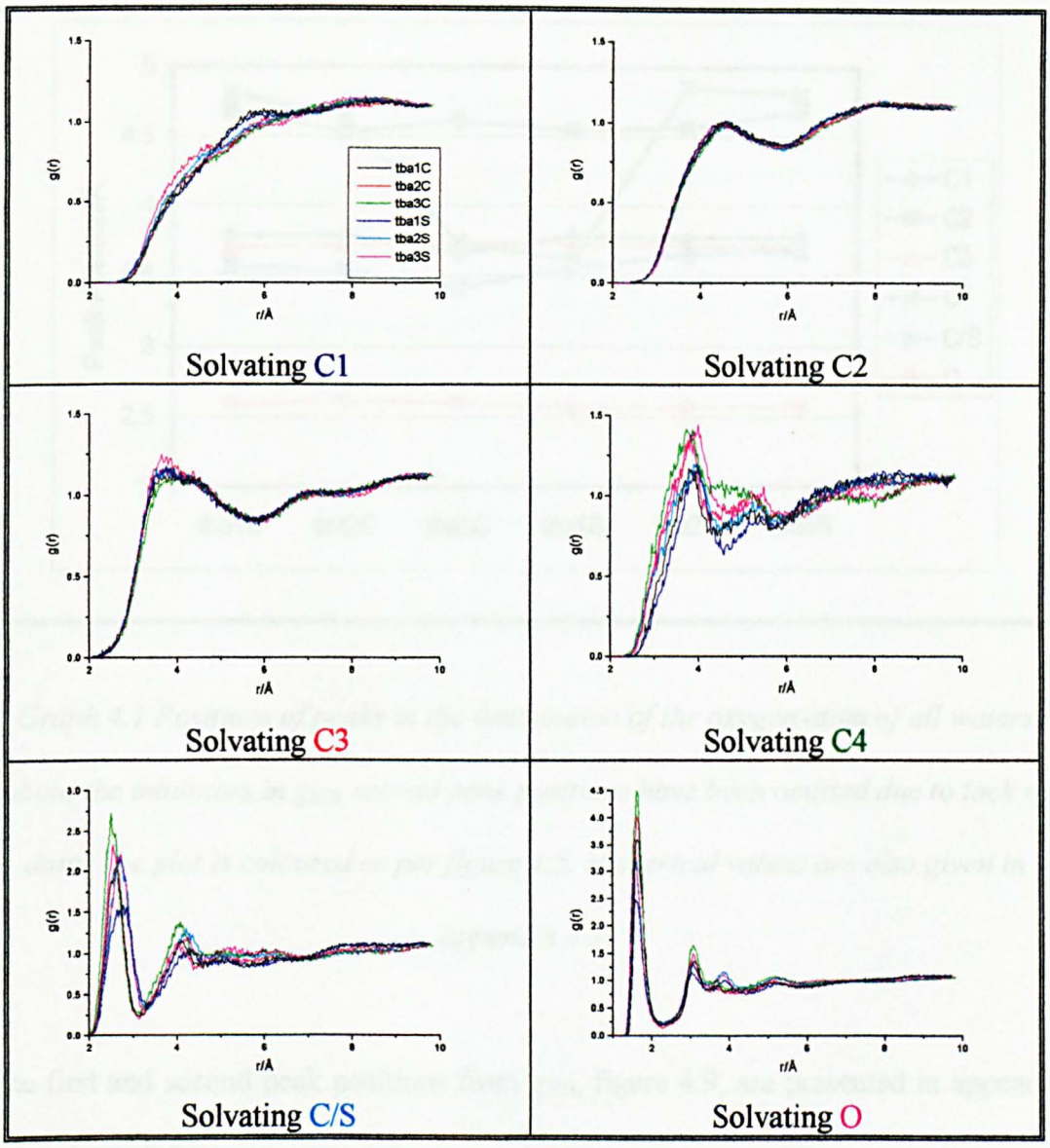

Figure 4.9 The radial distribution functions of the hydrogen atom of all waters around various solute atoms for the inhibited systems. The legend is the same for each plot and atom numbers are coloured as per figure 4.5.

The first and second peak positions from g_{XO}, figure 4.8, are presented in appendix 4.1 and graph 4.1.

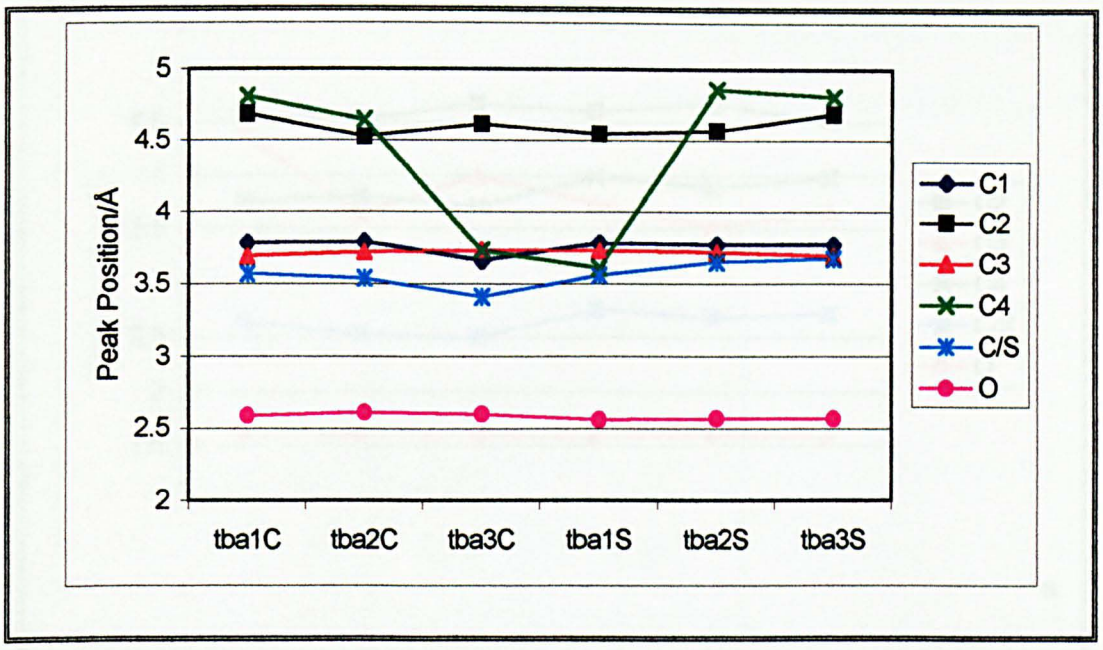

Graph 4.1 Positions of peaks in the distribution of the oxygen atom of all waters about the inhibitors in g_{XO}, second peak positions have been omitted due to lack of data. The plot is coloured as per figure 4.5. Numerical values are also given in appendix 4.1.

The first and second peak positions from g_{XH}, figure 4.9, are presented in appendix 4.2 and graph 4.2.

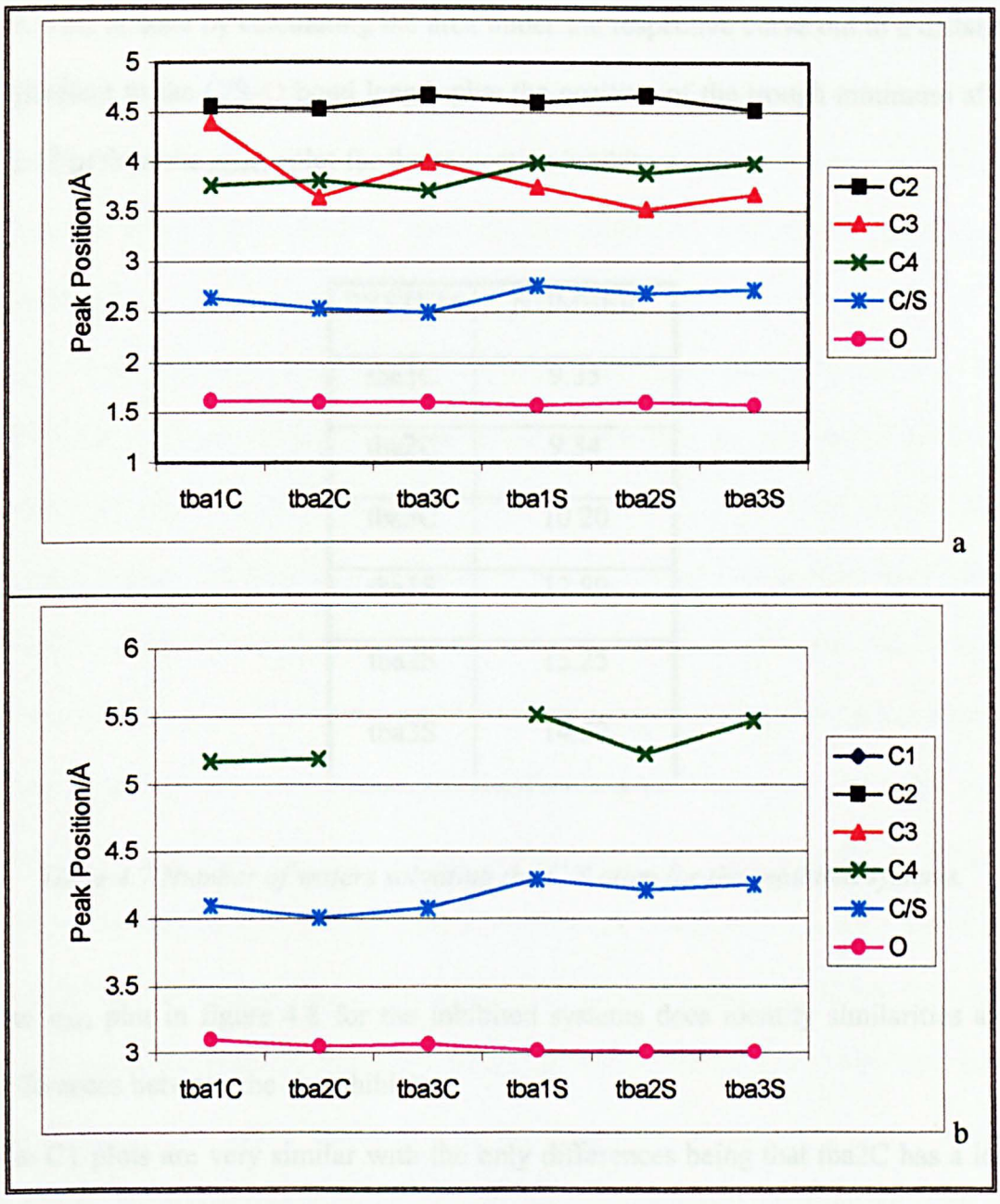

Graph 4.2 Positions of peaks in the distribution of the hydrogen atom of all waters about the inhibitors, first peak positions (a) and second peak positions (b), in g_{XH}, some of the second peak positions have been omitted due to lack of data. Graphs are coloured as per figure 4.5. Numerical values are also given in appendix 4.2.

In addition the number of waters solvating the C/S atom of the inhibitor headgroup have been calculated from the radial distribution functions and are presented in table

4.7. This is done by calculating the area under the respective curve out to a distance equivalent to the C/S–O bond length plus the position of the trough minimum after the 1st peak in the g_{OwOw} plot for the respective inhibitors.

SYSTEM	NUMBER
tba1C	9.35
tba2C	9.34
tba3C	10.20
tba1S	12.89
tba2S	15.25
tba3S	14.52

Table 4.7 Number of waters solvating the C/S atom for the inhibited systems.

The g_{XO} plot in figure 4.8 for the inhibited systems does identify similarities and differences between the six inhibitors.

The C1 plots are very similar with the only differences being that tba2C has a less well-defined peak at 3.79 Å and tba1C, tba1S show a broad shoulder at ~ 6 Å. This shoulder at ~ 6 Å may be a feature of all of the inhibitors but only shows up for tba1C and tba1S as these are the only two inhibitors studied with three C1 atoms as opposed to four for the other inhibitors; as a result of this there would be less averaging of the signal for tba1C and tba1S which may allow this shoulder to show up.

The C2 and C3 plots show no apparent differences for the inhibitors.

The fact that the respective plots for C1, C2 and C3 are almost identical is probably a reflection of the fact that these carbons are almost exclusively located in the hydrocarbon butyl chains of the inhibitors, *i.e.* in the hydrophobic region, and are displaced from the variations between the different zwitterionic headgroups considered.

The C4 plot appears to be split into two groups, the first comprising tba1S, tba2S and tba1C and the second tba2C, tba3C and tba3S. However if we consider the inhibitors in terms of the amine carboxylates and amine sulphonates we see that as the charge separation increases the first peak height in each of the two series increases. This is probably a reflection of the fact that as the charge separation increases the C4 atom moves further away from the sterically hindered nitrogen atom and therefore there is more 'room' for water molecules to solvate the C4 atom.

The C/S plot of the headgroup shows a similar trend to that observed for the C4 plot in that the first peak height increases with increasing charge separation for the amine carboxylates and amine sulphonates, although for tba2S and tba3S the first peak height is almost identical. Another interesting point is that as the charge separation increases for the amine carboxylates the first peak position moves to shorter distances indicating that there is stronger hydrogen-bonding, whereas an opposite effect is observed for amine sulphonates.

From table 4.7 it can be seen that the number of waters solvating the amine sulphonates headgroup is considerably greater than for the amine carboxylates. This is probably a result of the fact that the headgroup of the amine sulphonates contain one more oxygen atom than the amine carboxylates and is therefore able to hydrogen bond with more water molecules therefore increasing the number of waters around the amine sulphonates S atom in comparison to the amine carboxylates C atom.

Indeed if we find the ratio of the number of waters solvating the amine carboxylates headgroup to the number of waters solvating the amine sulphonates headgroup we find

a) tba1C : tba1S = 2 : 2.8

b) tba2C : tba2S = 2 : 3.3

c) tba3C : tba3S = 2 : 2.8

which are very close to the ratio of number of oxygens in the headgroups, 2 : 3.

The O plot of the headgroup in g_{XO}, which can be compared with g_{OwOw} for bulk water in the control and inhibited systems, does show differences from bulk water. The first peak position in the O plot occurs at ~ 2.60 Å whereas for bulk water this peak occurs at 2.75 Å, which indicates that the hydrogen-bonding between the O atom solvated water is stronger than found between bulk water molecules. In addition the first peak heights for the amine carboxylates are higher whereas the amine sulphonates show lower first peak heights when compared with bulk water in the control system. However if we consider the second peak position in the O plot we see that it is at longer distances than for g_{OwOw} in bulk water which indicates weaker hydrogen-bonding in this region, especially for the amine sulphonates, but with all of the inhibitors showing higher second peak heights than found for bulk water in the control system. This indicates that the second solvation shell is larger than for bulk water, but that it is still a more prominent feature than found in liquid water. This gives rise to the picture of a smaller more well-defined first solvation shell surrounded by a larger but still more well-defined second solvation shell than is found in bulk water. In addition the trough after the first peak in the O plot is at a lower value than for g_{OwOw} in bulk water, again suggesting that the inhibitor–solvated

water hydrogen bond may be more precisely defined than the bulk water–bulk water hydrogen bond.

The g_{XH} plot in figure 4.9 shows similar trends to those observed for g_{XO}.

The C1 plot is very similar apart from tba2C showing a slight difference with a broad shoulder at 6 Å.

The C2 and C3 plots are also very similar for each of the inhibitors with only a small difference being observed for tba2C in the C3 plot with a better-defined first peak.

The C4 plot shows the same ranking of the inhibitor series with the first peak height increasing as the charge separation increases for the amine carboxylates and amine sulphonates. In addition the first peak position is at longer distances for the amine sulphonates when compared with the amine carboxylates. A second peak is also apparent at ~ 5.2 Å for each of the inhibitors except tba3C, which seems to have a broad shoulder on the first peak which encompasses the position of the second peak. The second peak position is coincident with the trough in the g_{XO} plot for C4.

The C/S plot of the headgroup shows that the first peak height increases with increasing charge separation for the amine carboxylates and amine sulphonates, although for tba2S and tba3S the first peak height is almost identical. Another interesting point is that as the charge separation increases for the amine carboxylates the first peak position moves to shorter distances indicating that there is stronger hydrogen-bonding. We note, however, that the peak positions for the amine sulphonates do not show the same trend across the series. In this case the first peak position for tba1S is at longer distances than for tba2S and tba3S, however these two inhibitors do exhibit a movement of the first peak position to longer distances as the charge separation increases.

The O plot of the headgroup in g_{XH}, which can be compared with g_{OwHw} for bulk water in the control and inhibited systems, does reveal some differences from bulk water. The first obvious point to note is that there are in fact four peaks in the O plot compared with two in the g_{OwHw} plot for bulk water. Both the first and second peak positions are at shorter distances in the O plot with the first peak height being significantly higher for the inhibitors when compared with the g_{OwHw} plot for bulk water—indicating a more structured first and second solvation shell. In addition the appearance of a third/fourth peak in the O plot shows that there is much longer-range solvent order around the inhibitor O than is found around a bulk water molecule. The trough after the first peak is also more pronounced, which once again indicates increased structuring due to a better-defined inhibitor–water hydrogen bond.

4.3.2 Co-ordination Number

The frequency distribution of waters with a specified co-ordination number (see section 3.5), ranging from 1–10, has been calculated for the seven systems. In the following sections the most popular co-ordination number is tabulated along with the percentage of waters with co-ordination numbers 3, 4 or 5; this is useful in determining if the inhibitors distort the co-ordination number of water away from that for a perfect tetrahedral network. In all systems the distributions have been expressed as a percentage of the total number of each type of water in the system, to allow for direct comparison between results.

Control and Inhibited Systems: Bulk Water

The favoured co-ordination number and percentage of bulk waters with a co-ordination number of 3, 4 or 5 for the control and inhibited systems is presented in table 4.8 and graph 4.3.

SYSTEM	MODAL CO-ORDINATION NUMBER	AVERAGE CO-ORDINATION NUMBER	% OF BULK WATERS WITH CO-ORDINATION NUMBER		
			3	4	5
Control	4	4.48	11	42	32
tba1C	5	4.76	7	34	36
tba2C	4	4.65	9	37	35
tba3C	4	4.56	10	40	33
tba1S	5	4.82	7	33	36
tba2S	4	4.72	8	36	35
tba3S	5	4.74	8	35	35

Table 4.8 Co-ordination number summary for bulk water in the control and inhibited systems.

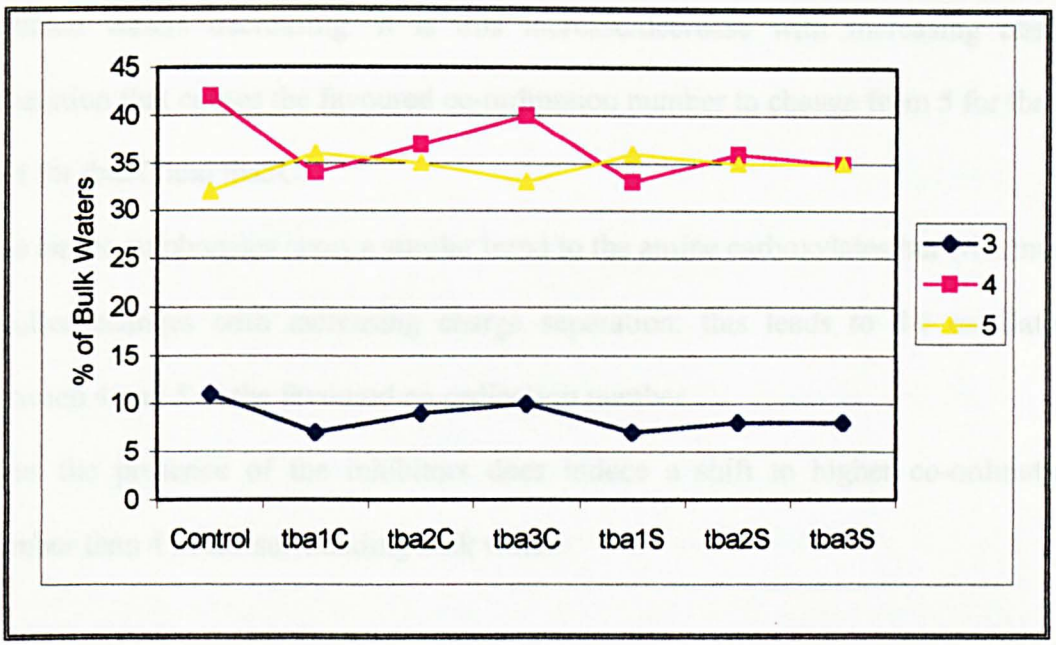

Graph 4.3 The percentage of bulk waters with co-ordination number 3, 4 or 5.

From table 4.8 it can be seen that the control system yields a value of 4 for the most likely co-ordination number, which is consistent with the random tetrahedral network model. This value is also obtained for tba2C, tba3C and tba2S, although tba1C, tba1S and tba3S favour 5-co-ordinate water. In all inhibited systems, however, the preference is small and 4- and 5-co-ordinate waters are almost equally likely (graph 4.3). A better measure of this subtle balance between 4- and 5-co-ordinate waters can be found from the average co-ordination number. This shows a clear increase in the presence of the inhibitors, with the tendency for this increase to be greatest when the zwitterionic length is shortest. This increase indicates that the inhibitors are indeed distorting the co-ordination number of water away from the usual value of 4 expected in a tetrahedral network to a co-ordination number of 5.

For the amine carboxylates there is a higher percentage of 5-co-ordinate waters than in the control system. In addition as the charge separation increases then the percentage of 3- and 4-co-ordinate waters both increase with the number of 5-co-

ordinate waters decreasing. It is this increase/decrease with increasing charge separation that causes the favoured co-ordination number to change from 5 for tba1C to 4 for tba2C and tba3C.

The amine sulphonates show a similar trend to the amine carboxylates but with much smaller changes with increasing charge separation; this leads to the oscillation between 4 and 5 as the favoured co-ordination number.

Thus the presence of the inhibitors does induce a shift to higher co-ordination number than 4 in the surrounding bulk water.

Inhibited Systems: Solvated Water

Data for the co-ordination number distribution of solvated water in the different solvation environments is presented in appendix 4.3 and graph 4.4.

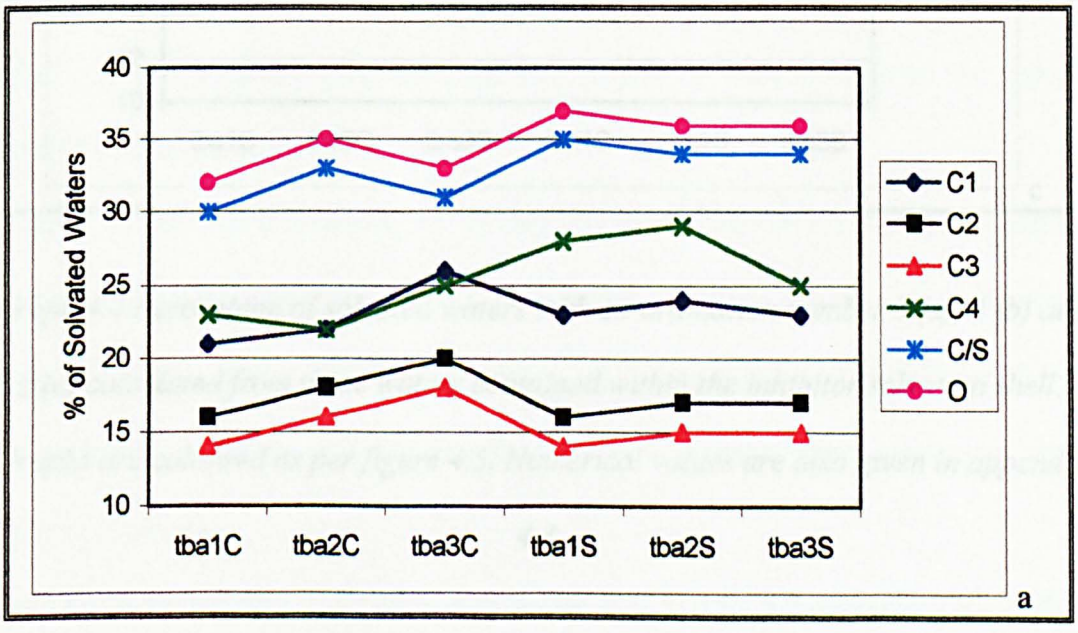

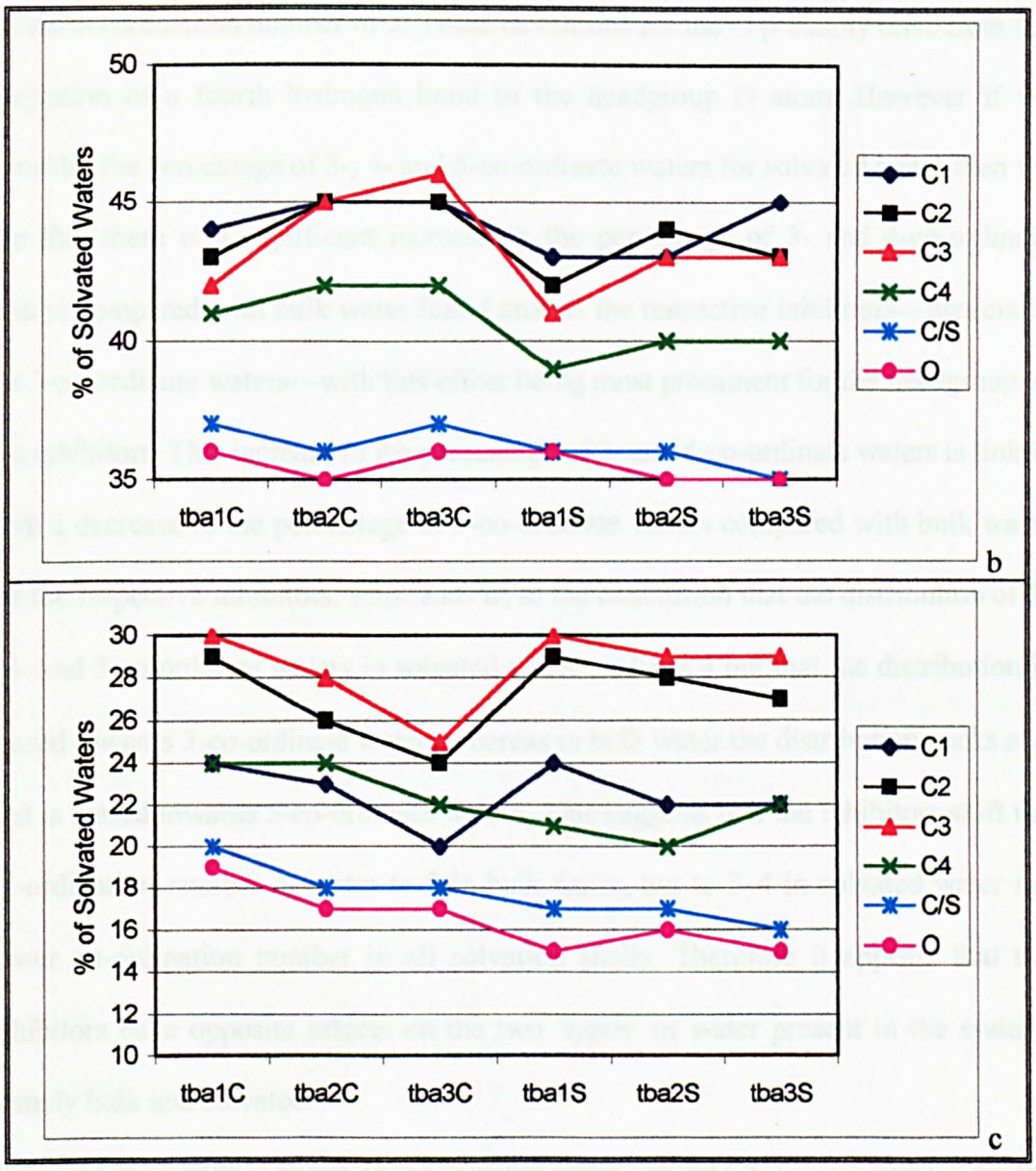

Graph 4.4 Percentage of solvated waters with co-ordination number 3 (a), 4 (b) and 5 (c) calculated from those waters contained within the inhibitor solvation shell. Graphs are coloured as per figure 4.5. Numerical values are also given in appendix 4.3.

The data shows that the modal co-ordination number for solvated water in the inhibited systems is in nearly all cases 4, with only the O atom in some inhibitor headgroups deviating from this: for tba2C and the amine sulphonates which have a

modal co-ordination number of 3. These deviations for the O probably arise from the formation of a fourth hydrogen bond to the headgroup O atom. However if we consider the percentage of 3-, 4- and 5-co-ordinate waters for solvated water then we see that there is a significant increase in the percentage of 3- and 4-co-ordinate waters compared with bulk water found around the respective inhibitors—especially for 3-co-ordinate waters—with this effect being most prominent for the headgroup of the inhibitors. This increase in the percentage of 3- and 4-co-ordinate waters is linked with a decrease in the percentage of 5-co-ordinate waters compared with bulk water for the respective inhibitors. This leads us to the conclusion that the distribution of 3-, 4- and 5-co-ordinate waters in solvated water peaks at 4 but that the distribution is biased towards 3-co-ordinate waters whereas in bulk water the distribution peaks at 4 and is biased towards 5-co-ordinate waters. This suggests that the inhibitors shift the co-ordination number of water to 5 in bulk water, but to 3–4 in solvated water *i.e.* lower co-ordination number in all solvation shells. Therefore it appears that the inhibitors have opposite effects on the two 'types' of water present in the system, namely bulk and solvated.

A similar behaviour is observed for solvated water around C1, C2, C3 and C4 for the amine carboxylates as was observed in bulk water, with an increase in the percentage of 3- and 4-co-ordinate waters with increasing charge separation accompanied by a corresponding decrease in the percentage of 5-co-ordinate waters; however, these effects are small.

Once again the amine sulphonates show a similar trend for solvated water as for bulk water in the case of C1, C2, C3 and C4. The results observed for solvated waters around the C/S and O atom of the headgroup are different from those observed for C1, C2, C3 and C4, with the number of 3-, 4- and 5-co-ordinate waters being almost

constant throughout the amine carboxylates and amine sulphonates. This leads us to believe that there are two distinct solvation regions, surrounding the hydrocarbon atoms C1, C2, C3 and C4 or surrounding the headgroup C/S and O atoms.

In summary for C1, C2, C3 and C4 there are more 3-, slightly more 4- and fewer 5-co-ordinate waters for solvated water compared with bulk water. For C/S and O there are many more 3-, a similar number of 4-, and significantly fewer 5-co-ordinate waters for solvated water compared with bulk water.

4.3.3 Order Parameters: F_3, $F_{4\varphi}$ and F_{4t}

The order parameters F_3, $F_{4\varphi}$ and F_{4t} (see section 3.4) for co-ordination numbers ranging from 1–10 have been calculated for the seven systems.

Control and Inhibited Systems: Bulk Water

Plots of F_3, $F_{4\varphi}$ and F_{4t} against co-ordination number for bulk water in the control and inhibited systems are shown in figure 4.10.

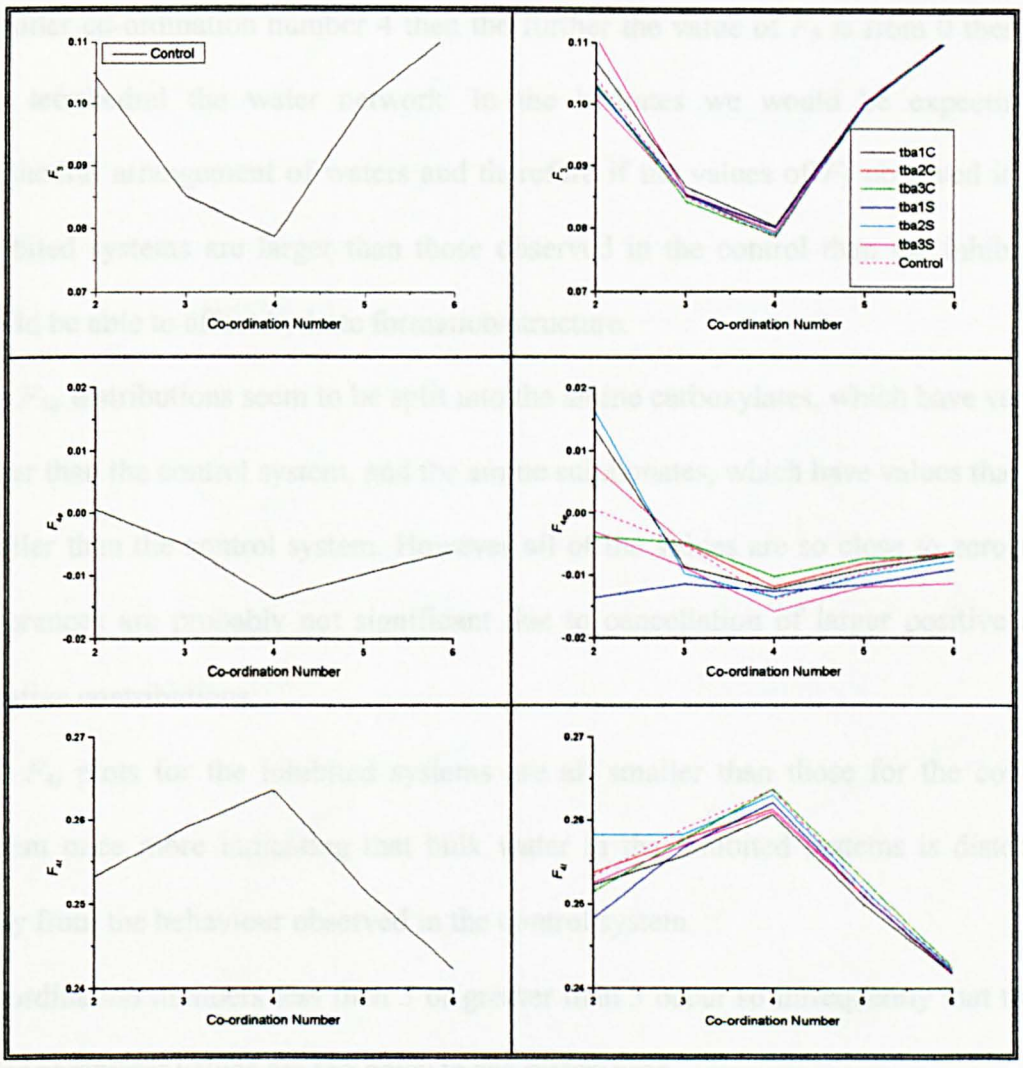

Figure 4.10 F_3, $F_{4\varphi}$ and F_{4t} for bulk water in the control system (left) and bulk water in the control and inhibited systems (right). The legend is the same for each plot on the left and each plot on the right.

From figure 4.10 it can be seen that the general appearance of the plots for the inhibited systems is similar to that for the control system and hence liquid water. However from the F_3 plots for the inhibited systems we can observe that the values of F_3 for co-ordination numbers 3, 4 or 5 are, in general, for all inhibitors larger than those for the control system, indicating that bulk water in the inhibited systems is

distorted away from the behaviour observed in the control system. Specifically if we consider co-ordination number 4 then the further the value of F_3 is from 0 then the less tetrahedral the water network. In the hydrates we would be expecting a tetrahedral arrangement of waters and therefore if the values of F_3 observed in the inhibited systems are larger than those observed in the control then the inhibitors would be able to affect hydrate formation/structure.

The $F_{4\varphi}$ distributions seem to be split into the amine carboxylates, which have values larger than the control system, and the amine sulphonates, which have values that are smaller than the control system. However all of the values are so close to zero that differences are probably not significant due to cancellation of larger positive and negative contributions.

The F_{4t} plots for the inhibited systems are all smaller than those for the control system once more indicating that bulk water in the inhibited systems is distorted away from the behaviour observed in the control system.

Co-ordination numbers less than 3 or greater than 5 occur so infrequently that these order parameter values are too noisy to see differences.

Inhibited Systems: Solvated Water

Plots of F_3, $F_{4\varphi}$ and F_{4t} against co-ordination number for solvated water in the inhibited systems are shown in figures 4.11, 4.12 and 4.13.

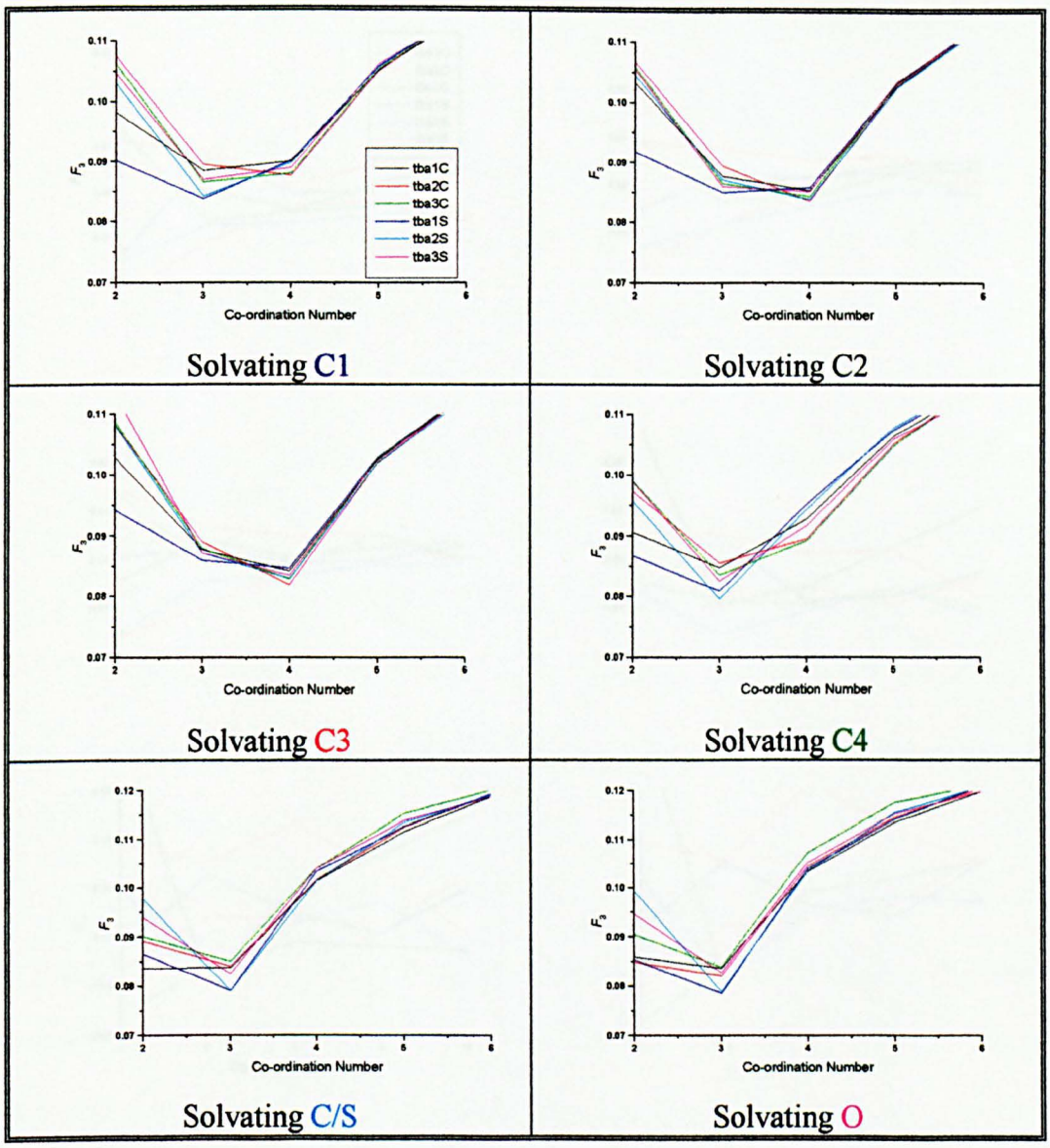

Figure 4.11 F_3 for solvated water around various solute atoms for the inhibited systems. The legend is the same for each plot and atom numbers are coloured as per figure 4.5.

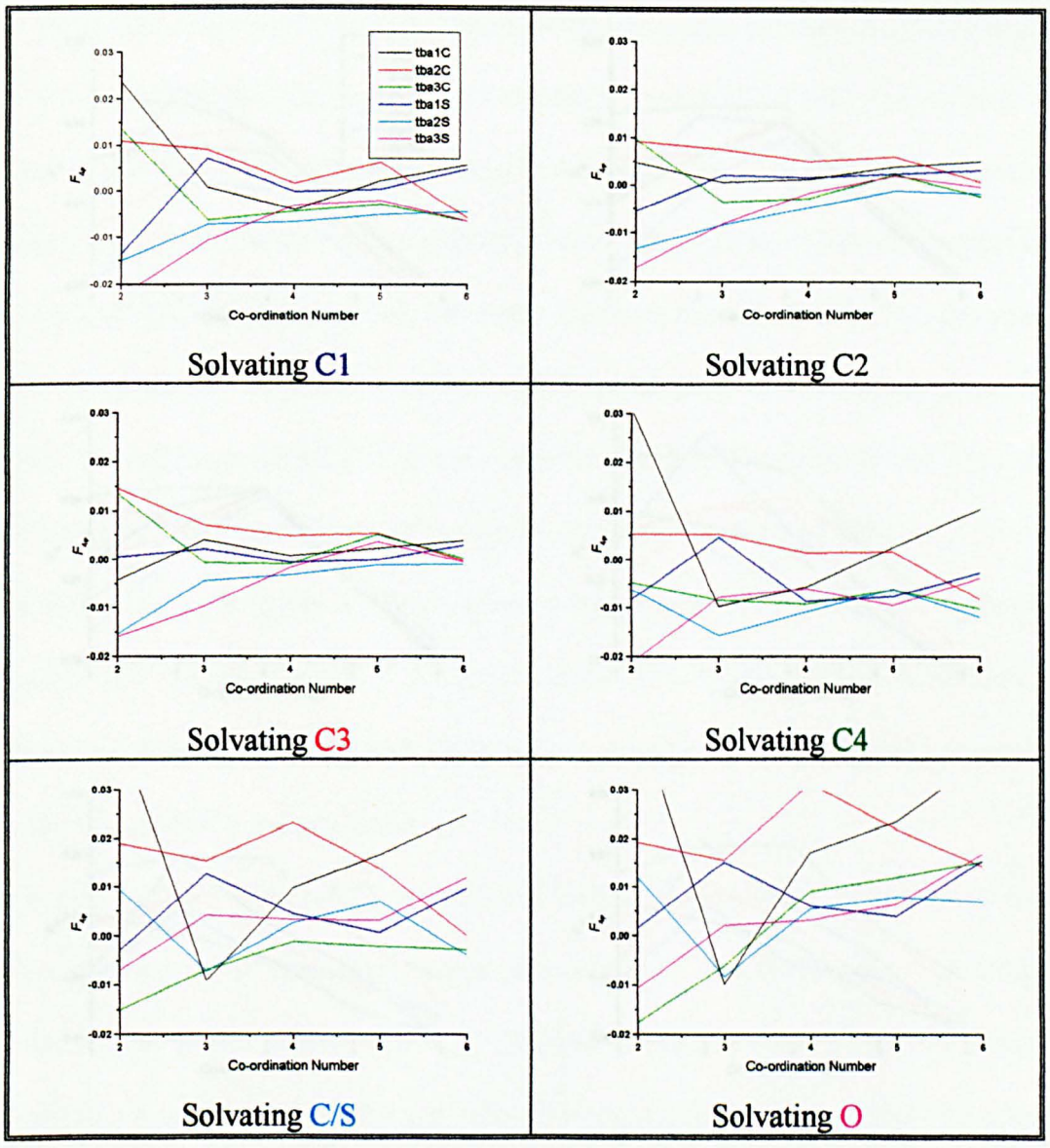

Figure 4.12 $F_{4\varphi}$ for solvated water around various solute atoms for the inhibited systems. The legend is the same for each plot and atom numbers are coloured as per figure 4.5.

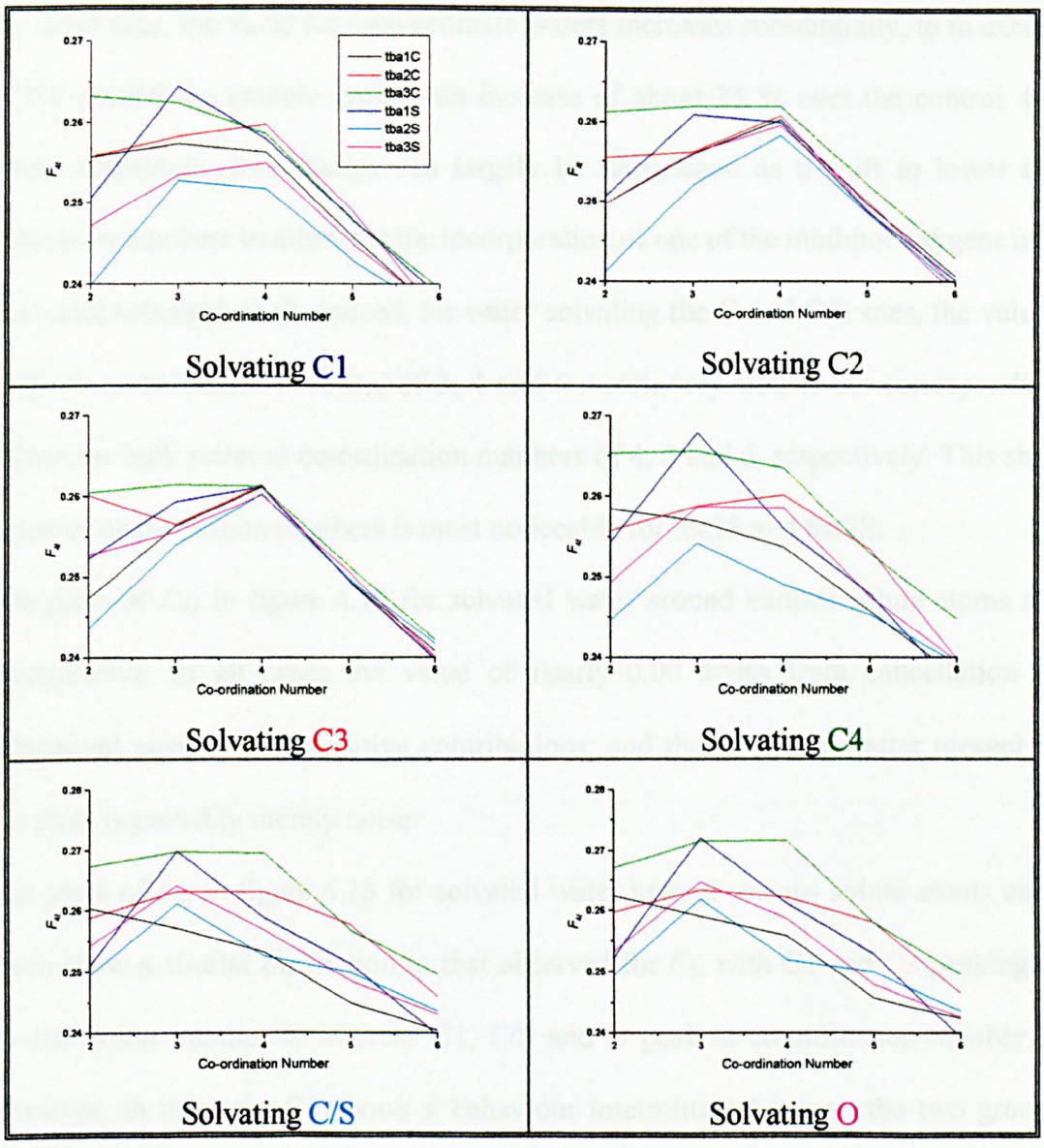

Figure 4.13 F_{4i} for solvated water around various solute atoms for the inhibited systems. The legend is the same for each plot and atom numbers are coloured as per figure 4.5.

From the plots of F_3 in figure 4.11 for solvated water around the solute atoms C2 and C3 we can see a similar behaviour to that for bulk water with a minimum at co-ordination number 4, albeit it at a higher value (0.085 compared with 0.080); however the plots for solvated water around the solute atoms C1, C4, C/S and O show a different profile, with the minimum shifting to a co-ordination number 3. At

the same time, the value for 4-co-ordinate waters increases substantially, to in excess of 0.1 around the anionic group—an increase of about 25 % over the control. On closer inspection, this change can largely be understood as a shift to lower co-ordination numbers to allow for the incorporation of one of the inhibitor oxygens into the water solvation shell. Indeed, for water solvating the O and C/S sites, the values of F_3 at co-ordination numbers of 3, 4 and 5 match very well to the corresponding values for bulk water at co-ordination numbers of 4, 5 and 6, respectively. This shift to lower co-ordination numbers is most noticeable for tba1S and tba2S.

The plots of $F_{4\varphi}$ in figure 4.12 for solvated water around various solute atoms are inconclusive. In all cases the value of nearly 0.00 arises from cancellation of substantial positive and negative contributions, and therefore the scatter present in the plots is probably merely noise.

The plots of F_{4t} in figure 4.13 for solvated water around various solute atoms once more show a similar distinction to that observed for F_3, with C2 and C3 peaking at co-ordination number 4, whereas C1, C/S and O peak at co-ordination number 3, However, in this case C1 shows a behaviour intermittent between the two groups with some inhibitors peaking at co-ordination number 3 others at co-ordination number 4.

The values observed in all solvation shells for F_3, $F_{4\varphi}$ and F_{4t} are not consistent with hydrate formation. In particular the values around the C3 atom are nowhere near the values of 0.01 for F_3, 0.69 for $F_{4\varphi}$, and 0.47 for F_{4t}, found in hydrates.

Control and Inhibited Systems: Local Phase Assignments

By combining the instantaneous values of F_3, $F_{4\varphi}$ and F_{4t} (see section 3.4) it is possible to assign the water molecules within each of the seven systems as belonging

to one of three phases: hydrate, ice or water. This is achieved by comparing the F_3, $F_{4\varphi}$ and F_{4t} values and if they are sufficiently close to a set to bulk phase values then they are assigned to that phase. In order to define 'sufficiently close' the covariance matrix for F_3, $F_{4\varphi}$ and F_{4t} was calculated in each bulk phase. The order parameters were then deemed to be sufficiently close when all three distances were simultaneously within three standard deviations of their respective bulk average.[21] The local phase assignments obtained for water molecules in each of the seven systems can be seen in table 4.9. In all of the inhibited systems the number of waters in the system have been scaled so that they are the same as in the control system, namely 256, to allow for direct comparison between results.

SYSTEM	NUMBER OF WATERS IN EACH PHASE		
	HYDRATE	ICE	LIQUID
Control	14	12	230
tba1C	11	8	237
tba2C	13	10	233
tba3C	14	11	230
tba1S	11	8	237
tba2S	12	10	235
tba3S	12	9	235

Table 4.9 Water molecule local phase assignments for the control and inhibited systems.

With respect to these local phase assignments, the water molecules in the inhibited systems show no large deviations from those in the control system. Small differences can be observed for tba1C, tba2C and tba1S, tba2S and tba3S, all of which show more 'liquid-like' water molecules than are present in the control system. In addition, in all cases except tba3C, there are fewer 'hydrate-like' and 'ice-like' water molecules in the inhibited systems than in the control system, which suggests that the water in the inhibited systems is not as structured as in the control system.

4.3.4 Residence Time Correlation Functions

The residence time correlation functions (see section 3.1.1) have been calculated from all six inhibited systems. From these, the time taken for half the water molecules to leave a solvation shell has been determined. This quantity provides an indication of the residence time for water molecules in the various environments. Discontinuities arise in the plots from the condition that waters must remain in the solvation shell of the atom of interest for the whole time step. In these plots four different time steps have been used and therefore when the time step is changed/doubled it is possible that a number of waters may have left the solvation shell of the atom of interest leading to a discontinuity. In the following sections the residence time correlation functions are presented along with the residence times for bulk and solvated water in the seven systems.

Control and Inhibited Systems: Bulk Water

The residence time correlation functions for bulk water in the inhibited systems can be seen in figure 4.14.

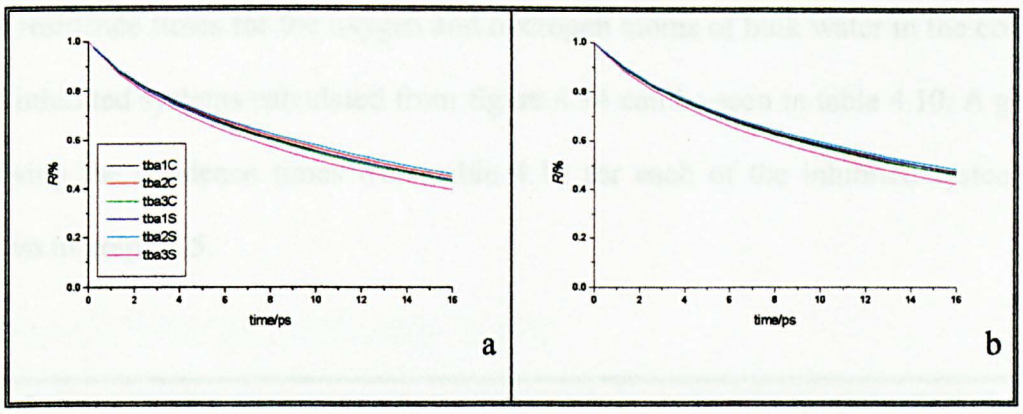

Figure 4.14 Residence time correlation functions, of the oxygen atom of bulk water (a) and of the hydrogen atom of bulk water (b), for the inhibited systems. The legend is the same for each plot.

SYSTEM	OXYGEN ATOM/ps	HYDROGEN ATOM/ps
Control	-	-
tba1C	12.9	13.9
tba2C	13.3	14.5
tba3C	12.3	13.8
tba1S	12.6	14.5
tba2S	13.9	15.1
tba3S	10.9	12.1

Table 4.10 Residence times for the oxygen and hydrogen atoms of bulk water for the control and inhibited systems. N.B. residence times have not been calculated for the control system, as by definition the water is always bulk water and therefore the residence time correlation function is constant at 1 and does not decay.

The residence times for the oxygen and hydrogen atoms of bulk water in the control and inhibited systems calculated from figure 4.14 can be seen in table 4.10. A graph showing the residence times from table 4.10 for each of the inhibited systems is shown in graph 4.5.

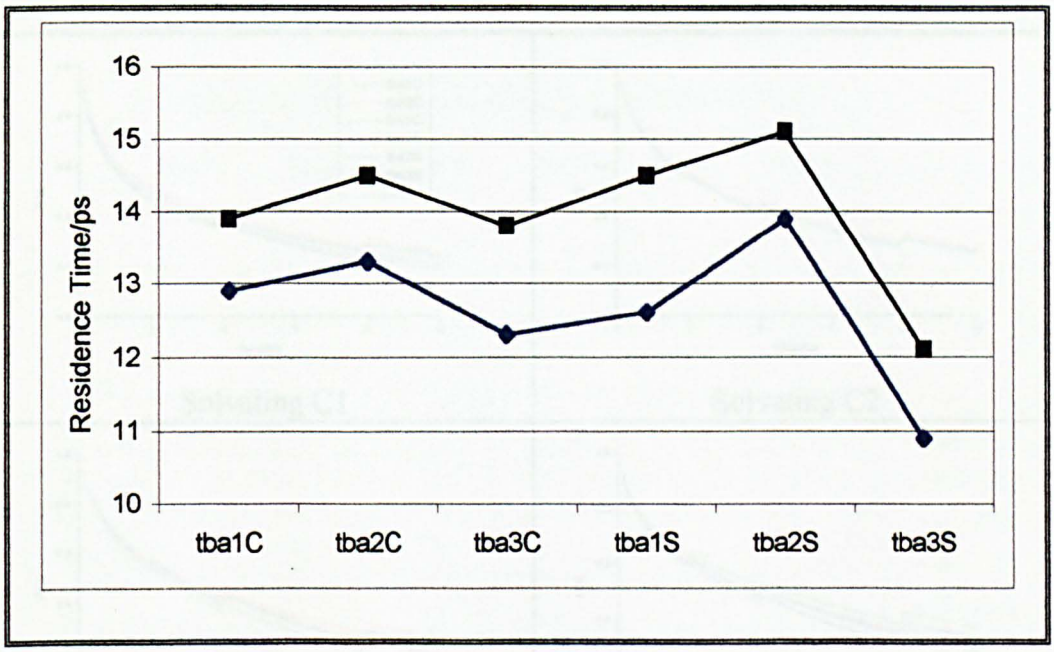

Graph 4.5 Residence times, of the oxygen atom of bulk water (blue) and of the hydrogen atom of bulk water (black), for the inhibited systems. The control system is not included for the reason stated above.

Residence times for the oxygen and hydrogen atoms of bulk water are listed in table 4.10 and presented in graph 4.5. It can be seen that the residence time for the hydrogen atom of the inhibitors is higher than the corresponding value for the oxygen atom in all cases.

There also seems to be optima in the oxygen and hydrogen residence times for each of the two inhibitor series for tba2C and tba2S. This may be a reflection of the moderation of the N^+ and headgroup$^-$ centres *i.e.* for tba1C and tba1S the two groups

are very close and therefore may merge into one whereas for tba3C and tba3S the separation is such that there are distinct positive and negative centres; for tba2C and tba2S there is a balancing of these two effects.

Inhibited Systems: Solvated Water

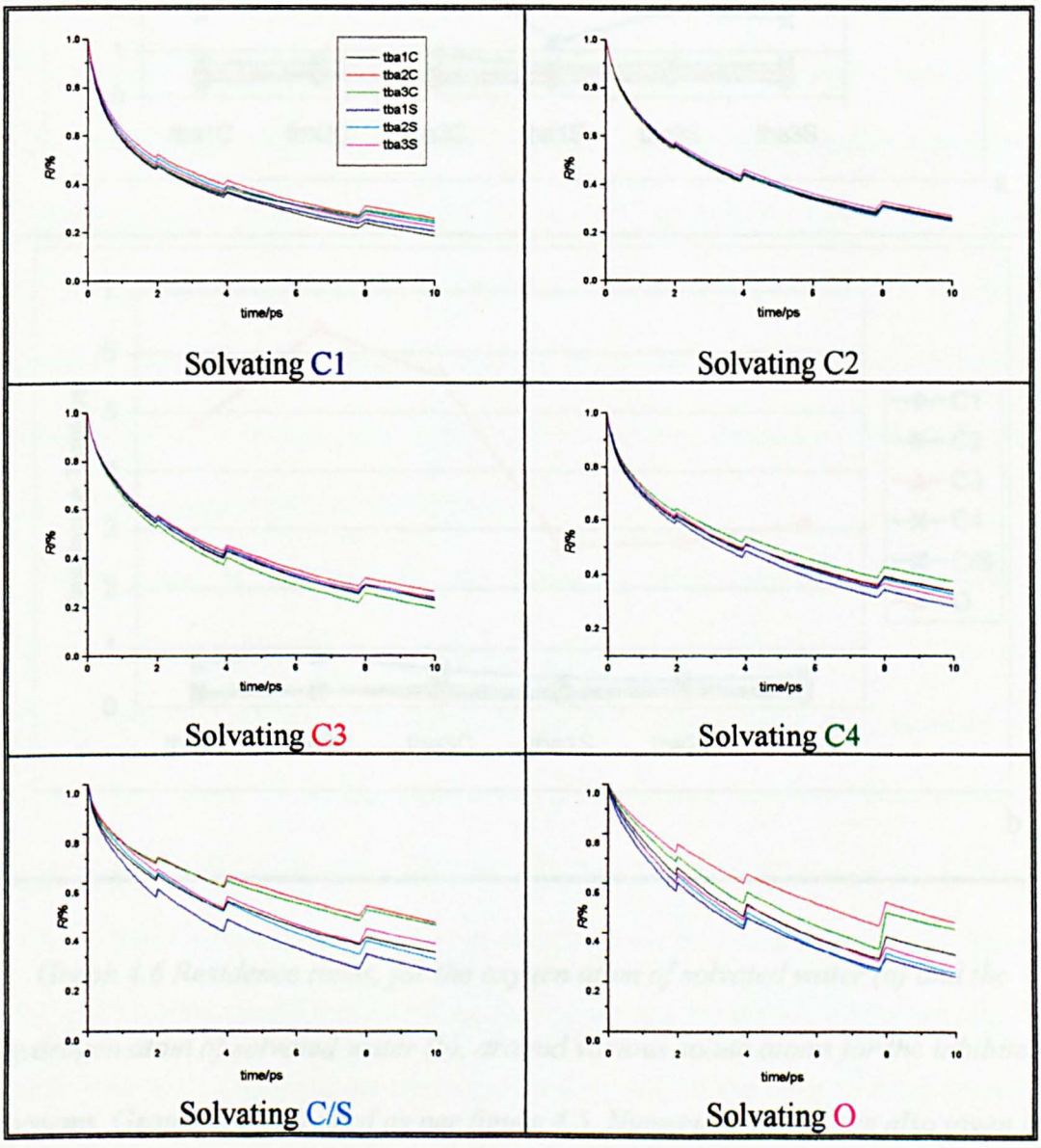

Figure 4.15 Residence time correlation functions of the oxygen atom of solvated water around various solute atoms for the inhibited systems. The legend is the same for each plot and atom numbers are coloured as per figure 4.5.

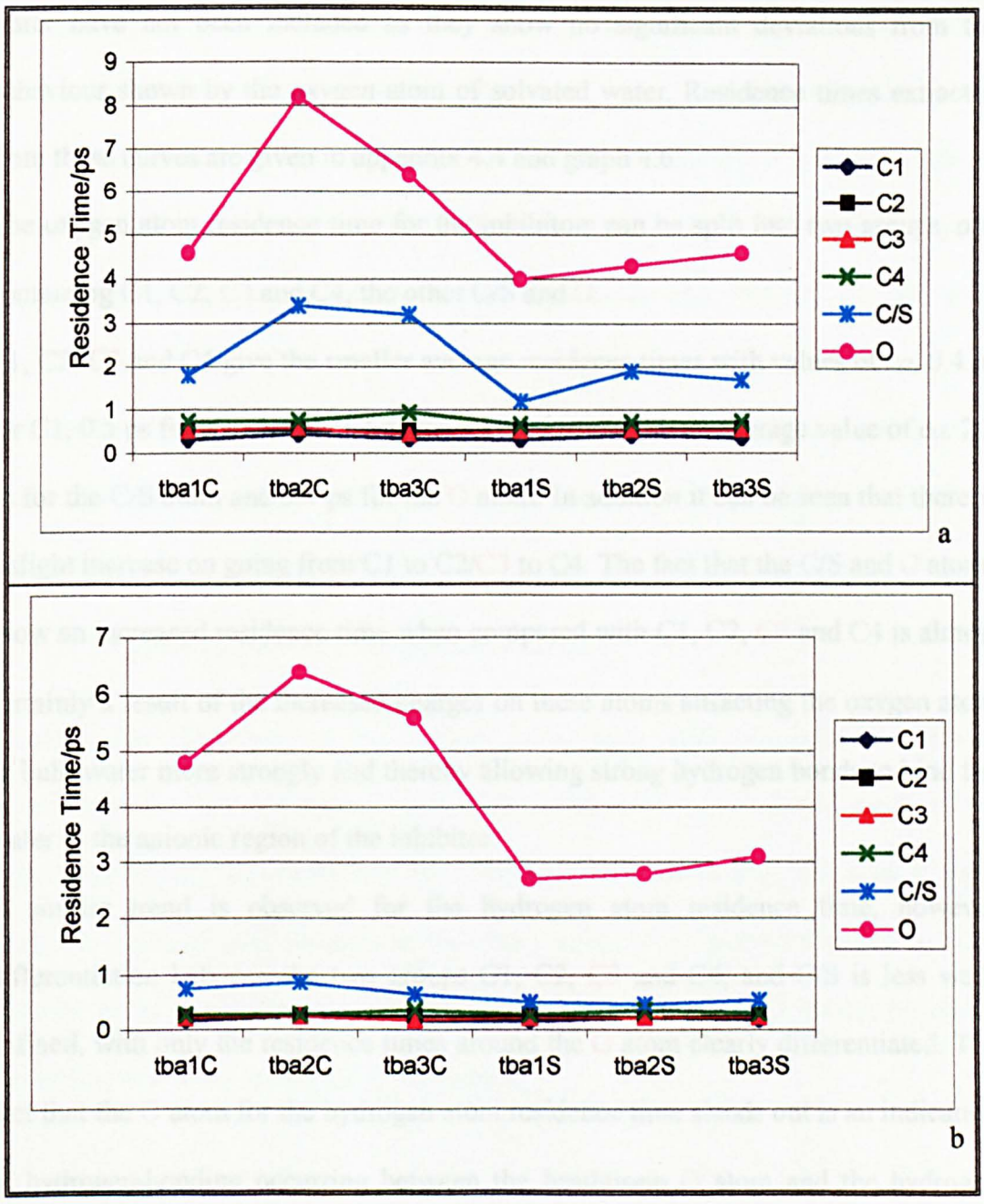

Graph 4.6 Residence times, for the oxygen atom of solvated water (a) and the hydrogen atom of solvated water (b), around various solute atoms for the inhibited systems. Graphs are coloured as per figure 4.5. Numerical values are also given in appendix 4.4.

The residence time correlation functions for the oxygen atom of solvated water in the inhibited systems can be seen in figure 4.15, plots for the hydrogen atom of solvated

water have not been included as they show no significant deviations from the behaviour shown by the oxygen atom of solvated water. Residence times extracted from these curves are given in appendix 4.4 and graph 4.6.

The oxygen atom residence time for the inhibitors can be split into two groups, one containing C1, C2, C3 and C4, the other C/S and O.

C1, C2, C3 and C4 give the smaller average residence times with values of *ca.* 0.4 ps for C1, 0.5 ps for C2/C3 and 0.7 ps for C4 compared with an average value of *ca.* 2.2 ps for the C/S atom and 5.4 ps for the O atom. In addition it can be seen that there is a slight increase on going from C1 to C2/C3 to C4. The fact that the C/S and O atoms show an increased residence time when compared with C1, C2, C3 and C4 is almost certainly a result of the increased charges on these atoms attracting the oxygen atom of bulk water more strongly and thereby allowing strong hydrogen bonds to bind the water to the anionic region of the inhibitor.

A similar trend is observed for the hydrogen atom residence time, however differentiation between the two groups C1, C2, C3 and C4, and C/S is less well-defined, with only the residence times around the O atom clearly differentiated. The fact that the O atom for the hydrogen atom residence time stands out is an indication of hydrogen-bonding occurring between the headgroup O atom and the hydrogen atom therefore increasing the hydrogen atom residence time. It is surprising that the average residence time for the hydrogen atom around the C4 and C/S atoms are not higher than those observed, as one would expect that if the oxygen atom residence time is higher for these atoms, then by connectivity arguments of the water molecule then so should the hydrogen atom residence time.

The O atom of the amine carboxylates is interesting when compared with the amine sulphonates, as the residence times for both the oxygen and hydrogen atoms are

considerably higher for the carboxylates. This is possibly counter-intuitive in that the amine sulphonates have one extra oxygen atom when compared with the amine carboxylates and can therefore undergo more hydrogen-bonding; however this can be rationalised by the assumption that the hydrogen bonds are most probably stronger for the amine carboxylates than the amine sulphonates and therefore the residence times are higher.

The mechanism for the mode of action of the amine carboxylates may be linked to the fact that the two groups C1, C2, C3 and C4 and C/S, O are well differentiated.

4.3.5 Mean Square Displacements

Mean square displacements (see section 3.1.3) have been calculated for various atomic sites in the seven systems and used to determine self-diffusion coefficients. The mean square displacements are calculated for molecules that remain in a specified solvation shell throughout the time interval (0, t). In the following sections both the mean square displacements and the self-diffusion coefficients are presented for bulk water in the seven different systems.

Control and Inhibited Systems: Bulk Water

The mean square displacement plots for the control and inhibited systems can be seen in figures 4.16 and 4.17.

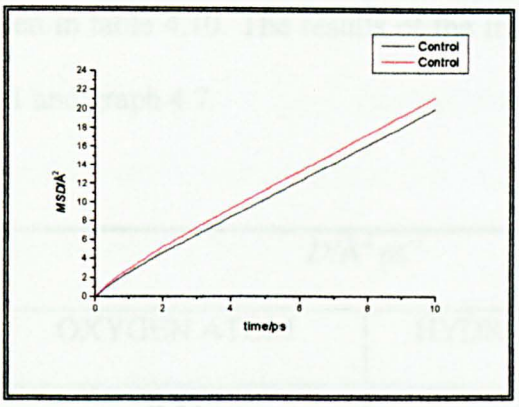

Figure 4.16 Mean square displacement, of the oxygen atom of bulk water (black) and the hydrogen atom of bulk water (red), for the control system.

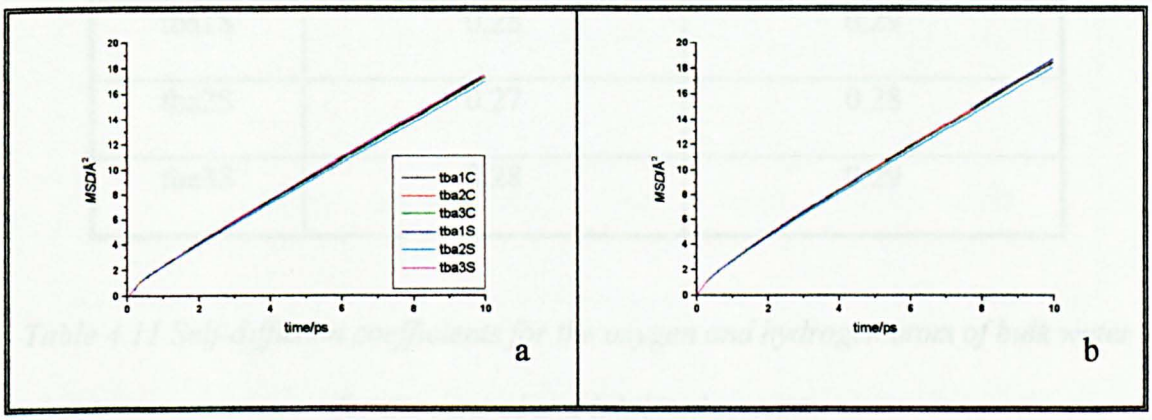

Figure 4.17 Mean square displacement, of the oxygen atom of bulk water (a) and the hydrogen atom of bulk water (b), for the inhibited systems. The legend is the same for each plot.

These curves show the clear linear behaviour characteristic of diffusive motion. The self-diffusion coefficients have been determined for the oxygen and hydrogen atom in the control and inhibited systems by carrying out a linear regression of the mean square displacement in figures 4.16 and 4.17. The linear regression was carried out over the time interval (1ps, $\tau_{residence}$) where $\tau_{residence}$ is the residence time for the

respective atoms as given in table 4.10. The results of the linear regression analysis can be seen in table 4.11 and graph 4.7.

SYSTEM	$D/Å^2 ps^{-1}$	
	OXYGEN ATOM	HYDROGEN ATOM
Control	0.32	0.34
tba1C	0.28	0.29
tba2C	0.28	0.29
tba3C	0.28	0.29
tba1S	0.28	0.29
tba2S	0.27	0.28
tba3S	0.28	0.29

Table 4.11 Self-diffusion coefficients for the oxygen and hydrogen atom of bulk water for the control and inhibited systems.

The mean square displacement is related to the self-diffusion coefficient by the equation

$$D = \lim_{t\to\infty} \frac{1}{6t} \langle | r(t) - r(0) |^2 \rangle$$

where D is the self-diffusion coefficient. It must however be noted that the value of D obtained by this method will be an under-estimate in our case: the mean square displacement has been calculated only for those molecules that remain in the given region, and so for longer times fast moving waters will escape, and thereafter be excluded from the calculation, such that at long times the only waters remaining

around the solute atoms would be those that were in essence 'physically bound' to the solute atoms. Since the bulk region is large, this will be a small effect in figure 4.17, and so estimates of the diffusion coefficient from these plots should give a good estimate of the diffusion coefficient for bulk water.

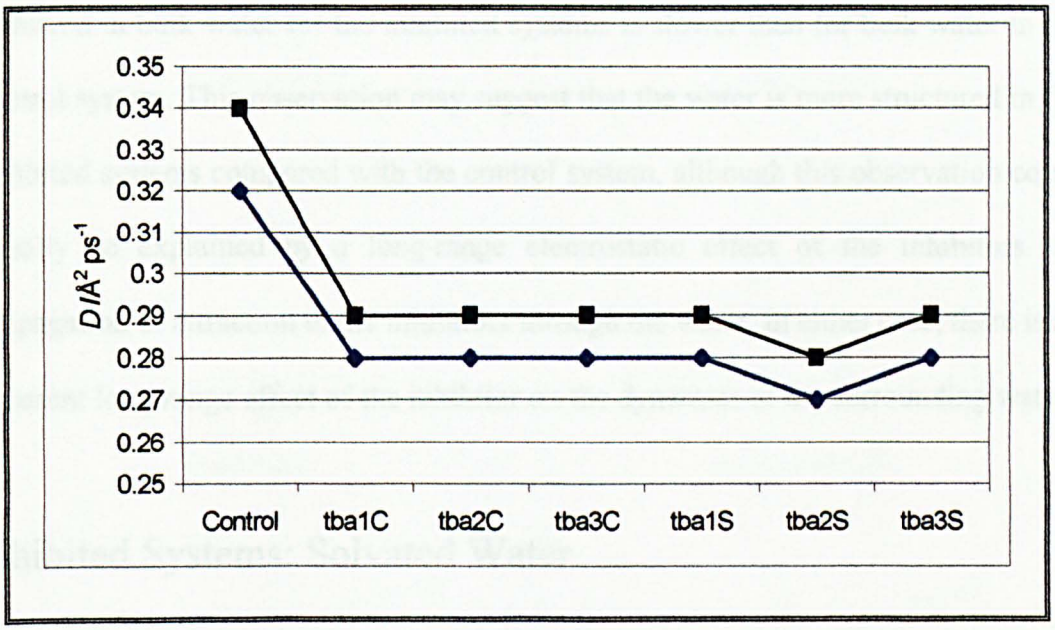

Graph 4.7 Self-diffusion coefficients, for the oxygen atom of bulk water (blue) and hydrogen atom of bulk water (black), for the control and inhibited systems.

From this data it is possible to note that the self-diffusion coefficient obtained for the hydrogen atom in the control system is higher than the corresponding value for the oxygen atom. This arises from the fact that a water molecule can rotate about its centre of mass, which is nearly coincident with the oxygen atom; this rotation leads to additional movement of the hydrogen atoms but not the oxygen atom and therefore an apparently higher self-diffusion coefficient; at long times this difference would become negligible.

A more significant observation is that in all cases the self-diffusion coefficients for water atoms in the inhibited systems are smaller than the respective self-diffusion coefficients in the control system. It is unlikely that this is due to the fast molecule exclusion artefact mentioned above, since in this case there should be a pronounced curvature to the MSDs, and this is not apparent in figure 4.17. We conclude that diffusion in bulk water for the inhibited systems is slower than for bulk water in the control system. This observation may suggest that the water is more structured in the inhibited systems compared with the control system, although this observation could equally be explained by a long-range electrostatic effect of the inhibitors *i.e.* propagation of attraction to the inhibitors through the water. In either case, there is an apparent long-range effect of the inhibitor on the dynamics of the surrounding water.

Inhibited Systems: Solvated Water

The mean square displacement plots for the inhibited systems can be seen in figures 4.18 and 4.19, while diffusion coefficients—again calculated by linear regression over the time interval (1ps, $\tau_{residence}$)—are given in appendix 4.5 and graph 4.8. Residence times were taken from appendix 4.4.

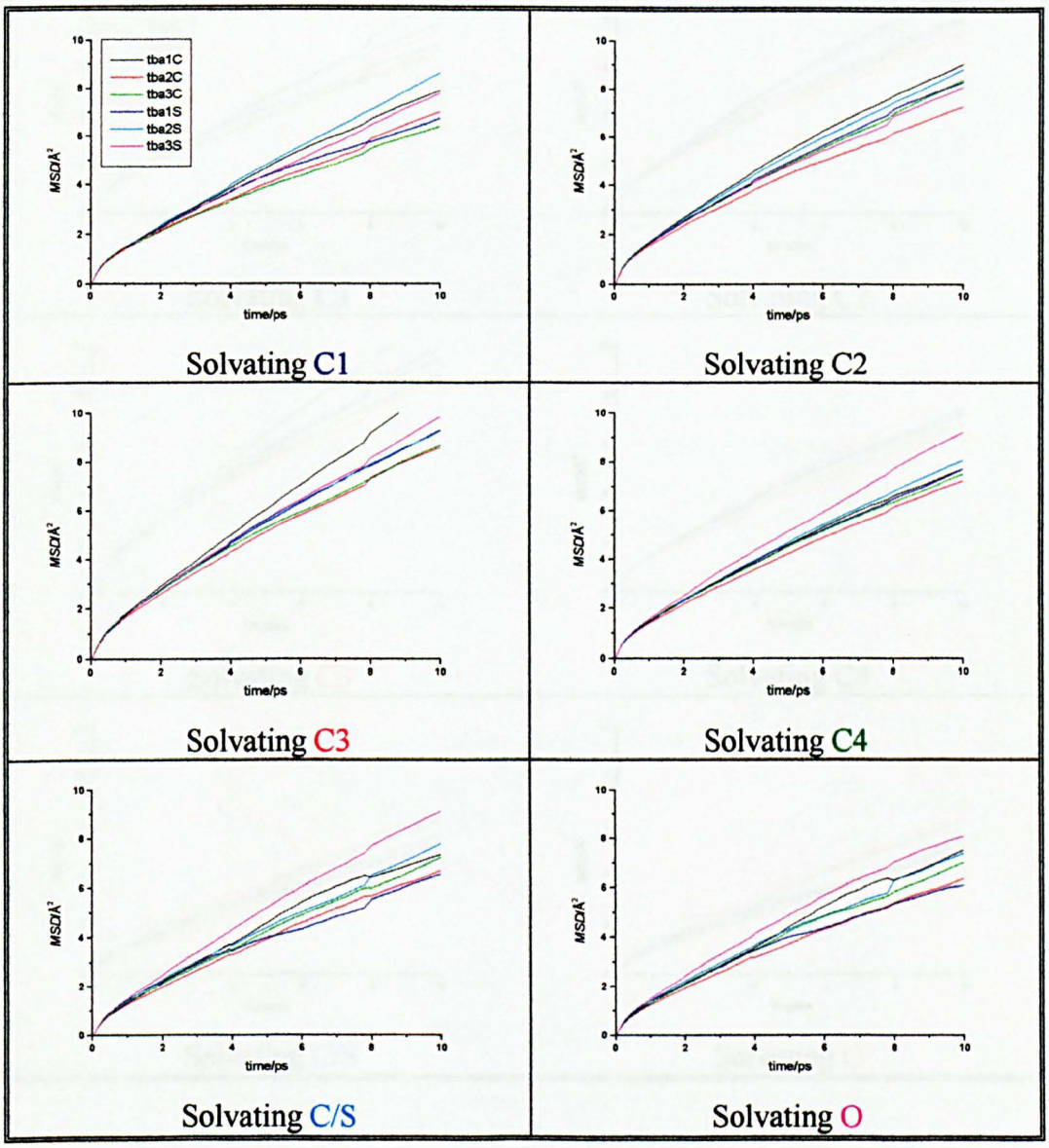

Figure 4.18 Mean square displacement of the oxygen atom of solvated water around various solute atoms for the inhibited systems. The legend is the same for each plot and atom numbers are coloured as per figure 4.5.

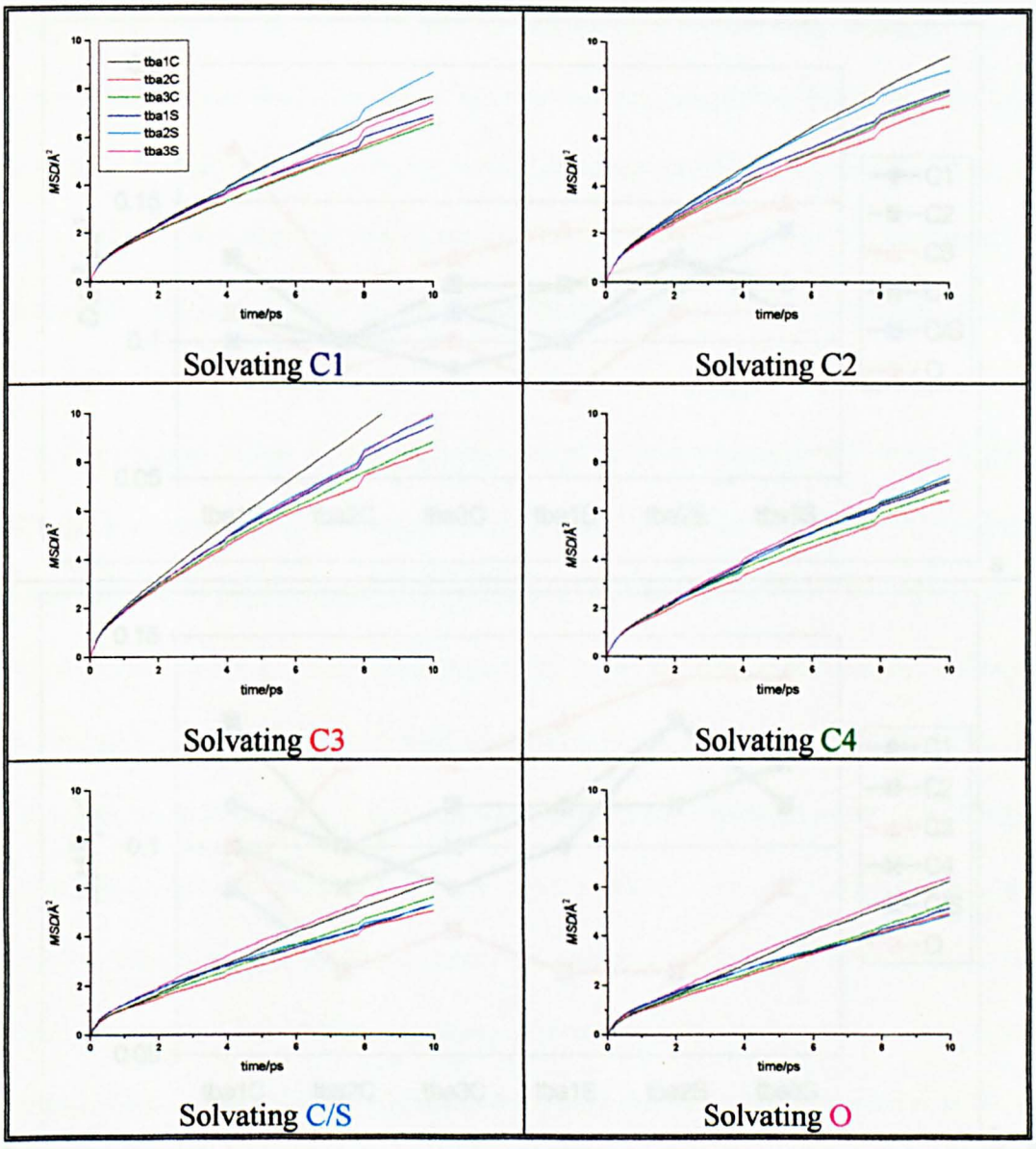

Figure 4.19 Mean square displacement of the hydrogen atom of solvated water around various solute atoms for the inhibited systems. The legend is the same for each plot and atom numbers are coloured as per figure 4.5.

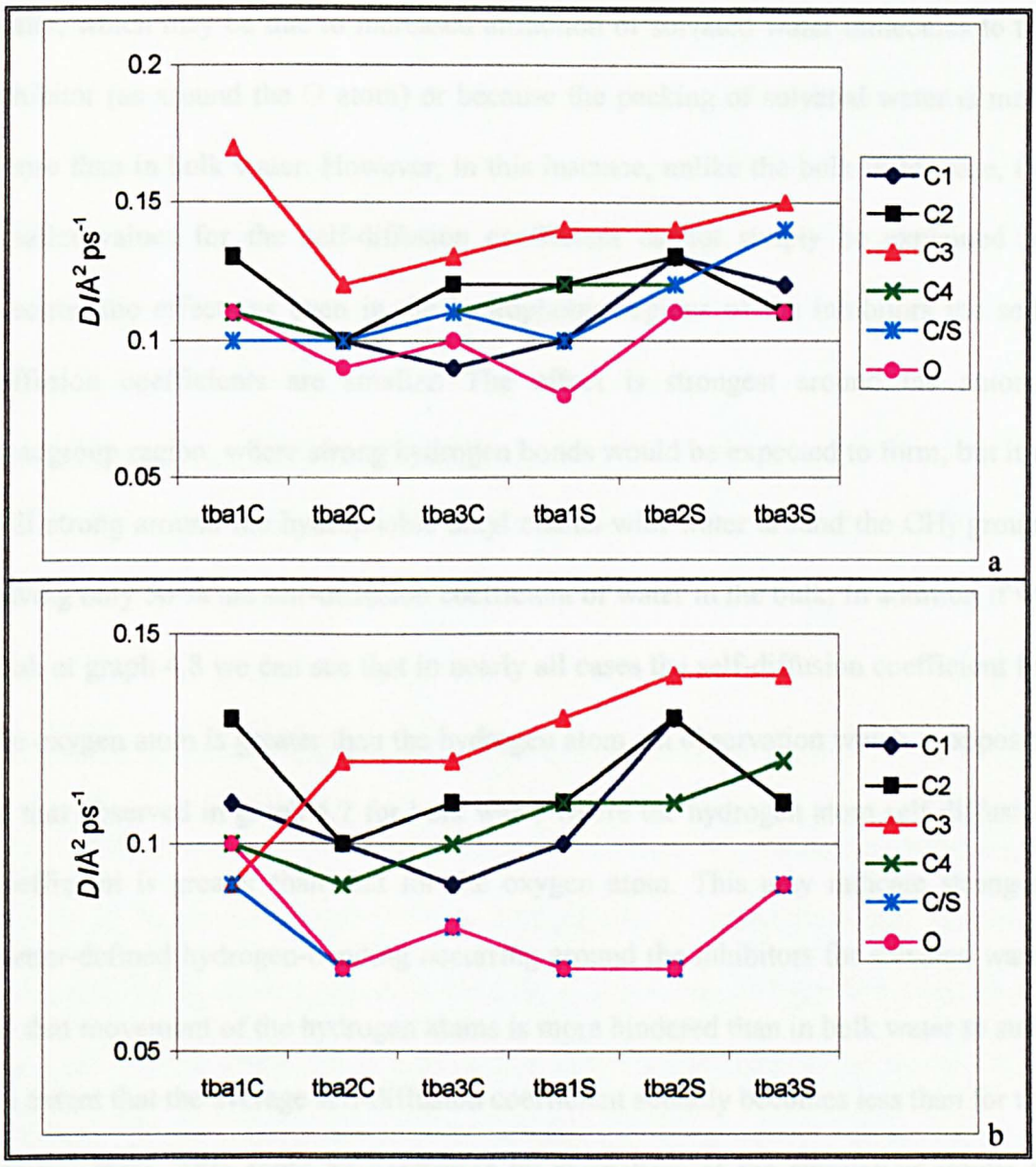

Graph 4.8 Self-diffusion coefficients, for the oxygen of solvated water (a) and the hydrogen atom of solvated water (b), around various solute atoms. Graphs are coloured as per figure 4.5. Numerical values are also given in appendix 4.5.

It can be seen that the self-diffusion coefficient for the oxygen and hydrogen atoms in all solvated cases is substantially lower than the self-diffusion coefficient obtained for bulk water in either the control or inhibited systems–typically by *ca.* 60 %. This reduction indicates that diffusion of solvated water is much slower than in bulk

water, which may be due to increased attraction of solvated water molecules to the inhibitor (as around the O atom) or because the packing of solvated water is more dense than in bulk water. However, in this instance, unlike the bulk water case, the smaller values for the self-diffusion coefficient cannot simply be explained by electrostatic effects as even in the hydrophobic regions of the inhibitors the self-diffusion coefficients are smaller. The effect is strongest around the anionic headgroup region, where strong hydrogen bonds would be expected to form, but it is still strong around the hydrophobic alkyl chains with water around the CH_3 groups having only 50 % the self-diffusion coefficient of water in the bulk. In addition if we look at graph 4.8 we can see that in nearly all cases the self-diffusion coefficient for the oxygen atom is greater than the hydrogen atom, an observation which is opposite to that observed in graph 4.7 for bulk water where the hydrogen atom self-diffusion coefficient is greater than that for the oxygen atom. This may indicate stronger-/better-defined hydrogen-bonding occurring around the inhibitors for solvated water so that movement of the hydrogen atoms is more hindered than in bulk water to such an extent that the average self-diffusion coefficient actually becomes less than for the oxygen atom. This could be confirmed by re-analysis of the simulation results to calculate hydrogen bond lifetimes or the orientation of the hydrogen atom of water relative to the headgroup O atom throughout the course of the simulation.

If we consider C1, C2 and C3 for the inhibitors we can see that there is a general increase in the self-diffusion coefficient for both the hydrogen and oxygen atoms on going from C1, C2 to C3. This is probably due to the fact that we are moving further away from the charged nitrogen atom and therefore the attraction felt by the water molecules in the environments of these atoms decreases and therefore the diffusion of the oxygen and hydrogen atoms is easier.

A similar but opposite effect is seen for C4, C/S and O in that on going from C4 to C/S to O then the average self-diffusion coefficient for both hydrogen and oxygen atoms decreases indicating that the diffusion of water molecules is becoming more difficult. This is because on going from C4 to C/S to O you are approaching the region with both the highest charge density and the strongest hydrogen bond acceptors and therefore diffusion becomes more difficult.

In essence what we are observing is that the water is more tightly bound around the highly charge centres and as you move away from these this decreases and diffusion becomes easier.

4.3.6 Legendre Orientational Correlation Functions

The time correlations functions for the second Legendre polynomial coefficients (see section 3.1.2) for the direction of the principal axes of water molecules have been calculated for the seven systems. In the following sections the Legendre orientational functions for the *z*-axis are presented; the *z*-axis corresponds to the dipole vector direction. If the rotational dynamics of the system are governed by rotational diffusion then these plots should be exponential in nature such that

$$P_l(t) = e^{-\frac{t}{l(l+1)\tau}}$$

where l is the order of the Legendre polynomial, t the time and τ the rotational lifetime. Therefore a plot of $\ln P_l(t)$ *vs.* t should be linear and the slope of the graph should give the rotational lifetime. However when this was attempted it was found that the plots of $\ln P_l(t)$ *vs.* t were not linear. This has two possible implications:

a) the method of calculation of $P_l(t)$—specifically, limiting calculation to molecules that remain within the solvation sphere over the time interval (0, t)—obscures the diffusional processes;

b) rotational dynamics of the system are not governed by rotational diffusion.

The second of these two options is the most likely in this case as this calculation method has been used before and yielded linear plots for $\ln P_l(t)$ *vs.* t.[22] As a consequence of this non-linearity, we have used the time taken for second Legendre polynomial coefficients to fall to 50 % to quantify the rotational lifetimes for water molecules in the various environments.

Control and Inhibited Systems: Bulk Water

The Legendre orientational correlation functions for the control and inhibited systems can be seen in figures 4.20 and 4.21.

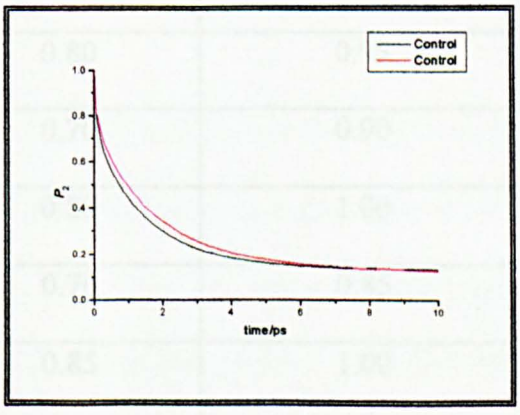

Figure 4.20 Legendre orientational correlation functions, parallel to the water dipole vector (black) and perpendicular to the water dipole vector (red), of bulk water for the control system.

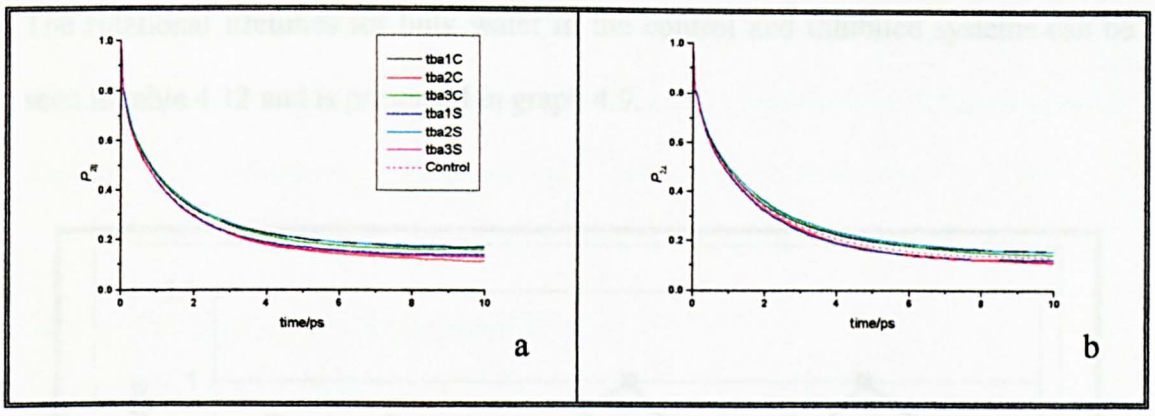

Figure 4.21 Legendre orientational correlation functions, parallel to the water dipole vector (a) and perpendicular to the water dipole vector (b), of bulk water for the control and inhibited systems. The legend is the same for each plot.

SYSTEM	ROTATIONAL LIFETIME/ps		$P_{2\perp}/P_{2\parallel}$ as a ratio.
	From $P_{2\parallel}$	From $P_{2\perp}$	
Control	0.70	0.95	+36
tba1C	0.80	0.95	+19
tba2C	0.70	0.90	+29
tba3C	0.80	1.00	+25
tba1S	0.70	0.85	+21
tba2S	0.85	1.00	+18
tba3S	0.70	0.90	+29

Table 4.12 Rotational lifetime summary for bulk water of the control and inhibited systems.

The rotational lifetimes for bulk water in the control and inhibited systems can be seen in table 4.12 and is presented in graph 4.9.

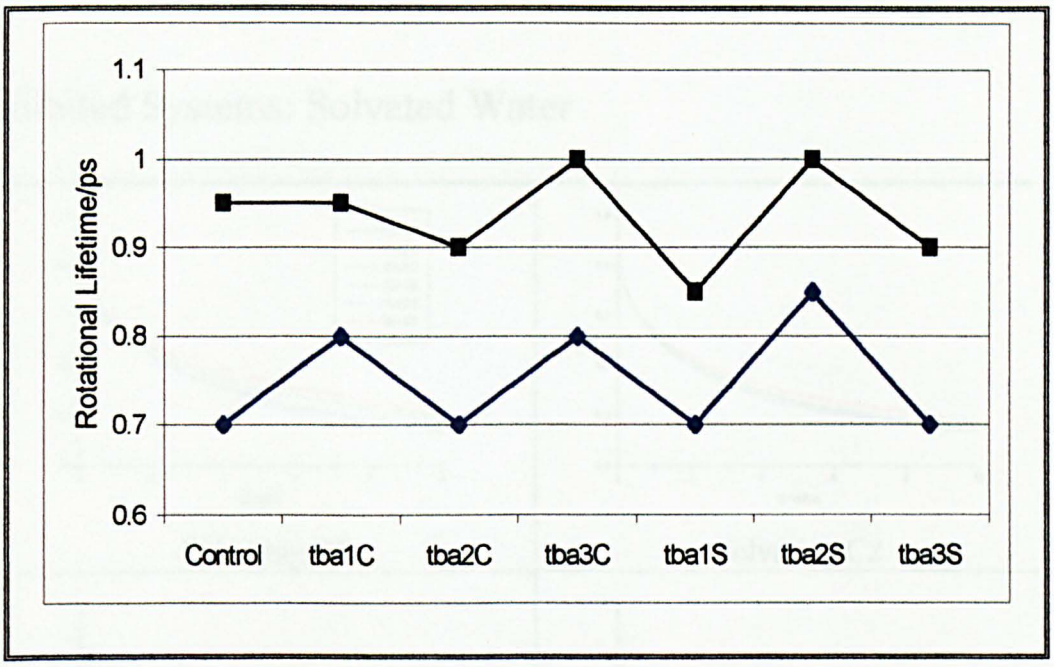

Graph 4.9 Rotational lifetimes for motion, parallel to the dipole vector of water (blue) and perpendicular to the dipole vector of water (black), of bulk water.

The rotational lifetimes from $P_{2\|}$ and $P_{2\perp}$ are listed in table 4.12 and graph 4.9. It can be seen that the rotational lifetime parallel to the dipole vector of the water molecules is smaller than for the corresponding perpendicular rotation in the control and inhibited systems. This indicates that rotation parallel to the dipole vector is more facile than rotation perpendicular to the dipole vector. In addition, in most cases the value of the rotational lifetime for parallel or perpendicular rotation is equivalent or larger in the inhibited systems when compared with the control system. This indicates slower dynamics and suggests that the water is potentially more tightly bound and therefore the rotational lifetimes are longer due to the increased binding, and at worst the structuring of water is equivalent in the inhibited systems when

compared with the control system. The choice of a 50 % decay for rotational lifetimes actually understates the apparent differences between the different systems, and larger differences would be observed at, say, decay to 37 % ($1/e$ = 36.8 %).

Inhibited Systems: Solvated Water

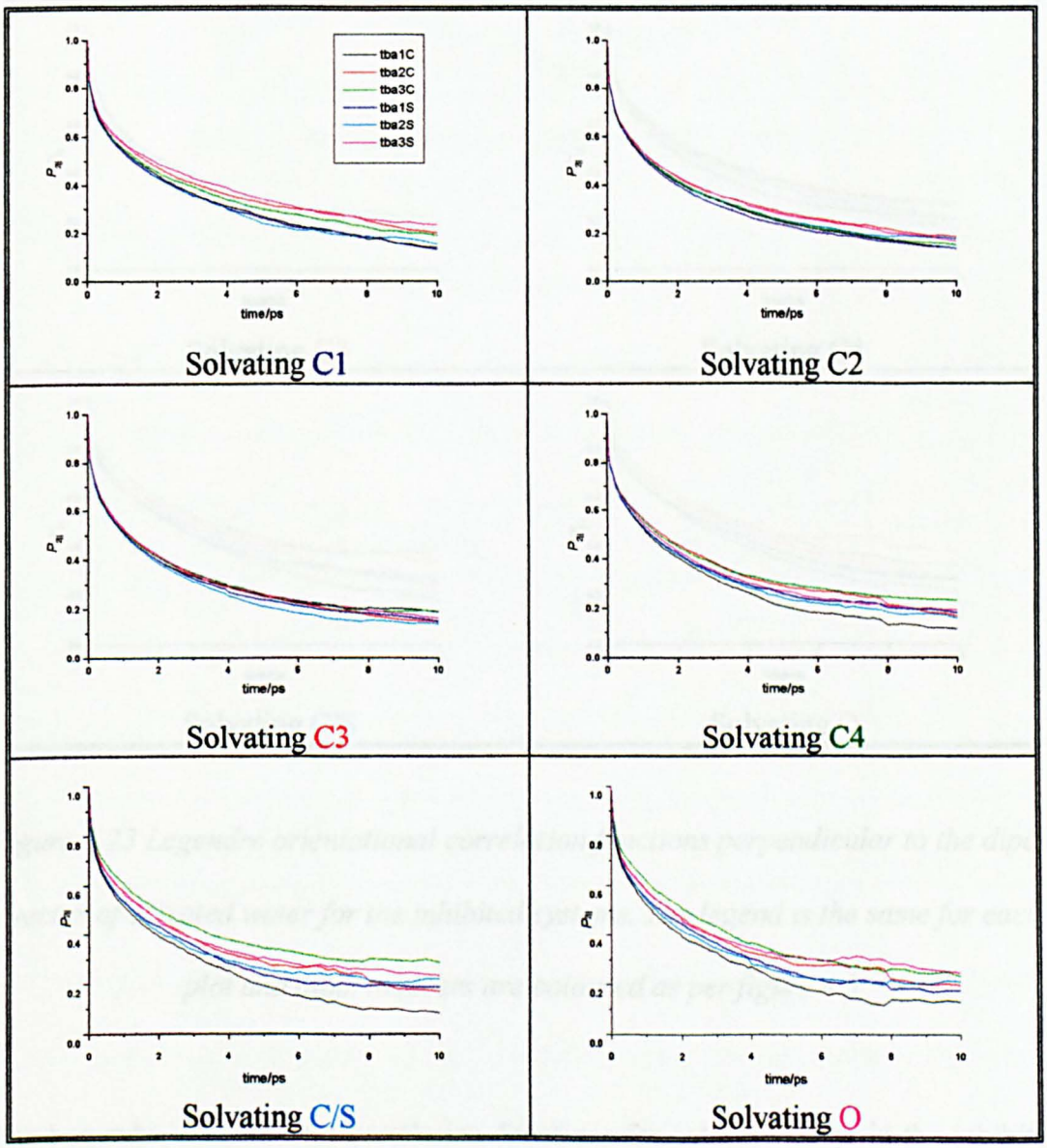

Figure 4.22 Legendre orientational correlation functions parallel to the dipole vector of solvated water for the inhibited systems. The legend is the same for each plot and atom numbers are coloured as per figure 4.5.

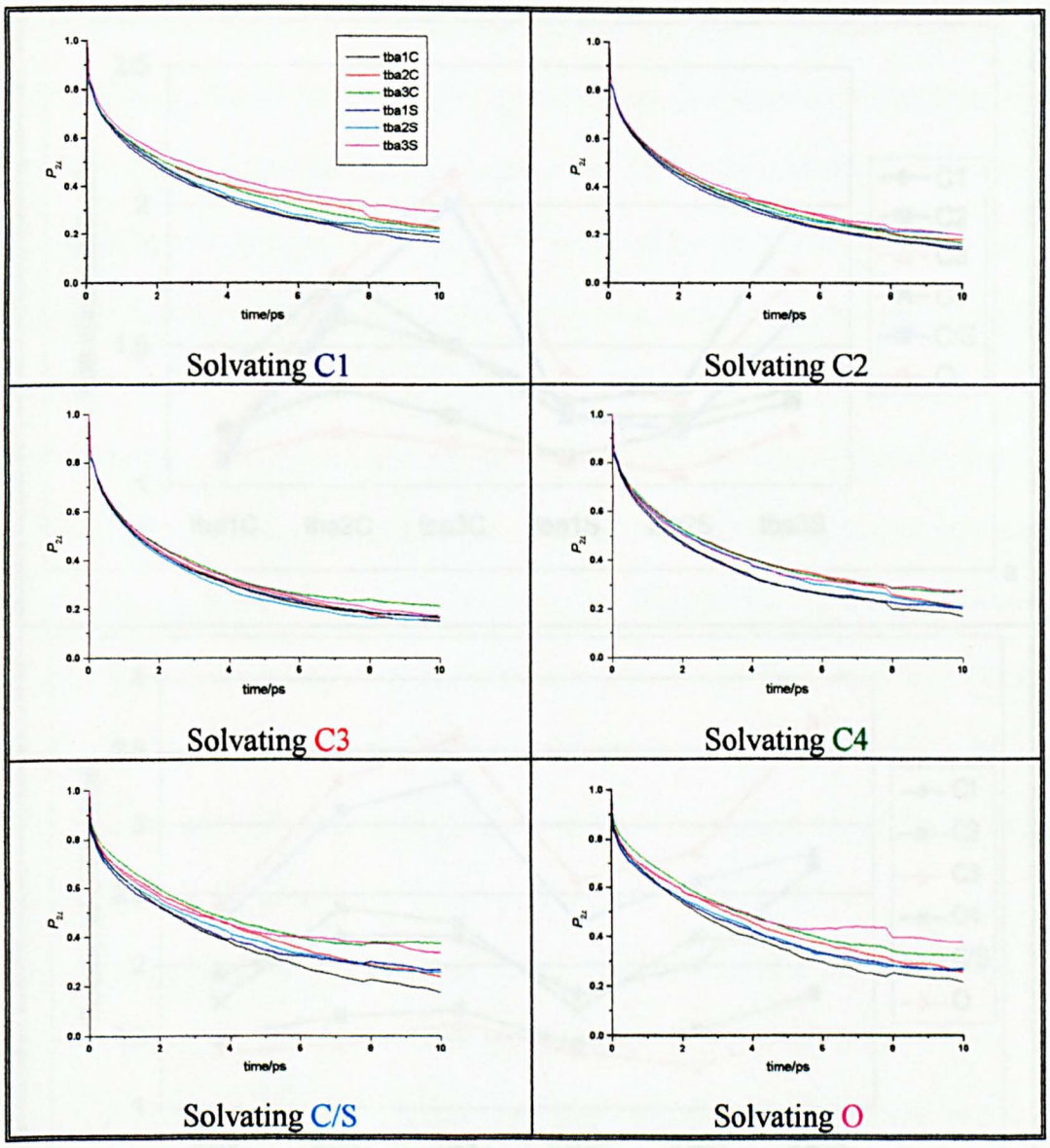

Figure 4.23 Legendre orientational correlation functions perpendicular to the dipole vector of solvated water for the inhibited systems. The legend is the same for each plot and atom numbers are coloured as per figure 4.5.

The Legendre orientational correlation functions for solvated water in the inhibited systems can be seen in figures 4.22 and 4.23. Corresponding lifetimes are tabulated in appendix 4.6 and graph 4.10.

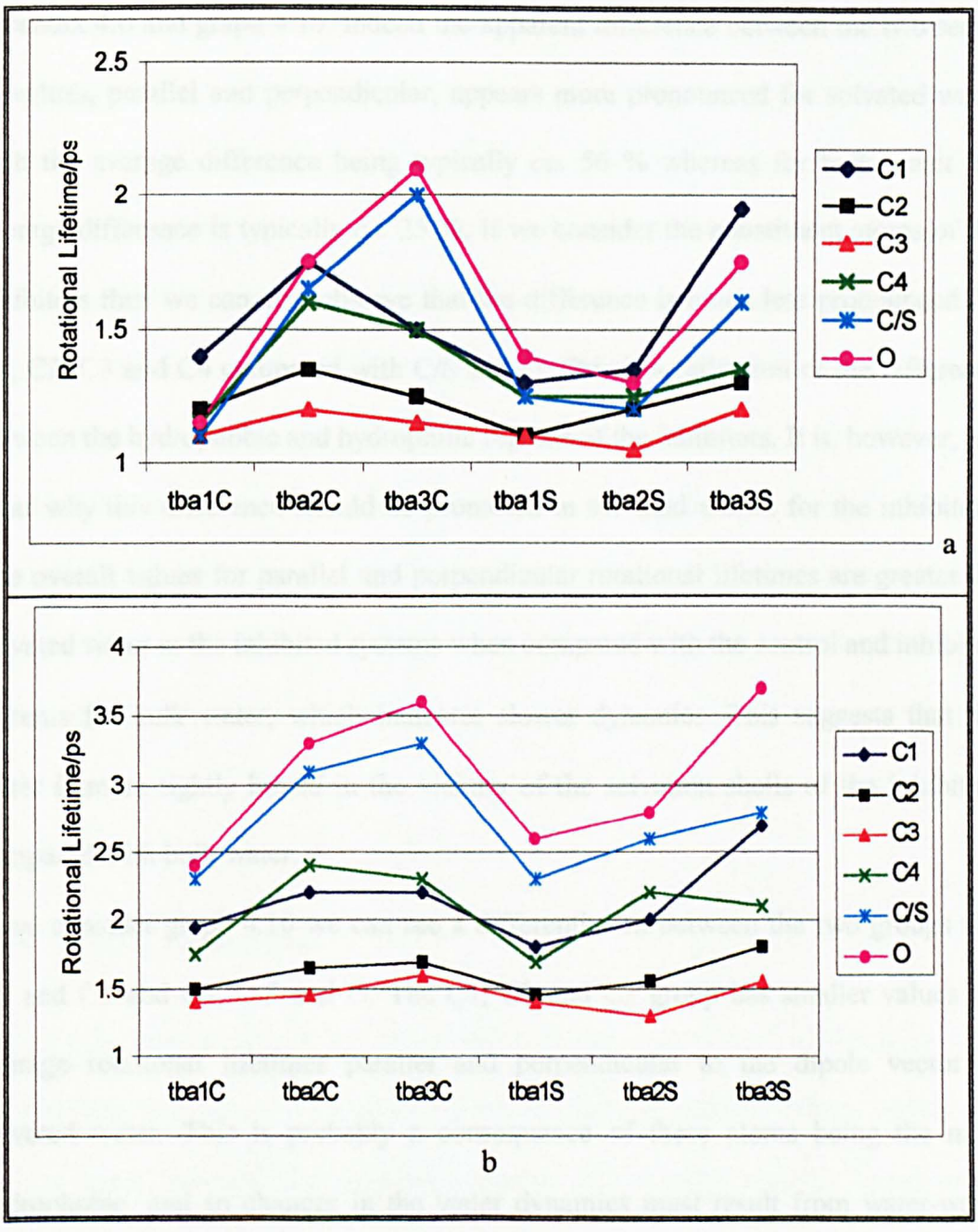

Graph 4.10 Rotational lifetimes for motion, parallel to the dipole vector (a) and perpendicular to the dipole vector (b), of solvated water around various solute atoms for the inhibited systems. Graphs are coloured as per figure 4.5. Numerical values are also given in appendix 4.6.

Once again the increased value for rotation perpendicular to the dipole vector of water when compared with the corresponding parallel rotation can be observed in

appendix 4.6 and graph 4.10. Indeed the apparent difference between the two series of values, parallel and perpendicular, appears more pronounced for solvated water with the average difference being typically *ca.* 56 % whereas for bulk water the average difference is typically *ca.* 25 %. If we consider the constituent atoms of the inhibitors then we can also observe that the difference is much less pronounced for C1, C2, C3 and C4 compared with C/S and O. This is a reflection of the difference between the hydrophobic and hydrophilic regions of the inhibitors. It is, however, not clear why this difference should be promoted in solvated waters for the inhibitors. The overall values for parallel and perpendicular rotational lifetimes are greater for solvated water in the inhibited systems when compared with the control and inhibited systems for bulk water, which indicates slower dynamics. This suggests that the water is more tightly bound in the vicinity of the solvation shells of the inhibitors compared with bulk water.

If we consider graph 4.10 we can see a differentiation between the two groups C1, C2 and C3 and C4, C/S and O. The C1, C2 and C3 group has smaller values for average rotational lifetimes parallel and perpendicular to the dipole vector of solvated water. This is probably a consequence of these atoms being the most hydrophobic, and so changes in the water dynamics must result from water-water interactions at the hydrophobic surface, rather than from direct water-solute interactions. Indeed it is C3, corresponding to the CH_3 group and so furthest from the charged centres, which has the smallest average rotational lifetimes. Even so, the rotational lifetimes around C3 are still longer than was observed for bulk water in the control and inhibited systems.

Considering the C4, C/S and O group we see that the average rotational lifetimes increase on going from C4 to C/S to O — especially for rotation perpendicular to the

dipole vector. This suggests stronger hydrogen-bonding of water around the inhibitor headgroup O atoms which propagates through space towards the C/S and C4 atoms but decreases with increasing distance from the inhibitor headgroup O atoms. This observation coupled with the observation of slower rotational dynamics in bulk water for the inhibited systems suggests that the effect is longer-ranged than just the 1st solvation shell of the inhibitors and implies long-range water structure around the inhibitors.

It is also interesting to note that the rotational lifetimes parallel and perpendicular to the dipole vector of water show a general increase with increasing charge separation for the amine carboxylates and the amine sulphonates for each of the constituent atoms of the inhibitor *i.e.* C1, C2 and C3 *etc.* However it is not clear what would cause such a phenomenon.

4.4 Conclusions

The results obtained from the simulations of the control and inhibited systems suggest that bulk water observed in the control and inhibited systems is similar but not the same; however the solvated water in the inhibited systems shows much greater differences from the behaviour of bulk water in both the control and inhibited systems.

The radial distribution functions for bulk water are very similar for the control and inhibited systems with only a slight movement of the second peak position in g_{OwOw} in the presence of the inhibitors; the movement is to longer distances for the amine carboxylates and shorter distances for the amine sulphonates.

The radial distribution functions for all waters highlight the two functional areas of the inhibitors with g_{XO} and g_{XH} forming two distinct behavioural groups: C1, C2 and

C3 (*i.e.* hydrophobic regions) or C4, C/S and O (*i.e.* hydrophilic regions). The former group are the same for all the inhibitors while the latter group show differences between the inhibitors.

The g_{XO} plot for the headgroup O atom, which can be compared with the g_{OwOw} plot for bulk water in the control and inhibited systems, shows movement of the first peak to shorter distances for the amine carboxylates, with a corresponding increase in the height of the peak; whereas there is a reduction of the peak height for the amine sulphonates. The second peak is higher and occurs at longer distances for all of the inhibitors. This indicates a small, well-defined first solvation shell surrounded by a larger better-defined second solvation shell compared with bulk water in the control and inhibited systems.

The g_{XH} plot for the headgroup O atom, which can be compared with g_{OwHw} for bulk water, shows four peaks as opposed to two for bulk water, indicating longer range structuring in solvated water. Both the first and second peaks are at shorter distances with the first peak height being greater for the inhibitors compared with bulk water, which suggests increased structuring of solvated water, by the inhibitors.

The co-ordination number for bulk water in the control system gives a value of 4 as the most frequent co-ordination number, with 4 or 5 for bulk water in the inhibited systems. The percentage of 5-co-ordinate waters is higher for the amine carboxylates and amine sulphonates compared with the control system, while the percentage of 3- and 4-co-ordinate waters is smaller. This suggests that the water in the inhibited systems is being disrupted away from the distribution observed for the control system.

The picture obtained for solvated water is that the water is typically 4-co-ordinate about most sites, but 3-co-ordinate around the O atom for tba2C and the amine

sulphonates. The co-ordination number of 3 around the O atom may be due to the fact that the O atom is acting as the 4th co-ordination site.

The set of order parameters F_3, $F_{4\varphi}$ and F_{4t} designed to identify ice- and clathrate-like clusters yield values for bulk water and solvated water that are very similar suggesting no differences between bulk water in the inhibited and control systems and solvated water in the inhibited systems. However differences are observed in the shapes of the plots for F_3 and F_{4t} against co-ordination number.

The residence times obtained for solvated water in the inhibited systems are smaller than those obtained for bulk water in the control and inhibited systems suggesting less structuring of solvated water when compared with bulk water.

The mean square displacements obtained for bulk water in the control and inhibited systems indicates slower dynamics for bulk water in the presence of the inhibitors compared with the control and that solvated water shows slower dynamics than bulk water in either the control or inhibited systems, indicated by the smaller self-diffusion coefficients obtained for solvated water in the inhibited systems.

Finally the Legendre orientational correlation functions indicate slower dynamics of bulk water around the inhibitors compared with the control system, and slower dynamics of solvated water compared with bulk water in the control and inhibited systems.

It can be seen from this brief résumé that the majority of results obtained support the picture that the inhibitors generate an increase in the short and long range structure of solvated water. This increased structure of solvated water may well be implicated in the mode of action of the inhibitors. It is believed that the hydrate lattice templates the liquid water above the lattice and so facilitates the growth of the hydrate lattice. Therefore it is possible that if the inhibitors alter the water structure then the growth

of the hydrate lattice would be retarded. This could be envisaged as a two-stage process, with migration of the inhibitor to the hydrate lattice and subsequent adsorption through hydrogen-bonding followed by alteration of the water structure in the vicinity of the inhibitor. It would also explain why the inhibitors do not completely stop the growth of the hydrate lattice, as it is conceivable that the hydrate lattice can overcome this modified water structure, but that this process would obviously be slower than growth of pure hydrate by templating of 'raw' unstructured water. Note that the bi-functional nature of these inhibitors may be important in determining their activity. The results presented in this chapter clearly show that the behaviour of the water around the alkyl groups is consistent with hydrophobic hydration structure—hydrophobic hydration is believed to be important in the formation of methane hydrates in the first place. At the same time, a very different water structure was observed around the hydrophilic end of the inhibitors. Thus one could imagine a mechanism in which the hydrophilic end targeted the growing hydrate crystals, while the hydrophobic end then disrupted further growth of the hydrate, and in particular, changed the intrinsic structure of water at the hydrate interface.

4.5 References

[1] Roentgen W.K., *Ann. Phys.* **45**, 1892, 91.

[2] Pauling L., *Hydrogen Bonding*, D. Hadzi ed., Pergamon Press, 1959.

[3] Bernal J.D., Fowler R.H., *J. Chem. Phys.*, **1**, 1933, 515.

[4] Niesar U., Corongiu G., Clementi E., Keller G.R., Bhattacharya D.K., *J. Phys. Chem.*, **94**, 1990, 7949.

[5] Jorgensen W.L., *J. Am. Chem. Soc.*, **103**, 1981, 335.

[6] Jorgensen W.L., Chandrasekhar J., Madura J.D., Impey R.W., Klein M.L., *J. Chem. Phys.*, **79**, 1983, 926.

[7] Berensden H.J.C., Postma J.P.M., van Gunsteren W.F., Hermans J., *Intermolecular Forces*, B. Pullman ed., D. Reidel Publishing Co., 1981, 331.

[8] Berensden H.J.C., Grigera J.R., Straatsma T.P., *J. Phys. Chem.*, **91**, 1987, 6269.

[9] Jorgensen W.L., *J. Chem. Phys.*, **77**, 1982, 4156.

[10] Stillinger F.H., Rahman A., *J. Chem. Phys.*, **60**, 1974, 1545.

[11] Ben-Naim A., Stillinger F.H., *Structure and Transport Processes in Water and Aqueous Solutions*, R.A. Horne ed., Wiley-Interscience, 1972.

[12] Singh U.C., Kollman P.A., *J. Comp. Chem.*, **5**, 1984, 129.

[13] Cerius^2, Molecular Simulations Inc., San Diego, USA.

[14] Rappe A.K., Casewit C.J., Colwell K.S., Goddard III W.A., Skiff W.M, *J. Am. Chem. Soc.*, **114**, 1992, 10024.

[15] Fletcher R., Reeves C.M., *Comput J.*, **7**, 1964, 149.

[16] Gaussian 92/DFT, Revision F.2, Frisch M.J., Trucks G. W., Schlegel H. B., Gill P. M. W., Johnson B. G., Wong M. W., Foresman J. B., Robb M. A., Head-Gordon M., Replogle E. S., Gomperts R., Andres J. L., Raghavachari K., Blinkley J. S., Gonzalez C., Martin R. L., Fox D. J., Defrees D. J., Baker J., Stewart J. J. P., Pople J. A., Gaussian, Inc., Pittsburgh PA, 1993.

[17] Ryckaert J.P. Cicotti G, Berensden H.J.C., *J. Comp. Phys.*, **23**, 1977, 327.

[18] Brooks, B.R., Bruccoleri R.E., Olafson B.D., States D.J., Swaminathan S., CHARMm: A Program for Macromolecular Energy, Minimisation and Dynamics Calculations, *J. Comp. Chem.*, **4**, 1983, 187.

[19] Smith W., Forester T.R., *J. Mol. Graphics*, **14**, 1996, 136.

[20] Ewald P., *Ann. Phys.*, **64**, 1921, 253.

[21] Fidler J., Rodger P.M., *J Phys Chem B*, **103**, 1999, 7695.

[22] Carver T.J., Drew M.G.B., Rodger P.M., *Phys. Chem. Chem. Phys.*, **1**, 1999, 1807.

CHAPTER 5

STRUCTURE II HYDRATES–PHASE BEHAVIOUR

5 Introduction

In this chapter the simulation work carried out to investigate the phase behaviour of a structure II gas hydrate in order to determine a set of operating conditions for later simulations is detailed. The chapter is divided into four parts as outlined below.

5.1 A literature review of the phase behaviour of structure I and II gas hydrates and the effect of pressure in forming unusual structures.

5.2 Simulation details—outlining the 'preparation' of the systems studied along with the simulations carried out.

5.3 Results and discussion of the simulations performed.

5.4 Conclusions.

5.1 Literature Review

5.1.1 Pressure Behaviour of Gas Hydrates

Structure I Gas Hydrates

The high-pressure behaviour of structure I gas hydrates is a subject of some interest in the literature. For example Handa *et al.*[1] studied the pressure-induced phase transitions in structure I gas hydrates incorporating both an experimental study of xenon hydrate and a computer modelling comparison of ethylene oxide hydrate with the empty structure I gas hydrate lattice (often called the β-hydrate). In their experimental study xenon hydrate was compressed to 17.2 kbar at 77 K with no structural transformation being observed. In the computer modelling study of the β-hydrate, an abrupt densification was observed which was similar to a first-order transition, such that within a pressure increase of ~ 2 kbar the volume of the empty structure I gas hydrate lattice decreased by more than 30 %. The transition pressure was found to be 9.8 kbar, which was taken as the midpoint of the sharp rise observed in the ρ–P curve. For the simulated ethylene oxide hydrate a different behaviour was observed, with the gas hydrate compressing elastically below 10 kbar while from 20–40 kbar a slow and less well-defined transformation than that observed for the β-hydrate was observed. The transition pressure, once again estimated from the ρ–P curve, was estimated to be 26 kbar. The densification in ethylene oxide hydrate for the transition was 12 %, compared to 26 % for the empty gas hydrate lattice. The ethylene oxide hydrate structure was analysed using oxygen–oxygen radial distribution functions. It was found that the effect of increasing pressure was to shorten the oxygen–oxygen distances with a concomitant

broadening of the distribution for the second co-ordination shell. Below 20 kbar the ethylene oxide hydrate structure seemed to compress elastically; between 30–40 kbar a fundamental structural change was observed. The second co-ordination shell peak at 4.5 Å widened with the hint of a new peak at 3.2 Å and a broad distribution centred around 4.4 Å. When the pressure was released at 60 kbar the radial distribution function obtained showed a structure similar to that at zero pressure and the density of the phase was close to that of the starting material. The radial distribution functions obtained for the empty gas hydrate lattice were similar to those for the ethylene oxide hydrate except that on release of the pressure they did not transform back to the original RDFs but to RDFs that were similar to those of high-density amorphous ice; the density also relaxed to a density close to that of HDA ice.

Dyadin *et al.*[2] also carried out an experimental investigation into xenon hydrate up to a pressure of 15 kbar. They studied the water–xenon system in the temperature range –25 to 100 °C at pressures up to 15 kbar. From their water–xenon phase diagram they concluded that throughout the pressure and temperature range studied that xenon hydrate did not undergo any phase transition—a result which was also observed in reference 1. This observation was explained in terms of the fact that structure I hydrates are highly compact, with xenon hydrate at low pressures (1.545 kbar) filling 71.6% of the small cavities and 98.0% of the large cavities; this amounts to a packing coefficient for gas hydrates of 0.564, which is remarkably high.[3,4]

Structure II Gas Hydrates

In 1971 Davidson and Gough[5] carried out an investigation into the effect of pressure upon the decomposition of tetrahydrofuran hydrate. Part of their study was concerned with the phase equilibrium of tetrahydrofuran hydrate. It was found that at pressures below 3.05 kbar the hydrate melts to yield a liquid of greater density while at higher pressures the hydrate melts to give ice III and a liquid. However there was no evidence of the formation of a denser hydrate phase.

Dyadin *et al.*[6] studied the water–tetrahydrofuran system two years later at temperatures in the range –33 to 47 °C and pressures up to 9 kbar. Four intermediate phases were identified with nominal compositions of $THF.17H_2O$, $THF.7.1H_2O$, $THF.4.6H_2O$ and $THF.2.2H_2O$. These four phases were named α, β, γ and δ respectively by Ross and Anderson[7] who investigated phases α, β and γ. Phase α had previously been identified as structure II tetrahydrofuran hydrate by Sargent and Calvert,[8] whose ideal composition was suggested as $THF.16.86H_2O$ by Gough and Davidson.[5] Phase β was suggested as being a gas hydrate, probably of structure II; this assignment was on the basis of composition data, since phase β was only stable under pressure, no structural data was available. As suggested by Dyadin *et al.*,[6] structure II may become less stable than structure I under pressure, leading to the formation of structure I. Phase γ was not identified but was assigned as not being a gas hydrate on the basis of composition data. In addition, during their experimental study they also identified an α′ phase which arose from a transition of the α phase at 11 kbar and –143 °C. The temperature dependence of the thermal conductivity for the α′ phase suggested that it was probably a gas hydrate. It

was suggested that the α′ phase arises from a densification of the host lattice of the structure II gas hydrate.

Handa *et al.*[1] also carried out an experimental investigation into THF hydrate along with sulphur hexafluoride hydrate and a computer modelling study of both krypton hydrate and the empty structure II gas hydrate lattice. In the experimental study a sharp transition was observed at a nominal pressure of 13.1 ± 1 kbar with a volume decrease of ~ 19 % for tetrahydrofuran hydrate, indicating the formation of a high-pressure phase. However, after the pressure was reduced to 0.7 kbar over ten minutes and subsequent recovery of the sample at –196 °C and ambient pressure the high-pressure phase reverted back to the structure II hydrate. A similar transformation was observed for sulphur hexafluoride hydrate at a pressure of 15.8 ± 1 kbar. Upon reducing the pressure to 4 kbar at –196 °C the sample transformed within a few seconds to the original sulphur hexafluoride structure II hydrate. This indicates that the high-pressure phase of sodium hexafluoride hydrate is much less stable than that of tetrahydrofuran hydrate.

In the computer modelling study, an abrupt transformation in the empty lattice was observed whilst in the krypton hydrate the transformation was gradual. The transition pressures for the empty structure II gas hydrate lattice and krypton hydrate were comparable to those for the structure I empty gas hydrate lattice and ethylene oxide hydrate as outlined in the section on structure I hydrates. When the pressure of the empty gas hydrate lattice was reduced to zero the density of the phase obtained was similar to that of high-density amorphous ice, whereas the krypton hydrate reverted to its original hydrate.

Van Hinsberg *et al.*[9] investigated the gas hydrate of nitrogen using Raman spectroscopy. They observed a phase transition in the nitrogen hydrate at 8.4 kbar, indicated by a

sudden change in Raman frequency as a function of pressure along with the appearance of two new peaks in the Raman spectrum. They postulated that their observations could be due to one of several mechanisms:

i) a transition between the two gas hydrate structures, structure I and II, with low-pressure nitrogen hydrate being a structure II hydrate;

ii) a transition to an unknown gas hydrate phase;

iii) a sudden orientational ordering of the molecules within the cages;

iv) a sudden increase of the probability for double occupancy in the cavities.

Zakrzewski *et al.*[10] once more investigated the gas hydrate of THF at high pressure. They employed two methods for sample preparation: the first was to freeze a liquid phase of overall composition $THF.7H_2O$ under a pressure of 3.0 kbar; the second was to pressurise the solid structure II tetrahydrofuran hydrate at –18 °C to 3.4 kbar. Unfortunately, upon recovery of the products at –196 °C the materials obtained were always mixed phase materials (as shown by X-ray powder diffraction). A number of diffraction lines could be indexed in terms of a structure I gas hydrate with a slightly expanded lattice parameter of 12.08 Å. This lattice parameter is slightly larger than those normally obtained for structure I hydrate, but this can be explained in terms of the fact that the guest molecule is larger than is usual for a structure I hydrate. These observations suggest that the phase transition observed at 3.4 kbar and –18 °C is due to the conversion of structure II tetrahydrofuran hydrate to structure I tetrahydrofuran hydrate.

The water–argon system was investigated at pressures and temperatures up to 30 kbar and 140 °C by Lotz and Schouten.[11] They discovered two new quadruple points for the system: at 105 °C and 20 kbar (Q_4) and 136 °C and 29 kbar (Q_5). The lower pressure

region below 10 kbar shows two breaks in the decomposition curve at 31.5 °C and 6.2 kbar (Q_2) and 37.5 °C and 9.6 kbar (Q_3). From their study they proposed the existence of three phases, C1, C2 and C3, with C1 being present between Q_1 and Q_2, C2 between Q_2 and Q_3 and C3 above Q_3. C1 is proposed to be structure II argon hydrate, C2 to be structure I argon hydrate. They were unable to detect C3, but they found no indication of an amorphous phase transition.

Unusual Hydrates

Londono *et al.*[12] announced the discovery of one of the first unusual gas hydrates in 1988. They found that when powders of D_2O ice Ih were pressurised with helium gas that at 2.8 kbar and –21 °C a phase transformation of the ice Ih into helium hydrate was observed whose idealised formula was $He.6D_2O$. The structure of the helium hydrate was found to resemble closely that of ice II. As in ice II, the hydrogen atoms are fully ordered in this structure. There are two types of water molecules in the structure, each type building up six-membered rings. The hexagon formed by water-2 molecules is quite flat, while the ring formed by water-1 molecules is more puckered. The latter ring connects two flatter water-1 hexagons by donating protons in hydrogen bonds to oxygen atoms. The resulting structure has channels running along the unique axis providing voids of sufficient size to host small atoms or molecules. The helium atoms are found in positions roughly halfway between the six-membered rings with a slight shift towards the flatter ring formed by the second type of water molecules.

The same authors carried out a further study into helium hydrate in 1992.[13] They found that although the helium hydrate resembled ice II in structure, the stability range of the

helium hydrate was considerably more extensive than that of ice II. In addition, helium hydrate was found to be more stable than ice III/IV or ice V up to 5 kbar. The helium content increases with increasing pressure/decreasing temperature but does not appear to follow an ideal solution behaviour. The lattice parameters of the helium hydrate were found to be significantly different from those of ice II; however the atomic arrangement of the host lattice is very similar, exhibiting full orientational order of the water molecules.

Another type of novel hydrate was discovered by Vos *et al.*[14] They found that when water and hydrogen were pressurised a rhombohedral hydrate with a water sub-lattice similar to ice II and a H_2 : H_2O ratio of 1 : 6 formed between 7.5 and 31 kbar at 22 °C. Above 23 kbar a new hydrate began to form with water molecules in a cubic diamond structure similar to ambient pressure metastable ice Ic but with the interstitials filled with H_2. The structure has a H_2 : H_2O ratio of 1 : 1. The hydrogen molecules occupy voids in the water framework therefore improving the packing efficiency and stabilising the hydrate to pressures at least as high as 300 kbar.

Summary

In summary, it can be seen that the effect of high pressure is threefold.

Firstly, for structure I hydrates high pressures induce slight compression of the structure rather than a phase transition.

Secondly, for structure II hydrates high pressures have two effects:

i) at ~ 3 kbar and –13 °C there is a structural transition from structure II to structure I hydrate;

ii) at ~ 13 kbar and –196 °C there is a structural transition to a high density phase.

Thirdly, high pressures have the effect of creating/stabilising unusual clathrate hydrates such as those of helium or hydrogen.

5.2 Simulation Details

5.2.1 System Overview

In this section the methods used to prepare and simulate structure II hydrates under pressure are outlined.

5.2.2 System Preparation

Gas Hydrate Lattice

A simulation cell was created by cleaving the bulk structure II hydrate in such a way as to expose its {1,1,1; -0.001} surface.[15] The oxygen positions were taken from neutron diffraction data[16] and hydrogens assigned in a manner consistent with two-fold crystallographic disorder. The resulting simulation cell had dimensions of 21.2 x 24.48 x 29.982 Å and contained 408 water molecules. Initially the small cavities of the gas hydrate lattice were filled with methane molecules and the large cavities with propane, such that 48 methane and 24 propane molecules were contained within the structure.

Potentials

The water in these simulations was modelled using the SPC model.[17] This model was chosen for being able to give a reasonable structural and thermodynamic description of liquid water[18] and hydrates as well as for its ease of implementation being a three interaction site model and as a result computationally inexpensive.

Methane and propane were modelled using the united atom model of Jorgensen *et al.*[19]

The van der Waals cross terms for the hydrocarbons/water molecules were derived from the Lorenz-Berthelot mixing rules.

Simulation Cell

The cell containing the gas hydrate lattice outlined above was taken and the *z*-dimension increased by 30 Å such that the simulation cell was 21.2 x 24.48 x 59.982 Å in size. This cell was taken as the control simulation cell in order to investigate the behaviour of the gas hydrate lattice under zero pressure. In order to investigate the behaviour of the gas hydrate lattice under pressure a second, pressurised, cell was constructed by taking the control cell and adding 55 methane and 33 propane molecules to the headspace around the gas hydrate lattice. The hydrocarbon gas was introduced by using the SORPTION module in Cerius^{2}.[20] Periodic boundary conditions in three dimensions were employed to give an infinite hydrate film *ca.* 30 Å thick.

Simulations Performed

A series of simulations were performed at both 277 and 300 K to investigate the effect of temperature on the pressure behaviour of the gas hydrate lattice. The series at 277 K

consisted of 8, while the series at 300 K consisted of 7, separate simulations, each using a different value for the *z*-dimension of the simulation cell (compression of the gas hydrate lattice was uniaxial along the *z*-axis), and chosen so that the set of simulations spanned pressures in the range 0 to 30 kbar. As the details of the phase diagram for SPC hydrate were not known, a large set of short simulations (2×20=40 ps duration) were performed. These were then examined to identify significant regions of the phase diagram, and then a subset of the systems modelled in longer (an additional 3×20 ps trajectories) simulations. A final selection was made to choose four systems at each temperature which were then simulated for another 100 ps (2×50 ps at 277 K) and (5×20 at 300 K), giving total trajectory lengths of 200 ps for these systems. At each stage in the selection process the time dependence of a number of properties, including radial distribution functions and pressures, was monitored to assess the stability of the dominant water phase in each system. In all instances the final configuration of the previous simulation was used as the starting point for the next simulation. A summary of the simulations at 277 and 300 K can be seen in tables 5.1 and 5.2.

RUN	*Z*-DIMENSION/Å	NUMBER CH_4	NUMBER C_3H_8	DURATION OF TRAJECTORY /ps
1a-g (Control)	59.982	48	24	200
2a-e	59.982	103	57	100
3a-b	55.882	103	57	40
4a-g	50.882	103	57	200
5a-e	45.782	103	57	100
6a-g	40.882	103	57	200
7a-e	35.882	103	57	100
8a-g	32.882	103	57	200

Table 5.1 Summary of the simulations carried out at 277 K. Systems investigated for a total of 200 ps are coloured blue.

RUN	Z-DIMENSION/Å	NUMBER CH_4	NUMBER C_3H_8	DURATION OF TRAJECTORY /ps
1a-j	59.982	103	57	200
2a-b	50.882	103	57	40
3a-j	42.882	103	57	200
4a-b	39.882	103	57	40
5a-j	36.882	103	57	200
6a-e	33.882	103	57	100
7a-j	32.882	103	57	200

Table 5.2 Summary of the simulations carried out at 300 K. Systems investigated for a total of 200 ps are coloured blue.

All simulations were carried out using DL_POLY[21] in the [*N*, *V*, *T*] ensemble with a thermostat value of 0.1 ps and a time step of 1 fs. Periodic boundary conditions were employed in all three dimensions. Long-range electrostatic interactions were evaluated with an Ewald summation,[22] while all other interactions were truncated for distances in excess of 9.5 Å. Water and propane molecules were constrained to be rigid using the SHAKE[23] algorithm.

Simulation Analysis

The simulations performed at 277 and 300 K were analysed using the techniques outlined in chapter 3 to determine radial distribution functions for the oxygen–oxygen distribution g_{OO}, and also for the guest–guest distribution g_{XX}. For the calculation of the radial distribution functions the gas hydrate lattice was split into six slabs each with dimensions 21.2 x 24.48 x 5 Å; the width of the slabs were such that they were *ca.* half the crystallographic repeat distance for this surface, and therefore the properties of slabs 1, 3 and 5 may differ from slabs 2, 4 and 6. Slab 1 refers to the bottom slab (*i.e.* the {1,1,1; 0.999} surface[15]), and slab 6 refers to the top slab (*i.e.* the {1,1,1; -0.001} surface[15]), of the gas hydrate lattice, *i.e.* the two surfaces. Within each of the six slabs the radial distribution functions were then calculated. In addition, the *z*-density distribution through the gas hydrate lattice was calculated.

5.3 Results

The results will be presented in three sections:

i) the phase behaviour of all the systems previously outlined in tables 5.1 and 5.2;

ii) the bulk behaviour, *i.e.* slabs 2, 3, 4 and 5, of the systems simulated to 200 ps previously outlined in tables 5.1 and 5.2;

iii) the surface behaviour, *i.e.* slabs 1 and 6, of the systems simulated to 200 ps previously outlined in tables 5.1 and 5.2.

5.3.1 Phase Behaviour–277 and 300 K

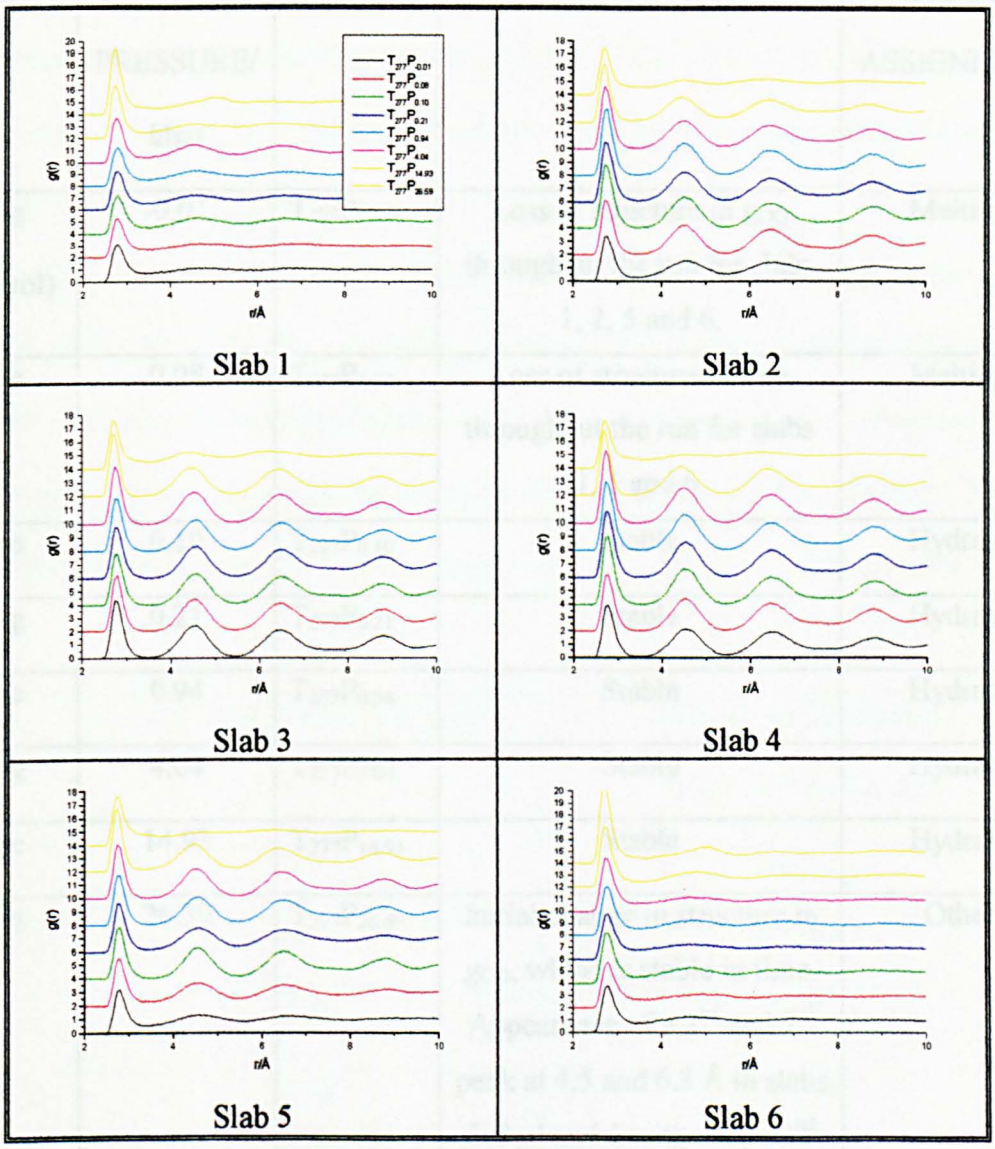

Figure 5.1 Oxygen–oxygen radial distribution functions for the six slabs in the simulations carried out at 277 K. The legend is the same for each plot, and symbols are from table 5.3. Plots are for the last run of each simulation series.

RUN	AVERAGE PRESSURE/ kbar	SYMBOL	OBSERVATION	PHASE ASSIGNMENT
1a-g (Control)	-0.01	$T_{277}P_{-0.01}$	Loss of structure in g_{OO} throughout the run for slabs 1, 2, 5 and 6.	Melting
2a-e	0.08	$T_{277}P_{0.08}$	Loss of structure in g_{OO} throughout the run for slabs 1, 5 and 6.	Melting
3a-b	0.10	$T_{277}P_{0.10}$	Stable	Hydrate
4a-g	0.21	$T_{277}P_{0.21}$	Stable	Hydrate
5a-e	0.94	$T_{277}P_{0.94}$	Stable	Hydrate
6a-g	4.04	$T_{277}P_{4.04}$	Stable	Hydrate
7a-e	14.93	$T_{277}P_{14.93}$	Stable	Hydrate
8a-g	26.59	$T_{277}P_{26.59}$	Initial change in structure in g_{OO}, which is stable in time. Appearance of a 2nd and 3rd peak at 4.5 and 6.3 Å in slabs 2, 3, 4 and 5 with only a 2nd peak in slabs 1 and 6 at 5 Å.	Other

Table 5.3 Summary of the simulations carried out at 277 K. Phase assignments are based upon the appearance of the oxygen–oxygen radial distribution functions in figure 5.1.

Oxygen–oxygen radial distribution functions (see section 3.3) for simulations carried out at 277 K are presented in figure 5.1.

A summary of all the simulations carried out at 277 K is given in table 5.3 along with the average pressures, brief comments and phase assignments; phase assignments were deduced from the g_{OO} (figure 5.1).

From table 5.3 it can be seen that melting is seen in $T_{277}P_{-0.01}$ and $T_{277}P_{0.08}$, stable type II hydrate in $T_{277}P_{0.10}$, $T_{277}P_{0.21}$, $T_{277}P_{0.94}$, $T_{277}P_{4.04}$ and $T_{277}P_{14.93}$, and a substantially different behaviour, denoted 'other', in $T_{277}P_{26.59}$. These phase assignments are supported by the calculation of the average density of the central 9 Å of the gas hydrate lattice from z-density plots of oxygen atoms–$\rho_O(Z)$, for each of the runs (see table 5.4).

RUN	AVERAGE DENSITY/g cm^{-3}	PHASE ASSIGNMENT (FROM TABLE 5.3)
$T_{277}P_{-0.01}$	0.75	Melting
$T_{277}P_{0.08}$	0.74	Melting
$T_{277}P_{0.10}$	0.82	Hydrate
$T_{277}P_{0.21}$	0.82	Hydrate
$T_{277}P_{0.94}$	0.82	Hydrate
$T_{277}P_{4.04}$	0.85	Hydrate
$T_{277}P_{14.93}$	0.88	Hydrate
$T_{277}P_{26.59}$	1.00	Other

Table 5.4 Summary of the average density for the 277 K simulations

From table 5.4 it can be concluded that: melting occurs when the average density of the hydrate falls below *ca.* 0.80 g cm^{-3}, hydrate is present and apparently stable when the average density of the system is 0.82–0.88 g cm^{-3}, and the 'other' phase is characterised by an average density of 1.00 g cm^{-3}. It must be noted that the ranges above are deduced from the values in table 5.4 for the three phases; this data is necessarily limited and the actual ranges may be more extensive in reality. However it does seem that there is a distinct change in the average density range observed for the three phases that is in agreement with the phase assignments in table 5.3.

Oxygen–oxygen radial distribution functions for simulations carried out at 300 K are presented in figure 5.2 and a summary of the data and phase assignments given in table 5.5.

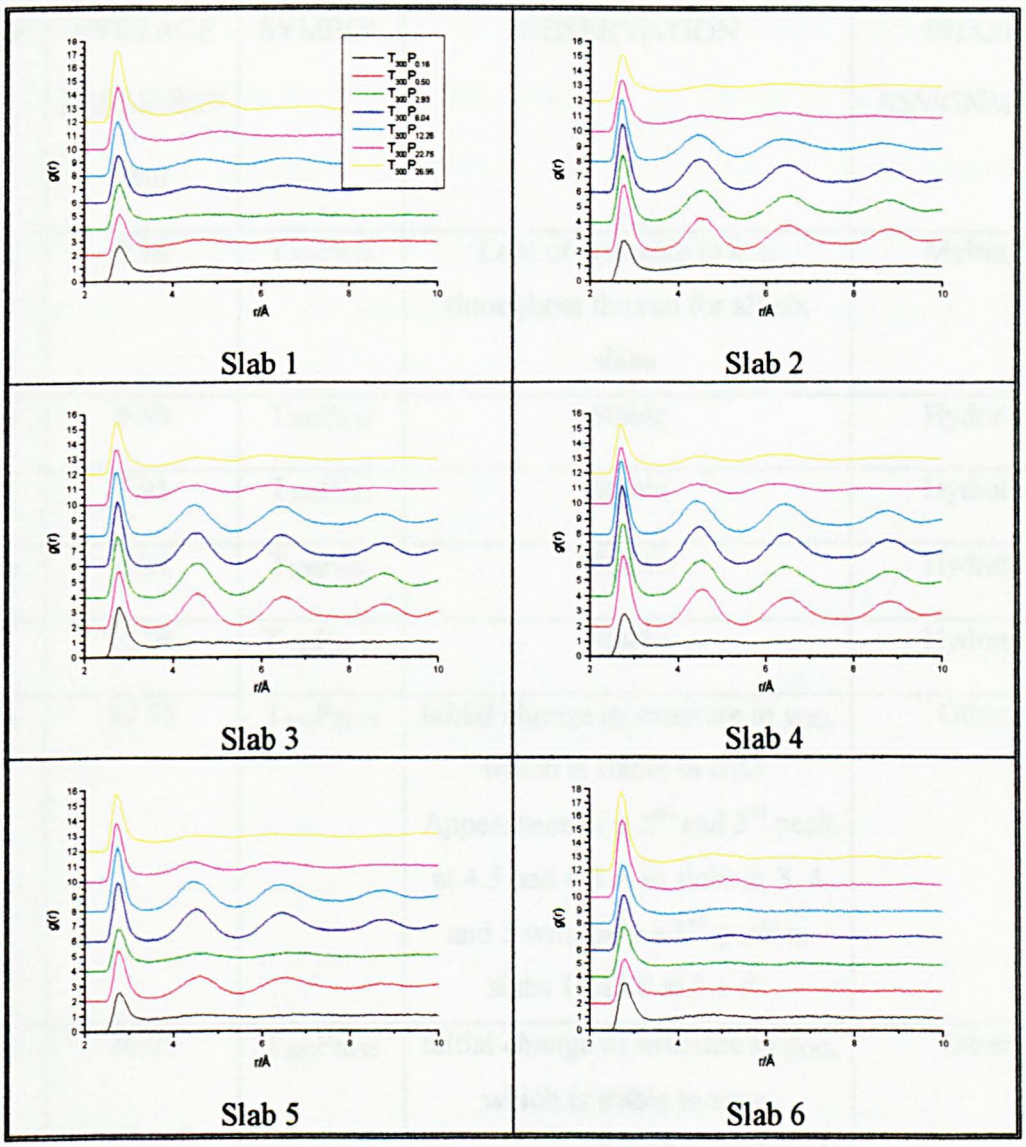

Figure 5.2 Oxygen–oxygen radial distribution functions for the six slabs in the simulations carried out at 300 K. The legend is the same for each plot, and symbols are from table 5.5. Plots are for the last run of each simulation series.

RUN	AVERAGE PRESSURE/ kbar	SYMBOL	OBSERVATION	PHASE ASSIGNMENT
1a-j	0.16	$T_{300}P_{0.16}$	Loss of structure in g_{OO} throughout the run for all six slabs.	Melting
2a-b	0.50	$T_{300}P_{0.50}$	Stable	Hydrate
3a-j	2.93	$T_{300}P_{2.93}$	Stable	Hydrate
4a-b	6.04	$T_{300}P_{6.04}$	Stable	Hydrate
5a-j	12.26	$T_{300}P_{12.26}$	Stable	Hydrate
6a-e	22.75	$T_{300}P_{22.75}$	Initial change in structure in g_{OO}, which is stable in time. Appearance of a 2nd and 3rd peak at 4.5 and 6.3 Å in slabs 2, 3, 4 and 5 with only a 2nd peak in slabs 1 and 6 at 5.1 Å.	Other
7a-j	26.95	$T_{300}P_{26.95}$	Initial change in structure in g_{OO}, which is stable in time. Appearance of a 2nd and 3rd peak at 4.4 and 6.1 Å in slabs 2, 3, 4 and 5 with only a 2nd peak in slabs 1 and 6 at 4.9 Å.	Other

Table 5.5 Summary of the simulations carried out at 300 K. Phase assignments are based upon the appearance of the oxygen–oxygen radial distribution functions in figure 5.2.

From table 5.5 it can be seen that melting is implicated in $T_{300}P_{0.16}$, stable hydrate in $T_{300}P_{0.50}$, $T_{300}P_{2.93}$, $T_{300}P_{6.04}$ and $T_{300}P_{12.26}$ and an unassigned, 'other' phase in $T_{300}P_{22.75}$ and $T_{300}P_{26.95}$. As with the 277 K simulations, these phases assignments are also consistent with the average density obtained from the central 9 Å of the hydrate slab (table 5.6), which again reveal three distinct density ranges: 0.70 g cm^{-3} for the melting hydrate, 0.81–0.86 g cm^{-3} for the stable hydrate, and 0.99–1.00 g cm^{-3} for the 'other' phase.

RUN	AVERAGE DENSITY/g cm^{-3}	PHASE ASSIGNMENT (FROM TABLE 5.5)
$T_{300}P_{0.16}$	0.70	Melting
$T_{300}P_{0.50}$	0.81	Hydrate
$T_{300}P_{2.93}$	0.82	Hydrate
$T_{300}P_{6.04}$	0.83	Hydrate
$T_{300}P_{12.26}$	0.86	Hydrate
$T_{300}P_{22.75}$	0.99	Other
$T_{300}P_{26.95}$	1.00	Other

Table 5.6 Summary of the average density for the 300 K simulations

5.3.2 Bulk Behaviour–277 K

A summary of the average pressures and phase assignments in the four 200 ps simulations at 277 K are presented in appendix 5.1 and graph 5.1.

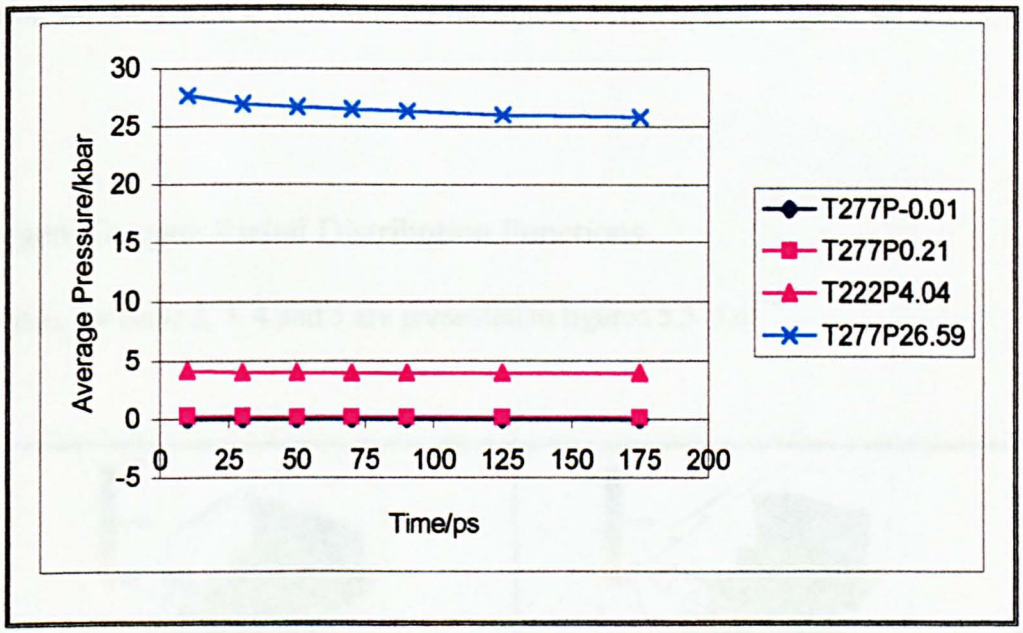

Graph 5.1 Average pressures in the four 200 ps simulations at 277 K. Phase assignments of the simulations are denoted by: dark blue for melting, pink for hydrate and turquoise for 'other'. Time values are plotted at the central time point for each of the constituent simulations. Numerical values are also given in appendix 5.1.

From graph 5.1 it can be seen that for runs $T_{277}P_{-0.01}$, $T_{277}P_{0.21}$ and $T_{277}P_{4.04}$ that the pressure stabilises with time. For run $T_{277}P_{26.59}$ the pressure continued to decrease throughout the simulation, indicating that structural relaxation was still continuing at the end of the simulation, however the rate of pressure change was substantially smaller at the end of the simulation, suggesting that convergence had almost been achieved.

Radial Distribution Functions

The radial distribution function (see section 3.3) for water in the gas hydrate lattice, namely g_{OO}, has been calculated for each of the simulations, along with the radial distribution function for guest atoms, g_{XX} where X is any C site in CH_4 or C_3H_8. In this section we discuss these functions for the inner ('bulk') hydrate region: slabs 2, 3, 4 and 5.

Oxygen–Oxygen Radial Distribution Functions

The g_{OO}, for slabs 2, 3, 4 and 5 are presented in figures 5.3–5.6.

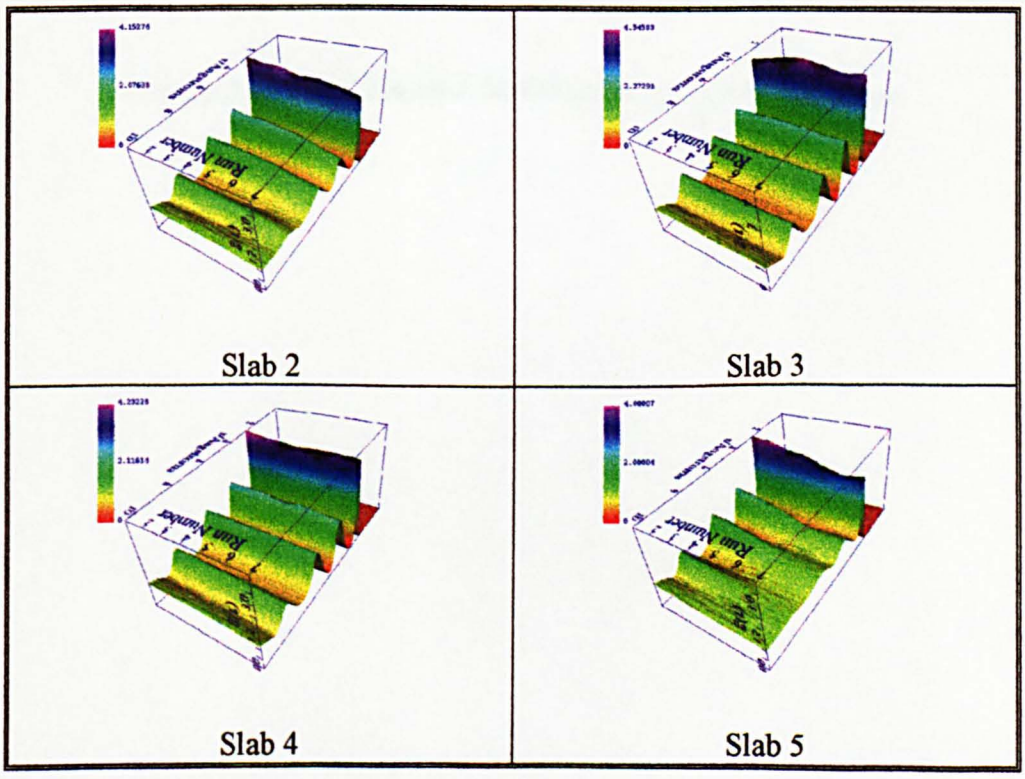

Figure 5.3 Radial distribution functions g_{OO} for run $T_{277}P_{0.01}$.

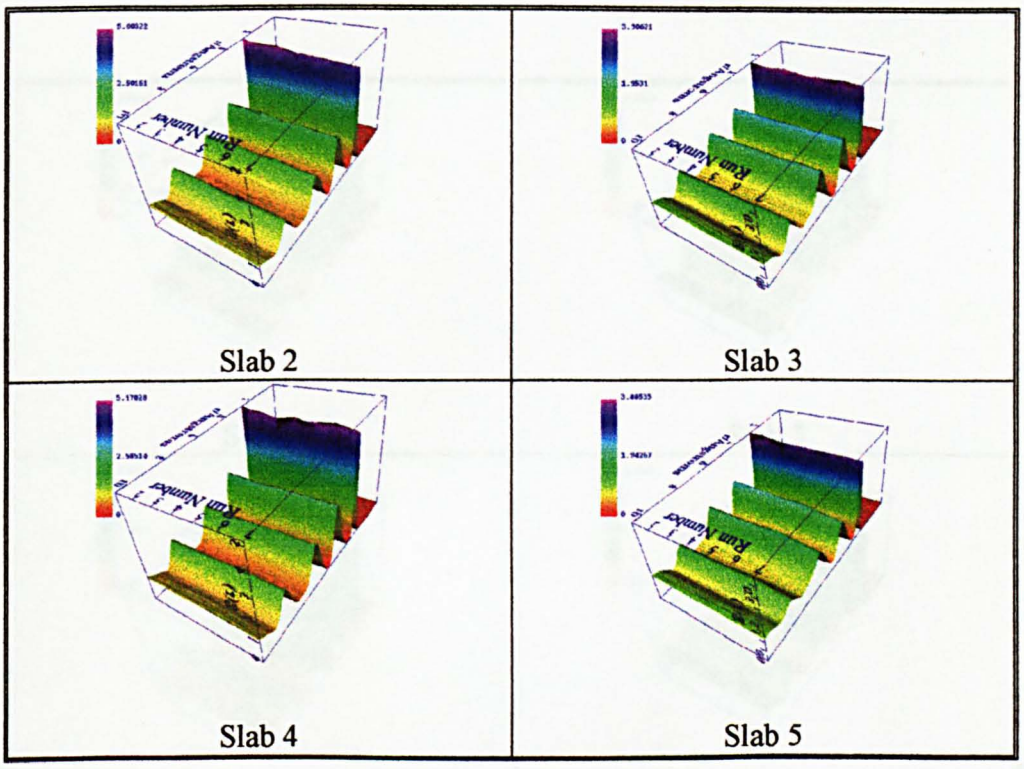

Figure 5.4 Radial distribution functions g_{OO} for run $T_{277}P_{0.21}$.

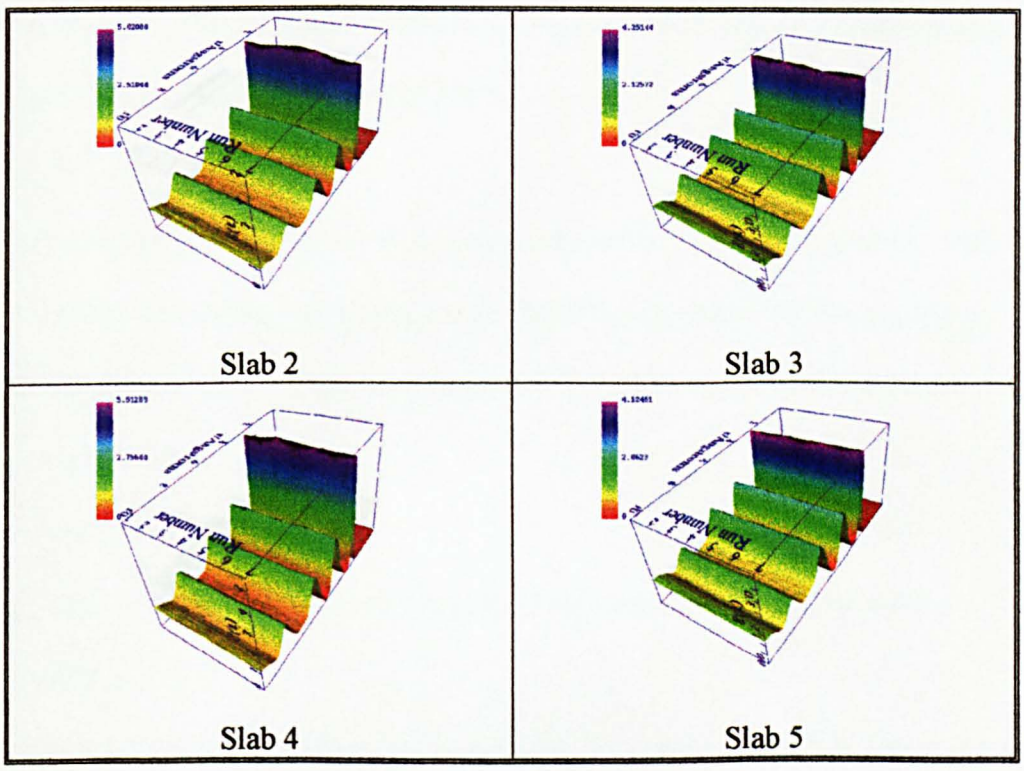

Figure 5.5 Radial distribution functions g_{OO} for run $T_{277}P_{4.04}$.

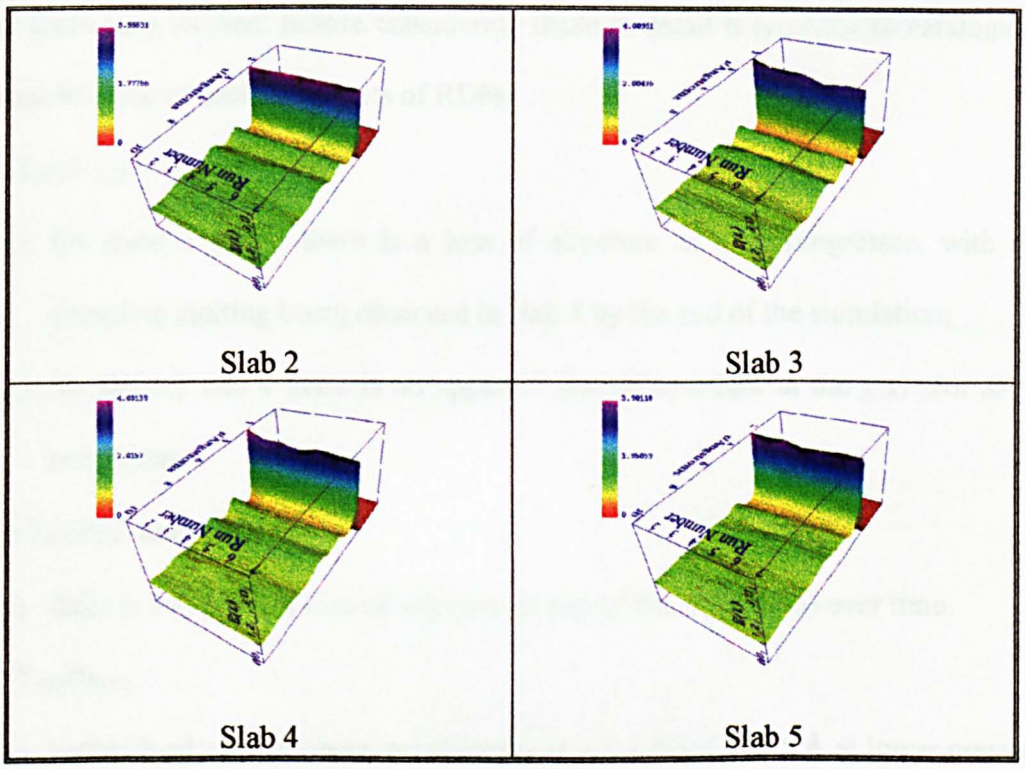

Figure 5.6 Radial distribution functions g_{OO} for run $T_{277}P_{26.59}$.

The first point to note from figures 5.3–5.6 is the apparent symmetry that is present in the four slabs. In runs $T_{277}P_{-0.01}$ and $T_{277}P_{26.59}$, slabs 2 and 5 are very similar, as are slabs 3 and 4, while for runs $T_{277}P_{0.21}$ and $T_{277}P_{4.04}$ all of the four sets of RDFs appear identical. This equivalence is a direct measure of the stability of the hydrate region on the simulation time scale, as melting might be expected to lead to a loss of structure that is seen first closest to the surface (slabs 2 and 5 in the current discussion).

It is also apparent that runs $T_{277}P_{-0.01}$, $T_{277}P_{0.21}$ and $T_{277}P_{4.04}$ give similar structures, but that the RDFs for run $T_{277}P_{26.59}$ are qualitatively different. Run $T_{277}P_{26.59}$ is the simulation in which the predicted phase assignment was of 'other', and it can now be

seen from the g_{OO} plots that this 'other' phase has a distinct structural difference to the other three runs studied. Before considering these in detail it is useful to catalogue the general features of each of the sets of RDFs.

Run $T_{277}P_{-0.01}$:

a) for slabs 2 and 5 there is a loss of structure as time progresses, with near-complete melting being observed in slab 5 by the end of the simulation;

b) for slabs 3 and 4 there is no apparent loss of structure in the g_{OO} plot as time progresses.

Runs $T_{277}P_{0.21}$ and $T_{277}P_{4.04}$:

a) there is no apparent loss of structure in any of the slabs (2–5) over time.

Run $T_{277}P_{26.59}$:

a) a new third peak appears immediately at ~ 6.3 Å (*cf.* ~ 6.5 Å at lower pressures) in all four slabs; the height and shape of this peak is stable in time;

b) a new fourth peak appears at ~ 8.4 Å (*cf.* ~ 8.7 Å for lower pressures) in slabs 3 and 4; again, this peak is stable in time.

The following comments can be made in summary.

a) For run $T_{277}P_{-0.01}$ melting is apparent in slabs 2 and 5, but occurs sufficiently slowly that no melting is seen in slabs 3 or 4 on the simulation time scale. Run $T_{277}P_{-0.01}$ was identified as unstable in the previous sections, and this phase assignment is supported by the behaviour of slabs 2 and 5. It is probable that with longer simulations slabs 3 and 4 would also show signs of melting.

b) Runs $T_{277}P_{0.21}$ and $T_{277}P_{4.04}$ give a hydrate core that is stable on the simulation time scale. This is consistent with the phase assignments made earlier.

c) In run $T_{277}P_{26.59}$ the hydrate core shows an immediate change in structure, which then appears to be stable on the simulation time scale. Again, this is consistent with the phase assignments made earlier.

Guest–Guest Radial Distribution Functions

The guest–guest radial distribution functions, g_{XX}, for the core of the hydrate region (*i.e.* slabs 2, 3, 4 and 5) are presented in figures 5.7–5.10.

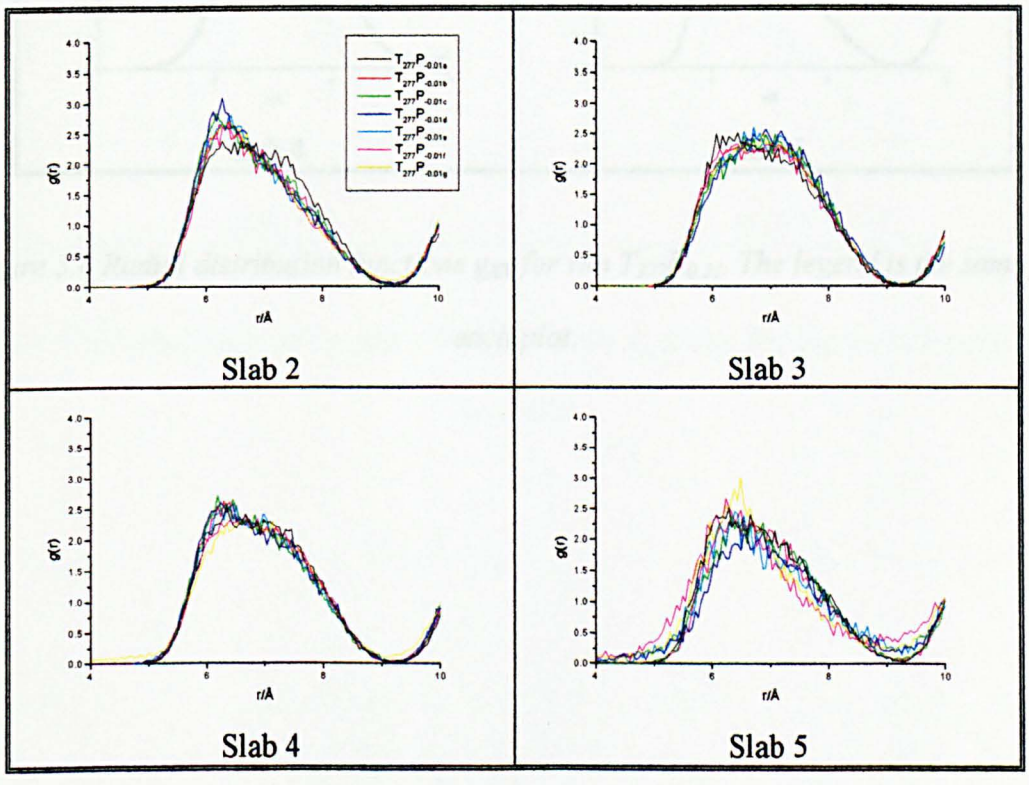

Figure 5.7 Radial distribution functions g_{XX} for run $T_{277}P_{-0.01}$. The legend is the same for each plot.

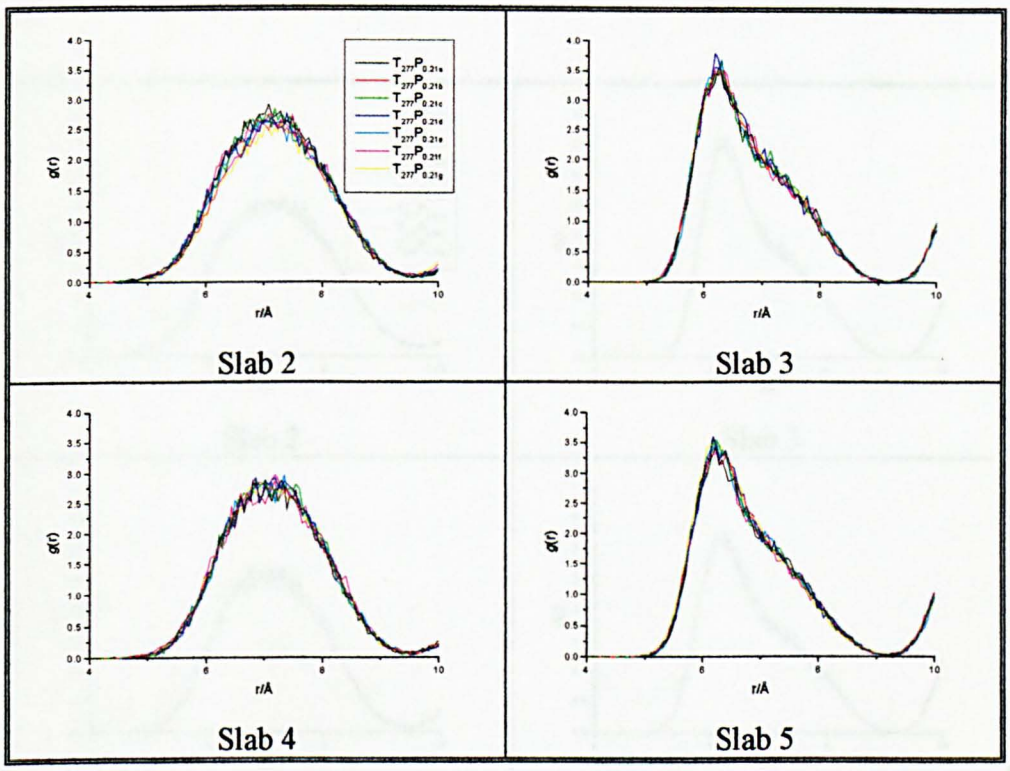

Figure 5.8 Radial distribution functions g_{XX} for run $T_{277}P_{0.21}$. The legend is the same for each plot.

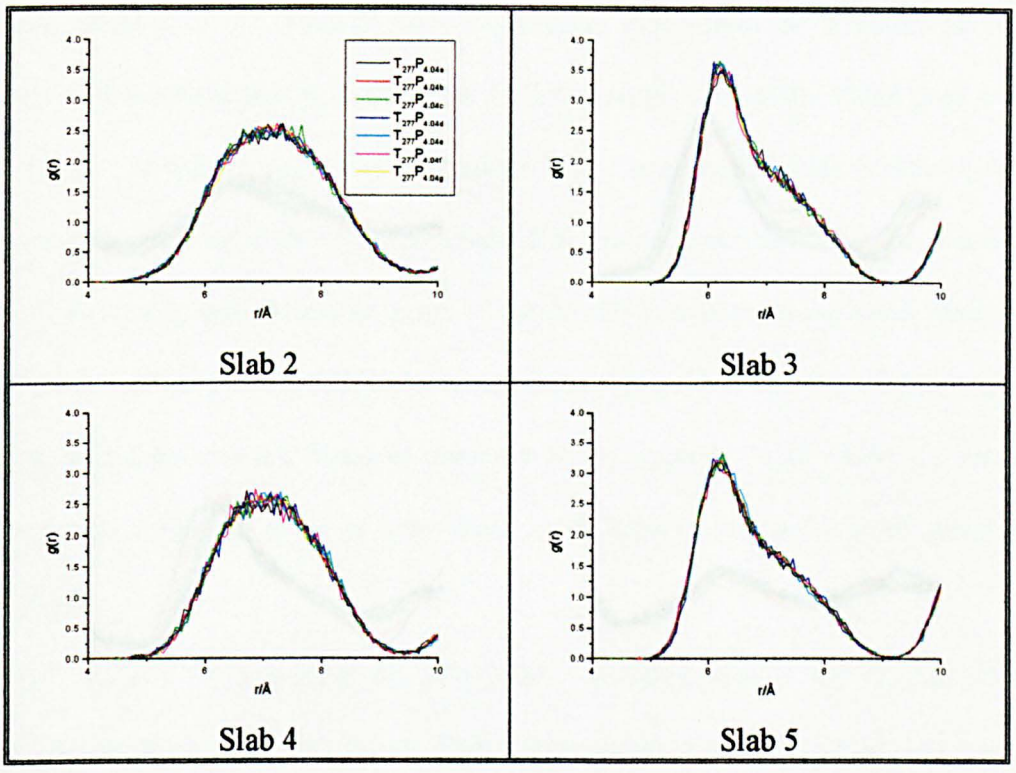

Figure 5.9 Radial distribution functions g_{XX} for run $T_{277}P_{4.04}$. The legend is the same for each plot.

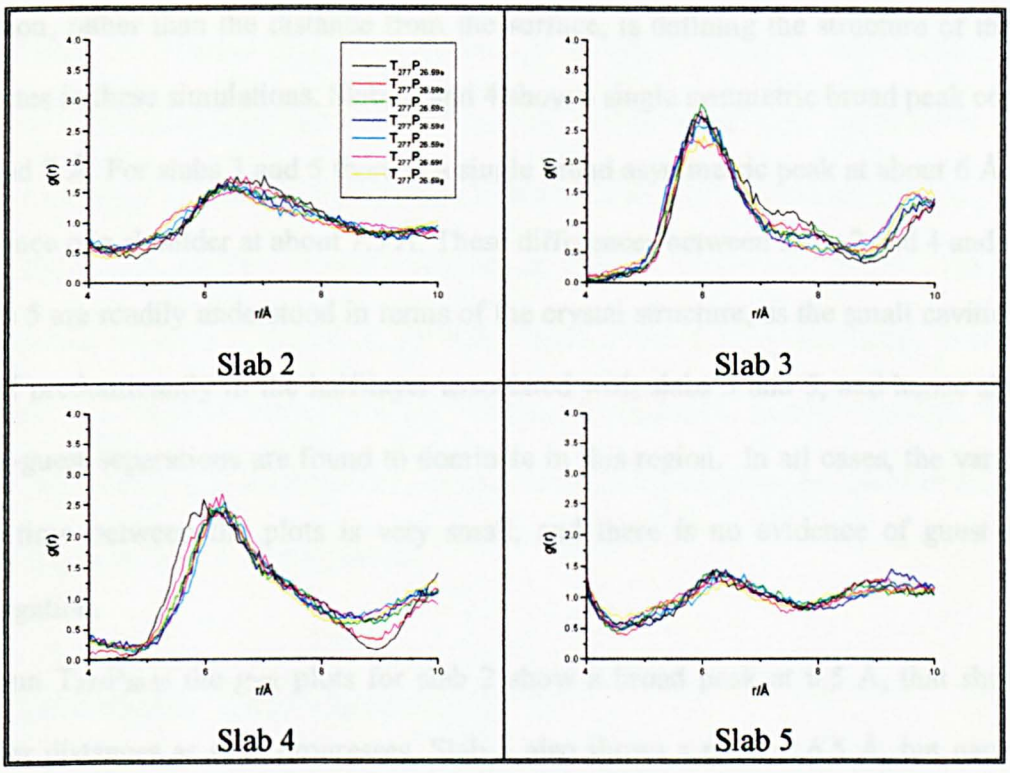

Figure 5.10 Radial distribution functions g_{XX} for run $T_{277}P_{26.59}$. The legend is the same for each plot.

From figures 5.7–5.10 it is possible to define three groups of simulation: run $T_{277}P_{-0.01}$, runs $T_{277}P_{0.21}$ and $T_{277}P_{4.04}$, and run $T_{277}P_{26.59}$.

For run $T_{277}P_{-0.01}$ it can be seen all four RDFs show a single broad, flat peak from 5–9 Å. For slabs 2 and 5 there is a sharp peak at ~ 6 Å that grows in time. Further, for slab 5 there is a growing density below 4 Å, indicative of guest-guest aggregation, and hence implies degradation of the gas hydrate cage structure.

For runs $T_{277}P_{0.21}$ and $T_{277}P_{4.04}$ once more all four RDFs are stable in time. Slabs 2 and 4 form an equivalent pair, as do slabs 3 and 5. This is consistent with the crystal structure

(slabs correspond to half the repeat distance), and hence shows that crystallographic position, rather than the distance from the surface, is defining the structure of the gas hydrates in these simulations. Slabs 2 and 4 show a single symmetric broad peak centred around 7 Å. For slabs 3 and 5 there is a single broad asymmetric peak at about 6 Å with evidence of a shoulder at about 7.5 Å. These differences between slabs 2 and 4 and slabs 3 and 5 are readily understood in terms of the crystal structure, as the small cavities are found predominantly in the half-layer associated with slabs 3 and 5, and hence shorter guest-guest separations are found to dominate in this region. In all cases, the variation with time between the plots is very small, and there is no evidence of guest-guest aggregation.

For run $T_{277}P_{26.59}$ the g_{XX} plots for slab 2 show a broad peak at 6.5 Å, that shifts to shorter distances as time progresses. Slab 5 also shows a peak at 6.5 Å, but narrower than for slab 2, while there is also a second peak at 8 Å. There is little evidence of time dependence in this layer. Slabs 3 and 4 relax towards similar structures, dominated by a sharp, symmetric peak at 6 Å, but with some evidence of a weak shoulder at 7.5 Å in slab 4. Slabs 2 and 5 show strong evidence of guest-guest contact, while slabs 3 and 4 show only very weak evidence of guest-guest contact.

This data is again consistent with the phase assignments made earlier. Most significantly, there is no evidence of any degradation of the clathrate cage structure in runs $T_{277}P_{0.21}$ or $T_{277}P_{4.04}$, and there is unusual long-lived and long-ranged structure evident in run $T_{277}P_{26.59}$, consistent with a high-pressure phase.

z-density Distributions–$\rho_O(Z)$ and $\rho_G(Z)$

The density of oxygen atoms along the surface normal to the gas hydrate lattice, $\rho_O(Z)$, has been calculated from each of the four runs and the results are presented in figure 5.11. Analogous calculations have been made for the density distribution of guest carbon sites, $\rho_G(Z)$, and resulting plots are depicted in figure 5.12. For run $T_{277}P_{-0.01}$ the lattice was located between 0 and 30 Å, for runs $T_{277}P_{0.21}$ and $T_{277}P_{4.04}$ the lattice is situated between −11.5 and 18.5 Å and for run $T_{277}P_{26.59}$ the lattice is situated between −13 and 17 Å. All of the $\rho_O(Z)$ distributions are characterised by a central trough corresponding to the centre of the gas hydrate lattice.

Oxygen z-density Distributions–$\rho_O(Z)$

Plots of $\rho_O(Z)$ are shown in figure 5.11. These curves again show variations that are entirely consistent with the identification of three separate phases, as described above. For run $T_{277}P_{-0.01}$ there are a large number of well-defined peaks with a clear central trough. For runs $T_{277}P_{0.21}$ and $T_{277}P_{4.04}$ there are once more a large number of well-defined peaks with a clear central trough. However in these two cases the peaks are better-defined than for run $T_{277}P_{-0.01}$, and the peaks for run $T_{277}P_{4.04}$ are better-defined than for run $T_{277}P_{0.21}$. For run $T_{277}P_{26.59}$ it can be seen that there are no longer a large number of well-defined peaks and no clearly discernible central trough. In addition it can be seen that the baseline of the plot appears to have translated up the z-density axis by 0.5 units and that the maximum z-density values observed have fallen by around 1 unit. None-the-less, run $T_{277}P_{26.59}$ still gives a density profile with evidence of distinctive crystallographic behaviour.

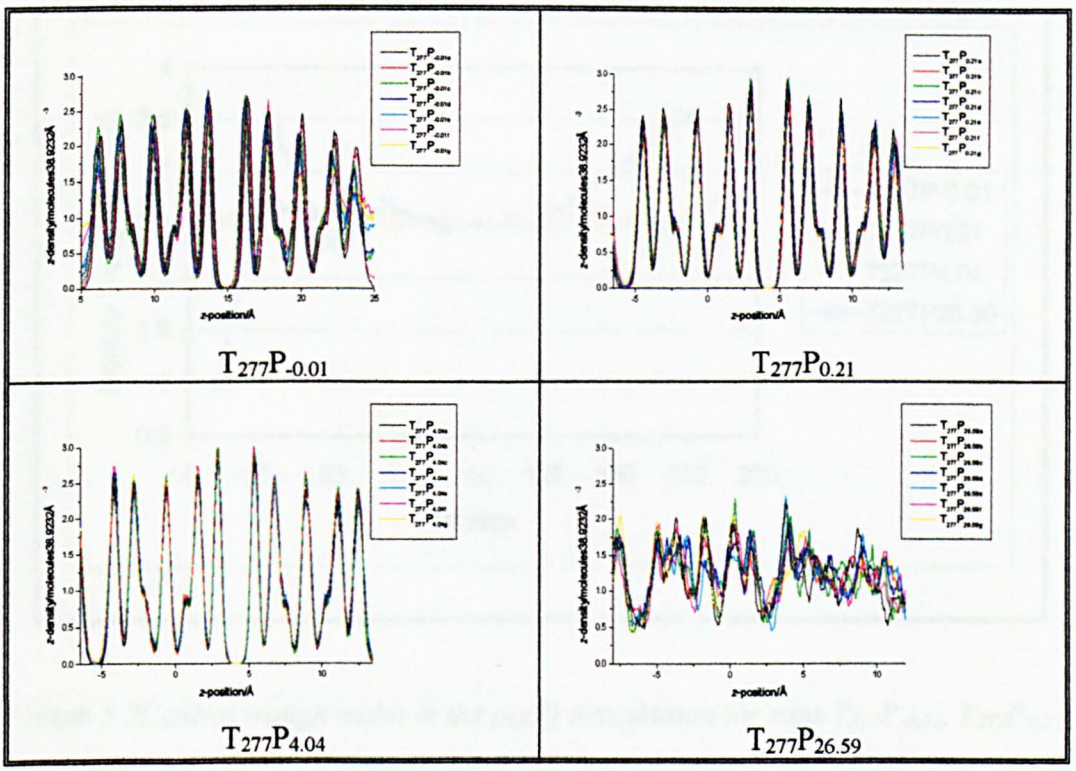

Figure 5.11 $\rho_O(Z)$ distributions for runs $T_{277}P_{-0.01}$, $T_{277}P_{0.21}$, $T_{277}P_{4.04}$ and $T_{277}P_{26.59}$. Differences in the z-axis scale are merely due to translational shifts of the hydrate slab prior to simulation.

A graph of the central trough width in the $\rho_O(Z)$ distribution for runs $T_{277}P_{-0.01}$, $T_{277}P_{0.21}$, $T_{277}P_{4.04}$ and $T_{277}P_{26.59}$ can be seen in graph 5.2. The central trough width is calculated by subtracting the right peak position from the left peak position. The right peak position refers to the peak immediately to the right of the central trough in the $\rho_O(Z)$ distribution, with the left peak position referring to the peak immediately to the left of the central trough in the $\rho_O(Z)$ distribution. For run $T_{277}P_{26.59}$ the central trough was assigned based upon the knowledge of the position of the gas hydrate lattice.

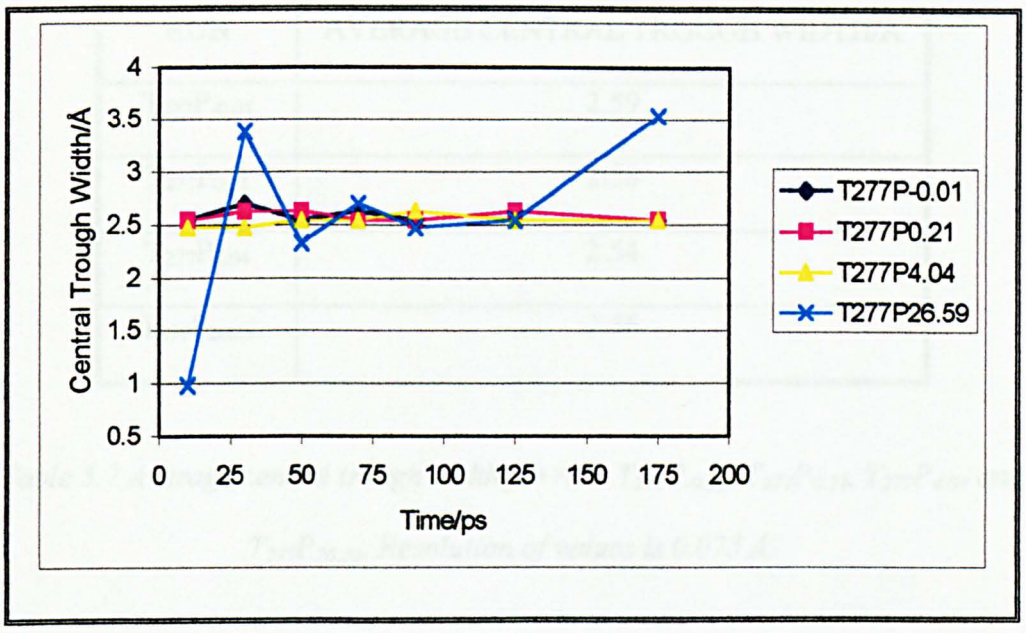

Graph 5.2Central trough width in the $\rho_O(Z)$ distribution for runs $T_{277}P_{-0.01}$, $T_{277}P_{0.21}$, $T_{277}P_{4.04}$ and $T_{277}P_{26.59}$. Resolution of the values is 0.075 Å.

From graph 5.2 we can see that the central trough width for runs $T_{277}P_{-0.01}$, $T_{277}P_{0.21}$ and $T_{277}P_{4.04}$ fluctuates slightly in time, but always lies within the ranges 2.5–2.7 Å. For run $T_{277}P_{26.59}$ there is a much greater variation in the central trough width: from 1.0–3.5 Å. This may be a real effect, but may also be a reflection of the fact that it is much harder to pick the peaks at either side of the centre of the gas hydrate lattice for run $T_{277}P_{26.59}$. The average central trough width for each run is summarised in table 5.7, and shows that no significant difference is found between any of the average central trough widths.

RUN	AVERAGE CENTRAL TROUGH WIDTH/Å
$T_{277}P_{-0.01}$	2.59
$T_{277}P_{0.21}$	2.58
$T_{277}P_{4.04}$	2.54
$T_{277}P_{26.59}$	2.56

Table 5.7 Average central trough width for runs $T_{277}P_{-0.01}$, $T_{277}P_{0.21}$, $T_{277}P_{4.04}$ and $T_{277}P_{26.59}$. Resolution of values is 0.075 Å.

Guest *z*-density Distributions–$\rho_G(Z)$

The $\rho_G(Z)$ (figure 5.12) show two distinctive behaviours. For runs $T_{277}P_{-0.01}$, $T_{277}P_{0.21}$ and $T_{277}P_{4.04}$ the distributions are well-defined with a central triplet bounded by a sharp well-defined peak on either side. However as the pressure in the system increases the definition of the $\rho_G(Z)$ plot increases, such that run $T_{277}P_{4.04}$ is better-defined than run $T_{277}P_{0.21}$, which is better-defined than run $T_{277}P_{-0.01}$. If we consider the extremities of the plots for runs $T_{277}P_{-0.01}$, $T_{277}P_{0.21}$ and $T_{277}P_{4.04}$ it is possible to propose a further subdivision of the runs into run $T_{277}P_{-0.01}$ and runs $T_{277}P_{0.21}$ and $T_{277}P_{4.04}$. For run $T_{277}P_{-0.01}$ the peak at the far right of the plot vanishes over time, whereas the corresponding peak in runs $T_{277}P_{0.21}$ and $T_{277}P_{4.04}$ is stable. Also, for run $T_{277}P_{-0.01}$ there is a single peak at the extreme left, whereas for runs $T_{277}P_{0.21}$ and $T_{277}P_{4.04}$ there is a clearly defined doublet. Thus again we see evidence of a stable hydrate phase in runs $T_{277}P_{0.21}$ and $T_{277}P_{4.04}$, but melting of this phase in run $T_{277}P_{-0.01}$.

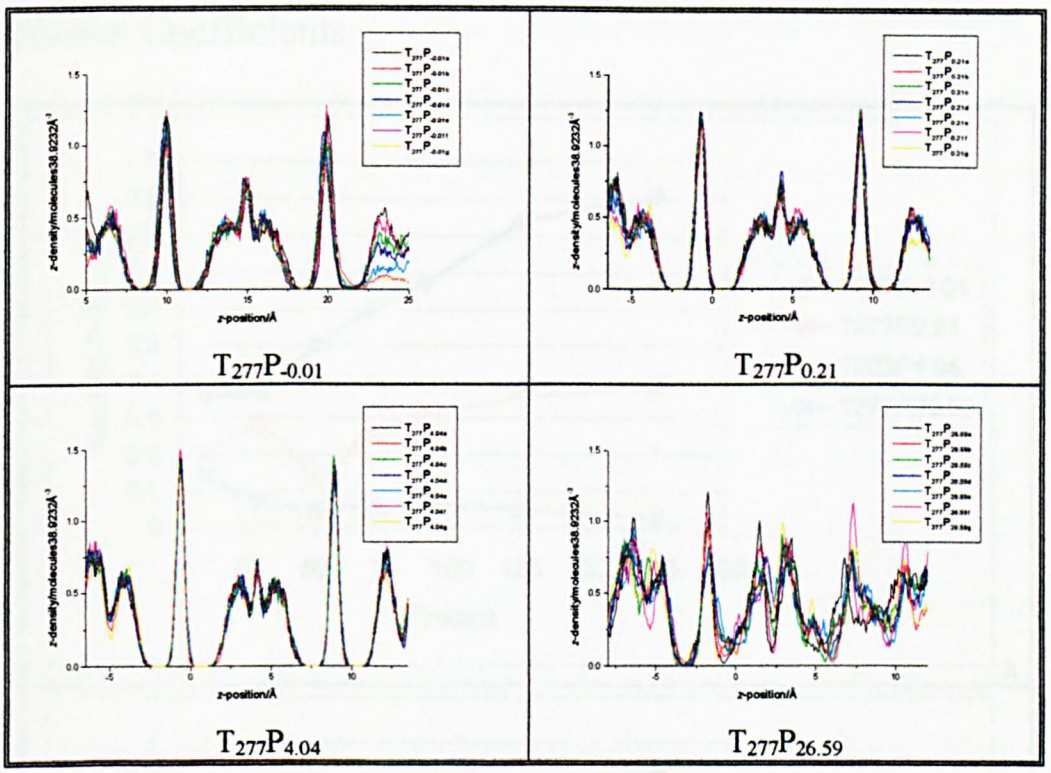

Figure 5.12 $\rho_G(Z)$ distributions for runs $T_{277}P_{-0.01}$, $T_{277}P_{0.21}$, $T_{277}P_{4.04}$ and $T_{277}P_{26.59}$. Differences in the z-axis scale are merely due to translational shifts of the hydrate slab prior to simulation.

For run $T_{277}P_{26.59}$ the central triplet found in the other runs transforms into a doublet, and that the sharp isolated peaks either side of the central triplet for the other runs are no longer so well resolved. For the extremities of the plot it seems as if there is an underlying structure similar to that observed for runs $T_{277}P_{0.21}$ and $T_{277}P_{4.04}$, with a doublet at the far left and a singlet at the far right. However these peaks are not as well resolved as in runs $T_{277}P_{0.21}$ and $T_{277}P_{4.04}$.

Diffusion Coefficients

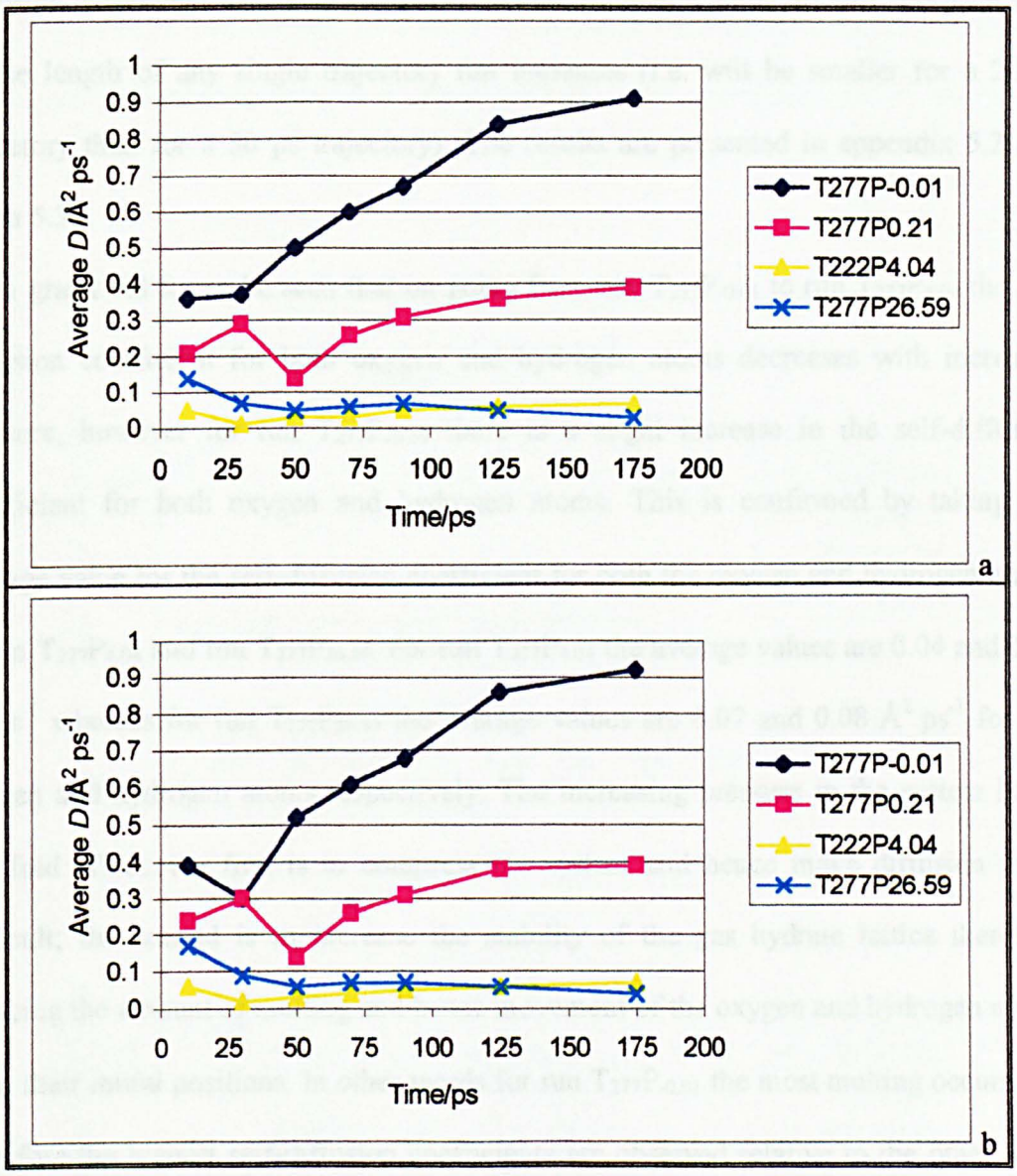

Graph 5.3 Average self-diffusion coefficients, for the oxygen atom (a) and hydrogen atom (b). Numerical values are also given in appendix 5.2.

The self-diffusion coefficients (see section 3.2) for oxygen and hydrogen have been taken from the DL_POLY[21] output file, and so are taken from $\langle(\boldsymbol{r}_0-\boldsymbol{r}_t)^2\rangle/6t$, rather than

from the limiting slope of the MSD. One significant consequence of this is that the self-diffusion coefficient for stable solids will appear to be non-zero, but will approach zero as the length of any single trajectory run increases (i.e. will be smaller for a 20 ps trajectory than for a 50 ps trajectory). The results are presented in appendix 5.2 and graph 5.3.

From graph 5.3 it can be seen that on going from run $T_{277}P_{-0.01}$ to run $T_{277}P_{4.04}$ the self diffusion coefficient for both oxygen and hydrogen atoms decreases with increased pressure, however for run $T_{277}P_{26.59}$ there is a slight increase in the self-diffusion coefficient for both oxygen and hydrogen atoms. This is confirmed by taking the average value for the self-diffusion coefficient for both the oxygen and hydrogen atoms in run $T_{277}P_{4.04}$ and run $T_{277}P_{26.59}$. For run $T_{277}P_{4.04}$ the average values are 0.04 and 0.05 $Å^2\ ps^{-1}$ whereas for run $T_{277}P_{26.59}$ the average values are 0.07 and 0.08 $Å^2\ ps^{-1}$ for the oxygen and hydrogen atoms respectively. The increasing pressure in the system has a two-fold effect: the first is to compress the system and hence make diffusion more difficult; the second is to increase the stability of the gas hydrate lattice therefore reducing the amount of melting and hence movement of the oxygen and hydrogen atoms from their initial positions. In other words for run $T_{277}P_{-0.01}$ the most melting occurs and therefore the highest self-diffusion coefficients are observed relative to the other three runs. However it is not clear what causes the effect observed for run $T_{277}P_{26.59}$.

As expected from graph 5.3 the values for the oxygen and hydrogen self-diffusion coefficients are almost identical.

Co-ordination Number

The co-ordination number (see section 3.5) of water molecules within slabs 2, 3, 4 and 5 of the gas hydrate lattice have been calculated and can be seen in appendix 5.3 and graph 5.4.

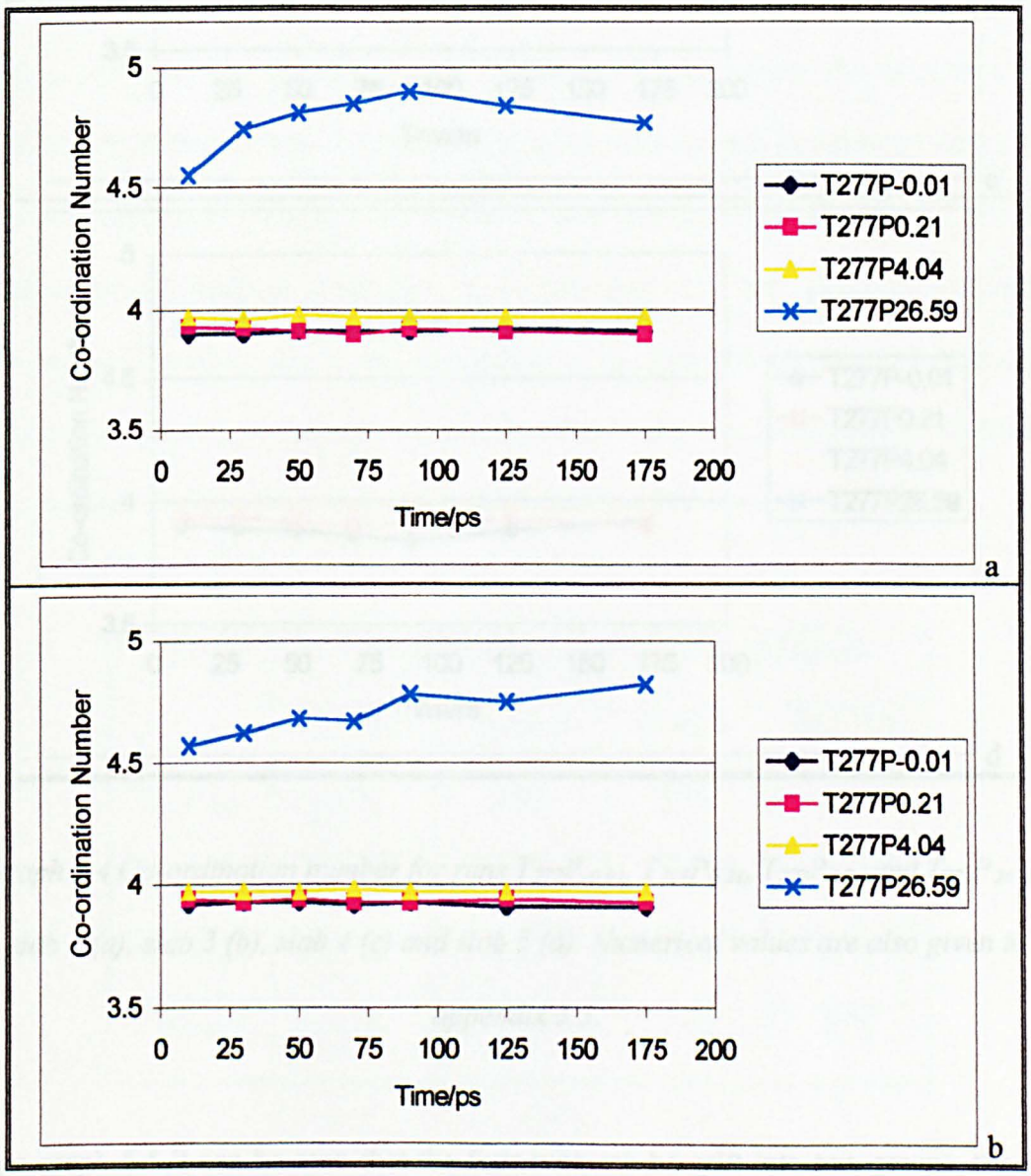

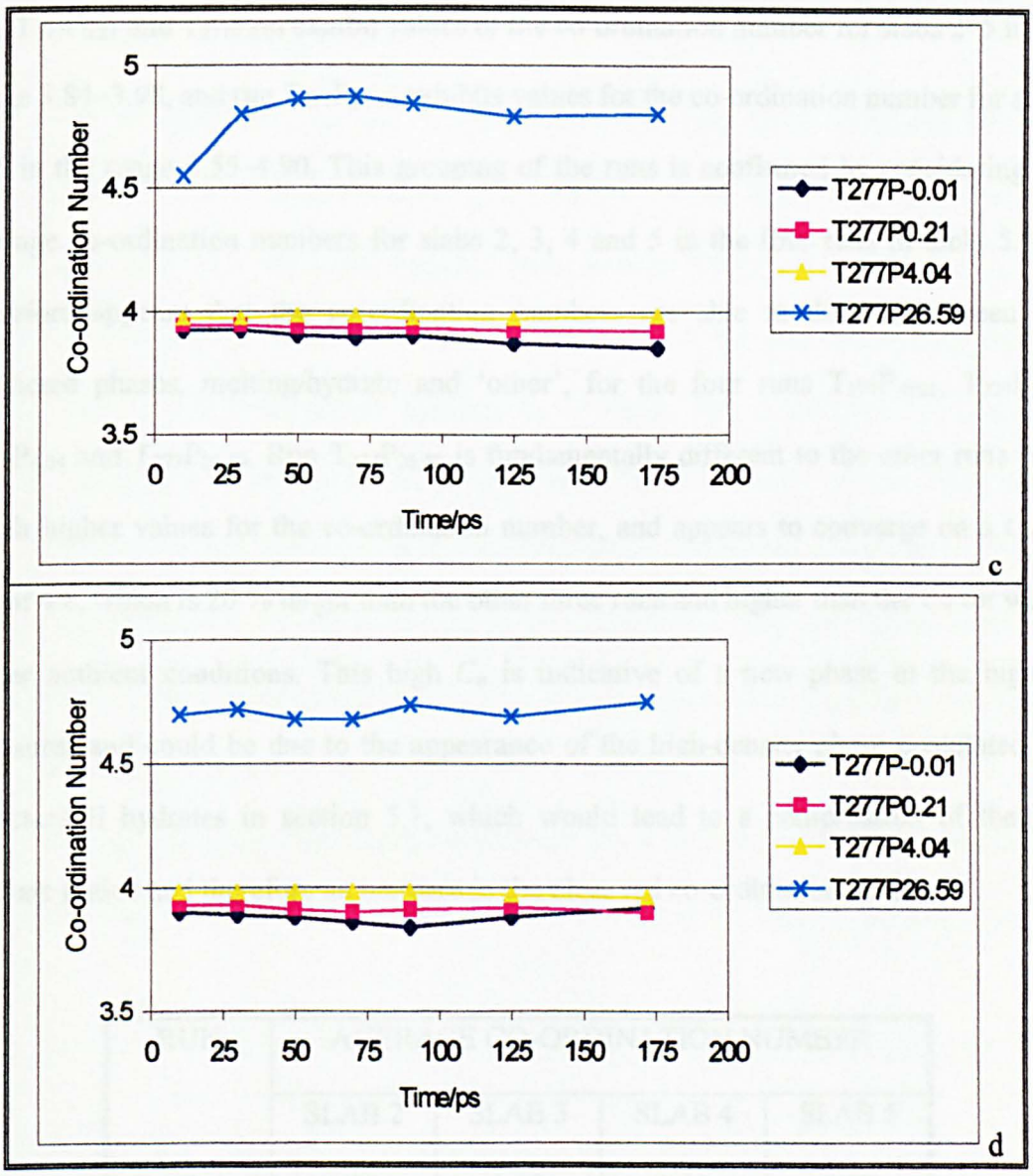

Graph 5.4 Co-ordination number for runs $T_{277}P_{-0.01}$, $T_{277}P_{0.21}$, $T_{277}P_{4.04}$ and $T_{277}P_{26.59}$: slab 2 (a), slab 3 (b), slab 4 (c) and slab 5 (d). Numerical values are also given in appendix 5.3.

From graph 5.4 it can be seen that the four runs can be split into two groups; the first being for runs $T_{277}P_{-0.01}$, $T_{277}P_{0.21}$ and $T_{277}P_{4.04}$ the second for run $T_{277}P_{26.59}$. Runs $T_{277}P_{-}$

$_{0.01}$, $T_{277}P_{0.21}$ and $T_{277}P_{4.04}$ exhibit values of the co-ordination number for slabs 2–5 in the range 3.84–3.98, and run $T_{277}P_{26.59}$ exhibits values for the co-ordination number for slabs 2–5 in the range 4.55–4.90. This grouping of the runs is confirmed by considering the average co-ordination numbers for slabs 2, 3, 4 and 5 in the four runs in table 5.8. It therefore appears that the co-ordination numbers are able to discern between the predicted phases, melting/hydrate and 'other', for the four runs $T_{277}P_{-0.01}$, $T_{277}P_{0.21}$, $T_{277}P_{4.04}$ and $T_{277}P_{26.59}$. Run $T_{277}P_{26.59}$ is fundamentally different to the other runs with much higher values for the co-ordination number, and appears to converge on a C_n of about 4.8, which is 20 % larger than the other three runs and higher than the C_n for water under ambient conditions. This high C_n is indicative of a new phase at the highest pressures and could be due to the appearance of the high-density phase postulated for structure II hydrates in section 5.1, which would lead to a compression of the gas hydrate lattice and therefore an increase in the observed co-ordination number.

RUN	AVERAGE CO-ORDINATION NUMBER			
	SLAB 2	SLAB 3	SLAB 4	SLAB 5
$T_{277}P_{-0.01}$	3.91	3.92	3.89	3.88
$T_{277}P_{0.21}$	3.91	3.93	3.93	3.91
$T_{277}P_{4.04}$	3.97	3.97	3.97	3.98
$T_{277}P_{26.59}$	4.78	4.70	4.79	4.78

Table 5.8 Average co-ordination number for slabs 2, 3, 4 and 5 in runs $T_{277}P_{-0.01}$, $T_{277}P_{0.21}$, $T_{277}P_{4.04}$ and $T_{277}P_{26.59}$.

Local Phase Assignments

The order parameters F_3, $F_{4\varphi}$ and F_{4t} (see section 3.4) have been calculated for water molecules in the four simulation cells, the calculation of these order parameters is outlined in chapter 3. By combining the instantaneous values of F_3, $F_{4\varphi}$ and F_{4t} it is possible to assign the water molecules within each of the four simulation cells as belonging to one of three phases: hydrate, ice or water. This is achieved by comparing the F_3, $F_{4\varphi}$ and F_{4t} values and if they are sufficiently close to the set of bulk phase values then they are assigned to that phase. In order to define 'sufficiently close' the covariance matrix for F_3, $F_{4\varphi}$ and F_{4t} was calculated in each bulk phase. The order parameters were then deemed to be sufficiently close when all three distances were simultaneously within three standard deviations of their respective bulk average.[24]

The resulting frequency distribution for the local phase of water molecules in each of the four runs $T_{277}P_{-0.01}$, $T_{277}P_{0.21}$, $T_{277}P_{4.04}$ and $T_{277}P_{26.59}$ can be seen in appendix 5.4 and graph 5.5.

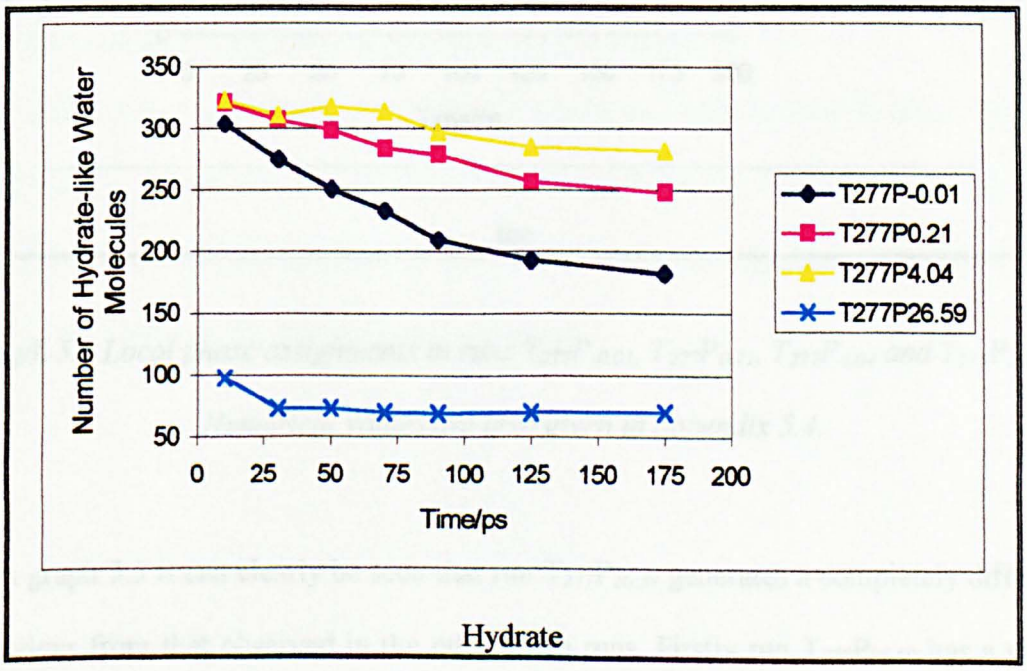

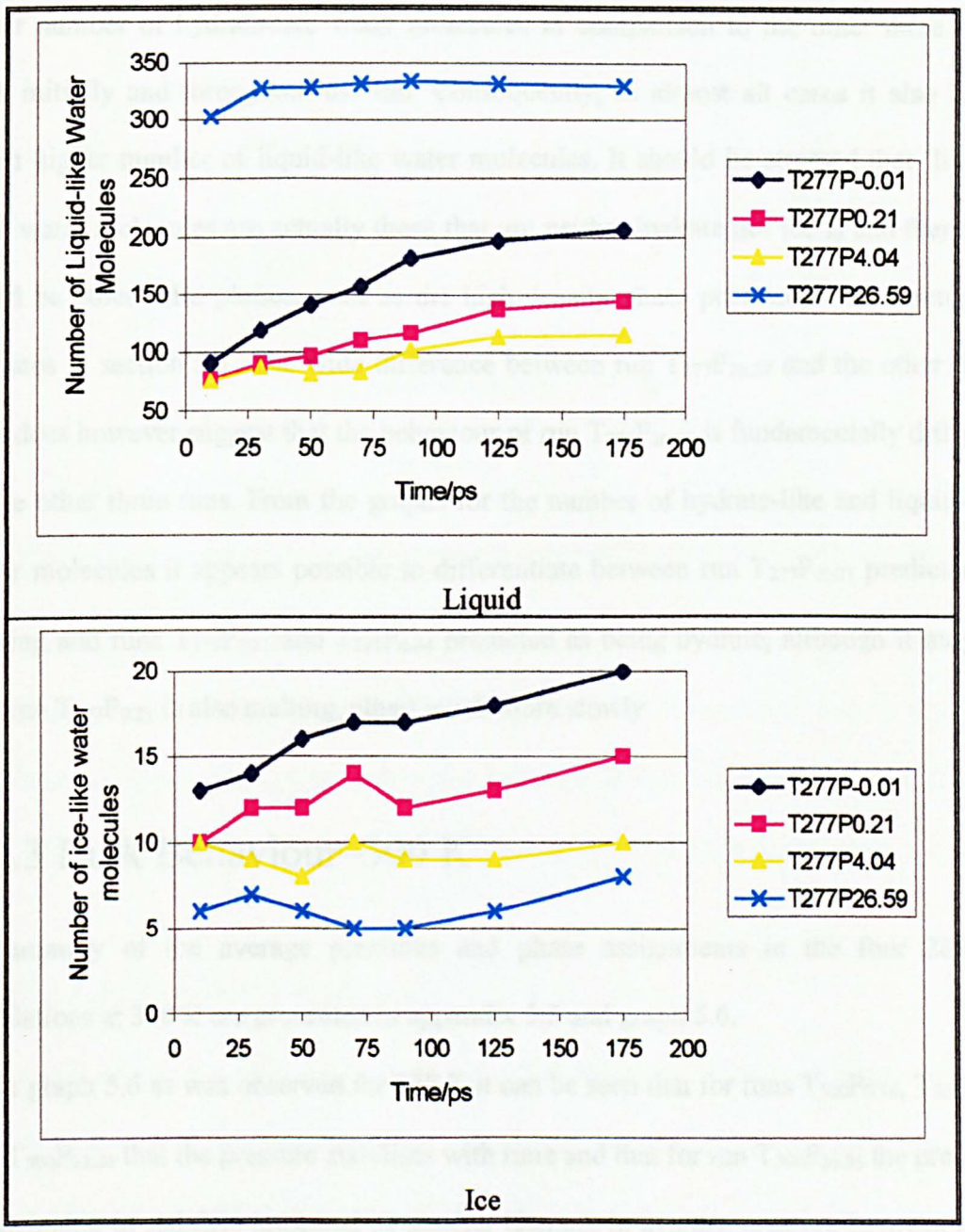

Graph 5.5 Local phase assignments in runs $T_{277}P_{-0.01}$, $T_{277}P_{0.21}$, $T_{277}P_{4.04}$ and $T_{277}P_{26.59}$.

Numerical values are also given in appendix 5.4.

From graph 5.5 it can clearly be seen that run $T_{277}P_{26.59}$ generates a completely different behaviour from that observed in the other three runs. Firstly run $T_{277}P_{26.59}$ has a much

lower number of hydrate-like water molecules in comparison to the other three runs, both initially and throughout the run. Consequently, in almost all cases it also has a much higher number of liquid-like water molecules. It should be stressed that 'liquid-like' water molecules are actually those that are neither hydrate nor ice I_h and therefore could be other solid phases, such as the high-density phase postulated for structure II hydrates in section 5.1. The wide difference between run $T_{277}P_{26.59}$ and the other three runs does however suggest that the behaviour of run $T_{277}P_{26.59}$ is fundamentally different to the other three runs. From the graphs for the number of hydrate-like and liquid-like water molecules it appears possible to differentiate between run $T_{277}P_{-0.01}$ predicted as melting and runs $T_{277}P_{0.21}$ and $T_{277}P_{4.04}$ predicted as being hydrate, although it may be that run $T_{277}P_{0.21}$ is also melting, albeit much more slowly.

5.3.3 Bulk Behaviour–300 K

A summary of the average pressures and phase assignments in the four 200 ps simulations at 300 K are presented in appendix 5.5 and graph 5.6.

From graph 5.6 as was observed for 277 K it can be seen that for runs $T_{300}P_{0.16}$, $T_{300}P_{2.93}$ and $T_{300}P_{12.26}$ that the pressure stabilises with time and that for run $T_{300}P_{26.95}$ the pressure is beginning to stabilise indicated by smaller changes in average pressure between runs, but that convergence has not quite been achieved.

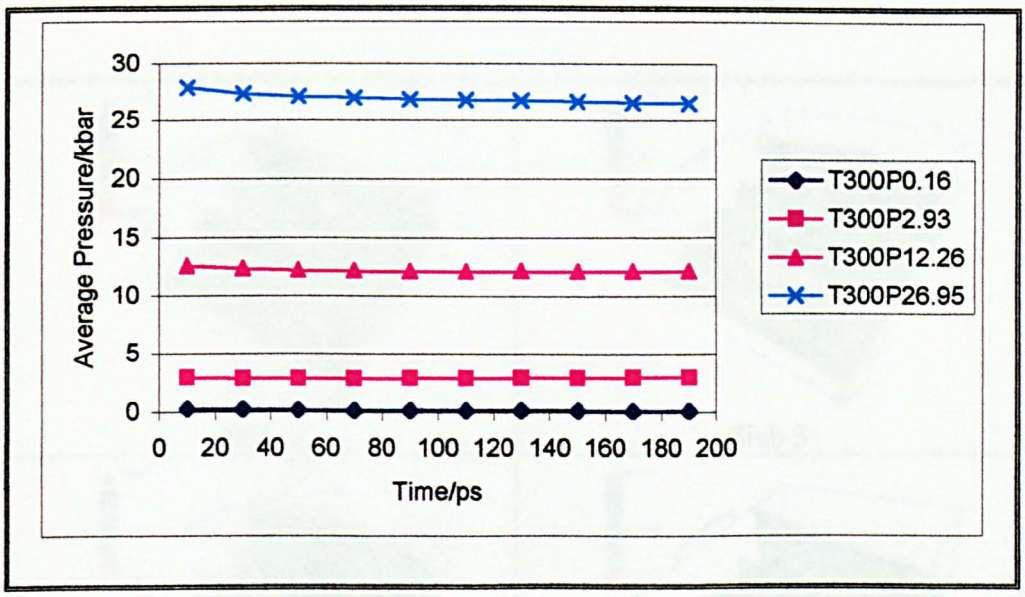

Graph 5.6 Average pressures in the four 200 ps simulations at 300 K. Phase assignments of the simulations are denoted by: dark blue for melting, pink for hydrate and turquoise for 'other'. Time values are plotted at the central time point for each of the constituent simulations. Numerical values are also given in appendix 5.5.

Radial Distribution Functions

The radial distribution function (see section 3.3) for water in the gas hydrate lattice, namely g_{OO}, has been calculated for each of the simulations, along with the radial distribution function for guest atoms, g_{XX} where X is any C site in CH_4 or C_3H_8. In this section we discuss these functions for the inner ('bulk') hydrate region: slabs 2, 3, 4 and 5.

Oxygen–Oxygen Radial Distribution Functions

The g_{OO}, for slabs 2, 3, 4 and 5 are presented in figures 5.13–5.16.

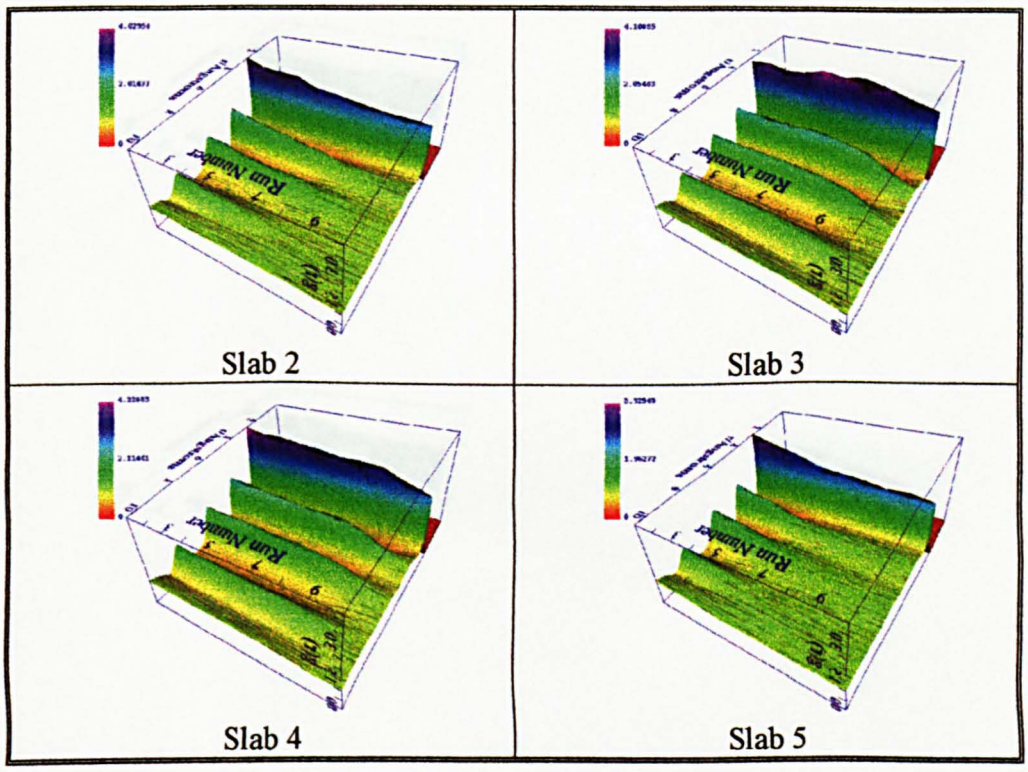

Figure 5.13 Radial distribution functions g_{OO} for run $T_{300}P_{0.16}$.

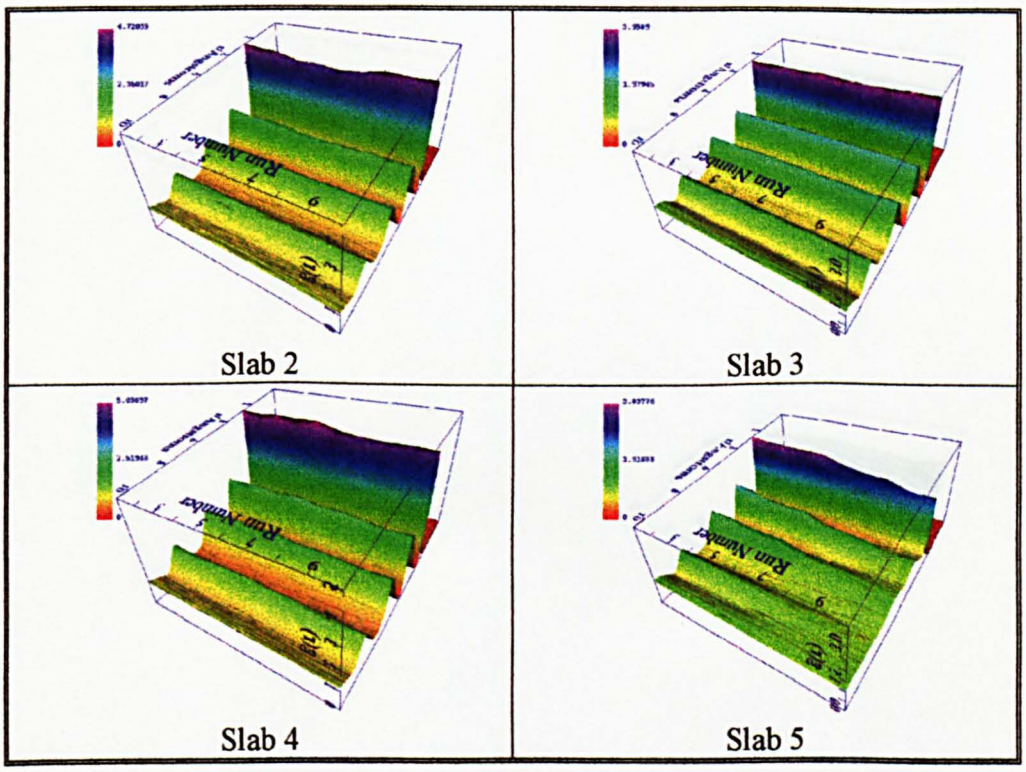

Figure 5.14 Radial distribution functions g_{OO} for run $T_{300}P_{2.93}$.

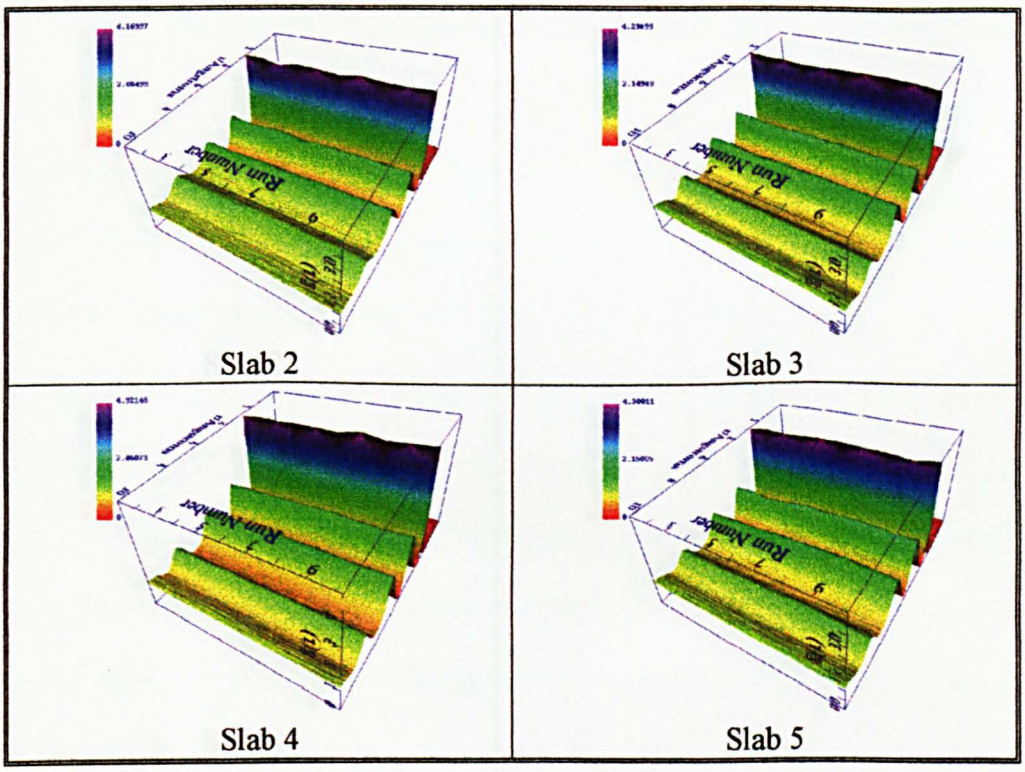

Figure 5.15 Radial distribution functions g_{OO} for run $T_{300}P_{12.26}$.

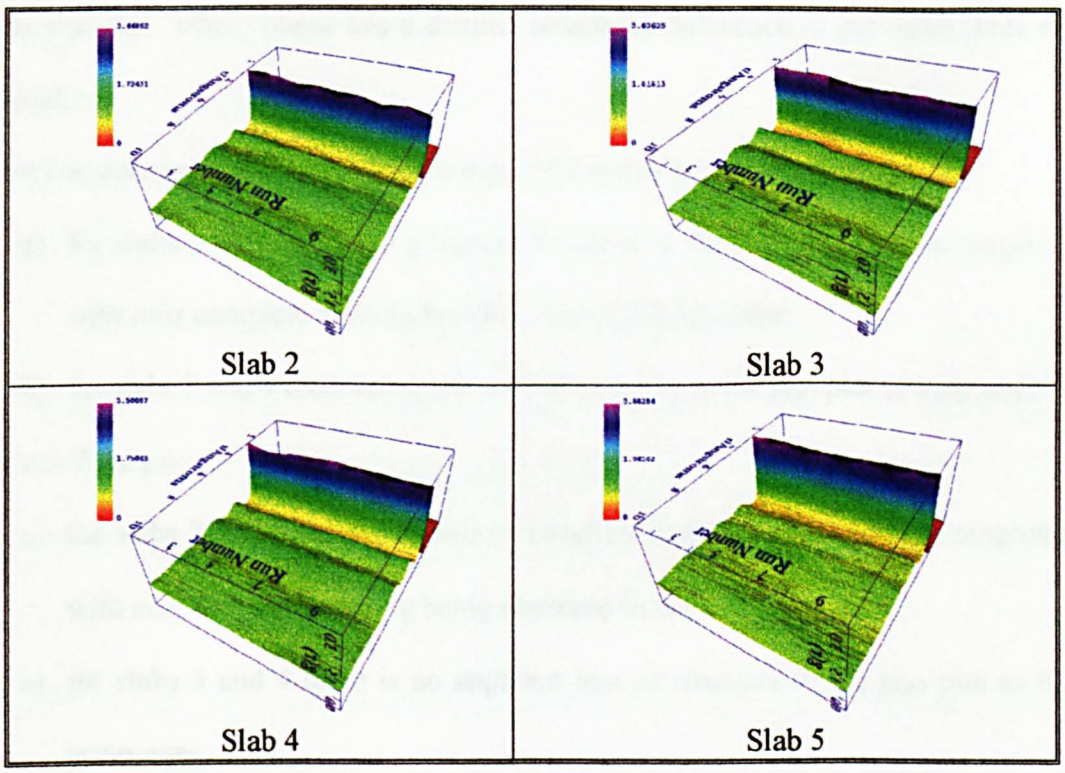

Figure 5.16 Radial distribution functions g_{OO} for run $T_{300}P_{26.95}$.

The first point to note from figures 5.13–5.16 is the apparent symmetry that is present in the four slabs. Slabs 2 and 5 are comparable in terms of the appearance of the plots, as are slabs 3 and 4 for runs $T_{300}P_{0.16}$ and $T_{300}P_{26.95}$ and that in runs $T_{300}P_{2.93}$ and $T_{300}P_{12.26}$ all of the four slabs appear identical. This observation is as for 277 K for slabs 2 and 5 and 3 and 4 in runs $T_{277}P_{-0.01}$ and $T_{277}P_{26.59}$ and for runs $T_{277}P_{0.21}$ and $T_{277}P_{4.04}$ for all of the slabs.

In addition as for run $T_{277}P_{26.59}$ at 277 K it is possible to note that for run $T_{300}P_{26.95}$ there is an obvious difference in the appearance of the plots when compared with the other three runs, namely runs $T_{300}P_{0.16}$, $T_{300}P_{2.93}$ and $T_{300}P_{12.26}$. Run $T_{300}P_{26.95}$ is the simulation

in which the predicted phase assignment was of 'other', and it can be seen from the g_{OO} plots that this 'other' phase has a distinct structural difference to the other three runs studied.

If we consider each of the runs in turn then we see that in run $T_{300}P_{0.16}$:

a) for slabs 2 and 5 there is a loss of structure in the g_{OO} plot as time progresses, with near complete melting being observed in both slabs;

b) for slabs 3 and 4 there is a slight loss of structure in the g_{OO} plot at long times.

For run $T_{300}P_{2.93}$:

a) for slabs 2 and 5 there is a loss of structure in the g_{OO} plot as time progresses, with near complete melting being observed in slab 5;

b) for slabs 3 and 4 there is no apparent loss of structure in the g_{OO} plot as time progresses.

For run $T_{300}P_{12.26}$:

a) for slabs 2–5 there is no apparent loss of structure in the g_{OO} plot as time progresses.

For run $T_{300}P_{26.95}$:

a) for slabs 2 and 5 there is the immediate appearance of a third peak in the g_{OO} plot which is stable in time;

b) for slabs 3 and 4 there is the immediate appearance of a third and fourth peak in the g_{OO} plot which is stable in time.

There are similarities and differences between the four runs at 300 K and the four runs at 277 K as outlined in table 5.9.

277 K RUN	SLABS	OBSERVATION	SLABS	300 K RUN
$T_{277}P_{-0.01}$	2 and 5	Same for 277 and 300 K.	2 and 5	$T_{300}P_{0.16}$
$T_{277}P_{-0.01}$	3 and 4	Different for 277 and 300 K.	3 and 4	$T_{300}P_{0.16}$
$T_{277}P_{0.21}$	2 and 5	Different for 277 and 300 K.	2 and 5	$T_{300}P_{2.93}$
$T_{277}P_{0.21}$	3 and 4	Same for 277 and 300 K.	3 and 4	$T_{300}P_{2.93}$
$T_{277}P_{4.04}$	2 and 5	Same for 277 and 300 K.	2 and 5	$T_{300}P_{12.26}$
$T_{277}P_{4.04}$	3 and 4	Same for 277 and 300 K.	3 and 4	$T_{300}P_{12.26}$
$T_{277}P_{26.59}$	2 and 5	Same for 277 and 300 K.	2 and 5	$T_{300}P_{26.95}$
$T_{277}P_{26.59}$	3 and 4	Same for 277 and 300 K.	3 and 4	$T_{300}P_{26.95}$

Table 5.9 Similarities and differences between the four runs at 277 K and the four runs at 300 K.

In general it can be summarised that:

a) for run $T_{300}P_{0.16}$ slabs 2–5 are unstable on the simulation time scale. Run $T_{300}P_{0.16}$ was predicted as melting and this phase assignment is supported by the behaviour of slabs 2–5;

b) for runs $T_{300}P_{2.93}$ and $T_{300}P_{12.26}$ slabs 2–5 in nearly all cases, apart from run $T_{300}P_{2.93}$ slabs 2 and 5, appear stable on the simulation time scale. Runs $T_{300}P_{2.93}$ and $T_{300}P_{12.26}$ were predicted as being hydrate and this phase assignment is supported by the behaviour of slabs 2–5;

c) For run $T_{300}P_{26.95}$ slabs 2–5 show an immediate change in structure, which appears stable on the simulation time scale. Run $T_{300}P_{26.95}$ was predicted as being 'other' and this phase assignment is supported by the behaviour of slabs 2–5.

Guest–Guest Radial Distribution Functions

The guest–guest radial distribution functions, g_{XX}, for slabs 2, 3, 4 and 5 of the four runs show identical trends to the corresponding runs at 277 K. The only observable difference was for run $T_{300}P_{0.16}$ at 300 K, which showed less well-defined plots for all four slabs, when compared with run $T_{277}P_{0.01}$ at 277 K. However the shape and position of peaks in the four slabs at 300 K was analogous with those at 277 K. Again, the RDFs are consistent with the phase assignments made in table 5.5.

z-density Distributions–$\rho_O(Z)$ and $\rho_G(Z)$

The oxygen ($\rho_O(Z)$) and guest ($\rho_G(Z)$) density distributions along the surface normal of the gas hydrate lattice has been calculated for the four simulations cells.

Oxygen *z*-density Distributions–$\rho_O(Z)$

The $\rho_O(Z)$ distributions for each of the four runs (figure 5.17) show an almost identical behaviour to the four runs at 277 K. The only observable differences are for run $T_{300}P_{0.16}$ where the $\rho_O(Z)$ distribution shows less well-defined peaks indicative of more complete melting compared with run $T_{277}P_{0.01}$ at 277 K and for run $T_{300}P_{26.95}$ where the $\rho_O(Z)$ distribution shows less well-defined behaviour to that observed for run $T_{277}P_{26.59}$ at 277 K. However it is still possible to split the $\rho_O(Z)$ distributions into three groups, those for

run $T_{300}P_{0.16}$–melting, those for runs $T_{300}P_{2.93}$ and $T_{300}P_{12.26}$–stable hydrate and those for run $T_{300}P_{26.95}$–high-pressure phase, which correspond to the phase assignments predicted for the four runs.

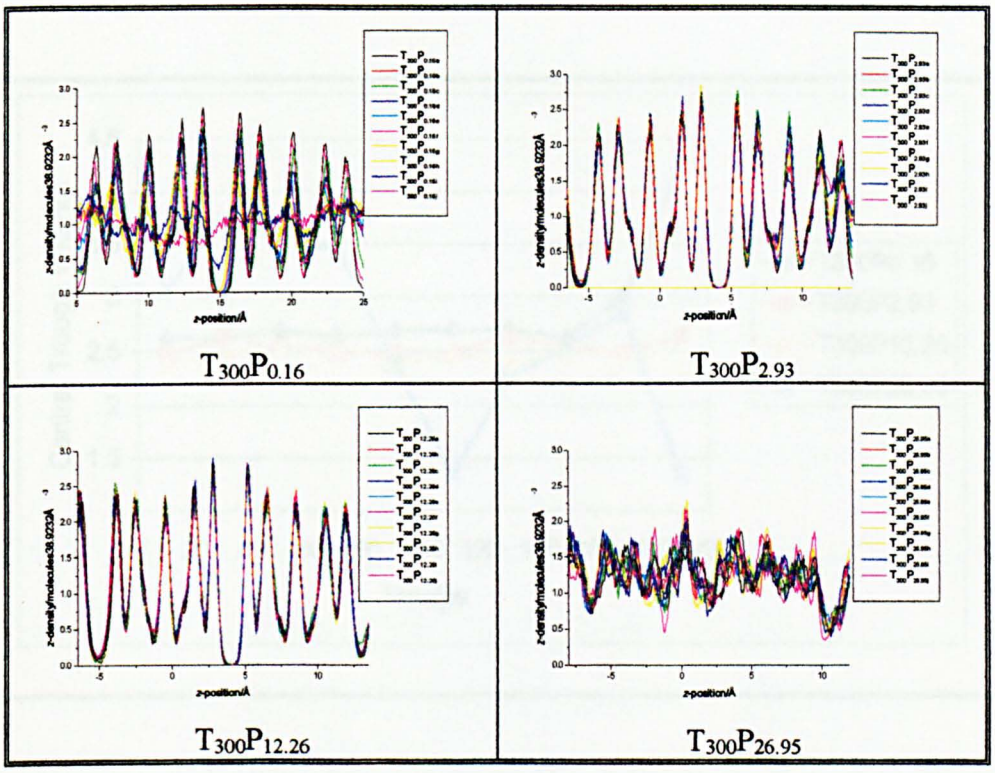

Figure 5.17 $\rho_O(Z)$ distributions for runs $T_{300}P_{0.16}$, $T_{300}P_{2.93}$, $T_{300}P_{12.26}$ and $T_{300}P_{26.95}$. Differences in the z-axis scale are merely due to translational shifts of the hydrate slab prior to simulation.

A graph of the central trough width in the $\rho_O(Z)$ distribution for the different runs can be seen in graph 5.7. The central trough width is calculated by subtracting the right peak position from the left peak position. The right peak position refers to the peak immediately to the right of the central trough in the $\rho_O(Z)$ distribution, with the left peak

position referring to the peak immediately to the left of the central trough in the $\rho_O(Z)$ distribution. For run $T_{300}P_{26.95}$ the right and left peak positions were assigned based upon the knowledge of the position of the gas hydrate lattice and picking peaks directly to the left and right of the centre of the gas hydrate lattice.

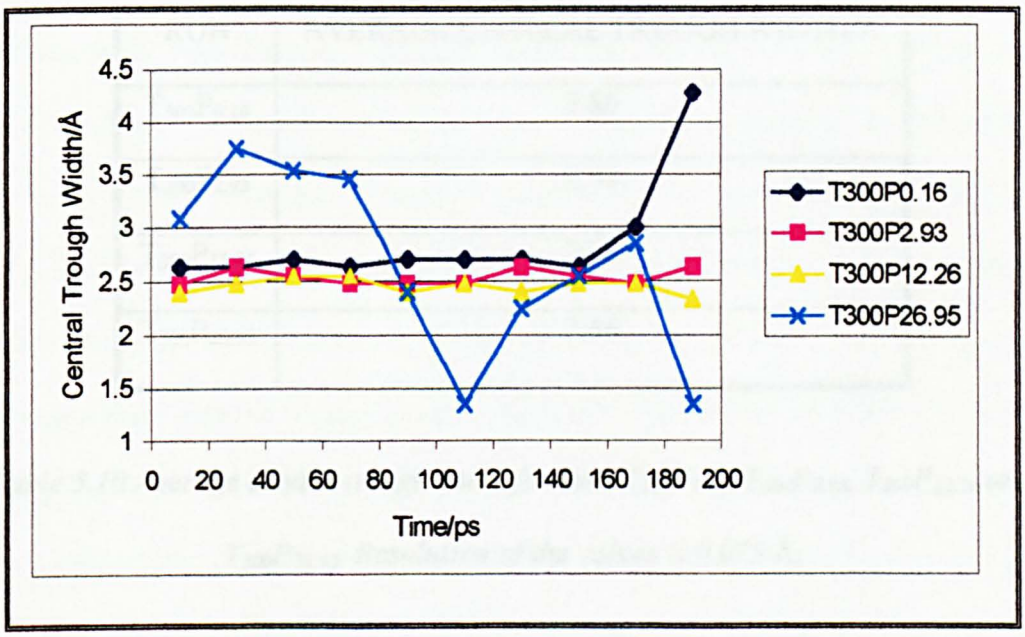

Graph 5.7 Central trough width in the $\rho_O(Z)$ distribution for runs $T_{300}P_{0.16}$, $T_{300}P_{2.93}$, $T_{300}P_{12.26}$ and $T_{300}P_{26.95}$. Resolution of values is 0.075 Å.

It can be seen that the central trough width for runs $T_{300}P_{0.16}$, $T_{300}P_{2.93}$, $T_{300}P_{12.26}$ ranges from 2.3–2.6 Å excluding the last two values for run $T_{300}P_{0.16}$, which are from times at which the hydrate has completely melted (*cf.* figure 5.13) and so the definition of the central peaks becomes uncertain. For these three runs the peak spacing is found to decrease as pressure is increased. A much greater variation in the overall peak spacing is apparent for run $T_{300}P_{26.95}$: from 1.4–3.8 Å. As with the 277 K simulations, it is not

possible to be sure whether this is a real effect, or merely a reflection of the fact that it is much harder to pick the peaks at either the side of the gas hydrate lattice for run $T_{300}P_{26.95}$.

The average central trough width for each run is summarised in table 5.10.

RUN	AVERAGE CENTRAL TROUGH WIDTH/Å
$T_{300}P_{0.16}$	2.86
$T_{300}P_{2.93}$	2.54
$T_{300}P_{12.26}$	2.46
$T_{300}P_{26.95}$	2.66

Table 5.10 Average central trough width for runs $T_{300}P_{0.16}$, $T_{300}P_{2.93}$, $T_{300}P_{12.26}$ and $T_{300}P_{26.95}$. Resolution of the values is 0.075 Å.

From table 5.10 we can see that as the pressure increases the average central trough width decreases for runs $T_{300}P_{0.16}$, $T_{300}P_{2.93}$, $T_{300}P_{12.26}$ as would be expected. However for run $T_{300}P_{26.95}$ the average central trough width is greater than for runs $T_{300}P_{2.93}$ and $T_{300}P_{12.26}$ even though the pressure in run $T_{300}P_{26.95}$ is greater than that for runs $T_{300}P_{2.93}$ and $T_{300}P_{12.26}$. This is as opposed to the four runs at 277 K where the average central trough width values were identical for each run.

Guest z-density Distributions–$\rho_G(Z)$

The $\rho_G(Z)$ distributions can be seen in figure 5.18 for each of the four runs. It can be seen that the $\rho_G(Z)$ distributions are also consistent with three different phases: melting for run $T_{300}P_{0.16}$; stable type II hydrate for runs $T_{300}P_{2.93}$ and $T_{300}P_{12.26}$ and; 'other' for run $T_{300}P_{26.95}$. The $\rho_G(Z)$ distribution for run $T_{300}P_{0.16}$ does bear similarities to the $\rho_G(Z)$ distributions for runs $T_{300}P_{2.93}$ and $T_{300}P_{12.26}$ but the amount of disorder present in the $\rho_G(Z)$ distribution is much greater and it is clearly approaching a homogeneous distribution as time increases. The $\rho_G(Z)$ distributions for runs $T_{300}P_{0.16}$, $T_{300}P_{2.93}$ and $T_{300}P_{12.26}$ all exhibit a central triplet bounded by a sharp well-defined peak on either side. It is interesting to note that for runs $T_{300}P_{0.16}$ and $T_{300}P_{2.93}$ the central triplet is composed of a central peak with the greatest peak height with a smaller peak on either side, but that for run $T_{300}P_{12.26}$ the central triplet has been inverted such that the central peak has a lower peak height compared to the peak at either side. It is possible to observe that as the pressure increases that the definition increases in the $\rho_G(Z)$ distribution, but this has an upper limit, and the trend is not continued to run $T_{300}P_{26.95}$. In other respects, the characteristics and trends in the density profiles are consistent with the discussion of the lower temperature data given above, albeit with considerably faster melting in run $T_{300}P_{0.16}$.

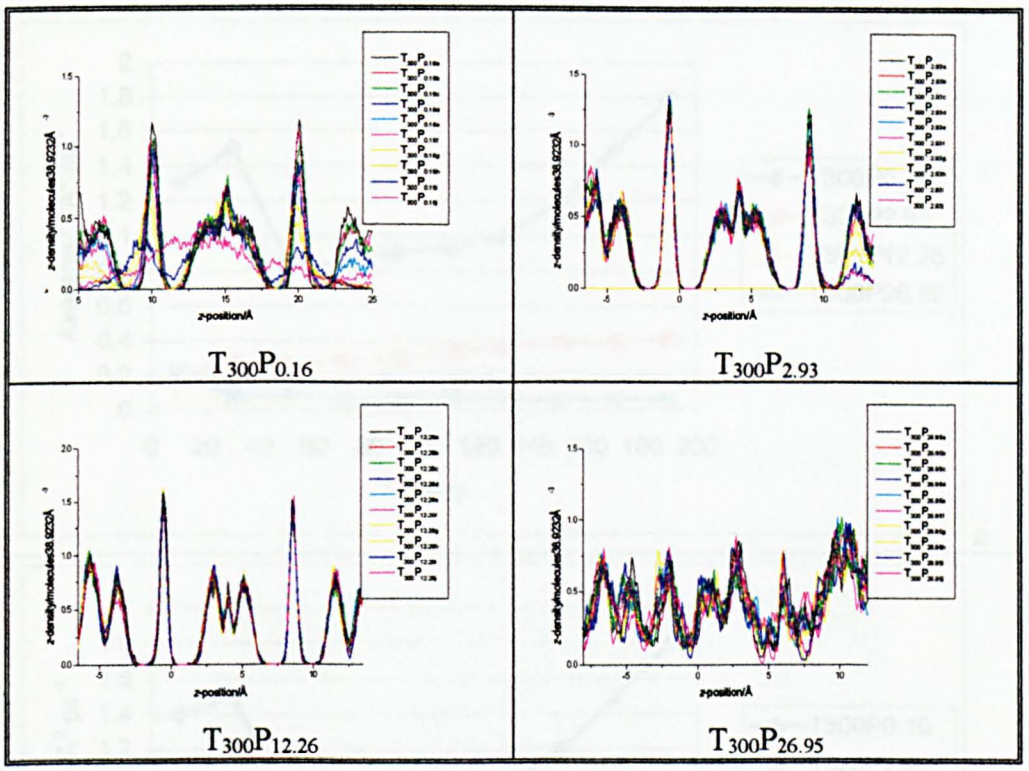

Figure 5.18 $\rho_G(Z)$ distributions for runs $T_{300}P_{0.16}$, $T_{300}P_{2.93}$, $T_{300}P_{12.26}$ and $T_{300}P_{26.95}$. Differences in the z-axis scale are merely due to translational shifts of the hydrate slab prior to simulation.

Diffusion Coefficients

The self-diffusion coefficients (see section 3.2) for water oxygen and hydrogen atoms have been taken from the DL_POLY OUTPUT file and are presented in appendix 5.6 and graph 5.8.

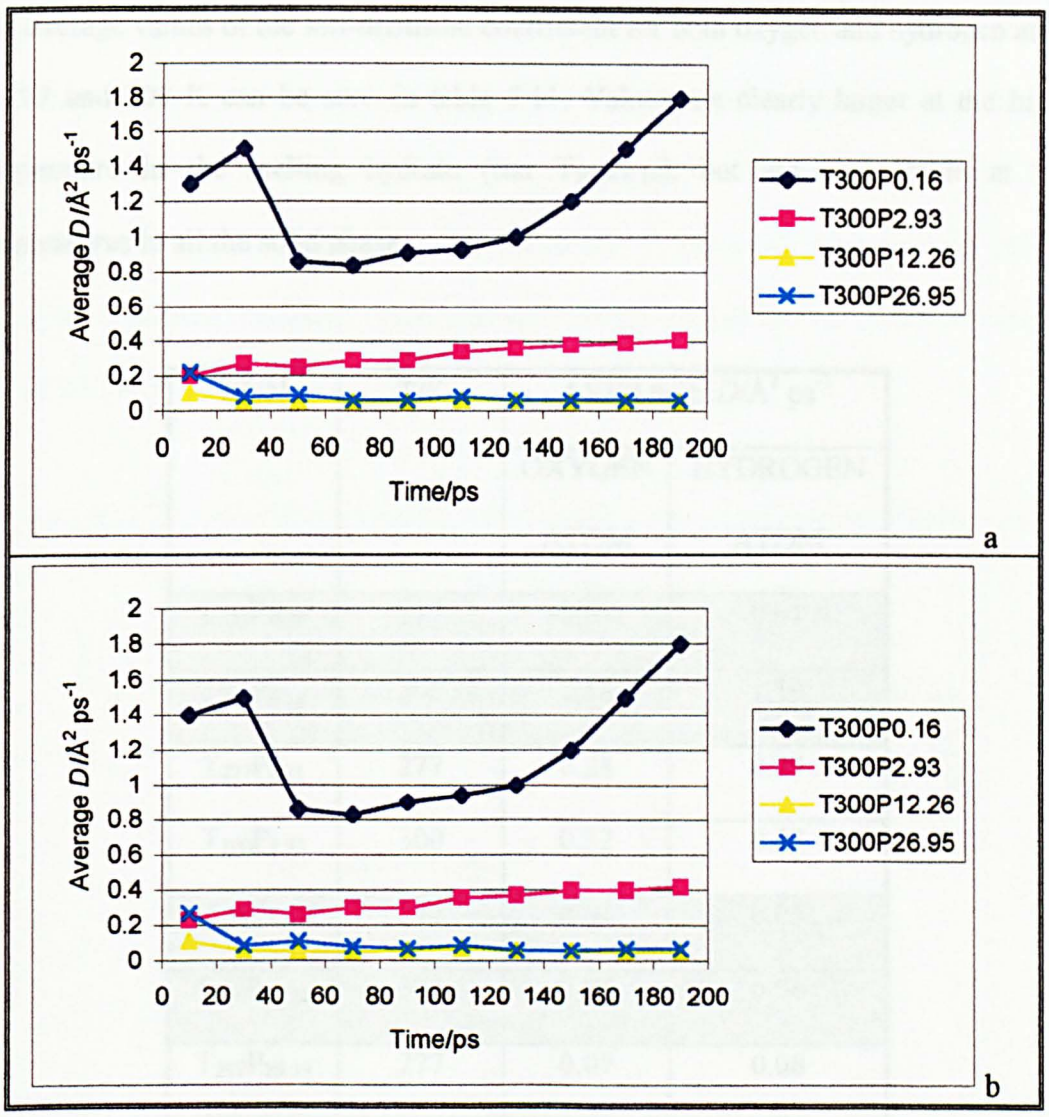

Graph 5.8 Average self-diffusion coefficients, for the oxygen atom (a) and the hydrogen atom (b). Numerical values are also given in appendix 5.6.

General trends are again consistent with those discussed at 277 K. The main difference is that there is apparent convergence of self-diffusion coefficients for runs $T_{300}P_{12.26}$ and $T_{300}P_{26.95}$.

The average values of the self-diffusion coefficient for both oxygen and hydrogen atoms at 277 and 300 K can be seen in table 5.11. Values are clearly larger at the higher temperature in the melting hydrate (run $T_{300}P_{0.16}$), but are comparable at both temperatures in all the solid phases.

RUN	T/K	AVERAGE $D/Å^2\ ps^{-1}$	
		OXYGEN ATOM	HYDROGEN ATOM
$T_{277}P_{-0.01}$	277	0.61	0.61
$T_{300}P_{0.16}$	300	1.18	1.19
$T_{277}P_{0.21}$	277	0.28	0.29
$T_{300}P_{2.93}$	300	0.32	0.33
$T_{277}P_{4.04}$	277	0.04	0.05
$T_{300}P_{12.26}$	300	0.06	0.06
$T_{277}P_{25.59}$	277	0.07	0.08
$T_{300}P_{26.95}$	300	0.07	0.10

Table 5.11 Average values of the self-diffusion coefficient for both the oxygen and hydrogen atoms at 277 and 300 K.

Co-ordination Number

The co-ordination number (see section 3.5) of water molecules within slabs 2, 3, 4 and 5 of the gas hydrate lattice for runs $T_{300}P_{0.16}$, $T_{300}P_{2.93}$, $T_{300}P_{12.26}$ and $T_{300}P_{26.95}$ are given in

appendix 5.7 and graph 5.9, with average C_n calculated across the entire 200 ps accumulated trajectories presented in table 5.12. As with the 277 K data, the co-ordination number tends to increase with pressure. The difference between the three lower pressure runs is greater at 300 K than at 277 K, but again there is a big increase when the high-pressure phase forms. Greater fluctuations in the C_n are also evident at 300 K than were apparent at 277 K.

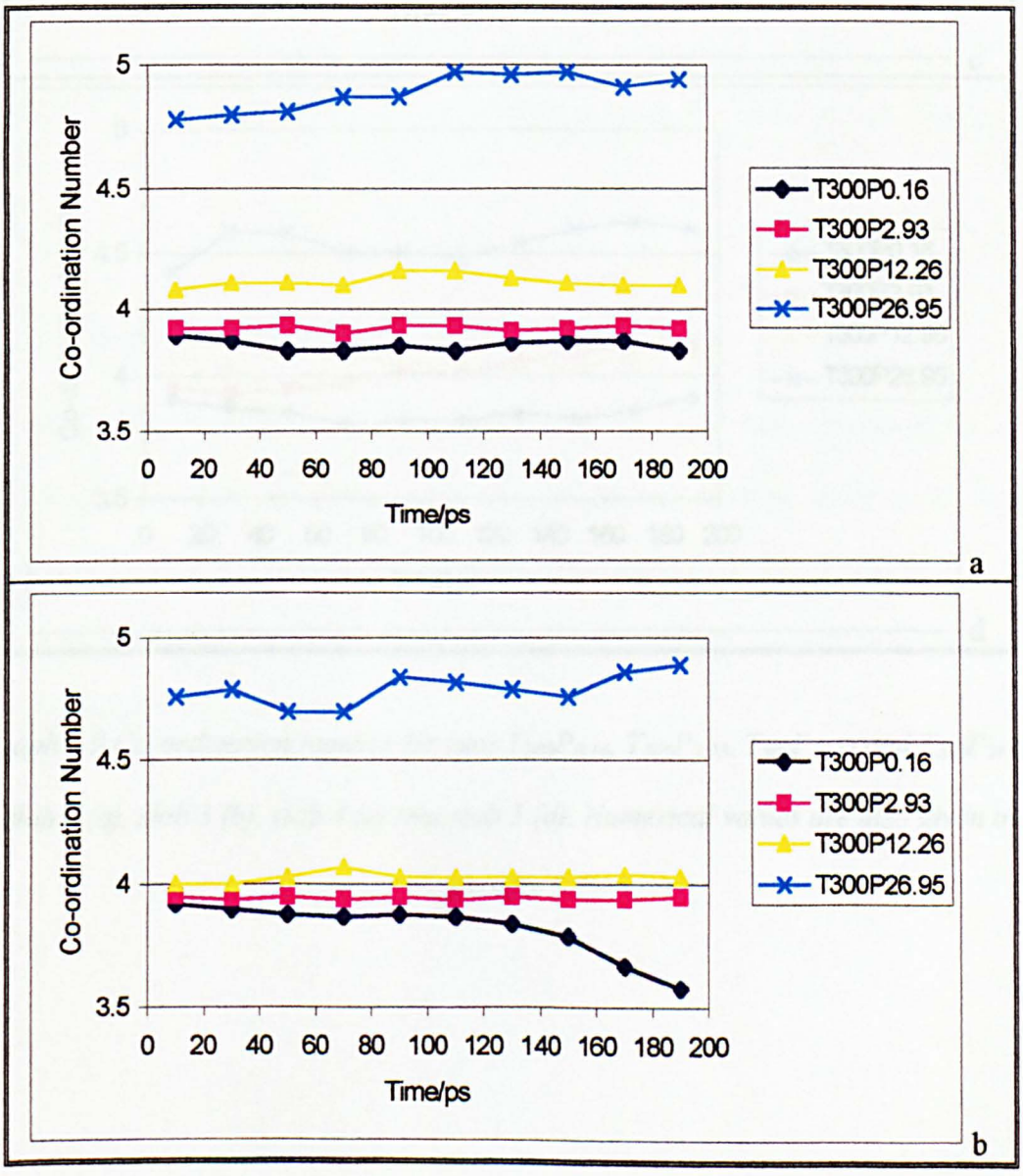

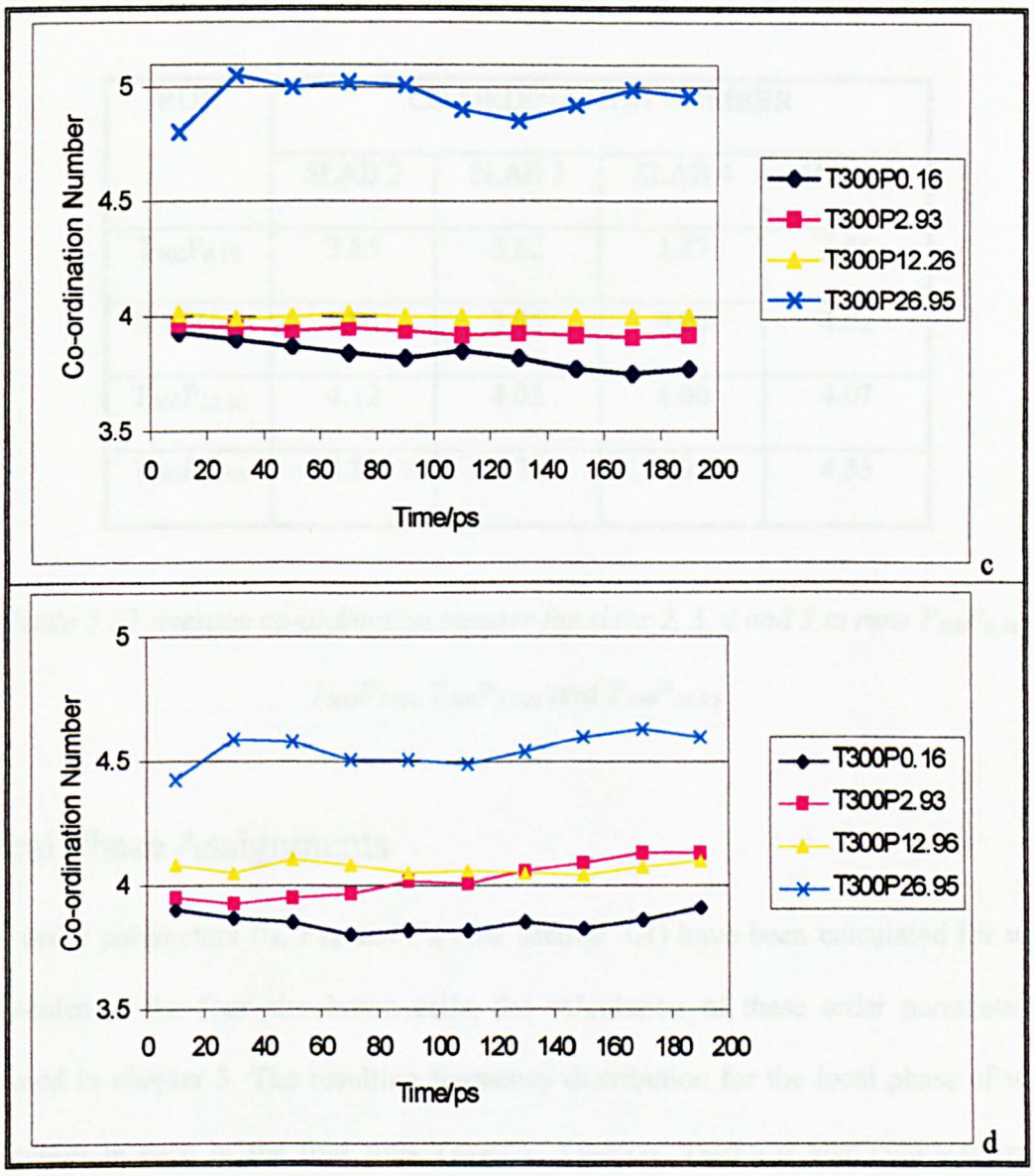

Graph 5.9 Co-ordination number for runs $T_{300}P_{0.16}$, $T_{300}P_{2.93}$, $T_{300}P_{12.26}$ and $T_{300}P_{26.95}$: slab 2 (a), slab 3 (b), slab 4 (c) and slab 5 (d). Numerical values are also given in appendix 5.7.

RUN	CO-ORDINATION NUMBER			
	SLAB 2	SLAB 3	SLAB 4	SLAB 5
$T_{300}P_{0.16}$	3.85	3.82	3.83	3.85
$T_{300}P_{2.93}$	3.92	3.95	3.93	4.02
$T_{300}P_{12.26}$	4.12	4.03	4.00	4.07
$T_{300}P_{26.95}$	4.89	4.79	4.95	4.55

Table 5.12 Average co-ordination number for slabs 2, 3, 4 and 5 in runs $T_{300}P_{0.16}$, $T_{300}P_{2.93}$, $T_{300}P_{12.26}$ and $T_{300}P_{26.95}$.

Local Phase Assignments

The order parameters F_3, $F_{4\varphi}$ and F_{4t} (see section 3.4) have been calculated for water molecules in the four simulation cells, the calculation of these order parameters is outlined in chapter 3. The resulting frequency distribution for the local phase of water molecules in each of the four runs $T_{300}P_{0.16}$, $T_{300}P_{2.93}$, $T_{300}P_{12.26}$ and $T_{300}P_{26.95}$ can be seen in appendix 5.8 and graph 5.10.

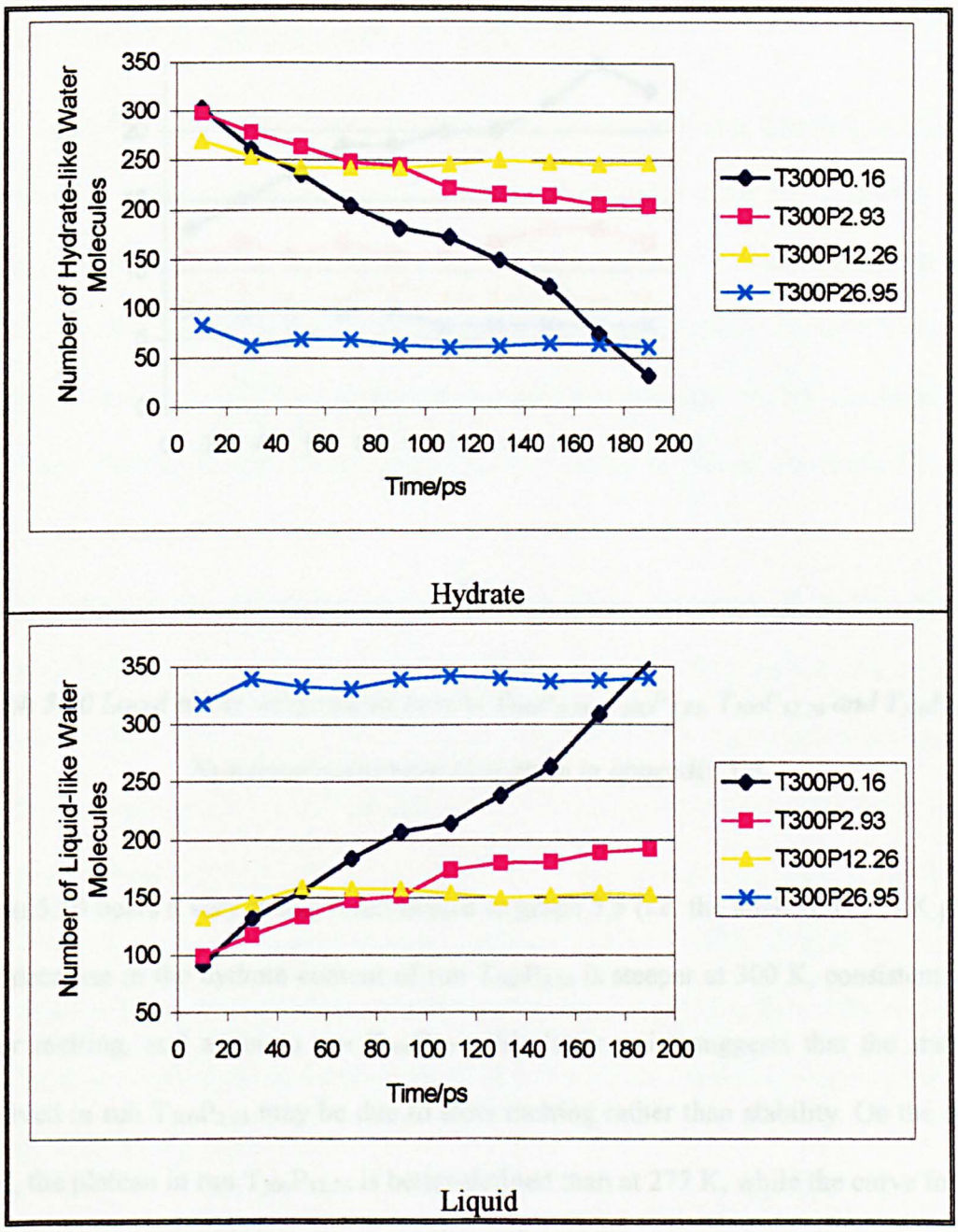
Number of Hydrate-like Water Molecules
350
300
250
200
150
100
50
0
0 20 40 60 80 100 120 140 160 180 200
Time/ps
T300P0.16
T300P2.93
T300P12.26
T300P26.95
Hydrate
Number of Liquid-like Water Molecules
350
300
250
200
150
100
50
0 20 40 60 80 100 120 140 160 180 200
Time/ps
T300P0.16
T300P2.93
T300P12.26
T300P26.95
Liquid

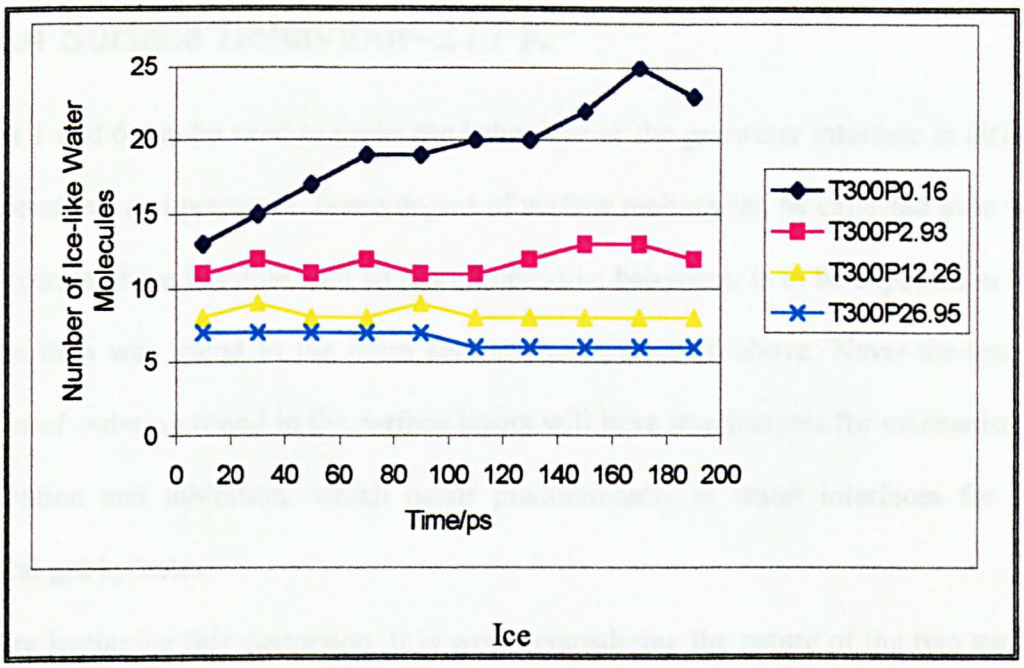

Graph 5.10 Local phase assignments in runs $T_{300}P_{0.16}$, $T_{300}P_{2.93}$, $T_{300}P_{12.26}$ and $T_{300}P_{26.95}$. Numerical values are also given in appendix 5.8.

Graph 5.10 bears a very strong resemblance to graph 5.5 (*i.e.* the analogous 277 K plot). The decrease in the hydrate content of run $T_{300}P_{0.16}$ is steeper at 300 K, consistent with faster melting, and again in run $T_{300}P_{2.93}$; this latter point suggests that the stability observed in run $T_{300}P_{2.93}$ may be due to slow melting rather than stability. On the other hand, the plateau in run $T_{300}P_{12.26}$ is better-defined than at 277 K, while the curve for run $T_{300}P_{26.95}$ is essentially the same as run $T_{277}P_{26.59}$. In general, the data is again consistent with melting at low pressure, stable hydrate at intermediate pressures, and an alternative phase at high pressures.

5.3.4 Surface Behaviour–277 K

Slabs 1 and 6 can be used to probe the behaviour of the gas/water interface at different temperatures and pressures. Some degree of surface melting can be expected even when the hydrate phase is stable, and so more liquid-like behaviour is to be expected in these layers than was found in the more central slabs discussed above. Never-the-less, the extent of ordering found in the surface layers will have implications for mechanisms of nucleation and inhibition, which occur predominantly at water interfaces for most natural gas hydrates.

Before beginning this discussion, it is worth considering the nature of the two surfaces involved. Slab 6 contains the surface layer of the {1,1,1; -0.001} surface. As described elsewhere[15] this surface is created by cleaving just below a layer of hexagonal rings, and so exposes deep potholes on the surface (*ca.* 9 Å deep). One might expect ready loss of guests from these potholes unless the conditions favour strong adsorption to the hydrate surface. Slab 1 is the complementary surface ({1,1,1; 0.999}), which is therefore characterised by hexagonal islands that complete large cavities just below the surface. In general, these differences in topology mean that the stability and characteristics of these two surfaces should differ.

Radial Distribution Functions

The radial distribution function (see section 3.3) for water in the gas hydrate lattice, g_{OO}, has been calculated for the four runs, along with the guest–guest RDFs, g_{XX}. In the following sections these plots are presented for slabs 1 and 6, the surface slabs of the gas hydrate lattice.

Oxygen–Oxygen Radial Distribution Functions

The oxygen–oxygen radial distribution functions, g_{OO}, for slabs 1 and 6 of the four runs are presented in figures 5.19–5.22.

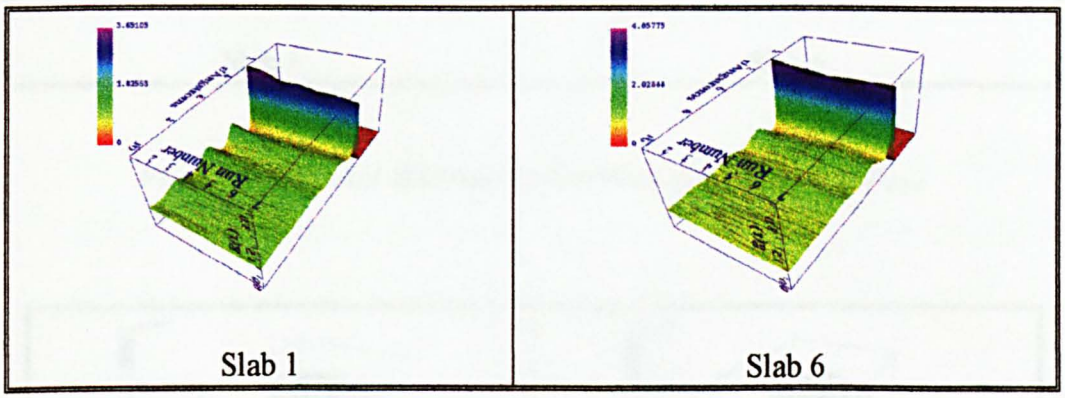

Figure 5.19 Radial distribution functions g_{OO} for run $T_{277}P_{-0.01}$.

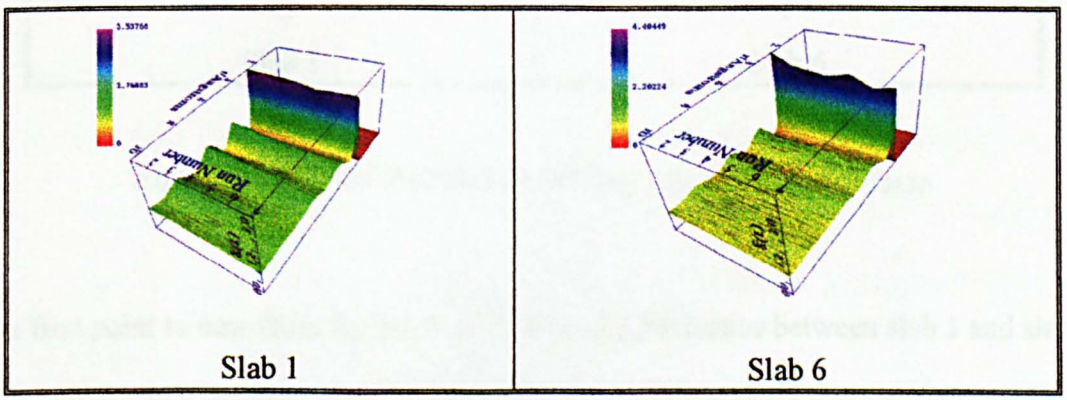

Figure 5.20 Radial distribution functions g_{OO} for run $T_{277}P_{0.21}$.

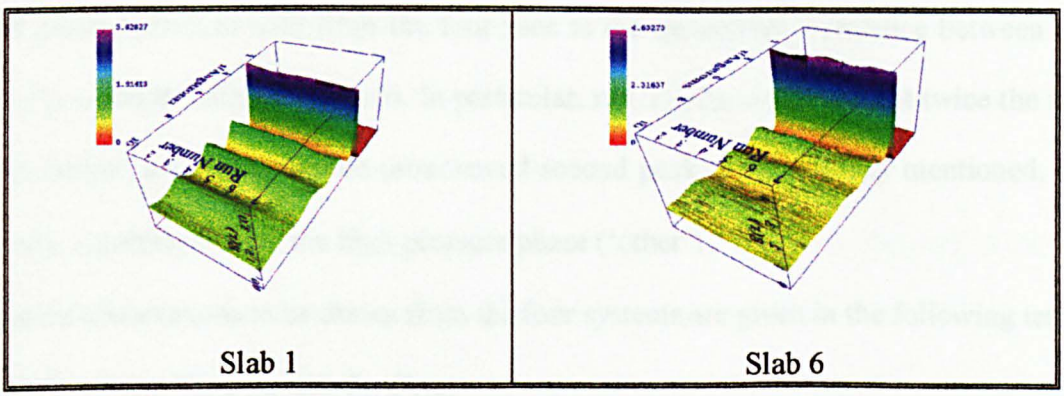

Figure 5.21 Radial distribution functions g_{OO} for run $T_{277}P_{4.04}$.

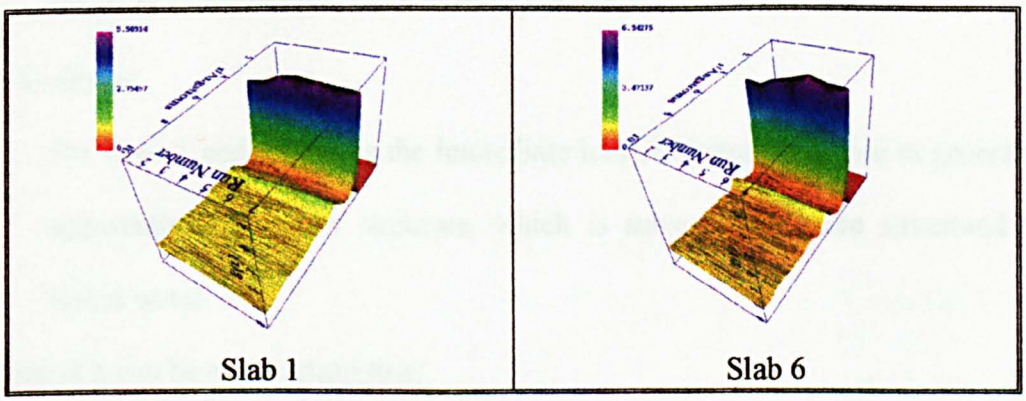

Figure 5.22 Radial distribution functions g_{OO} for run $T_{277}P_{26.59}$.

The first point to note from figures 5.19–5.22 is the difference between slab 1 and slab 6 in the three lower pressure runs: although both describe a hydrate surface, slab 6 exhibits considerably less structure in g_{OO} than slab 1. However it does appear that although there is less structure in g_{OO} for slab 6 that this structure in general remains throughout the run, whereas for slab 1 there may initially be more structure in g_{OO}, but by the end of the run the structure in slabs 1 and 6 is comparable. In essence slab 6 melts more rapidly than slab 1, but that both of these surfaces end up with RDFs that look like liquid water.

The second point to note from the four runs is the qualitative difference between run $T_{277}P_{26.59}$ and the other three runs. In particular, run $T_{277}P_{26.59}$ gives about twice the first peak height, and a much more pronounced second peak. As previously mentioned, run $T_{277}P_{26.59}$ corresponds to the high-pressure phase ('other').

General observations to be drawn from the four systems are given in the following text.

Runs $T_{277}P_{-0.01}$, $T_{277}P_{0.21}$ and $T_{277}P_{4.04}$:

For slabs 1 and 6 there is a loss of structure in the g_{OO} plot as time progresses, with near complete melting being observed in both slabs, such that the final structure is indistinguishable from liquid water.

Run $T_{277}P_{26.59}$:

For slabs 1 and 6 there is the immediate loss of hydrate structure to generate an apparently stable new structure, which is substantially more structured than liquid water.

In general it can be summarised that:

a) for runs $T_{277}P_{-0.01}$, $T_{277}P_{0.21}$ and $T_{277}P_{4.04}$ slabs 1 and 6 are unstable on the simulation time scale; however it is noticeable that as the pressure in these three runs increases, the time at which liquid-like structure is observed becomes longer;

b) for run $T_{277}P_{26.59}$, both slabs 1 and 6 show a rapid change to a new structure, which appears stable on the simulation time scale.

A graph of the 1st and 2nd peak positions and heights in g_{OO} for slab 1 can be seen in graph 5.11. It can be seen that the simulations can be split into two groups: runs $T_{277}P_{-0.01}$, $T_{277}P_{0.21}$ and $T_{277}P_{4.04}$, and then run $T_{277}P_{26.59}$. This split is clearest in the 1st peak height, where runs $T_{277}P_{-0.01}$, $T_{277}P_{0.21}$ and $T_{277}P_{4.04}$ exhibit 1st peak heights in the region

3.02–3.83, but run $T_{277}P_{26.59}$ exhibits 1st peak heights in the region 4.79–5.51. A similar segregation of the four runs is observed for the 2nd peak position, with the second peak in run $T_{277}P_{26.59}$ occurring at substantially longer distances. This is particularly significant as it implies considerable strain in the hydrogen-bonding network: a second peak position in excess of 5.0 Å, coupled with a first peak position of 2.75 Å implies an O…O…O angle in excess of 130°—considerably larger than the 109° expected for a tetrahedral water network. The distinction in the second peak heights can be seen in that for runs $T_{277}P_{-0.01}$, $T_{277}P_{0.21}$ and $T_{277}P_{4.04}$ these decay to a value below 1.2, whereas for run $T_{277}P_{26.59}$ the second peak height grows to a value in excess of 1.3

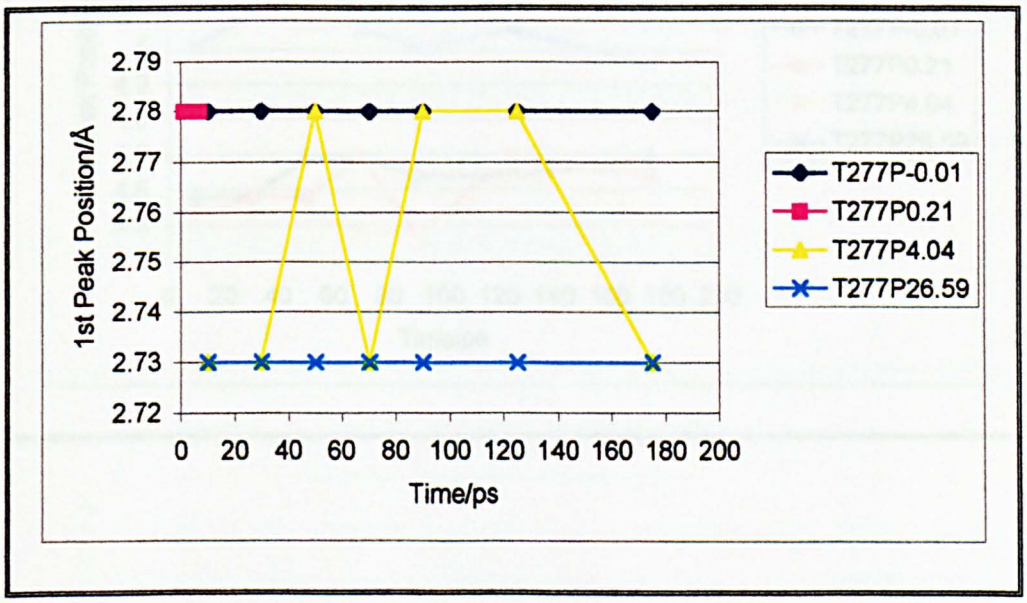

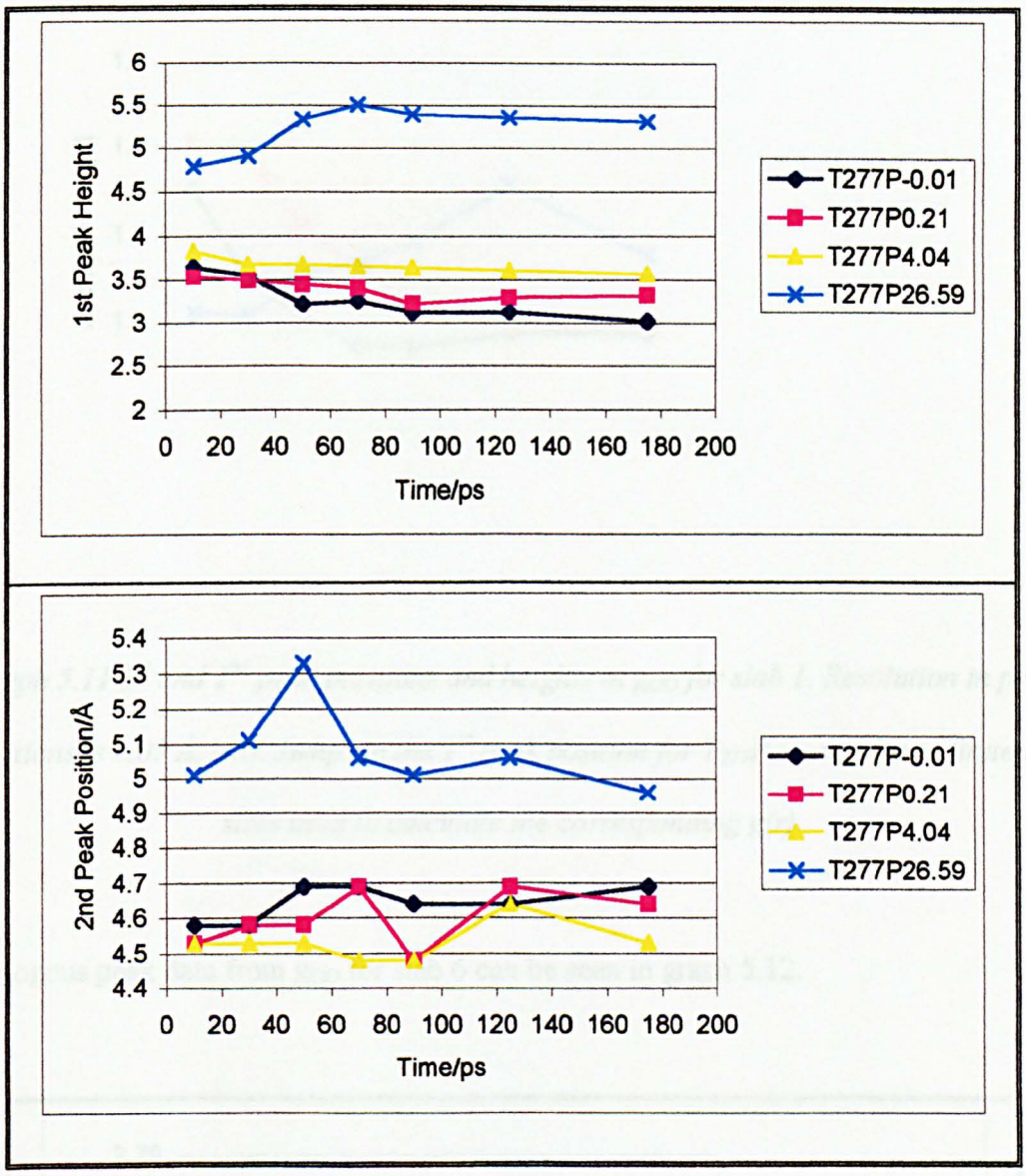
1st Peak Height
6
5.5
5
4.5
4
3.5
3
2.5
2
0 20 40 60 80 100 120 140 160 180 200
Time/ps
T277P-0.01
T277P0.21
T277P4.04
T277P26.59
2nd Peak Position/Å
5.4
5.3
5.2
5.1
5
4.9
4.8
4.7
4.6
4.5
4.4
0 20 40 60 80 100 120 140 160 180 200
Time/ps
T277P-0.01
T277P0.21
T277P4.04
T277P26.59

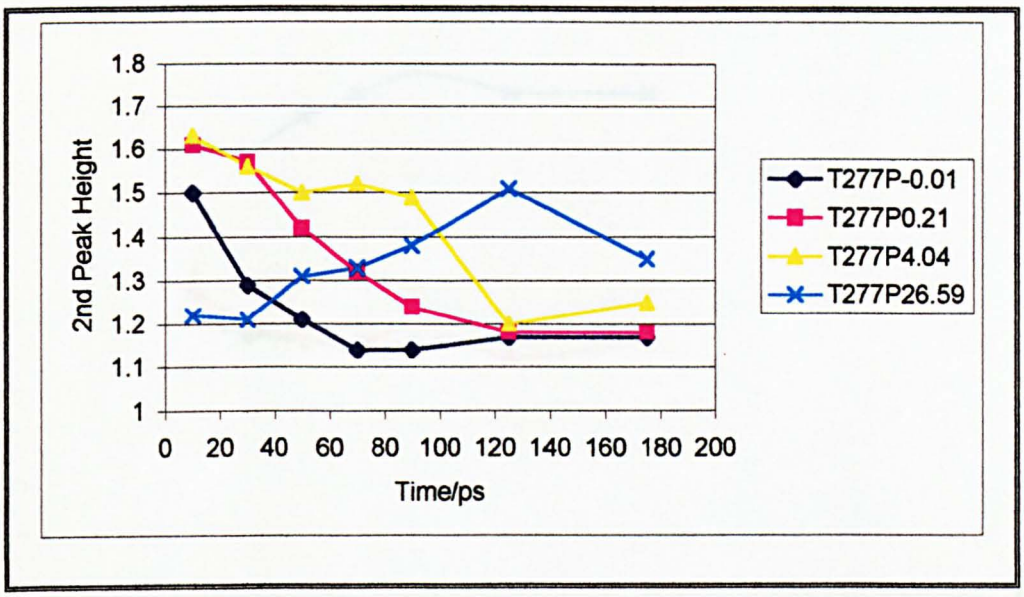

Graph 5.11 1st and 2nd peak positions and heights in g_{OO} for slab 1. Resolution in peak positions is 0.05 Å. N.B. Jumps in the 1st peak position for $T_{277}P_{4.04}$ are due to finite bin sizes used to calculate the corresponding g(r).

Analogous peak data from g_{OO} for slab 6 can be seen in graph 5.12.

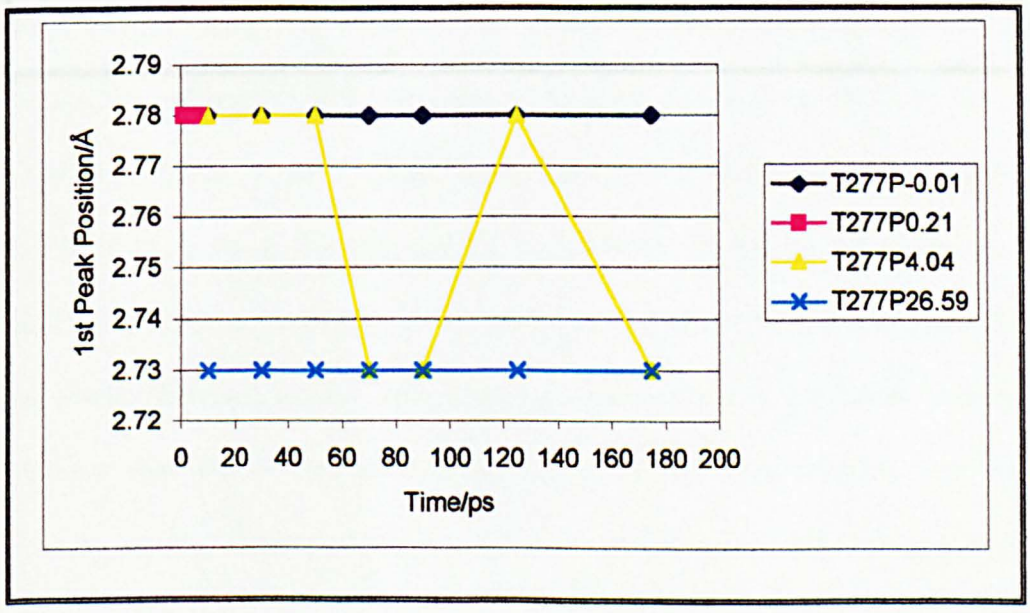

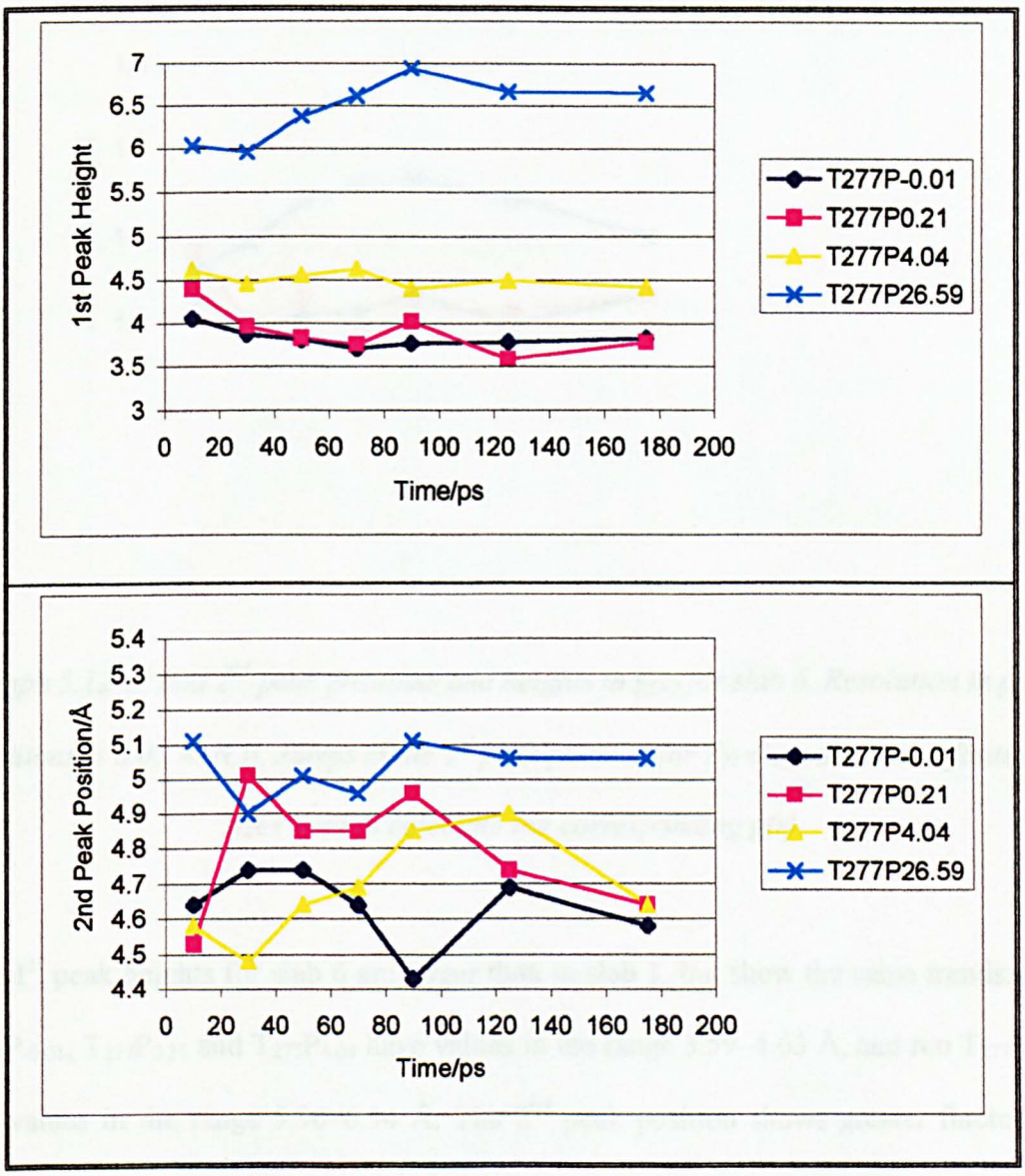
1st Peak Height
7
6.5
6
5.5
5
4.5
4
3.5
3
0 20 40 60 80 100 120 140 160 180 200
Time/ps
T277P-0.01
T277P0.21
T277P4.04
T277P26.59
2nd Peak Position/Å
5.4
5.3
5.2
5.1
5
4.9
4.8
4.7
4.6
4.5
4.4
0 20 40 60 80 100 120 140 160 180 200
Time/ps
T277P-0.01
T277P0.21
T277P4.04
T277P26.59

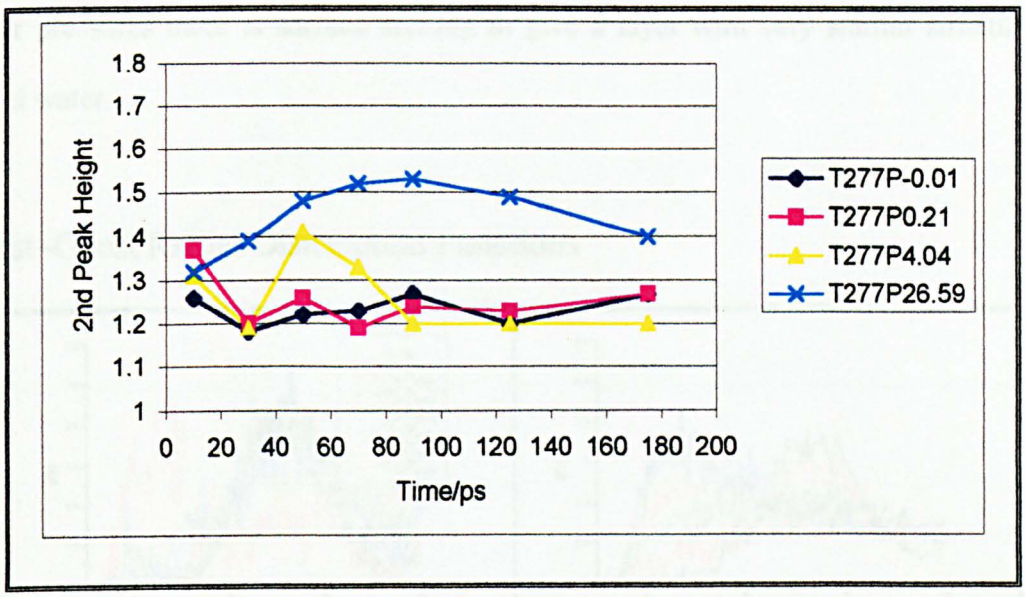

Graph 5.12 1st and 2nd peak positions and heights in g_{OO} for slab 6. Resolution in peak positions is 0.05 Å. N.B. Jumps in the 1st peak position for $T_{277}P_{4.04}$ are due to finite bin sizes used to calculate the corresponding g(r).

The 1st peak heights for slab 6 are larger than in slab 1, but show the same trends: runs $T_{277}P_{-0.01}$, $T_{277}P_{0.21}$ and $T_{277}P_{4.04}$ have values in the range 3.59–4.63 Å, and run $T_{277}P_{26.59}$ has values in the range 5.96–6.94 Å. The 2nd peak position shows greater fluctuation during surface melting, but still converges to the same values as for slab 1 by the end of the trajectory. Similarly, the 2nd peak height can again be split into two distinct groups: the first for runs $T_{277}P_{-0.01}$, $T_{277}P_{0.21}$ and $T_{277}P_{4.04}$, and the second for run $T_{277}P_{26.59}$.

The general conclusion from graphs 5.11 and 5.12 is that run $T_{277}P_{26.59}$ appears to show fundamentally different results, with a stable structure that is consistent with neither liquid water, nor with a tetrahedral network. This is consistent with the idea that run $T_{277}P_{26.59}$ is the high-density phase postulated for structure II hydrates in section 5.1 At

lower pressures there is surface melting to give a layer with very similar structure to liquid water.

Guest–Guest Radial Distribution Functions

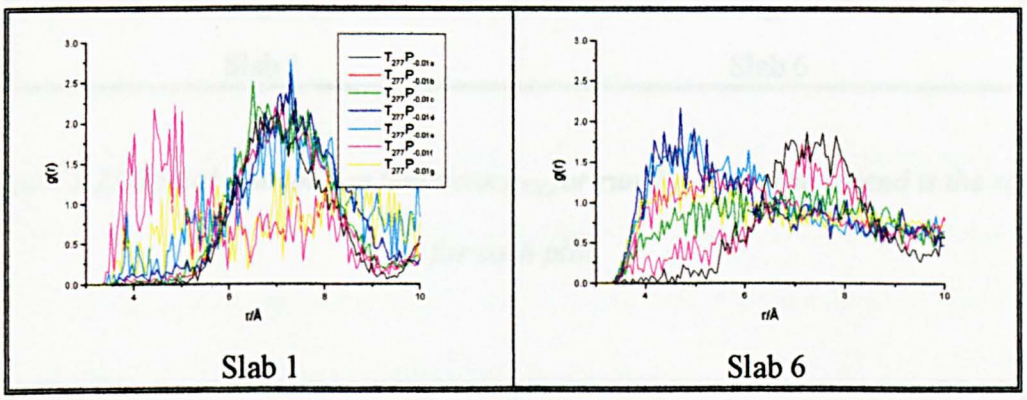

Figure 5.23 Radial distribution functions g_{XX} for run $T_{277}P_{-0.01}$. The legend is the same for each plot.

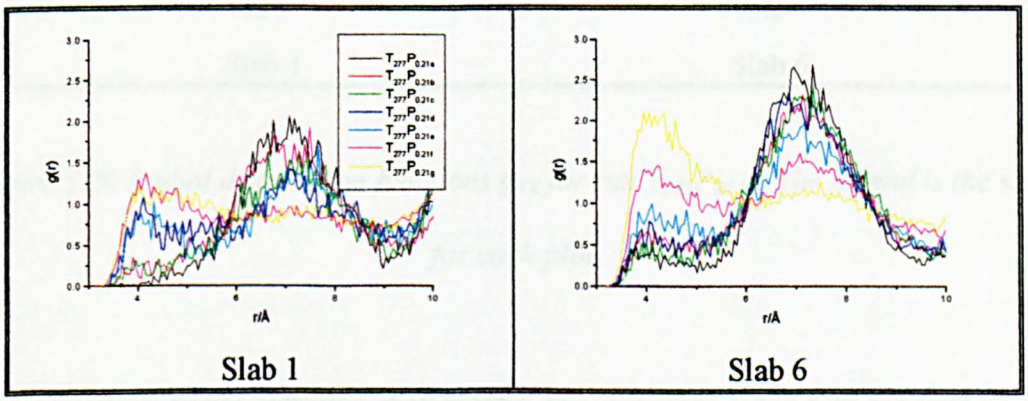

Figure 5.24 Radial distribution functions g_{XX} for run $T_{277}P_{0.21}$. The legend is the same for each plot.

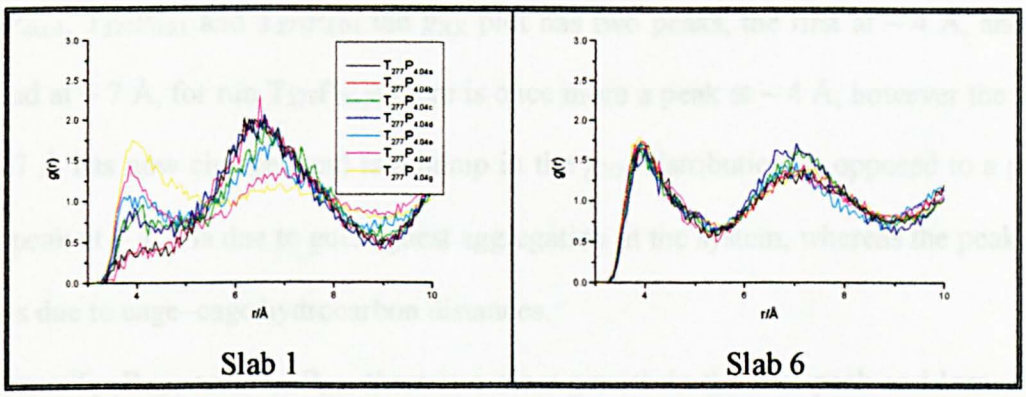

Figure 5.25 Radial distribution functions g_{XX} for run $T_{277}P_{4.04}$. The legend is the same for each plot.

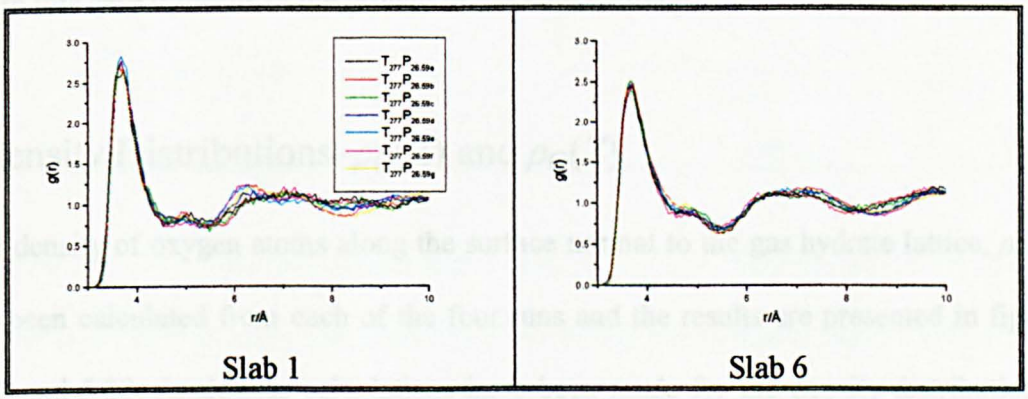

Figure 5.26 Radial distribution functions g_{XX} for run $T_{277}P_{26.59}$. The legend is the same for each plot.

The guest–guest radial distribution functions, g_{XX}, for slabs 1 and 6 of the four runs are presented in figures 5.23–5.26. From figures 5.23–5.26 it can be seen that as the pressure in the runs increases the disorder observed in the g_{XX} plots decreases up to and including run $T_{277}P_{26.59}$, however it can clearly be seen that the structure present in g_{XX} for run $T_{277}P_{26.59}$ is fundamentally different to that observed for the other three runs. For runs

$T_{277}P_{-0.01}$, $T_{277}P_{0.21}$ and $T_{277}P_{4.04}$ the g_{XX} plot has two peaks, the first at ~ 4 Å, and the second at ~ 7 Å, for run $T_{277}P_{26.59}$ there is once more a peak at ~ 4 Å, however the peak at ~ 7 Å has now changed and is a hump in the g_{XX} distribution as opposed to a peak. The peak at ~ 4 Å is due to guest-guest aggregation in the system, whereas the peak at ~ 7 Å is due to cage–cage hydrocarbon distances.

For runs $T_{277}P_{-0.01}$ and $T_{277}P_{0.21}$ there is a clear growth in the first peak and loss of the second peak with time. This is also seen in slab 1 run $T_{277}P_{4.04}$, whereas slab 6 run $T_{277}P_{4.04}$ appears completely stable, with two peaks of equal height. Run $T_{277}P_{26.59}$ gives a stable slab 6, and almost stable slab 1–with the latter showing some time dependence, but in this case it results in the growth of the second hump.

z-density Distributions–$\rho_O(Z)$ and $\rho_G(Z)$

The density of oxygen atoms along the surface normal to the gas hydrate lattice, $\rho_O(Z)$, has been calculated from each of the four runs and the results are presented in figures 5.27 and 5.28. Analogous calculations have been made for the density distribution of guest carbon sites, $\rho_G(Z)$, and resulting plots are depicted in figures 5.29 and 5.30. For run $T_{277}P_{-0.01}$ the lattice was located between 0 and 30 Å, for runs $T_{277}P_{0.21}$ and $T_{277}P_{4.04}$ the lattice is situated between –11.5 and 18.5 Å and for run $T_{277}P_{26.59}$ the lattice is situated between –13 and 17 Å. All of the $\rho_O(Z)$ distributions are characterised by a central trough corresponding to the centre of the gas hydrate lattice. In the following sections these plots are presented along with a tabulated summary of the $\rho_O(Z)$ distribution central peak positions.

Oxygen z-density Distributions–$\rho_o(Z)$

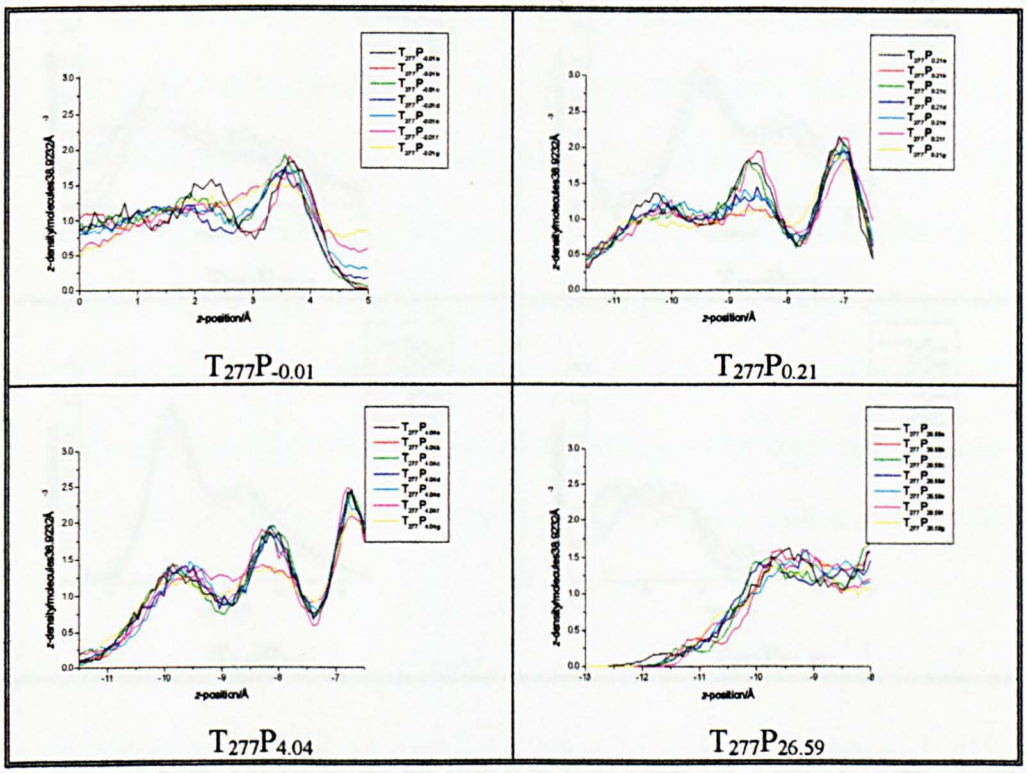

Figure 5.27 $\rho_O(Z)$ distributions for slab 1 in runs $T_{277}P_{-0.01}$, $T_{277}P_{0.21}$ and $T_{277}P_{4.04}$ and $T_{277}P_{26.59}$. Differences in the z-axis scale are merely due to translational shifts of the hydrate slab prior to simulation.

From figure 5.27 it can be seen that as the pressure in the system increases the $\rho_O(Z)$ distributions for slab 1 develop a better-defined peak structure up to run $T_{277}P_{4.04}$, then for run $T_{277}P_{26.59}$ the appearance of $\rho_O(Z)$ changes fundamentally. For run $T_{277}P_{-0.01}$ there are two peaks in the $\rho_O(Z)$ distribution whereas for runs $T_{277}P_{0.21}$ and $T_{277}P_{4.04}$ a third peak in the $\rho_O(Z)$ distribution has developed at the edge of the gas hydrate lattice. For run $T_{277}P_{26.59}$ there is only one broad peak present in the $\rho_O(Z)$ distribution, suggesting an amorphous solid for this phase.

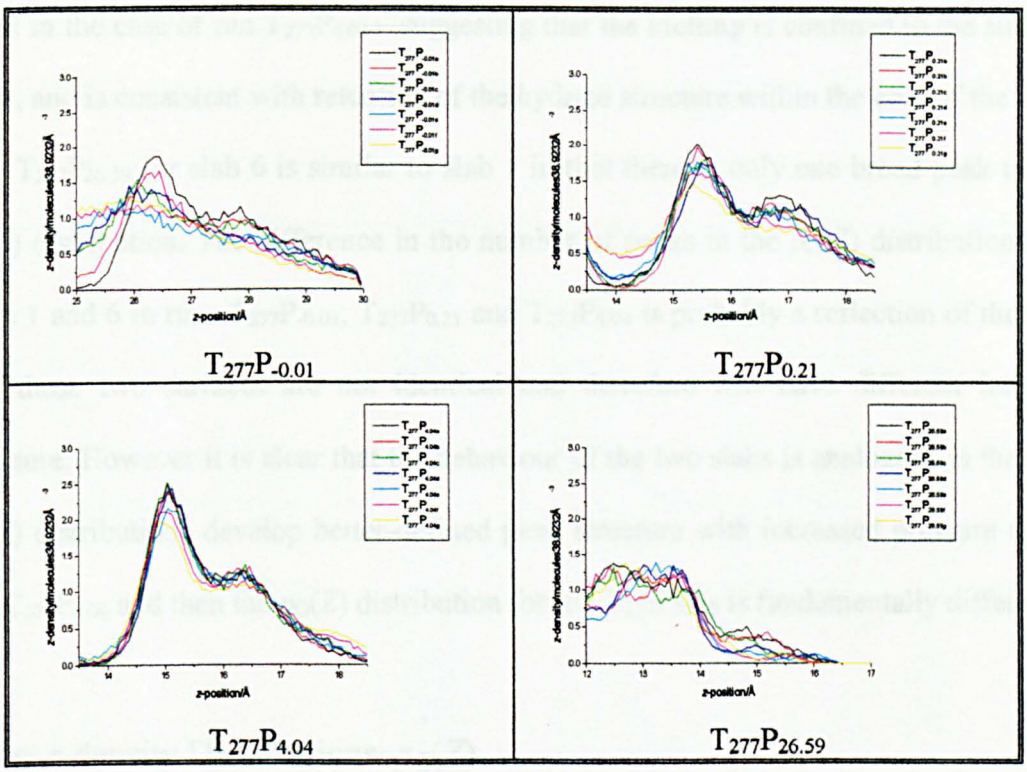

Figure 5.28 $\rho_O(Z)$ distributions for slab 6 in runs $T_{277}P_{-0.01}$, $T_{277}P_{0.21}$, $T_{277}P_{4.04}$ and $T_{277}P_{26.59}$. Differences in the z-axis scale are merely due to translational shifts of the hydrate slab prior to simulation.

A similar behaviour can be observed in figure 5.28 for slab 6 as was seen for slab 1 in figure 5.27. That is to say that as the pressure in the system increases the $\rho_O(Z)$ distributions for slab 6 develop a better-defined peak structure up to run $T_{277}P_{4.04}$, then for run $T_{277}P_{26.59}$ the appearance of $\rho_O(Z)$ changes fundamentally. However in the case of slab 6 there are only two peaks present in all of the $\rho_O(Z)$ distributions for runs $T_{277}P_{-0.01}$, $T_{277}P_{0.21}$ and $T_{277}P_{4.04}$, as opposed to up to three peaks in slab 1, and these peaks are less well resolved in slab 6. This is consistent with faster melting on this surface. However, the figures also indicate a very distinct trough at the bottom of this surface—vanishingly

small in the case of run $T_{277}P_{4.04}$—suggesting that the melting is confined to the surface layer, and is consistent with retention of the hydrate structure within the core of the slab. Run $T_{277}P_{26.59}$ for slab 6 is similar to slab 1 in that there is only one broad peak in the $\rho_O(Z)$ distribution. The difference in the number of peaks in the $\rho_O(Z)$ distributions for slabs 1 and 6 in runs $T_{277}P_{-0.01}$, $T_{277}P_{0.21}$ and $T_{277}P_{4.04}$ is probably a reflection of the fact that these two surfaces are not identical and therefore will have different internal structure. However it is clear that the behaviour of the two slabs is analogous in that the $\rho_O(Z)$ distributions develop better-defined peak structure with increased pressure up to run $T_{277}P_{4.04}$ and then the $\rho_O(Z)$ distribution for run $T_{277}P_{26.59}$ is fundamentally different.

Guest *z*-density Distributions–$\rho_G(Z)$

These distributions once more show the same grouping as observed with other properties, with run $T_{277}P_{26.59}$ being fundamentally different to runs $T_{277}P_{-0.01}$, $T_{277}P_{0.21}$ and $T_{277}P_{4.04}$. However in this case the $\rho_G(Z)$ distributions for runs $T_{277}P_{-0.01}$, $T_{277}P_{0.21}$ and $T_{277}P_{4.04}$ do not show much detail apart from an apparent increase in the guest density at the edges of the gas hydrate lattice with increasing pressure. This increase in the guest density at the edges of the gas hydrate lattice is due to methane adsorption. This is not due to release of methane on melting as that would lead to an opposite effect with increasing pressure. That is to say hydrate melting would give a reduction in the guest density at the edges of the gas hydrate lattice with increasing pressure, as the gas hydrate lattice would become more stable with increasing pressure. This increase in guest density with increasing pressure may be due to templating of the stable gas hydrate

lattice on the hydrocarbon phase above, causing the methane to aggregate on the gas hydrate lattice surface prior to the next layer of cages being completed.

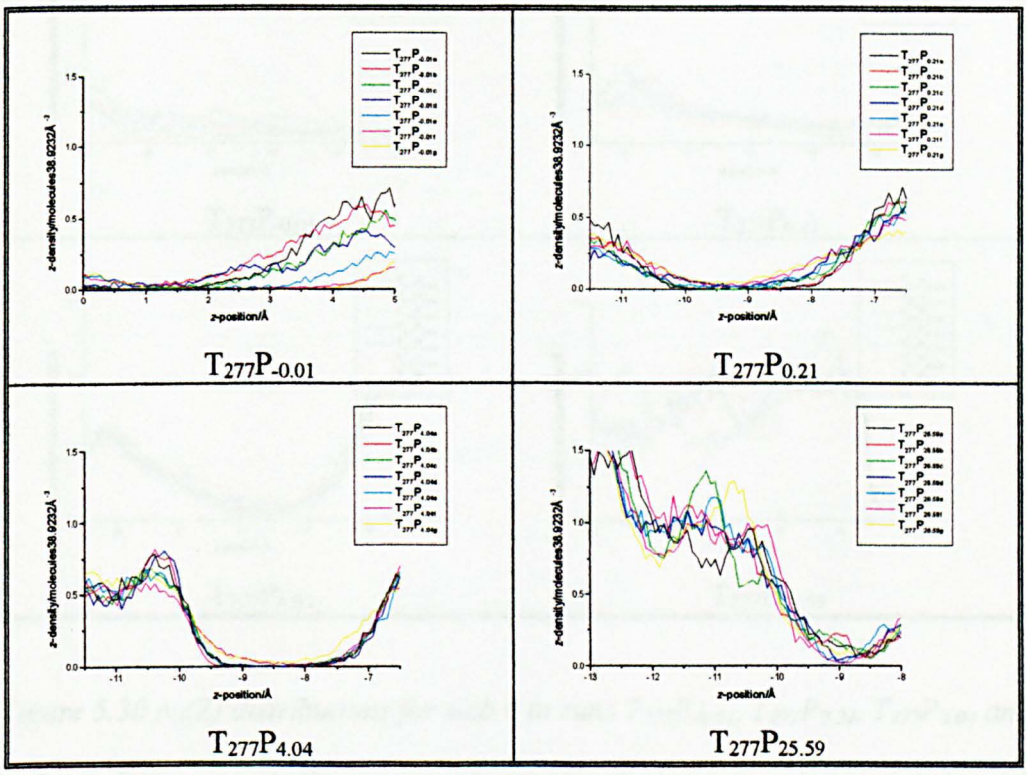

Figure 5.29 $\rho_G(Z)$ distributions for slab 1 in runs $T_{277}P_{-0.01}$, $T_{277}P_{0.21}$, $T_{277}P_{4.04}$ and $T_{277}P_{26.59}$. Differences in the z-axis scale are merely due to translational shifts of the hydrate slab prior to simulation.

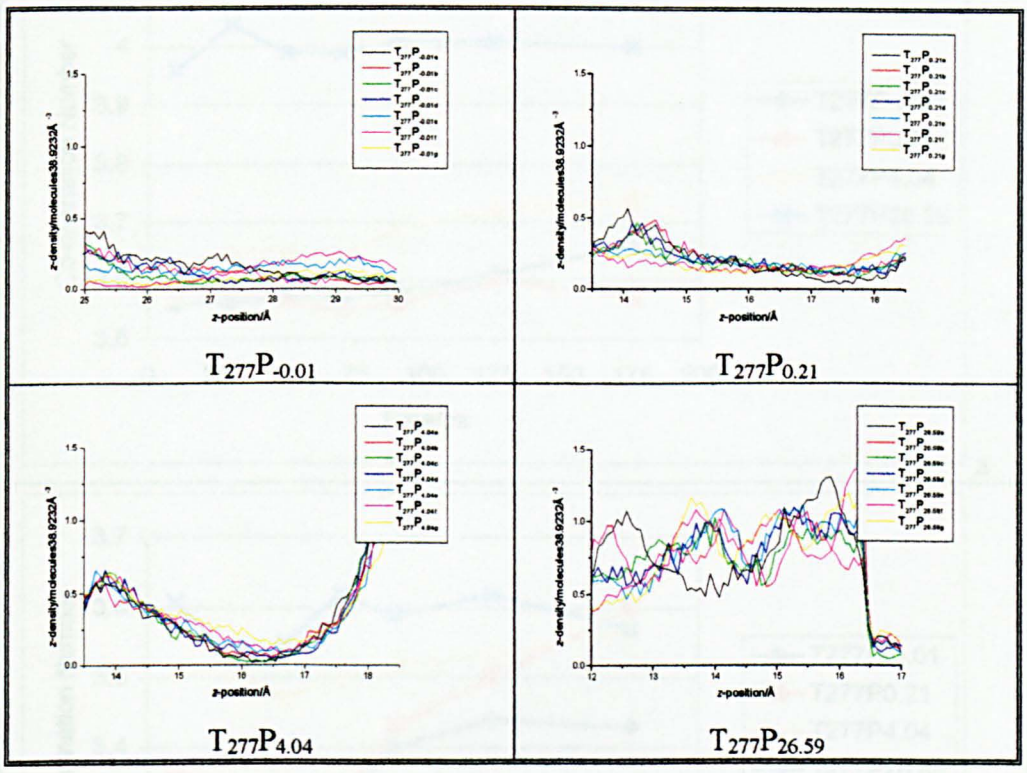

Figure 5.30 $\rho_G(Z)$ distributions for slab 6 in runs $T_{277}P_{-0.01}$, $T_{277}P_{0.21}$, $T_{277}P_{4.04}$ and $T_{277}P_{26.59}$. Differences in the z-axis scale are merely due to translational shifts of the hydrate slab prior to simulation.

Co-ordination Number

The co-ordination number (see section 3.5) of water molecules within the gas hydrate lattice for slabs 1 and 6 have been calculated for the four simulation cells and are given in appendix 5.9 and graph 5.13.

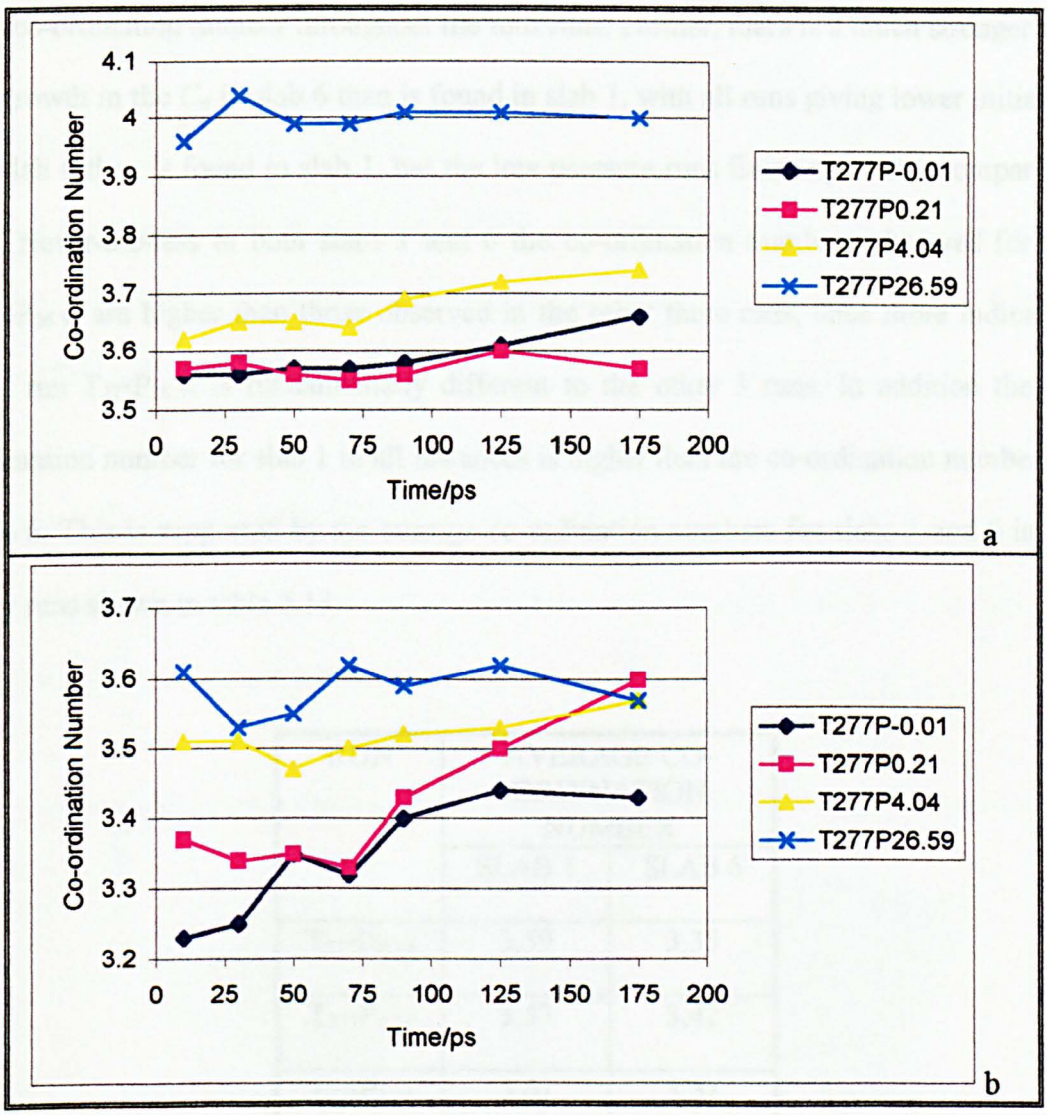

Graph 5.13 Co-ordination number for runs $T_{277}P_{-0.01}$, $T_{277}P_{0.21}$, $T_{277}P_{4.04}$ and $T_{277}P_{26.59}$: slab 1 (a) and slab 6 (b). Numerical values are also given in appendix 5.9.

For both surfaces it can be seen that the co-ordination number increases with increasing pressure. For slab 1 there seems to be a gradual increase in the co-ordination number up to run $T_{277}P_{4.04}$ which is then followed by a much larger increase in the co-ordination number for run $T_{277}P_{26.59}$. However for slab 6 there appears to be a gradual increase in

the co-ordination number throughout the four runs. Further, there is a much stronger rate of growth in the C_n in slab 6 than is found in slab 1, with all runs giving lower initial C_n in slab 6 than is found in slab 1, but the low pressure runs finishing with a comparable C_n. Never-the-less in both slabs 1 and 6 the co-ordination numbers observed for run $T_{277}P_{26.59}$ are higher than those observed in the other three runs, once more indicating that run $T_{277}P_{26.59}$ is fundamentally different to the other 3 runs. In addition the co-ordination number for slab 1 in all instances is higher than the co-ordination number for slab 6. This is supported by the average co-ordination numbers for slabs 1 and 6 in the four runs shown in table 5.13.

RUN	AVERAGE CO-ORDINATION NUMBER	
	SLAB 1	SLAB 6
$T_{277}P_{-0.01}$	3.59	3.35
$T_{277}P_{0.21}$	3.57	3.42
$T_{277}P_{4.04}$	3.67	3.52
$T_{277}P_{26.59}$	4.00	3.58

Table 5.13 Average co-ordination number for slabs 1 and 6 in $T_{277}P_{-0.01}$, $T_{277}P_{0.21}$, $T_{277}P_{4.04}$ and $T_{277}P_{26.59}$.

5.3.5 Surface Behaviour–300 K

Radial Distribution Functions

Oxygen and guest RDFs (see section 3.3) have been calculated from the four 200 ps runs performed at 300 K. In the following sections these plots are presented for slabs 1 and 6, the surface slabs of the gas hydrate lattice.

Oxygen–Oxygen Radial Distribution Functions

The oxygen–oxygen radial distribution functions, g_{OO}, for slabs 1 and 6 of the four runs are presented in figures 5.31–5.34.

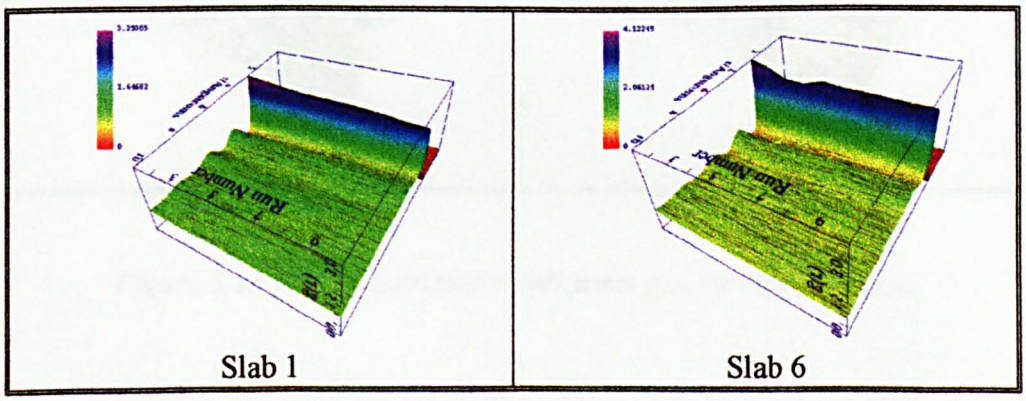

Figure 5.31 Radial distribution functions g_{OO} for run $T_{300}P_{0.16}$.

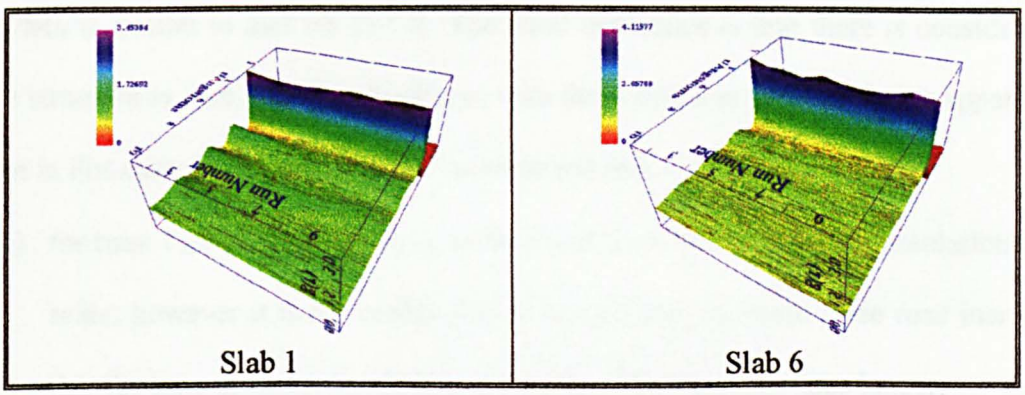

Figure 5.32 Radial distribution functions g_{OO} for run $T_{300}P_{2.93}$.

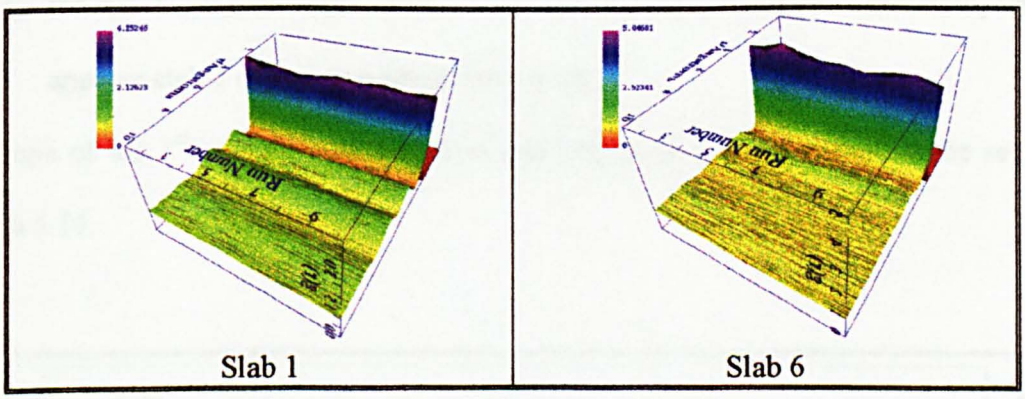

Figure 5.33 Radial distribution functions g_{OO} for run $T_{300}P_{12.26}$.

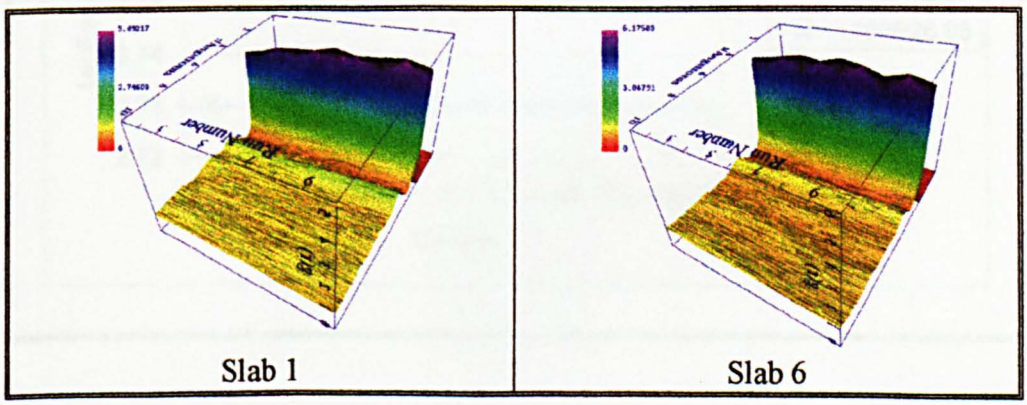

Figure 5.34 Radial distribution functions g_{OO} for run $T_{300}P_{26.95}$.

The data is similar to that for 277 K. The main difference is that there is considerably more structure in slab 1 for run $T_{300}P_{12.26}$, with three peaks in the RDF being apparently stable in this case. In general it can be summarised that:

a) for runs $T_{300}P_{0.16}$ and $T_{300}P_{2.93}$, slabs 1 and 6 are unstable on the simulation time scale; however it is noticeable that as the pressure in these three runs increases that the time at which liquid-like structure is observed becomes longer;

b) for run $T_{300}P_{12.26}$, slabs 1and 6 are stable on the simulation time scale, and slab 1 shows considerable structure;

c) for run $T_{300}P_{26.95}$, slabs 1 and 6 show an immediate change in structure, which appears stable on the simulation time scale.

A graph of the 1st and 2nd peak positions and heights in g_{OO} for slab 1 can be seen in graph 5.14.

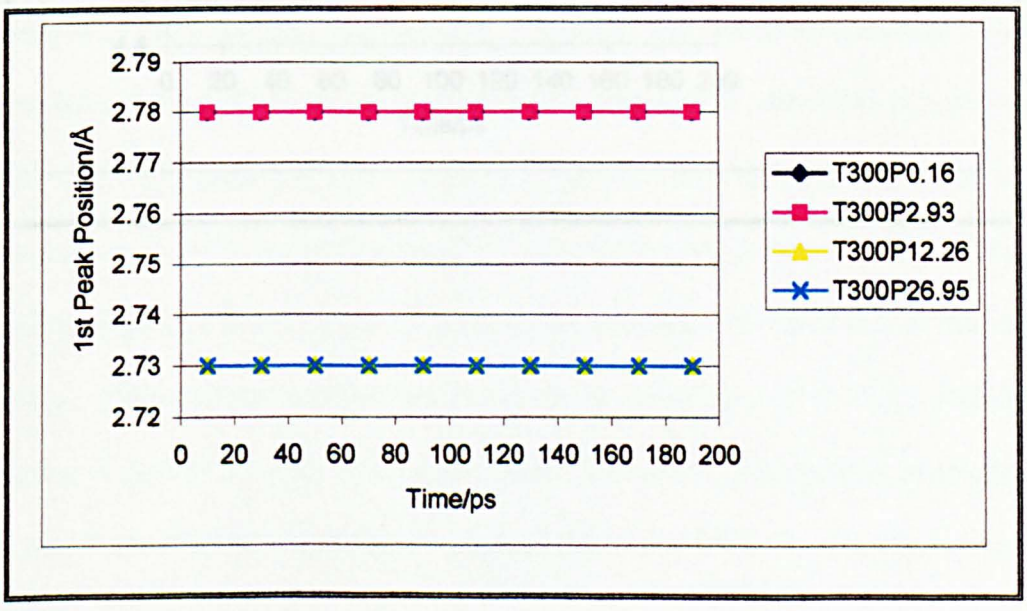

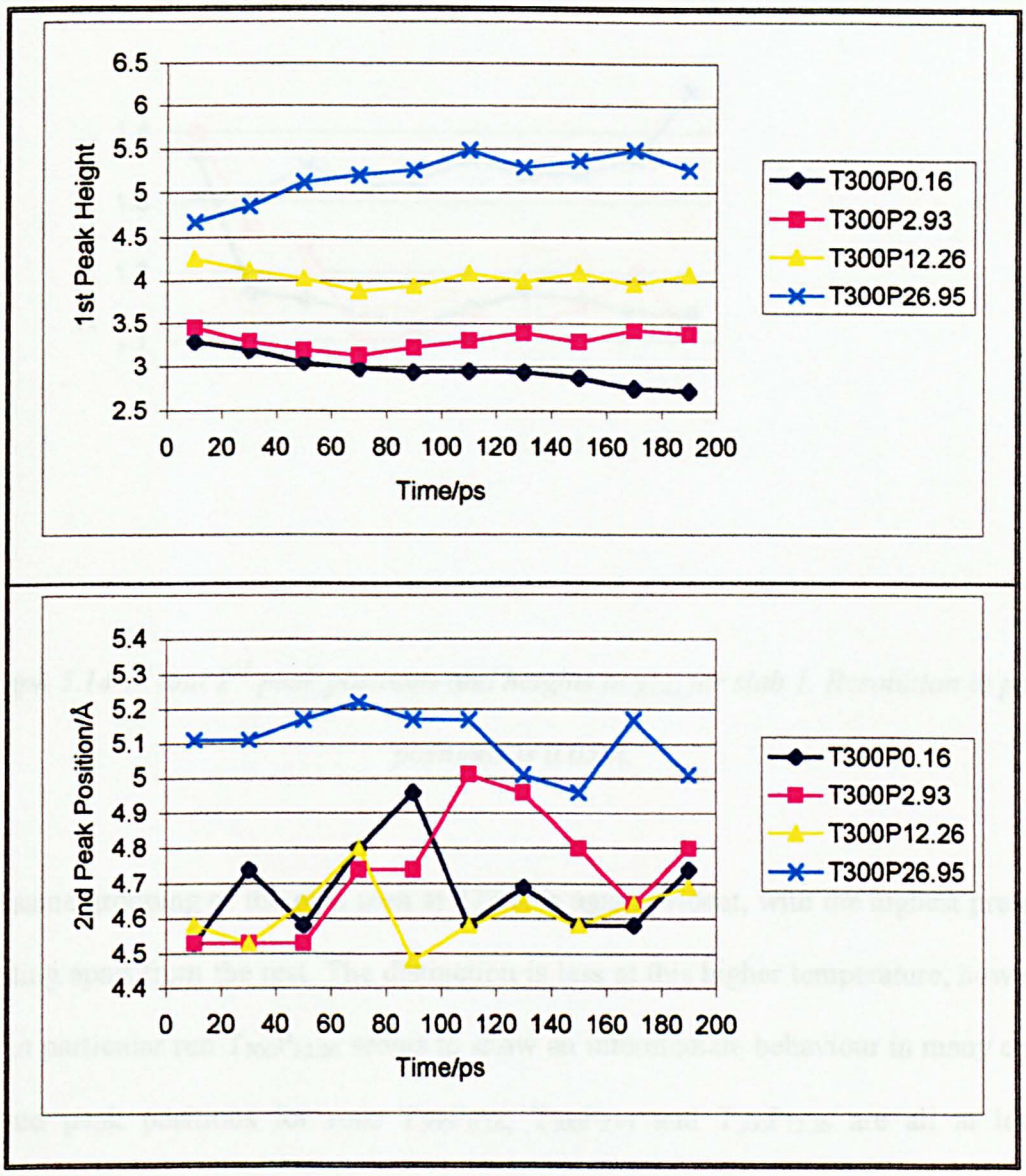
1st Peak Height
6.5
6
5.5
5
4.5
4
3.5
3
2.5
0 20 40 60 80 100 120 140 160 180 200
Time/ps
T300P0.16
T300P2.93
T300P12.26
T300P26.95
2nd Peak Position/Å
5.4
5.3
5.2
5.1
5
4.9
4.8
4.7
4.6
4.5
4.4
0 20 40 60 80 100 120 140 160 180 200
Time/ps
T300P0.16
T300P2.93
T300P12.26
T300P26.95

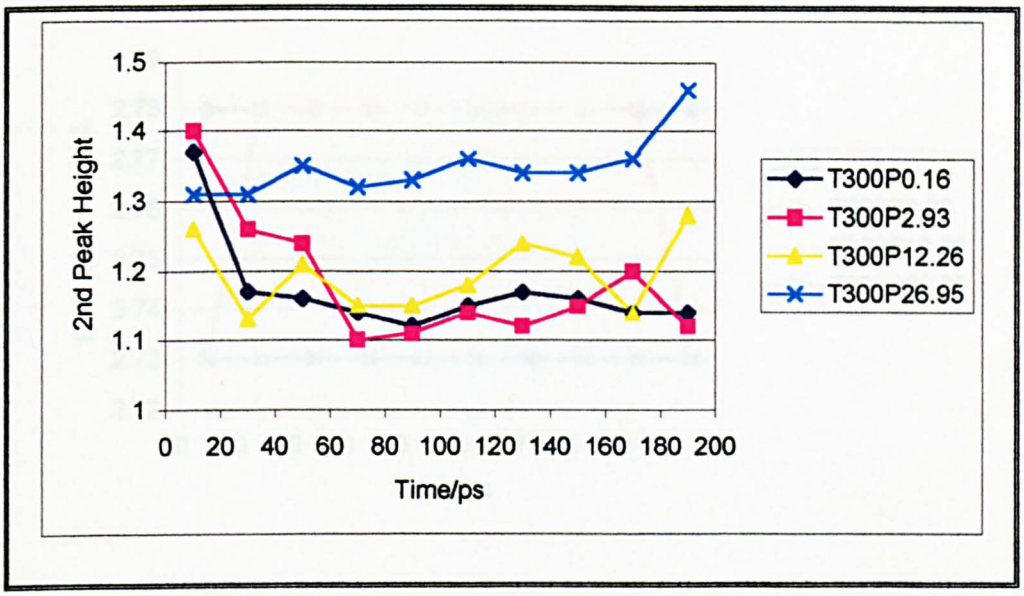

Graph 5.14 1st and 2nd peak positions and heights in g_{OO} for slab 1. Resolution in peak positions is 0.05 Å.

The same grouping of the runs seen at 277 K is again evident, with the highest pressure standing apart from the rest. The distinction is less at this higher temperature, however, and in particular run $T_{300}P_{12.26}$ seems to show an intermediate behaviour in many cases. Second peak positions for runs $T_{300}P_{0.16}$, $T_{300}P_{2.93}$ and $T_{300}P_{12.26}$ are all at longer distances than found in the analogous 277 K simulations, suggesting that thermal motion is leading to greater stress in the hydrogen bond network. The same is not true for run $T_{300}P_{26.95}$, which shows comparable positions to those seen at 277 K, presumably because it is already a highly compressed phase, and so has little room to accommodate large amplitude thermal vibrations. A graph of the 1st and 2nd peak positions and heights in g_{OO} for slab 6 can be seen in graph 5.15.

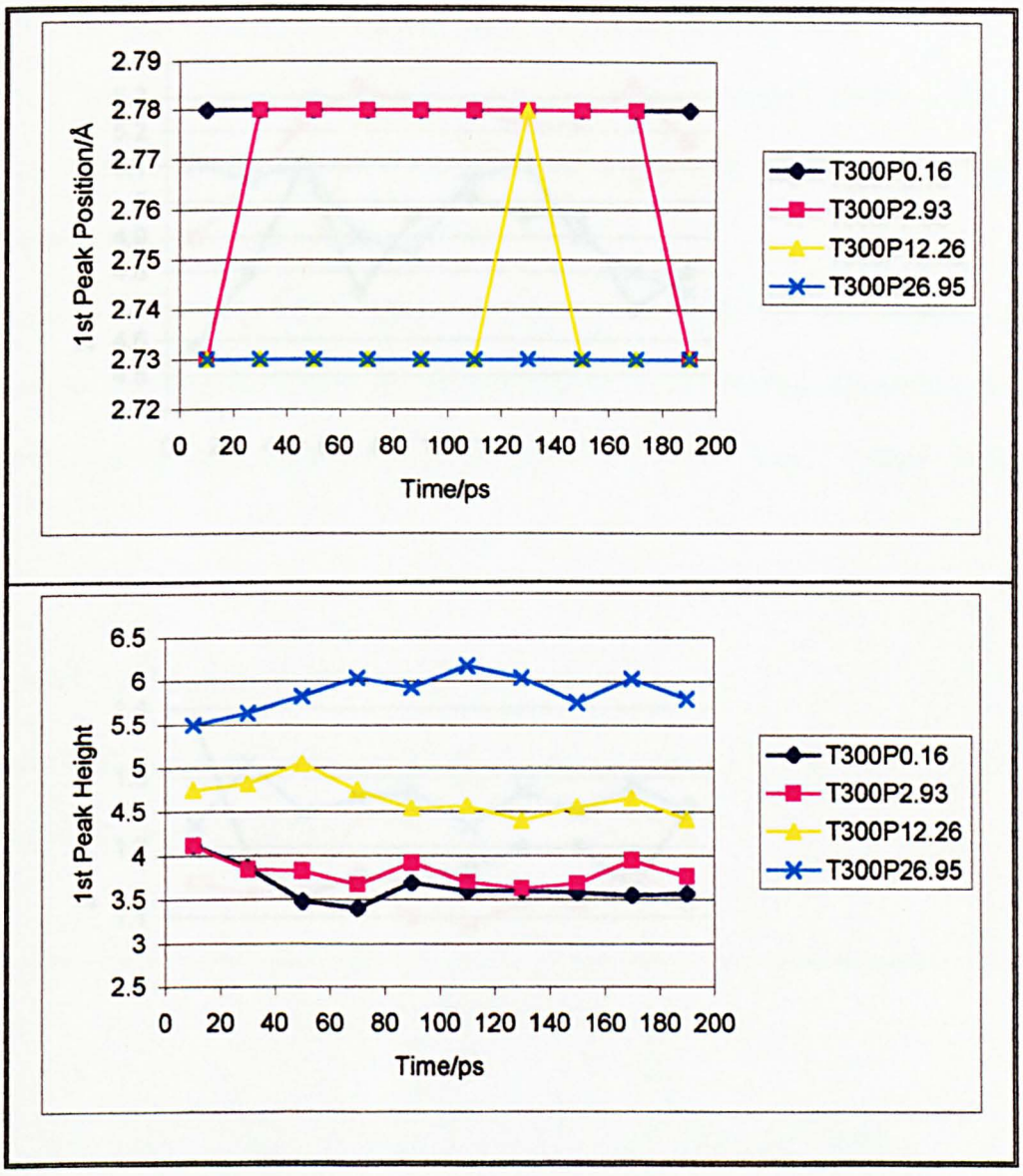
2.79
2.78
2.77
2.76
2.75
2.74
2.73
2.72
1st Peak Position/Å
0 20 40 60 80 100 120 140 160 180 200
Time/ps
T300P0.16
T300P2.93
T300P12.26
T300P26.95
6.5
6
5.5
5
4.5
4
3.5
3
2.5
1st Peak Height
0 20 40 60 80 100 120 140 160 180 200
Time/ps
T300P0.16
T300P2.93
T300P12.26
T300P26.95

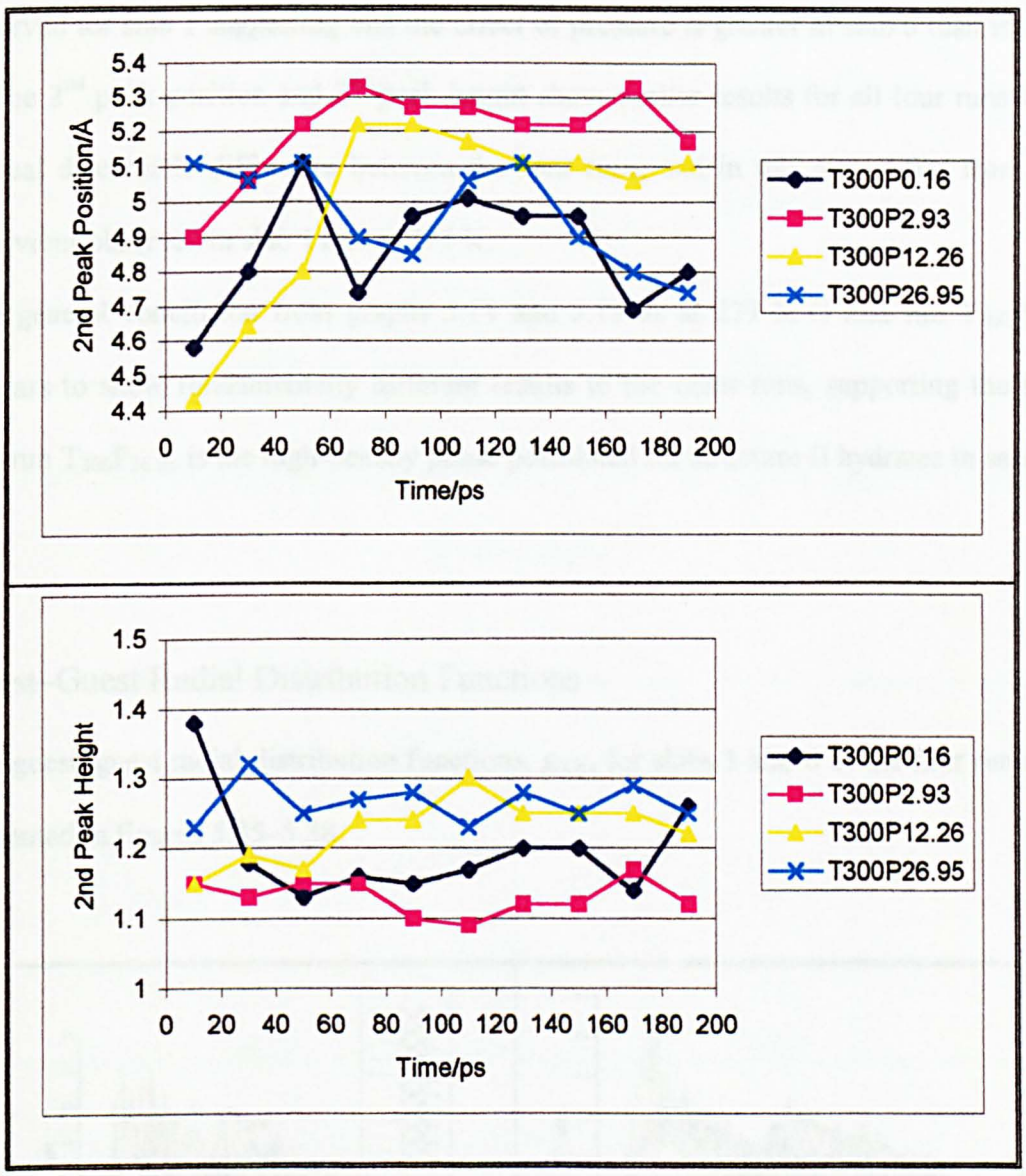

Graph 5.15 1st and 2nd peak positions and heights in g_{OO} for slab 6. Resolution in peak positions is 0.05 Å.

The 1st peak height for slab 6 shows a similar behaviour to slab 1 except that the range of values exhibited by the three groups is different. Runs $T_{300}P_{0.16}$ and $T_{300}P_{2.93}$ have values in the range 3.40–4.12 Å, run $T_{300}P_{12.26}$ has values in the range 4.40–5.05 Å, and run $T_{300}P_{26.95}$ has values in the range 5.50–6.18 Å. These values are larger than those

observed for slab 1 suggesting that the effect of pressure is greater in slab 6 than in slab 1. The 2nd peak position and 2nd peak height show similar results for all four runs with no real discernible difference between the four runs, and in this they differ from the behaviour observed in slab 1 and at 277 K.

The general conclusion from graphs 5.14 and 5.15 as at 277 K is that run $T_{300}P_{26.95}$ appears to show fundamentally different results to the other runs, supporting the idea that run $T_{300}P_{26.95}$ is the high-density phase postulated for structure II hydrates in section 5.1

Guest–Guest Radial Distribution Functions

The guest–guest radial distribution functions, g_{XX}, for slabs 1 and 6 of the four runs are presented in figures 5.35–5.38.

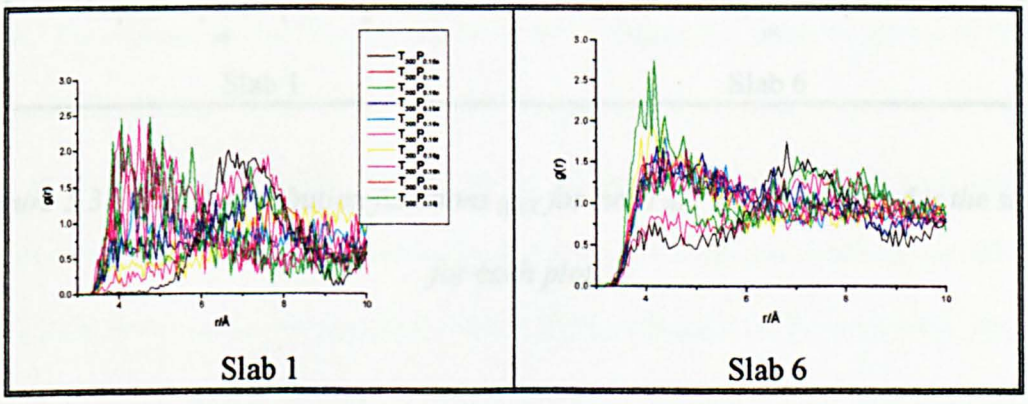

Figure 5.35 Radial distribution functions g_{XX} for run $T_{300}P_{0.16}$. The legend is the same for each plot.

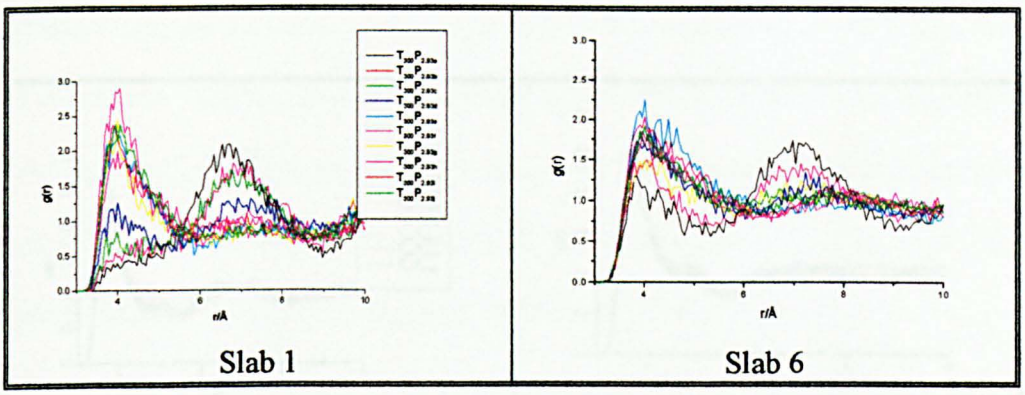

Figure 5.36 Radial distribution functions g_{XX} for run $T_{300}P_{2.93}$. The legend is the same for each plot.

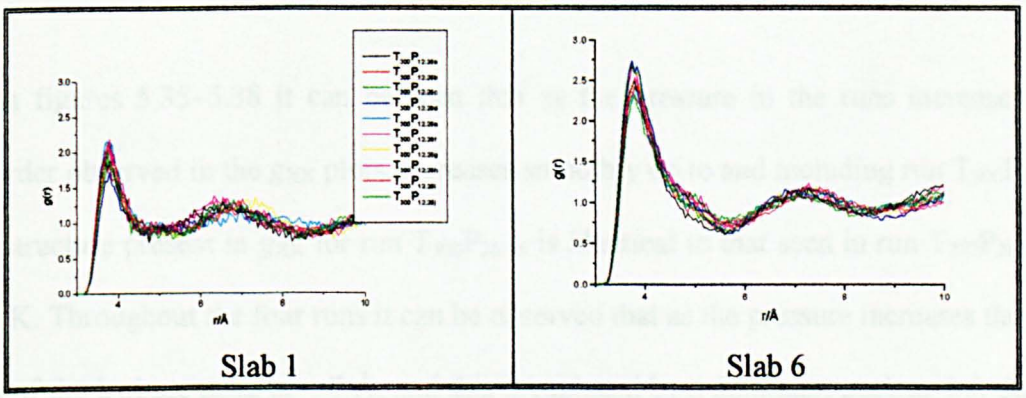

Figure 5.37 Radial distribution functions g_{XX} for run $T_{300}P_{12.26}$. The legend is the same for each plot.

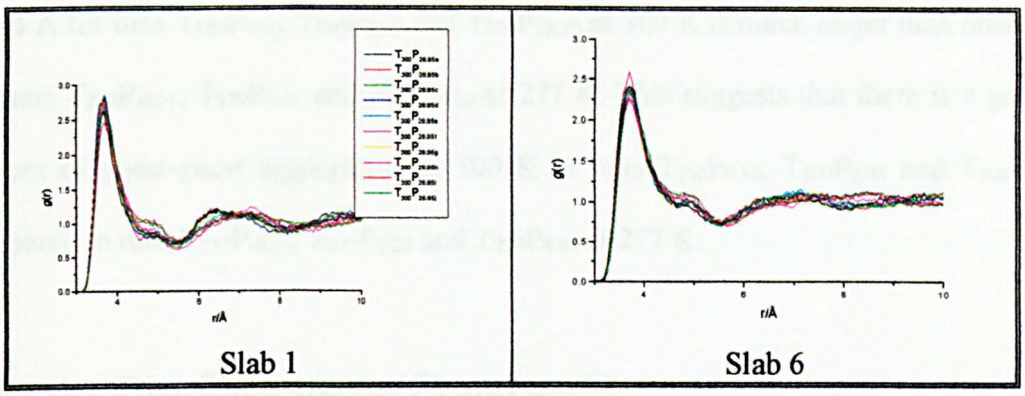

Figure 5.38 Radial distribution functions g_{XX} for run $T_{300}P_{26.95}$. The legend is the same for each plot.

From figures 5.35–5.38 it can be seen that as the pressure in the runs increases the disorder observed in the g_{XX} plots decreases smoothly up to and including run $T_{300}P_{26.95}$, the structure present in g_{XX} for run $T_{300}P_{26.95}$ is identical to that seen in run $T_{277}P_{26.59}$ at 277 K. Throughout the four runs it can be observed that as the pressure increases there is loss of the hydrate peak at ~ 7 Å, and this is replaced by a dominant peak at 4 Å due to guest-guest aggregation in the system. As the pressure increase this first peak becomes narrower, taller, and more symmetric. By the time we reach run $T_{300}P_{12.26}$ the RDF for slab 1 now seems like a symmetric two-peak RDF, with peaks at 3.9 and 6.8 Å, however for run $T_{300}P_{12.26}$ slab 6 this has shifted to peaks at 3.9 and 7.2 Å, with the hint of a shoulder growing at just below 5 Å. For run $T_{300}P_{26.95}$, we then see a peak below 4 Å, a clear shoulder at just below 5 Å, and a second peak at about 7 Å; this is stable in slab 6, but grows in slab 1.

The main difference between the g_{XX} plots at 300 K compared to 277 K is that the peak at ~ 4 Å for runs $T_{300}P_{0.16}$, $T_{300}P_{2.93}$ and $T_{300}P_{12.26}$ at 300 K is much larger than observed for runs $T_{277}P_{-0.01}$, $T_{277}P_{0.21}$ and $T_{277}P_{4.04}$ at 277 K. This suggests that there is a greater amount of guest-guest aggregation at 300 K in runs $T_{300}P_{0.16}$, $T_{300}P_{2.93}$ and $T_{300}P_{12.26}$ compared to runs $T_{277}P_{-0.01}$, $T_{277}P_{0.21}$ and $T_{277}P_{4.04}$ at 277 K.

z-density Distributions–$\rho_O(Z)$ and $\rho_G(Z)$

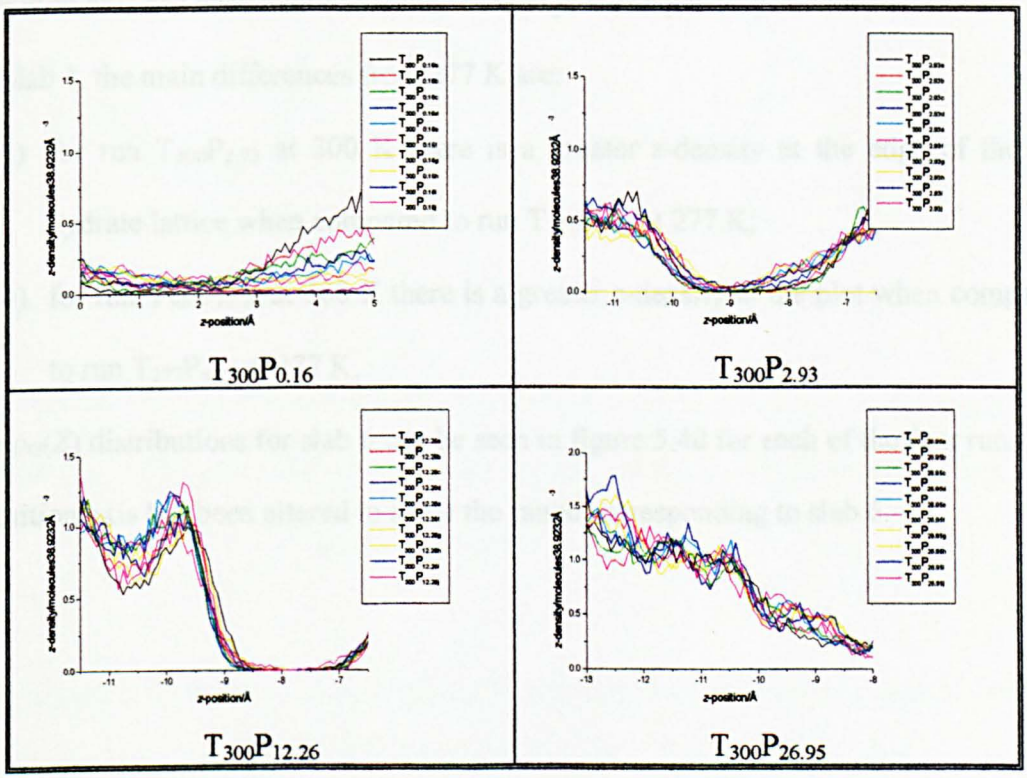

Figure 5.39 $\rho_G(Z)$ distributions for slab 1 in runs $T_{300}P_{0.16}$, $T_{300}P_{2.93}$, $T_{300}P_{12.26}$ and $T_{300}P_{26.95}$. Differences in the z-axis scale are merely due to translational shifts of the hydrate slab prior to simulation.

The distribution of oxygen and guest carbon sites along the surface normal have been calculated from each of the four systems. The distribution of O atoms across the two interfaces showed no interesting departures from the behaviour at 277 K, and so are not discussed further here. The distribution of guest methane and propane molecules is also similar to that seen at 277 K, but some differences are apparent (see figures 5.39 and 5.40).

The $\rho_G(Z)$ distributions for slab 1 can be seen in figure 5.39 for each of the four runs, the z-position axis has been altered to show the range corresponding to slab 1.

For slab 1, the main differences from 277 K are:

a) for run $T_{300}P_{2.93}$ at 300 K there is a greater z-density at the edge of the gas hydrate lattice when compared to run $T_{277}P_{0.21}$ at 277 K;

b) for run $T_{300}P_{12.26}$ at 300 K there is a greater z-density in the plot when compared to run $T_{277}P_{4.04}$ at 277 K.

The $\rho_G(Z)$ distributions for slab 6 can be seen in figure 5.40 for each of the four runs, the z-position axis has been altered to show the range corresponding to slab 6.

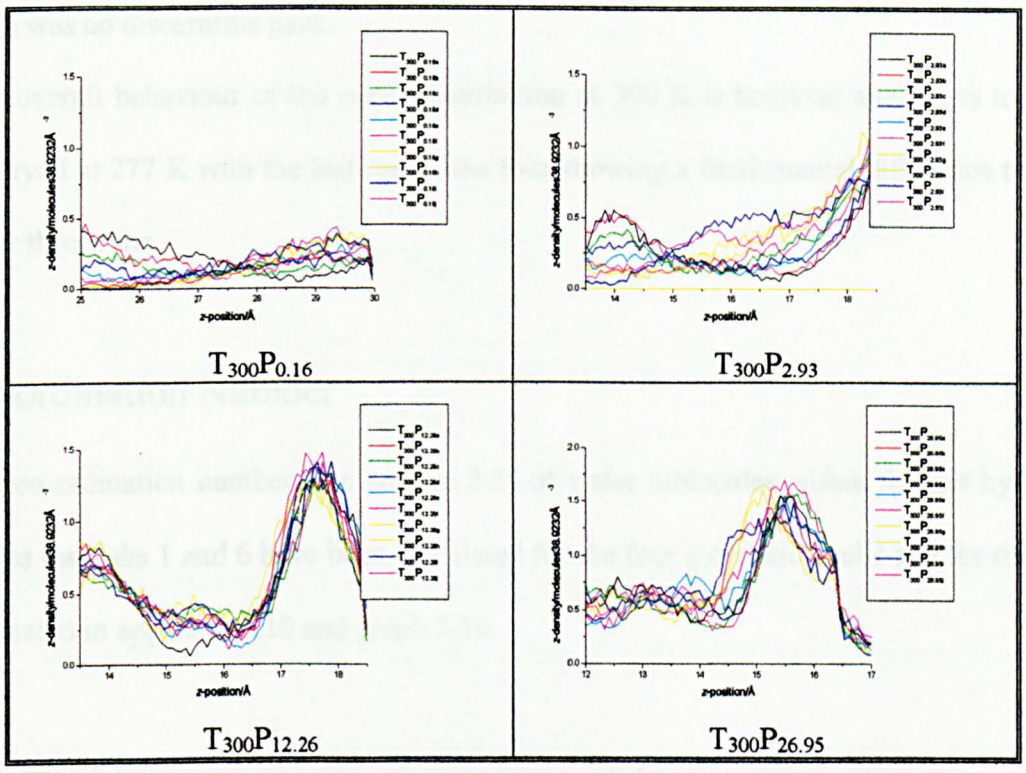

Figure 5.40 $\rho_G(Z)$ distributions for slab 6 in runs $T_{300}P_{0.16}$, $T_{300}P_{2.93}$, $T_{300}P_{12.26}$ and $T_{300}P_{26.95}$. Differences in the z-axis scale are merely due to translational shifts of the hydrate slab prior to simulation.

From figure 5.40 the $\rho_G(Z)$ distributions for slab 6 show a similar behaviour to slab 6 at 277 K. Run $T_{300}P_{0.16}$ at 300 K shows an identical behaviour to that observed for run $T_{277}P_{-0.01}$ at 277 K. Run $T_{300}P_{2.93}$ at 300 K shows a similar behaviour to that observed for run $T_{277}P_{0.21}$ at 277 K, however there is a much larger peak observed for run $T_{300}P_{2.93}$ at ~ 18.5 Å in the $\rho_O(Z)$ distribution when compared to 277 K. Run $T_{300}P_{12.26}$ at 300 K as for run $T_{300}P_{2.93}$ shows a much larger peak observed at ~ 18.5 Å in the $\rho_O(Z)$ distribution when compared to run $T_{277}P_{4.04}$ at 277 K. Run $T_{300}P_{26.95}$ at 300 K shows a single broad

peak in the $\rho_O(Z)$ distribution at ~ 15.5 Å as opposed to run $T_{277}P_{26.59}$ at 277 K where there was no discernible peak.

The overall behaviour of the $\rho_O(Z)$ distribution at 300 K is however analogous to that observed at 277 K with the last run of the four showing a fundamental difference to the other three runs.

Co-ordination Number

The co-ordination number (see section 3.5) of water molecules within the gas hydrate lattice for slabs 1 and 6 have been calculated for the four simulation cells and the data is presented in appendix 5.10 and graph 5.16.

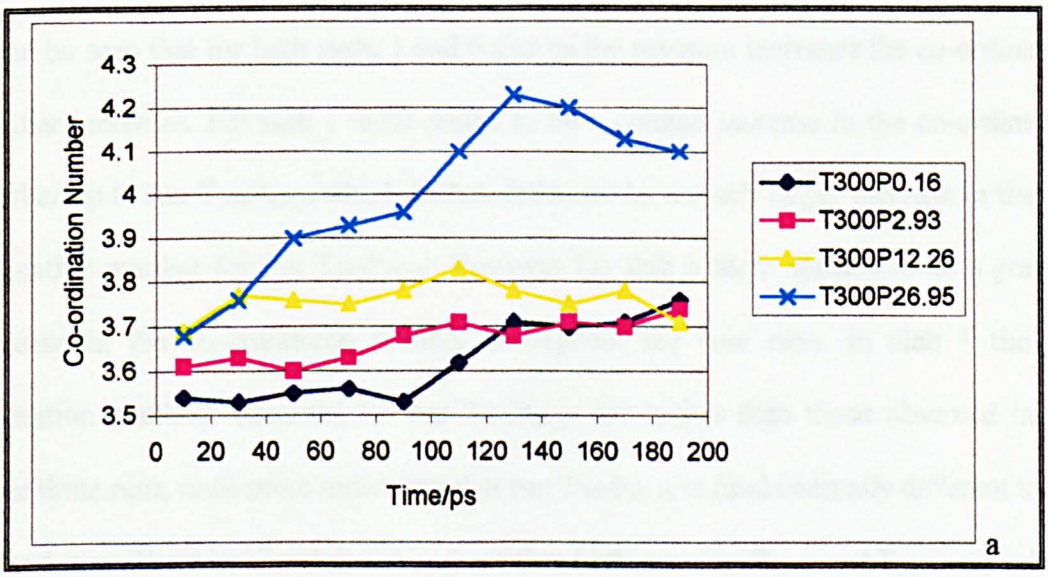

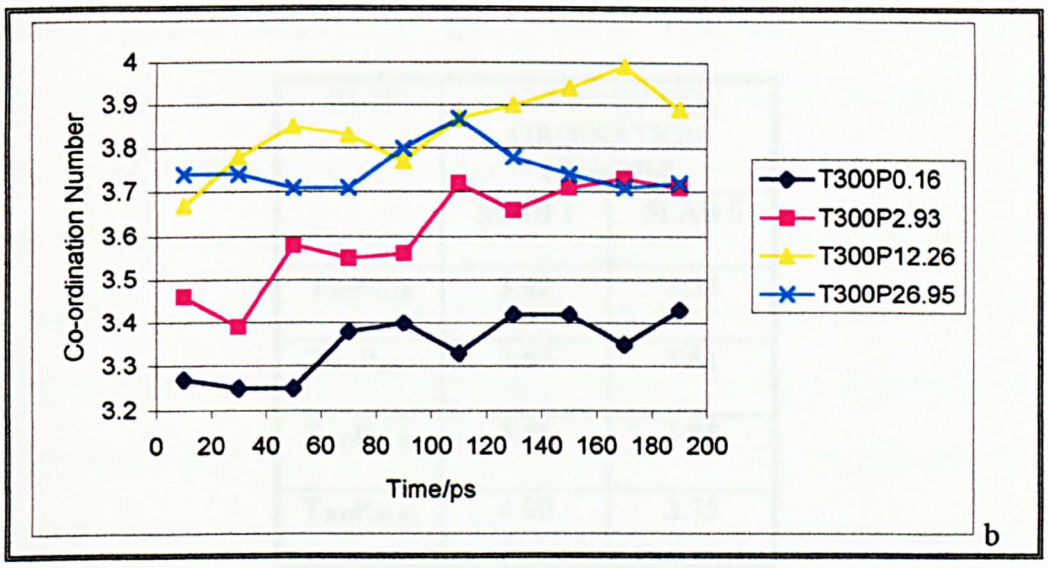

Graph 5.16 Co-ordination number for runs $T_{300}P_{0.16}$, $T_{300}P_{2.93}$, $T_{300}P_{12.26}$ and $T_{300}P_{26.95}$: slab 1 (a) and slab 6 (b). Numerical values are also given in appendix 5.10.

It can be seen that for both slabs 1 and 6 that as the pressure increases the co-ordination number increases. For slab 1 there seems to be a gradual increase in the co-ordination number up to run $T_{300}P_{12.26}$ which is then followed by a much larger increase in the co-ordination number for run $T_{300}P_{26.95}$. However for slab 6 there appears to be a gradual increase in the co-ordination number throughout the four runs. In slab 1 the co-ordination numbers observed for run $T_{300}P_{26.95}$ are higher than those observed in the other three runs, once more indicating that run $T_{300}P_{26.95}$ is fundamentally different to the other 3 runs. However for slab 6 it appears that both runs $T_{300}P_{12.26}$ and $T_{300}P_{26.95}$ exhibit a similar behaviour with higher co-ordination numbers than observed for runs $T_{300}P_{0.16}$ and $T_{300}P_{2.93}$. In general the co-ordination number for slab 1 in nearly all instances is higher than the co-ordination number for slab 6. This is supported by the average co-ordination numbers for slabs 1 and 6 in the four runs shown in table 5.14.

RUN	AVERAGE CO-ORDINATION NUMBER	
	SLAB 1	SLAB 6
$T_{300}P_{0.16}$	3.62	3.35
$T_{300}P_{2.93}$	3.67	3.61
$T_{300}P_{12.26}$	3.76	3.85
$T_{300}P_{26.95}$	4.00	3.75

Table 5.14 Average co-ordination number for slabs 1 and 6 in runs $T_{300}P_{0.16}$, $T_{300}P_{2.93}$, $T_{300}P_{12.26}$ and $T_{300}P_{26.95}$.

5.4 Conclusions

In this chapter we presented the results of a series of molecular dynamics simulations on a structure II gas hydrate lattice exhibiting the {1,1,1; -0.001} and {1,1,1; 0.999} surfaces.[15] The simulation results were characterised using radial distribution functions, *z*-density distributions, self-diffusion coefficients, co-ordination numbers and by examining the local order around water. This analysis was done separately for the central ('bulk') and surface regions of a thin hydrate film under a methane/propane gas mixture. Simulations were carried out at 277 K for pressures in the range –0.01–26.59 kbar and at 300 K for pressures in the range 0.16–26.95 kbar.

The results of the simulations indicate a number of interesting features. Firstly the 26.59 kbar run at 277 K and the 26.95 kbar run at 300 K exhibited a distinctly different

behaviour to that shown by the other systems studied. This difference of behaviour led to the conclusion that the gas hydrate lattice in these systems was fundamentally different to that found in the other systems suggesting the presence of a distinct high-density phase. The phase transition occurred somewhere between 14.93 and 26.59 kbar at 277 K and between 12.26 and 22.75 kbar at 300 K. The high-density phase could not be completely characterised, as it did show some indications of being an amorphous solid; however it did show clear evidence of a hydrogen bond network that was strongly perturbed away from tetrahedral, with typical O...O...O angles being in excess of 130° and co-ordination numbers that differed substantially from 4.

Secondly on increasing the pressure within the system the degree of melting observed decreased such that little melting was observed in the core of the hydrate film at 277 K between 0.10 and 0.94 kbar and between 0.50 and 6.04 kbar at 300 K the bulk of the system appeared stable on the time scale of simulations carried out, namely 200 ps. In addition at 277 K the 4.04 kbar system and at 300 K the 12.26 kbar system were completely stable on the time scale of simulations carried out. These two systems will now be further investigated in the following chapter to investigate the behaviour of the carboxylates and sulphonates upon the gas hydrate lattice.

Finally, although slabs 1 and 6, 2 and 5 and 3 and 4 are in the same relative position in the gas hydrate lattice, *i.e.* slab 6 being at the top and slab 1 at the bottom of the gas hydrate lattice, there were differences noted in the behaviour of the pairs of slabs. The differences observed between the two surfaces correspond to real topological variations between the two interfaces, and perhaps suggest that this might have implications for how inhibitors should be targeted at growing gas hydrate micro-crystals.

5.5 References

[1] Handa Y.P., Tse J.S., Klug D.D., Whalley E., *J. Chem. Phys.*, **94**, 1991, 623.

[2] Dyadin Y.A., Larionov E.G., Mirinskij D.S., Mikina T.V., Aladko E.Y., Starostina L.I., *J. Inclusion Phenom. Mol. Recogn.*, **28**, 1997, 271.

[3] Collins M.J., Ratcliffe C.I., Ripmeester J.A., *J. Phys. Chem.*, **94**, 1990, 157.

[4] Davidson D.W., Handa Y.P., Ripmeester J.A., *J. Phys. Chem.*, **90**, 1986, 6549.

[5] Gough S.R., Davidson D.W., *Can. J. Chem.*, **49**, 1971, 2691.

[6] Dyadin Y.A., Kuznetsov P.N., Yakovlev I.I., Pyrinova A.V., *Dokl. Chem.*, **208**, 1973, 9.

[7] Ross R.G., Andersson P., *Can. J. Chem.*, **60**, 1982, 881.

[8] Sargent D.F., Calvert L.D., *J. Phys. Chem.*, **70**, 1966, 2689.

[9] van Hinsberg M.G.E., Scheerboom M.I.M., Schouten J.A., *J. Chem. Phys.*, **99**, 1993, 752.

[10] Zakrzewski M., Klug D.D., Ripmeester J.A., *J. Inclusion Phenom. Mol. Recogn.*, **17**, 1994, 237.

[11] Lotz H.T., Schouten J.A., *J. Chem. Phys.*, **111**, 1991, 10242.

[12] Londono D., Kuhs W.F., Finney J.L., *Nature*, **332**, 1988, 141.

[13] Londono D., Kuhs W.F., Finney J.L., *J. Chem. Phys.*, **97**, 1992, 547.

[14] Vos W.L., Finger L.W., Henley R.J., Mao H-K., *Phys. Rev. Letts.*, **71**, 1993, 3150.

[15] Carver T.J., Drew M.G.B., Rodger P.M., *J. Chem. Soc. Faraday Trans.*, **92**, 1996, 5029.

[16] McMullan R.K., Kvick A., *Acta. Cryst.*, **B46**, 1990, 390.

[17] Berensden H.J.C., Postma J.P.M., van Gunsteren W.F., Hermans J., *Intermolecular Forces*, B. Pullman ed., D. Reidel Publishing Co., 1981, 331.

[18] Jorgensen W.L., Chandrasekhar J., Madura J.D., *J. Chem. Phys.*, **79**, 1983, 926.

[19] Jorgensen J.L., Madura J.D., Swenson C.J., *J. Am. Chem. Soc.*, **106**, 1984, 6638.

[20] Cerius^2, Molecular Simulations Inc., San Diego, USA.

[21] Smith W., Forester T.R., *J. Mol. Graphics*, **14**, 1996, 136.

[22] Ewald P., *Ann. Phys.*, **64**, 1921, 253.

[23] Ryckaert J.P. Cicotti G, Berensden H.J.C., *J. Comp. Phys.*, **23**, 1977, 327.

[24] Fidler J., Rodger P.M., *J Phys Chem B*, **103**, 1999, 7695.

CHAPTER 6

INHIBITOR BEHAVIOUR AT GAS HYDRATE SURFACES

6 Introduction

In this chapter the investigation into the gas hydrate surface behaviour of the sulphonates and carboxylates is outlined. This work was undertaken because kinetic inhibitors act at the liquid water/hydrate interface; however it is not clear whether the kinetic inhibitors affect the hydrate surface or liquid water structure or a mixture of the two. Therefore by investigating the gas hydrate surface behaviour alone we can identify any activity in this region. In addition, the results obtained from chapter 4 on the liquid behaviour of the sulphonates and carboxylates can be coupled with the results obtained in this chapter to gain a clearer understanding of the mode of action of kinetic inhibitors. The investigation into the surface behaviour of the kinetic inhibitors was achieved by taking a stable gas hydrate film identified in chapter 5 and adding the inhibitors to the system. The chapter is divided into three parts as outlined below.

6.1 Simulation details—outlining the 'preparation' of the systems studied along with the simulations carried out.

6.2 Results and discussion of the simulations performed.

6.3 Conclusions.

6.1 Simulation Details

6.1.1 System Overview

In this section the preparation of the systems for the study of the carboxylates and sulphonates in the presence of a structure II gas hydrate lattice is outlined.

6.1.2 System Preparation

Molecules Studied

The molecules studied are the same as those used in chapter 4, and as described in section 4.2.2. The names and formulas of the three carboxylates and the three sulphonates are shown in table 6.1 along with the abbreviations used throughout this thesis.

MOLECULE	FORMULA	ABBREVIEATION
N,N,N-tributylammonium-1-(2-ethylcarboxylate)	$(C_4H_9)_3N^+CH_2COO^-$	tba1C
N,N,N-tributylammonium-1-(3-propylcarboxylate)	$(C_4H_9)_3N^+(CH_2)_2COO^-$	tba2C
N,N,N-tributylammonium-1-(4-butylcarboxylate)	$(C_4H_9)_3N^+(CH_2)_3COO^-$	tba3C
N,N,N-tributylammonium-1-(1-methylsulphonate)	$(C_4H_9)_3N^+CH_2SO_3^-$	tba1S
N,N,N-tributylammonium-1-(2-ethylsulphonate)	$(C_4H_9)_3N^+(CH_2)_2SO_3^-$	tba2S
N,N,N-tributylammonium-1-(3-propylsulphonate)	$(C_4H_9)_3N^+(CH_2)_3SO_3^-$	tba3S

Table 6.1 Molecular formulas and abbreviations. Note 1, 2, 3 in the abbreviations refers to the number of CH_2 spacer groups, while C and S refers to whether the inhibitor is an amine Carboxylate or amine Sulphonate.

Molecular Conformations/Charges

Inhibitor conformations and charges are the same as those used in chapter 4, and as described in section 4.2.2. A summary of the initial conformations of the six molecules studied is reproduced in figure 6.1.

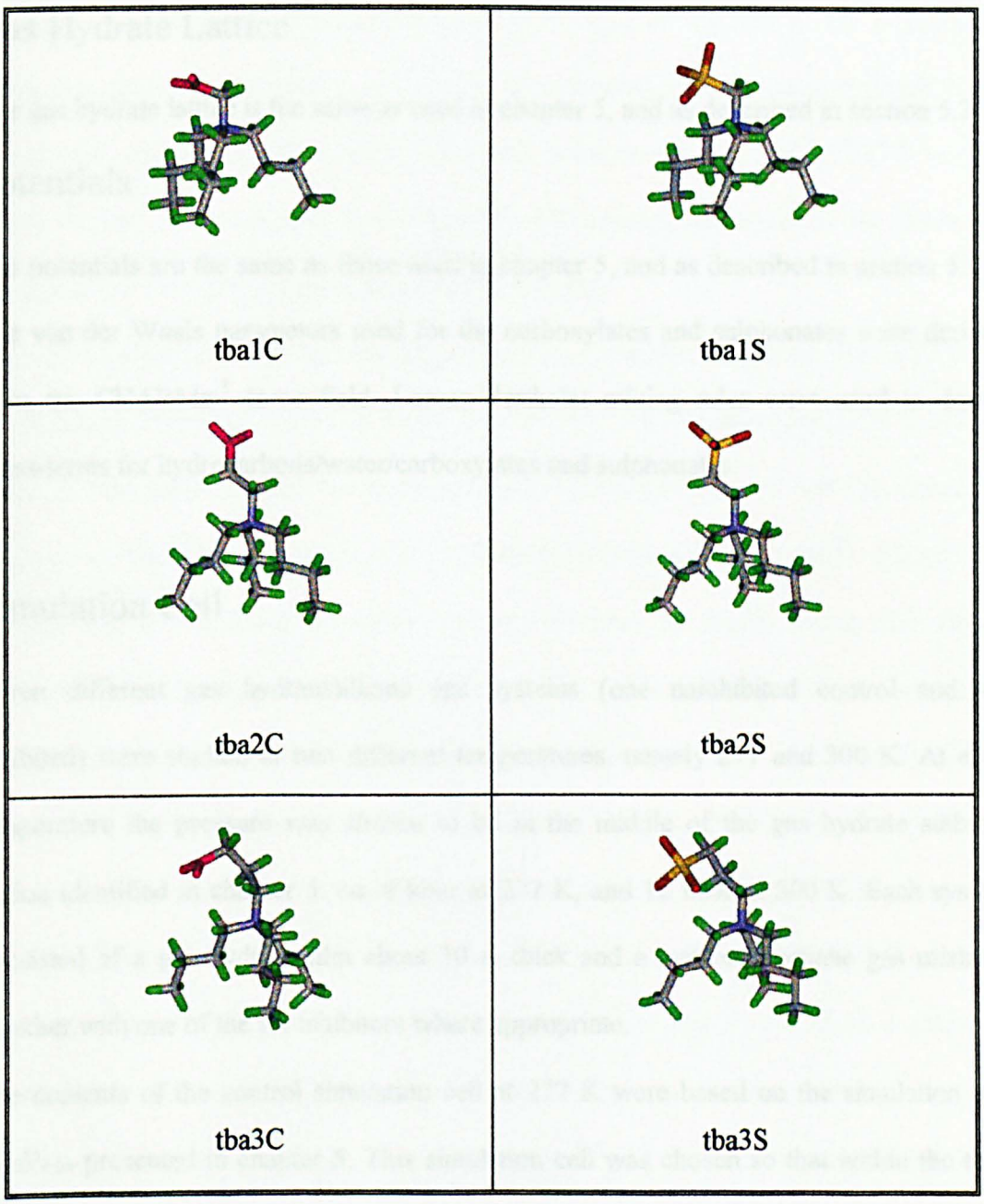

Figure 6.1 The initial conformations of the six potential inhibitors listed in table 6.1. Carbon–grey, hydrogen–green, nitrogen–blue, sulphur–yellow, carboxylate oxygen–pink, sulphonate oxygen–red.

Gas Hydrate Lattice

The gas hydrate lattice is the same as used in chapter 5, and as described in section 5.2.2.

Potentials

The potentials are the same as those used in chapter 5, and as described in section 5.2.2. The van der Waals parameters used for the carboxylates and sulphonates were derived from the CHARMm[1] force field. Lorenz-Berthelot mixing rules were used to derive cross-terms for hydrocarbons/water/carboxylates and sulphonates.

Simulation Cell

Seven different gas hydrate/alkane gas systems (one uninhibited control and six inhibited) were studied at two different temperatures, namely 277 and 300 K. At each temperature the pressure was chosen to be in the middle of the gas hydrate stability region identified in chapter 5: *ca.* 4 kbar at 277 K, and 12 kbar at 300 K. Each system consisted of a gas hydrate film about 30 Å thick and a methane/propane gas mixture, together with one of the six inhibitors where appropriate.

The contents of the control simulation cell at 277 K were based on the simulation cell $T_{277}P_{4.04}$ presented in chapter 5. This simulation cell was chosen so that within the time scale of investigation in chapter 5, namely 200 ps, the gas hydrate lattice appeared stable, with the average pressure being 4.04 kbar.

Upon inspection of $T_{277}P_{4.04}$ it was found that approximately 30 propane and 50 methane molecules occupied the headspace above the gas hydrate film, with the *z*-dimension of the headspace being ~ 10.9 Å. This was then used as the basis for the creation of the 277 K control simulation cell in this chapter.

Two cells were created with dimensions of 21.20 x 24.48 x 43.60 Å, the *z*-dimension being 4 x 10.9 Å to ensure a sufficiently large headspace was created to allow the subsequent addition of the carboxylates and sulphonates. The SORPTION module within Cerius^{2},^{2} was then used to add 4 x 30 = 120 propane molecules to one of the two boxes and 4 x 50 = 200 methane molecules to the other.

The cell containing the gas hydrate lattice ($T_{277}P_{4.04}$ from chapter 5) was taken and the *z*-dimension of the cell increased by 43.60 Å to create a cell of dimensions 21.20 x 24.48 x 73.58 Å. Into the headspace above the gas hydrate lattice in this cell was introduced the contents of both the simulation cells created previously within Cerius^{2},^{2} namely 120 propane and 200 methane molecules; this was achieved by simply cutting and pasting the contents of the two cells. The dimension of the resultant simulation cell (containing the gas hydrate lattice and methane/propane gas mixture) was then increased by 2 Å in the *z*-direction and the contents of the cell translated + 1 Å in the *z*-dimension. This was done so as to avoid difficulties that may arise from bad contacts across the boundaries of the simulation cell. This led to a final control simulation cell at 277 K with dimensions of 21.20 x 24.48 x 75.58 Å. This cell was then taken and subjected to a series of equilibration runs, outlined in figure 6.2, to relieve internal stresses within the system. These simulations were carried out with DL_POLY[3] and, unless otherwise stated, were in the [*N*, *V*, *T*] ensemble with a thermostat value of 0.1 ps and a time step of 1 fs. Long-range electrostatic interactions were evaluated using an Ewald summation,[4] while all other interactions were truncated for distances in excess of 9.5 Å. Periodic boundary conditions in three dimensions were employed to give an infinite hydrate film *ca.* 30 Å thick. Bond lengths, bond angles and torsions for the carboxylates and sulphonates were

treated dynamically as described in chapter 2. A summary of the equilibration simulations performed can be seen in figure 6.2.

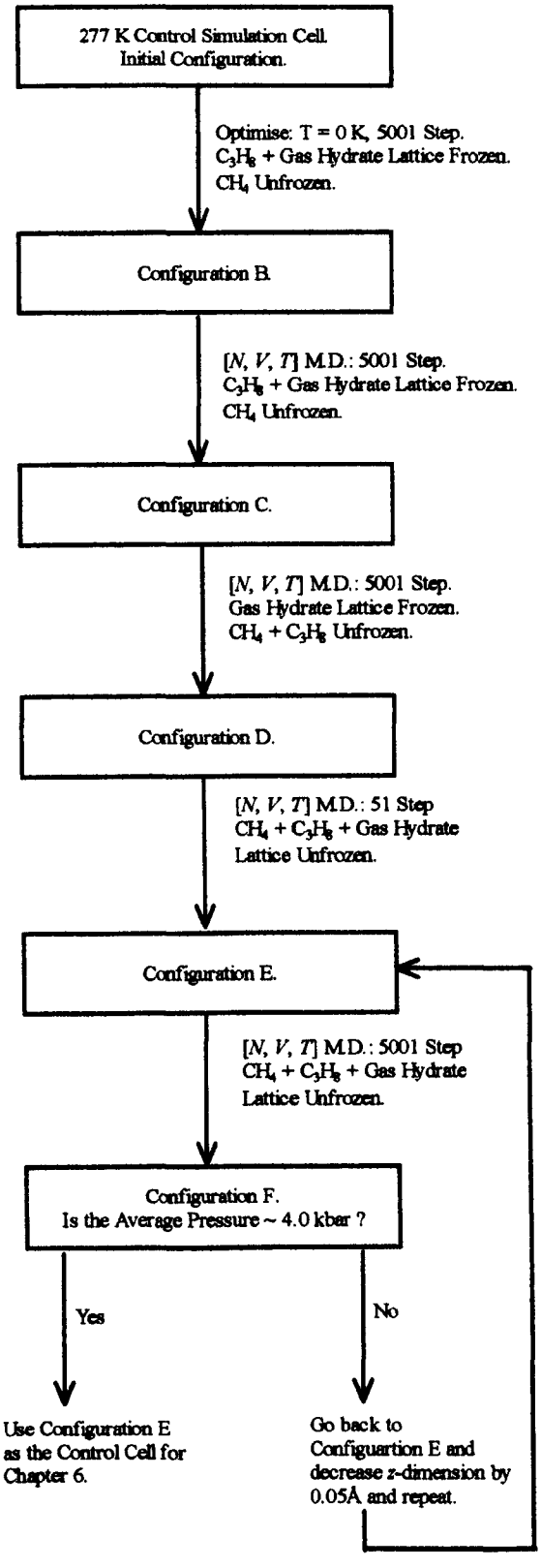

Figure 6.2 Equilibration procedure for the control simulation cell at 277 K.

The simulation cells for the carboxylates and sulphonates were created by taking a copy of the configuration E control cell outlined in figure 6.2 and inserting one of the solute molecules. The inhibitor was inserted in such a way that any gas molecules, namely hydrocarbons, that created a bad contact were removed; bad contacts were defined using the van der Waals radius of the respective atoms. Therefore any solvent atoms that overlapped with the molecule were removed along with the rest of the solvent molecule to which they belonged. Upon insertion of the carboxylates and sulphonates, the position of each of the molecules was inspected to ensure that the molecules were positioned close to the surface of the gas hydrate lattice, but not within it. Once each of the carboxylates and sulphonates had been inserted into a copy of the configuration E control cell then the system iterated through the E↔F cycle in figure 6.2 until a pressure of *ca.* 4 kbar was obtained. Throughout this process the inhibitor was kept immobile. A summary of the simulation cells prepared for investigation at 277 K is given in table 6.2.

CELL	BOX DIMENSIONS/Å			AVERAGE PRESSURE - over 5001 steps/kbar	HEADSPACE GAS COMPOSITION (NO. MOLECULES)		TOTAL NUMBER OF 'GAS' MOLECULES	
	X	Y	Z		CH_4	C_3H_8	CH_4	C_3H_8
Control	21.2	24.48	72.6	4.08	200	120	248	144
tba1C	21.2	24.48	71.9	4.07	192	117	240	141
tba2C	21.2	24.48	70.9	4.08	191	113	239	137
tba3C	21.2	24.48	71.3	4.08	190	115	238	139
tba1S	21.2	24.48	71.9	4.09	188	114	236	138
tba2S	21.2	24.48	71.2	4.09	190	115	238	139
tba3S	21.2	24.48	71.8	4.12	193	116	241	140

Table 6.2 Summary of the seven simulation cells at 277K. Note the total number of gas molecules = the headspace gas molecules + the gas hydrate lattice gas molecules, (48 CH_4 and 24 C_3H_8).

The contents of the control simulation cell at 300 K were based on the simulation cell $T_{300}R_{12.26}$ presented in chapter 5. This simulation cell was chosen so that within the time scale of investigation in chapter 5, namely 200 ps, the gas hydrate lattice appeared stable, with average pressure being 12.26 kbar. The simulation cells were prepared using

the same technique outlined above. In this case, 150 propane molecules and 250 methane molecules were inserted into a 21.20 × 24.48 × 34.50 Å cell, and as before the *iteration through steps E↔F continued until the pressure was ca. 12.3 kbar. A summary* of the simulation cells prepared at 300 K is given in table 6.3.

CELL	BOX DIMENSIONS/Å			AVERAGE PRESSURE –over 5001 steps/kbar	HEADSPACE GAS COMPOSITION (NO. MOLECULES)		TOTAL NUMBER OF 'GAS' MOLECULES	
	X	Y	Z		CH_4	C_3H_8	CH_4	C_3H_8
Control	21.2	24.48	73.0	12.32	250	150	298	174
tba1C	21.2	24.48	72.25	12.39	244	145	292	169
tba2C	21.2	24.48	72.1	12.37	244	144	292	168
tba3C	21.2	24.48	71.6	12.31	241	142	289	166
tba1S	21.2	24.48	72.0	12.31	242	144	290	168
tba2S	21.2	24.48	71.6	12.35	243	141	291	165
tba3S	21.2	24.48	71.95	12.33	241	144	289	168

Table 6.3 Summary of the seven simulation cells at 300 K. Note the total number of gas molecules = the headspace gas molecules + the gas hydrate lattice gas molecules (48 CH_4 and 24 C_3H_8).

6.1.3 System Study

Simulations Performed

The fourteen simulation cells described above were then subjected to longer simulations in order to study the effect of the six molecules upon the surface of a structure II gas hydrate. Once again all of the simulations were carried out using DL_POLY,[3] in the [*N*, *V*, *T*] ensemble with a thermostat value of 0.1 ps. Simulations were carried out at 277 K and 300 K for 200 000 steps with a time step of 1 fs.

Simulation Analysis

The simulations performed at 277 and 300 K were analysed using the techniques outlined in chapter 3 to determine radial distribution functions for the oxygen–oxygen distribution, g_{OO}, and also for the guest–guest distribution, g_{XX}. For the calculation of the radial distribution functions the gas hydrate lattice was split into six slabs each with dimensions 21.2 x 24.48 x 5 Å; the width of the slabs were such that they were *ca.* half the crystallographic repeat distance for this surface, and therefore the properties of slabs 1, 3 and 5 may differ from slabs 2, 4 and 6. Slab 1 refers to the bottom slab (i.e. the {1,1,1; 0.999} surface[6]), and slab 6 refers to the top slab (i.e. the {1,1,1; -0.001} surface[6]), of the gas hydrate lattice, *i.e.* the two surfaces. Within each of the six slabs the radial distribution functions were then calculated. Other properties reported in this chapter included the *z*-density profiles for O and C atoms, orientational time correlation functions, mean square displacements and various order parameters.

In addition to the layer decomposition, analyses have also been performed for water in various solvation shells around the inhibitor. For this purpose it was decided to split the carboxylates and sulphonates into chemically/symmetrically similar regions as shown in figure 6.3. The rationale for this grouping of carbon sites is summarised below:

a) C1, which is the carbons immediately next to the nitrogen atom;

b) C2, which is the central carbons of the butyl chains;

c) C3, which is the terminal carbons of the butyl chains.

d) C4, which is the carbons immediately next to the headgroup moiety.

Note that these definitions (and the associated colour coding) are the same as those used in chapter 4.

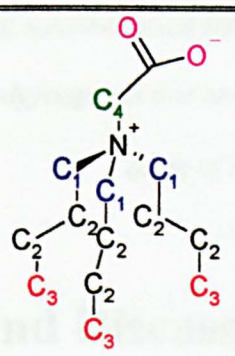 tba1C	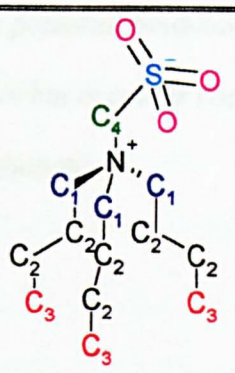 tba1S
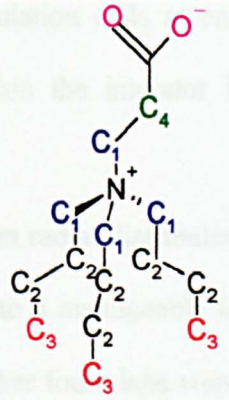 tba2C	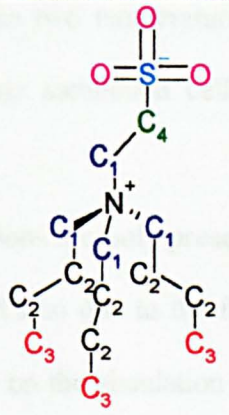 tba2S
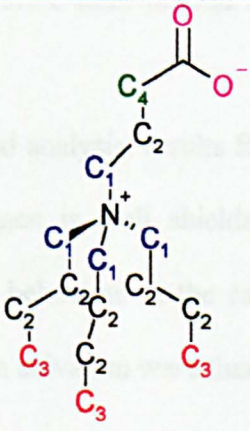 tba3C	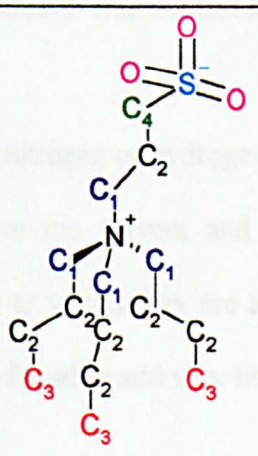 tba3S

Figure 6.3 Numbering schemes used for the six potential inhibitors. Note the C atom of the carboxylates headgroup has not been shown but is colour coded the same as the S atom of the sulphonates.

6.2 Results and Discussion

The results in this section are decomposed according to: i) location within the hydrate film in the seven simulation cells at each of the two temperatures; or ii) proximity to functional groups within the inhibitor in the six simulation cells at each of the two temperatures.

For the gas hydrate film radial distribution functions are only presented for slabs 1 and 6 in order to keep data to a manageable level and also due to the fact that in chapter 5 it was shown that the other four slabs were stable on the simulation time scale. In addition none of these simulations in this chapter showed evidence of the inhibitors accessing the inner slabs of the hydrate film; instead the inhibitor was confined to the region in and above slab 6.

For the inhibitor-based analysis, results for the nitrogen or hydrogen solute atoms are not discussed. The nitrogen is well shielded from the solvent and the hydrogen atoms generate very similar behaviour to the carbons to which they are attached. The data for nitrogen and hydrogen solvation were therefore found to add very little to the discussion.

6.2.1 277 K Interfacial Analysis

Radial Distribution Functions

The radial distribution functions (see section 3.2) for oxygen atoms, g_{OO}, and for guest atoms, g_{XX}, have been calculated for each of the simulations. In the following sections these plots are presented along with a summary of the first and second peak positions.

Interfacial Analysis Oxygen–Oxygen Radial Distribution Functions

The g_{OO} for slabs 1 and 6 can be seen in figure 6.4 and a summary of the peak positions in table 6.4 and 6.5.

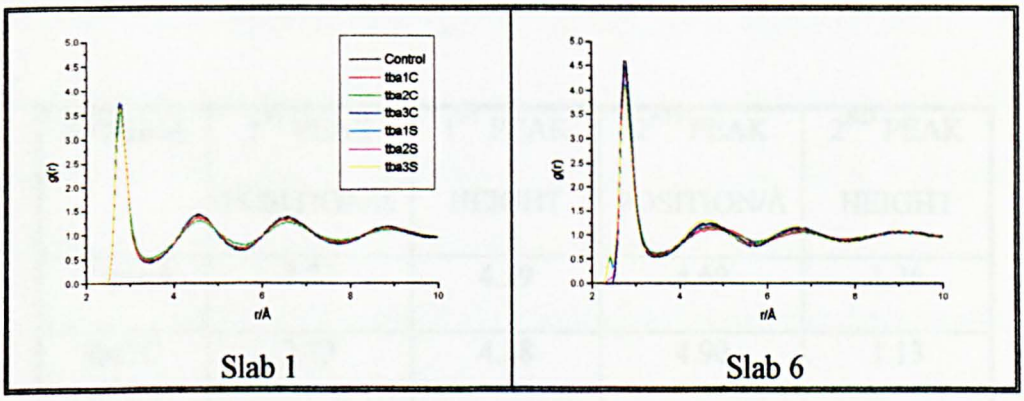

Figure 6.4 Radial distribution functions g_{OO} for slab 1 and 6. The legend is the same for each plot.

SYSTEM	1ST PEAK POSITION/Å	1ST PEAK HEIGHT	2ND PEAK POSITION/Å	2ND PEAK HEIGHT
Control	2.73	3.70	4.53	1.43
tba1C	2.73	3.67	4.53	1.36
tba2C	2.73	3.56	4.53	1.29
tba3C	2.73	3.76	4.53	1.42
tba1S	2.78	3.69	4.53	1.44
tba2S	2.73	3.66	4.58	1.39
tba3S	2.73	3.67	4.58	1.40

Table 6.4 g_{OO} summary for slab 1. Resolution of values is 0.05 Å.

SYSTEM	1ST PEAK POSITION/Å	1ST PEAK HEIGHT	2ND PEAK POSITION/Å	2ND PEAK HEIGHT
Control	2.73	4.59	4.69	1.26
tba1C	2.73	4.38	4.90	1.13
tba2C	2.78	4.43	4.74	1.16
tba3C	2.73	4.50	4.53	1.25
tba1S	2.73	4.13	4.69	1.25
tba2S	2.73	4.34	4.74	1.20
tba3S	2.73	4.09	4.64	1.31

Table 6.5 g_{OO} summary for slab 6. Resolution of values is 0.05 Å.

From this data we can see that for slab 1 the 1st and 2nd peak positions are constant within the resolution of the plots, and there is only a small variation in the 1st and 2nd peak heights. This is a useful check on the reproducibility of the simulations, as the inhibitors were introduced on the slab 6 surface and so should not influence slab 1. The data for slab 6 indicate that the 1st peak positions are constant within the resolution of the plots and that there is only a small variation in the 2nd peak heights. However the 1st peak heights and 2nd peak positions show noticeable variations that depend on the nature of the inhibitor. All the inhibitors tend to lower the height of the first peak, with the effect being greatest for the shorter sulphonates. In contrast, it is the carboxylates that have the greatest effect on the position of the second peak

If we compare slab 6 with slab 1 then we see that the peak positions are essentially the same, the 1st peak height is larger, while the 2nd peak height is smaller for slab 6.

In order to gauge the significance of these variations it is important to determine the variability expected within the simulations. A good way to do this is to compare the results of the control system with the results presented in chapter 5 for $T_{277}P_{4.04}$—the simulation on which the simulations in this chapter were based. The corresponding data for this simulation, averaged over 200 ps, is: the 1st peak position was at 2.76 Å, the 1st peak height was 4.51, the 2nd peak position was at 4.68 Å and the 2nd peak height was 1.26. This shows that the variation between chapter 5 $T_{277}P_{4.04}$ and the control system in this section is: 1st peak position ± 0.03 Å; 1st peak height ± 0.08; 2nd peak position ± 0.01 Å; and 2nd peak height ± 0.00. This variation now allows us to compare the results obtained for the control system and the inhibited systems to quantify whether the differences are due to inhibitor effect or merely variation in the results as was observed for the control run. For the 1st peak position no effect is observed, for the 1st peak height

we can see that the values obtained for all six inhibitors are outside the variation, for the 2nd peak position we can see that values obtained for all inhibitors except tba1S are outside the variation, and for the 2nd peak height we can see that the values obtained for all six inhibitors are outside the variation between the $T_{277}P_{4.04}$ and the control system in this section. This suggests that the differences observed between the control and inhibited systems for slab 6 are indeed real effects and that the inhibitors are affecting the structure of slab 6.

If we consider the results obtained for slab 6 with and without the inhibitor then we can see that:

a) there is no change in the 1st peak position;

b) the 1st peak height shows a reduction for all of the inhibitors;

c) the 2nd peak position decreases with increasing charge separation for the carboxylates, but is constant and in agreement with the control for the sulphonates;

d) the 2nd peak height increases with increasing charge separation for the carboxylates, but is constant and in agreement with the control for the sulphonates.

Interfacial Analysis Guest–Guest Radial Distribution Functions

The guest–guest radial distribution functions, g_{XX}, for slabs 1 and 6 can be seen in figure 6.5. It can be seen that the behaviour of slab 1 and slab 6 are very different. Slab 1 exhibits a g_{XX} radial distribution function with two distinct peaks, at ~ 4 Å and ~ 7 Å, with the peak at ~ 7 Å being much more pronounced than the peak at ~ 4 Å. In contrast

slab 6 exhibits one distinct peak at ~ 4 Å and a small hump at ~ 7.5 Å. The peak observed in g_{XX} at ~ 4 Å is due to guest-guest aggregation in the slab. It can therefore be seen that there is slow guest-guest aggregation in slab 1, but that in slab 6 there is fast guest-guest aggregation. In a completely stable hydrate no guest-guest aggregation would be observed and so based upon this observation we can conclude that slab 6 is less stable than slab 1.

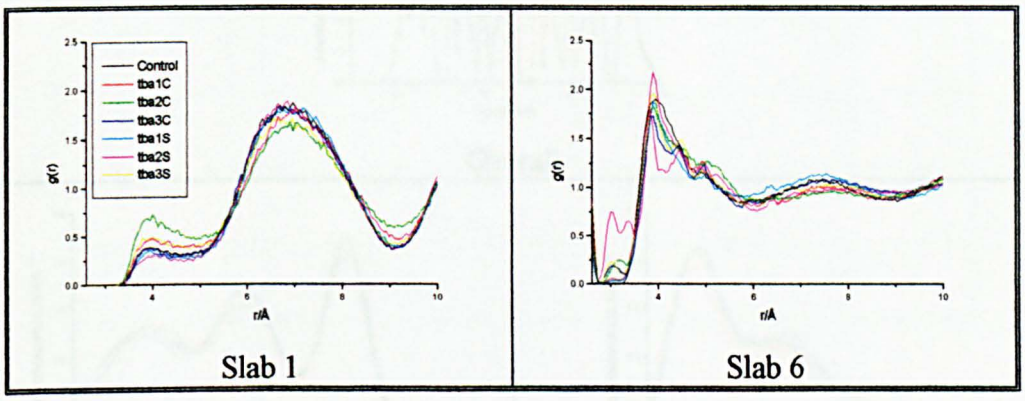

Figure 6.5 Radial distribution functions g_{XX} for slab 1 and 6. The legend is the same for each plot.

z-density Distributions–$\rho_O(Z)$ and $\rho_G(Z)$

The oxygen density distribution along the surface normal ($\rho_O(Z)$) of the gas hydrate lattice has been calculated along with the analogous function for all atoms other than O and H, ($\rho_G(Z)$); note that inhibitor O atoms are included in $\rho_O(Z)$, while other inhibitor atoms (apart from H) are included with the natural gas in $\rho_G(Z)$. All of the $\rho_O(Z)$ distributions are characterised by a central trough corresponding to the centre of the gas

hydrate lattice. In the following sections these plots are presented along with a summary of the central peak spacings.

Interfacial Analysis Oxygen *z*-density Distributions–$\rho_O(Z)$

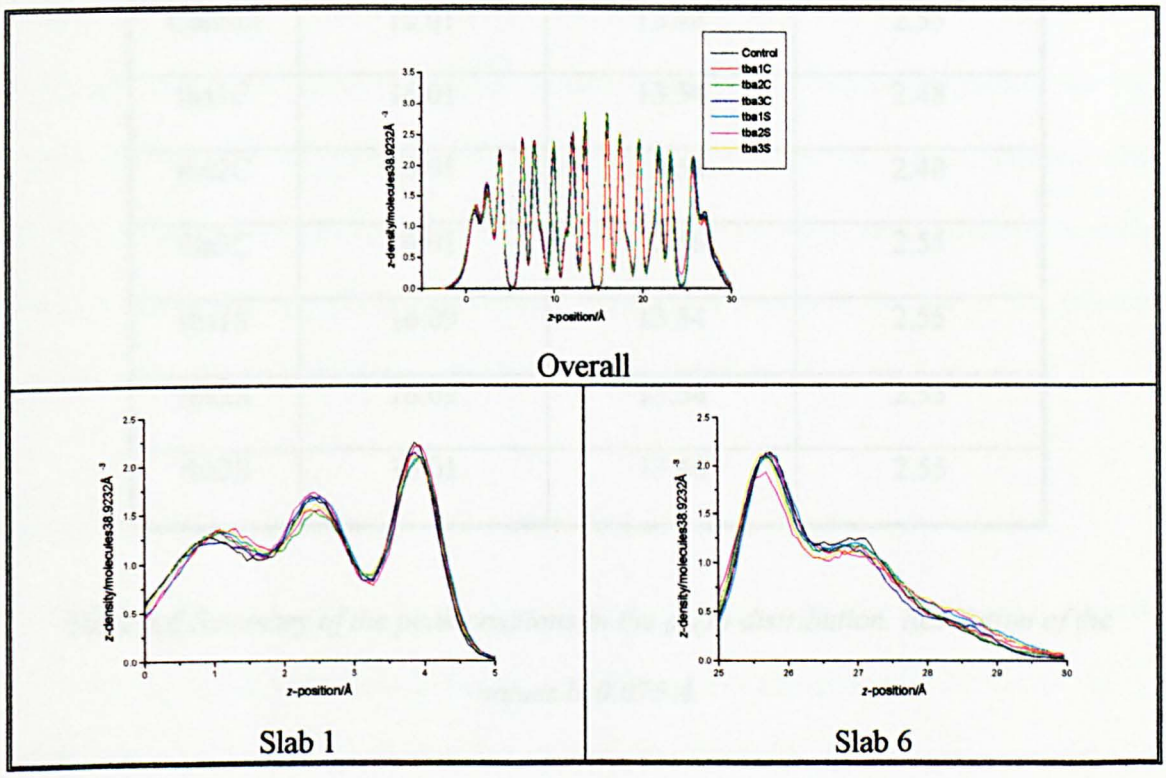

Figure 6.6 $\rho_O(Z)$ distributions for the seven systems. The legend is the same for each plot.

SYSTEM	RIGHT PEAK POSITION/Å	LEFT PEAK POSITION/Å	CENTRAL TROUGH WIDTH/Å
Control	16.01	13.46	2.55
tba1C	16.01	13.54	2.48
tba2C	16.01	13.54	2.48
tba3C	16.01	13.46	2.55
tba1S	16.09	13.54	2.55
tba2S	16.09	13.54	2.55
tba3S	16.01	13.46	2.55

Table 6.6 Summary of the peak positions in the $\rho_O(Z)$ distribution. Resolution of the values is 0.075 Å.

The $\rho_O(Z)$ distributions can be seen in figure 6.6, and a summary of the central trough width is given in table 6.6. The central trough width is calculated by subtracting the right peak position from the left peak position. The right peak position refers to the peak immediately to the right of the central trough in the $\rho_O(Z)$ distribution, with the left peak position referring to the peak immediately to the left of the central trough in the $\rho_O(Z)$ distribution.

From figure 6.6 it can be seen that there is a central crystalline region with melting occurring over the outer 5 Å of the gas hydrate lattice. The central peak spacings in table

6.6 are the same in all seven systems. Differences are limited to fairly subtle differences in the surface regions.

From the expanded view of the $\rho_O(Z)$ distribution (figure 6.6) in the region of slab 1 we see that there is no discernible pattern: for some of the peaks the control system shows the highest peaks whereas for others the inhibitors show the highest peaks. More differences are evident in the region of slab 6, where the two peaks present for the inhibited systems are equivalent or smaller in height than the control system. The biggest difference occurs with tba2S. This apparent reduction in oxygen density may be due to a restructuring of the gas hydrate lattice, but may also be due to the volume occupied by the inhibitor, and so it is not clear if this effect is significant or not.

Interfacial Analysis Guest *z*-density Distributions–$\rho_G(Z)$

From the $\rho_G(Z)$ presented in figure 6.7 it can be seen that there is a regular arrangement of peaks in the central region of the gas hydrate lattice, namely between ~ 5 and ~ 25 Å. This observation ties in with that from the $\rho_O(Z)$ distribution that the centre of the gas hydrate lattice was stable during the length of the simulation and indicates that the inhibitors are not affecting the stability of the hydrate core.

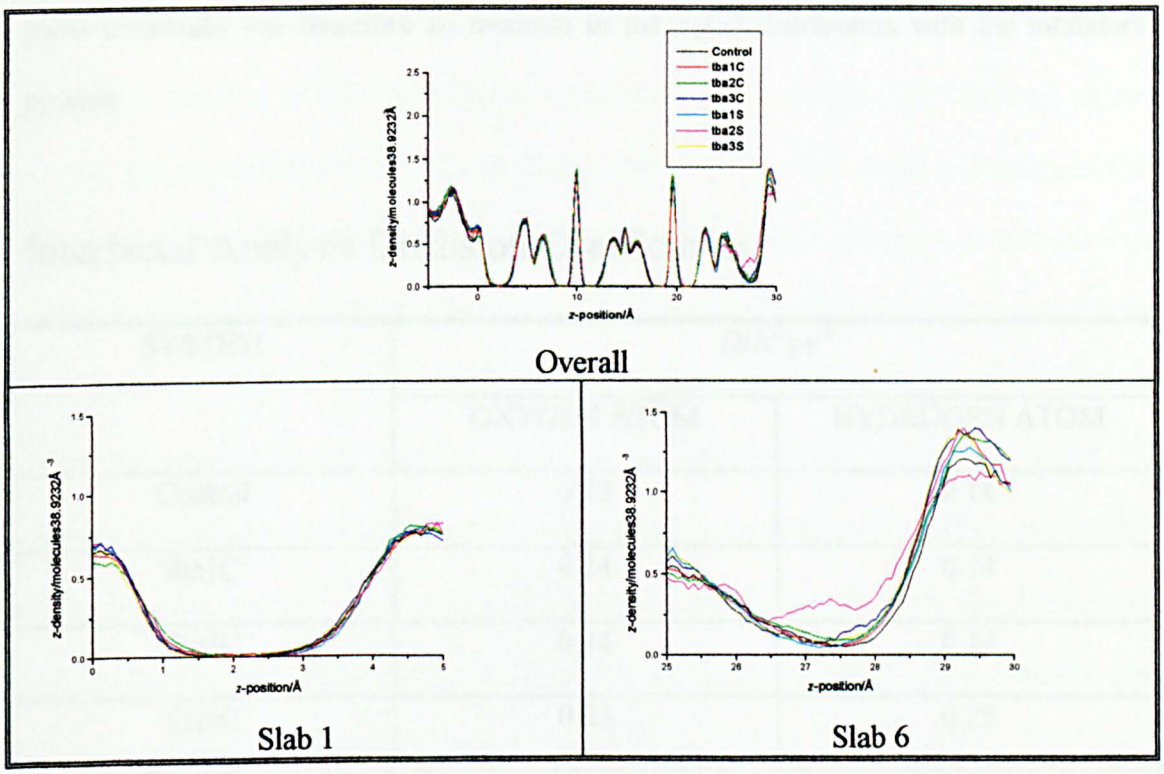

Figure 6.7 $\rho_G(Z)$ distributions for the seven systems. The legend is the same for each plot.

From the expanded view of the gas hydrate lattice in the region of slab 1 one can see that the structure is essentially the same in each of the seven systems. The same is not true for the region of slab 6 where differences between the control and inhibited systems are apparent. In particular, there is an increase in the outer peaks of the $\rho_G(Z)$ distributions for the inhibited compared with the control system. This correlates with the observations from the $\rho_O(Z)$ distributions. If the reduction with the inhibitors present in the $\rho_O(Z)$ distributions was due to the inhibitors causing the gas hydrate lattice to melt/change structure then it is possible that this would lead to the release of the encaged guest

molecules. This release of encaged guest molecules could lead to an aggregation of guest molecules and therefore an increase in the $\rho_G(Z)$ distribution with the inhibitors present.

Interfacial Analysis Diffusion Coefficients

SYSTEM	D/Å^2 ps^{-1}	
	OXYGEN ATOM	HYDROGEN ATOM
Control	0.13	0.14
tba1C	0.14	0.14
tba2C	0.14	0.14
tba3C	0.25	0.25
tba1S	0.14	0.15
tba2S	0.08	0.08
tba3S	0.32	0.33

Table 6.7 Summary of oxygen and hydrogen atom self-diffusion coefficients.

The self-diffusion coefficients (see section 3.5) for oxygen and hydrogen have been taken from the DL_POLY[3] output file, and so are taken from $\langle(\boldsymbol{r}_0-\boldsymbol{r}_t)^2\rangle/6t$, rather than from the limiting slope of the MSD. One significant consequence of this is that the self-diffusion coefficient for stable solids will appear to be non-zero, but will approach zero as the length of any single trajectory run increases (*i.e.* will be smaller for a 20 ps trajectory than for a 50 ps trajectory). These self-diffusion coefficients are a composite

of the whole system, and have not been decomposed into values associated with specific regions. The results are presented in table 6.7. From table 6.7 we can see that there is a significant increase in the self-diffusion coefficients of the oxygen and hydrogen atoms for the systems containing tba3C and tba3S. This indicates that water molecules in the presence of tba3C and tba3S are more mobile than the other inhibitors or without any additive. This effect may be due to increased melting present in these systems but this is not obvious from the *z*-density distributions. Another alternative is that these inhibitors affect the structuring properties of water in the neighbouring gas hydrate lattice, in essence weakening the interactions between water molecules and therefore increasing their apparent mobility. A final possibility could be due to the fact that these two inhibitors have the largest charge separation and hence the alkyl chain between the nitrogen and the headgroup may be sufficiently long to allow the headgroup to curl back towards the nitrogen atom, hence merging the two highly charged centres and cancelling out their effects on water, namely attracting water molecules strongly. In contrast, tba2S shows a significantly smaller value for the oxygen and hydrogen self-diffusion coefficients, indicating that water is less mobile in this system compared with the control system. Note that the values in table 6.7 are averaged over all the waters in the system, and so if the effect of the inhibitor is local the values will understate the effect of the inhibitors. The other systems are in accord with the control system.

Interfacial Analysis Co-ordination Number

The co-ordination number (see section 3.4) of water molecules within slabs 1–6 of the gas hydrate lattice have been calculated and can be seen in table 6.8.

SYSTEM	CO-ORDINATION NUMBER					
	SLAB 1	SLAB 2	SLAB 3	SLAB 4	SLAB 5	SLAB 6
Control	3.74	3.97	3.94	3.97	3.97	3.48
tba1C	3.76	3.97	3.98	3.97	3.97	3.42
tba2C	3.75	3.96	3.97	3.97	3.97	3.48
tba3C	3.77	3.98	3.95	3.97	3.97	3.42
tba1S	3.76	3.97	3.95	3.97	3.97	3.56
tba2S	3.75	3.97	3.94	3.97	4.02	3.53
tba3S	3.76	3.95	3.98	3.97	3.97	3.55

Table 6.8 Summary of co-ordination numbers for slabs 1–6 in the seven systems.

The co-ordination number for water molecules in the six slabs for the seven systems are given in table 6.8. It is immediately apparent that the co-ordination numbers for slabs 2–5 are constant at around 3.97. The is very close to the value one would expect for tetrahedrally bonded water, 4, and so indicates that the central region of the gas hydrate lattice is stable and not decomposing.

The value for slab 1 for each of the seven systems are 3.74–3.77, *i.e.* essentially the same for each system. This value is smaller than that for slabs 2–5, consistent with some melting occurring in slab 1, and with some deficit of hydrogen bonds at a surface.

For slab 6 there is a segregation of the behaviour of the two inhibitor series, with the carboxylates showing co-ordination numbers equal to or smaller than the control system whereas the sulphonates exhibit co-ordination numbers larger than the control system.

These effects are weak, but may show that the carboxylates cause a slight decrease in the structuring of the gas hydrate lattice, whereas the sulphonates appear to increase the structuring of the gas hydrate lattice relative to the control system.

Interfacial Analysis Local Phase Assignments

The order parameters F_3, $F_{4\varphi}$ and F_{4t} (see section 3.3) have been calculated for water molecules in the seven systems, the calculation of these order parameters is outlined in chapter 3. By combining the instantaneous values of F_3, $F_{4\varphi}$ and F_{4t} it is possible to assign the water molecules within each of the seven systems as belonging to one of three phases: hydrate, ice or water. This is achieved by comparing the F_3, $F_{4\varphi}$ and F_{4t} values and if they are sufficiently close to the set of bulk phase values then they are assigned to that phase. In order to define 'sufficiently close' the covariance matrix for F_3, $F_{4\varphi}$ and F_{4t} was calculated in each bulk phase. The order parameters were then deemed to be sufficiently close when all three distances were simultaneously within three standard deviations of their respective bulk average.[5] The local phase assignments for water molecules in each of the seven systems can be seen in table 6.9. The data clearly shows that the percentage of ice-like water molecules present in the seven systems is small and much less than 5 %. Considering the hydrate-like and liquid-like water molecules we see that only tba2C and tba2S exhibit any real differences from the control. tba2C and tba2S, which are both the middle members of the inhibitor families, show smaller numbers of hydrate-like water molecules and a corresponding increased number of liquid-like water molecules. This suggests that both tba2C and tba2S are reducing the structuring of the gas hydrate lattice possibly through localised melting; that is to say

that tba2C and tba2S increase the chemical potential of water molecules in the hydrate state in their vicinity.

SYSTEM	NUMBERS OF WATERS IN EACH PHASE		
	HYDRATE	ICE	LIQUID
Control	297	10	101
tba1C	294	9	105
tba2C	290	9	109
tba3C	298	10	101
tba1S	299	9	100
tba2S	285	11	112
tba3S	298	9	101

Table 6.9 Local phase assignment summary for the seven systems.

6.2.2 277 K Inhibitor-based Analysis

Whereas in the previous section the analysis was systematised by reference to the form and location of the hydrate slab, in this section the analysis will be decomposed according to proximity to the inhibitor. This analysis should be particularly useful in identifying local variations induced by the inhibitor, but does have the drawback that there is no obvious control with which to compare. In order to identify any general trends data for all X atoms will be produced but we will only consider the classic hydrophilic groups C/S and O and the classic hydrophobic group C3.

Radial Distribution Functions

RDFs (see section 3.2) for all waters, namely g_{XO} and g_{XH} where X is an inhibitor atom and O/H is any water atom, have been calculated from the inhibited systems. The RDFs for bulk water, namely g_{OwOw} and g_{OwHw} where Ow/Hw refers to bulk water, have not been calculated. This is because there is no bulk water in these systems, as almost all water surrounds a CH_4 or C_3H_8 molecule in a gas hydrate. In the following sections these plots are presented along with a summary of the first and second peak positions and where applicable the area of the first peak.

Inhibitor-based Radial Distribution Functions–g_{XO} and g_{XH}

The radial distribution functions g_{XO} and g_{XH} for the inhibited systems can be seen in figures 6.8 and 6.9; g_{XO}, (g_{XH}), corresponds to the oxygen, (hydrogen), distribution around the X atom where X is C1, C2, C3, C4 or the headgroup C/S, O. Corresponding peak positions are tabulated in appendices 6.1 and 6.2 and plotted in graphs 6.1 and 6.2.

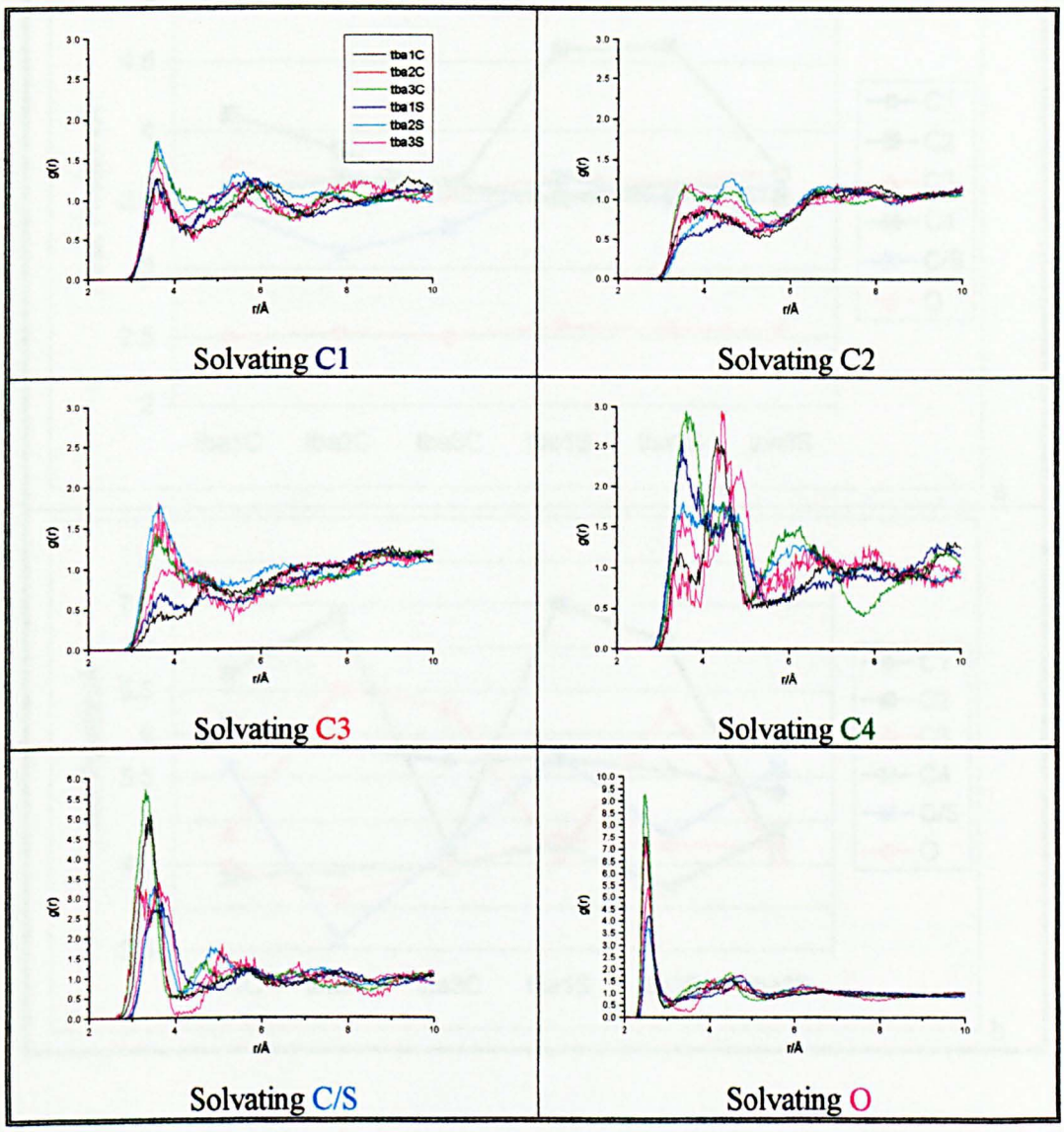

Figure 6.8 The radial distribution functions of the oxygen atom of all waters around various solute atoms for the inhibited systems. The legend is the same for each plot and atom numbers are coloured as per figure 6.3.

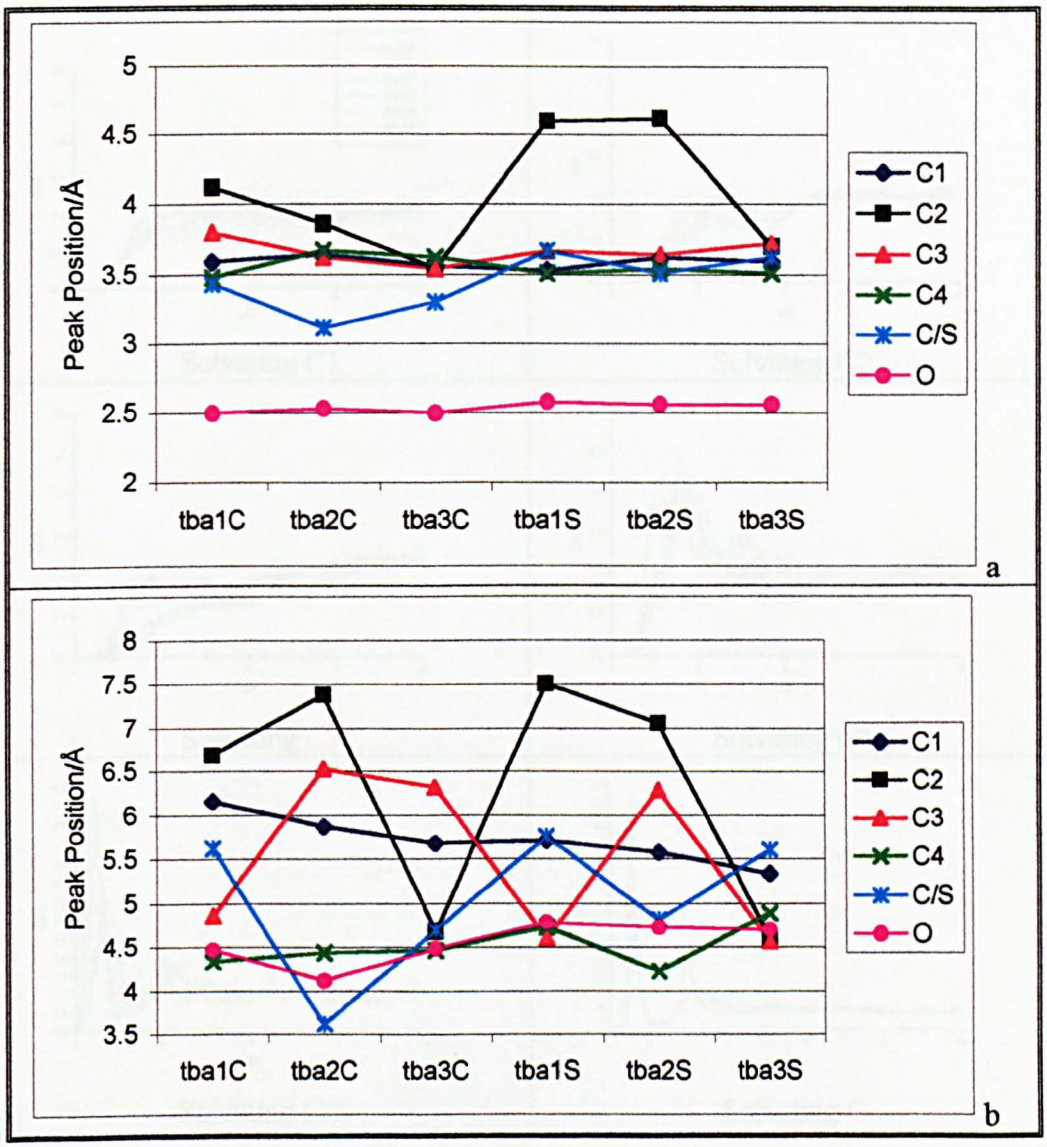

Graph 6.1 Positions of peaks in the distribution of the oxygen atom of all waters about the inhibitors, first peak positions (a) and second peak positions (b), in g_{XO}. The plot is coloured as per figure 6.3. Numerical values are also given in appendix 6.1.

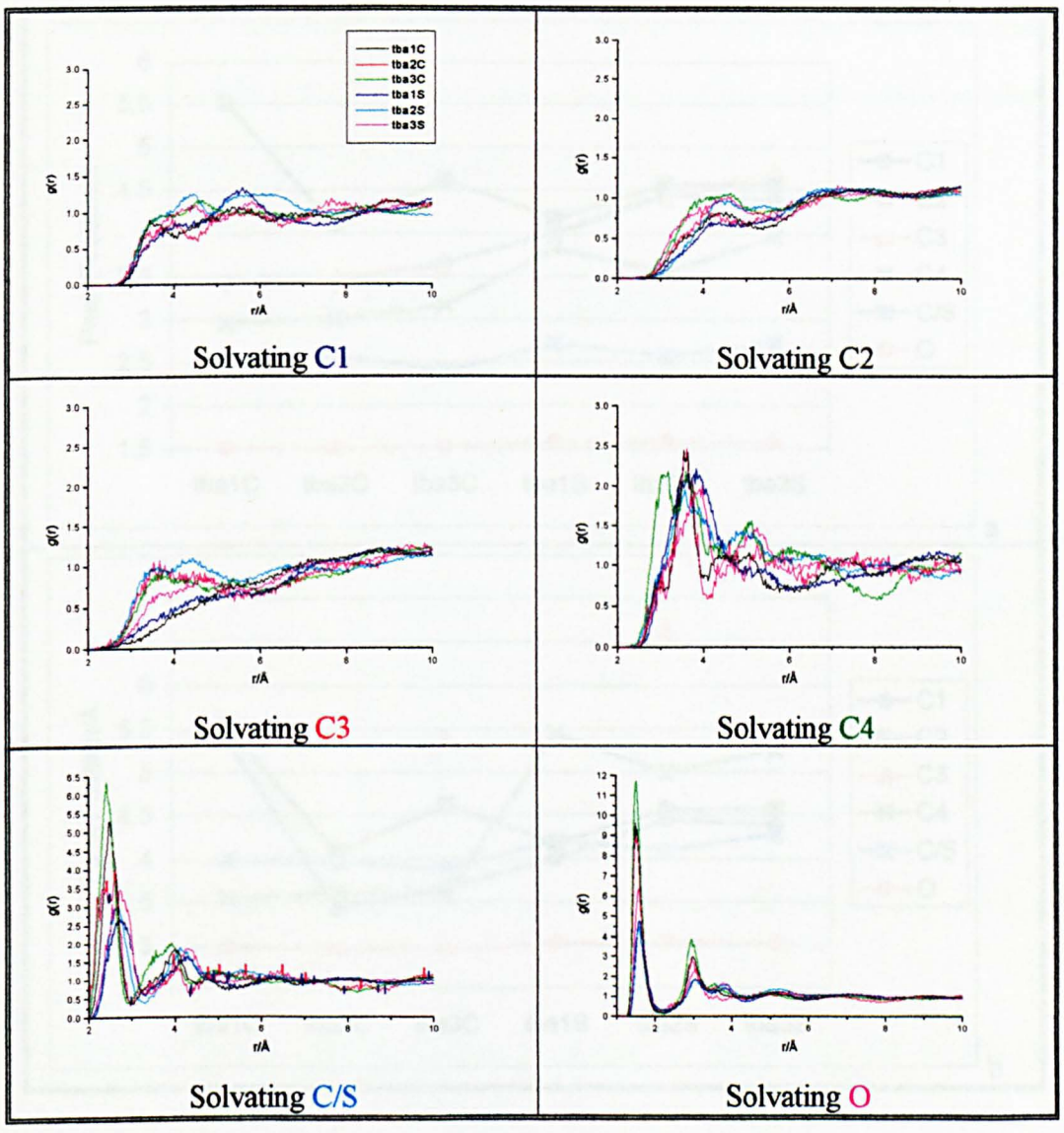

Figure 6.9 The radial distribution functions of the hydrogen atom of all waters around various solute atoms for the inhibited systems. The legend is the same for each plot and atom numbers are coloured as per figure 6.3.

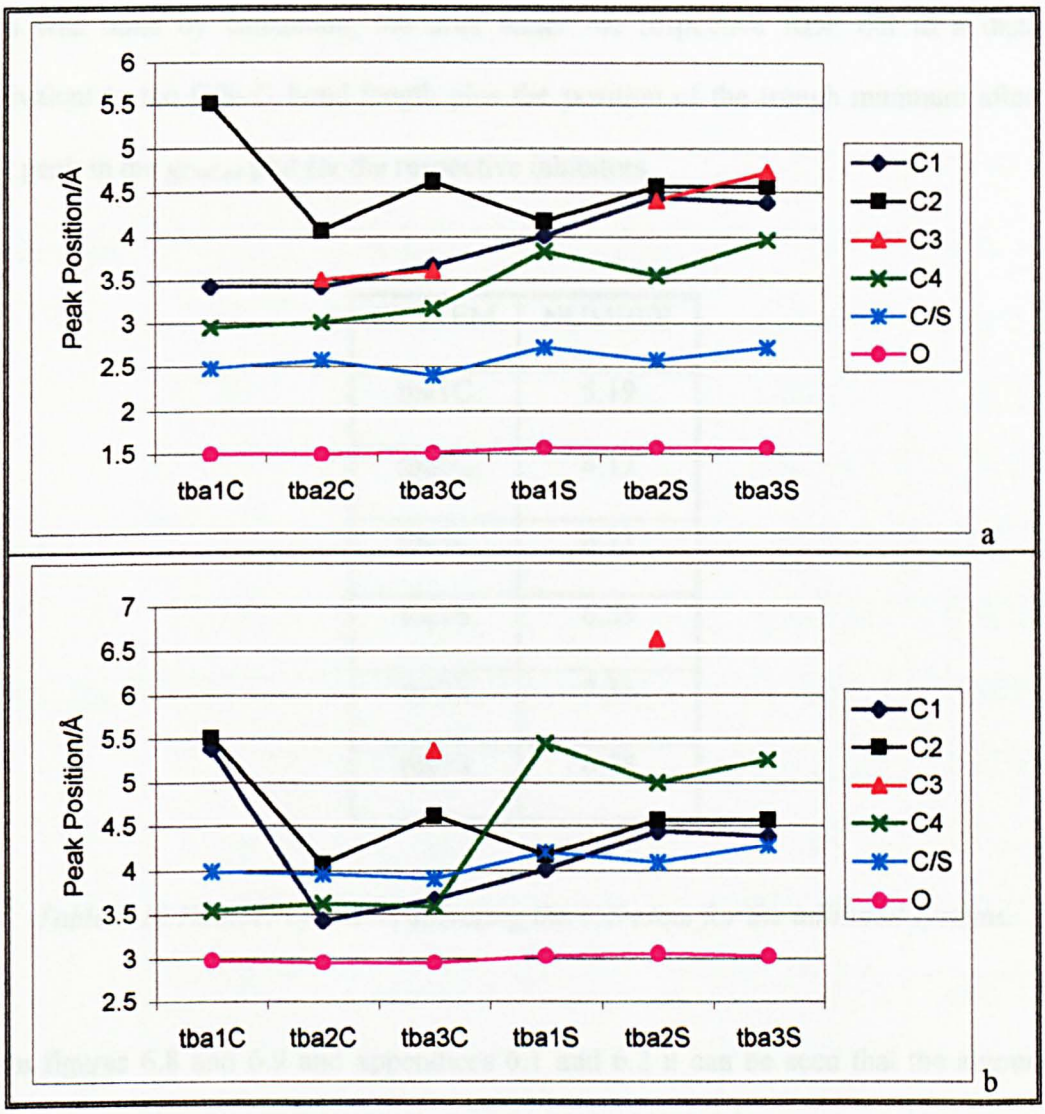

Graph 6.2 Positions of peaks in the distribution of the hydrogen atom of all waters about the inhibitors, first peak positions (a) and second peak positions (b), in g_{XH}. The plot is coloured as per figure 6.3, some of the peak positions have been omitted due to an inability to resolve the data. Numerical values are also given in appendix 6.2.

In addition, the number of waters solvating the C/S atom of the inhibitor headgroup have been calculated from the radial distribution functions and are presented in table 6.10.

This was done by calculating the area under the respective RDF out to a distance equivalent to the C/S–O bond length plus the position of the trough minimum after the first peak in the g_{OwOw} plot for the respective inhibitors.

SYSTEM	NUMBER
tba1C	5.19
tba2C	4.17
tba3C	6.21
tba1S	6.35
tba2S	7.33
tba3S	6.78

Table 6.10 Number of waters solvating the C/S atom for the inhibited systems.

From figures 6.8 and 6.9 and appendices 6.1 and 6.2 it can be seen that the amount of data is extensive. So, in order to simplify any trends in the data, the net effect of increasing charge separation in the carboxylates and sulphonates on the 1st and 2nd peak position in the g_{XO} radial distribution function is summarised in table 6.11. A stepwise increase/decrease with increasing charge separation is denoted increase/decrease, whereas if the central member of the carboxylates/sulphonates shows a maximum/minimum this is denoted maximum/minimum. In addition the position/range within which the 1st and 2nd peak positions in g_{XO} are found for the carboxylates/sulphonates is tabulated.

INHIBITOR FAMILY	ATOM	EFFECT ON PEAK POSITION IN g_{XO}.		RANGE OF PEAK POSITIONS /Å	
		1st	2nd	1st	2nd
Carboxylate	O	Constant	Constant	~ 2.5	4.12–4.49
	C	Minimum	Minimum	3.11–3.43	3.62–5.63
	C4	Maximum	Increase	3.48–3.67	4.33–4.47
	C3	Decrease	Maximum	3.54–3.80	4.86–6.53
	C2	Decrease	Maximum	3.54–4.12	4.68–7.38
	C1	Constant	Decrease	3.56–3.64	5.68–6.18
Sulphonate	O	Constant	Decrease	~ 2.6	4.70–4.78
	S	Minimum	Minimum	3.51–3.67	4.81–5.76
	C4	Constant	Minimum	~ 3.5	4.23–4.89
	C3	Increase	Maximum	3.64–3.72	4.57–6.29
	C2	Maximum	Decrease	3.70 – 4.62	4.60–7.51
	C1	Maximum	Decrease	3.53–3.63	5.34–5.71

Table 6.11 Effect on 1st and 2nd peak position in g_{XO} of increasing zwitterionic charge separation for the carboxylates and sulphonates.

It can be seen from table 6.11 for the carboxylates that the net effect on the 1st peak position in g_{XO} with increasing charge separation for C and O atoms is mirrored by the net effect on the 2nd peak position. The fact that an identical behaviour is seen for the net effect of the carboxylates upon the 1st and 2nd peak positions for these atoms suggests

that these atoms are affecting both the 1st and 2nd solvation shells of solvated water in a similar fashion and is probably a result of the strong hydrophilic nature of these atoms. The C3 atom shows no such correlation between the net effect upon the 1st and 2nd peak positions and indeed shows an opposite behaviour to the C and O atoms in the net effect on the peak position in g_{XO} as one would expect for a hydrophobic *vs.* hydrophilic comparison.

In addition it can be seen for the C atom of tba2C that a minimum is observed for the net effect on the 1st and 2nd peak position in g_{XO} and that for the C3 atom a maximum is observed for the net effect on the 2nd peak position in g_{XO}. This seems to suggest that the nature of the hydrophilic and hydrophobic atoms in tba2C are being enhanced and that the overall differentiation between hydrophilic and hydrophobic atoms is greater for tba2C than for the other two carboxylates.

Considering the number of waters solvating the C atom of the carboxylate headgroup in table 6.10 it can be seen that there is a minimum in the distribution for tba2C.

From figure 6.8 it can also be seen that the amount of structure present in g_{XO} is considerably less for carboxylate C3 solvated water molecules when compared with gas hydrate lattice water molecules in the region of slab 6 (see section 6.2.1), however an opposite effect is observed for the C and O atoms.

It can be seen from table 6.11 that for the sulphonates the net effect on the 1st peak position in g_{XO} with increasing charge separation is mirrored by the net effect on the 2nd peak position for the S atom but not the O atom. This suggests that the effect of the S atom of the sulphonates on the structure of solvated water is stronger/longer ranged than the O atom. The C3 atom shows no such correlation between the net effect upon the 1st and 2nd peak positions and indeed shows an opposite behaviour to the C and O atoms in

the net effect on the peak position in g_{XO} as one would expect for a hydrophobic *vs.* hydrophilic comparison.

A similar behaviour to that observed for the hydrophilic and hydrophobic atoms of tba2C is also observed for tba2S.

Considering the number of waters solvating the S atom of the sulphonates headgroup in table 6.10 it can be seen that there is a maximum in the distribution for tba2S, the opposite to that observed for the carboxylates.

From figure 6.8 it can also be seen that the amount of structure present in g_{XO} is considerably less for the sulphonate C3 than for the gas hydrate in the region of slab 6 (section 6.2.1), but more structure is observed for the S and O atoms.

Comparing the two families of inhibitors leads to the following observations.

i) The net effect of the carboxylates upon the 1st peak position is mirrored by that of the 2nd peak position for the C and O atoms, whereas for the sulphonates this is true for only the S atom.

ii) The nature of deviation of both tba2C and tba2S from the predicted value is almost identical, namely to shorter distances than predicted for hydrophilic atoms and to longer distances than predicted for hydrophobic atoms.

iii) The net trend for both the carboxylates and sulphonates in the number of waters solvating the headgroup C/S atom is identical, but tba2C exhibits a smaller than predicted value, whereas tba2S exhibits a larger than predicted value. Similarly the number of waters solvating the C atom of the carboxylates headgroup is smaller than the S atom of the sulphonates headgroup.

iv) The nature of the C3 and the C/S, O groups of atoms in g_{XO} show similar behaviour for the carboxylates and sulphonates when compared with the gas

hydrate lattice water molecules, with the C3 atom showing less structure, and the C/S and O group of atoms showing more structure, than in the region of slab 6 (section 6.2.1). However the C/S and O atoms of the carboxylates have 1st peak positions at shorter distances than the sulphonates indicating a tighter bound 1st solvation shell. In addition, the C/S and O atoms of the carboxylates have in general higher 1st peak heights than for the sulphonates.

From figure 6.8 it is apparent that for the C and O atoms of tba2C that the trough after the 1st peak is much lower than for all the other inhibitors indicating the 1st solvation shell is more distinct, there is also more structure apparent in these plots at longer distances for tba2C.

An analogous table to that presented for the carboxylates and sulphonates for g_{XO} can be seen in table 6.12 for the g_{XH}.

INHIBITOR FAMILY	ATOM	EFFECT ON PEAK POSITION IN g_{XH}.		RANGE OF PEAK POSITIONS /Å	
		1st	2nd	1st	2nd
Carboxylate	O	Constant	Constant	~ 1.5	~ 3.0
	C	Maximum	Decrease	2.40–2.58	3.91–3.99
	C4	Increase	Maximum	2.95–3.17	3.54–3.62
	C3	N.A.	N.A.	N.A.	N.A.
	C2	Minimum	N.A.	4.07–5.52	N.A.
	C1	Minimum	Minimum	3.43–3.67	3.96–5.39
Sulphonate	O	Constant	Constant	~ 1.6	~ 3.0
	S	Minimum	Minimum	2.58–2.72	4.09–4.28
	C4	Minimum	Minimum	3.56–3.96	5.00–5.45
	C3	N.A.	N.A.	N.A.	N.A.
	C2	Maximum	N.A.	4.17–4.57	N.A.
	C1	Maximum	Maximum	4.01–4.44	5.58–6.06

Table 6.12 Effect on 1st and 2nd peak position in g_{XH} with increasing inhibitor charge separation for the carboxylates and sulphonates.

It can be seen from table 6.12 for the carboxylates that the net effect on the 1st peak position in g_{XH} with increasing charge separation is mirrored by the net effect on the 2nd peak position for the O atom but not the C atom as was the case for g_{XO}.

In addition it can be seen for the C atom of tba2C that a maximum is observed for the net effect on 1st peak position in g_{XH}, which is opposite to that observed for g_{XO}.

From figure 6.9 it can also be seen that the amount of structure present in g_{XH} is considerably less for carboxylate C3 solvated water molecules when compared with gas hydrate lattice water molecules in the region of slab 6 (section 6.2.1), however an opposite effect is observed for the C and O atoms.

It can be seen from table 6.12 that for the sulphonates the net effect on the 1st peak position in g_{XH} with increasing charge separation is mirrored by the net effect on the 2nd peak position for all atoms where data is available.

Further it can be seen for the S atom of tba2S that minimums are observed in the distribution for the net effect on the 1st and 2nd peak position in g_{XH} as was observed for g_{XO}.

From figure 6.9 it can also be seen that the amount of structure present in g_{XH} is considerably less for sulphonate C3 solvated water molecules when compared with gas hydrate lattice water molecules in the region of slab 6 (see section 6.2.1), however an opposite effect is observed for the S and O atoms.

Comparing the observations for g_{XH} with those for g_{XO} we see that in general the behaviour of the two families of potential inhibitors is the same. The most noticeable difference is for the carboxylates and specifically tba2C, which in the g_{XO} distributions gives a minimum for the C atom and a maximum for the C3 atom as one would expect. However in the g_{XH} distributions this behaviour is the opposite with the C atom giving a maximum, no values are available for the C3 atom and so no conclusion can be drawn for this atom.

From figure 6.9 it is apparent that for the C and O atoms of tba2C that there is more structure apparent in these plots at longer distances.

Co-ordination Number

The frequency distribution of waters with a specified co-ordination number (see section 3.4), ranging from 1–10, has been calculated from the six inhibited systems. These values refer to the number of water molecules found around a specified water, when the specified water is next to X. In the following sections the most popular co-ordination number is tabulated along with the percentage of waters with co-ordination number 2, 3 or 4; this differs from the practice adopted in chapter 4, where the percentage of waters for co-ordination numbers 3, 4 or 5 was tabulated. This is due to the fact that the distribution around the inhibitor at the hydrate interface was found to be shifted to lower co-ordination numbers than was found in aqueous solution. In all of the inhibited systems the number of waters is the same and as a result the percentage of waters with co-ordination numbers 1–10 around each type of inhibitor atom has been presented.

Inhibitor-based Co-ordination Number

Data for the co-ordination number distribution of solvated water in the different solvation environments is presented in appendix 6.3 and graph 6.3.

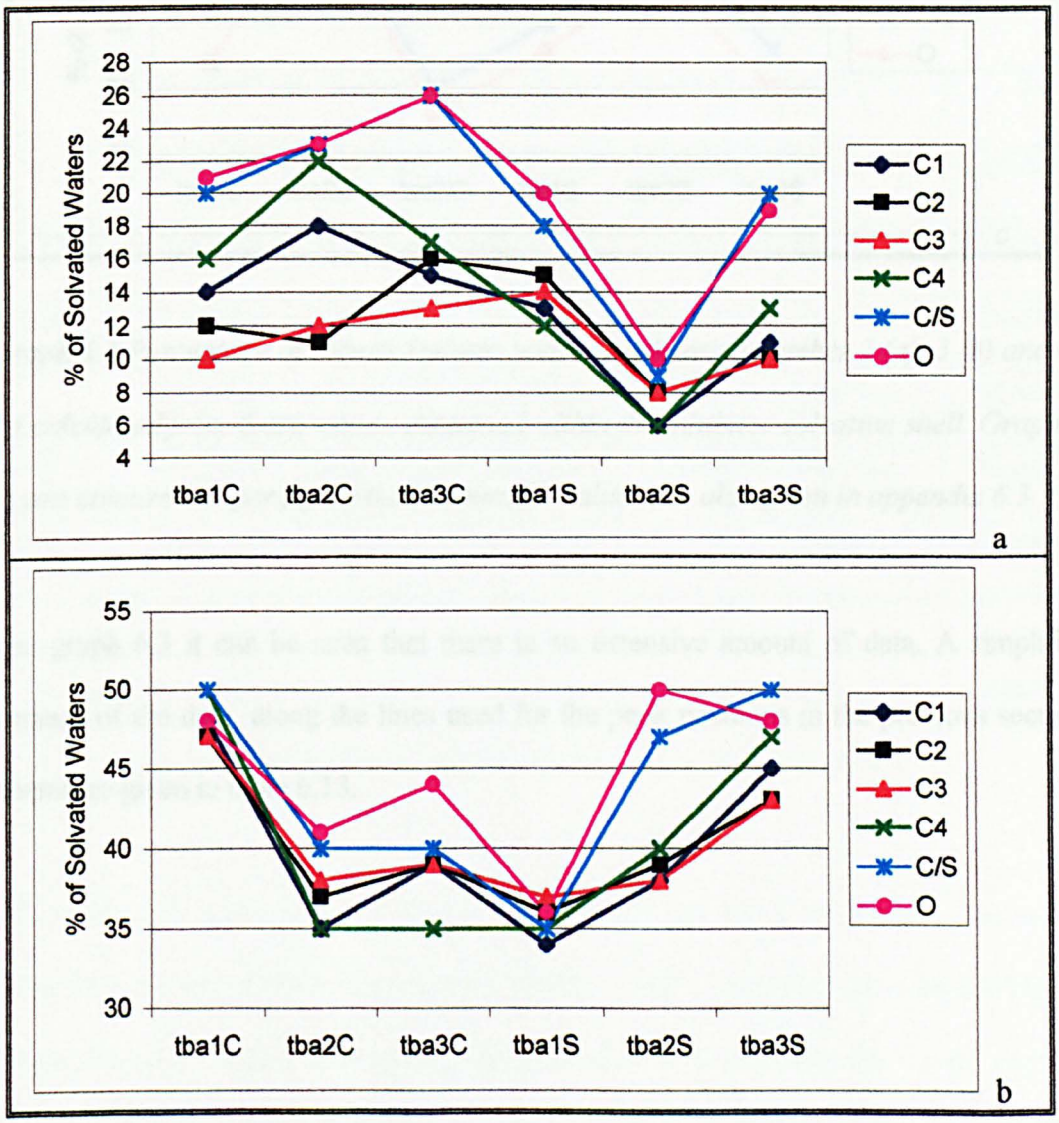

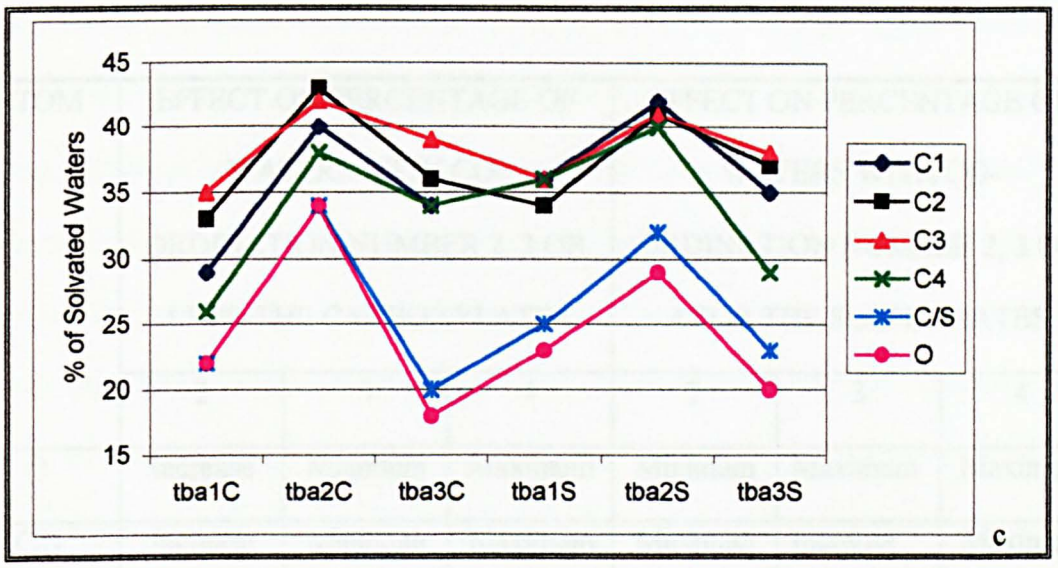

Graph 6.3 Percentage of solvated waters with co-ordination number 2 (a), 3 (b) and 4 (c) calculated from those waters contained within the inhibitor solvation shell. Graphs are coloured as per figure 6.3. Numerical values are also given in appendix 6.3.

From graph 6.3 it can be seen that there is an extensive amount of data. A simplified summary of the data, along the lines used for the peak positions in the previous section, is therefore given in table 6.13.

ATOM	EFFECT ON PERCENTAGE OF WATERS WITH CO-ORDINATION NUMBER 2, 3 OR 4 FOR THE CARBOXYLATES			EFFECT ON PERCENTAGE OF WATERS WITH CO-ORDINATION NUMBER 2, 3 OR 4 FOR THE SULPHONATES		
	2	3	4	2	3	4
O	Increase	Minimum	Maximum	Minimum	Maximum	Maximum
C/S	Increase	Minimum	Maximum	Minimum	Increase	Maximum
C4	Maximum	Minimum	Maximum	Minimum	Increase	Maximum
C3	Increase	Minimum	Maximum	Minimum	Increase	Maximum
C2	Minimum	Minimum	Maximum	Minimum	Increase	Maximum
C1	Maximum	Minimum	Maximum	Minimum	Increase	Maximum

Table 6.13 Effect on the percentage of waters with co-ordination 2, 3 or 4 with increasing inhibitor charge separation for the carboxylates.

From table 6.13 it can be seen for the carboxylates that for a particular co-ordination number that the net effect is the same for the C, O and C3 atoms, with a net increase in the percentage of waters with co-ordination number 2, a minimum for waters with co-ordination number 3 and a maximum for waters with co-ordination number 4. Therefore the behaviour of these three atoms with respect to the co-ordination number of solvated water molecules is the same as opposed to the effect seen in g_{XO} and g_{XH} where there was a clear delineation between hydrophilic and hydrophobic atoms.

It can also be seen from table 6.13 that in general we are not seeing a steady increase or decrease in the percentage of waters with co-ordination number 2, 3 or 4 with increasing charge separation but that in most cases we see either a maximum or minimum at tba2C.

From appendix 6.3 it can be seen that the modal co-ordination number for C3 is 3–4, whereas for O and C the modal co-ordination number is 3. This is compared with the liquid simulations in chapter 4 where the modal co-ordination number for C3 and C was 4 and for O 3–4.

The average co-ordination number for waters around a particular solute atom of the carboxylates is presented in table 6.14.

INHIBITOR	AVERAGE CO-ORDINATION NUMBER FOR WATER AROUND ATOM					
	C1	C2	C3	C4	C	O
tba1C	3.22	3.30	3.33	3.14	3.03	3.01
tba2C	3.33	3.47	3.44	3.22	3.14	3.15
tba3C	3.31	3.30	3.37	3.30	2.98	2.92

Table 6.14 Average co-ordination number for water around the carboxylates constituent atoms.

From table 6.14 it can be seen that average co-ordination number for water around each atom of the carboxylates is substantially less than the value of 4 that would be for tetrahedrally bonded water, suggesting that the carboxylates are breaking/disrupting the

co-ordination of water. This effect is most pronounced for the C and O atoms. The fact that this was not observed in chapter 4 could be due to two possible explanations: the first is that the carboxylates have a weak ability to break/disrupt the co-ordination number of water *i.e.* in the region of the gas hydrate lattice surface where melting has occurred; the second explanation is due to whether the molecule is above the gas hydrate lattice or immersed in the gas hydrate lattice open surface cages. However although the average co-ordination number for water around each atom of the carboxylates is substantially less than 4 we can see from table 6.14 that in every case except one tba2C has the higher average co-ordination number for water around each atom of the carboxylates. This seems to suggest that tba2C is better at preserving the average co-ordination number for water around each atom close to the expected value of 4 for tetrahedrally bonded water molecules than the other carboxylates.

From table 6.13 we can see as for the carboxylates that for a particular co-ordination number then the net effect is the same for the S, O and C3 atoms. However for the sulphonates the net effect on the percentage of waters with co-ordination number 2 or 3 is different to that for the carboxylates. For the sulphonates we see a minimum in the percentage of waters with co-ordination number 2 for S, O and C3 atoms as opposed to the carboxylates where an increase was observed for C, O and C3 atoms and that the percentage of waters with co-ordination number 3 show an increase for the sulphonates as opposed to a minimum for the carboxylates.

As with the carboxylates, it can also be observed that in general a maximum or minimum is observed for tba2S as opposed to a steady increase or decrease with increasing charge separation.

The behaviour of the modal co-ordination number is as per the carboxylates.

The average co-ordination number for waters around a particular solute atom of the sulphonates is presented in table 6.15.

INHIBITOR	AVERAGE CO-ORDINATION NUMBER FOR WATER AROUND ATOM					
	C1	C2	C3	C4	S	O
tba1S	3.30	3.23	3.29	3.31	3.03	2.93
tba2S	3.63	3.56	3.59	3.61	3.44	3.39
tba3S	3.31	3.35	3.37	3.19	3.15	2.97

Table 6.15 Average co-ordination number for water around the sulphonates constituent atoms.

A similar behaviour can be seen from table 6.15 for the sulphonates as was seen for the carboxylates but it is noticeable that the average co-ordination number for water around the sulphonates constituent atoms is in general higher than that for the carboxylates suggesting that the sulphonates have a weaker effect upon the co-ordination number of waters than the carboxylates.

Comparing the behaviour of the two families of inhibitors it can be observed.

i) The behaviour of the C, O and C3 atoms for waters with a particular co-ordination number is the same for the carboxylates and also the behaviour of the S, O and C3 atoms for waters with a particular co-ordination number is the same for the sulphonates. However the carboxylates and sulphonates do exhibit

differences with increasing charge separation in their effect upon waters with co-ordination number 2 and 3, whereas the effect upon waters with co-ordination number 4 is the same for both families of inhibitors

ii) Both the carboxylates and sulphonates in general exhibit a maximum or minimum for the central member of the series as opposed to a steady increase or decrease with increasing charge separation.

iii) The modal co-ordination number for waters around C3 is 3–4 for both the carboxylates and sulphonates, and for waters around the C/S and O atoms is 3.

iv) In all cases except one the average co-ordination number of waters around each atom of the central member of the sulphonates or carboxylates is higher than for the other two members of the inhibitor series.

Finally it can be seen (appendix 6.3) that in all cases tba1S exhibits the lowest total percentage of waters with co-ordination number 2, 3 and 4, this is especially so for the headgroup S and O atoms.

Order Parameters: F_3, $F_{4\varphi}$ and F_{4t}

The order parameters F_3, $F_{4\varphi}$ and F_{4t} (see section 3.3) for co-ordination numbers ranging from 1–10 have been calculated for the seven systems and are discussed below.

Inhibitor-based F_3

Values of F_3 for waters with co-ordination number 2, 3 or 4 are presented in appendix 6.4 and graph 6.4.

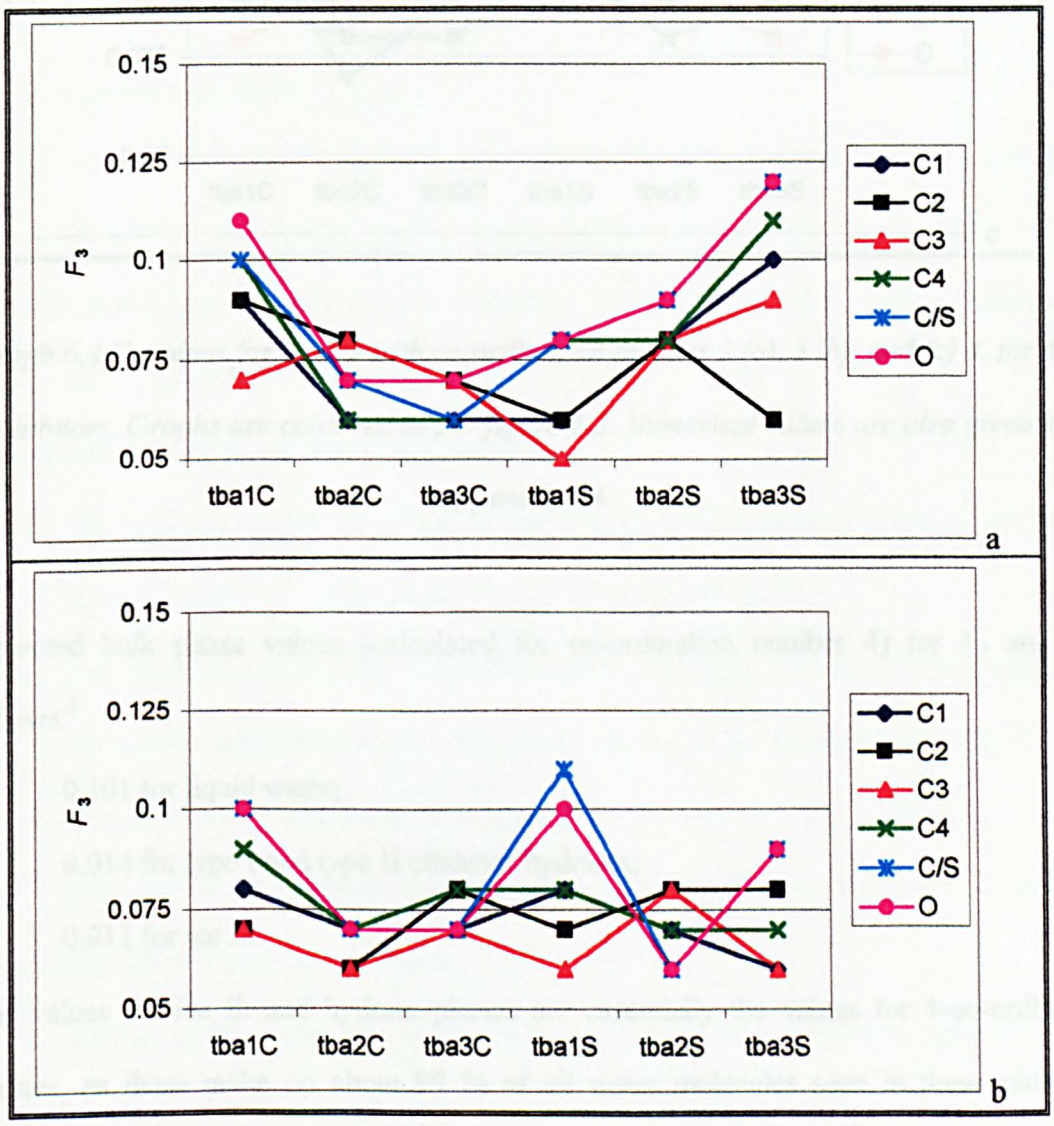

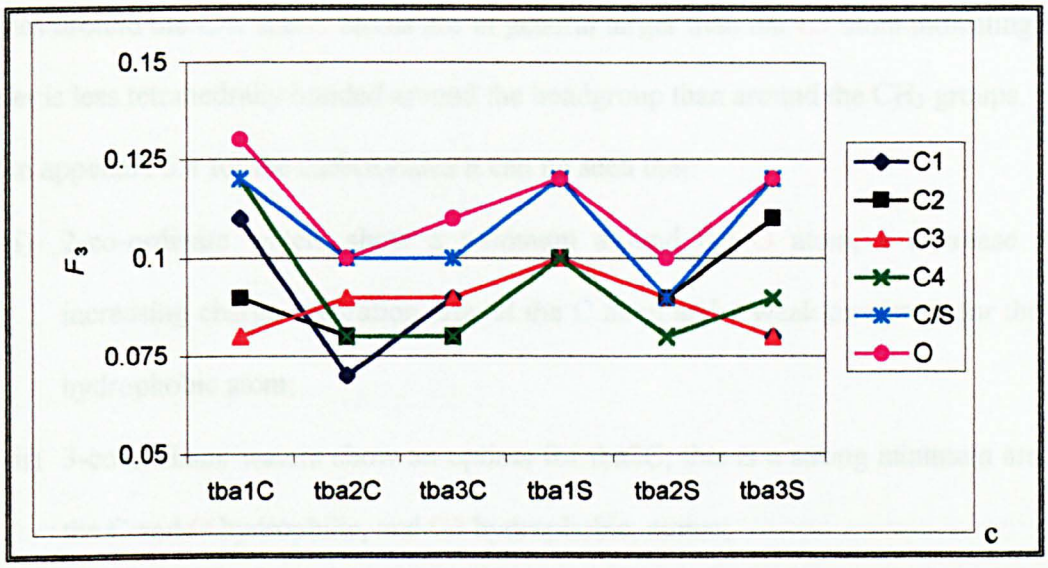

Graph 6.4 F_3 values for waters with co-ordination number 2 (a), 3 (b), and (c) 4, for the inhibitors. Graphs are coloured as per figure 6.3. Numerical values are also given in appendix 6.4.

Expected bulk phase values (calculated for co-ordination number 4) for F_3 are as follows:[5]

0.101 for liquid water;

0.014 for type I and type II clathrate hydrates;

0.011 for ice Ih.

The values for ice Ih and hydrate phases are essentially the values for 4-co-ordinate species, as these make up about 99 % of all water molecules seen in these phases. Values for 3- and 5-co-ordinate waters in the solid phases are more typically about 0.05. From appendix 6.4 for waters with co-ordination number 2, 3 or 4 of F_3 it can be seen that all the values for the carboxylates and sulphonates are indicative of liquid-like behaviour albeit a more tetrahedrally structured liquid than liquid water, and that the F_3

values around the C/S and O atoms are in general larger than the C3 atom indicating that water is less tetrahedrally bonded around the headgroup than around the CH_3 groups.

From appendix 6.4 for the carboxylates it can be seen that:

i) 2-co-ordinate waters show a minimum around the O atom, a decrease with increasing charge separation around the C atom and a weak maximum for the C3 hydrophobic atom;

ii) 3-co-ordinate waters show an optima for tba2C; this is a strong minimum around the C and O hydrophilic, and C3 hydrophobic, atoms;

iii) 4-co-ordinate waters show a minimum in F_3 around the C and O atoms for tba2C, but a maximum around the hydrophobic C3 atom.

From graph 6.4 for the sulphonates it can be seen that:

i) 2-co-ordinate waters show an increase in F_3 with increasing charge separation around the S and O hydrophilic, and C3 hydrophobic, atoms;

ii) 3-co-ordinate waters tend to show an optima for tba2S; this is a strong minimum around the hydrophilic atoms, and a weak maximum for the hydrophobic atoms;

iii) 4-co-ordinate waters show a minimum in F_3 around the S and O atoms for tba2S, but decrease with increasing charge separation around the hydrophobic C3 atom.

Comparing the two families of inhibitors we see that:

i) for the carboxylates and sulphonates F_3 values for waters with co-ordination number 2, 3 or 4 generally show an optima which in most cases is a minimum;

ii) the F_3 values for both families of inhibitors are in almost all cases indicative of liquid-like behaviour, albeit a fairly structured liquid.

From graph 6.4 it is apparent that for waters with co-ordination number 2 tba3S and to some extent tba1C exhibit values that are larger than for the other inhibitors. For waters

with co-ordination number 4 the C/S and O atoms of all the inhibitors are clearly differentiated from the other atoms.

Inhibitor-based $F_{4\varphi}$

Values of $F_{4\varphi}$ have been calculated for waters with co-ordination number 2, 3 or 4 and are presented in appendix 6.5 and graph 6.5.

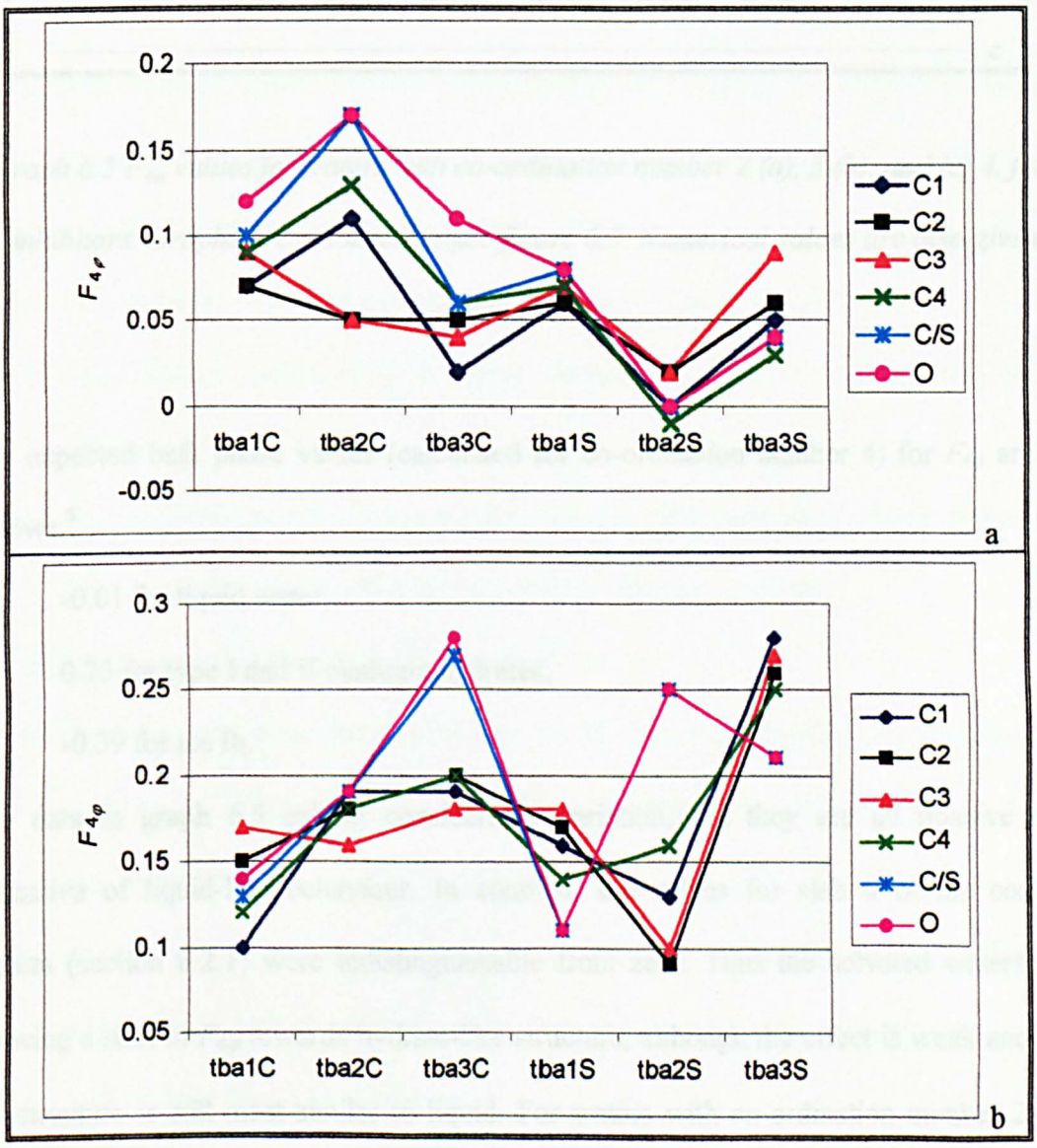

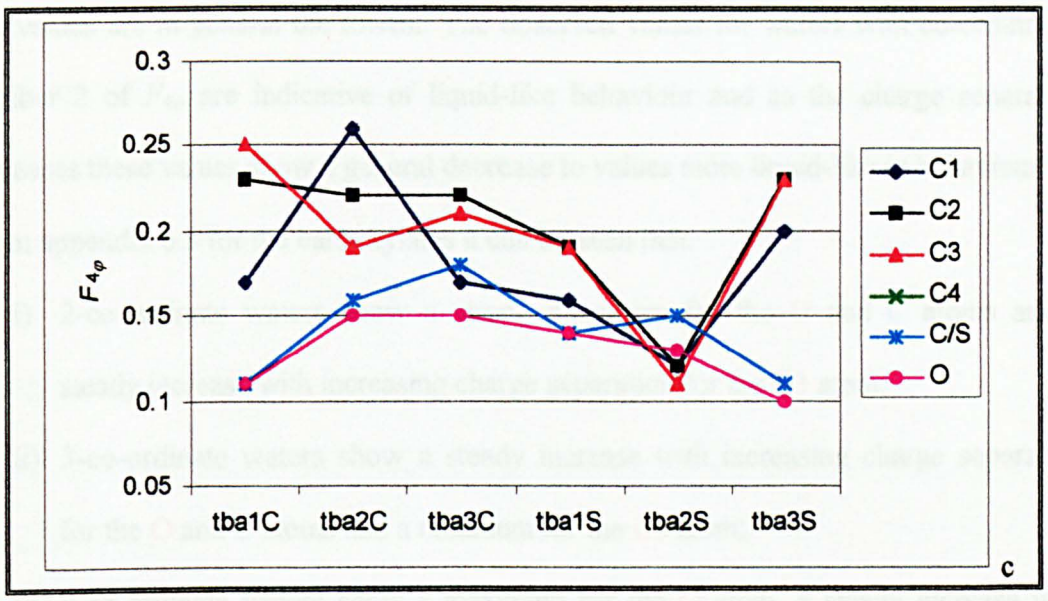

Graph 6.5 $F_{4\varphi}$ values for waters with co-ordination number 2 (a), 3 (b), and (c) 4, for the inhibitors. Graphs are coloured as per figure 6.3. Numerical values are also given in appendix 6.5.

The expected bulk phase values (calculated for co-ordination number 4) for $F_{4\varphi}$ are as follows:[5]

-0.01 for liquid water;

0.73 for type I and II clathrate hydrates;

-0.39 for ice Ih.

The data in graph 6.5 exhibit considerable variation, but they are all positive and indicative of liquid-like behaviour. In contrast, the values for slab 6 of the control system (section 6.2.1) were indistinguishable from zero. Thus the solvated waters are showing a shift in $F_{4\varphi}$ towards hydrate-like structure, although the effect is weak and the net structure is still most similar to liquid. For waters with co-ordination number 2 the

$F_{4\varphi}$ values are in general the lowest. The observed values for waters with co-ordination number 2 of $F_{4\varphi}$ are indicative of liquid-like behaviour and as the charge separation increases these values show a general decrease to values more liquid-like in behaviour.

From appendix 6.5 for the carboxylates it can be seen that:

i) 2-co-ordinate waters show a strong maximum for the O and C atoms and a steady increase with increasing charge separation for the C3 atom;

ii) 3-co-ordinate waters show a steady increase with increasing charge separation for the O and C atoms and a minimum for the C3 atom;

iii) 4-co-ordinate waters show a maximum for the O atom, a steady increase with increasing charge separation for the C atom and a minimum for the C3 atom.

From graph 6.5 for the sulphonates it can be seen that:

i) 2-co-ordinate waters show a strong minimum for the O, S and C3 atoms;

ii) 3-co-ordinate waters show a strong maximum for the O and S atoms and a minimum for the C3 atom;

iii) 4-co-ordinate waters show a steady decrease with increasing charge separation for the O and S atoms and a strong minimum for the C3 atom.

Comparing the two families of inhibitors we see that:

i) for the carboxylates and sulphonates the $F_{4\varphi}$ values for waters with co-ordination number 2, 3 or 4 generally show an optima as opposed to a steady increase/decrease;

ii) the $F_{4\varphi}$ values for both families are in almost all cases indicative of liquid-like behaviour, but show more structure than is apparent in the surface region of the pure hydrate film control system.

From graph 6.5 it is apparent that for waters with co-ordination number 2 tba2C exhibits values that are larger than for the other inhibitors for nearly all atoms. For waters with co-ordination number 3 tba3S stand out from the other inhibitors with larger values for almost all atoms, while tba3C gives the largest values for the C and O atoms.

Inhibitor-based F_{4t}

Values of F_{4t} for waters with co-ordination number 2, 3 or 4 are presented in appendix 6.6 and graph 6.6.

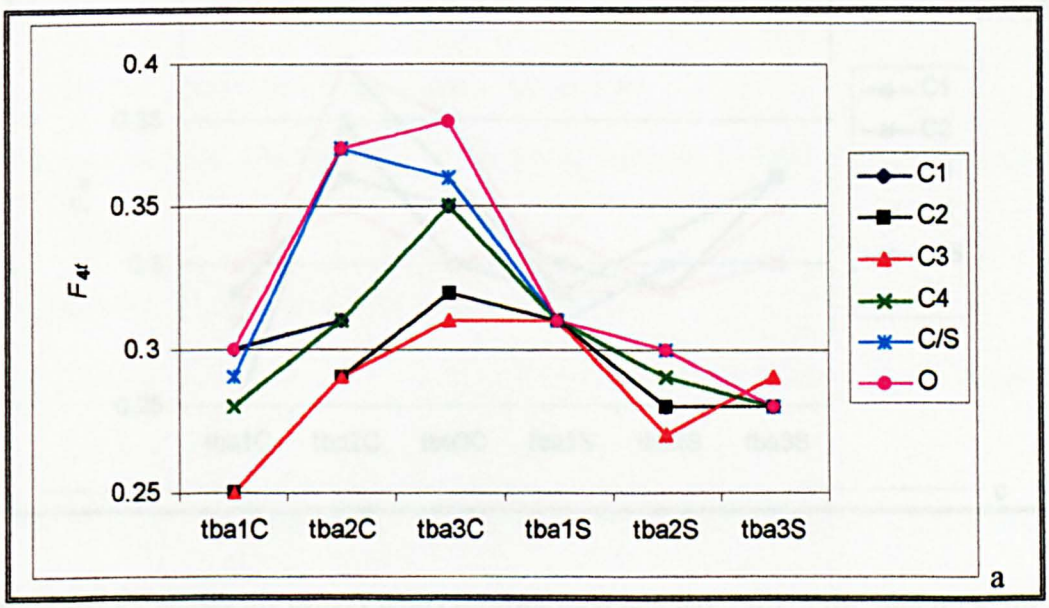

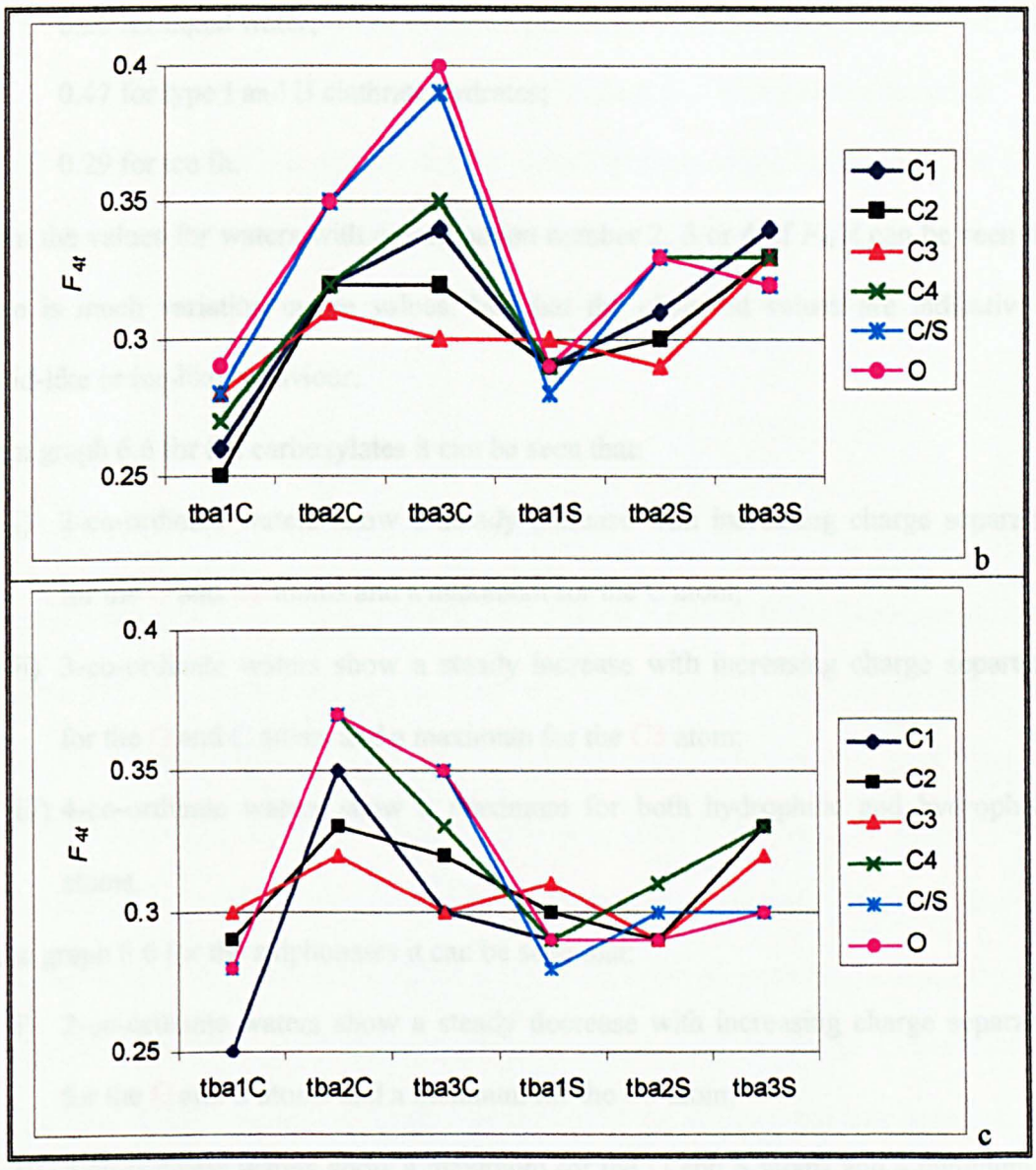

Graph 6.6 F_{4t} values for waters with co-ordination number 2 (a), 3 (b), and (c) 4, for the inhibitors. Graphs are coloured as per figure 6.3. Numerical values are also given in appendix 6.6.

The average bulk phase values (calculated predominantly from 4-co-ordinate waters for the solid phases) for F_{4t} are as follows:

0.26 for liquid water;

0.47 for type I and II clathrate hydrates;

0.29 for ice Ih.

From the values for waters with co-ordination number 2, 3 or 4 of F_{4t} it can be seen that there is much variation in the values, but that the observed values are indicative of liquid-like or ice-like behaviour.

From graph 6.6 for the carboxylates it can be seen that:

i) 2-co-ordinate waters show a steady increase with increasing charge separation for the O and C3 atoms and a maximum for the C atom;

ii) 3-co-ordinate waters show a steady increase with increasing charge separation for the O and C atoms and a maximum for the C3 atom;

iii) 4-co-ordinate waters show a maximum for both hydrophilic and hydrophobic atoms.

From graph 6.6 for the sulphonates it can be seen that:

i) 2-co-ordinate waters show a steady decrease with increasing charge separation for the O and S atoms and a minimum for the C3 atom;

ii) 3-co-ordinate waters show a maximum for the O and S atoms and a minimum for the C3 atom;

iii) 4-co-ordinate waters show a minimum for the O and C3 atoms and a maximum for the S atom.

Comparing the two families of inhibitors we can make the following observations.

i) In most cases the F_{4t} values for both families are most similar to liquid-like or ice-like behaviour, but shifted towards clathrate-like structure. For the

hydrophilic end of the longer carboxylates, the F_{4t} values may actually be better described as hydrate-like, but perturbed towards ice- or liquid-like structure.

ii) From graph 6.6 we can see that for waters with co-ordination number 2 or 3 that the values for the carboxylate headgroup atoms particularly stand out and that in addition the carboxylates exhibit a much wider spread of values than is observed for the sulphonates.

Residence Time Correlation Functions

The residence time correlation functions (see section 3.1.1) have been calculated for the inhibited systems, these plots give an indication of the residence time for solvated water molecules in the various environments. Discontinuities arise in the plots from the condition that waters must remain in the solvation shell of the atom of interest for the whole time step. In these plots four different time steps have been used and therefore when the time step is changed/doubled it is possible that a number of waters may have left the solvation shell of the atom of interest leading to a discontinuity. In the following sections the residence time correlation functions for the oxygen and hydrogen atoms of solvated water are presented for the inhibited systems.

Inhibitor-based Residence Times

The residence time correlation functions for oxygen atoms of solvated water molecules in the inhibited systems are presented in figure 6.10. The residence time correlation functions for the hydrogen atoms of solvated water molecules are not shown, as they do not differ significantly in their behaviour from the oxygen plots in figure 6.10.

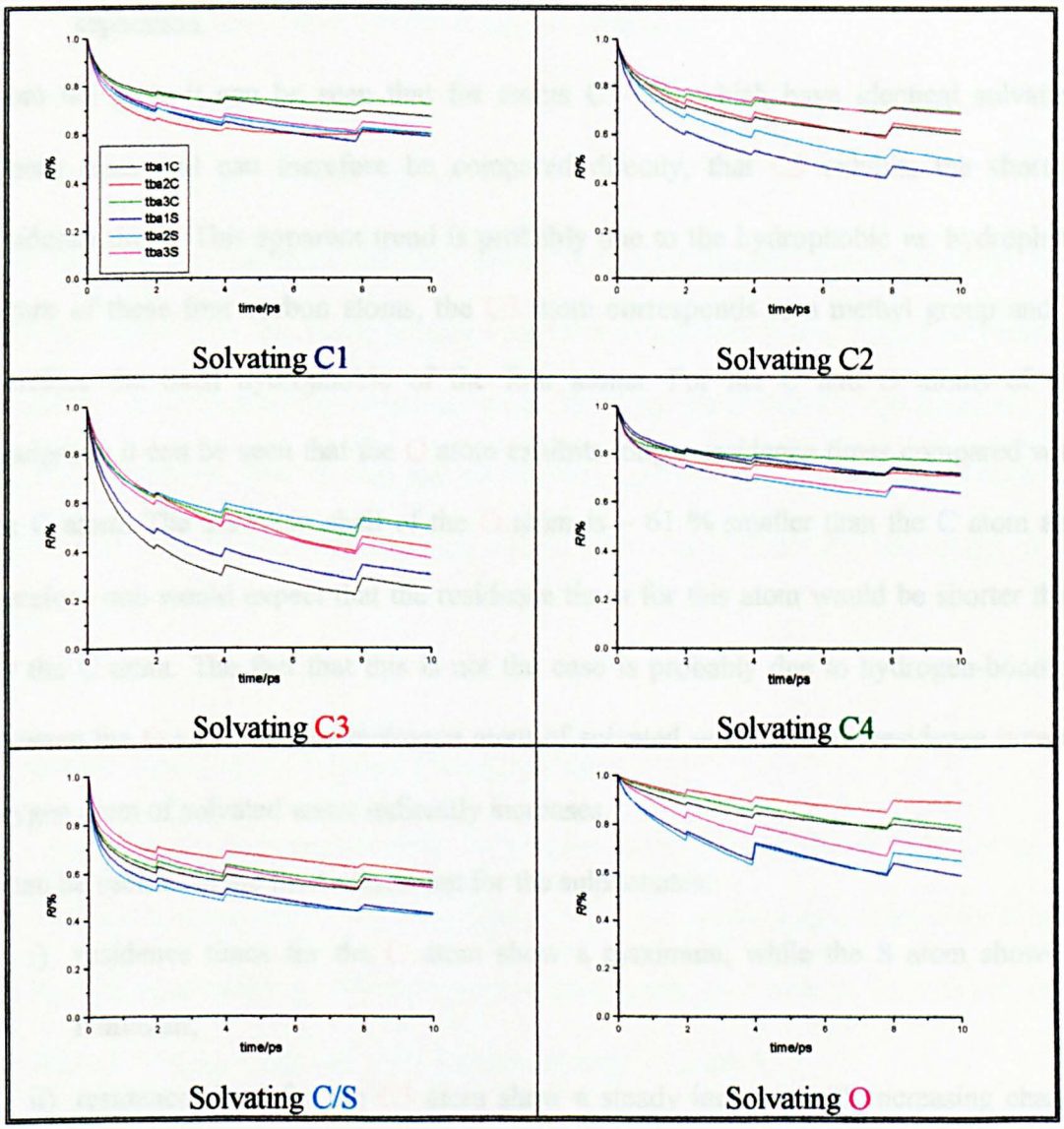

Figure 6.10 Residence time correlation functions of the oxygen atom of solvated water around various solute atoms for the inhibited systems. The legend is the same for each plot and atom numbers are coloured as per figure 6.3.

It can be seen from the final values that for the carboxylates:

i) residence times for the O and C atoms show a maximum;

ii) residence times for the C3 atom show a steady increase with increasing charge separation.

From the plots it can be seen that for atoms C1–C4, which have identical solvation sphere sizes and can therefore be compared directly, that C3 exhibits the shortest residence times. This apparent trend is probably due to the hydrophobic *vs.* hydrophilic nature of these four carbon atoms, the C3 atom corresponds to a methyl group and is therefore the most hydrophobic of the four atoms. For the C and O atoms of the headgroup it can be seen that the O atom exhibits longer residence times compared with the C atom. The solvation shell of the O atom is ~ 61 % smaller than the C atom and therefore one would expect that the residence times for this atom would be shorter than for the C atom. The fact that this is not the case is probably due to hydrogen-bonding between the O atom and the hydrogen atom of solvated water that the residence time of oxygen atom of solvated water indirectly increases.

It can be seen from the final values that for the sulphonates:

i) residence times for the O atom show a maximum, while the S atom shows a minimum;

ii) residence times for the C3 atom show a steady increase with increasing charge separation.

Once more as per the carboxylates the sulphonates C3 atom shows the shortest residence times, while the O atom shows the longest residence times.

Comparing the two families of inhibitors we see that:

i) for almost all C/S and O atoms of the carboxylates and sulphonates there is a maximum in the residence times, whereas for the C3 atom a steady increase is observed with increasing charge separation for the carboxylates and sulphonates;

ii) the residence time for the C3 atom is shortest for both groups of inhibitors, and longest for the O atom in both groups of inhibitors.

Mean Square Displacements

The mean square displacements (see section 3.1.3) of solvated water molecules have been calculated from the seven systems and used to estimate self-diffusion coefficients. Recall that mean square displacements were calculated for molecules that remained in a specified solvation shell during the entire time interval (0, *t*), and so self-diffusion coefficients must be extracted from the intermediate, rather than long, time slope of the MSD.

Inhibitor-based Mean Square Displacements

The mean square displacement plots for oxygen atoms of solvated water molecules in the inhibited systems are presented in figures 6.11. The mean square displacement plots for the hydrogen atoms of solvated water molecules are not shown, as they do not differ significantly in their behaviour from the oxygen plots in figure 6.11.

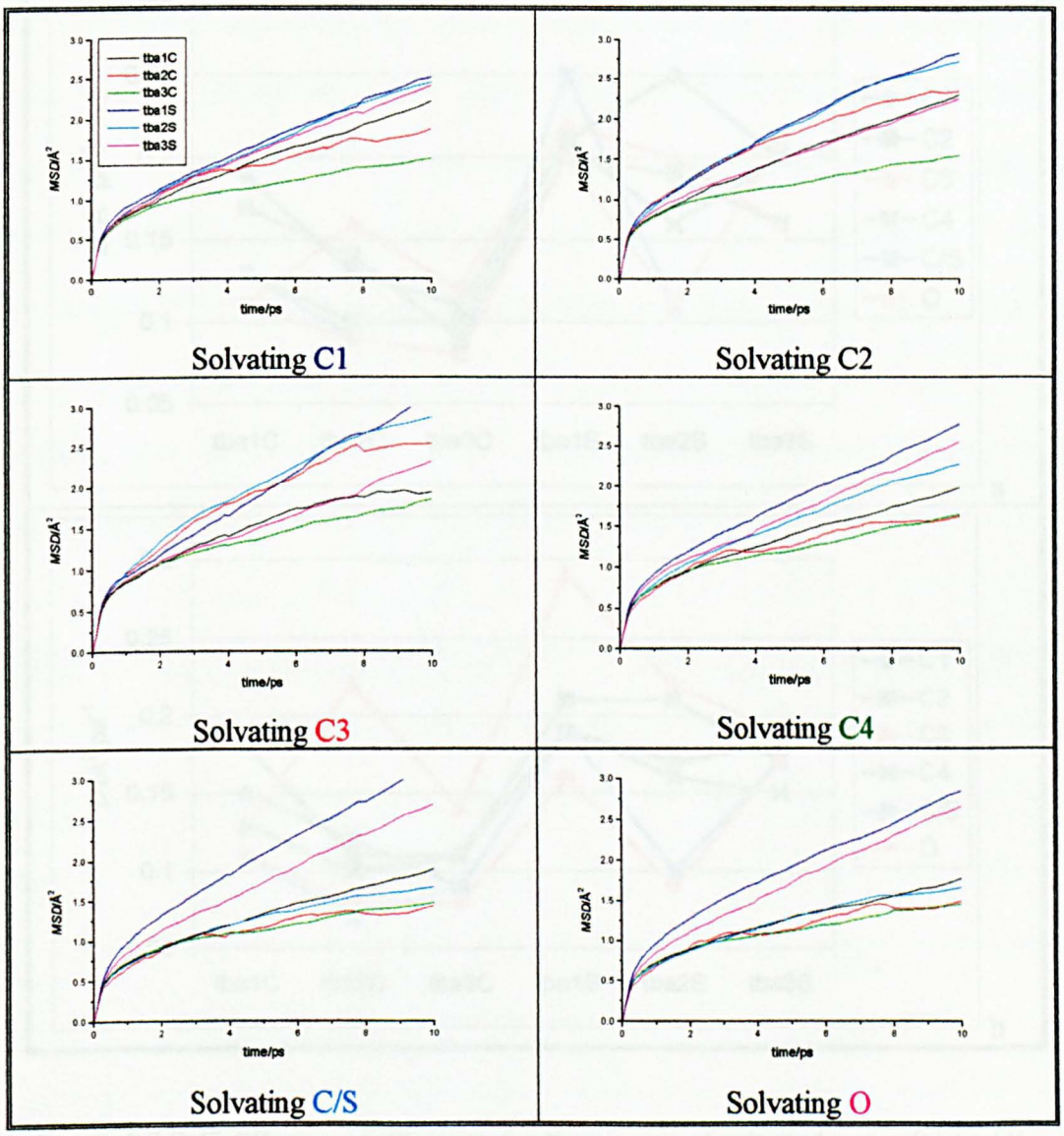

Figure 6.11 Mean square displacement of the oxygen atom of solvated water around various solute atoms for the inhibited systems. The legend is the same for each plot and atom numbers are coloured as per figure 6.3.

The self-diffusion coefficients for the hydrogen and oxygen atom of solvated water for each of the solute atoms as in appendix 6.7 are presented in graph 6.7.

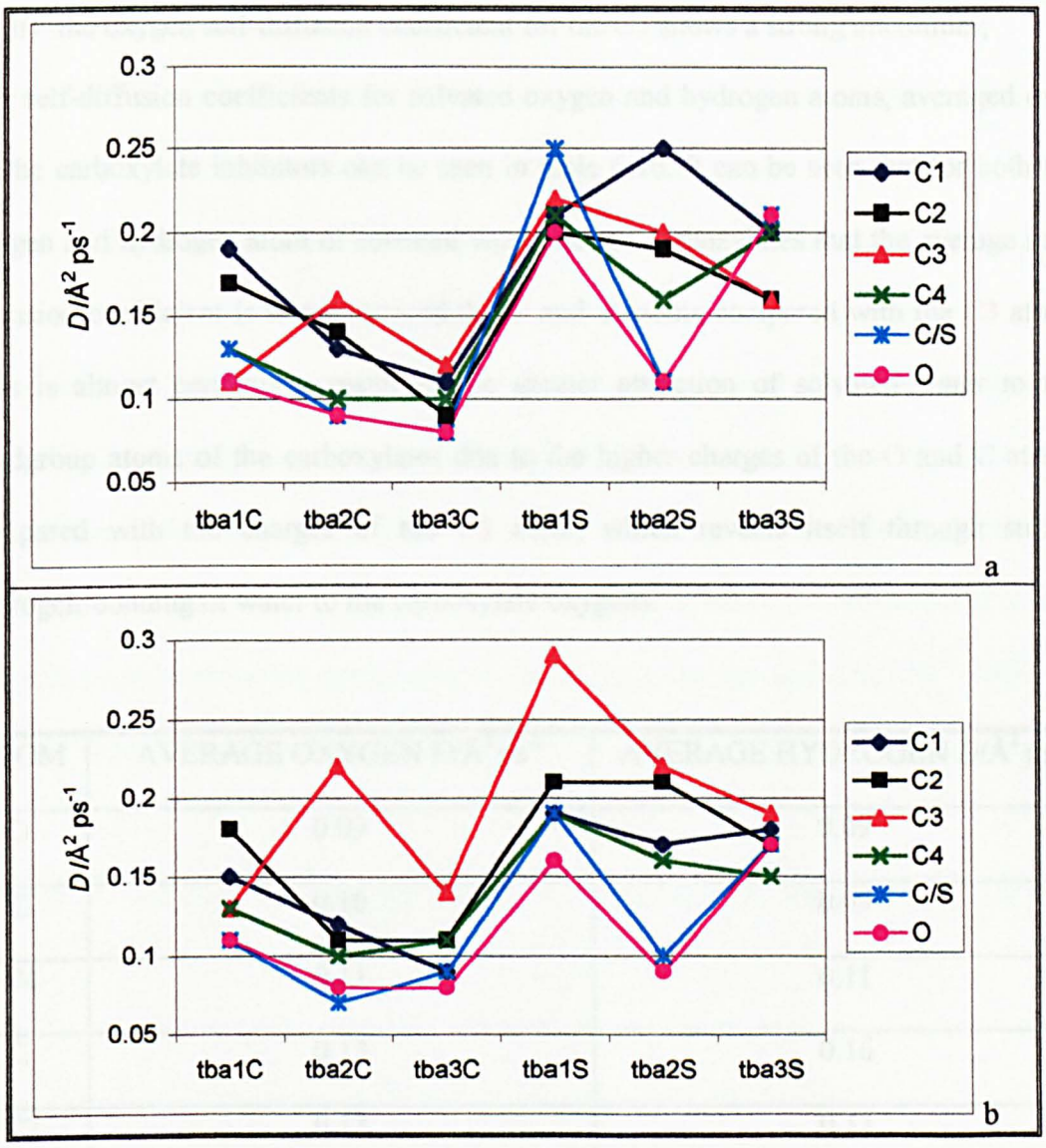

Graph 6.7 Self-diffusion coefficients, for the oxygen of solvated water (a) and the hydrogen atom of solvated water (b), around various solute atoms. Graphs are coloured as per figure 6.3. Numerical values are also given in appendix 6.7.

It can be seen from graph 6.7 for the carboxylates that:

i) the oxygen self-diffusion coefficient for the O and C atom shows a steady decrease with increasing charge spearation;

ii) the oxygen self-diffusion coefficient for the C3 shows a strong maximum;

The self-diffusion coefficients for solvated oxygen and hydrogen atoms, averaged over all the carboxylate inhibitors can be seen in table 6.16. It can be seen that for both the oxygen and hydrogen atom of solvated water for the carboxylates that the average self-diffusion coefficient is slower around the O and C atoms compared with the C3 atom. This is almost certainly a result of the greater attraction of solvated water to the headgroup atoms of the carboxylates due to the higher charges of the O and C atoms compared with the charges of the C3 atom, which reveals itself through strong hydrogen-bonding of water to the carboxylate oxygens.

ATOM	AVERAGE OXYGEN D/Å^2 ps^{-1}	AVERAGE HYDROGEN D/Å^2 ps^{-1}
O	0.09	0.09
C	0.10	0.09
C4	0.11	0.11
C3	0.13	0.16
C2	0.13	0.13
C1	0.14	0.12

Table 6.16 Average self-diffusion coefficients of the oxygen and hydrogen atom of solvated water for the carboxylates.

It can be from graph 6.7 for the sulphonates that:

i) the oxygen self-diffusion coefficient for the O and S atoms shows a strong minimum;

ii) the oxygen self-diffusion coefficient for the C3 atom shows a steady decrease with increasing charge separation;

The average self-diffusion coefficients of the oxygen and hydrogen atom of solvated water for the sulphonates can be seen in table 6.17. From table 6.17 it can be seen, as for the carboxylates, that similar trends are observed for the average self-diffusion coefficients around the headgroup atoms O, S and the C3 atom. However the differentiation between the two groups for the oxygen average self-diffusion coefficient is not as clear as for the carboxylates.

ATOM	AVERAGE OXYGEN $D/Å^2 ps^{-1}$	AVERAGE HYDROGEN $D/Å^2 ps^{-1}$
O	0.17	0.14
S	0.19	0.15
C4	0.19	0.17
C3	0.19	0.23
C2	0.18	0.20
C1	0.22	0.18

Table 6.17 Average self-diffusion coefficients of the oxygen and hydrogen atom of solvated water for the sulphonates.

Comparing the two families of inhibitors we see that:

i) the oxygen self-diffusion coefficient for hydrophilic atoms in the carboxylates shows a steady decrease with increasing charge separation whereas for the sulphonates a minimum is observed, while the hydrophobic atom of the carboxylates shows a maximum compared to a steady decrease with increasing charge separation for the sulphonates;

ii) from graph 6.7 it can be seen that in every case except one the sulphonates give rise to a larger self-diffusion coefficient for solvated water than do the carboxylates. This suggests that water is more strongly bound to the carboxylates than the sulphonates;

iii) the average self-diffusion coefficients of the oxygen and hydrogen atom of solvated water show similar trends for the carboxylates and the sulphonates.

From figure 6.11 it can be seen that tba3C has mean square displacement plots that are in general much lower than for all the other inhibitors.

Legendre Orientational Correlation Functions

The time correlation functions for the second Legendre polynomial coefficients (see section 3.1.2) for the direction of the principal axes of water molecules have been calculated for the inhibited systems. In the following sections the Legendre orientational functions for the *z*-axis are presented; the *z*-axis corresponds to the dipole vector direction.

If the rotational dynamics of the system are governed by rotational diffusion then these plots should be exponential in nature such that

$$P_l(t) = e^{-\frac{t}{l(l+1)\tau}}$$

where l is the order of the Legendre polynomial, t the time and τ the rotational lifetime. Therefore a plot of $\ln P_l(t)$ *vs.* t should be linear and the slope of the graph should give the rotational lifetime. However when this was attempted it was found that the plots of $\ln P_l(t)$ *vs.* t were not linear which has two possible implications:

a) the method of calculation of $P_l(t)$ is incorrect;

b) rotational dynamics of the system are not governed by rotational diffusion.

The second of these two options is the most likely in this case as this calculation method has been used before and yielded linear plots for $\ln P_l(t)$ *vs.* t, see Carver *et al.*[6] Therefore the value of the second Legendre polynomial coefficients plots after 10 ps have been measured. This is different to chapter 4 where the time taken for second Legendre polynomial coefficients plots to fall to 50 % were measured and is due to the fact that in this chapter the second Legendre polynomial coefficients plots decay much slower than in chapter 4.

Inhibitor-based Legendre Orientational Correlation Functions

The Legendre orientational correlation functions for solvated water in the inhibited systems can be seen in figures 6.12 and 6.13. Corresponding values of $P_{2\|}$ and $P_{2\perp}$ after 10 ps are tabulated in appendix 6.8 and graph 6.8.

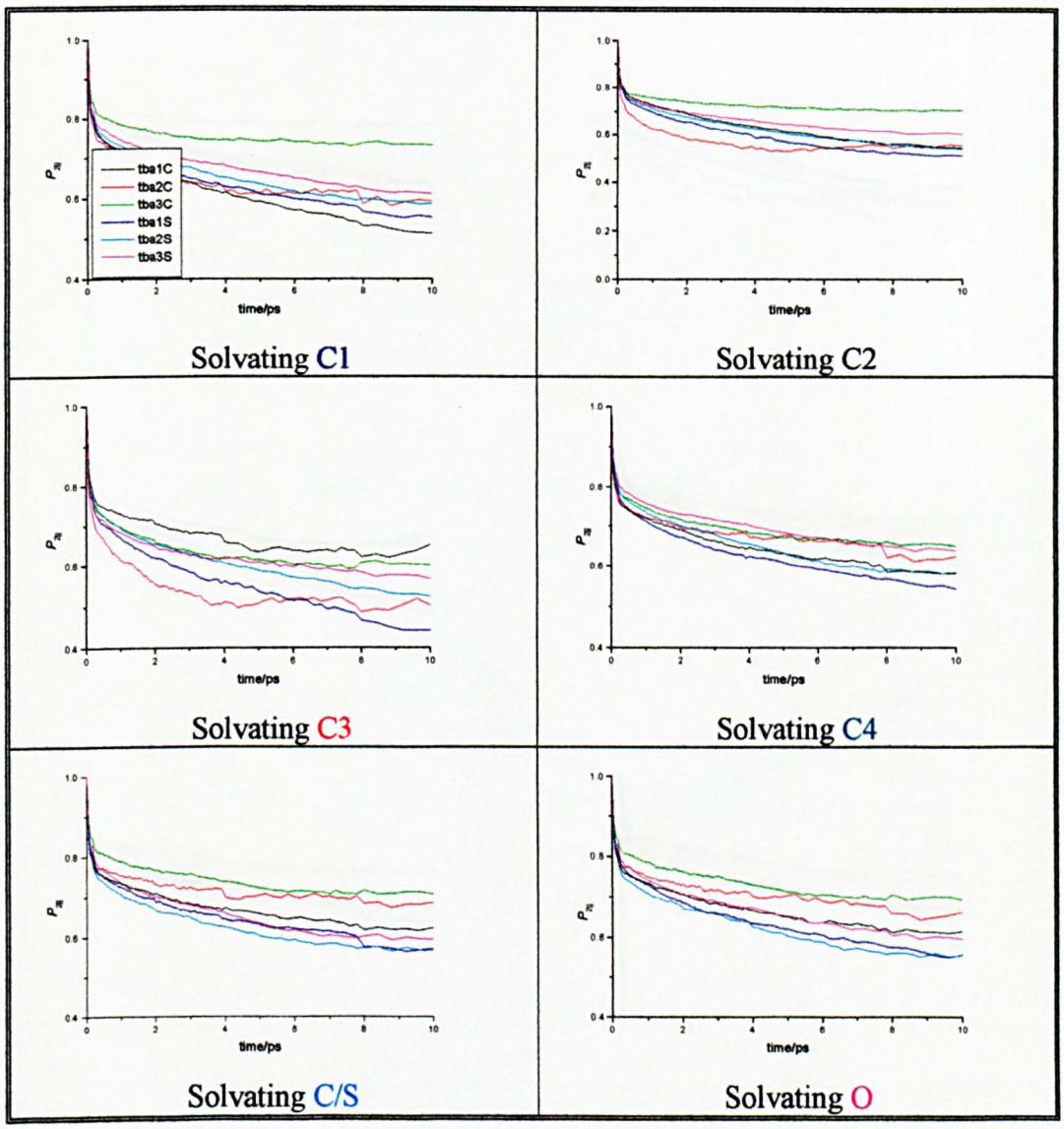

Figure 6.12 Legendre orientational correlation functions parallel to the water dipole vector of solvated water around various solute atoms for the inhibited systems. The legend is the same for each plot and atom numbers are coloured as per figure 6.3.

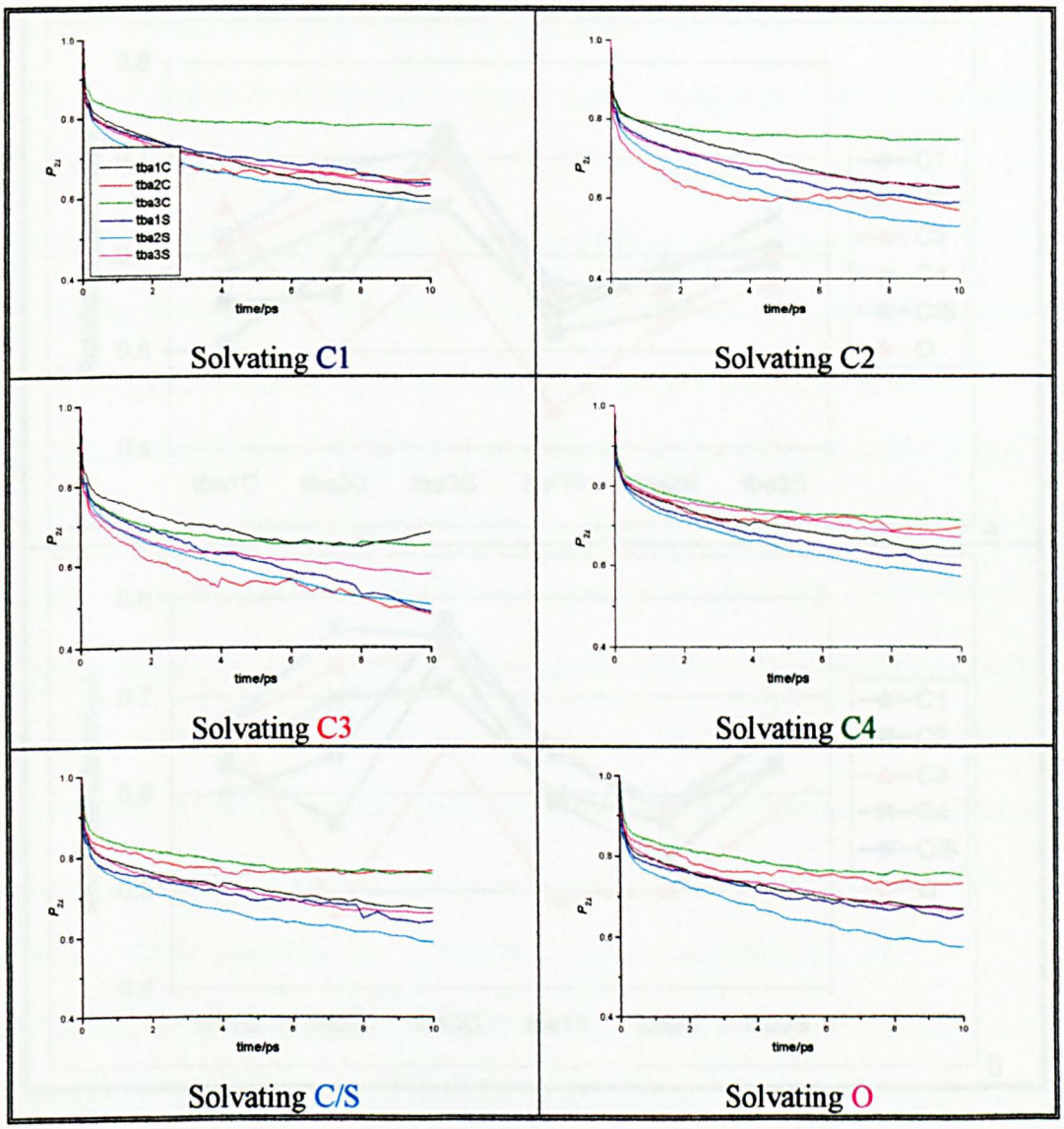

Figure 6.13 Legendre orientational correlation functions perpendicular to the water dipole vector of solvated water around various solute atoms for the inhibited systems. The legend is the same for each plot and atom numbers are coloured as per figure 6.3.

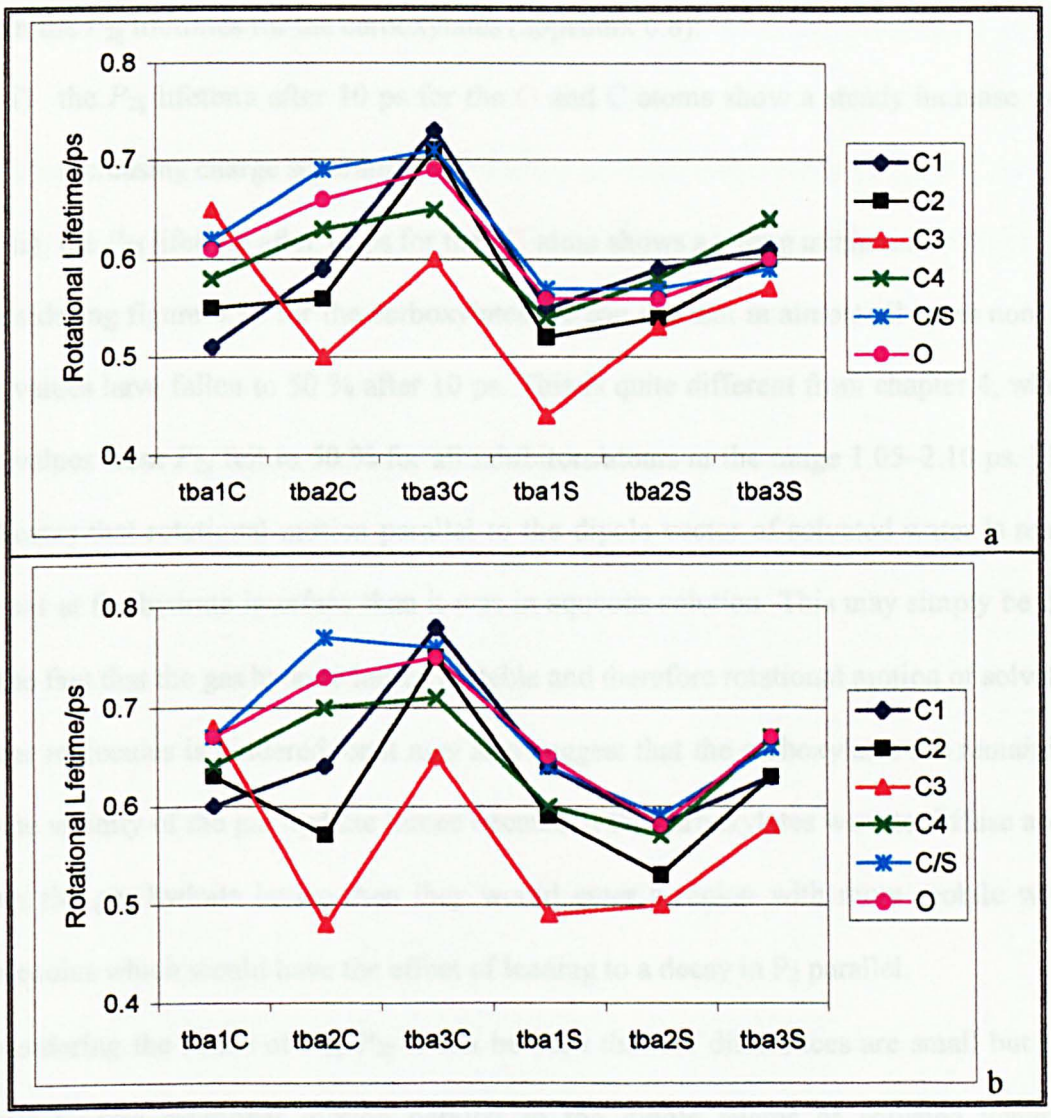

Graph 6.8 Rotational lifetimes for motion, parallel to the dipole vector (a) and perpendicular to the dipole vector (b), of solvated water around various solute atoms for the inhibited systems. Graphs are coloured as per figure 6.3. Numerical values are also given in appendix 6.8.

From the $P_{2\|}$ lifetimes for the carboxylates (appendix 6.8):

i) the $P_{2\|}$ lifetime after 10 ps for the O and C atoms show a steady increase with increasing charge separation

ii) the $P_{2\|}$ lifetime after 10 ps for the C3 atom shows a strong minimum.

Considering figure 6.12 for the carboxylates we can see that in almost all cases none of the values have fallen to 50 % after 10 ps. This is quite different from chapter 4, where the values from $P_{2\|}$ fell to 50 % for all inhibitors/atoms in the range 1.05–2.10 ps. This indicates that rotational motion parallel to the dipole vector of solvated water is much slower at the hydrate interface than it was in aqueous solution. This may simply be due to the fact that the gas hydrate lattice is stable and therefore rotational motion of solvated water molecules is hindered, or it may also suggest that the carboxylates are remaining in the vicinity of the gas hydrate lattice because if the carboxylates were to diffuse away from the gas hydrate lattice then they would enter a region with more mobile water molecules which would have the effect of leading to a decay in P_2 parallel.

Considering the ratios of $P_{2\perp}/P_{2\|}$ it can be seen that the differences are small but that never-the-less rotational motion parallel to the dipole vector of solvated water is favoured. This observation is consistent with the behaviour in aqueous solution (chapter 4), although the ratios are much smaller in this case. Given that rotational motion in general in this chapter is slower than in aqueous solution we can conclude that the inhibitor does retard rotational motion of water in its vicinity both parallel and perpendicular to the dipole vector of solvated water. Therefore the smaller ratios observed in this case must be due to a greater retardation for rotational motion parallel to the dipole vector of solvated water.

From graph 6.8 we can see that the values after 10 ps for the carboxylates from $P_{2\|}$ are much smaller for C3 than for other atoms of the carboxylates. This indicates that rotational motion parallel to the dipole vector of solvated water is fastest around the CH_3 groups of the carboxylates; the CH_3 groups are the most hydrophobic part of the carboxylates. The opposite effect is observed around the C and O atoms of the headgroup. In this case, strong hydrogen-bonding may be expected between water and the highly charged C and O carboxylate atoms, which clearly would retard the rotational motion of the solvated water.

From the $P_{2\|}$ lifetimes for the sulphonates (graph 6.8):

i) the $P_{2\|}$ lifetime after 10 ps for the O and S atoms show a minimum;

ii) the $P_{2\|}$ lifetime after 10 ps for the C3 atom shows a steady increase with increasing charge separation..

Similar observations can be made from the values of $P_{2\|}$ after 10 ps for the sulphonates as for the carboxylates.

The behaviour of $P_{2\perp}$ is very similar to that for $P_{2\|}$ and so will not be discussed.

Comparing the two families of inhibitors we see that:

i) rotational motion parallel to the dipole vector of solvated water shows a steady increase with increasing charge separation for the hydrophilic atoms of the carboxylates compared with a minimum for the sulphonates, whereas for the hydrophobic atoms of the carboxylates a minimum is observed and a steady increase with increasing charge separation for the sulphonates;

ii) rotational motion parallel to the water dipole vector of solvated water is slower for both the carboxylates and sulphonates than was observed in chapter 4;

iii) rotational motion parallel to the dipole vector of solvated water is retarded more than rotational motion perpendicular to the dipole vector of solvated water for both the carboxylates and sulphonates;

iv) rotational motion of solvated water is fastest around the C3 atom and slowest around the C/S and O atoms for both the carboxylates and sulphonates.

6.2.3 300 K Interfacial Analysis

Due to the constraints of length for this chapter in this section we will solely concern our selves with any substantially new behaviour found at 300 K that was not seen at 277 K. The discussion above will be considered sufficient to address trends in behaviour that are analogous to those seen at 277 K.

Radial Distribution Functions

The radial distribution functions (see section 3.2) for oxygen atoms, g_{OO}, and for guest atoms, g_{XX}, where X is anything that is not a water molecule, have been calculated for the each of the systems.

Interfacial Analysis Oxygen–Oxygen Radial Distribution Functions

The oxygen–oxygen radial distribution functions, g_{OO}, for slabs 1 and 6 can be seen in figure 6.14 and a summary of the 1st and 2nd peak positions in tables 6.18 and 6.19.

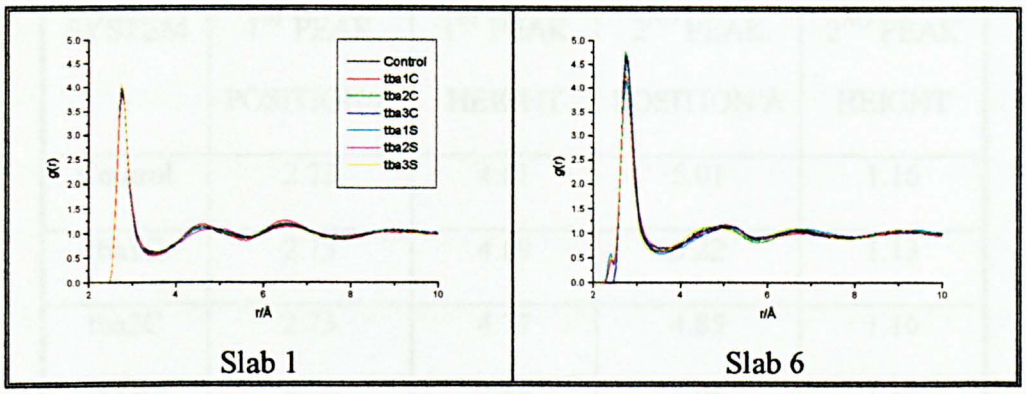

Figure 6.14 Radial distribution functions g_{OO} for slab 1 and 6. The legend is the same for each plot.

SYSTEM	1ST PEAK POSITION/Å	1ST PEAK HEIGHT	2ND PEAK POSITION/Å	2ND PEAK HEIGHT
Control	2.73	3.92	4.58	1.14
tba1C	2.73	3.99	4.58	1.19
tba2C	2.73	3.91	4.58	1.15
tba3C	2.73	4.01	4.58	1.15
tba1S	2.73	3.91	4.58	1.11
tba2S	2.73	3.87	4.85	1.09
tba3S	2.73	4.05	4.58	1.15

Table 6.18 g_{OO} summary for slab 1. Resolution of the values is 0.05 Å.

SYSTEM	1ST PEAK POSITION/Å	1ST PEAK HEIGHT	2ND PEAK POSITION/Å	2ND PEAK HEIGHT
Control	2.73	4.61	5.01	1.16
tba1C	2.73	4.69	5.22	1.13
tba2C	2.73	4.77	4.85	1.16
tba3C	2.73	4.69	5.06	1.14
tba1S	2.73	4.17	4.90	1.16
tba2S	2.73	4.29	5.06	1.19
tba3S	2.73	4.33	4.64	1.14

Table 6.19 g_{OO} summary for slab 6. Resolution of the values is 0.05 Å.

From this data we can be seen for slab 1 that the 1st and 2nd peak positions are essentially the same as those observed at 277 K in all cases. The 1st peak heights are much larger, and the 2nd peak heights much smaller, than observed at 277 K for all seven systems. From figure 6.14 and table 6.19 it can be seen for slab 6 that the 1st peak positions are essentially the same, while the 2nd peak positions are at longer distances than those observed at 277 K. As with slab 1, the 1st peak heights are larger, while the 2nd peak heights are in general smaller, than observed at 277 K for all seven systems. This suggest that the short range structure in the gas hydrate lattice at 300 K is more pronounced than at 277 K, while the medium range structure is relaxed and less pronounced.

Comparing slab 6 with slab 1 shows that in slab 6 the 1st peak position is the same, the 1st peak height is much larger, the 2nd peak position is either equivalent or larger and the 2nd peak height is essentially the same. These comparisons are as per 277 K except for the 2nd peak height, which was smaller for slab 6 than slab 1 at 277 K. The kinetic inhibitors are located in slab 6 but these effects are also observed for the control system. However, if we average over the whole 200 ps of $T_{300}P_{12.26}$, which is the simulation from chapter 5 that these simulations are based upon then we get that the 1st peak position was at 2.73 Å, the 1st peak height was 4.65, the 2nd peak position was at 4.99 Å and the 2nd peak height was 1.23. This shows that the variation between chapter 5 $T_{300}P_{12.26}$ and the control simulation in this section is: 1st peak position ± 0.00 Å; 1st peak height ± 0.04; 2nd peak position ± 0.02 Å; and 2nd peak height ± 0.07. This variation now allows us to compare the results obtained for the control system and the inhibitor simulations to quantify whether the differences are due to inhibitor effect or merely variation in the results as was observed for the control run. For the 1st peak position no effect is observed, for the 1st peak height we can see that the values obtained for all six inhibitors are outside the variation, for the 2nd peak position we can see that values obtained for all six inhibitors are outside the variation, and for the 2nd peak height we can see that the values obtained for all six inhibitors are within the variation, between $T_{300}P_{12.26}$ and the control simulation in this section. This suggests that the differences observed between that control and inhibitor simulations for slab 6 are indeed real effects and that the inhibitors are affecting the structure of slab 6 even at this elevated temperature.

If we consider the results obtained for slab 6 with the inhibitors present compared with the control then we can see that:

i) there is no change in the 1st peak position;

ii) the 1st peak height shows an increase for the carboxylates and a decrease for the sulphonates–this suggests an increase in the number of water molecules at this distance for the carboxylates and a decrease in the number of water molecules at this distance for the sulphonates;

iii) the 2nd peak position is at longer distances for the first and last members of the carboxylates while the central member is at shorter distances. The sulphonates exhibit an opposite effect with the first and last members at shorter distances while the central member is at longer distances–this suggests that the longer range water structure is relaxed for the first and last members of the carboxylates and the central member of the sulphonates, whereas an opposite effect is true for the central member of the carboxylates and the first and last members of the sulphonates;

iv) the 2nd peak heights are within the variation and therefore it is not possible to determine whether there is any effect of the inhibitors.

Interfacial Analysis Guest–Guest Radial Distribution Functions

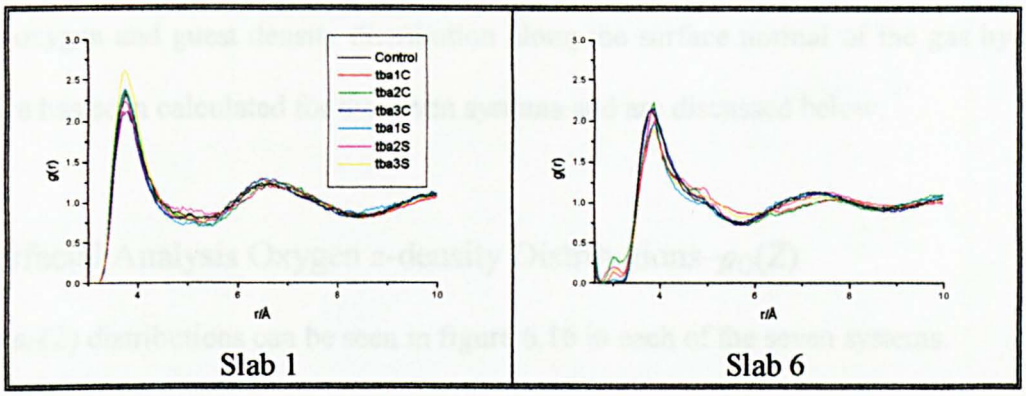

Figure 6.15 Radial distribution functions g_{XX} for slab 1 and 6. The legend is the same for each plot.

The guest–guest radial distribution functions, g_{XX}, for slabs 1 and 6 can be seen in figure 6.15 for the seven systems. The behaviour of both slabs 1 and 6 are similar, exhibiting two distinct peaks in g_{XX}, at ~ 4 Å and ~ 7 Å, with the peak at ~ 4 Å being more pronounced than the peak at ~ 7 Å. There is a hint of a shoulder at *ca.* 5 Å and some very small *r* structure in slab 6, but these are both intra-molecular inhibitor peaks. All these RDFs are quite different from the corresponding functions at 277 K. At 277 K there was only a small peak at ~ 4 Å with the major peak being at ~ 7 Å. The peak observed in g_{XX} at ~ 4 Å is due to guest-guest aggregation in the slab and therefore it can be seen that there is fast guest-guest aggregation in both slabs at 300 K as opposed to only fast guest-guest aggregation in slab 6 at 277 K. In completely stable hydrate no guest-guest aggregation would be observed and so based upon this observation we can conclude that slabs 1 and 6 both show surface melting.

z-density Distributions–$\rho_O(Z)$ and $\rho_G(Z)$

The oxygen and guest density distribution along the surface normal of the gas hydrate lattice has been calculated for the seven systems and are discussed below.

Interfacial Analysis Oxygen z-density Distributions–$\rho_O(Z)$

The $\rho_O(Z)$ distributions can be seen in figure 6.16 in each of the seven systems.

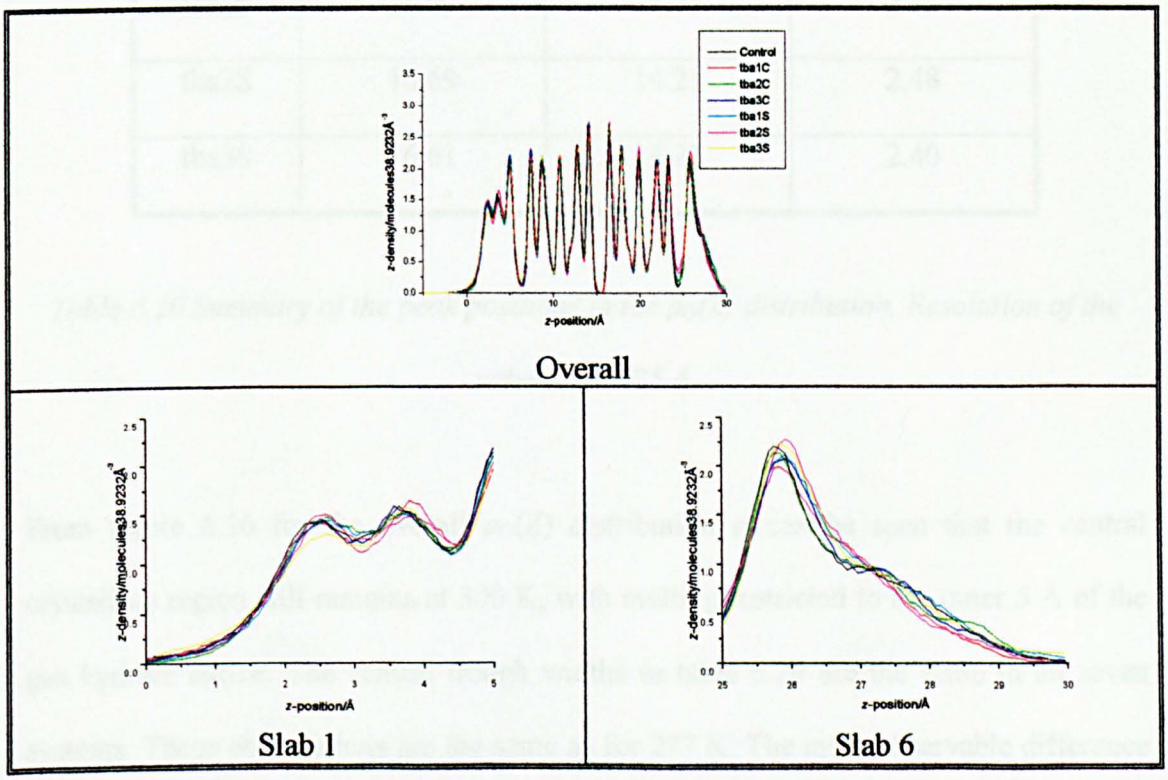

Figure 6.16 $\rho_O(Z)$ distributions for the seven systems. The legend is the same for each plot.

A summary of the central peak positions in the $\rho_O(Z)$ distribution can be seen in table 6.20 for the seven systems.

SYSTEM	RIGHT PEAK POSITION/Å	LEFT PEAK POSITION/Å	CENTRAL TROUGH WIDTH/Å
Control	16.61	14.14	2.47
tba1C	16.69	14.21	2.48
tba2C	16.69	14.21	2.48
tba3C	16.61	14.21	2.40
tba1S	16.69	14.21	2.48
tba2S	16.69	14.21	2.48
tba3S	16.61	14.21	2.40

Table 6.20 Summary of the peak positions in the $\rho_O(Z)$ distribution. Resolution of the values is 0.075 Å.

From figure 6.16 for the overall $\rho_O(Z)$ distribution it can be seen that the central crystalline region still remains at 300 K, with melting restricted to the outer 5 Å of the gas hydrate lattice. The central trough widths in table 6.20 are the same in all seven systems. These observations are the same as for 277 K. The main observable difference is that the shoulder on the peak at ~ 26 Å is much less pronounced at 300 K than at 277 K.

From the expanded view of the $\rho_O(Z)$ distribution in the region of slab 1 we see, as per 277 K that there is no discernible pattern in the order of the inhibitors/control systems.

For slab 6 there is also no discernible pattern, unlike 277 K, where the inhibitors exhibited peaks that were equivalent or smaller in height than the control system.

Interfacial Analysis Guest *z*-density Distributions–$\rho_G(Z)$

The $\rho_G(Z)$ distributions can be seen in figure 6.17 in each of the seven systems.

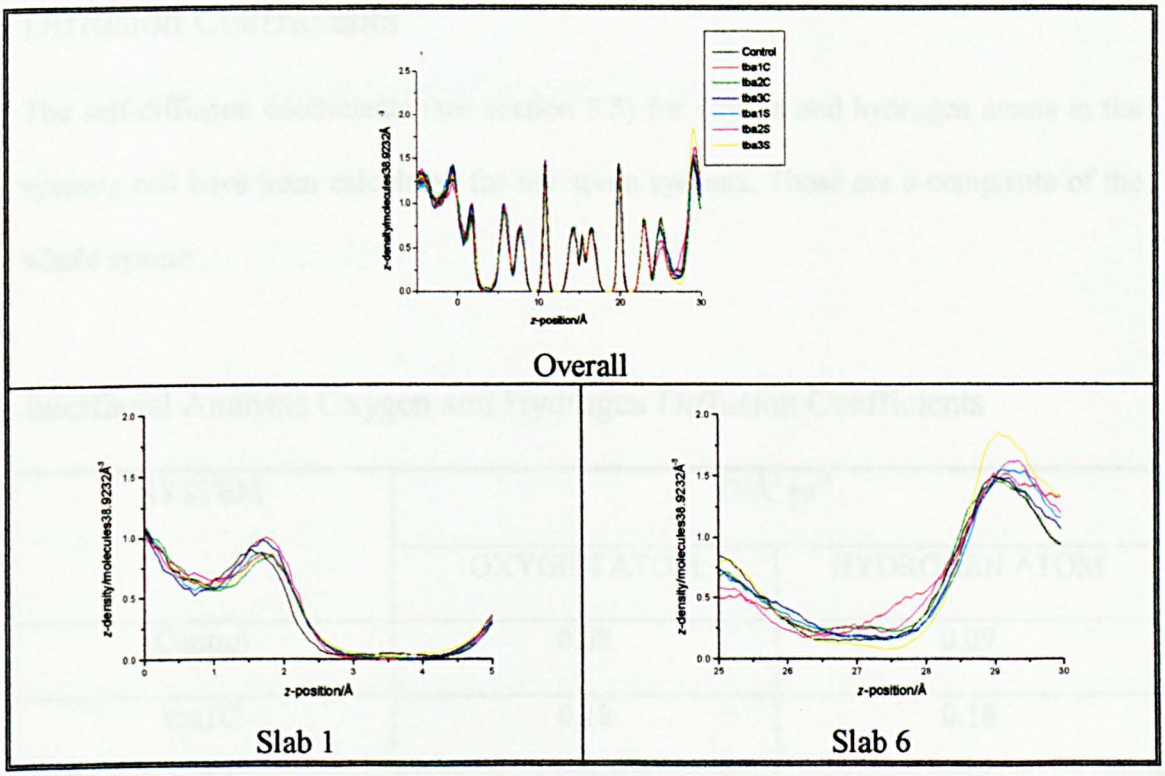

Figure 6.17 $\rho_G(Z)$ distributions for the seven systems. The legend is the same for each plot.

As with $\rho_O(Z)$, the overall $\rho_G(Z)$ distribution shows a regular crystalline arrangement of peaks in the central region of the gas hydrate lattice, namely between ~ 5 and ~ 25 Å, consistent with a stable hydrate core. A general increase in the peak heights is apparent

in $\rho_G(Z)$ at 300 K compared with 277 K. From the expanded view of the $\rho_G(Z)$ distribution in the region of slab 1 we see that there is more variation in the curves than was observed at 277 K. For slab 6 the behaviour of the inhibitor/control systems is as per 277 K, however it can be seen that the peak heights at 300 K have increased compared with 277 K

Diffusion Coefficients

The self-diffusion coefficients (see section 3.5) for oxygen and hydrogen atoms in the systems cell have been calculated for the seven systems. These are a composite of the whole system.

Interfacial Analysis Oxygen and Hydrogen Diffusion Coefficients

SYSTEM	D/Å^2 ps^{-1}	
	OXYGEN ATOM	HYDROGEN ATOM
Control	0.08	0.09
tba1C	0.18	0.18
tba2C	0.04	0.04
tba3C	0.05	0.05
tba1S	0.15	0.15
tba2S	0.05	0.05
tba3S	0.08	0.09

Table 6.21 Summary of oxygen and hydrogen atom self-diffusion coefficients.

The self-diffusion coefficients for the oxygen and hydrogen atoms as calculated by DL_POLY[3] are given in table 6.21. The oxygen and hydrogen self-diffusion coefficients are smaller at 300 K than those observed at 277 K except for tba1C and tba1S which show comparable results to those obtained at 277 K. Presumably the effect of higher temperature is compensated by the effects of higher pressure to the extent that lower overall mobility results.

Interfacial Analysis Co-ordination Number

The co-ordination number (see section 3.4) for water molecules in the six slabs for the seven systems are given in table 6.22.

SYSTEM	CO-ORDINATION NUMBER					
	SLAB 1	SLAB 2	SLAB 3	SLAB 4	SLAB 5	SLAB 6
Control	3.91	4.10	3.99	4.00	4.06	3.67
tba1C	3.82	4.10	4.00	4.00	4.16	3.76
tba2C	3.87	4.12	4.00	3.99	4.07	3.67
tba3C	3.85	4.11	4.00	3.99	4.05	3.68
tba1S	3.89	4.13	4.00	3.99	4.09	3.71
tba2S	3.88	4.11	4.00	4.00	4.21	3.84
tba3S	3.88	4.14	4.00	4.01	4.07	3.76

Table 6.22 Summary of co-ordination numbers for slabs 1–6 in the seven systems.

These values are in accord with the data at 277 K. All values are slightly higher than at 277 K, and the difference between slabs 1 and 6 is less pronounced at the higher temperature.

Interfacial Analysis Local Phase Assignments

The order parameters F_3, $F_{4\varphi}$ and F_{4t} (see section 3.3) have been calculated for water molecules as before. The corresponding local phase assignments for water molecules can be seen in table 6.23.

SYSTEM	NUMBERS OF WATERS IN EACH PHASE		
	HYDRATE	ICE	LIQUID
Control	251	8	148
tba1C	245	9	154
tba2C	251	8	149
tba3C	255	8	144
tba1S	249	9	151
tba2S	240	8	160
tba3S	248	8	151

Table 6.23 Local phase assignment summary for the seven systems.

From table 6.23 it can be seen that the trends observed at 300 K are similar to those observed at 277 K, however in this instance only tba2S shows any real deviation from

the control values whereas at 277 K this was true for tba2S and also tba2C. In general, the number of hydrate-like water molecules is smaller by ~ 15 % at the higher temperature.

6.2.4 300 K Inhibitor-based Analysis

Radial Distribution Functions

Various radial distribution functions (see section 3.2) have been calculated. In the following sections these are presented along with a summary of the peak positions and, where applicable, the area of the first peak.

Inhibitor-based Radial Distribution Functions–g_{XO} and g_{XH}

The RDFs for the inhibited systems can be seen in figures 6.18 and 6.19. Corresponding peak positions have been extracted and presented in appendices 6.9 and 6.10 and graphs 6.9 and 6.10.

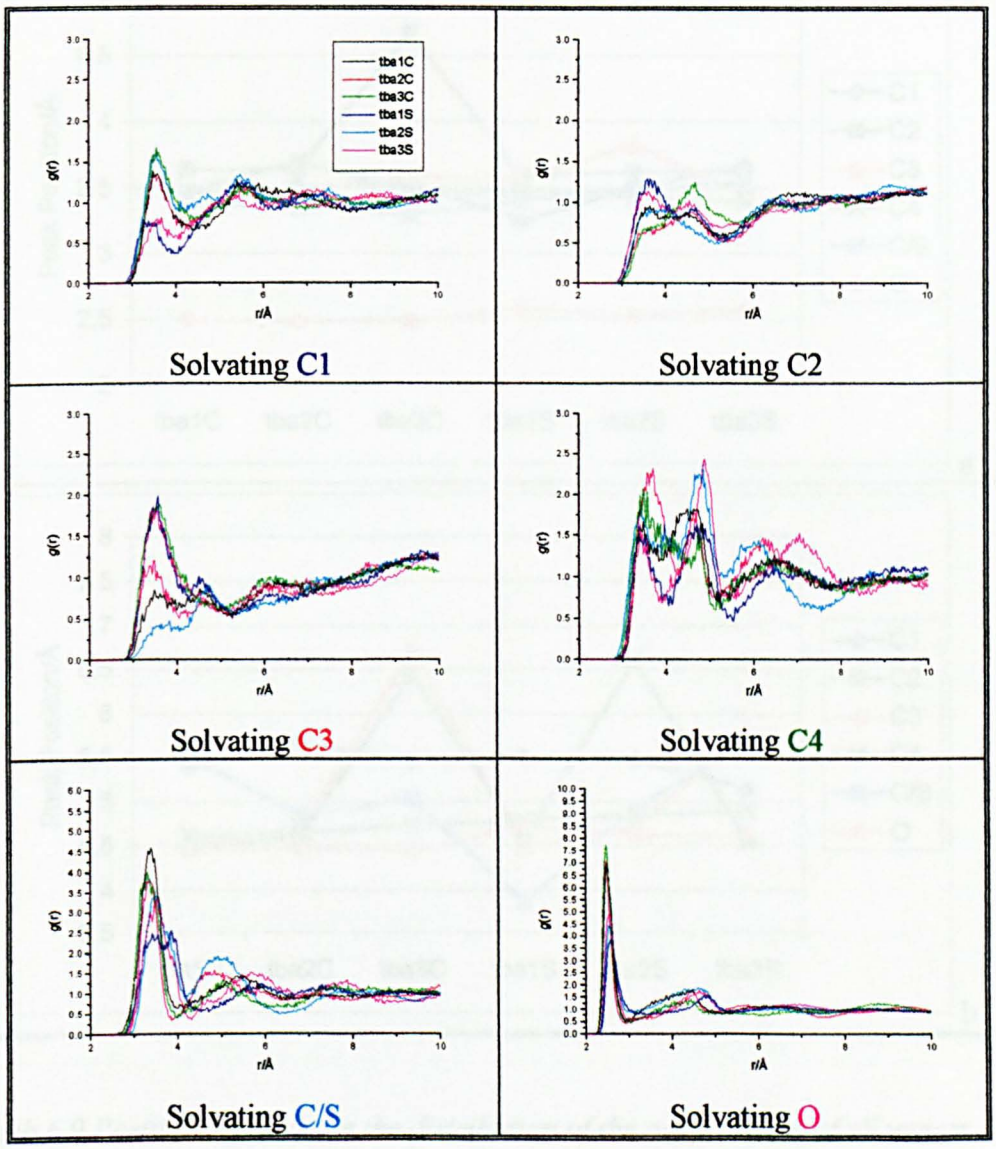

Figure 6.18 The radial distribution function of the oxygen atom of all waters around various solute atoms for the inhibited systems. The legend is the same for each plot and the atom numbers are coloured as per figure 6.3.

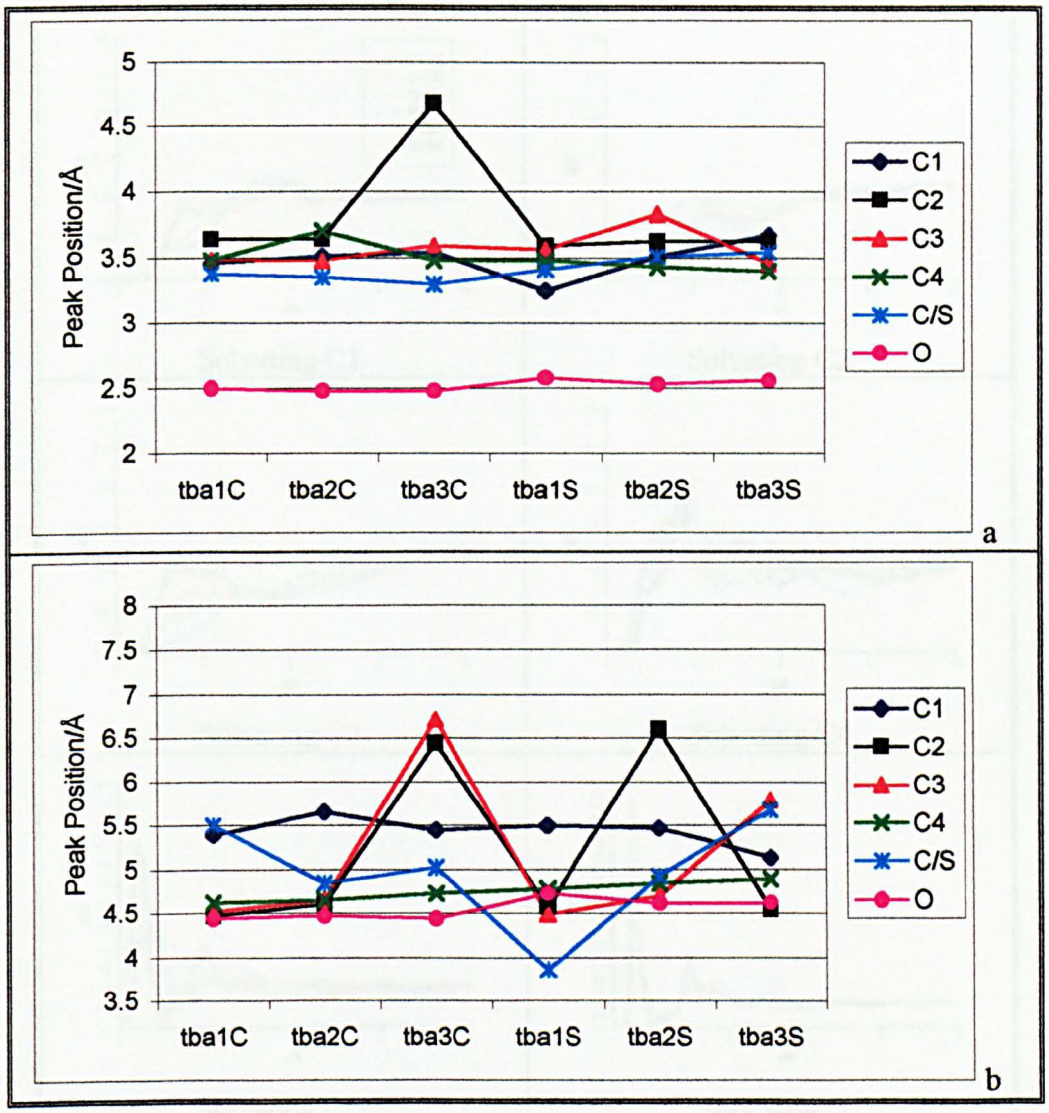

Graph 6.9 Positions of peaks in the distribution of the oxygen atom of all waters about the inhibitors, first peak positions (a) and second peak positions (b), in g_{XO}. The plot is coloured as per figure 6.3. Numerical values are also given in appendix 6.9.

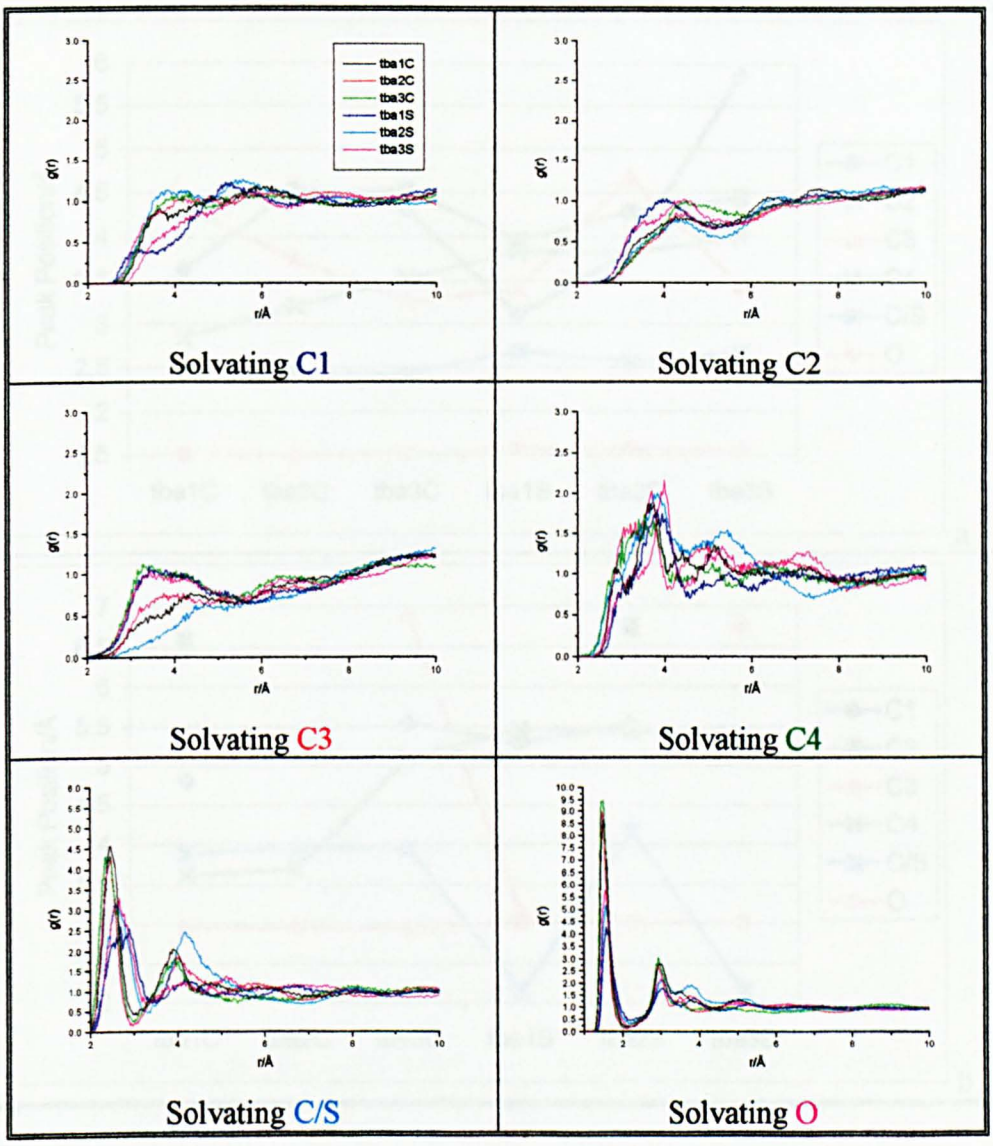

Figure 6.19 The radial distribution function of the hydrogen atom of all waters around various solute atoms for the inhibited systems. The legend is the same as per figure 6.3

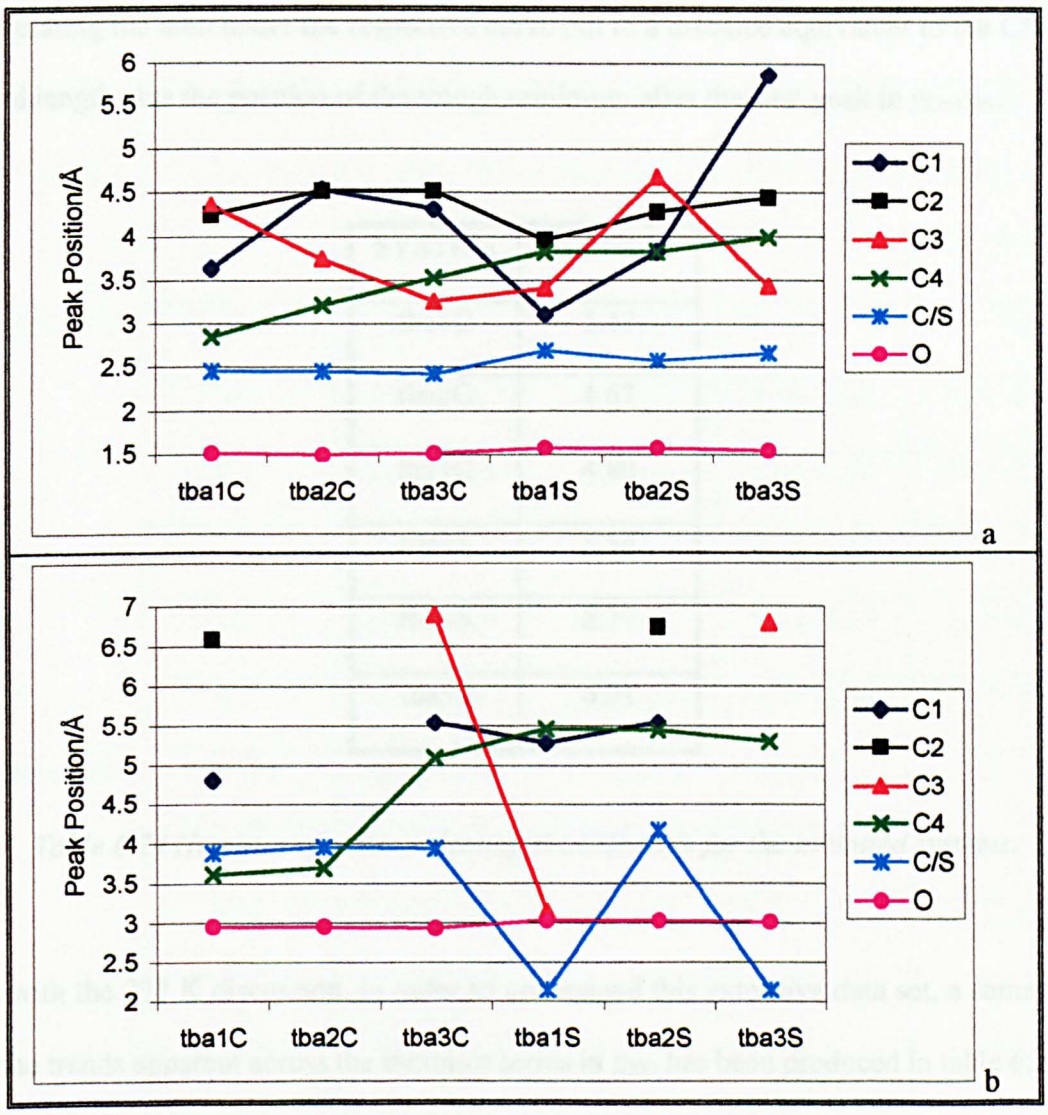

Graph 6.10 Positions of peaks in the distribution of the hydrogen atom of all waters about the inhibitors, first peak positions (a) and second peak positions (b), in g_{XH}. The plot is coloured as per figure 6.3, some of the peak positions have been omitted due to an inability to resolve the data. Numerical values are also given in appendix 6.10.

In addition the RDFs have been used to calculate the number of water molecules in the first solvation shell of the C/S atom and these are presented in table 6.24. This is done by

calculating the area under the respective curve out to a distance equivalent to the C/S–O bond length plus the position of the trough minimum after the first peak in g_{OwOw}.

SYSTEM	NUMBER
tba1C	5.47
tba2C	4.67
tba3C	4.80
tba1S	5.88
tba2S	8.77
tba3S	6.01

Table 6.24 Numbers of water solvating the C/S atom for the inhibited systems.

As with the 277 K discussion, in order to understand this extensive data set, a summary of the trends apparent across the inhibitor series in g_{XO} has been produced in table 6.25.

INHIBITOR FAMILY	ATOM	EFFECT ON PEAK POSITION IN g_{XO}.		RANGE OF PEAK POSITIONS/Å	
		1st	2nd	1st	2nd
Carboxylate	O	Constant	Constant	~ 2.5	~ 4.4
	C	Decrease	Minimum	3.30–3.38	4.84–5.50
	C4	Maximum	Increase	3.48–3.70	4.62–4.73
	C3	Minimum	Increase	3.48–3.59	4.52–6.72
	C2	Minimum	Increase	3.64–4.68	4.47–6.45
	C1	Increase	Maximum	3.46–3.54	5.39–5.66
Sulphonate	O	Constant	Minimum	~ 2.6	4.62–4.73
	S	Increase	Increase	3.41–3.54	3.86–5.68
	C4	Constant	Increase	~ 3.4	4.78–4.89
	C3	Maximum	Increase	3.46–3.83	4.49–5.79
	C2	Constant	Maximum	~ 3.6	4.54–6.61
	C1	Increase	Decrease	3.25–3.67	5.13–5.50

Table 6.25 Effect on 1st and 2nd peak position in g_{XO} of increasing zwitterionic charge separation for the carboxylates and sulphonates.

From the g_{XO} for the carboxylates it can be seen that:

i) the general appearance of the g_{XO} plots for the carboxylates are similar to those at 277 K;

ii) for the O and C atoms the effect on the 1st and 2nd peak positions is essentially the same as well as the general positions of the 1st and 2nd peaks, however the range exhibited by the 1st and 2nd peak positions is smaller than seen at 277 K;

iii) for the C3 atom the effect on the 1st and 2nd peak positions shows no correlation with 277 K but the same effect as for the O and C atoms is seen for the general positions and range exhibited by the 1st and 2nd peak positions;

iv) an analogous trend is observed for the number of waters solvating the C atom with tba2C showing a minimum.

From the g_{XO} for the sulphonates it can be seen that:

i) the general appearance of the g_{XO} plots for the sulphonates are similar to those at 277 K;

ii) for the O, S and C3 atoms the effect on the 1st and 2nd peak positions is different to that observed at 277 K. In addition the general positions of the 1st and 2nd peaks are generally at smaller distances, for the O, S and C3 atoms the range exhibited by the 1st and 2nd peak positions tends to be the same, as seen at 277 K;

iii) an analogous trend is observed for the number of waters solvating the S atom with tba2S showing a maximum.

It can therefore be concluded that the carboxylates show in general the same results as seen at 277 K, while the sulphonates behaviour is essentially changed at the increased temperature.

An analogous summary table for the g_{XH} is given in table 6.26.

INHIBITOR FAMILY	ATOM	EFFECT ON PEAK POSITION IN g_{XH}.		RANGE OF PEAK POSITIONS/Å	
		1st	2nd	1st	2nd
Carboxylate	O	Constant	Constant	~ 1.5	~ 3.0
	C	Constant	Maximum	~ 2.5	3.88–3.96
	C4	Increase	Increase	2.85–3.54	3.62–5.10
	C3	Decrease	N.A.	3.27–4.36	N.A.
	C2	Maximum	N.A.	4.25–4.52	N.A.
	C1	Maximum	N.A.	3.64–4.54	N.A.
Sulphonate	O	Constant	Constant	~ 1.6	~ 3.0
	S	Minimum	Maximum	2.58–2.69	2.15–4.17
	C4	Minimum	Decrease	3.83–3.99	5.31–5.47
	C3	Maximum	N.A.	3.41–4.68	N.A.
	C2	Increase	N.A.	3.96–4.44	N.A.
	C1	Increase	N.A.	3.11–5.87	N.A.

Table 6.26 Effect on 1st and 2nd peak position in g_{XH} of increasing zwitterionic charge separation for the carboxylates and sulphonates.

From the g_{XH} data for the carboxylates it can be seen that:

i) the general appearance of the g_{XH} plots for the carboxylates are similar to those at 277 K;

ii) for the O atom the effect on the 1st and 2nd peak positions is the same as well as the general positions and ranges exhibited by the 1st and 2nd peaks, as seen at 277 K;

iii) for the C atom the effect on the 1st and 2nd peak positions is different, while the general positions and ranges exhibited by the 1st and 2nd peaks are the same, as seen at 277 K;

iv) for the C3 atom the data is unable to be resolved.

From the g_{XH} for the sulphonates it can be seen that:

i) the general appearance of the g_{XO} plots for the sulphonates are similar to those at 277 K;

ii) for the O and S atoms the effect on the 1st and 2nd peak positions is generally the same as that observed at 277 K. In addition the general positions of the 1st and 2nd peaks and the range exhibited by the 1st and 2nd peak positions tends to be the same as seen at 277 K;

iii) for the C3 atom the data is unable to be resolved.

Co-ordination Number

The numbers of solvated waters with a certain co-ordination number (see section 3.4), ranging from 1–10, has been calculated for the six systems. The co-ordination number refers to the co-ordination number of water, when water is next to X. In the following sections the most popular co-ordination number is tabulated along with the percentage of waters with co-ordination number 3, 4 or 5, this is as opposed to 277 K where the percentage of waters for co-ordination numbers 2, 3 or 4 was tabulated. This is due to

the fact that upon inspection of the distributions it was found that a greater percentage of solvated waters existed for co-ordination number 5 when compared with co-ordination number 2. In all of the inhibited systems the number of waters is the same and as a result the percentage of waters solvating each inhibitor atom for co-ordination numbers 1–10 has been calculated. This is done by totalling the number of waters solvating each atom of the inhibitors for each co-ordination number 1–10, this total is then used to divide the number of waters solvating each inhibitor atom for each co-ordination number 1–10, leading to a percentage of waters solvating each atom for co-ordination numbers 1–10.

Inhibitor-based Co-ordination Number

Data for the co-ordination number distribution of solvated water is presented in appendix 6.11 and graph 6.11, with a summary of the trends in the data in table 6.27.

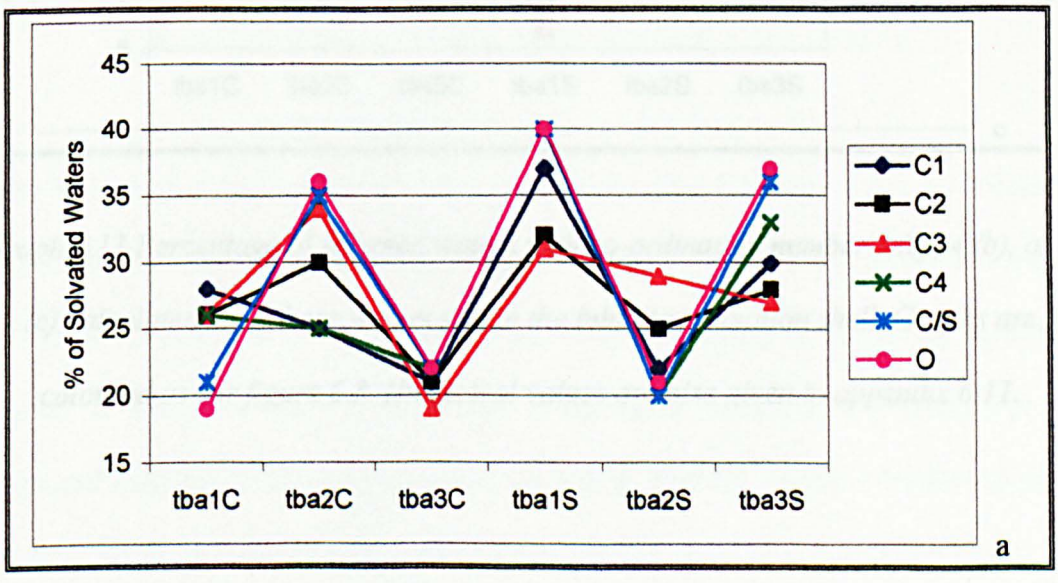

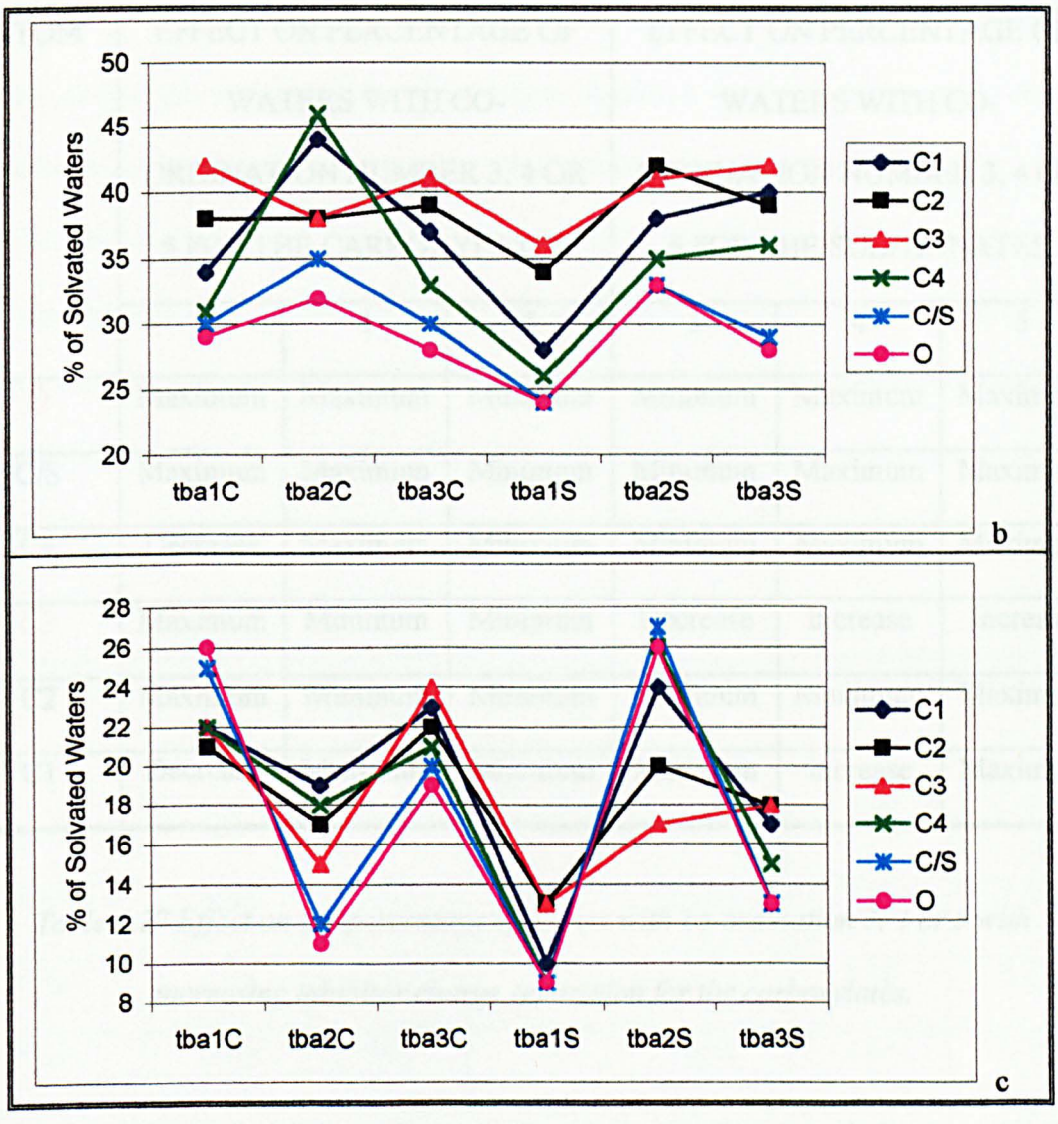

Graph 6.11 Percentage of solvated waters with co-ordination number 3 (a), 4 (b), or 5 (c) calculated from those waters within the inhibitor solvation shell. Graphs are coloured as per figure 6.3. Numerical values are also given in appendix 6.11.

ATOM	EFFECT ON PERCENTAGE OF WATERS WITH CO-ORDINATION NUMBER 3, 4 OR 5 FOR THE CARBOXYLATES			EFFECT ON PERCENTAGE OF WATERS WITH CO-ORDINATION NUMBER 3, 4 OR 5 FOR THE SULPHONATES		
	3	4	5	3	4	5
O	Maximum	Maximum	Minimum	Minimum	Maximum	Maximum
C/S	Maximum	Maximum	Minimum	Minimum	Maximum	Maximum
C4	Decrease	Maximum	Minimum	Minimum	Maximum	Maximum
C3	Maximum	Minimum	Minimum	Decrease	Increase	Increase
C2	Maximum	Minimum	Minimum	Minimum	Maximum	Maximum
C1	Decrease	Maximum	Minimum	Minimum	Increase	Maximum

Table 6.27 Effect on the percentage of waters with co-ordination 3, 4 or 5 with increasing inhibitor charge separation for the carboxylates.

From table 6.27 it can be seen for the carboxylates that for a particular co-ordination number the net effect is in general the same for the C, O and C3 atoms as was seen at 277. However at 277 K there was a minimum for waters with co-ordination number 3, whereas at 300 K we have a maximum, there was a maximum for waters with co-ordination number 4, which is also seen at 300 K, and for waters with co-ordination number 5 we see a minimum at 300 K.

As at 277 K we can see from table 6.27 that we do not see a steady increase or decrease in the percentage of waters with co-ordination number 3, 4 or 5 with increasing charge separation but that in most cases we see either a maximum or minimum at tba2C.

The modal co-ordination number for O is 3–4 and for C and C3 is 4 (see appendix 6.11 for details); this is as opposed to 277 K where the modal co-ordination number for C3 was 3–4 and for O and C was 3. That increasing the temperature increased the modal co-ordination number for these atoms is in line with the results observed for the modal co-ordination number for the liquid simulations in chapter 4.

INHIBITOR	AVERAGE CO-ORDINATION NUMBER FOR WATER AROUND ATOM					
	C1	C2	C3	C4	C	O
tba1C	3.90	3.91	3.97	3.87	3.94	3.97
tba2C	3.85	3.72	3.65	3.81	3.48	3.43
tba3C	3.89	3.88	3.96	3.75	3.60	3.55

Table 6.28 Average co-ordination number for water around the carboxylates constituent atoms.

The average co-ordination number for waters around a particular solute atom of the carboxylates is presented in table 6.28. The average co-ordination number for water around each atom of the carboxylates is much closer to 4 than was observed at 277 K. It can also be observed that the average co-ordination number for water around each atom

for tba2C is lower than for the other two inhibitors the opposite of the behaviour at 277 K where tba2C had the higher average co-ordination number for water around each atom.

From table 6.27 it can be seen for the sulphonates that for a particular co-ordination number the net effect is the same for the S and O atoms, but that the C3 atom shows a different behaviour, this is as opposed to 277 K where all 3 atoms showed the same net effect. As per the carboxylates it can be observed that in general a maximum or minimum is observed for tba2S as opposed to a steady increase or decrease with increasing charge separation.

The modal co-ordination number once more shows an increase compared to 277 K and is in line with the liquid simulations in chapter 4.

INHIBITOR	AVERAGE CO-ORDINATION NUMBER FOR WATER AROUND ATOM					
	C1	C2	C3	C4	S	O
tba1S	3.27	3.46	3.54	3.20	3.19	3.19
tba2S	4.01	3.91	3.76	4.05	4.07	4.03
tba3S	3.74	3.77	3.82	3.57	3.38	3.36

Table 6.29 Average co-ordination number for water around the sulphonates constituent atoms.

The average co-ordination number for waters around a particular solute atom of the sulphonates is presented in table 6.29. The average co-ordination number for water around each atom of the sulphonates has increased relative to 277 K, but the increase is not as marked as that seen for the carboxylates. At 277 K the sulphonates exhibited higher average co-ordination numbers for water around their constituent atoms whereas at 300 K we see due to the large increase in the carboxylates that this trend is reversed, with only tba2S being the exception It can also be observed that the average co-ordination number for water around each atom for tba2S is higher than for the other two inhibitors as seen at 277 K.

Order Parameters: F_3, $F_{4\varphi}$ and F_{4t}

The order parameters F_3, $F_{4\varphi}$ and F_{4t} (see section 3.3) for co-ordination numbers ranging from 1–10 have been calculated for the seven systems. In the following sections the values of F_3, $F_{4\varphi}$ and F_{4t} are tabulated for co-ordination numbers 3, 4 and 5.

Inhibitor-based F_3

Values for F_3 for the inhibitors are tabulated in appendix 6.12 and graph 6.12.

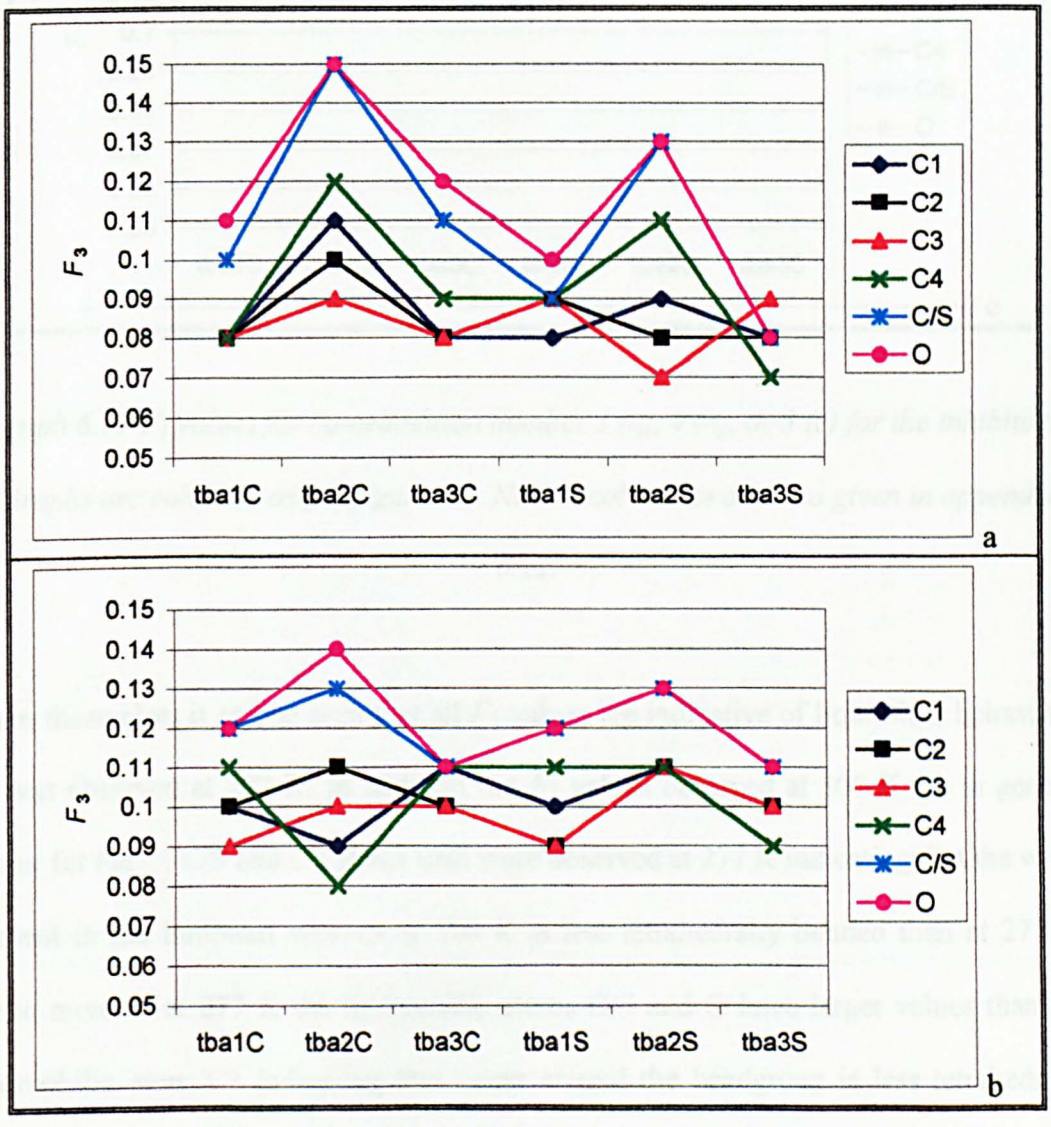

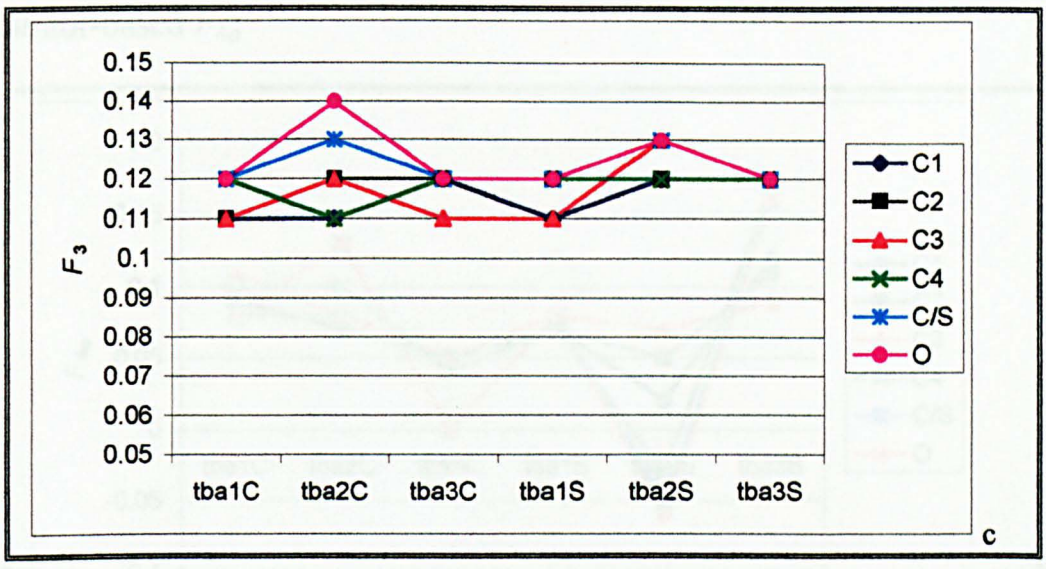

Graph 6.12 F_3 values for co-ordination number 3 (a), 4 (b), or 5 (c) for the inhibitors. Graphs are coloured as per figure 6.3. Numerical values are also given in appendix 6.12.

From these plots it can be seen that all F_3 values are indicative of liquid-like behaviour, as was observed at 277 K. In addition the F_3 values observed at 300 K are in general larger for the O, C/S and C3 atoms than were observed at 277 K indicating that the water present in the inhibited systems at 300 K is less tetrahedrally bonded than at 277 K. Once more as at 277 K the hydrophilic atoms C/S and O have larger values than the hydrophilic atom C3 indicating that water around the headgroup is less tetrahedrally bonded than around the CH_3 groups.

It can be seen from graph 6.12 that the F_3 values for waters with co-ordination number 3, 4 or 5 show a maximum for the central member of the inhibitor series, especially for tba2C compared with tba2S.

Inhibitor-based $F_{4\varphi}$

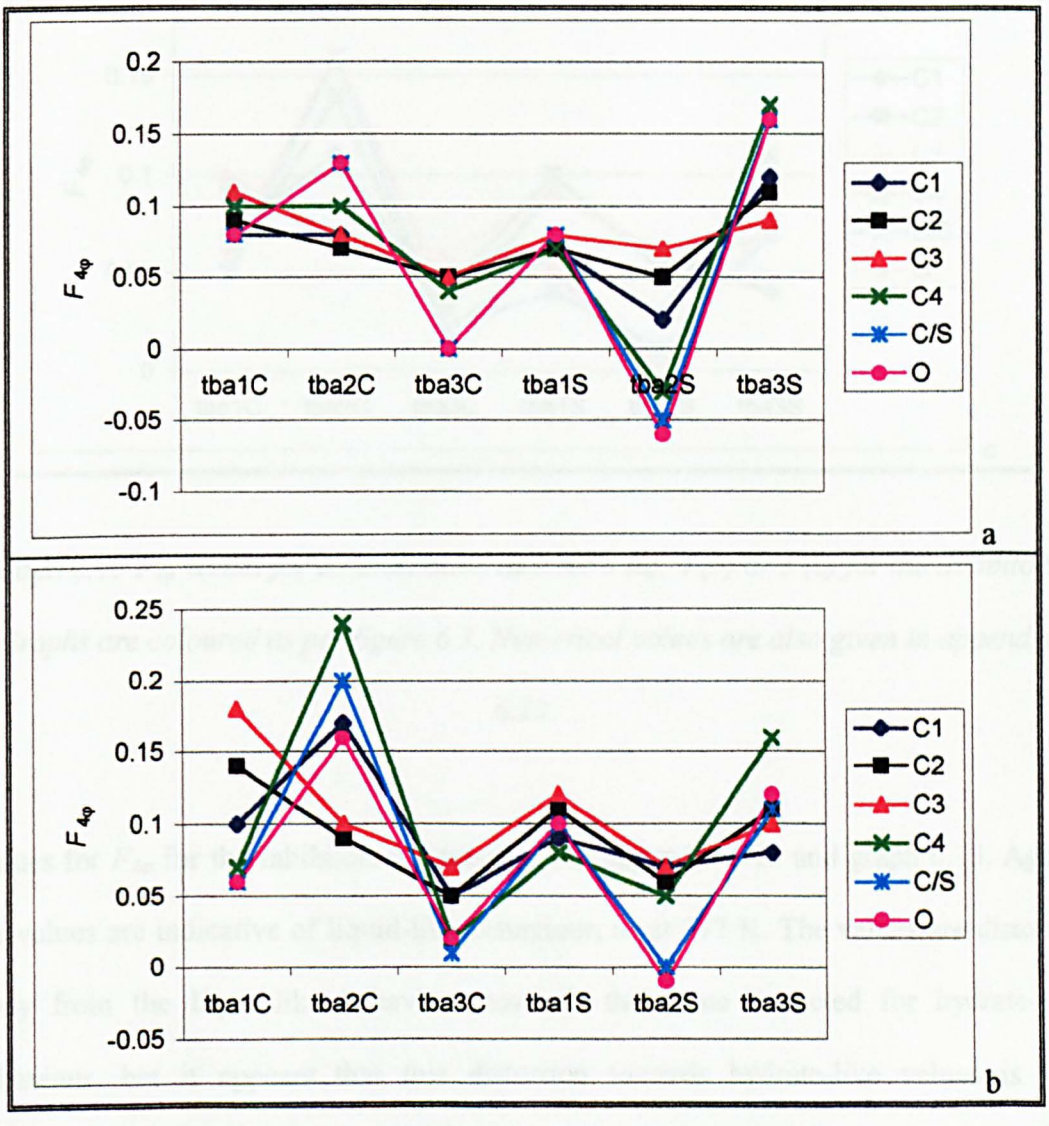

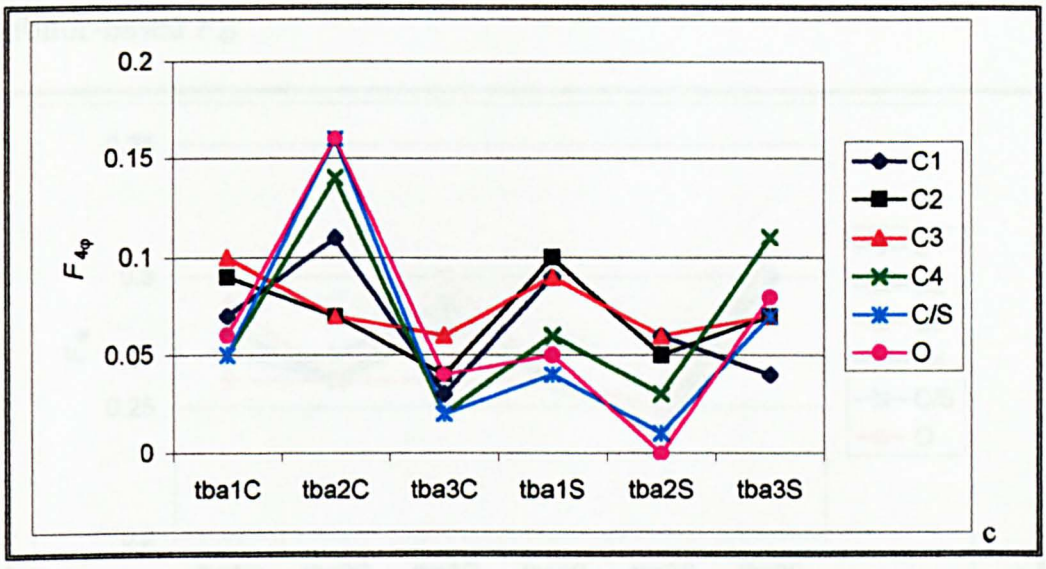

Graph 6.13 $F_{4\varphi}$ values for co-ordination number 3 (a), 4 (b) or 5 (c) for the inhibitors. Graphs are coloured as per figure 6.3. Numerical values are also given in appendix 6.13.

Values for $F_{4\varphi}$ for the inhibitors are tabulated in appendix 6.13 and graph 6.13. Again, the values are indicative of liquid-like behaviour, as at 277 K. The values are distorted away from the liquid-like behaviour towards the value expected for hydrate-like behaviour, but it appears that this distortion towards hydrate-like values is less pronounced in graph 6.13 than can be observed in graph 6.5 (the corresponding 277 K data). It can be seen from graph 6.13 that the $F_{4\varphi}$ values for waters with co-ordination number 3, 4 or 5 show a maximum for tba2C and a minimum for tba2S.

Inhibitor-based F_{4t}

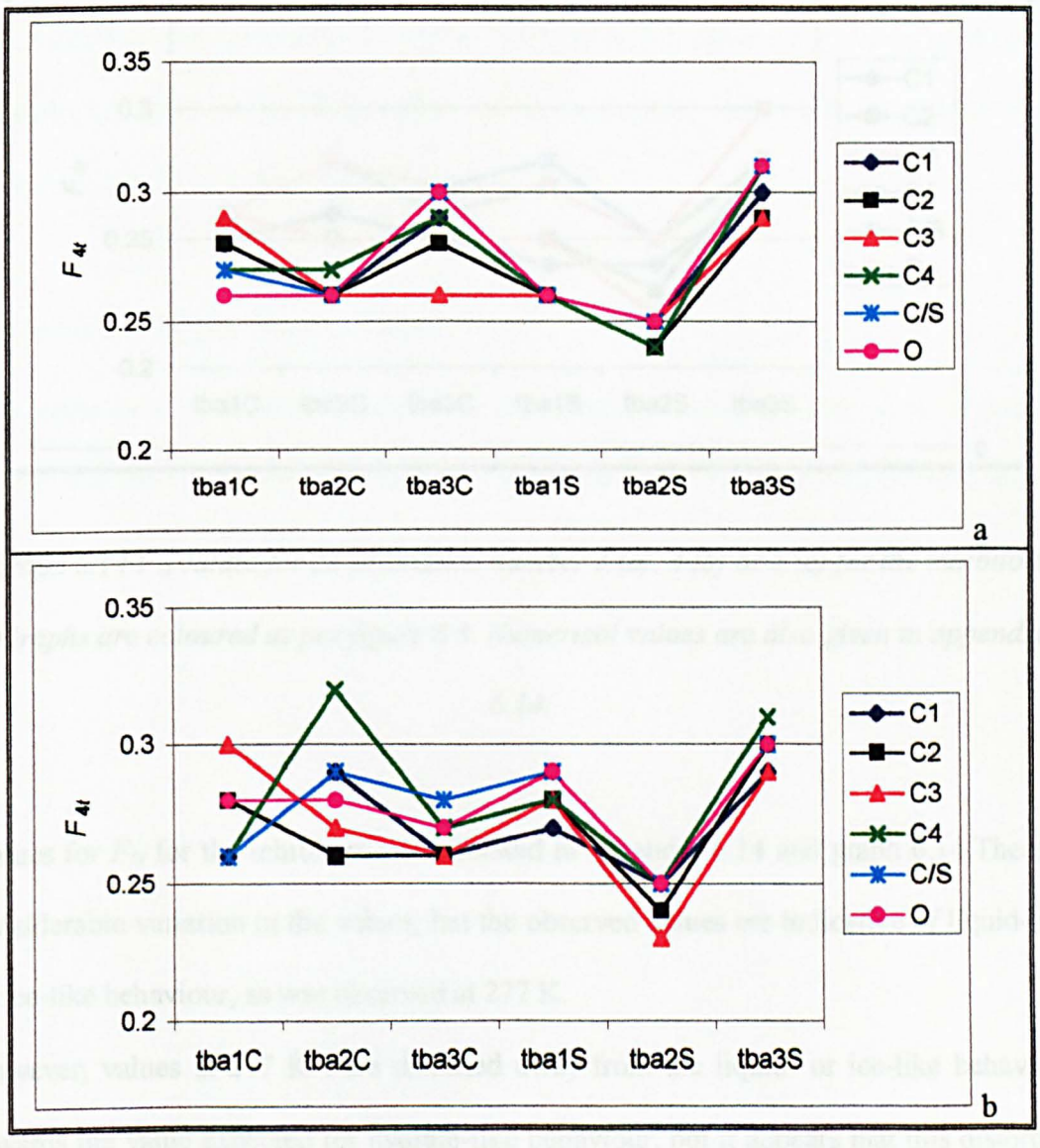

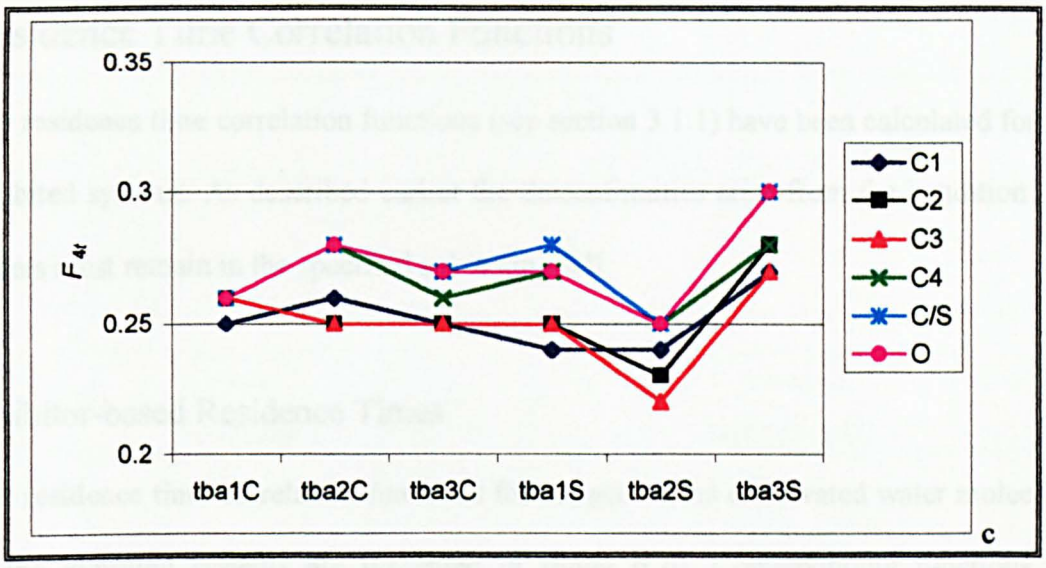

Graph 6.14 F_{4t} values for co-ordination number 3 (a), 4 (b) or 5 (c) for the inhibitors. Graphs are coloured as per figure 6.3. Numerical values are also given in appendix 6.14.

Values for F_{4t} for the inhibitors are tabulated in appendix 6.14 and graph 6.14.There is considerable variation in the values, but the observed values are indicative of liquid-like or ice-like behaviour, as was observed at 277 K.

However, values at 277 K were distorted away from the liquid- or ice-like behaviour towards the value expected for hydrate-like behaviour, but it appears that this distortion towards hydrate-like values is less pronounced at 300 K than can be observed in graph 6.6 (corresponding 277K data).

It can be seen from graph 6.14 that the F_{4t} values for waters with co-ordination number 3, 4 or 5 show a minimum for tba2S, with a minimum for tba2C being observed for waters with co-ordination number 3 only.

Residence Time Correlation Functions

The residence time correlation functions (see section 3.1.1) have been calculated for the inhibited systems. As described earlier the discontinuities arise from the condition that waters must remain in the specified solvation shell

Inhibitor-based Residence Times

The residence time correlation functions for oxygen atoms of solvated water molecules in the inhibited systems are presented in figure 6.20. Corresponding functions for hydrogen are essentially the same and so are not shown.

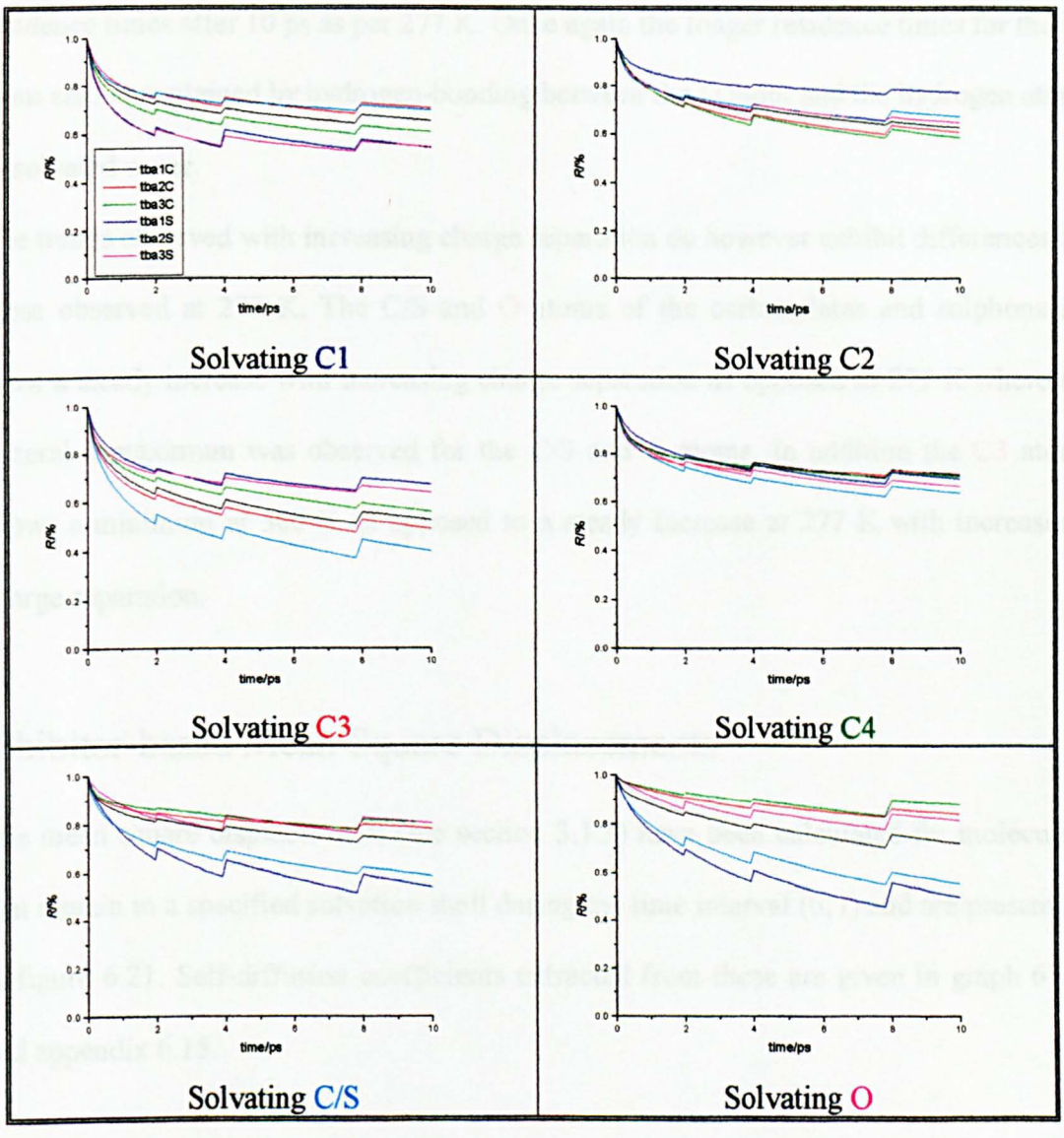

Figure 6.20 Residence time correlation function of the oxygen atom of solvated water around various solute atoms for the inhibited systems. The legend is the same for each plot and atom numbers are coloured as per figure 6.3.

The residence time correlation functions appear quantitatively the same as at 277 K with the C3 atom of the carboxylates and sulphonates once again showing the shortest

residence times after 10 ps of all atoms considered and the O atom showing the longest residence times after 10 ps as per 277 K. Once again the longer residence times for the O atom can be explained by hydrogen-bonding between the O atom and the hydrogen atom of solvated water.

The trends observed with increasing charge separation do however exhibit differences to those observed at 277 K. The C/S and O atoms of the carboxylates and sulphonates show a steady increase with increasing charge separation as opposed to 277 K where in general a maximum was observed for the C/S and O atoms. In addition the C3 atom shows a minimum at 300 K as opposed to a steady increase at 277 K with increasing charge separation.

Inhibitor-based Mean Square Displacements

The mean square displacements (see section 3.1.3) have been calculated for molecules that remain in a specified solvation shell during the time interval (0, t) and are presented in figure 6.21. Self-diffusion coefficients extracted from these are given in graph 6.15 and appendix 6.15.

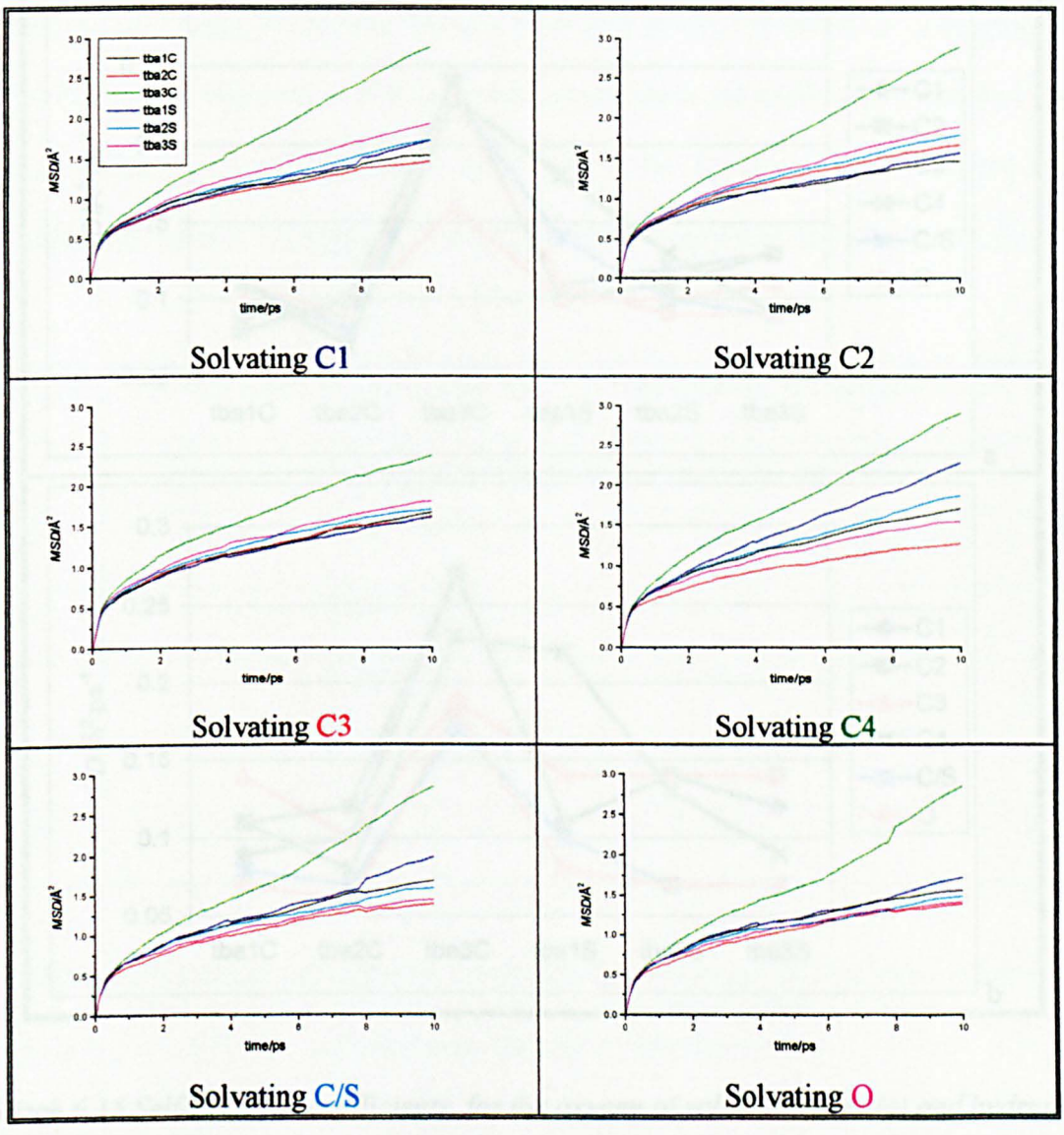

Figure 6.21 Mean square displacement of the oxygen atom of solvated water around various solute atoms for the inhibited systems. The legend is the same for each plot and atom numbers are coloured as per figure 6.3

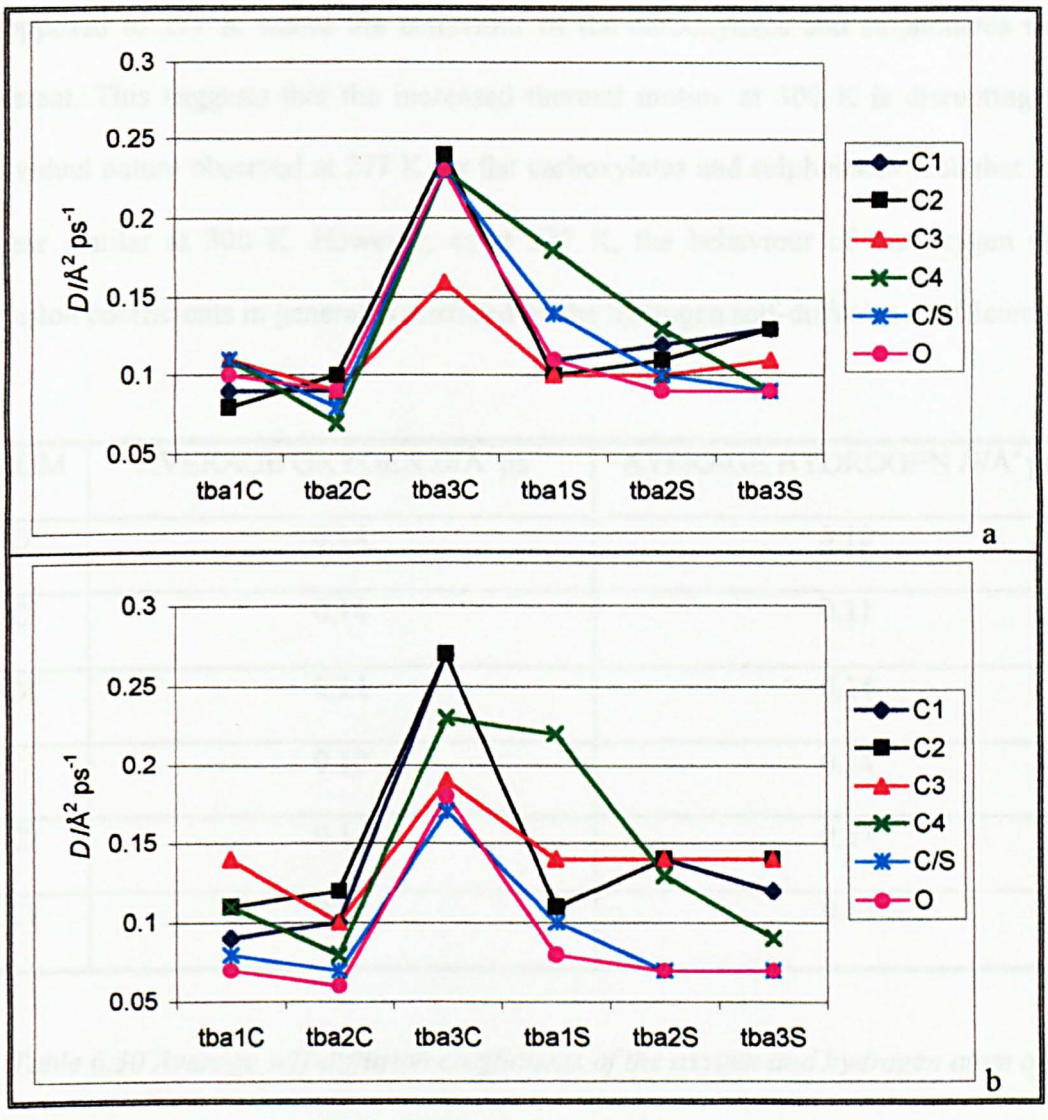

Graph 6.15 Self-diffusion coefficients, for the oxygen of solvated water (a) and hydrogen atom of solvated water (b), around various solute atoms for the inhibited systems. Graphs are coloured as per figure 6.3. Numerical values are also given in appendix 6.15.

From graph 6.15 it can be seen that in general the oxygen self-diffusion coefficient for the sulphonates and carboxylates show a minimum for the O, C/S and C3 atoms this is

as opposed to 277 K where the behaviour of the carboxylates and sulphonates were different. This suggests that the increased thermal motion at 300 K is disrupting the individual nature observed at 277 K for the carboxylates and sulphonates such that they appear similar at 300 K. However, as at 277 K, the behaviour of the oxygen self-diffusion coefficients in general is mirrored by the hydrogen self-diffusion coefficients.

ATOM	AVERAGE OXYGEN $D/Å^2 ps^{-1}$	AVERAGE HYDROGEN $D/Å^2 ps^{-1}$
O	0.14	0.10
C	0.14	0.11
C4	0.14	0.14
C3	0.12	0.14
C2	0.14	0.17
C1	0.14	0.15

Table 6.30 Average self-diffusion coefficients of the oxygen and hydrogen atom of solvated water for the carboxylates.

The average self-diffusion coefficients of the oxygen and hydrogen atom of solvated water for the carboxylates can be seen in table 6.30. From this table we can observe that the hydrophilic and hydrophobic atoms give rise to similar self-diffusion coefficients for the oxygen atom but that the hydrophilic and hydrophobic atoms are clearly separated by the hydrogen atom self-diffusion coefficients. This is as opposed to 277 K where both the oxygen and hydrogen atom self-diffusion coefficients were clearly delineated for

hydrophilic and hydrophobic atoms. As expected at the higher the temperature the average self-diffusion coefficients are larger for the oxygen and hydrogen atom than at 277 K.

ATOM	AVERAGE OXYGEN $D/Å^2 ps^{-1}$	AVERAGE HYDROGEN $D/Å^2 ps^{-1}$
O	0.10	0.07
S	0.11	0.08
C4	0.13	0.15
C3	0.10	0.14
C2	0.11	0.13
C1	0.12	0.12

Table 6.31 Average self-diffusion coefficients of the oxygen and hydrogen atom of solvated water for the sulphonates.

The average self-diffusion coefficients of the oxygen and hydrogen atom of solvated water for the sulphonates can be seen in table 6.31. This table shows that the sulphonates unexpectedly have smaller self-diffusion coefficients for the oxygen and hydrogen atom of solvated water than at 277 K, an opposite effect to that observed above for the carboxylates and in addition the carboxylates appear to have larger self-diffusion coefficients than the sulphonates the opposite to that seen at 277 K

From figure 6.21 it can be seen that tba3C exhibits a behaviour that is different to all the other inhibitors, with the mean square displacement plots being much higher than for the

other inhibitors. A similar anomalous behaviour was observed at 277 K, however in that instance tba3C had mean square displacement plots showing much smaller values for almost all solute atoms compared with the other inhibitors.

Inhibitor-based Legendre Orientational Correlation Functions

The time correlations functions for the second Legendre polynomial coefficients (see section 3.1.2) for the direction of the principal axes of water molecules have been calculated for the inhibited systems and are presented in figures 6.22 and 6.23. Once again, these functions do not exhibit exponential behaviour and so values at 10 ps have been taken as a measure of rotational lifetimes see appendix 6.16 and graph 6.16.

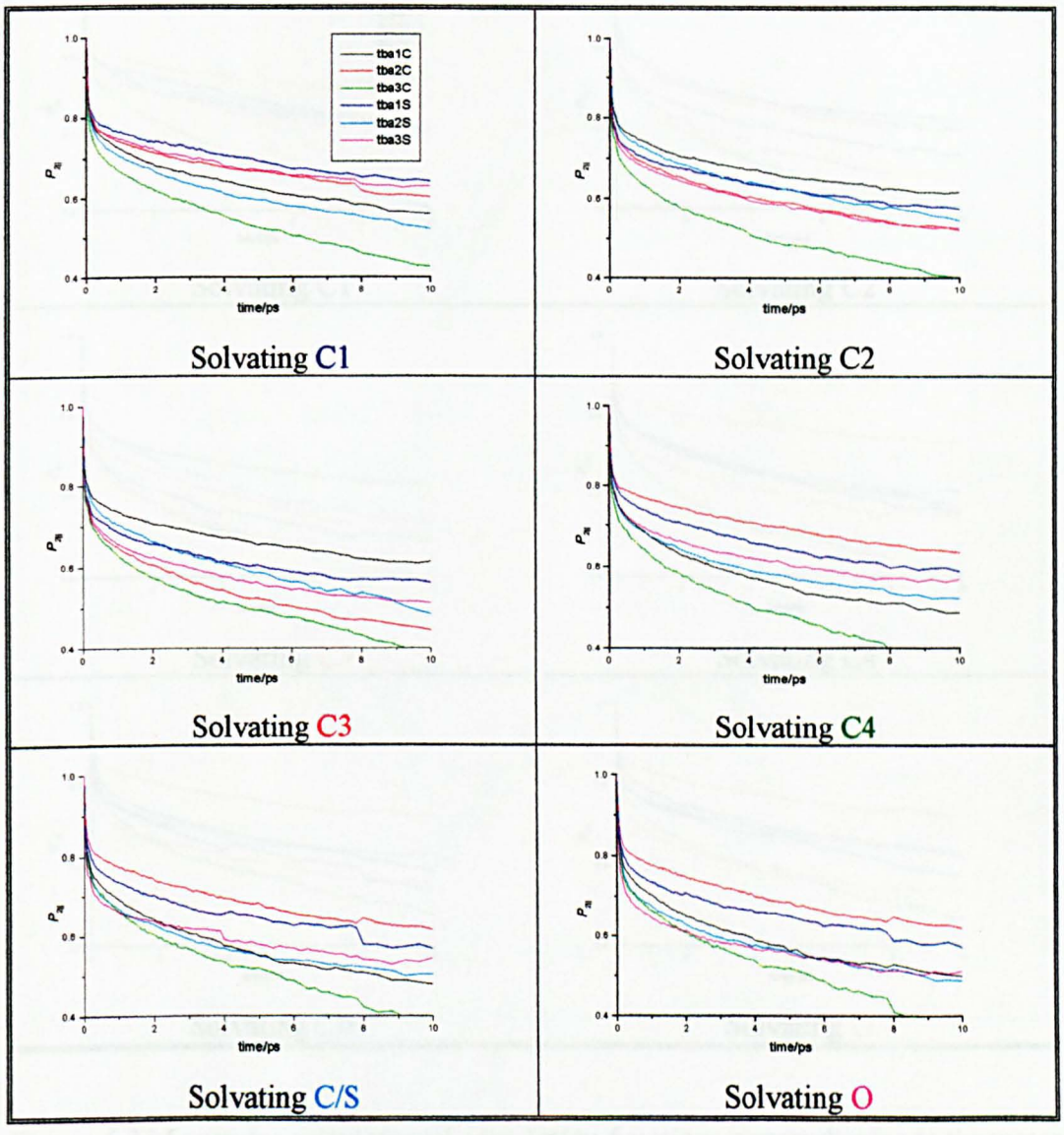

Figure 6.22 Legendre orientational correlation functions parallel to the water dipole vector of solvated water around various solute atoms for the inhibited systems. The legend is the same for each plot and atom numbers are coloured as per figure 6.3.

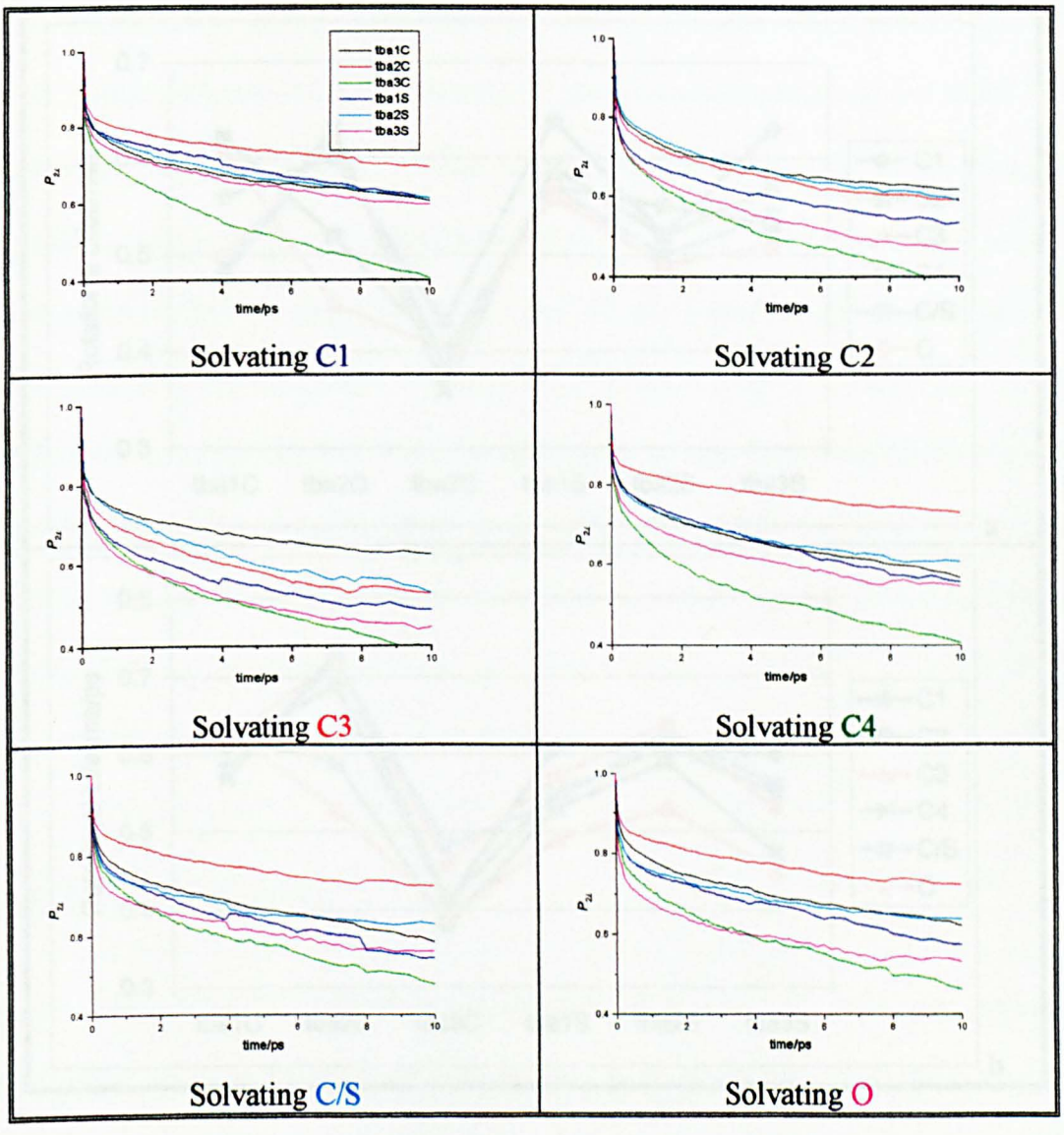

Figure 6.23 Legendre orientational correlation functions perpendicular to the water dipole vector of solvated water around various solute atoms for the inhibited systems. The legend is the same for each plot and atom numbers are coloured as per figure 6.3.

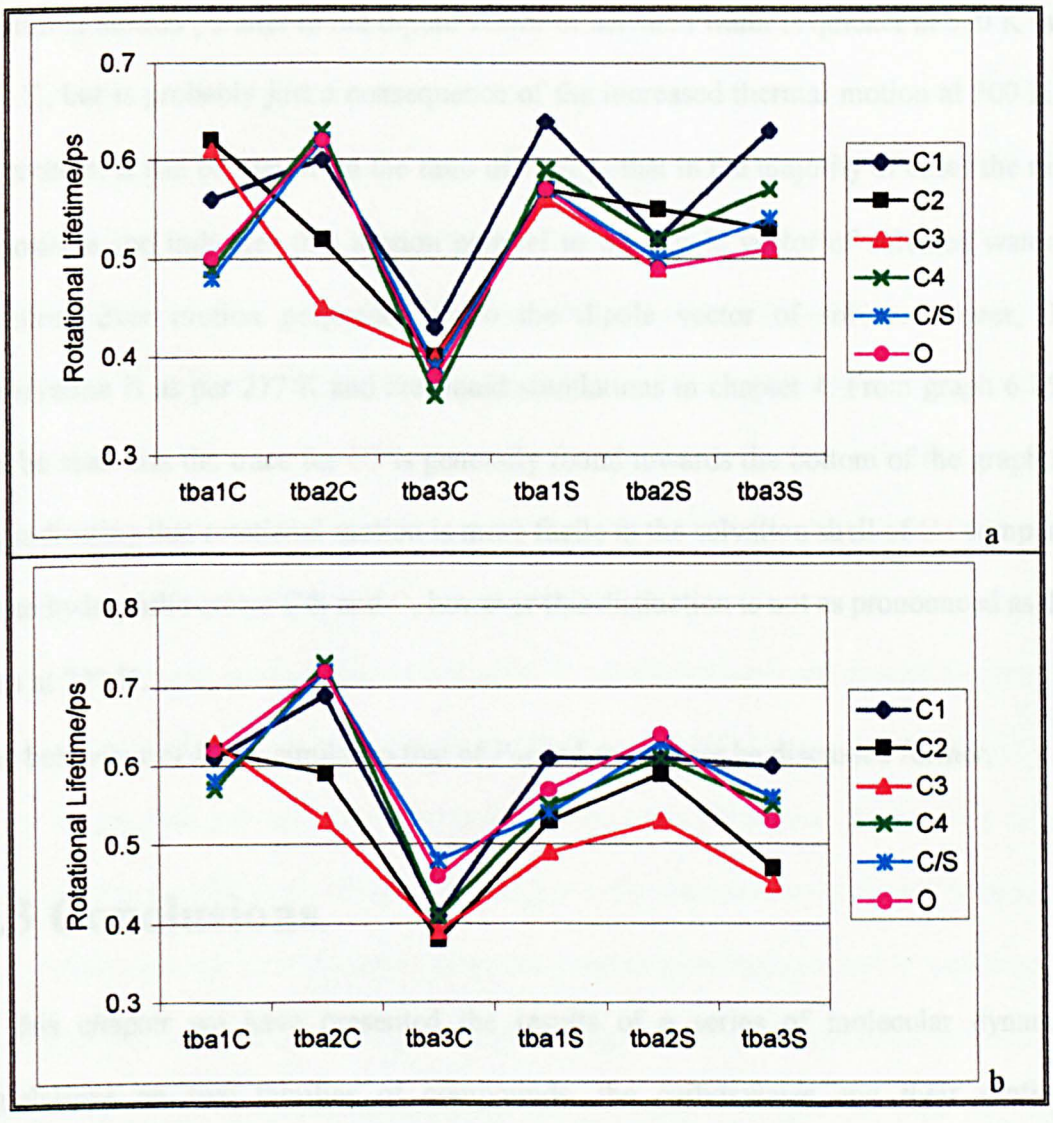

Graph 6.16 Rotational lifetimes for motion, parallel to the dipole vector (a) and perpendicular to the dipole vector (b), of solvated water around various solute atoms for the inhibited systems. Graphs are coloured as per figure 6.3. Numerical values are also given in appendix 6.16.

Considering appendix 6.16 and graph 6.16 it can be seen that there are many more cases of $P_{2\|}$ falling to 50 % or below in 10 ps than was observed at 277 K, this indicates that

rotational motion parallel to the dipole vector of solvated water is quicker at 300 K than 277 K, but is probably just a consequence of the increased thermal motion at 300 K in the system. It can be seen from the ratio of $P_{2\|}/P_{2\perp}$ that in the majority of cases the ratio is positive and indicates that motion parallel to the dipole vector of solvated water is favoured over motion perpendicular to the dipole vector of solvated water, this observation is as per 277 K and the liquid simulations in chapter 4. From graph 6.16 it can be seen that the trace for C3 is generally found towards the bottom of the graph for $P_{2\|}$ indicating that rotational motion is more facile in the solvation shell of C3 compared to the hydrophilic atoms C/S and O, however this distinction is not as pronounced as that seen at 277 K.

The behaviour of $P_{2\perp}$ is similar to that of $P_{2\|}$ and so will not be discussed further.

6.3 Conclusions

In this chapter we have presented the results of a series of molecular dynamics simulations on two families of compounds, the carboxylates and their synthetic analogues the sulphonates, in the presence of a type II gas hydrate lattice. Simulations have been carried out at two temperatures namely 277 and 300 K for each of the two families and also of a pure type II gas hydrate lattice to act as a control.

From the simulations performed a number of distributions and characteristic parameters have been calculated to allow for comparison of the control with the inhibited systems and in addition for comparison between the inhibited systems.

The simulations carried out at 277 K indicate that for the gas hydrate lattice in slab 6 there are some differences observed for the inhibitors studied. The radial distribution

function g_{OO} indicates that for the first two members of each inhibitor family that the water network structure is more relaxed than in the control system whereas for the last member of each inhibitor family the water network shows an opposite effect. The oxygen density distribution shows lower oxygen densities with the inhibitors present whereas the guest density distribution shows increased guest densities for the inhibited systems. The co-ordination numbers seems to identify differences between the carboxylates and the sulphonates, with the carboxylates having co-ordination numbers that are equivalent or smaller to the control system while the sulphonates show co-ordination numbers larger than the control system.

Analysing the solvent structure around specific inhibitor functional groups was used to develop comparisons between the two families. At 277 K the radial distribution functions g_{XO} and g_{XH} both show the carboxylates having first peak positions at shorter distances for the C/S and O atom indicating a contracted water network. The g_{XO} and g_{XH} distributions for the C/S and O atoms in general show higher water populations for the carboxylates due to an increased first peak height when compared to the sulphonates. The co-ordination numbers obtained for the inhibitors indicate for both the amine carboxylates and sulphonates that there is a disruption from the ideal tetrahedral co-ordination from 4 towards 3. All of the phase assignment results show the water molecules present in the six systems to be liquid-like, but with a weak tendency towards hydrate-like structure. The indication of possible increased structuring around the C/S and O atom for the carboxylates in the g_{XO} and g_{XH} radial distribution functions is complemented by the fact that diffusion is slower for the carboxylates than the amines sulphonates.

The simulations carried out at 300 K indicate that for the gas hydrate lattice in slab 6 there are some differences observed for the inhibitors studied. The radial distribution function g_{OO} indicates that for the carboxylates the first solvation shell is more highly populated than for the sulphonates given the increased first peak height and in addition the second peak is at longer distances indicating a relaxation in the water network at longer distances. The oxygen density distribution shows lower oxygen densities with the majority of the inhibitors present whereas the guest density distribution shows increased peak heights relative to 277 K. The co-ordination number summary shows higher co-ordination numbers for water around the inhibitors.

At 300 K the radial distribution functions g_{XO} and g_{XH} both show the carboxylates having first peak positions at shorter distances for the C/S and O atoms indicating a contracted water network with a corresponding increase in the first peak height for the carboxylates indicating a more highly populated first solvation shell. The co-ordination numbers obtained for the inhibitors indicate for both the amines carboxylates and sulphonates that the co-ordination number is as one would expect for tetrahedrally bonded water, namely 4. All of the phase assignment results show the water molecules present in the six systems to be liquid-like. The indication of possible increased structuring around the C/S and O atom for the carboxylates in the g_{XO} and g_{XH} radial distribution functions is complemented by the fact that diffusion is slower for the carboxylates than the amine sulphonates.

6.4 References

[1] Brooks, B.R., Bruccoleri R.E., Olafson B.D., States D.J., Swaminathan S., CHARMm: A Program for Macromolecular Energy, Minimisation and Dynamics Calculations, *J. Comp. Chem.*, **4**, 1983, 187.

[2] Cerius[2], Molecular Simulations Inc., San Diego, USA.

[3] Smith, W., Forester T.R., *J. Mol. Graphics*, **14**, 1996, 136.

[4] Ewald P., *Ann. Phys.*, **64**, 1921, 253.

[5] Fidler J., Rodger P.M., *J Phys Chem B*, **103**, 1999, 7695.

[6] Carver T.J., Drew M.G.B., Rodger P.M., *Phys. Chem. Chem. Phys.*, **1**, 1999, 1807.

CHAPTER 7

EXPERIMENTAL STUDY OF THE INHIBITION PROPERTIES OF TBA3S

7 Introduction

In this chapter the investigation into the behaviour of the inhibitor tba3S upon the formation of two hydrates, namely tetrahydrofuran and ethane, is outlined. Experiments upon tetrahydrofuran were performed at the Universite de Pau et des Pays de l'Adour in collaboration with M. L. Zanota, while the experiments on ethane were performed at ENSIGCT in Toulouse in collaboration with J.P. Monfort and L. Jussaume. Synthesis of tba3S was performed by P. Taylor at the University of Warwick. This work was undertaken because kinetic inhibitors act at the liquid water/hydrate interface, however it is not clear whether the kinetic inhibitors affect the hydrate surface or liquid water structure. Therefore by investigating the effect of tba3S upon the formation of two hydrates we can identify any activity in the hydrate region and also it allows for comparison with the computational experiments carried out in chapter 6. The chapter is divided into six parts as outlined below.

7.1 A brief introduction to tetrahydrofuran (THF) hydrate and ethane hydrate.

7.2 An outline of the synthesis of tba3S.

7.3 Nucleation and growth of THF hydrate.

7.4 Morphology of THF hydrate.

7.5 Nucleation and growth of ethane hydrate.

7.6 Conclusions.

7.1 Brief Introduction to THF/C_2H_6 Hydrate

In the following sections the properties of the two hydrates upon which our experiments have been performed, namely THF and C_2H_6, are outlined along with the reasons for the choice of these two hydrates.

7.1.1 THF

Physical Properties of THF

THF is a colourless, volatile liquid, which is completely miscible with water as well as with a number of other solvents. Its formula is C_4H_8O, it has a molar weight of 72.11 g mol^{-1} and its structure is shown in figure 7.1. Some of the physical properties of THF are outlined in table 7.1.

Formula	C_4H_8O
Molar Weight/g	72.11
CAS-RN	109-99-9
Melting Point/°C	-108.3
Boiling Point/°C	65

Table 7.1 Physical Properties of THF.

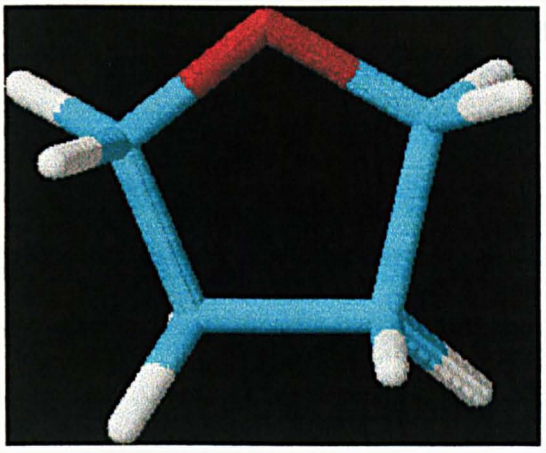

Figure 7.1 Structure of THF. Blue is carbon, red oxygen and white hydrogen.

Why use THF Hydrate?

THF hydrate is an appealing system for studying gas hydrate properties as well as for high throughput screening of inhibitors for a number of reasons. These include:

a) THF forms a structure II hydrate, which is the structure of most hydrates of natural gas;

b) the thermodynamic and experimental considerations associated with the THF/water system are not complicated, as a 23.56 wt.% THF in water solution will form hydrate at 5 °C and 1 atm;

c) unlike natural gas components THF is miscible with water and so formation of THF hydrate is therefore not limited by mass transfer problems across the liquid-gas interface.

THF Hydrate

THF hydrate was first reported in 1950 by Palmer.[1] THF hydrate forms a structure II face centred cubic hydrate with composition $THF.17H_2O$ just as the hydrates of natural gas. The unit cell contains 16 pentagonal dodecahedral cages (d ~ 5 Å) and 8

hexakaidecahedral cages (d ~ 6 Å) constructed from 136 water molecules. The THF molecules are trapped in each of the hexakaidecahedral cages by a weak van der Waals interaction.

THF hydrate has three different types of disorder in the crystal. The first is related to the configuration of protons in the hydrogen-bonded host lattice formed by water molecules. The second is the orientational disorder of the guest molecules in the hexakaidecahedral cages. The third is due to incomplete occupancy of the hexakaidecahedral cages by the THF molecules.

The THF hydrate molecules continue to rotate rapidly even at very low temperatures, with the rotational barriers being 3.9 kJ mol^{-1}.[2,3,4,5,6,7] This barrier has been estimated from nmr[3] and dielectric relaxation data.[4,5,6] Recently, neutron diffraction studies on THF hydrate samples partially ordered by KOH doping indicate that at low temperatures the THF molecules have preferred orientations and that the low temperature phase exhibits local lattice distortions leading to a quasi-tetragonal structure.[8]

7.1.2 Ethane

Physical Properties of Ethane

Ethane is a colourless, flammable gas, which is soluble in benzene. Its formula is C_2H_6, and it has a molar weight of 30.07 g mol^{-1} and its structure is shown in figure 7.2. Some of the physical properties of ethane are outlined in table 7.2.

Formula	C_2H_6
Molar Weight/g	30.07
CAS-RN	74-84-0
Melting Point/°C	-182.8
Boiling Point/°C	-88.6

Table 7.2 Physical Properties of Ethane,

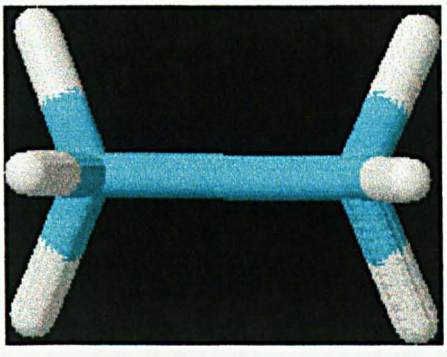

Figure 7.2 Structure of ethane. Blue is carbon and white hydrogen.

Why use Ethane Hydrate?

In the present work ethane hydrate was the system of choice for more complex gas hydrate experiments. This is due to the fact that it is a significant component of natural gas constituting (~ 6 %) and ethane hydrate will form at much lower pressures than the hydrate of the major component of natural gas, namely methane. For example at 277.6 K ethane hydrate will form at 0.8 MPa whereas methane hydrate will form at 4.2 MPa.

Ethane Hydrate

Ethane hydrate was first reported in 1888 by Villard.[9] Just as for methane, carbon dioxide, xenon and hydrogen sulphide, it forms as structure I, which is a body centred cubic hydrate with the unit cell containing two pentagonal dodecahedral cages and six tetrakaidecahedral cages constructed from 46 water molecules. The ideal composition is $C_2H_6.7\frac{2}{3}H_2O$, with the ethane molecules trapped in each of the tetrakaidecahedral cages. Ethane hydrate shows the same three types of disorder in the crystal as found with THF hydrate. The ethane molecules are restricted in their rotation due to the shape of the molecules; the rotational barrier is 5.0 kJ mol^{-1}.[10]

7.2 Synthesis of tba3S

7.2.1 Experimental Setup

tba3S was prepared using a modified literature procedure.[11] Reaction of 1,3-propane sultone and tributylamine in dichloroethane solution followed by a simple work-up gave a 60 % yield tba3S as a white powder.

7.2.2 Experimental Procedure

1,3-Propane sultone, (2 g, 0.16 mol), was added to a mixture of tributylamine, (200 ml, 0.84 mol), and dichloroethane, (200 ml). The solution was stirred at room temperature for 60 hours. Hexane was added until an oil separated. The solvents and excess amine were decanted away. Acetone was added until there were signs of crystallisation; the mixture was then left standing at 4 °C overnight. The white precipitate which formed was collected by filtration and washed with cold acetone.

After drying under vacuum, the product was collected and characterised by melting point determination, ir, CHN analysis, ^{1}H nmr, ^{13}C nmr, and mass spectrometry.

7.2.3 Results and Discussion

After crystallisation, 30 g of a white powder at 60 % yield, assuming 100 % purity, was collected.

The analytical results were as follows: melting point 213–214.5 °C; ν_{max} (nujol) 1201, 1036, 721 cm^{-1}; C 57.48 %, H 10.61 %, N 4.52 %, ($C_{15}H_{33}NO_3S$ requires C 58.59 %, H 10.82 %, N 4.56 %); δ_H (300 MHz, $CDCl_3$), 3.75 (2H, m, CH_2N), 3.21 (6H, m, CH_2N), 2.93 (2H, t, CH_2S), 2.18 (2H, m, CH_2), 1.71 (6H, m, CH_2), 1.43 (6H, m, CH_2), 1.02 (9H, t, CH_3); δ_C (100 MHz, $CDCl_3$), 58.53 (CH_2N of Bu), 57.91 (CH_2N), 47.14 (CH_2S), 23.61 (CH_2 of Bu), 19.57 (CH_2 of Bu), 18.64 (CH_2), 13.47 (CH_3); m/z 258 $[(M-C_4H_8)H]^+$.

The structure of the proposed product was supported by the ^{1}H and ^{13}C nmr spectra. Particularly helpful were the signals for the two different methylene groups adjacent to the quaternary nitrogen centre, which appeared in the ^{1}H nmr spectrum at 3.75 and 3.21 ppm, integrating as expected in a ratio of 1:3, and in the ^{13}C spectrum at 58.53 and 57.91 ppm in a qualitative 3:1 ratio. No molecular ion for tba3S was observed in either the EI or CI mass spectrum, but a molecular ion was observed at m/z 258 in the CI spectrum, which suggests a facile elimination of butene must occur before ionisation.

7.3 Nucleation and Growth of THF Hydrate

7.3.1 Experimental Setup[12]

The THF hydrate experimental setup can be seen in figure 7.3.

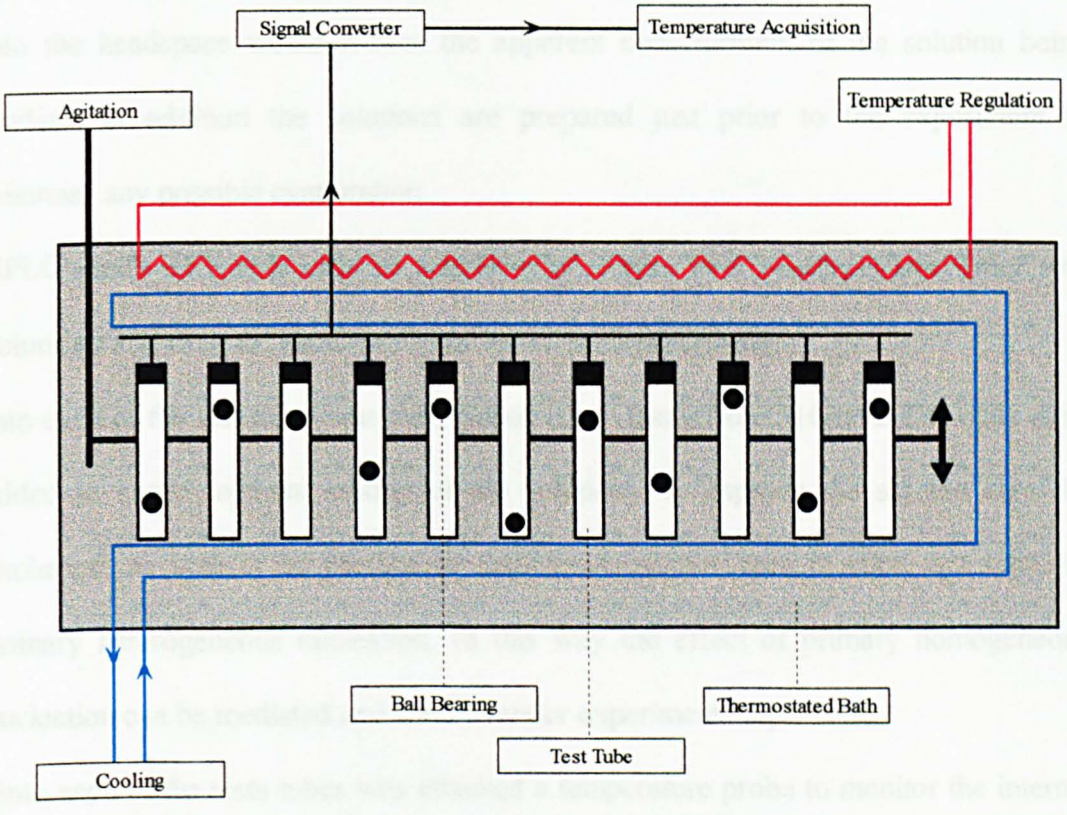

Figure 7.3 Nucleation and growth of THF hydrate experimental setup.

The principle of the experiment is quite simple; the test tubes are filled with the solution of choice and a temperature probe attached to each. Continual agitation of the test tubes is begun at 6 °C and the system cooled to 2 °C and then kept at this temperature. The experiment is continued until THF hydrate has formed in each of the test tubes. The time to formation of THF hydrate is then determined by observing the temperature *vs.* time profile recorded for each of the test tubes by the temperature probes.

7.3.2 Experimental Procedure[13]

Eight 8 ml test tubes were filled with 7.5 ml of solution, either THF 20 wt.% + water or THF 20 wt.% + water + X where X is the potential inhibitor of interest at the required concentration by weight of water. The test tubes are filled to this extent to reduce the effect of air upon the formation of the THF hydrate as evaporation of THF into the headspace would reduce the apparent concentration of the solution being studied; in addition the solutions are prepared just prior to the experiment to minimise any possible evaporation.

HPLC grade THF was used as supplied by Fluka (99.8 % pure). The water was deionised and from the same local source for each experiment.

Into each of the test tubes was then placed a ball made from 316Inox. The balls were added to ensure optimal mixing of the solutions, to improve the surface area for exchange, as well as to provide an equivalent surface area in each test tube for primary heterogeneous nucleation. In this way the effect of primary homogeneous nucleation can be mediated and should render experiments repeatable.

Onto each of the tests tubes was attached a temperature probe to monitor the internal temperature of each test tube, and these temperature probes were then connected to a temperature acquisition device as shown in figure 7.3. The test tubes were then immersed into a thermostated bath which was held at 6 °C and left for ten minutes to achieve thermal equilibrium with the bath. The bath was at 6 °C as this is above the temperature of formation of THF hydrate at 1atm (5 °C). The bath was then cooled to 2 °C at 0.2 °C per minute and then held at 2 °C until the experiment was finished.

A typical temperature profile is given in graph 7.1. The onset of hydrate formation is indicated by the vertical step in the temperature *vs.* time profile, due to the fact heat of crystallisation for THF hydrate is exothermic and so hydrate formation causes

local heating. These curves were analysed for each of the test tubes and the time at which THF hydrate was formed noted.

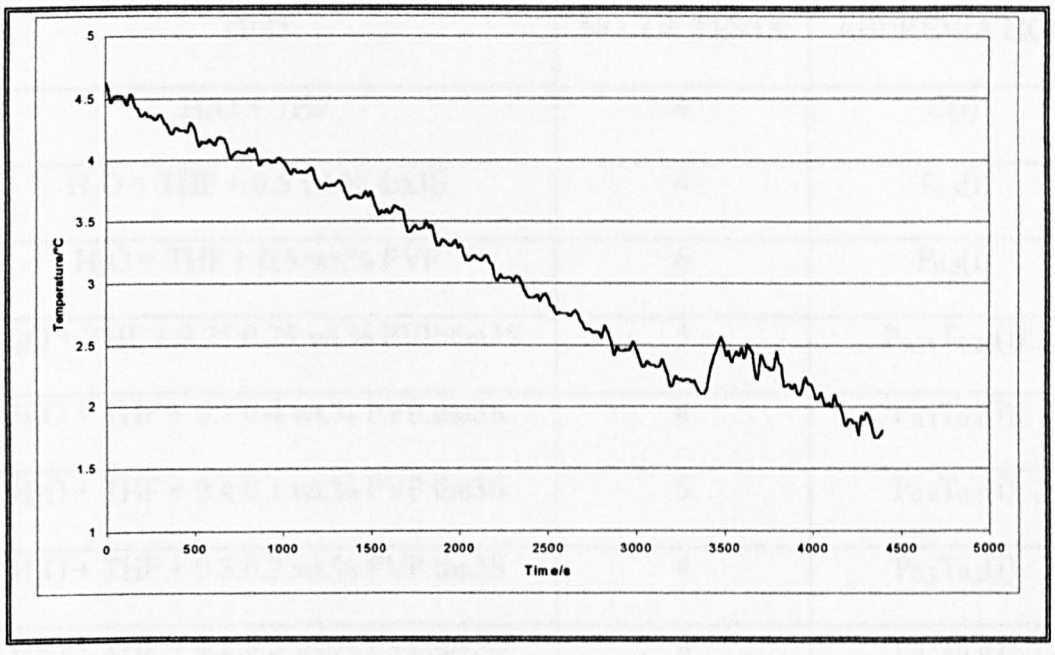

Graph 7.1 A typical temperature vs time profile.

7.3.3 Results Format

The results obtained from the nucleation and growth of THF hydrate experiments are the induction time for THF hydrate formation. This is the time from when the system reaches 4 °C until THF hydrate formation is measured via the temperature probe.

7.3.4 Results and Discussion

A summary of the nucleation and growth of THF hydrate experiments can be seen in table 7.3 along with the abbreviations used for the experiments. Some of the tests in table 7.3 did not yield eight results and this is because upon inspection of the

temperature *vs.* time profile it was not possible to identify a vertical step in the profile. Corresponding induction times are given in table 7.4 and graph 7.2.

TEST	NO. OF TESTS	ABBREVIATION
H_2O + THF	4	C(i)
H_2O + THF + 0.5 wt.% tba3S	4	$T_{0.5}$(i)
H_2O + THF + 0.5 wt.% PVP	6	$P_{0.5}$(i)
H_2O + THF + 0.25:0.25 wt.% PVP:tba3S	5	$P_{0.25}T_{0.25}$(i)
H_2O + THF + 0.1:0.4 wt.% PVP:tba3S	4	$P_{0.1}T_{0.4}$(i)
H_2O + THF + 0.4:0.1 wt.% PVP:tba3S	5	$P_{0.4}T_{0.1}$(i)
H_2O + THF + 0.3:0.2 wt.% PVP:tba3S	4	$P_{0.3}T_{0.2}$(i)
H_2O + THF + 0.2:0.3 wt.% PVP:tba3S	8	$P_{0.2}T_{0.3}$(i)

Table 7.3 Nucleation and growth of THF hydrate experiments.

RUN	SYSTEM							
	Control	$T_{0.5}$	$P_{0.5}$	$P_{0.25}T_{0.25}$	$P_{0.1}T_{0.4}$	$P_{0.4}T_{0.1}$	$P_{0.3}T_{0.2}$	$P_{0.2}T_{0.3}$
1	6100	5900	7000	5400	5800	6600	3900	5200
2	3500	8900	4600	5200	4200	3800	4200	5700
3	3300	7800	5100	5500	10300	4500	4900	4000
4	3800	4000	5200	5200	5800	4300	5300	7500
5			6200	4900		4600		9400
6			6700					5700
7								7000
8								5400
Average	4175	6650	5800	5240	6525	4760	4575	6238
S.D.	1300	2158	970	230	2627	1074	640	1671
Rank	8	1	4	5	2	6	7	3

Table 7.4 THF hydrate induction times. Results not available for some tests due to the inability to resolve the vertical step in the temperature vs. time profile.

The first observation to note from this data is that the uninhibited system, C(i), does have the shortest average induction time of all the systems studied, namely 4175 s. This average induction time is the benchmark by which to study the efficiency of tba3S, PVP and mixtures of the two.

The second point to note is that in the system containing 0.5 wt.% PVP, $P_{0.5}$(i),the average observed induction time of 5800s is greater than that for the uninhibited system, C(i). This difference borders on being significant at a 95 % confidence level

(*t*-test gives 2.28, *cf* 2.31 for 95 % confidence with 8 degrees of freedom). PVP is a known kinetic inhibitor and therefore the fact that it does appear active with respect to inhibiting THF hydrate formation gives us confidence in this test at identifying inhibitor activity.

If we now consider the system containing 0.5 wt.% tba3S, $T_{0.5}(i)$, we see that the average induction time of 6650 s is greater than that observed in either the uninhibited system, C(i), or the system containing 0.5 wt.% PVP, $P_{0.5}(i)$. The comparison with the control is significant at a 90 % confidence level (t = 1.97, *cf* 1.94 for 90 % confidence with 6 degrees of freedom). This observation suggests that tba3S at 0.5 wt.% is both a kinetic inhibitor and more effective than PVP at the same concentration, although as an isolated result, the latter observation cannot be confirmed as statistically significant without further experiments.

The other mixed systems studied in the nucleation and growth of THF hydrate experiments were used to investigate if there was any synergism between tba3S and PVP. Synergism is a deviation from a simple linear relationship between the two pure systems *i.e.* mixtures of tba3S and PVP would be more active than either tba3S or PVP on there own, and this can be identified by studying graph 7.2.

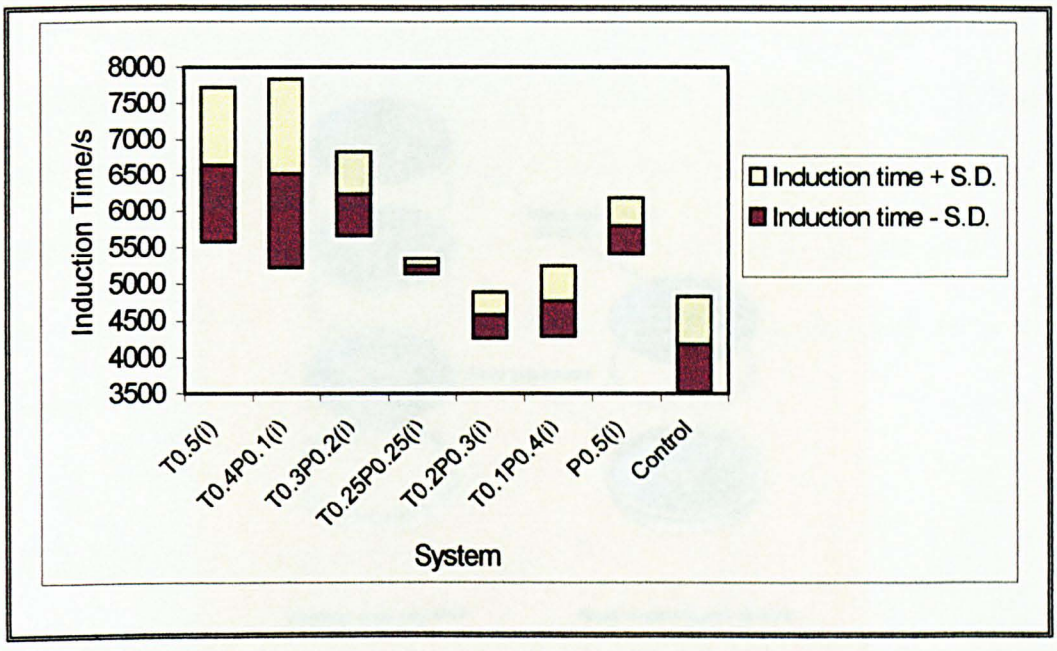

Graph 7.2 Plot of average induction time vs. system.

If we consider graph 7.2 then we see that upon moving from $T_{0.5}(i)$ to $PVP_{0.5}(i)$ that we do not have simply a mixing effect as if this was the case then we would expect a straight line with negative slope going from $T_{0.5}(i)$ to $PVP_{0.5}(i)$. From graph 7.2 it can be seen that the data shows a clear U-shaped curve with a minimum at $P_{0.3}(i)T_{0.2}(i)$ which is substantially below the linear curve. In other words, the mixtures are less effective than the combination of the two inhibitors. Therefore there must be some destructive interference going on, which may be due to the fact that upon mixing the two chemicals aggregate together therefore reducing the amount of either inhibitor available.

7.4 Morphology of THF Hydrate

7.4.1 Experimental Setup[14]

The morphology of THF hydrate experimental setup can be seen in figure 7.4.

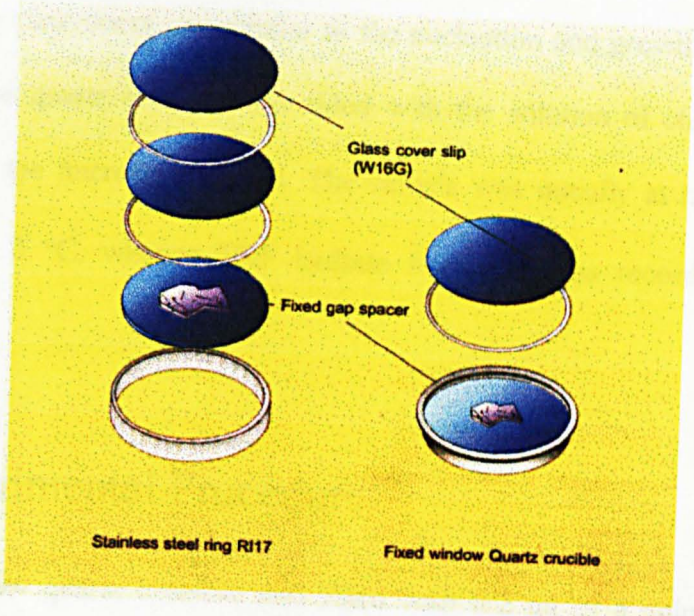

Figure 7.4a The fixed window quartz crucible.

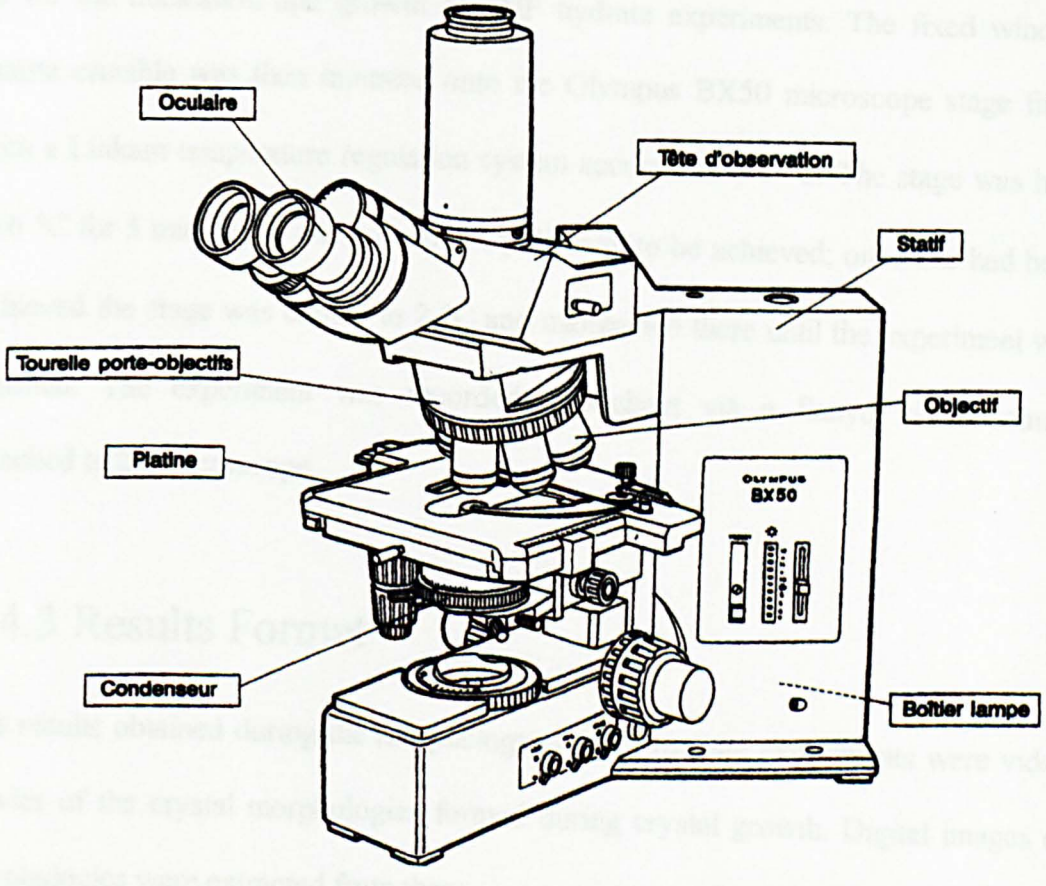

Figure 7.4b Crystallographic study microscope.

The sample crucible is depicted in figure 7.4a and the microscope in figure 7.4b. The principle of the experiment was similar to the nucleation and growth of THF hydrate experiments: the quartz crucible was filled with the solution of choice, which was then placed on the microscope stage. The sample was initially at held at 6 °C and then cooled to 2 °C, whence THF hydrate formation was recorded via a video camera.

7.4.2 Experimental Procedure[14]

The fixed window quartz crucible was filled with 0.2 ml of a solution containing THF (20 wt.%) + water + X, where X was the potential inhibitor of interest at the required concentration by weight of water. The THF and water used were the same as for the nucleation and growth of THF hydrate experiments. The fixed window quartz crucible was then mounted onto the Olympus BX50 microscope stage fitted with a Linkam temperature regulation system accurate to 0.1 °C. The stage was held at 6 °C for 5 minutes to allow thermal equilibrium to be achieved; once this had been achieved the stage was cooled to 2 °C and maintained there until the experiment was finished. The experiment was recorded throughout via a Sanyo video camera attached to the microscope.

7.4.3 Results Format

The results obtained during the morphology of THF hydrate experiments were video movies of the crystal morphologies formed during crystal growth. Digital images of morphologies were extracted from these.

7.4.4 Results and Discussion

A summary of the morphology of THF hydrate experiments can be seen in table 7.6 along with the abbreviations used for the experiments.

TEST	NO. OF PICTURES	ABBREVIATION
H_2O + THF	4	C(i)
H_2O + THF + 0.5wt.% PVP	1	$P_{0.5}$(i)
H_2O + THF + 0.5wt.% tba3S	3	$T_{0.5}$(i)

Table 7.6 Morphology of THF hydrate experiments.

The pictures taken during the morphology of THF hydrate experiments of the control system, C(i) are shown in pictures 7.1–7.4.

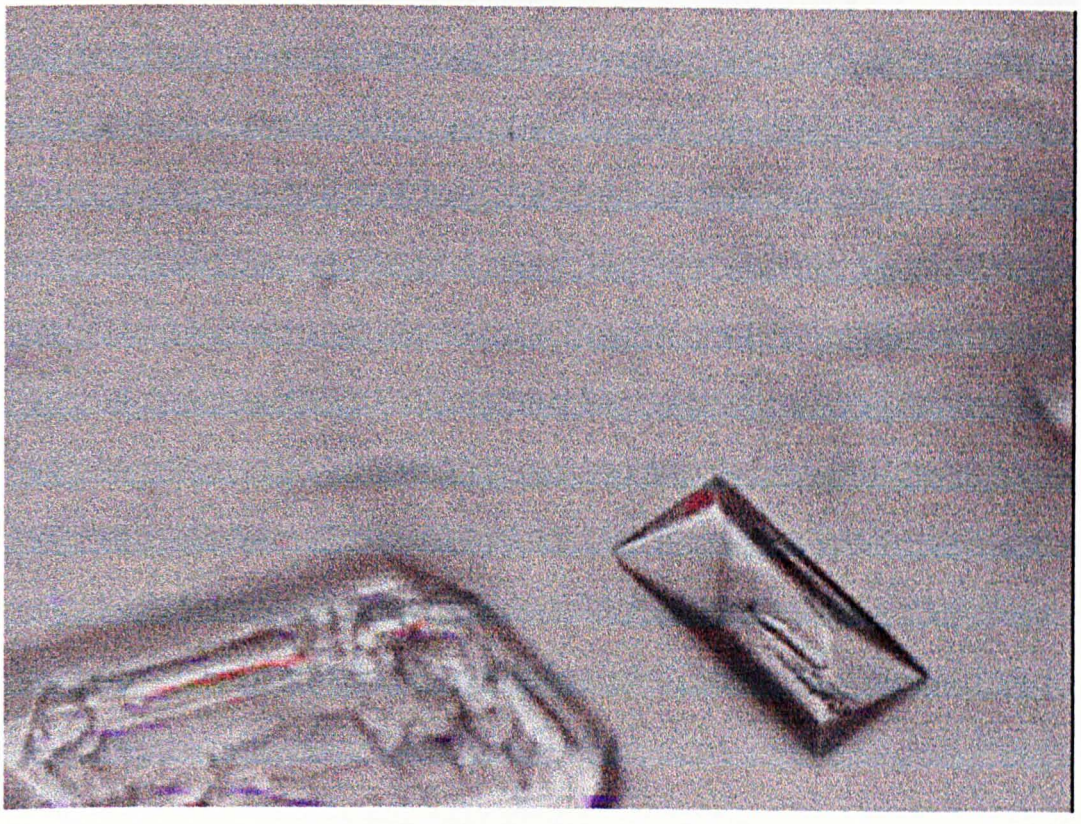

Picture 7.1 THF hydrate C(1).

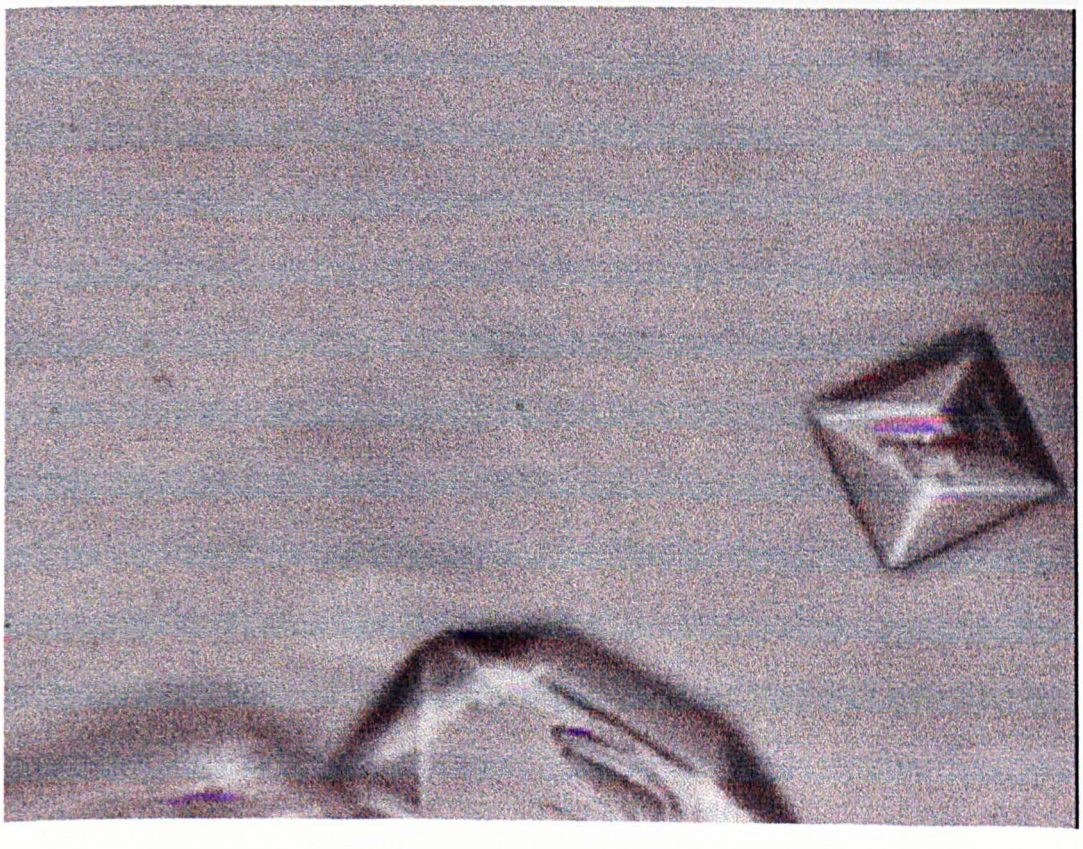

Picture 7.2 THF hydrate C(2).

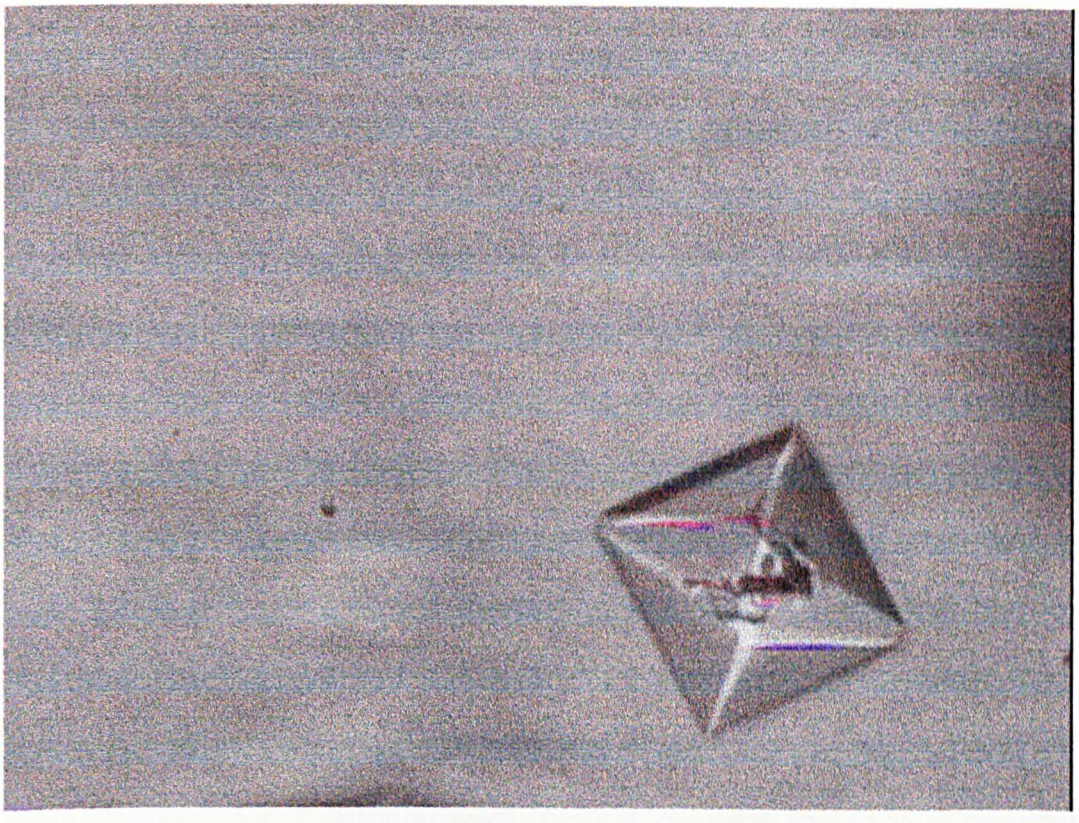

Picture 7.3 THF hydrate C(3).

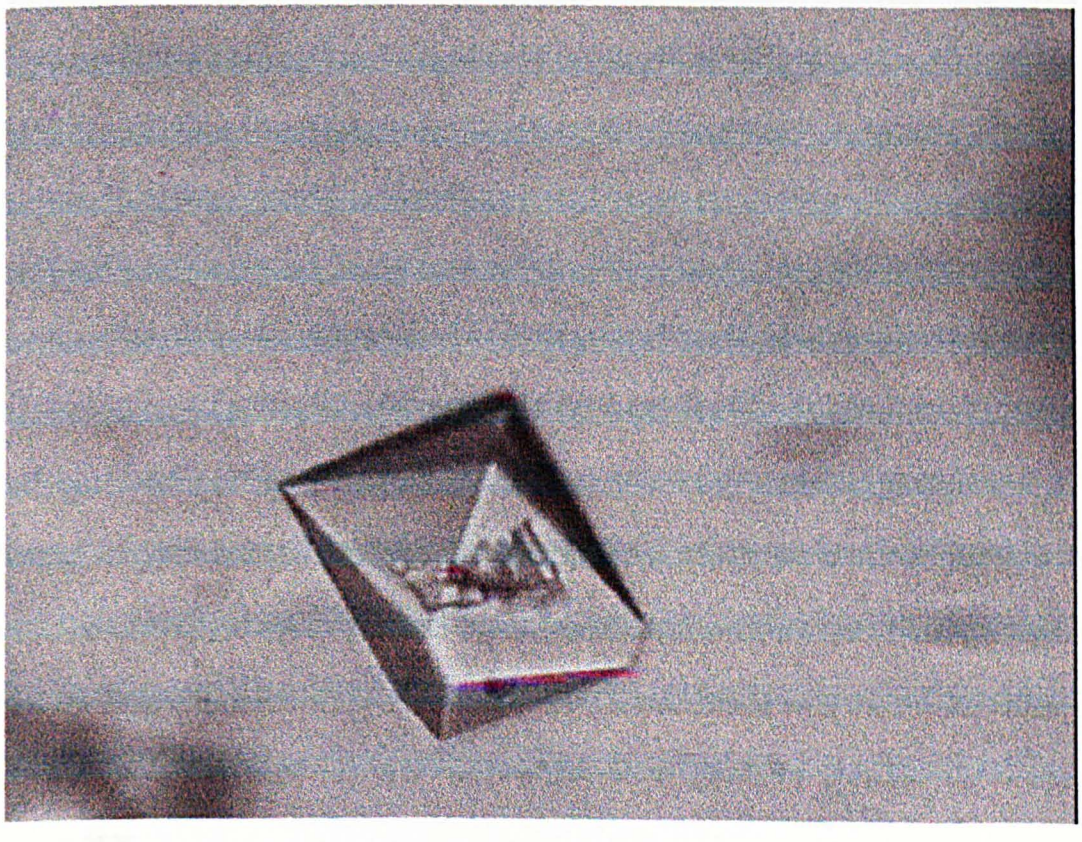

Picture 7.4 THF hydrate C(4).

Pictures 7.1–7.4 show that THF hydrate forms octahedral crystals in the absence of inhibitors. This is consistent with the results obtained for the crystal growth of THF hydrate in uninhibited systems from previous studies.[33,76]

The picture taken during the morphology of THF hydrate experiments of the PVP system, $P_{0.5}(i)$ is shown in picture 7.5.

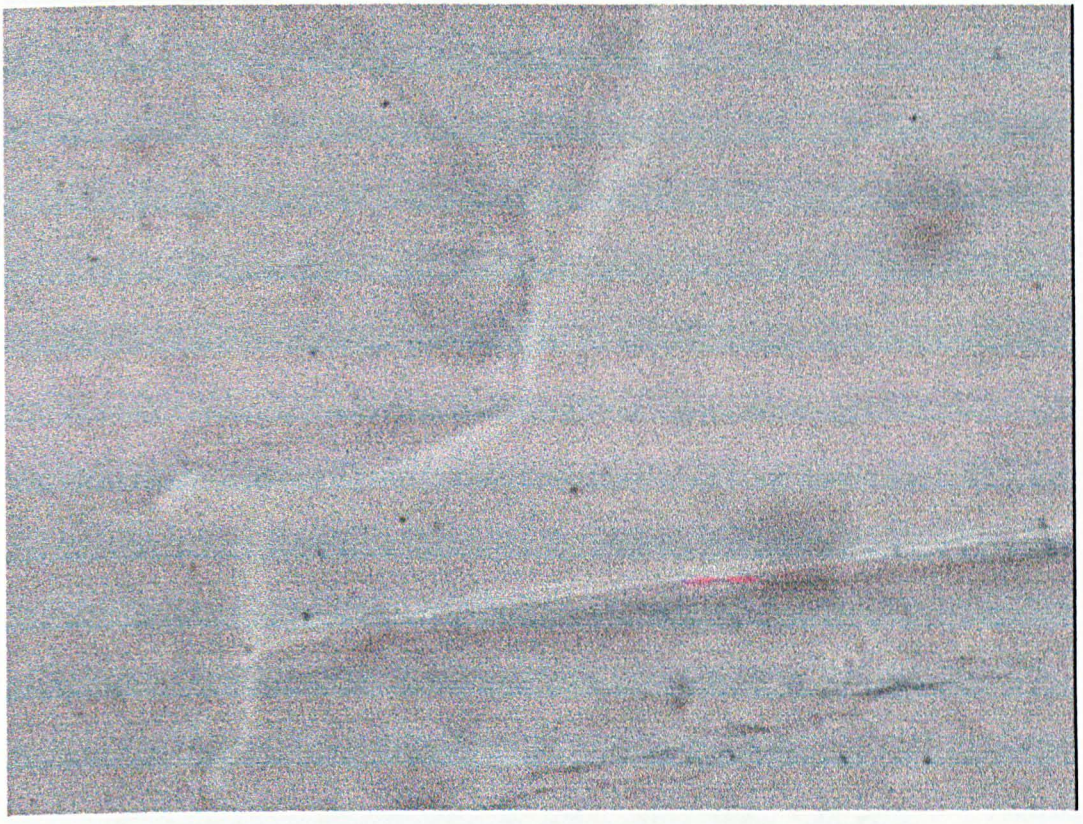

Picture 7.5 THF hydrate with 0.5wt.% PVP: $P_{0.5}(1)$.

Picture 7.5 shows that THF hydrate forms crystals which are planar in habit in the presence of PVP; to the extent that it is very difficult to observe/photo the crystals as they are almost transparent in appearance. This is consistent with the results obtained for the crystal growth of THF hydrate in PVP inhibited systems in previous studies.[33,76]

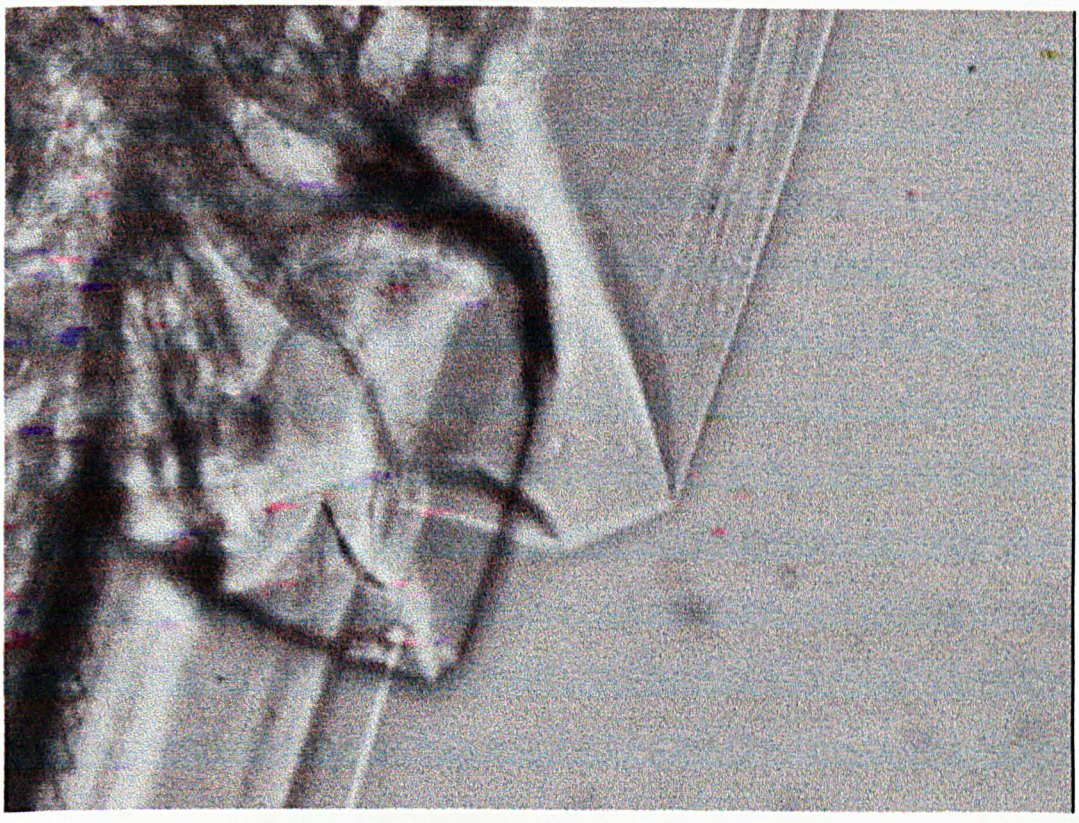

Picture 7.6 THF hydrate with 0.5wt.% tba3S: $T_{0.5}(1)$.

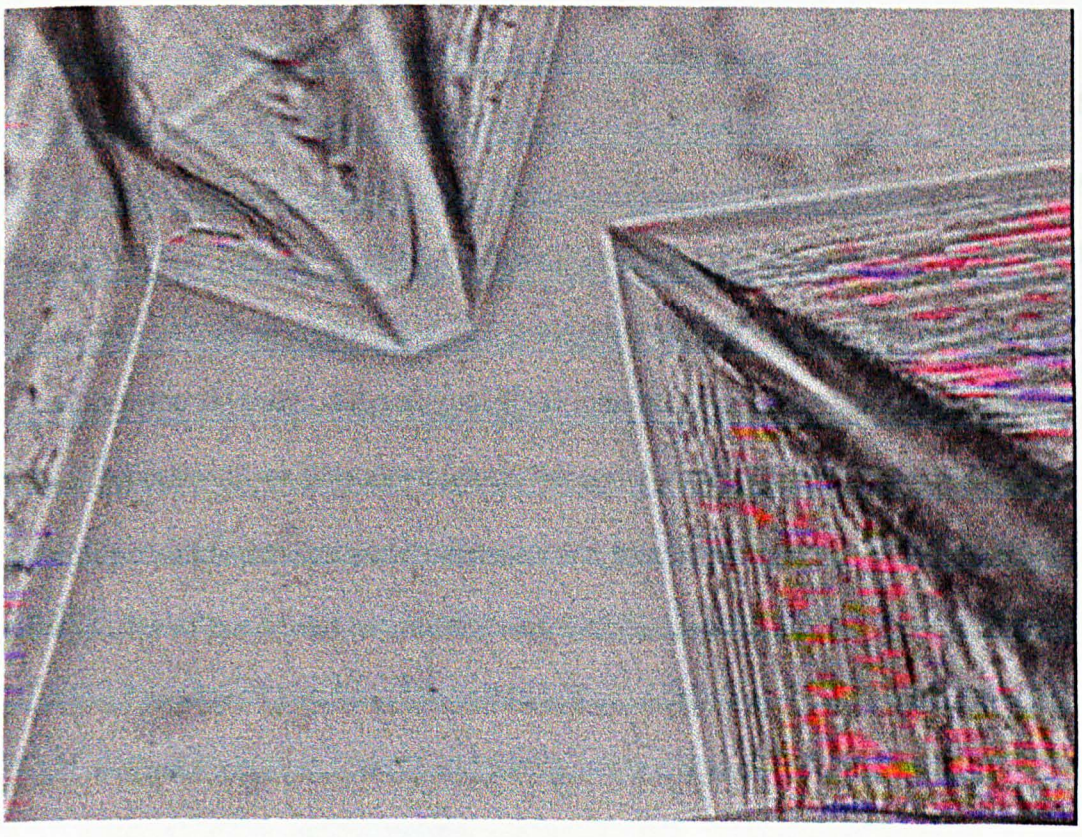

Picture 7.7 THF hydrate with 0.5wt.% tba3S: $T_{0.5}(2)$.

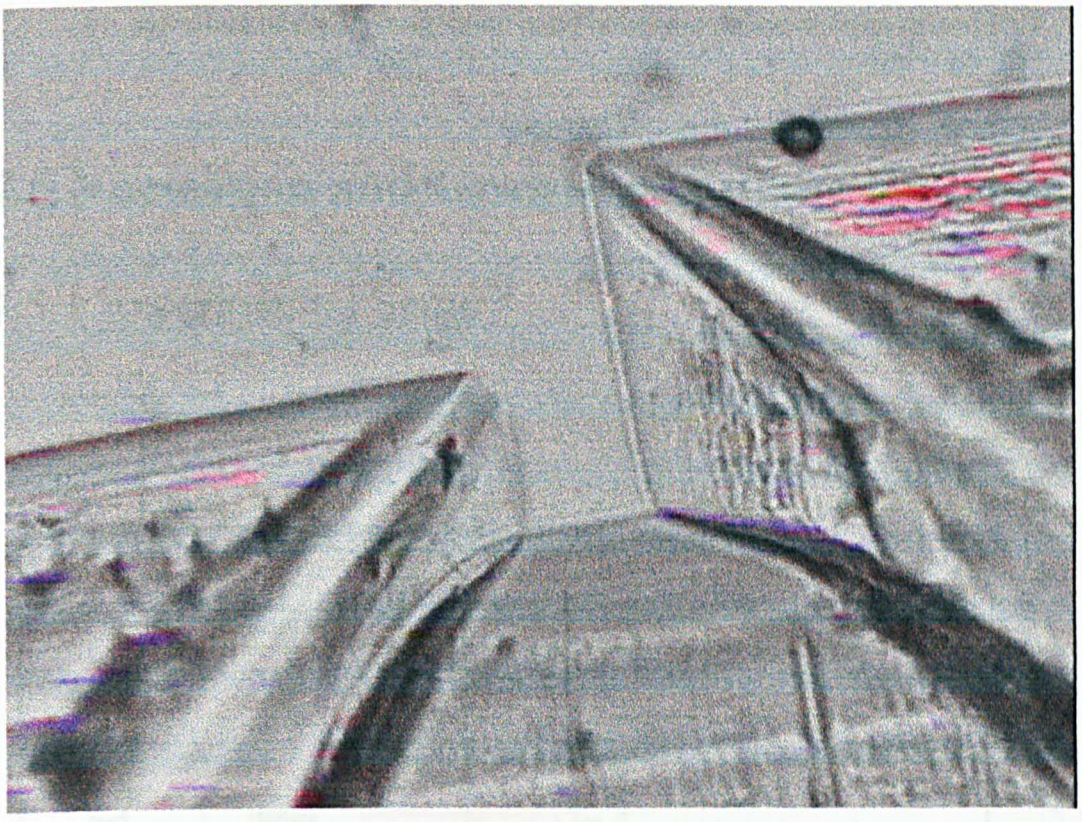

Picture 7.8 THF hydrate with 0.5wt.% tba3S: $T_{0.5}(3)$.

The pictures taken during the morphology of THF hydrate experiments of the tba3S system, $T_{0.5}(i)$ are shown in pictures 7.6–7.8. Pictures 7.6–7.8 show that THF hydrate forms crystals exhibiting similarities to those obtained for pure, and PVP inhibited, THF hydrate. Firstly they are plate-like in appearance, but the fact that they are more visible than the crystals obtained with PVP inhibited systems suggests that they are thicker. Secondly if we consider picture 7.6 and 7.7 then there does appear to be a number of crystals that resemble octahedra but they seem to have grown much more at the equator of the crystal to produce very wide and flat octahedra. However it must be stressed that both of these points are based upon observation, and they are the first results of THF hydrate crystals inhibited by tba3S available.

These results however illustrate two points:

a) tba3S does affect the morphology of THF hydrate crystals;

b) the effect of tba3S on hydrate morphology is different from that of PVP.

7.5 Nucleation and Growth of Ethane Hydrate

7.5.1 Experimental Setup[15]

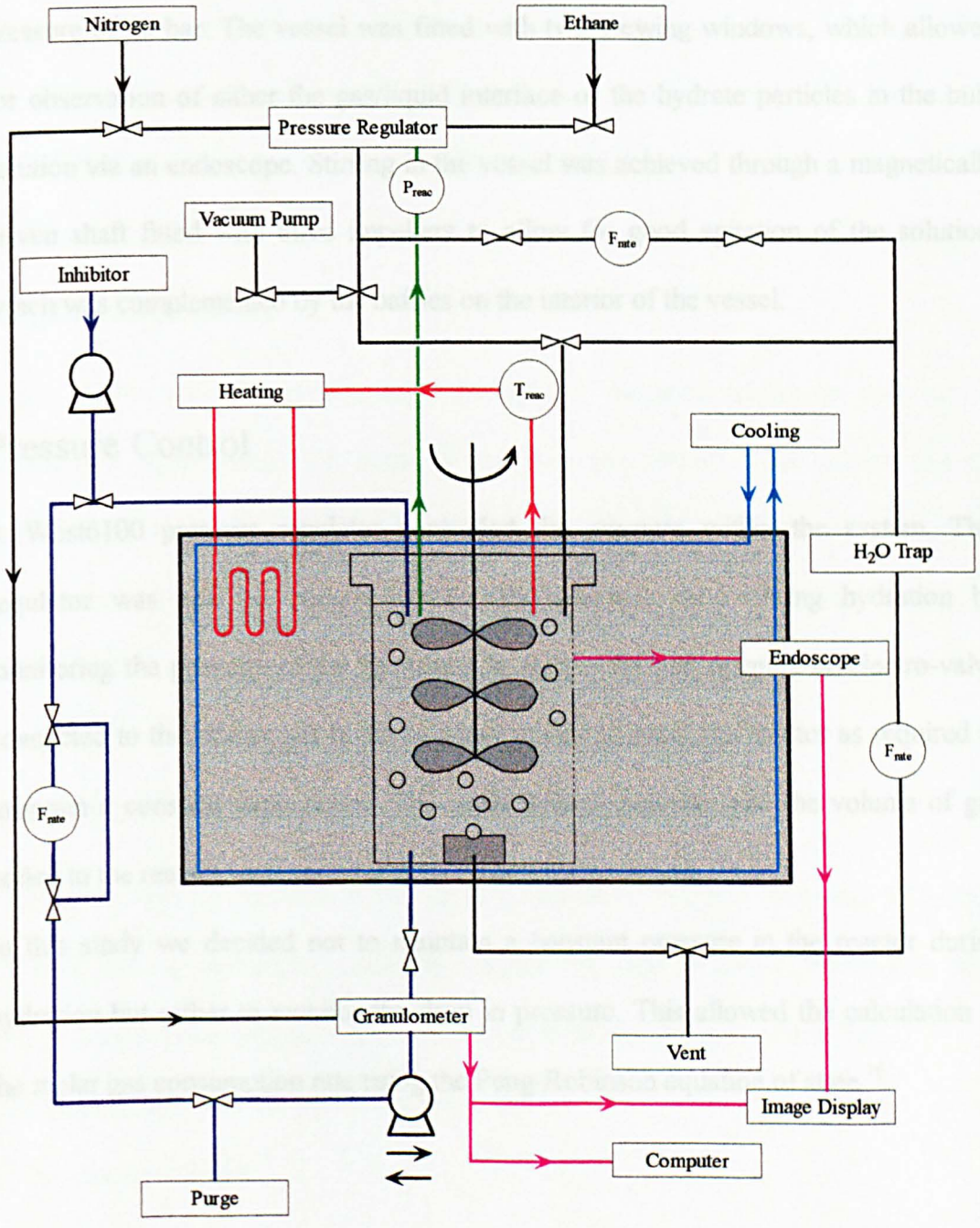

Figure 7.5 Nucleation and growth of ethane hydrate experimental setup.

The nucleation and growth of ethane hydrate experimental setup can be seen in figure 7.5.

The Reactor

The reactor was a baffled 1litre stainless steel vessel, rated to a maximum operational pressure of 30 bar. The vessel was fitted with two viewing windows, which allowed for observation of either the gas/liquid interface or the hydrate particles in the bulk solution via an endoscope. Stirring in the vessel was achieved through a magnetically driven shaft fitted with three impellers to allow for good agitation of the solution, which was complemented by the baffles on the interior of the vessel.

Pressure Control

A West6100 pressure regulator controlled the pressure within the system. This regulator was able to compensate for the pressure drop during hydration by monitoring the pressure of the gas phase in the reactor and opening an electro-valve connected to the ethane gas bottle to allow ethane to enter the reactor as required to maintain a constant temperature. The instantaneous pressure and the volume of gas added to the reactor were monitored by a personal computer.

In this study we decided not to maintain a constant pressure in the reactor during hydration but rather to monitor the drop in pressure. This allowed the calculation of the molar gas consumption rate using the Peng-Robinson equation of state.[16]

Temperature Control

A Shimaden SR50 temperature regulator controlled the temperature within the system. The thermostated bath was cooled at a constant rate by the cooling system and the temperature of the bath was monitored via a PT100 resistance probe, with the amount of heating in the bath being adjusted as required.

The temperature of the bath was recorded along with the temperature of the liquid in the reactor. The main temperature of interest was that of the liquid in the reactor which allowed us to follow/characterise the hydration.

Liquid Circulation

Liquid in the reactor was circulated through ¼" insulated tubing for analysis by means of a liquid pump. The liquid flowed from the bottom of the reactor into the granulometer for analysis and then through the liquid pump and back into the reactor via the top. The pump was positioned after the granulometer to minimise damage to ethane hydrate crystals prior to analysis by the granulometer.

The Granulometer

The ethane hydrate particles in the liquid phase were analysed by means of a Galai Cis1000 laser granulometer, specially adapted for high pressures, which was fitted with a thermostated analysis cell rated to an operational pressure of 100 bar.

The granulometer has two modes of operation:

a) visual analysis;

b) laser analysis.

Visual analysis is by means of a monitor connected to the granulometer and allows for observation of the ethane hydrate particles with and without inhibitor.

Laser analysis is the main mode of operation and allows the particle size distribution to be measured throughout the experiment. The main drawback of the laser analysis mode is the assumption that the particles are spherical. Analysis was carried out in the 2–100 μm range. Ethane hydrate particles quickly began to agglomerate after they grew to *ca.* 10–20 μm, and as we were interested in single particle sizes, it made no sense to analyse to the full range of particle sizes accessible with the granulometer.

The Injection Pump

A Gilson HPLC injection pump was used to add inhibitors to the reactor once it was pressurised. This was achieved by means of an anti-return valve which allowed for the flow of fluid into the reactor once the pressure within the pump was ~ 7 bar greater than the pressure within the reactor.

This method of adding inhibitors to the reactor does have its drawbacks:

a) it is not feasible to add large volumes of liquid to the reactor;

b) it is not possible to use viscous solutions in the pump.

Data Acquisition

A personal computer was used to record the reactor temperature and pressure. The signal was recorded as a voltage and then converted by means of experimentally derived correlations,[13] *viz.*

Absolute Pressure/bar = 2.47326 * V_P / volts + 1.134.

Absolute Temperature/K = 4.95042 * V_T / volts + 273.095.

Where V_P refers to the voltage measured relating to the pressure and V_T refers to the voltage measured relating to the temperature.

Chemicals

Ethane gas was used as supplied by AGA and was dry and of high purity. The deionised water used was from the same local source for all of the experiments. The inhibitor was as described in section 7.3.1 and was more than 99 % pure.

7.5.2 Experimental Procedure

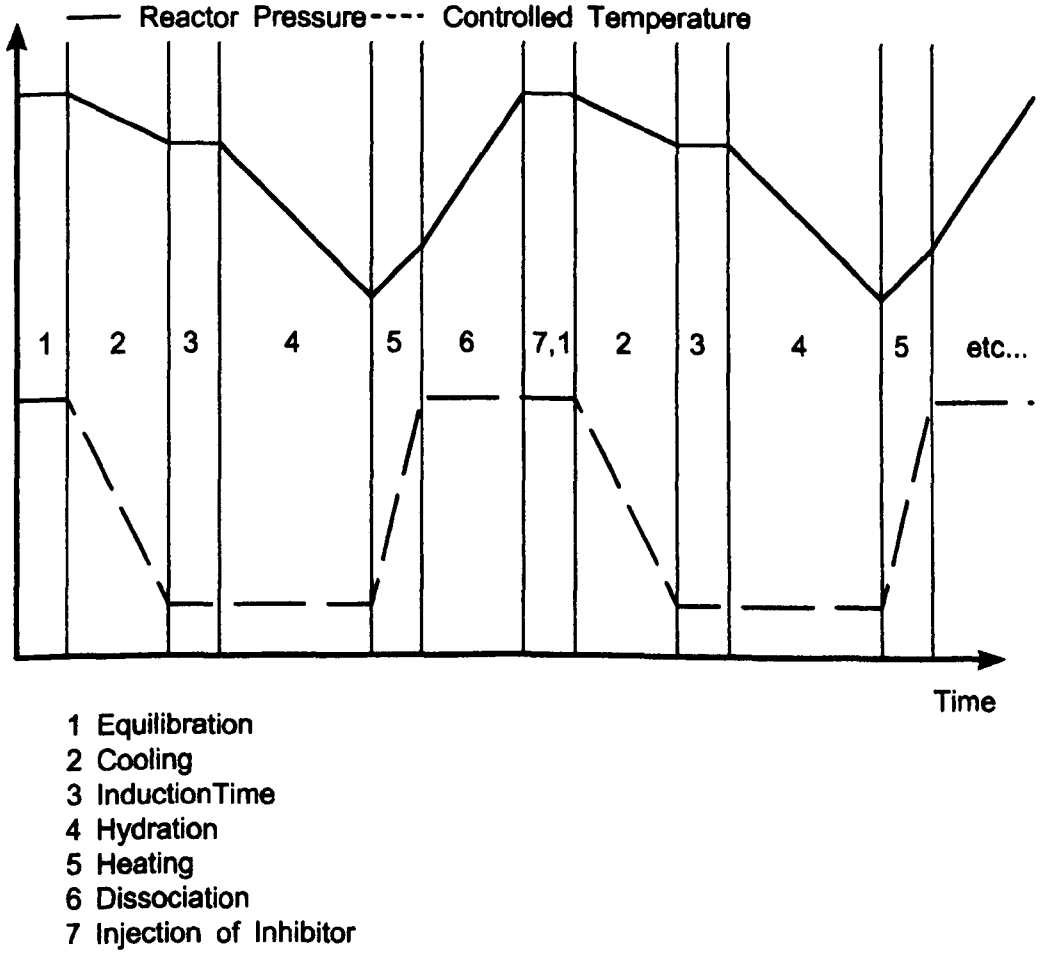

Figure 7.6 Schematic representation of the experimental procedure.

A schematic representation of the experimental procedure is shown in figure 7.6. A series of hydration cycles were performed in which each hydration cycle (steps 1–7 in figure 7.6) represents one experiment.

The reactor was charged with deionised water and the system pressurised to 12 bar at 8 °C. The system was then left to equilibrate in order to dissolve ethane in the deionised water; once saturation and thermal equilibrium had been achieved the gas inlet was closed.

The first hydration cycle was then carried out, which was equivalent to a study of primary nucleation in the uninhibited system. The system was held at 8 °C for 15 minutes, then cooled to 4 °C at 0.13 °C minute^{-1} and held at 4 °C until hydrate equilibrium was achieved. Once the pressure was equal to the equilibrium pressure of ethane hydrate at 4 °C (see graph 7.3) the system was heated back to 8 °C at 0.13 °C minute^{-1}.

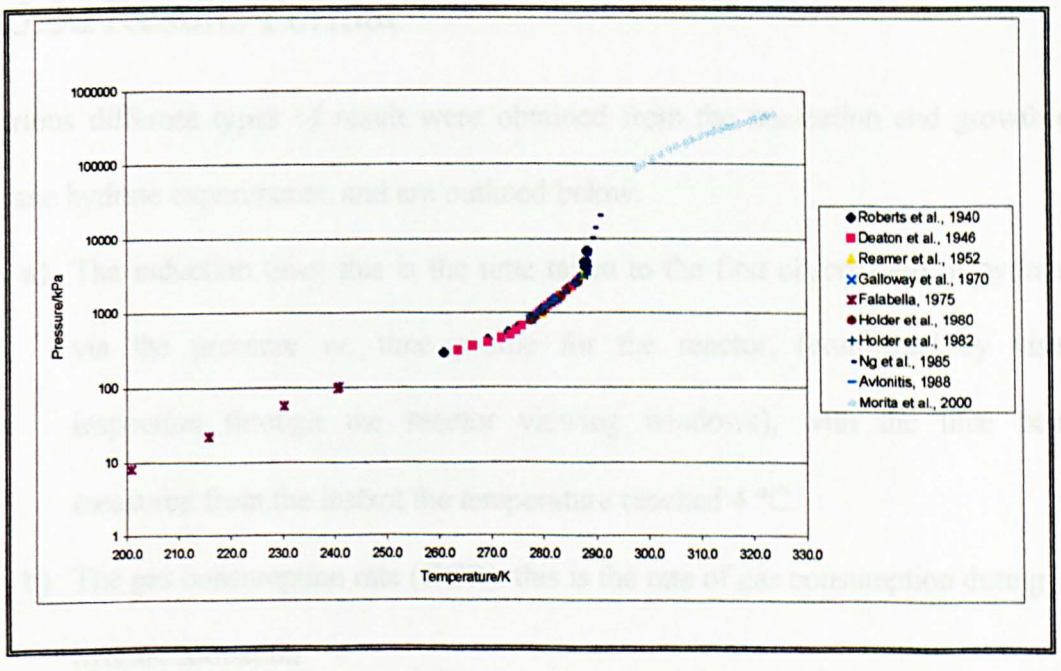

Graph 7.3 Three phase coexistence data for ethane hydrate. Experimental data taken from[17,18,19,20,21,22,23,24,25,26].

Once the first hydration cycle had been carried out, the hydrate memory effect insured that there was sufficient residual structure to seed crystallisation in subsequent experiments, so subsequent cycles avoided long induction times and were repeatable.[13]

The general experimental procedure was then to characterise the nucleation of ethane hydrate followed by the addition of the inhibitor of interest and subsequent characterisation of the nucleation of ethane hydrate in the presence of the inhibitor.

The inhibitor was added by removing 80 ml of liquid from the system and then adding 60 ml of solution containing the inhibitor at the required concentration, followed by a 20 ml water rinse. The water rinse was used to ensure that all of the inhibitor solution was washed from the injection pump and liquid lines into the reactor. Repeats of this cycle thus gave measurements at increasing inhibitor concentrations.

7.5.3a Results Format

Various different types of result were obtained from the nucleation and growth of ethane hydrate experiments, and are outlined below.

a) The induction time: this is the time taken to the first observation of hydrates via the pressure *vs.* time profile for the reactor, (confirmed by visual inspection through the reactor viewing windows), with the time being measured from the instant the temperature reached 4 °C.

b) The gas consumption rate (GCR): this is the rate of gas consumption during hydrate formation.

c) The nucleation rate: this is the rate of increase of the number of separate hydrate particles obtained from the granulometer during hydrate growth. The

lower the nucleation rate the greater the efficiency of the inhibitor at inhibiting hydrate nucleation.

d) The growth rate: this is the rate at which the mean particle diameter increased, and was obtained from the granulometer during hydrate growth. The lower the growth rate the greater the efficiency of the inhibitor at inhibiting hydrate growth.

The last two data sets allow for the classification of the inhibitor as a nucleation or growth inhibitor, or possibly a composite of the two.

7.5.3b Data Manipulation

The format of the raw data obtained from the granulometer is outlined in table 7.7.

TIME/minutes	1	TO	30
Conc./ml^{-1}	X_1	TO	X_{30}
Number Population	1	TO	30
2 μm	Y_2		Y_2
TO	TO		TO
100 μm	Y_{100}		Y_{100}
Total	1		1

Table 7.7 Summary of the raw data obtained from the granulometer. X_a refers to the total concentration of particles at time a. Y_a refers to relative population of particles with size a.

As can be seen from table 7.7 the data from the granulometer is of two types.

a) The total concentration of particles over the time range of analysis. In most cases the time range was 30 minutes with a reading being taken every minute, but this was altered where the inhibitor slowed the hydration process significantly.

b) The relative population of particles over the time range of analysis for the chosen size distribution of particles, which in this case was 2–100 μm.

The data obtained from the granulometer for control test C(2) is used to demonstrate how the data was processed to extract nucleation and growth rates.

Nucleation Rate

In order to calculate the nucleation rate the period of hydrate growth in the experiment must be determined. In order to achieve this a graph of the concentration of particles *vs.* time is plotted as in graph 7.4.

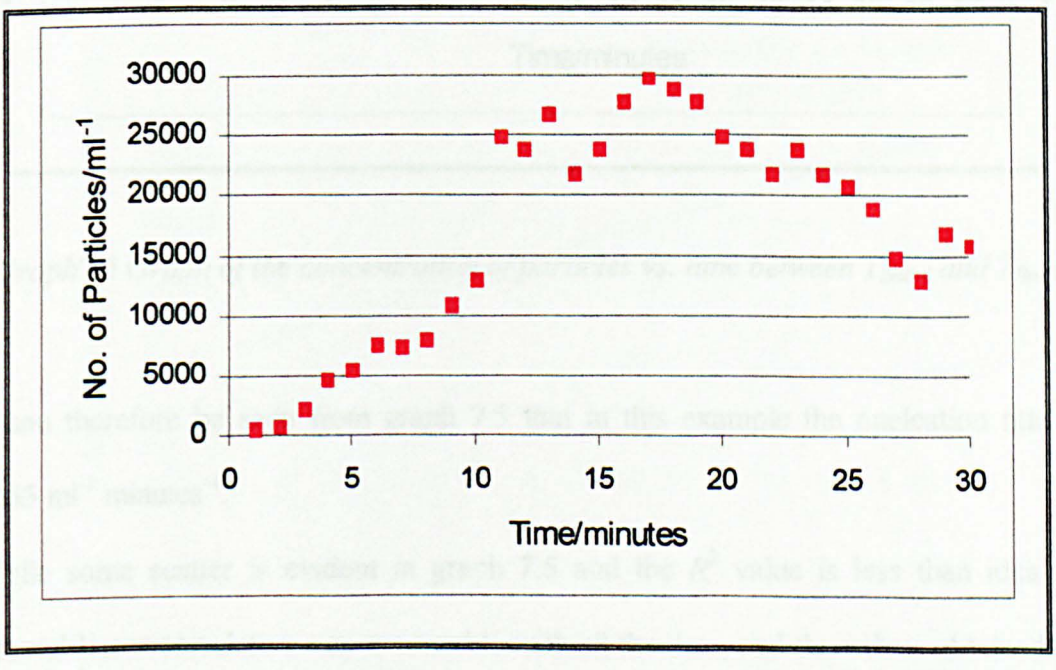

Graph 7.4 Graph of the concentration of particles vs. time.

From graph 7.4 the time at which the distribution begins to grow ($T_{initial}$) was noted along with the time at which the distribution plateaus (T_{final}). In this case these values are:

a) $T_{initial}$: 2 minutes;

b) T_{final} 17 minutes.

Graph 7.4 was then replotted for the time range $T_{initial}$ to T_{final}, and a linear regression carried out from which the nucleation rate was determined as the slope of the growth region. This process is illustrated in graph 7.5

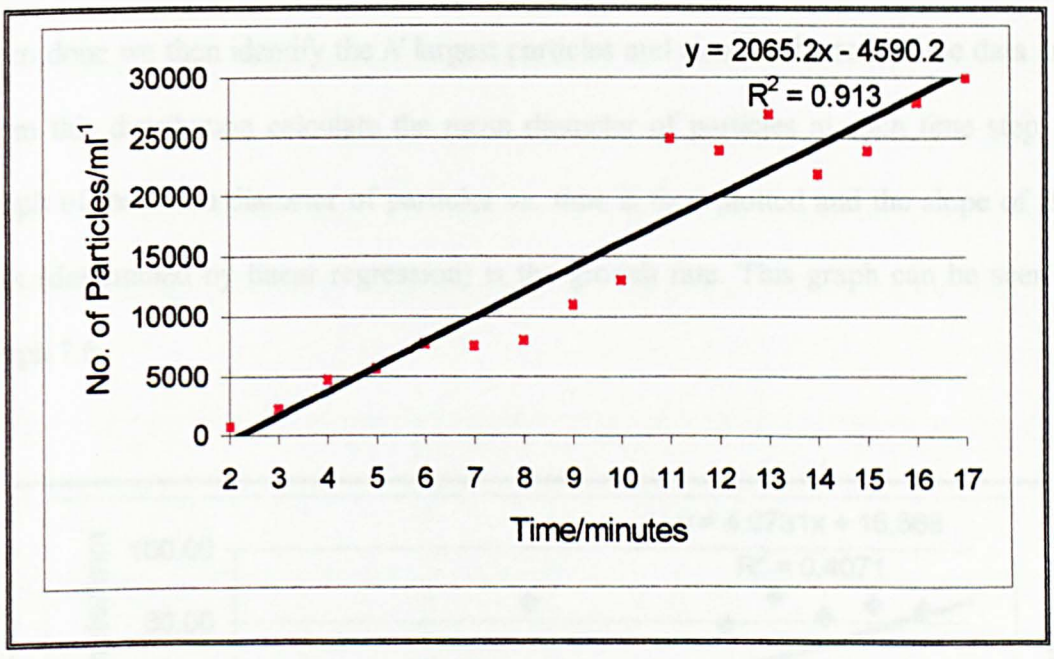

Graph7.5 Graph of the concentration of particles vs. time between $T_{initial}$ and T_{final}.

It can therefore be seen from graph 7.5 that in this example the nucleation rate is 2065 ml^{-1} $minutes^{-1}$.

While some scatter is evident in graph 7.5 and the R^2 value is less than ideal, a general linear correlation was reasonable with all the data, and the values obtained by this procedure do provide a reasonable, reproducible estimate of nucleation rates.

Growth Rate

In order to calculate the growth rate we need to separate particle growth from the appearance of new particles *i.e.* separate growth from nucleation. In order to achieve this we assume that the initial particles are always going to be the largest, and that no aggregation occurs. Thus, if we start with N particles at $T_{initial}$, then the N largest particles at any other time will be what these initial particles have grown into, which in this instance was 770 ml^{-1}. The next step is to determine the number of particles of each size in the distribution; this is achieved by multiplying the relative populations of each particle size by the total number of particles at each time step. Once this has been done we then identify the N largest particles and remove the rest of the data and from this distribution calculate the mean diameter of particles at each time step. A graph of the mean diameter of particles *vs.* time is then plotted and the slope of this plot (determined by linear regression) is the growth rate. This graph can be seen in graph 7.6.

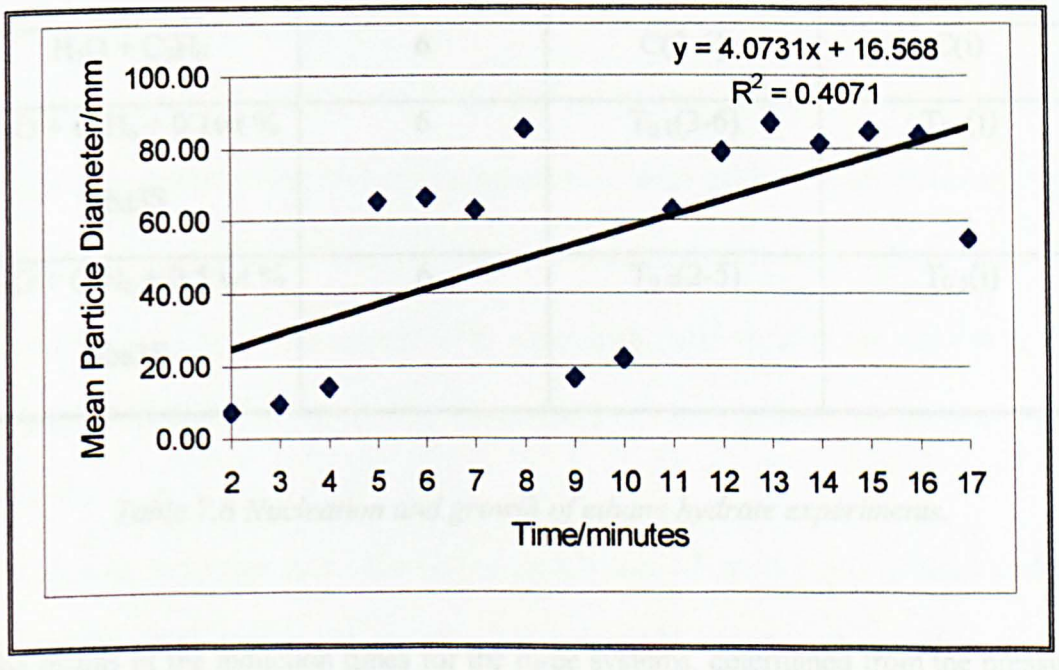

Graph 7.6 Graph of the mean particle diameter vs. time.

It can therefore be seen from graph 7.6 that in this example the growth rate is 4.07 $\mu m\ min^{-1}$.

It is clear in graph 7.6 that there is considerable noise in the plot of mean radius against time, and that there is considerable uncertainty in the growth rates extracted with this procedure. The data is likely to be useful in giving a general idea of growth rates in the presence of different inhibitors, but clearly there should not be too much emphasis placed on the precise numerical comparison of these growth rates.

7.5.4 Results and Discussion

A summary of the nucleation and growth of ethane hydrate experiments can be seen in table 7.8 along with the abbreviations used for the experiments. In some instances there is no granulometry data for certain runs, this is due to operational difficulties with the granulometer due to condensation on the analysis cell obscuring the laser.

TEST	NO. OF TESTS	USABLE TESTS	ABBREVIATION
$H_2O + C_2H_6$	6	C(2-6)	C(i)
$H_2O + C_2H_6$ + 0.1wt.% tba3S	6	$T_{0.1}$(3-6)	$T_{0.1}$(i)
$H_2O + C_2H_6$ + 0.5 wt.% tba3S	6	$T_{0.5}$(2-5)	$T_{0.5}$(i)

Table 7.8 Nucleation and growth of ethane hydrate experiments.

The results of the induction times for the three systems, determined from the pressure *vs.* time profile for that run are shown in table 7.9.

TEST	INDUCTION TIME/s	TEST	INDUCTION TIME/s	TEST	INDUCTION TIME/s
C(1)	–50	$T_{0.1}(1)$	1560	$T_{0.5}(1)$	3080
C(2)	–130	$T_{0.1}(2)$	940	$T_{0.5}(2)$	2610
C(3)	–120	$T_{0.1}(3)$	1930	$T_{0.5}(3)$	2540
C(4)	–70	$T_{0.1}(4)$	1950	$T_{0.5}(4)$	2400
C(5)	–70	$T_{0.1}(5)$	2120	$T_{0.5}(5)$	2740
C(6)	–100	$T_{0.1}(6)$	1730	$T_{0.5}(6)$	2700
Average	–90		1705		2678
S.D.	32		422		231

Table 7.9 Ethane hydrate induction times.

There is an increase in the induction time on going from C(i) to $T_{0.1}(i)$ through to $T_{0.5}(i)$, which is a clear indication that increasing [tba3S] increases the induction time for ethane hydrate formation

The average induction time, –90 s, for the uninhibited system, C(1-6), is negative. This indicates that ethane hydrate formation was observed before the temperature of the reactor had reached 4 °C. Since the equilibrium temperature for ethane hydrate at 12 bar is 8 °C, 4 °C represents 4 °C subcooling, and so it is not surprising that hydrate formation occurs in the uninhibited system before this subcooling is achieved.

The average induction time observed in the 0.1 and 0.5 wt.% tba3S systems studied, namely $T_{0.1}(1\text{-}6)$ and $T_{0.5}(1\text{-}6)$ are 1705 and 2678 s respectively. This average induction time shows that tba3S does retard the formation of ethane hydrate with the

effectiveness of tba3S increasing with increasing concentration. However the delay in ethane hydrate formation does not appear to be linear with respect to tba3S concentration. This result could be due to a number of reasons. The first is that tba3S may be targeting a particular part of the water/ethane/ethane hydrate system *e.g.* adsorption to a specific area. Therefore at low tba3S concentrations, 0.1 wt.%, all the adsorption sites are free; however as the concentration is increased, 0.5 wt.%, the number of available adsorption sites falls and therefore adsorption, and consequently activity, of tba3S becomes more difficult. The resulting effect would be that at higher concentrations the retardation in ethane hydrate formation is not as high as would be expected if we simply scaled the 0.1 wt.% tba3S results. A second possibility is that as the concentration of tba3S is increased there may be clustering of tba3S, which would in effect reduce the amount of free tba3S for adsorption. Therefore the activity observed at 0.5 wt.% would not simply be five times that observed at 0.1 wt.% but somewhat less than expected. Finally it may be that the solubility of tba3S is small and that at 0.5 wt.% we are at threshold solubility at room temperature, therefore as the reactor is cooled during the hydration cycle then this would lead to tba3S precipitating out of solution and reducing the actual wt.% of the solution under testing; however, no evidence of such precipitation was seen during the experiments.

The results of the gas consumption rates for the three systems studied in the nucleation and growth of ethane hydrate experiments are shown in table 7.10. These data give an indication of the total amount of hydrate formed during each experiment. Gas consumption rates are almost identical for each of the three systems, and indeed any variations are well within experimental uncertainties and cannot be called significant.

This observation suggests that tba3S does not affect the amount of ethane hydrate that is produced during hydration, as the amount of gas consumed during a hydration cycle is almost identical. However it must be noted that this observation does not indicate whether the ethane hydrate produced has the same physical characteristics (particle size, aggregate strength ...) in each case, and this will be investigated from the results obtained from the granulometer.

TEST	GCR/bar h^{-1}	TEST	GCR/bar h^{-1}	TEST	GCR/bar h^{-1}
C(1)	0.38	$T_{0.1}(1)$	0.97	$T_{0.5}(1)$	0.40
C(2)	0.59	$T_{0.1}(2)$	0.67	$T_{0.5}(2)$	0.50
C(3)	0.54	$T_{0.1}(3)$	0.47	$T_{0.5}(3)$	0.65
C(4)	0.66	$T_{0.1}(4)$	0.39	$T_{0.5}(4)$	0.55
C(5)	0.61	$T_{0.1}(5)$	0.62	$T_{0.5}(5)$	0.51
C(6)	0.50	$T_{0.1}(6)$	0.63	$T_{0.5}(6)$	0.47
Average	0.55		0.63		0.51
S.D.	0.10		0.20		0.08

Table 7.10 Ethane hydrate gas consumption rate.

The results obtained from the granulometer for the three systems studied in the nucleation and growth of ethane hydrate experiments are shown in table 7.11. As mentioned earlier in each of the three systems there is not a full complement of results for the number of tests ran on each system; due to operational difficulties with the granulometer during some runs.

TEST	NUCLEATION RATE/ml^{-1} minutes^{-1}	R^2	GROWTH RATE/μm minutes^{-1}	R^2
C(2)	2065	0.91	4.07	0.41
C(3)	2947	0.95	0.22	0.07
C(4)	913	0.69	0.36	0.54
C(5)	707	0.86	0.24	0.67
C(6)	561	0.55	-0.14	0.05
Average	1439		1.56	
S.D.	1031		2.18	
$T_{0.1}(3)$	41	0.13	0.44	0.67
$T_{0.1}(4)$	-13	0.01	0.06	0.01
$T_{0.1}(5)$	89	0.40	0.77	0.82
$T_{0.1}(6)$	-26	0.21	0.03	0.02
Average	89		0.61	
S.D.	N.A.		0.23	
$T_{0.5}(2)$	115	0.52	1.22	0.69
$T_{0.5}(3)$	135	0.84	0.84	0.94
$T_{0.5}(4)$	103	0.83	0.72	0.85
$T_{0.5}(5)$	113	0.82	0.67	0.95
Average	116		0.86	
S.D.	13		0.25	

Table 7.11 Granulometry data.

The data presented in table 7.11 for some of the experiments has a very poor signal:noise ratio–sufficiently small that in some instances the data has not been used in the calculation of the average values. Therefore all fits with correlation coefficients less than 0.4 have been removed when determining the average properties.

From table 7.11 we can see that the nucleation rate is very difficult to determine in $T_{0.1}(i)$, and that the only moderately good result gives a nucleation rate close to that for $T_{0.5}(i)$, but is probably not reliable. Growth rates are difficult to determine for C(i) and $T_{0.1}(i)$, but some of the runs did give moderate correlations. However both the nucleation and growth rates give surprisingly good correlations for $T_{0.5}(i)$, perhaps suggesting that the inhibitor is involved in the nucleation mechanism, and so is making this a more reproducible process. The nucleation rates are consistent with the induction times, with the inhibitor giving slower nucleation times, consistent with longer times to each nucleation event. However the data is not reliable enough to say whether or not $T_{0.1}(i)$ fits this trend. The growth rates are probably too unreliable to compare closely, but the data does seem to indicate comparable growth rates in each system, which is consistent with the gas consumption data.

7.6 Conclusions

In this chapter we reported the synthesis of tba3S and presented results of a series of tests to characterise its influence on hydrate formation. These tests included an investigation into the effect of tba3S upon the induction time to crystal formation, and morphology, of THF hydrate, together with a more comprehensive study of the effect of tba3S upon ethane hydrate formation.

The results obtained for THF hydrate formation show an increased average induction time in systems containing either solely PVP or tba3S when compared to the uninhibited system. The addition of tba3S gives longer induction times than addition of either PVP or mixtures of tba3S/PVP. The mixtures appear to show a negative synergism, giving shorter induction times than would be predicted from the weighted average of the pure tba3S and PVP results.

The crystals grown from THF/water mixtures exhibit different crystal habits when tba3S or PVP is present compared with the crystals produced in the uninhibited system. The uninhibited system produces octahedral crystals whereas the PVP inhibited system produces thin, almost transparent plate-like crystals. The crystals produced in the tba3S inhibited system appear to be a composite of the other two systems, in that they resemble plate-like octahedra.

The results obtained in the nucleation and growth of ethane hydrate experiments show higher average induction times when tba3S is present than in the simple ethane/water mixture. The gas consumption rate, within experimental error, shows no difference in any of the three systems studied. The average nucleation rate is smaller when tba3S is present with respect to the control system while the average growth rate is the same, within experimental error, for all three systems studied.

From these results we conclude that tba3S is active as a kinetic inhibitor and affects the formation of both THF and ethane hydrate. The mode of action is primarily inhibition of hydrate crystal nucleation rather than by retarding subsequent growth, as demonstrated by the increased induction times and nucleation rates, but comparable gas consumption and growth rates.

However the crystallisation study shows that tba3S does posses some growth modifying properties, and that these are not the same as those observed for PVP. The

fact that different morphologies are produced by these additives does suggest that they will give different rheological properties for hydrate slurries in addition to any beneficial effects on nucleation time.

7.7 References

[1] Palmer H.A., Diss., U. of Oklahoma, 1950.

[2] Bertie J.E., Jacobs S.M., *J. Chem. Phys.*, **69**, 1978, 4105.

[3] Garg S.R., Davidson D.W., Ripmeester J.A., *J. Magn. Reson.*, **15**, 1974, 295.

[4] Gough S.R., Hawkins R.E., Morris B., Davidson D.W., *J. Phys. Chem.*, **77**, 1973, 2969.

[5] Morris B., Davidson D.W., *J. Chem. Phys.*, **49**, 1971, 1243.

[6] Davidson D.W., *Can. J. Chem.*, **49**, 1971, 1224.

[7] Klug D.D., Whalley E., *Can. J. Chem.*, **51**, 1973, 4062.

[8] Yamamuro O., Matsuo T., Suga H., David W.I.F., Ibberson R.M., Leadbetter A.J., *Physica B*, **213**, 1995, 405.

[9] Villard P., *Compt. Rend.*, **106**, 1888, 1602.

[10] Davidson D.W., Garg S.K., Gough S.R., Hawkins R.E., Ripmeester J.A., *Can. J. Chem.*, **55**, 1977, 3641.

[11] Linfield W.M., Abend P.G., Davis G.A., *J. Am. Oil Chem. Assoc.*, **40B**, 1963, 114.

[12] Jussaume L., Canselier J.P., Monfort J.P., Proceedings AIChE Spring National Meeting, Houston, USA, 14-18 March, 1999.

[13] Jussaume L., Etude D'Inhibiteurs Cinetiques D'Hydrates De Gaz: Methods Experimentales Et Modelisations Numeriques, PhD Diss. ENSIGCT, 1999.

[14] Zanota M.L. PhD Diss., Universite de Pau et des Pays de l'Adour, To Be Published.

[15] El Hafaia T. Monfort J.P., Proceedings AIChE Spring National Meeting, Houston, USA, 14-18 March, 1999.

[16] Peng D., Robinson D.B., *Ind. Eng. Chem. Fundam.*, **15**, 1976, 59.

[17] Roberts O.L., Brownscombe E.R., Howe L.S., *Oil and Gas J.*, **39**, 1940, 37.

[18] Deaton W.M., Frost E.M., Gas Hydrates and Their Relation to the Operation of Natural-Gas Pipe Lines, US Bureau of Mines Monograph, **8**, 1946, 101.

[19] Reamer H.H., Selleck F.T., Sage B.H., *J. Petrol Tech.*, **4**, 1952, 197.

[20] Galloway T.J., Ruska W., Chappelear P.S., Kobayashi R., *Ind. Eng. Chem. Fundam.*, **9**, 1970, 237.

[21] Falabella B.J., A Study of Natural Gas Hydrates, PhD Diss., U. of Mass., 1975.

[22] Holder G.D., Grigoriou G.C., *J. Chem. Thermo.*, **12**, 1980, 1093.

[23] Holder G.D., Hand J.H., *AIChE Journal*, **28**, 1982, 44.

[24] Ng H.J., Robonson D.B., *Fluid Phase Equilibria*, **21**, 1985, 145.

[25] Avlonitis D., Danesh A., Todd A.C., Measurement and Prediction of Hydrate Dissociation Pressure of Oil-Gas Systems, BHRA Conference On Operational Consequences of Hydrate Formation and Inhibition Offshore, Cranfield, UK, 3 November, 1988.

[26] Morita K., Nakano S., Ohgaki K., *Fluid Phase Equilibria*, **169**, 2000, 167.

CHAPTER 8

CONCLUSIONS

8 General Conclusions

8.1 Summary of the Problem

Clathrate hydrates, or gas hydrates as they are more commonly called, are members of a family of compounds known as inclusion compounds, in which small guest molecules are encaged by a crystalline host lattice. Gas hydrates usually form in one of three main crystal structures: type I, which has a body centred cubic crystal structure; type II, with a diamond lattice structure; or structure H, which has a hexagonal structure. These structures are all favoured by relatively low temperatures and high pressures. Indeed conditions found during natural gas exploration and production can be ideal for the formation and growth of gas hydrates and so there is significant risk of pipeline blockages. Thus there is considerable interest in developing better methods of inhibiting hydrate formation and growth.

Various options for controlling this problem have been tried. These include decreasing the pressure or increasing the temperature of the pipeline, removing water from the pipeline or adding inhibitors to the pipeline. Of these, the use of inhibitors is usually the only financially viable alternative. The inhibitors themselves can be divided into two categories: thermodynamic or kinetic. Thermodynamic inhibitors act by altering the phase diagram of gas hydrates *i.e.* altering the temperature or pressure at which the hydrate forms. Historically these have been the inhibitors of choice, however they are required in large amounts—typically 10–50 wt. %—so that the cost of using the most common inhibitor, methanol, is estimated at $500 million a year.[1]

Over the last decade, interest has turned to the kinetic inhibitors, which act to slow either nucleation or the rate of growth of the hydrate crystals, and are believed to act via a mechanism involving selective adsorption of the KI onto particular crystal growth surfaces. This selective adsorption has been likened to the lock and key mechanism used to explain enzyme specificity towards substrates in biology. According to this model activity arises from a complementarity between the shapes of the inhibitor and surface adsorption sites, in much the same way as a key fits into a lock. The attraction of such inhibitors is that they are required in much smaller amounts than their thermodynamic counterparts and therefore afford the potential for significant financial savings.

In this thesis we presented results from work designed to investigate the mode of action of small zwitterionic kinetic inhibitors. Results are presented for two families of potential KIs interacting with a methane–propane double hydrate. This system adopts the hydrate structure that forms under most operating conditions, *i.e.* type II.

8.2 Results of the Investigation

Results from chapter 4 indicate that both families of inhibitors appear to have an effect upon the second solvation shell structure of bulk water, and that they do increase short and long-range structure in solvated water. It is clear from the radial distribution functions for water around solute atoms, g_{XO} and g_{XH}, that two distinct regions can be identified within the inhibitors: the hydrophobic regions (*i.e.* C1, C2 and C3) and the hydrophilic regions (*i.e.* C4, C/S and O).* This dual character of the inhibitors may well

* This notation refers to different chemical centres within the inhibitor, and is explained on pages 113–114

be important in the mode of action of kinetic inhibitors, with the hydrophilic region targeting growing hydrate crystals while the hydrophobic region disrupts further growth of the hydrate, possibly by changing the structure of solvated water at the hydrate interface. That is to say adsorption via the hydrophilic region of the inhibitor would allow for the possibility of the alkyl chains to either stick up into the liquid water region above the hydrate surface or to lie along the hydrate surface disrupting further growth of the crystal.

The simulations performed in chapter 5 allowed for elucidation of part of the SPC hydrate phase diagram at 277 and 300 K, which ultimately led to a set of operating conditions for simulations in chapter 6. In addition, a high-density phase was identified at pressures in excess of 20 kbar at both 277 and 300 K. This high-density phase had a fundamentally different structure to that observed at lower pressures and is in agreement with a number of papers that postulate the existence of such a phase as outlined in chapter 5 section 5.1.1.

Chapter 6 was concerned with the most complex system studied in this thesis and as a result led to probably the least conclusive set of results. This is, perhaps, as was to be expected, as there are so many different interactions occurring which can mask those effects that are most significant for inhibition. For example, no constraint was imposed to force the inhibitor to remain immediately above the gas hydrate surface for the whole of the simulation, which could lead to a dilution of the effects of the inhibitors upon gas hydrate surface structure. Never-the-less differences were identified in g_{OO} for the region of the surface to which the inhibitor was added. At 277 K there was in general a relaxation of the water network structure whereas at 300 K this effect was only observed

for the carboxylates. However at both 277 and 300 K g_{XO} and g_{XH} showed a contracted water network for the carboxylates compared with the sulphonates for C/S and O. This is a recurrence of the competition between hydrophilic and hydrophobic regions of these inhibitors identified in chapter 4, and suggests that the hydrophilic region of the inhibitor is the region that invokes the most important changes upon the water network structure for hydrate inhibition.

The experimental study carried out in chapter 7 confirmed that our newly proposed inhibitor, tba3S, did indeed show substantial activity in inhibiting the formation of both THF and ethane hydrate as well as some growth modifying properties. The delay of nucleation was longer than is found with PVP. These results led to the conclusion that tba3S is active as a kinetic inhibitor and primarily affects hydrate crystal nucleation rather than retarding growth.

8.3 References

[1] Sloan, E.D., Subramanian S., Matthews P.N., Lederhos J.P., Khokar A.A., *Ind. Eng. Chem. Res.* **37**, 1998, 3124.

APPENDIX

Appendix

Chapter 4

Data listed in this appendix is contained upon the included CD.

Appendix 4.1 g_{XO} summary for the inhibited systems – Appendix4.1.doc.

Appendix 4.2 g_{XH} summary for the inhibited systems – Appendix4.2.doc.

Appendix 4.3 Co-ordination number summary for solvated water in the inhibited systems – Appendix4.3.doc.

Appendix 4.4 Residence times for the oxygen and hydrogen atoms of solvated water for the inhibited systems – Appendix4.4.doc.

Appendix 4.5 Self-diffusion coefficients for the oxygen and hydrogen atom of solvated water around various solute atoms for the inhibited systems – Appendix4.5.doc.

Appendix 4.6 Rotational lifetime summary for solvated water in the inhibited systems – Appendix4.6.doc.

Chapter 5

Appendix 5.1 Summary of the simulations and average pressures obtained at 277 K – Appendix5.1.doc.

Appendix 5.2 Summary of oxygen and hydrogen atom self-diffusion coefficients in the four runs $T_{277}P_{-0.01}$, $T_{277}P_{0.21}$, $T_{277}P_{4.04}$ and $T_{277}P_{26.59}$ – Appendix5.2.doc.

Appendix 5.3 Summary of co-ordination number for slabs 2, 3, 4 and 5 in runs $T_{277}P_{-0.01}$, $T_{277}P_{0.21}$, $T_{277}P_{4.04}$ and $T_{277}P_{26.59}$ – Appendix5.3.doc.

Appendix 5.4 Phase assignment summary for runs $T_{277}P_{-0.01}$, $T_{277}P_{0.21}$, $T_{277}P_{4.04}$ and $T_{277}P_{26.59}$ – Appendix5.4.doc.

Appendix 5.5 Summary of the simulations and average pressures obtained at 300 K – Appendix5.5.doc.

Appendix 5.6 Summary of oxygen and hydrogen atom self-diffusion coefficients in the four runs $T_{300}P_{0.16}$, $T_{300}P_{2.93}$, $T_{300}P_{12.26}$ and $T_{300}P_{26.95}$ – Appendix5.6.doc.

Appendix 5.7 Summary of co-ordination number for slabs 2, 3, 4 and 5 in runs $T_{300}P_{0.16}$, $T_{300}P_{2.93}$, $T_{300}P_{12.26}$ and $T_{300}P_{26.95}$ – Appendix5.7.doc.

Appendix 5.8 Phase assignment summary for runs $T_{300}P_{0.16}$, $T_{300}P_{2.93}$, $T_{300}P_{12.26}$ and $T_{300}P_{26.95}$ – Appendix5.8.doc.

Appendix 5.9 Summary of co-ordination number for slabs 1 and 6 in runs $T_{277}P_{-0.01}$, $T_{277}P_{0.21}$, $T_{277}P_{4.04}$ and $T_{277}P_{26.59}$ – Appendix5.9.doc.

Appendix 5.10 Summary of co-ordination number for slabs 1 and 6 in runs $T_{300}P_{0.16}$, $T_{300}P_{2.93}$, $T_{300}P_{12.26}$ and $T_{300}P_{26.95}$ – Appendix5.10.doc.

Chapter 6

Appendix 6.1 g_{XO} summary for the inhibited systems – Appendix6.1.doc.

Appendix 6.2 g_{XH} summary for the inhibited systems – Appendix6.2.doc.

Appendix 6.3 Co-ordination number summary for solvated water in the inhibited systems – Appendix6.3.doc.

Appendix 6.4 F_3 summary for the inhibited systems – Appendix6.4.doc.

Appendix 6.5 $F_{4\varphi}$ summary for the inhibited systems – Appendix6.5.doc.

Appendix 6.6 F_{4t} summary for the inhibited systems – Appendix6.6.doc.

Appendix 6.7 Self-diffusion coefficient summary for the oxygen and hydrogen atom of solvated water around various solute atoms for the inhibited systems – Appendix6.7.doc.

Appendix 6.8 Rotational lifetime summary for solvated water in the inhibited systems – Appendix6.8.doc.

Appendix 6.9 g_{XO} summary for the inhibited systems – Appendix6.9.doc.

Appendix 6.10 g_{XH} summary for the inhibited systems – Appendix6.10.doc.

Appendix 6.11 Co-ordination number summary for solvated water in the inhibited systems – Appendix6.11.doc.

Appendix 6.12 F_3 summary for the inhibited systems – Appendix6.12.doc.

Appendix 6.13 $F_{4\varphi}$ summary for the inhibited systems – Appendix6.13.doc.

Appendix 6.14 F_{4t} summary for the inhibited systems – Appendix6.14.doc.

Appendix 6.15 Self-diffusion coefficient summary for the oxygen and hydrogen atom of solvated water around various solute atoms for the inhibited systems – Appendix6.15.doc.

Appendix 6.16 Rotational lifetime summary for solvated water in the inhibited systems – Appendix6.16.doc.

SYSTEM	ATOM	1st PEAK POSITION/Å	2nd PEAK POSITION/Å
tba1C	C1	3.78	-
tba2C	C1	3.79	-
tba3C	C1	3.66	-
tba1S	C1	3.78	-
tba2S	C1	3.77	-
tba3S	C1	3.77	-
tba1C	C2	4.69	-
tba2C	C2	4.53	-
tba3C	C2	4.62	-
tba1S	C2	4.55	-
tba2S	C2	4.57	-
tba3S	C2	4.69	-
tba1C	C3	3.69	-
tba2C	C3	3.72	-
tba3C	C3	3.73	-
tba1S	C3	3.73	-
tba2S	C3	3.72	-
tba3S	C3	3.69	-
tba1C	C4	4.81	-
tba2C	C4	4.65	-

tba3C	C4	3.73	-
tba1S	C4	3.61	-
tba2S	C4	4.86	-
tba3S	C4	4.81	-
tba1C	C	3.57	-
tba2C	C	3.54	-
tba3C	C	3.41	-
tba1S	S	3.56	-
tba2S	S	3.65	-
tba3S	S	3.67	-
tba1C	O	2.59	4.51
tba2C	O	2.61	4.57
tba3C	O	2.60	4.60
tba1S	O	2.56	4.70
tba2S	O	2.57	4.74
tba3S	O	2.57	4.83

Appendix 4.1 g_{XiOs} summary for the inhibited systems. Resolution of the positions is 0.025 Å.

SYSTEM	ATOM	1st PEAK POSITION/Å	2nd PEAK POSITION/Å
tba1C	C1	-	-
tba2C	C1	-	-
tba3C	C1	-	-
tba1S	C1	-	-
tba2S	C1	-	-
tba3S	C1	-	-
tba1C	C2	4.56	-
tba2C	C2	4.53	-
tba3C	C2	4.67	-
tba1S	C2	4.60	-
tba2S	C2	4.67	-
tba3S	C2	4.52	-
tba1C	C3	4.39	-
tba2C	C3	3.64	-
tba3C	C3	4.00	-
tba1S	C3	3.75	-
tba2S	C3	3.52	-
tba3S	C3	3.67	-
tba1C	C4	3.76	5.17
tba2C	C4	3.81	5.19

tba3C	C4	3.71	-
tba1S	C4	3.99	5.52
tba2S	C4	3.89	5.23
tba3S	C4	3.98	5.47
tba1C	C	2.64	4.10
tba2C	C	2.54	4.01
tba3C	C	2.50	4.08
tba1S	S	2.76	4.29
tba2S	S	2.69	4.21
tba3S	S	2.72	4.25
tba1C	O	1.62	3.10
tba2C	O	1.61	3.05
tba3C	O	1.61	3.07
tba1S	O	1.57	3.02
tba2S	O	1.60	3.01
tba3S	O	1.57	3.01

Appendix 4.2 g_{XiHs} summary for the inhibited systems. Resolution of the values is 0.025 Å.

SYSTEM	ATOM	MODAL CO-ORDINATION NUMBER	% OF SOLVATED WATERS WITH CO-ORDINATION NUMBER		
			3	4	5
tba1C	C1	4	21	44	24
tba2C	C1	4	22	45	23
tba3C	C1	4	26	45	20
tba1S	C1	4	23	43	24
tba2S	C1	4	24	43	22
tba3S	C1	4	23	45	22
tba1C	C2	4	16	43	29
tba2C	C2	4	18	45	26
tba3C	C2	4	20	45	24
tba1S	C2	4	16	42	29
tba2S	C2	4	17	44	28
tba3S	C2	4	17	43	27
tba1C	C3	4	14	42	30
tba2C	C3	4	16	45	28
tba3C	C3	4	18	46	25
tba1S	C3	4	14	41	30

tba2S	C3	4	15	43	29
tba3S	C3	4	15	43	29
tba1C	C4	4	23	41	24
tba2C	C4	4	22	42	24
tba3C	C4	4	25	42	22
tba1S	C4	4	28	39	21
tba2S	C4	4	29	40	20
tba3S	C4	4	25	40	22
tba1C	C	4	30	37	20
tba2C	C	4	33	36	18
tba3C	C	4	31	37	18
tba1S	S	4	35	36	17
tba2S	S	4	34	36	17
tba3S	S	4	34	35	16
tba1C	O	4	32	36	19
tba2C	O	3 – 4	35	35	17
tba3C	O	4	33	36	17
tba1S	O	3	37	36	15
tba2S	O	3	36	35	16
tba3S	O	3	36	35	15

Appendix 4.3 Co-ordination number summary for solvated water in the inhibited systems.

SYSTEM	ATOM	OXYGEN ATOM/ps	HYDROGEN ATOM/ps
tba1C	C1	0.32	0.18
tba2C	C1	0.45	0.25
tba3C	C1	0.34	0.18
tba1S	C1	0.32	0.17
tba2S	C1	0.42	0.23
tba3S	C1	0.36	0.20
tba1C	C2	0.51	0.23
tba2C	C2	0.53	0.25
tba3C	C2	0.51	0.25
tba1S	C2	0.53	0.25
tba2S	C2	0.55	0.23
tba3S	C2	0.57	0.26
tba1C	C3	0.51	0.22
tba2C	C3	0.57	0.25
tba3C	C3	0.45	0.18
tba1S	C3	0.51	0.22
tba2S	C3	0.53	0.23
tba3S	C3	0.55	0.23
tba1C	C4	0.73	0.28
tba2C	C4	0.75	0.28
tba3C	C4	0.95	0.35

tba1S	C4	0.65	0.28
tba2S	C4	0.71	0.35
tba3S	C4	0.73	0.31
tba1C	C	1.8	0.75
tba2C	C	3.4	0.86
tba3C	C	3.2	0.64
tba1S	S	1.2	0.50
tba2S	S	1.9	0.47
tba3S	S	1.7	0.54
tba1C	O	4.6	4.8
tba2C	O	8.2	6.4
tba3C	O	6.4	5.6
tba1S	O	4.0	2.7
tba2S	O	4.3	2.8
tba3S	O	4.6	3.1

Appendix 4.4 Residence times for the oxygen and hydrogen atoms of solvated water for the inhibited systems. The values have been scaled relative to the water oxygen or water hydrogen solvation shell to allow for direct comparison between values.

SYSTEM	ATOM	D/Å^2 ps^{-1}	
		OXYGEN ATOM	HYDROGEN ATOM
tba1C	C1	0.11	0.11
tba2C	C1	0.10	0.10
tba3C	C1	0.09	0.09
tba1S	C1	0.10	0.10
tba2S	C1	0.13	0.13
tba3S	C1	0.12	0.11
tba1C	C2	0.13	0.13
tba2C	C2	0.10	0.10
tba3C	C2	0.12	0.11
tba1S	C2	0.12	0.11
tba2S	C2	0.13	0.13
tba3S	C2	0.11	0.11
tba1C	C3	0.17	0.09
tba2C	C3	0.12	0.12
tba3C	C3	0.13	0.12
tba1S	C3	0.14	0.13
tba2S	C3	0.14	0.14
tba3S	C3	0.15	0.14
tba1C	C4	0.11	0.10

tba2C	C4	0.10	0.09
tba3C	C4	0.11	0.10
tba1S	C4	0.12	0.11
tba2S	C4	0.12	0.11
tba3S	C4	0.14	0.12
tba1C	C	0.10	0.09
tba2C	C	0.10	0.07
tba3C	C	0.11	0.08
tba1S	S	0.10	0.07
tba2S	S	0.12	0.07
tba3S	S	0.14	0.09
tba1C	O	0.11	0.10
tba2C	O	0.09	0.07
tba3C	O	0.10	0.08
tba1S	O	0.08	0.07
tba2S	O	0.11	0.07
tba3S	O	0.11	0.09

Appendix 4.5 Self-diffusion co-efficients for the oxygen and hydrogen atom of solvated water around various solute atoms for the inhibited systems.

SYSTEM	ATOM	ROTATIONAL LIFETIME/ps		$P2_{\perp}/P2_{\parallel}$ as a ratio.
		From $P_{2\parallel}$	From $P_{2\perp}$	
tba1C	C1	1.40	1.95	+39
tba2C	C1	1.75	2.20	+26
tba3C	C1	1.50	2.20	+47
tba1S	C1	1.30	1.80	+38
tba2S	C1	1.35	2.00	+48
tba3S	C1	1.95	2.70	+38
tba1C	C2	1.20	1.50	+25
tba2C	C2	1.35	1.65	+22
tba3C	C2	1.25	1.70	+36
tba1S	C2	1.10	1.45	+32
tba2S	C2	1.20	1.55	+29
tba3S	C2	1.30	1.80	+38
tba1C	C3	1.10	1.40	+27
tba2C	C3	1.20	1.45	+21
tba3C	C3	1.15	1.60	+39
tba1S	C3	1.10	1.40	+27

tba2S	C3	1.05	1.30	+24
tba3S	C3	1.20	1.55	+29
tba1C	C4	1.15	1.75	+52
tba2C	C4	1.60	2.40	+50
tba3C	C4	1.50	2.30	+53
tba1S	C4	1.25	1.70	+36
tba2S	C4	1.25	2.20	+76
tba3S	C4	1.35	2.10	+56
tba1C	C	1.10	2.30	+109
tba2C	C	1.65	3.10	+88
tba3C	C	2.00	3.30	+65
tba1S	S	1.25	2.30	+84
tba2S	S	1.20	2.60	+117
tba3S	S	1.60	2.80	+75
tba1C	O	1.15	2.40	+109
tba2C	O	1.75	3.30	+89
tba3C	O	2.10	3.60	+71
tba1S	O	1.40	2.60	+86
tba2S	O	1.30	2.80	+115
tba3S	O	1.75	3.70	+111

Appendix 4.6 Rotational lifetime summary for solvated water in the inhibited systems.

RUN	DURATION OF TRAJECTORY /ps	AVERAGE PRESSURE/kbar	PHASE ASSIGNMENT
$T_{277}P_{-0.01a}$	20	0.00	Melting
$T_{277}P_{-0.01b}$	20	-0.01	Melting
$T_{277}P_{-0.01c}$	20	-0.01	Melting
$T_{277}P_{-0.01d}$	20	-0.01	Melting
$T_{277}P_{-0.01e}$	20	-0.01	Melting
$T_{277}P_{-0.01f}$	50	-0.02	Melting
$T_{277}P_{-0.01g}$	50	-0.02	Melting
$T_{277}P_{0.21a}$	20	0.28	Hydrate
$T_{277}P_{0.21b}$	20	0.22	Hydrate
$T_{277}P_{0.21c}$	20	0.19	Hydrate
$T_{277}P_{0.21d}$	20	0.17	Hydrate
$T_{277}P_{0.21e}$	20	0.18	Hydrate
$T_{277}P_{0.21f}$	50	0.21	Hydrate
$T_{277}P_{0.21g}$	50	0.21	Hydrate
$T_{277}P_{4.04a}$	20	4.20	Hydrate
$T_{277}P_{4.04b}$	20	4.06	Hydrate
$T_{277}P_{4.04c}$	20	4.03	Hydrate
$T_{277}P_{4.04d}$	20	4.00	Hydrate

$T_{277}P_{4.04e}$	20	3.98	Hydrate
$T_{277}P_{4.04f}$	50	4.01	Hydrate
$T_{277}P_{4.04g}$	50	4.00	Hydrate
$T_{277}P_{26.59a}$	20	27.65	Other
$T_{277}P_{26.59b}$	20	26.97	Other
$T_{277}P_{26.59c}$	20	26.71	Other
$T_{277}P_{26.59d}$	20	26.53	Other
$T_{277}P_{26.59e}$	20	26.38	Other
$T_{277}P_{26.59f}$	50	26.04	Other
$T_{277}P_{26.59g}$	50	25.86	Other

Appendix 5.1 Summary of the simulations and average pressures obtained at 277 K. a – g in the run column refers to the constituent simulations as outlined in table 5.3.

RUN	AVERAGE D/Å^2 ps^{-1}	
	OXYGEN ATOM	HYDROGEN ATOM
$T_{277}P_{-0.01a}$	0.36	0.39
$T_{277}P_{-0.01b}$	0.37	0.30
$T_{277}P_{-0.01c}$	0.50	0.52
$T_{277}P_{-0.01d}$	0.60	0.61
$T_{277}P_{-0.01e}$	0.67	0.68
$T_{277}P_{-0.01f}$	0.84	0.85
$T_{277}P_{-0.01g}$	0.91	0.92
$T_{277}P_{0.21a}$	0.21	0.24
$T_{277}P_{0.21b}$	0.29	0.30
$T_{277}P_{0.21c}$	0.14	0.14
$T_{277}P_{0.21d}$	0.26	0.26
$T_{277}P_{0.21e}$	0.31	0.31
$T_{277}P_{0.21f}$	0.36	0.38
$T_{277}P_{0.21g}$	0.39	0.39
$T_{277}P_{4.04a}$	0.05	0.06
$T_{277}P_{4.04b}$	0.01	0.02
$T_{277}P_{4.04c}$	0.03	0.03
$T_{277}P_{4.04d}$	0.03	0.04
$T_{277}P_{4.04e}$	0.05	0.05

$T_{277}P_{4.04f}$	0.06	0.06
$T_{277}P_{4.04g}$	0.07	0.07
$T_{277}P_{26.59a}$	0.14	0.17
$T_{277}P_{26.59b}$	0.07	0.09
$T_{277}P_{26.59c}$	0.05	0.06
$T_{277}P_{26.59d}$	0.06	0.07
$T_{277}P_{26.59e}$	0.07	0.07
$T_{277}P_{26.59f}$	0.05	0.06
$T_{277}P_{26.59g}$	0.03	0.04

Appendix 5.2 Summary of oxygen and hydrogen atom diffusion coefficients in the four runs $T_{277}P_{-0.01}$, $T_{277}P_{0.21}$, $T_{277}P_{4.04}$ and $T_{277}P_{26.59}$.

RUN	CO-ORDINATION NUMBER			
	SLAB 2	SLAB 3	SLAB 4	SLAB 5
$T_{277}P_{-0.01a}$	3.90	3.92	3.92	3.90
$T_{277}P_{-0.01b}$	3.90	3.93	3.92	3.89
$T_{277}P_{-0.01c}$	3.91	3.93	3.90	3.88
$T_{277}P_{-0.01d}$	3.91	3.92	3.89	3.86
$T_{277}P_{-0.01e}$	3.91	3.93	3.90	3.84
$T_{277}P_{-0.01f}$	3.92	3.91	3.87	3.88
$T_{277}P_{-0.01g}$	3.91	3.91	3.85	3.92
$T_{277}P_{0.21a}$	3.93	3.94	3.94	3.93
$T_{277}P_{0.21b}$	3.92	3.93	3.94	3.93
$T_{277}P_{0.21c}$	3.91	3.94	3.93	3.91
$T_{277}P_{0.21d}$	3.90	3.93	3.93	3.90
$T_{277}P_{0.21e}$	3.92	3.93	3.93	3.91
$T_{277}P_{0.21f}$	3.91	3.94	3.92	3.92
$T_{277}P_{0.21g}$	3.90	3.93	3.92	3.90
$T_{277}P_{4.04a}$	3.97	3.97	3.97	3.98
$T_{277}P_{4.04b}$	3.96	3.97	3.97	3.98
$T_{277}P_{4.04c}$	3.98	3.97	3.98	3.98
$T_{277}P_{4.04d}$	3.97	3.98	3.98	3.98
$T_{277}P_{4.04e}$	3.97	3.97	3.97	3.98
$T_{277}P_{4.04f}$	3.97	3.97	3.97	3.97

$T_{277}P_{4.04g}$	3.97	3.97	3.98	3.96
$T_{277}P_{26.59a}$	4.55	4.57	4.55	4.70
$T_{277}P_{26.59b}$	4.74	4.62	4.80	4.72
$T_{277}P_{26.59c}$	4.81	4.68	4.86	4.68
$T_{277}P_{26.59d}$	4.85	4.67	4.87	4.68
$T_{277}P_{26.59e}$	4.90	4.78	4.84	4.74
$T_{277}P_{26.59f}$	4.84	4.75	4.79	4.69
$T_{277}P_{26.59g}$	4.77	4.82	4.80	4.75

Appendix 5.3 Summary of co-ordination number for slabs 2, 3, 4 and 5 in runs $T_{277}P_{-0.01}$, $T_{277}P_{0.21}$, $T_{277}P_{4.04}$ and $T_{277}P_{26.59}$.

RUN	NUMBER OF WATERS IN EACH PHASE		
	HYDRATE	LIQUID	ICE
$T_{277}P_{-0.01a}$	304	91	13
$T_{277}P_{-0.01b}$	275	119	14
$T_{277}P_{-0.01c}$	251	141	16
$T_{277}P_{-0.01d}$	233	158	17
$T_{277}P_{-0.01e}$	209	182	17
$T_{277}P_{-0.01f}$	193	197	18
$T_{277}P_{-0.01g}$	182	206	20
$T_{277}P_{0.21a}$	321	77	10
$T_{277}P_{0.21b}$	307	90	12
$T_{277}P_{0.21c}$	299	97	12
$T_{277}P_{0.21d}$	284	111	14
$T_{277}P_{0.21e}$	279	117	12
$T_{277}P_{0.21f}$	257	138	13
$T_{277}P_{0.21g}$	249	145	15
$T_{277}P_{4.04a}$	323	76	10
$T_{277}P_{4.04b}$	311	88	9
$T_{277}P_{4.04c}$	318	82	8
$T_{277}P_{4.04d}$	314	84	10
$T_{277}P_{4.04e}$	297	102	9

$T_{277}P_{4.04f}$	285	114	9
$T_{277}P_{4.04g}$	282	116	10
$T_{277}P_{26.59a}$	98	303	6
$T_{277}P_{26.59b}$	73	328	7
$T_{277}P_{26.59c}$	73	329	6
$T_{277}P_{26.59d}$	70	332	5
$T_{277}P_{26.59e}$	69	334	5
$T_{277}P_{26.59f}$	70	332	6
$T_{277}P_{26.59g}$	70	330	8

Appendix 5.4 Phase assignment summary for runs $T_{277}P_{-0.01}$, $T_{277}P_{0.21}$, $T_{277}P_{4.04}$ and $T_{277}P_{26.59}$.

RUN	DURATION OF TRAJECTORY /ps	AVERAGE PRESSURE/kbar.	PHASE ASSIGNMENT
$T_{300}P_{0.16a}$	20	0.27	Melting
$T_{300}P_{0.16b}$	20	0.22	Melting
$T_{300}P_{0.16c}$	20	0.18	Melting
$T_{300}P_{0.16d}$	20	0.15	Melting
$T_{300}P_{0.16e}$	20	0.14	Melting
$T_{300}P_{0.16f}$	20	0.14	Melting
$T_{300}P_{0.16g}$	20	0.13	Melting
$T_{300}P_{0.16h}$	20	0.12	Melting
$T_{300}P_{0.16i}$	20	0.11	Melting
$T_{300}P_{0.16j}$	20	0.10	Melting
$T_{300}P_{2.93a}$	20	2.97	Hydrate
$T_{300}P_{2.93b}$	20	2.87	Hydrate
$T_{300}P_{2.93c}$	20	2.88	Hydrate
$T_{300}P_{2.93d}$	20	2.86	Hydrate
$T_{300}P_{2.93e}$	20	2.90	Hydrate
$T_{300}P_{2.93f}$	20	2.92	Hydrate
$T_{300}P_{2.93g}$	20	2.95	Hydrate
$T_{300}P_{2.93h}$	20	2.97	Hydrate

$T_{300}P_{2.93i}$	20	2.99	Hydrate
$T_{300}P_{2.93j}$	20	3.00	Hydrate
$T_{300}P_{12.26a}$	20	12.62	Hydrate
$T_{300}P_{12.26b}$	20	12.40	Hydrate
$T_{300}P_{12.26c}$	20	12.28	Hydrate
$T_{300}P_{12.26d}$	20	12.22	Hydrate
$T_{300}P_{12.26e}$	20	12.19	Hydrate
$T_{300}P_{12.26f}$	20	12.19	Hydrate
$T_{300}P_{12.26g}$	20	12.21	Hydrate
$T_{300}P_{12.26h}$	20	12.19	Hydrate
$T_{300}P_{12.26i}$	20	12.17	Hydrate
$T_{300}P_{12.26j}$	20	12.17	Hydrate
$T_{300}P_{26.95a}$	20	27.91	Other
$T_{300}P_{26.95b}$	20	27.33	Other
$T_{300}P_{26.95c}$	20	27.13	Other
$T_{300}P_{26.95d}$	20	26.98	Other
$T_{300}P_{26.95e}$	20	26.86	Other
$T_{300}P_{26.95f}$	20	26.79	Other
$T_{300}P_{26.95g}$	20	26.75	Other
$T_{300}P_{26.95h}$	20	26.67	Other
$T_{300}P_{26.95i}$	20	26.59	Other
$T_{300}P_{26.95j}$	20	26.52	Other

Appendix 5.5 Summary of the simulations and average pressures obtained at 300 K. Run numbers are the same as in tables 5.2 and 5.4.

RUN	AVERAGE D/Å^2 ps^{-1}	
	OXYGEN ATOM	HYDROGEN ATOM
$T_{300}P_{0.16a}$	1.30	1.40
$T_{300}P_{0.16b}$	1.50	1.50
$T_{300}P_{0.16c}$	0.86	0.86
$T_{300}P_{0.16d}$	0.84	0.83
$T_{300}P_{0.16e}$	0.91	0.90
$T_{300}P_{0.16f}$	0.93	0.94
$T_{300}P_{0.16g}$	1.00	1.00
$T_{300}P_{0.16h}$	1.20	1.20
$T_{300}P_{0.16i}$	1.50	1.50
$T_{300}P_{0.16j}$	1.80	1.80
$T_{300}P_{2.93a}$	0.20	0.23
$T_{300}P_{2.93b}$	0.27	0.29
$T_{300}P_{2.93c}$	0.25	0.26
$T_{300}P_{2.93d}$	0.29	0.30
$T_{300}P_{2.93e}$	0.29	0.30
$T_{300}P_{2.93f}$	0.34	0.36
$T_{300}P_{2.93g}$	0.36	0.37
$T_{300}P_{2.93h}$	0.38	0.40
$T_{300}P_{2.93i}$	0.39	0.40

$T_{300}P_{2.93j}$	0.41	0.42
$T_{300}P_{12.26a}$	0.10	0.11
$T_{300}P_{12.26b}$	0.05	0.06
$T_{300}P_{12.26c}$	0.05	0.05
$T_{300}P_{12.26d}$	0.05	0.05
$T_{300}P_{12.26e}$	0.05	0.06
$T_{300}P_{12.26f}$	0.06	0.07
$T_{300}P_{12.26g}$	0.06	0.06
$T_{300}P_{12.26h}$	0.05	0.06
$T_{300}P_{12.26i}$	0.05	0.05
$T_{300}P_{12.26j}$	0.05	0.05
$T_{300}P_{26.95a}$	0.22	0.27
$T_{300}P_{26.95b}$	0.08	0.09
$T_{300}P_{26.95c}$	0.09	0.11
$T_{300}P_{26.95d}$	0.06	0.08
$T_{300}P_{26.95e}$	0.06	0.07
$T_{300}P_{26.95f}$	0.08	0.09
$T_{300}P_{26.95g}$	0.06	0.06
$T_{300}P_{26.95h}$	0.06	0.06
$T_{300}P_{26.95i}$	0.06	0.07
$T_{300}P_{26.95j}$	0.06	0.07

Appendix 5.6 Summary of oxygen and hydrogen atom diffusion coefficients in the four runs $T_{300}P_{0.16}$, $T_{300}P_{2.93}$, $T_{300}P_{12.26}$ *and* $T_{300}P_{26.95}$.

RUN	CO-ORDINATION NUMBER			
	SLAB 2	SLAB 3	SLAB 4	SLAB 5
$T_{300}P_{0.16a}$	3.89	3.92	3.93	3.90
$T_{300}P_{0.16b}$	3.87	3.90	3.90	3.87
$T_{300}P_{0.16c}$	3.83	3.88	3.87	3.85
$T_{300}P_{0.16d}$	3.83	3.87	3.84	3.80
$T_{300}P_{0.16e}$	3.85	3.88	3.82	3.82
$T_{300}P_{0.16f}$	3.83	3.87	3.85	3.82
$T_{300}P_{0.16g}$	3.86	3.84	3.82	3.85
$T_{300}P_{0.16h}$	3.87	3.79	3.77	3.83
$T_{300}P_{0.16i}$	3.87	3.67	3.75	3.86
$T_{300}P_{0.16j}$	3.83	3.58	3.77	3.91
$T_{300}P_{2.93a}$	3.92	3.95	3.96	3.95
$T_{300}P_{2.93b}$	3.92	3.94	3.95	3.93
$T_{300}P_{2.93c}$	3.93	3.95	3.94	3.95
$T_{300}P_{2.93d}$	3.90	3.94	3.95	3.97
$T_{300}P_{2.93e}$	3.93	3.95	3.94	4.02
$T_{300}P_{2.93f}$	3.93	3.94	3.92	4.01
$T_{300}P_{2.93g}$	3.91	3.95	3.93	4.06
$T_{300}P_{2.93h}$	3.92	3.94	3.92	4.09
$T_{300}P_{2.93i}$	3.93	3.94	3.91	4.13
$T_{300}P_{2.93j}$	3.92	3.95	3.92	4.13

$T_{300}P_{12.26a}$	4.08	4.00	4.01	4.08
$T_{300}P_{12.26b}$	4.11	4.00	3.99	4.05
$T_{300}P_{12.26c}$	4.11	4.03	4.00	4.11
$T_{300}P_{12.26d}$	4.10	4.07	4.01	4.08
$T_{300}P_{12.26e}$	4.16	4.03	4.00	4.05
$T_{300}P_{12.26f}$	4.16	4.03	4.00	4.06
$T_{300}P_{12.26g}$	4.13	4.03	4.00	4.05
$T_{300}P_{12.26h}$	4.11	4.03	4.00	4.04
$T_{300}P_{12.26i}$	4.10	4.04	4.00	4.07
$T_{300}P_{12.26j}$	4.10	4.03	4.00	4.10
$T_{300}P_{26.95a}$	4.78	4.76	4.80	4.43
$T_{300}P_{26.95b}$	4.80	4.79	5.05	4.59
$T_{300}P_{26.95c}$	4.81	4.70	5.00	4.58
$T_{300}P_{26.95d}$	4.87	4.70	5.02	4.51
$T_{300}P_{26.95e}$	4.87	4.84	5.01	4.51
$T_{300}P_{26.95f}$	4.97	4.82	4.90	4.49
$T_{300}P_{26.95g}$	4.96	4.79	4.85	4.54
$T_{300}P_{26.95h}$	4.97	4.76	4.92	4.60
$T_{300}P_{26.95i}$	4.91	4.86	4.99	4.63
$T_{300}P_{26.95j}$	4.94	4.89	4.96	4.60

Appendix 5.7 Summary of co-ordination number for slabs 2, 3, 4 and 5 in runs $T_{300}P_{0.16}$, $T_{300}P_{2.93}$, $T_{300}P_{12.26}$ and $T_{300}P_{26.95}$.

RUN	NUMBER OF WATERS IN EACH PHASE		
	HYDRATE	LIQUID	ICE
$T_{300}P_{0.16a}$	303	92	13
$T_{300}P_{0.16b}$	261	132	15
$T_{300}P_{0.16c}$	236	156	17
$T_{300}P_{0.16d}$	205	184	19
$T_{300}P_{0.16e}$	182	207	19
$T_{300}P_{0.16f}$	173	214	20
$T_{300}P_{0.16g}$	150	238	20
$T_{300}P_{0.16h}$	123	263	22
$T_{300}P_{0.16i}$	75	309	25
$T_{300}P_{0.16j}$	32	353	23
$T_{300}P_{2.93a}$	298	99	11
$T_{300}P_{2.93b}$	278	117	12
$T_{300}P_{2.93c}$	263	134	11
$T_{300}P_{2.93d}$	248	148	12
$T_{300}P_{2.93e}$	244	152	11
$T_{300}P_{2.93f}$	222	174	11
$T_{300}P_{2.93g}$	216	180	12
$T_{300}P_{2.93h}$	214	181	13
$T_{300}P_{2.93i}$	206	189	13

$T_{300}P_{2.93j}$	204	192	12
$T_{300}P_{12.26a}$	269	132	8
$T_{300}P_{12.26b}$	253	146	9
$T_{300}P_{12.26c}$	242	159	8
$T_{300}P_{12.26d}$	242	158	8
$T_{300}P_{12.26e}$	242	158	9
$T_{300}P_{12.26f}$	246	154	8
$T_{300}P_{12.26g}$	250	150	8
$T_{300}P_{12.26h}$	248	152	8
$T_{300}P_{12.26i}$	246	154	8
$T_{300}P_{12.26j}$	247	153	8
$T_{300}P_{26.95a}$	83	318	7
$T_{300}P_{26.95b}$	62	339	7
$T_{300}P_{26.95c}$	69	333	7
$T_{300}P_{26.95d}$	69	331	7
$T_{300}P_{26.95e}$	63	339	7
$T_{300}P_{26.95f}$	61	342	6
$T_{300}P_{26.95g}$	62	340	6
$T_{300}P_{26.95h}$	65	337	6
$T_{300}P_{26.95i}$	64	338	6
$T_{300}P_{26.95j}$	61	340	6

Appendix 5.8 Phase assignment summary for runs $T_{300}P_{0.16}$, $T_{300}P_{2.93}$, $T_{300}P_{12.26}$ and $T_{300}P_{26.95}$.

RUN	CO-ORDINATION NUMBER	
	SLAB 1	SLAB 6
$T_{277}P_{-0.01a}$	3.56	3.23
$T_{277}P_{-0.01b}$	3.56	3.25
$T_{277}P_{-0.01c}$	3.57	3.35
$T_{277}P_{-0.01d}$	3.57	3.32
$T_{277}P_{-0.01e}$	3.58	3.40
$T_{277}P_{-0.01f}$	3.61	3.44
$T_{277}P_{-0.01g}$	3.66	3.43
$T_{277}P_{0.21a}$	3.57	3.37
$T_{277}P_{0.21b}$	3.58	3.34
$T_{277}P_{0.21c}$	3.56	3.35
$T_{277}P_{0.21d}$	3.55	3.33
$T_{277}P_{0.21e}$	3.56	3.43
$T_{277}P_{0.21f}$	3.60	3.50
$T_{277}P_{0.21g}$	3.57	3.60
$T_{277}P_{4.04a}$	3.62	3.51
$T_{277}P_{4.04b}$	3.65	3.51
$T_{277}P_{4.04c}$	3.65	3.47
$T_{277}P_{4.04d}$	3.64	3.50
$T_{277}P_{4.04e}$	3.69	3.52
$T_{277}P_{4.04f}$	3.72	3.53

$T_{277}P_{4.04g}$	3.74	3.57
$T_{277}P_{26.59a}$	3.96	3.61
$T_{277}P_{26.59b}$	4.04	3.53
$T_{277}P_{26.59c}$	3.99	3.55
$T_{277}P_{26.59d}$	3.99	3.62
$T_{277}P_{26.59e}$	4.01	3.59
$T_{277}P_{26.59f}$	4.01	3.62
$T_{277}P_{26.59g}$	4.00	3.57

Appendix 5.9 Summary of co-ordination number for slabs 1 and 6 in runs $T_{277}P_{-0.01}$, $T_{277}P_{0.21}$, $T_{277}P_{4.04}$ and $T_{277}P_{26.59}$.

RUN	CO-ORDINATION NUMBER	
	SLAB 1	SLAB 6
$T_{300}P_{0.16a}$	3.54	3.27
$T_{300}P_{0.16b}$	3.53	3.25
$T_{300}P_{0.16c}$	3.55	3.25
$T_{300}P_{0.16d}$	3.56	3.38
$T_{300}P_{0.16e}$	3.53	3.40
$T_{300}P_{0.16f}$	3.62	3.33
$T_{300}P_{0.16g}$	3.71	3.42
$T_{300}P_{0.16h}$	3.70	3.42
$T_{300}P_{0.16i}$	3.71	3.35
$T_{300}P_{0.16j}$	3.76	3.43
$T_{300}P_{2.93a}$	3.61	3.46
$T_{300}P_{2.93b}$	3.63	3.39
$T_{300}P_{2.93c}$	3.60	3.58
$T_{300}P_{2.93d}$	3.63	3.55
$T_{300}P_{2.93e}$	3.68	3.56
$T_{300}P_{2.93f}$	3.71	3.72
$T_{300}P_{2.93g}$	3.68	3.66
$T_{300}P_{2.93h}$	3.71	3.71
$T_{300}P_{2.93i}$	3.70	3.73
$T_{300}P_{2.93j}$	3.74	3.71

$T_{300}P_{12.26a}$	3.69	3.67
$T_{300}P_{12.26b}$	3.77	3.78
$T_{300}P_{12.26c}$	3.76	3.85
$T_{300}P_{12.26d}$	3.75	3.83
$T_{300}P_{12.26e}$	3.78	3.77
$T_{300}P_{12.26f}$	3.83	3.87
$T_{300}P_{12.26g}$	3.78	3.90
$T_{300}P_{12.26h}$	3.75	3.94
$T_{300}P_{12.26i}$	3.78	3.99
$T_{300}P_{12.26j}$	3.71	3.89
$T_{300}P_{26.95a}$	3.68	3.74
$T_{300}P_{26.95b}$	3.76	3.74
$T_{300}P_{26.95c}$	3.90	3.71
$T_{300}P_{26.95d}$	3.93	3.71
$T_{300}P_{26.95e}$	3.96	3.80
$T_{300}P_{26.95f}$	4.10	3.87
$T_{300}P_{26.95g}$	4.23	3.78
$T_{300}P_{26.95h}$	4.20	3.74
$T_{300}P_{26.95i}$	4.13	3.71
$T_{300}P_{26.95j}$	4.10	3.72

Appendix 5.10 Summary of co-ordination number for slabs 1 and 6 in runs $T_{300}P_{0.16}$, $T_{300}P_{2.93}$, $T_{300}P_{12.26}$ and $T_{300}P_{26.95}$.

SYSTEM	ATOM	1^{ST} PEAK POSITION/Å	2^{ND} PEAK POSITION/Å
tba1C	C1	3.59	6.16
tba2C	C1	3.64	5.87
tba3C	C1	3.56	5.68
tba1S	C1	3.53	5.71
tba2S	C1	3.62	5.58
tba3S	C1	3.59	5.34
tba1C	C2	4.12	6.69
tba2C	C2	3.86	7.38
tba3C	C2	3.54	4.68
tba1S	C2	4.60	7.51
tba2S	C2	4.62	7.06
tba3S	C2	3.70	4.60
tba1C	C3	3.80	4.86
tba2C	C3	3.62	6.53
tba3C	C3	3.54	6.32
tba1S	C3	3.67	4.60
tba2S	C3	3.64	6.29
tba3S	C3	3.72	4.57
tba1C	C4	3.48	4.33
tba2C	C4	3.67	4.44

tba3C	C4	3.62	4.47
tba1S	C4	3.51	4.73
tba2S	C4	3.54	4.23
tba3S	C4	3.51	4.89
tba1C	C	3.43	5.63
tba2C	C	3.11	3.62
tba3C	C	3.30	4.70
tba1S	S	3.67	5.76
tba2S	S	3.51	4.81
tba3S	S	3.62	5.61
tba1C	O	2.50	4.47
tba2C	O	2.53	4.12
tba3C	O	2.50	4.49
tba1S	O	2.58	4.78
tba2S	O	2.56	4.73
tba3S	O	2.56	4.70

Appendix 6.1 g_{XO} summary for the inhibited systems. Resolution of the values is 0.027 Å.

SYSTEM	ATOM	1^{ST} PEAK POSITION/Å	2^{ND} PEAK POSITION/Å
tba1C	C1	3.43	5.39
tba2C	C1	3.43	3.96
tba3C	C1	3.67	4.68
tba1S	C1	4.01	5.58
tba2S	C1	4.44	6.06
tba3S	C1	4.39	5.82
tba1C	C2	5.52	–
tba2C	C2	4.07	–
tba3C	C2	4.62	–
tba1S	C2	4.17	–
tba2S	C2	4.57	–
tba3S	C2	4.57	–
tba1C	C3	–	–
tba2C	C3	3.51	–
tba3C	C3	3.62	5.37
tba1S	C3	–	–
tba2S	C3	4.41	6.64
tba3S	C3	4.73	–
tba1C	C4	2.95	3.54
tba2C	C4	3.01	3.62

tba3C	C4	3.17	3.59
tba1S	C4	3.83	5.45
tba2S	C4	3.56	5.00
tba3S	C4	3.96	5.26
tba1C	C	2.48	3.99
tba2C	C	2.58	3.96
tba3C	C	2.40	3.91
tba1S	S	2.72	4.20
tba2S	S	2.58	4.09
tba3S	S	2.72	4.28
tba1C	O	1.50	2.98
tba2C	O	1.50	2.95
tba3C	O	1.52	2.95
tba1S	O	1.58	3.03
tba2S	O	1.58	3.06
tba3S	O	1.58	3.03

Appendix 6.2 g_{XH} summary for the inhibited systems. Resolution of the values is 0.027 Å.

SYSTEM	ATOM	MODAL CO-ORDINATION NUMBER	% OF SOLVATED WATERS WITH CO-ORDINATION NUMBER			TOTAL % OF WATERS WITH CO-ORDINATION NUMBERS 2, 3 AND 4
			2	3	4	
tba1C	C1	3	14	48	29	91
tba2C	C1	4	18	35	40	93
tba3C	C1	3	15	39	34	88
tba1S	C1	4	13	34	36	83
tba2S	C1	4	6	38	42	86
tba3S	C1	3	11	45	35	91
tba1C	C2	3	12	47	33	92
tba2C	C2	4	11	37	43	91
tba3C	C2	3	16	39	36	91
tba1S	C2	3	15	36	34	85
tba2S	C2	4	8	39	41	88
tba3S	C2	3	10	43	37	90
tba1C	C3	3	10	47	35	92
tba2C	C3	4	12	38	42	92
tba3C	C3	4	13	39	39	91
tba1S	C3	3	14	37	36	87

tba2S	C3	4	8	38	41	87
tba3S	C3	3	10	43	38	91
tba1C	C4	3	16	50	26	92
tba2C	C4	4	22	35	38	95
tba3C	C4	3	17	35	34	86
tba1S	C4	4	12	35	36	83
tba2S	C4	3	6	40	40	86
tba3S	C4	3	13	47	29	89
tba1C	C	3	20	50	22	92
tba2C	C	3	23	40	34	97
tba3C	C	3	26	40	20	86
tba1S	S	3	18	35	25	78
tba2S	S	3	9	47	32	88
tba3S	S	3	20	50	23	93
tba1C	O	3	21	48	22	91
tba2C	O	3	23	41	34	98
tba3C	O	3	26	44	18	88
tba1S	O	3	20	36	23	79
tba2S	O	3	10	50	29	89
tba3S	O	3	19	48	20	87

Appendix 6.3 Co-ordination number summary for solvated water in the inhibited systems.

SYSTEM	ATOM	F_3 FOR CO-ORDINATION NUMBER:		
		2	3	4
tba1C	C1	0.09	0.08	0.11
tba2C	C1	0.06	0.07	0.07
tba3C	C1	0.06	0.07	0.09
tba1S	C1	0.06	0.08	0.10
tba2S	C1	0.08	0.07	0.09
tba3S	C1	0.10	0.06	0.08
tba1C	C2	0.09	0.07	0.09
tba2C	C2	0.08	0.06	0.08
tba3C	C2	0.07	0.08	0.08
tba1S	C2	0.06	0.07	0.10
tba2S	C2	0.08	0.08	0.09
tba3S	C2	0.06	0.08	0.11
tba1C	C3	0.07	0.07	0.08
tba2C	C3	0.08	0.06	0.09
tba3C	C3	0.07	0.07	0.09
tba1S	C3	0.05	0.06	0.10
tba2S	C3	0.08	0.08	0.09
tba3S	C3	0.09	0.06	0.08
tba1C	C4	0.10	0.09	0.12
tba2C	C4	0.06	0.07	0.08

tba3C	C4	0.06	0.08	0.08
tba1S	C4	0.08	0.08	0.10
tba2S	C4	0.08	0.07	0.08
tba3S	C4	0.11	0.07	0.09
tba1C	C	0.10	0.10	0.12
tba2C	C	0.07	0.07	0.10
tba3C	C	0.06	0.07	0.10
tba1S	S	0.08	0.11	0.12
tba2S	S	0.09	0.06	0.09
tba3S	S	0.12	0.09	0.12
tba1C	O	0.11	0.10	0.13
tba2C	O	0.07	0.07	0.10
tba3C	O	0.07	0.07	0.11
tba1S	O	0.08	0.10	0.12
tba2S	O	0.09	0.06	0.10
tba3S	O	0.12	0.09	0.12

Appendix 6.4 F_3 summary for the inhibited systems.

SYSTEM	ATOM	$F_{4\varphi}$ FOR CO-ORDINATION NUMBER:		
		2	3	4
tba1C	C1	0.07	0.10	0.17
tba2C	C1	0.11	0.19	0.26
tba3C	C1	0.02	0.19	0.17
tba1S	C1	0.06	0.16	0.16
tba2S	C1	0.00	0.13	0.12
tba3S	C1	0.05	0.28	0.20
tba1C	C2	0.07	0.15	0.23
tba2C	C2	0.05	0.18	0.22
tba3C	C2	0.05	0.20	0.22
tba1S	C2	0.06	0.17	0.19
tba2S	C2	0.02	0.09	0.12
tba3S	C2	0.06	0.26	0.23
tba1C	C3	0.09	0.17	0.25
tba2C	C3	0.05	0.16	0.19
tba3C	C3	0.04	0.18	0.21
tba1S	C3	0.07	0.18	0.19
tba2S	C3	0.02	0.10	0.11
tba3S	C3	0.09	0.27	0.23
tba1C	C4	0.09	0.12	0.13

tba2C	C4	0.13	0.18	0.25
tba3C	C4	0.06	0.20	0.22
tba1S	C4	0.07	0.14	0.15
tba2S	C4	-0.01	0.16	0.16
tba3S	C4	0.03	0.25	0.21
tba1C	C	0.10	0.13	0.11
tba2C	C	0.17	0.19	0.16
tba3C	C	0.06	0.27	0.18
tba1S	S	0.08	0.11	0.14
tba2S	S	0.00	0.25	0.15
tba3S	S	0.04	0.21	0.11
tba1C	O	0.12	0.14	0.11
tba2C	O	0.17	0.19	0.15
tba3C	O	0.11	0.28	0.15
tba1S	O	0.08	0.11	0.14
tba2S	O	0.00	0.25	0.13
tba3S	O	0.04	0.21	0.10

Appendix 6.5 $F_{4\varphi}$ summary for the inhibited systems.

SYSTEM	ATOM	F_{4t} FOR CO-ORDINATION NUMBER:		
		2	3	4
tba1C	C1	0.30	0.26	0.25
tba2C	C1	0.31	0.32	0.35
tba3C	C1	0.35	0.34	0.30
tba1S	C1	0.31	0.29	0.29
tba2S	C1	0.28	0.31	0.29
tba3S	C1	0.28	0.34	0.33
tba1C	C2	0.25	0.27	0.29
tba2C	C2	0.29	0.32	0.33
tba3C	C2	0.32	0.32	0.32
tba1S	C2	0.31	0.29	0.30
tba2S	C2	0.28	0.30	0.29
tba3S	C2	0.28	0.33	0.33
tba1C	C3	0.25	0.28	0.30
tba2C	C3	0.29	0.31	0.32
tba3C	C3	0.31	0.30	0.30
tba1S	C3	0.31	0.30	0.31
tba2S	C3	0.27	0.29	0.29
tba3S	C3	0.29	0.33	0.32
tba1C	C4	0.28	0.27	0.28
tba2C	C4	0.31	0.32	0.37

tba3C	C4	0.35	0.35	0.33
tba1S	C4	0.31	0.29	0.29
tba2S	C4	0.29	0.33	0.31
tba3S	C4	0.28	0.33	0.33
tba1C	C	0.29	0.28	0.28
tba2C	C	0.37	0.35	0.37
tba3C	C	0.36	0.39	0.35
tba1S	S	0.31	0.28	0.28
tba2S	S	0.30	0.33	0.30
tba3S	S	0.28	0.32	0.30
tba1C	O	0.30	0.29	0.28
tba2C	O	0.37	0.35	0.37
tba3C	O	0.38	0.40	0.35
tba1S	O	0.31	0.29	0.29
tba2S	O	0.30	0.33	0.29
tba3S	O	0.28	0.32	0.30

Appendix 6.6 F_{4t} summary for the inhibited systems.

SYSTEM	ATOM	D/Å^2 ps^{-1}	
		OXYGEN ATOM	HYDROGEN ATOM
tba1C	C1	0.19	0.15
tba2C	C1	0.13	0.12
tba3C	C1	0.11	0.09
tba1S	C1	0.21	0.19
tba2S	C1	0.25	0.17
tba3S	C1	0.20	0.18
tba1C	C2	0.17	0.18
tba2C	C2	0.14	0.11
tba3C	C2	0.09	0.11
tba1S	C2	0.20	0.21
tba2S	C2	0.19	0.21
tba3S	C2	0.16	0.17
tba1C	C3	0.11	0.13
tba2C	C3	0.16	0.22
tba3C	C3	0.12	0.14
tba1S	C3	0.22	0.29
tba2S	C3	0.20	0.22
tba3S	C3	0.16	0.19
tba1C	C4	0.13	0.13

tba2C	C4	0.10	0.10
tba3C	C4	0.10	0.11
tba1S	C4	0.21	0.19
tba2S	C4	0.16	0.16
tba3S	C4	0.20	0.15
tba1C	C	0.13	0.11
tba2C	C	0.09	0.07
tba3C	C	0.08	0.09
tba1S	S	0.25	0.19
tba2S	S	0.11	0.10
tba3S	S	0.21	0.17
tba1C	O	0.11	0.11
tba2C	O	0.09	0.08
tba3C	O	0.08	0.08
tba1S	O	0.20	0.16
tba2S	O	0.11	0.09
tba3S	O	0.21	0.17

Appendix 6.7 Self-diffusion coefficient summary for the oxygen and hydrogen atom of solvated water around various solute atoms for the inhibited systems.

SYSTEM	ATOM	ROTATIONAL LIFETIME/ps		$P2_{\perp}/P2_{\parallel}$ as a ratio.
		From $P_{2\parallel}$	From $P_{2\perp}$	
tba1C	C1	0.51	0.60	+18
tba2C	C1	0.59	0.64	+8
tba3C	C1	0.73	0.78	+7
tba1S	C1	0.55	0.64	+16
tba2S	C1	0.59	0.58	-2
tba3S	C1	0.61	0.63	+3
tba1C	C2	0.55	0.63	+15
tba2C	C2	0.56	0.57	+2
tba3C	C2	0.71	0.75	+6
tba1S	C2	0.52	0.59	+13
tba2S	C2	0.54	0.53	+5
tba3S	C2	0.60	0.63	+5
tba1C	C3	0.65	0.68	+5
tba2C	C3	0.50	0.48	-4
tba3C	C3	0.60	0.65	+8
tba1S	C3	0.44	0.49	+11

tba2S	C3	0.53	0.50	-6
tba3S	C3	0.57	0.58	+2
tba1C	C4	0.58	0.64	+10
tba2C	C4	0.63	0.70	+11
tba3C	C4	0.65	0.71	+9
tba1S	C4	0.54	0.60	+11
tba2S	C4	0.58	0.57	-2
tba3S	C4	0.64	0.67	+5
tba1C	C	0.62	0.67	+8
tba2C	C	0.69	0.77	+12
tba3C	C	0.71	0.76	+7
tba1S	S	0.57	0.64	+12
tba2S	S	0.57	0.59	+4
tba3S	S	0.59	0.66	+12
tba1C	O	0.61	0.67	+10
tba2C	O	0.66	0.73	+11
tba3C	O	0.69	0.75	+9
tba1S	O	0.56	0.65	+16
tba2S	O	0.56	0.58	+4
tba3S	O	0.60	0.67	+12

Appendix 6.8 Rotational lifetime summary for solvated water in the inhibited systems.

SYSTEM	ATOM	1^{ST} PEAK POSITION/Å	2^{ND} PEAK POSITION/Å
tba1C	C1	3.46	5.39
tba2C	C1	3.51	5.66
tba3C	C1	3.54	5.45
tba1S	C1	3.25	5.50
tba2S	C1	3.51	5.47
tba3S	C1	3.67	5.13
tba1C	C2	3.64	4.47
tba2C	C2	3.64	4.60
tba3C	C2	4.68	6.45
tba1S	C2	3.59	4.57
tba2S	C2	3.62	6.61
tba3S	C2	3.62	4.54
tba1C	C3	3.48	4.52
tba2C	C3	3.48	4.65
tba3C	C3	3.59	6.72
tba1S	C3	3.56	4.49
tba2S	C3	3.83	4.70
tba3S	C3	3.46	5.79
tba1C	C4	3.48	4.62
tba2C	C4	3.70	4.65

tba3C	C4	3.48	4.73
tba1S	C4	3.38	4.78
tba2S	C4	3.43	4.84
tba3S	C4	3.40	4.89
tba1C	C	3.38	5.50
tba2C	C	3.35	4.84
tba3C	C	3.30	5.02
tba1S	S	3.41	3.86
tba2S	S	3.51	4.92
tba3S	S	3.54	5.68
tba1C	O	2.50	4.44
tba2C	O	2.48	4.47
tba3C	O	2.48	4.44
tba1S	O	2.58	4.73
tba2S	O	2.53	4.62
tba3S	O	2.56	4.62

Appendix 6.9 g_{XO} summary for the inhibited systems. Resolution of the values is 0.027 Å.

SYSTEM	ATOM	1^{ST} PEAK POSITION/Å	2^{ND} PEAK POSITION/Å
tba1C	C1	3.64	4.81
tba2C	C1	4.54	–
tba3C	C1	4.31	5.55
tba1S	C1	3.11	5.29
tba2S	C1	3.83	5.55
tba3S	C1	5.87	–
tba1C	C2	4.25	6.59
tba2C	C2	4.52	–
tba3C	C2	4.52	–
tba1S	C2	3.96	–
tba2S	C2	4.28	6.74
tba3S	C2	4.44	–
tba1C	C3	4.36	–
tba2C	C3	3.75	–
tba3C	C3	3.27	6.90
tba1S	C3	3.41	3.15
tba2S	C3	4.68	–
tba3S	C3	3.44	6.80
tba1C	C4	2.85	3.62
tba2C	C4	3.22	3.70

tba3C	C4	3.54	5.10
tba1S	C4	3.83	5.47
tba2S	C4	3.83	5.45
tba3S	C4	3.99	5.31
tba1C	C	2.45	3.88
tba2C	C	2.45	3.96
tba3C	C	2.42	3.94
tba1S	S	2.69	2.15
tba2S	S	2.58	4.17
tba3S	S	2.66	2.15
tba1C	O	1.52	2.95
tba2C	O	1.50	2.95
tba3C	O	1.52	2.93
tba1S	O	1.58	3.03
tba2S	O	1.58	3.03
tba3S	O	1.55	3.01

Appendix 6.10 g_{XH} summary for the inhibited systems. Resolution of the values is 0.027 Å.

SYSTEM	ATOM	MODAL CO-ORDINATION NUMBER	% OF WATERS WITH CO-ORDINATION NUMBER			TOTAL % OF WATERS WITH CO-ORDINATION NUMBERS 3, 4 AND 5
			3	4	5	
tba1C	C1	4	28	34	22	84
tba2C	C1	4	25	44	19	88
tba3C	C1	4	21	37	23	81
tba1S	C1	3	37	28	10	75
tba2S	C1	4	22	38	24	84
tba3S	C1	4	30	40	17	87
tba1C	C2	4	26	38	21	85
tba2C	C2	4	30	38	17	85
tba3C	C2	4	21	39	22	82
tba1S	C2	4	32	34	13	79
tba2S	C2	4	25	42	20	87
tba3S	C2	4	28	39	18	85
tba1C	C3	4	26	42	22	90
tba2C	C3	4	34	38	15	87
tba3C	C3	4	19	41	24	84
tba1S	C3	4	31	36	13	80

tba2S	C3	4	29	41	17	87
tba3S	C3	4	27	42	18	87
tba1C	C4	4	26	31	22	79
tba2C	C4	4	25	46	18	89
tba3C	C4	4	22	33	21	76
tba1S	C4	3	40	26	9	75
tba2S	C4	4	20	35	26	81
tba3S	C4	4	33	36	15	84
tba1C	C	4	21	30	25	76
tba2C	C	4	35	35	12	82
tba3C	C	4	22	30	20	72
tba1S	S	3	40	24	9	73
tba2S	S	4	20	33	27	80
tba3S	S	3	36	29	13	78
tba1C	O	4	19	29	26	74
tba2C	O	3	36	32	11	79
tba3C	O	4	22	28	19	69
tba1S	O	3	40	24	9	73
tba2S	O	4	21	33	26	80
tba3S	O	3	37	28	13	78

Appendix 6.11 Co-ordination number summary for solvated water in the inhibited systems.

SYSTEM	ATOM	F_3 FOR CO-ORDINATION NUMBER		
		3	4	5
tba1C	C1	0.08	0.10	0.11
tba2C	C1	0.11	0.09	0.11
tba3C	C1	0.08	0.11	0.12
tba1S	C1	0.08	0.10	0.11
tba2S	C1	0.09	0.11	0.12
tba3S	C1	0.08	0.10	0.12
tba1C	C2	0.08	0.10	0.11
tba2C	C2	0.10	0.11	0.12
tba3C	C2	0.08	0.10	0.12
tba1S	C2	0.09	0.09	0.12
tba2S	C2	0.08	0.11	0.12
tba3S	C2	0.08	0.10	0.12
tba1C	C3	0.08	0.09	0.11
tba2C	C3	0.09	0.10	0.12
tba3C	C3	0.08	0.10	0.11
tba1S	C3	0.09	0.09	0.11
tba2S	C3	0.07	0.11	0.13
tba3S	C3	0.09	0.10	0.12
tba1C	C4	0.08	0.11	0.12
tba2C	C4	0.12	0.08	0.11

tba3C	C4	0.09	0.11	0.12
tba1S	C4	0.09	0.11	0.12
tba2S	C4	0.11	0.11	0.12
tba3S	C4	0.07	0.09	0.12
tba1C	C	0.10	0.12	0.12
tba2C	C	0.15	0.13	0.13
tba3C	C	0.11	0.11	0.12
tba1S	S	0.09	0.12	0.12
tba2S	S	0.13	0.13	0.13
tba3S	S	0.08	0.11	0.12
tba1C	O	0.11	0.12	0.12
tba2C	O	0.15	0.14	0.14
tba3C	O	0.12	0.11	0.12
tba1S	O	0.10	0.12	0.12
tba2S	O	0.13	0.13	0.13
tba3S	O	0.08	0.11	0.12

Appendix 6.12 F_3 summary for the inhibited systems.

SYSTEM	ATOM	$F_{4\varphi}$ FOR CO-ORDINATION NUMBER		
		3	4	5
tba1C	C1	0.08	0.10	0.07
tba2C	C1	0.08	0.17	0.11
tba3C	C1	0.05	0.05	0.03
tba1S	C1	0.07	0.09	0.09
tba2S	C1	0.02	0.07	0.06
tba3S	C1	0.12	0.08	0.04
tba1C	C2	0.09	0.14	0.09
tba2C	C2	0.07	0.09	0.07
tba3C	C2	0.05	0.05	0.04
tba1S	C2	0.07	0.11	0.10
tba2S	C2	0.05	0.06	0.05
tba3S	C2	0.11	0.11	0.07
tba1C	C3	0.11	0.18	0.10
tba2C	C3	0.08	0.10	0.07
tba3C	C3	0.05	0.07	0.06
tba1S	C3	0.08	0.12	0.09
tba2S	C3	0.07	0.07	0.06
tba3S	C3	0.09	0.10	0.07
tba1C	C4	0.10	0.07	0.05
tba2C	C4	0.10	0.24	0.14

tba3C	C4	0.04	0.02	0.02
tba1S	C4	0.07	0.08	0.06
tba2S	C4	-0.03	0.05	0.03
tba3S	C4	0.17	0.16	0.11
tba1C	C	0.08	0.06	0.05
tba2C	C	0.13	0.20	0.16
tba3C	C	0.00	0.01	0.02
tba1S	S	0.08	0.10	0.04
tba2S	S	-0.05	0.00	0.01
tba3S	S	0.16	0.11	0.07
tba1C	O	0.08	0.06	0.06
tba2C	O	0.13	0.16	0.16
tba3C	O	0.00	0.02	0.04
tba1S	O	0.08	0.10	0.05
tba2S	O	-0.06	-0.01	0.00
tba3S	O	0.16	0.12	0.08

Appendix 6.13 $F_{4\varphi}$ summary for the inhibited systems.

SYSTEM	ATOM	F_{4t} FOR CO-ORDINATION NUMBER		
		3	4	5
tba1C	C1	0.28	0.26	0.25
tba2C	C1	0.26	0.29	0.26
tba3C	C1	0.29	0.26	0.25
tba1S	C1	0.26	0.27	0.24
tba2S	C1	0.25	0.25	0.24
tba3S	C1	0.30	0.29	0.27
tba1C	C2	0.28	0.28	0.26
tba2C	C2	0.26	0.26	0.25
tba3C	C2	0.28	0.26	0.25
tba1S	C2	0.26	0.28	0.25
tba2S	C2	0.24	0.24	0.23
tba3S	C2	0.29	0.30	0.28
tba1C	C3	0.29	0.30	0.26
tba2C	C3	0.26	0.27	0.25
tba3C	C3	0.26	0.26	0.25
tba1S	C3	0.26	0.28	0.25
tba2S	C3	0.25	0.23	0.22
tba3S	C3	0.29	0.29	0.27
tba1C	C4	0.27	0.26	0.26
tba2C	C4	0.27	0.32	0.28

tba3C	C4	0.29	0.27	0.26
tba1S	C4	0.26	0.28	0.27
tba2S	C4	0.24	0.25	0.25
tba3S	C4	0.31	0.31	0.28
tba1C	C	0.27	0.26	0.26
tba2C	C	0.26	0.29	0.28
tba3C	C	0.30	0.28	0.27
tba1S	S	0.26	0.29	0.28
tba2S	S	0.25	0.25	0.25
tba3S	S	0.31	0.30	0.30
tba1C	O	0.26	0.28	0.26
tba2C	O	0.26	0.28	0.28
tba3C	O	0.30	0.27	0.27
tba1S	O	0.26	0.29	0.27
tba2S	O	0.25	0.25	0.25
tba3S	O	0.31	0.30	0.30

Appendix 6.14 F_{4t} summary for the inhibited systems.

SYSTEM	ATOM	D/Å^2 ps^{-1}	
		OXYGEN ATOM	HYDROGEN ATOM
tba1C	C1	0.09	0.09
tba2C	C1	0.09	0.10
tba3C	C1	0.23	0.27
tba1S	C1	0.11	0.11
tba2S	C1	0.12	0.14
tba3S	C1	0.13	0.12
tba1C	C2	0.08	0.11
tba2C	C2	0.10	0.12
tba3C	C2	0.24	0.27
tba1S	C2	0.10	0.11
tba2S	C2	0.11	0.14
tba3S	C2	0.13	0.14
tba1C	C3	0.11	0.14
tba2C	C3	0.09	0.10
tba3C	C3	0.16	0.19
tba1S	C3	0.10	0.14
tba2S	C3	0.10	0.14
tba3S	C3	0.11	0.14
tba1C	C4	0.11	0.11

tba2C	C4	0.07	0.08
tba3C	C4	0.23	0.23
tba1S	C4	0.18	0.22
tba2S	C4	0.13	0.13
tba3S	C4	0.09	0.09
tba1C	C	0.11	0.08
tba2C	C	0.08	0.07
tba3C	C	0.23	0.17
tba1S	S	0.14	0.10
tba2S	S	0.10	0.07
tba3S	S	0.09	0.07
tba1C	O	0.10	0.07
tba2C	O	0.09	0.06
tba3C	O	0.23	0.18
tba1S	O	0.11	0.08
tba2S	O	0.09	0.07
tba3S	O	0.09	0.07

Appendix 6.15 Self-diffusion co-efficient summary for the oxygen and hydrogen atom of solvated water around various solute atoms for the inhibited systems.

SYSTEM	ATOM	ROTATIONAL LIFETIME/ps		$P2_{\perp}/P2_{\parallel}$ as a ratio.
		From $P_{2\parallel}$	From $P_{2\perp}$	
tba1C	C1	0.56	0.61	+9
tba2C	C1	0.60	0.69	+15
tba3C	C1	0.43	0.41	-5
tba1S	C1	0.64	0.61	-5
tba2S	C1	0.52	0.61	+19
tba3S	C1	0.63	0.60	-5
tba1C	C2	0.62	0.62	0
tba2C	C2	0.52	0.59	+13
tba3C	C2	0.40	0.38	-5
tba1S	C2	0.57	0.53	-7
tba2S	C2	0.55	0.59	+7
tba3S	C2	0.53	0.47	-11
tba1C	C3	0.61	0.63	+3
tba2C	C3	0.45	0.53	+18
tba3C	C3	0.40	0.39	-2
tba1S	C3	0.56	0.49	-12

tba2S	C3	0.49	0.53	+8
tba3S	C3	0.51	0.45	-12
tba1C	C4	0.49	0.57	+16
tba2C	C4	0.63	0.73	+16
tba3C	C4	0.36	0.41	+14
tba1S	C4	0.59	0.55	-7
tba2S	C4	0.52	0.61	+17
tba3S	C4	0.57	0.55	-4
tba1C	C	0.48	0.58	+21
tba2C	C	0.62	0.72	+16
tba3C	C	0.39	0.48	+23
tba1S	S	0.57	0.54	-5
tba2S	S	0.50	0.63	+26
tba3S	S	0.54	0.56	+4
tba1C	O	0.50	0.62	+24
tba2C	O	0.62	0.72	+16
tba3C	O	0.38	0.46	+21
tba1S	O	0.57	0.57	0
tba2S	O	0.49	0.64	+31
tba3S	O	0.51	0.53	+4

Appendix 6.16 Rotational lifetime summary for solvated water in the inhibited systems.